Complexity

Fractional-Order Chaotic Systems: Theory and Applications

Lead Guest Editor: Guillermo Huerta Cuellar
Guest Editors: Eric Campos, Rider Jaimes Reátegu, Ning Wang, and Cristiana Joao Silva

Fractional-Order Chaotic Systems: Theory and Applications

Complexity

Fractional-Order Chaotic Systems: Theory and Applications

Lead Guest Editor: Guillermo Huerta Cuellar
Guest Editors: Eric Campos, Rider Jaimes Reátegu, Ning Wang, and Cristiana Joao Silva

Contents

Hindawi
Complexity
Volume 2022, Article ID 3592422, 18 pages
https://doi.org/10.1155/2022/3592422

Research Article

A New Fractional-Order Map with Infinite Number of Equilibria and Its Encryption Application

Ahlem Gasri,[1] Amina-Aicha Khennaoui,[2] Adel Ouannas,[3] Giuseppe Grassi,[4] Apostolos Iatropoulos,[5] Lazaros Moysis,[6] and Christos Volos[6]

[1]*Department of Mathematics, University of Larbi Tebessi, Tebessa 12002, Algeria*
[2]*Laboratory of Dynamical Systems and Control, University of Larbi Ben M'hidi, Oum El Bouaghi, Algeria*
[3]*Department of Mathematics and Computer Science, University of Larbi Ben M'hidi, Oum El Bouaghi, Algeria*
[4]*Universita Del Salento, Dipartimento Ingegneria Innovazione, 73100 Lecce, Italy*
[5]*Department of Information and Electronic Engineering, International Hellenic University, Thessaloniki, Greece*
[6]*Laboratory of Nonlinear Systems Circuits and Complexity Physics Department, Aristotle University of Thessaloniki, Thessaloniki, Greece*

Correspondence should be addressed to Amina-Aicha Khennaoui; kamina_aicha@yahoo.fr

Received 5 April 2021; Revised 25 June 2021; Accepted 27 November 2021; Published 24 February 2022

Academic Editor: M. De Aguiar

The study of the chaotic dynamics in fractional-order discrete-time systems has received great attention over the last years. Some efforts have been also devoted to analyze fractional maps with special features. This paper makes a contribution to the topic by introducing a new fractional map that is characterized by both particular dynamic behaviors and specific properties related to the system equilibria. In particular, the conceived one dimensional map is algebraically simpler than all the proposed fractional maps in the literature. Using numerical simulation, we investigate the dynamic and complexity of the fractional map. The results indicate that the new one-dimensional fractional map displays various types of coexisting attractors. The approximate entropy is used to observe the changes in the sequence sequence complexity when the fractional order and system parameter. Finally, the fractional map is applied to the problem of encrypting electrophysiological signals. For the encryption process, random numbers were generated using the values of the fractional map. Some statistical tests are given to show the performance of the encryption.

1. Introduction

Fractional calculus is a topic which is developed more than 300 years. However, it is only the last decades that it has been extensively and intensively investigated, due to its wide application in signal mechanical controls and other fields [1]. Compared with integer order derivatives, fractional-order derivatives are more accurate as they provide excellent tool for the description of the memory effect in all kinds of materials and processing. Based on this consideration, the application of fractional-order systems have attracted more and more researchers attention [2]. At the same time, during the last decade, attention has been focused on discrete fractional calculus and fractional difference operators [3, 4]. Several papers regarding the presence of chaotic phenomena in fractional discrete-time systems (maps) have been published to date [5–9]. For example, in [10] the hyperchaotic dynamic of the fractional generalized Hénon map has been investigated, whereas in [11] the presence of chaos in the fractional discrete memristor system has been illustrated. In [6] the presence of chaos in the fractional sine map and in the fractional standard map has been analyzed in details. In [7], control laws for stabilizing the chaotic dynamics of the fractional Grassi-Miller map have been developed, whereas in [8] the fractional Hénon map and its chaotic attractors have been studied. In [12], the chaotic dynamics of three maps (i.e., the fractional flow map, the fractional Lozi map and the fractional Lorenz map) have been investigated, whereas in [13] the chaotic behavior of the fractional Tinkerbell map has been illustrated. To our knowledge, all of the

above reported systems have a finite number of equilibria. In general, systems with more equilibria may bring unexpected stabilities to some extent. Therefore, several efforts have been devoted to the study of fractional chaotic maps with some special features related to the system equilibria [14]. Among these studies, Zambrano-Serrano et al. [15] analyzed the dynamic properties and projective synchronization of the fractional difference map with no equilibrium, whereas in [16] Almatroud et al. found rich chaotic behaviours of a novel two-dimensional (2D) hyperchaotic fractional map with infinite line of equilibrium As a result, the analysis of chaotic dynamical behaviours of the fractional-order discrete-time systems without equilibrium points is an interesting topic.

In recent years, there has been a growing interest in discrete time systems with special complex dynamical behaviours, such as hidden attractors [17], coexisting multiple attractors [18] and hyperchaotic behaviours. For instance, in [19] the dynamic properties of a novel memristive hyperchaotic map and its application in secure communication have been illustrated. A 2D sine map was presented in [20] and several interesting behaviour like coexisting attractors and initial offset boosting were explored. General speaking, chaotic maps with coexisting attractors has drawn the attention of many researcher. Coexistence of attractors is a special phenomenon in nonlinear dynamical systems, which denotes that with fixed values of system parameters, a tiny disturbance in the initial condition can lead to the coexistence of different attractors. This property makes the chaotic maps very useful in the fields of secure communication and encryption. Since such phenomenon has not received enough attention with fractional discrete-time systems [21], this paper aims to make a contribution by introducing a new fractional map that is characterized by both particular dynamic behaviors and specific properties related to the system equilibria. Namely, the proposed map possesses infinite number of equilibria in a bounded domain, being this a new feature for fractional map, not published in literature to date. Dynamics and complexity of the conceived map are investigated in details. In particular, bifurcation diagrams, maximum Lyapunov exponents and 0-1 test are reported to highlight the coexistence of different periodic and chaotic attractors. Moreover, the map is applied to the problem of data encryption, which is a well established application of chaotic systems. As recent examples of fractional systems being applied to encryption, in the work [22] a technique to improve chaotic behavior in fractional maps is proposed, and applied to image encryption. An image encryption using the fractional logistic map is proposed in [23], and a different one in [24]. The 2D fractional Hénon map was also applied to image encryption in [25]. In [26] a graphical user interface is designed for random number generators based on integer and fractional order chaotic systems. In [27] another pseudo random number generator was designed based on the coupling of multiple fractional chaotic systems. The above works are just a small sample of the expanding use of continuous and discrete fractional systems to encryption. The use of fractional systems is drawing increasing attention by researchers, since they have more complex dynamics due to their memory effect, and a higher key space than their integer order analogues, since the fractional order and the finite memory order constitute additional key values.

In this work, the encryption of electrophysiological signals [28–33] is considered. To do so, first, a pseudo-random bit generator (PRBG) is designed using the values of the chaotic map. This chaotic PRBG is the basis for the encryption design, since it is used as the source of deterministic randomness [34–38]. Here, to take advantage of the fractional nature of the map that is used as the basis of the PRBG, a technique is proposed that takes into account its memory effect. So first, the map is implemented using finite memory, in order to reduce its computational cost. Then, in each iteration, all previous values of the map are taken into account in generating the bits, which leads in producing 459 bits per iteration. So the proposed technique reduces the computational load of the PRBG, since fewer iterations of the map are required to reach a desired bistream length, and is specifically designed for fractional order systems.

After the PRBG is designed, to encrypt a given electrophysiological signal, two rounds of masking are performed. First, the signal is modulated to mask its structure by combining it with the values of the fractional chaotic map. Then, the modulated signal is transformed into its binary representation, and combined with a bitstream generated from the PRBG, to yield the encrypted signal. This binary signal can then be safely transmitted through a communication channel. The original signal can be retrieved back at the receiver end, by following the reverse encryption procedure. The performance of the encryption is finally evaluated by a series of statistical tests performed on the original, modulated, and encrypted signals.

Finally, the encryption process is realised in a microcontroller board. This implementation helps verify the feasibility of simulating fractional maps in low cost hardware devices, a task that is of high interest, due to the potential implementability of chaotic systems in IoT related devices [39, 40]. Such realizations have already been explored in the literature, with positive results. For example, in [41] a fractional macro-economic model was established, and a microcontroller implementation was designed on an Arduino Due. In [42] the problem of impulsive synchronization for fractional order discrete chaotic maps is considered, and the design was again implemented in two Arduino Mega boards that simulated the master and observer systems. In [43] a hyperchaotic fractional order system was proposed and discretized. The system was then simulated in an Arduino Uno board and applied to the problem of text encryption. In [44], a fractional order modified Chua's circuit was designed and implemented in an Arduino Uno microcontroller. In [45] a generalized fractional logistic map was constructed and applied to random number generation and image encryption, implemented on a Virtex-5 field-programmable gate array FPGA. In the current work, the realization is done on an STM32F103 nucleo development board, and the encrypted signal from the microcontroller has the same statistical properties to the signal generated from Matlab, as indicated from all the statistical tests performed.

1.1. Fractional Calculus and Preliminaries. In this section, some preliminaries and basic concepts associated with discrete fractional calculus are presented here for completeness. In the following we consider that our domain is the time scale $\mathbb{N}_b = \{b, b+1, b+2, \ldots\}$ with $b \in \mathbb{R}$. Let X denote any function defined from $\mathbb{N}_b$, thus the μ-th fractional sum for $\mu > 0$ is defined by [46]:

$$\Delta_b^{-\mu} X(s) = \frac{1}{\Gamma(\mu)} \sum_{l=b}^{s-\mu} (s-l-1)^{(\mu-1)} X(l), \tag{1}$$

where $s \in \mathbb{N}_{b+\mu}$. Observe that the term s^{μ} indicates to the so-called a falling function which may be defined via Gamma function, Γ, as follows:

$$s^{(\mu)} = \frac{\Gamma(s+1)}{\Gamma(s+1-\mu)}. \tag{2}$$

Based on the above definition of the μ-th fractional sum, it is possible to define the μ-Caputo like difference operator. Let X denote any function defined from $\mathbb{N}_b$. The Caputo difference operator with order $\mu \notin \mathbb{N}$ is defined by:

Definition 1. For $n = \lceil \mu \rceil + 1$, *the* μ-th order Caputo-like operator can be defined as [47]:

$$\begin{aligned} {}^{C}\Delta b_{\mu} X(s) &= \Delta_b^{-(n-\mu)}, \\ \Delta^n X(s) &= \frac{1}{\Gamma(n-\mu)} \sum_{l=b}^{s-(n-\mu)} (s-l-1)^{(n-\mu-1)} \Delta_l^n X(l). \end{aligned} \tag{3}$$

For $s \in \mathbb{N}_{b+n-\mu}$.

Now a theorem is briefly summarized, in order to derive in the following the discrete formula of the new fractional map.

Theorem 1. *[48] For the fractional difference equation*

$$\begin{cases} {}^{C}\Delta\mu_b^{\mu} X(s) = f(s+\mu-1, X(s+\mu-1)), \\ \Delta^r X(b) = X_r, n = \lceil \mu \rceil + 1, r = 0, 1, \ldots, n-1. \end{cases} \tag{4}$$

Then, the discrete integral equation which is equivalent to equations in (4) is:

$$\begin{aligned} X_s = X_b + \frac{1}{\Gamma(\mu)} \sum_{l=b+n-\mu}^{s-\mu} (s-\sigma(l))^{(\mu-1)} \\ \cdot f(l+\mu-1, X(l+\mu-1)),\ t \in \mathbb{N}_{b+n}. \end{aligned} \tag{5}$$

Note that, for the purpose of numerical calculation, (5) can be written as [48]:

$$X_n = X_0 + \frac{1}{\Gamma(\mu)} \sum_{i=0}^{n-1} \frac{\Gamma(n-i+\mu)}{\Gamma(n-i+1)} f(i, X_i). \tag{6}$$

2. The New Fractional Map

Let us consider the following one dimensional map, which has been recently proposed in [49] as an example of an elegant map that can display chaotic behavior:

$$x_{n+1} = A \sin\left(\frac{C}{x_n}\right) + B, \tag{7}$$

where A, B and C are three positive parameters. In this work, we extend the original integer–order system to the fractional-order case. Specifically, we consider the effect of the fractional–order in the system dynamics by introducing the following new fractional difference equation:

$$\Delta_b^{\mu} x(s) = A \sin\left(\frac{C}{x(s+1-\mu)}\right) - x(s+1-\mu) + B, \tag{8}$$

where $s \in \mathbb{N}_{(b+1-\mu)}$ and μ is the fractional order with $0 < \mu \leq 1$. This fractional map is invariant under transformation $x \longrightarrow -x$ for all values of parameters A, B, C and order μ. Hence this map could display coexisting attractors for appropriate choice of initial conditions and fractional order values as well. In order to investigate this property, the numerical formula is designed as:

$$x_n = x_0 + \frac{1}{\Gamma(\mu)} \sum_{i=0}^{n-1} \frac{\Gamma(n-1-i+\mu)}{\Gamma(n-i)} \left(A \sin\left(\frac{C}{x_i}\right) - x_i + B \right). \tag{9}$$

According to the discrete (9), the proposed fractional map (8) has memory effect, which means that the iterated solution x_n is determined by all the previous states. In order to find the equilibrium points x_f of the fractional map (8), we solve the following equation

$$ApEn = \phi^m(r) - \phi^{m+1}(r), \tag{10}$$

Obviously, (10) is a trigonometrical equation that is very difficult to solve analytically, therefore, to analyze the equilibrium points we adopt the graphic analytic method. Taking the system parameters $A = 0.5$, $C = 3$, $B = 0$ as an example and the integer order value $\mu = 1$, Figure 1 shows the phase portrait obtained by simulating (9) in the $x_n - x_{n+1}$ plane along with the $y = x$ line. The black line in Figure 1, bisects the first and third quadrants at the interval $[-0.5, 0.5]$, and its crosses with the map are equilibrium points. As one can see, Figure 1 visually demonstrates that there are infinite equilibrium points in this case. On the other hand, Figure 2 shows different phase portraits obtained by simulating (9) for different values of order μ. In comparison to the integer-order case, the shape of the bounded attractors does not change much with the decrease of the value of μ, while the interval where equilibrium points exist is changed from $[-0.5, 0.5]$ into $[-0.6, 0.6]$.

3. Dynamics and Complexity of the New Fractional Map

In this Section the dynamic behaviors of the fractional-order map (8) are numerically investigated using bifurcation

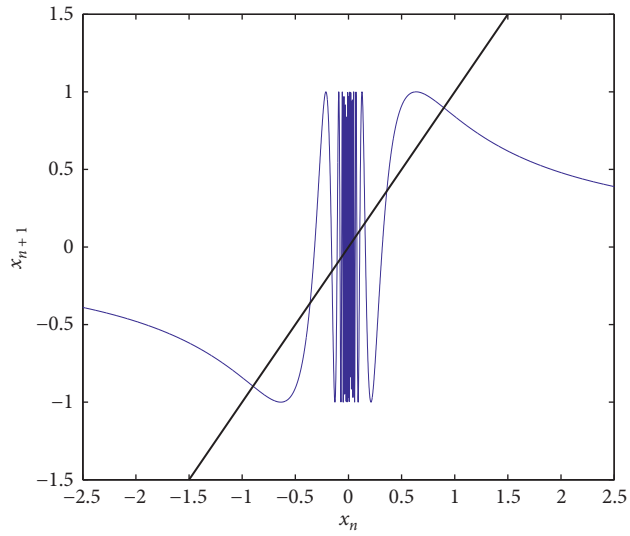

FIGURE 1: Phase diagram of fractional map (8) for $\mu = 1$, $A = 0.5$, $B = 0$, $C = 1$.

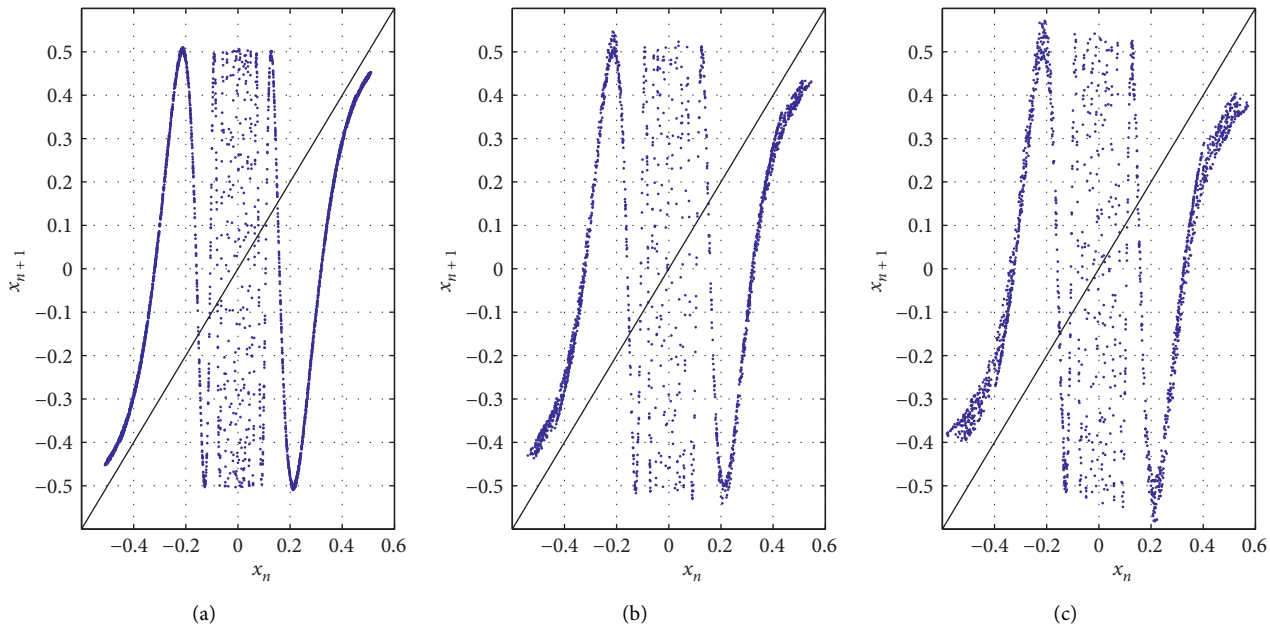

FIGURE 2: Different chaotic attractors of the fractional map (8) for system parameters $A = 0.5$, $B = 0$, $C = 3$ and different values of μ: (a)$\mu = 0.9$ and (b)$\mu = 0.8$. (c)$\mu = 0.8$.

diagrams and computation of maximum Lyapunov exponents, 0-1 test and entropy. Namely, the influence of both fractional order and initial conditions on the dynamics of the novel map are investigated in detail, with the aim to highlight the coexistence of different chaotic attractors. Namely, the influence of both fractional order and initial conditions on the dynamical behaviour of the novel map are investigated in detail, with the aim to highlight the coexistence of different chaotic attractors. To give a finer analysis of our fractional map we model its dynamics for two parameter sets, i.e for the above values $A = 0.5$, $B = 0, C = 3$ and for $A = 0.05, B = 0$, $C = 1$.

3.1. Bifurcation Diagrams and MLE. By changing the system parameters, the fractional map (8) can undertake different dynamic scenarios. Figure 3 gives the three-dimensional view of the bifurcation diagrams of the fractional map (8) for different values of μ (i.e., $\mu = 1$, $\mu = 0.6$, $\mu = 0.2$). We consider the parameter A as the bifurcation parameter and we take the other parameters as $B = 0$ and $C = 1$. We consider two values of symmetric initial conditions: $x_0 = 0.1$ and the negative one $x_0 = -0.1$. Clearly, these diagrams are different (see Figure 4). In particular, in Figure 4 the diagram in magenta color represents the dynamic behavior of the fractional map (8) for order $\mu = 1$ (i.e., for the integer-order

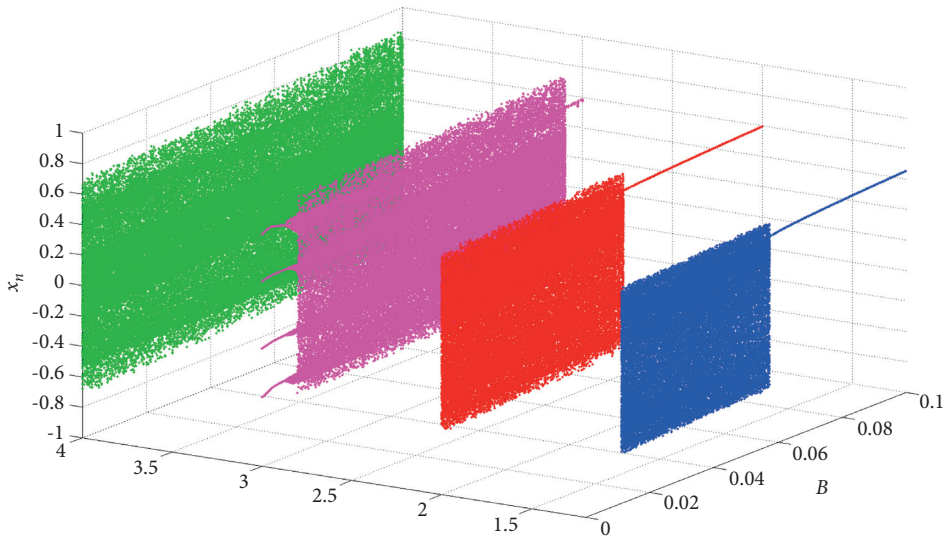

FIGURE 3: Different bifurcation diagrams of the fractional map (8) in three-dimensional space with the variation of system parameter B: blue diagram for $\mu = 1$; red diagram for $\mu = 0.8$; magneta diagram for $\mu = 0.6$; green diagram for $\mu = 0.4$.

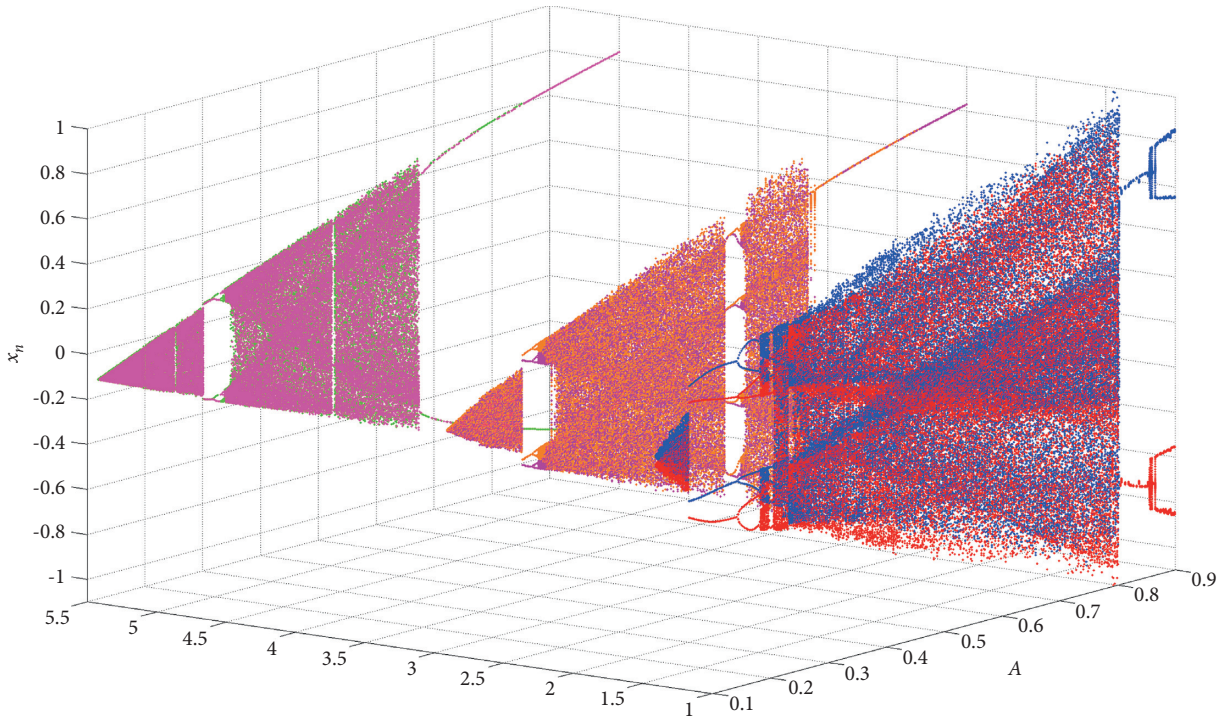

FIGURE 4: Different bifurcation diagrams of the fractional map (8) in three-dimensional space with the variation of system parameter A, and for two initial conditions: blue diagram for $\mu = 0.2$ and for initial condition $x_0 = 0.1$; red diagram $\mu = 0.2$ and for initial condition $x_0 = -0.1$; brown and green diagram for order $\mu = 0.6$; magenta diagram for order $\mu = 1$.

case). As it can be seen, the fractional map is chaotic over most of the range and is changed from chaotic to periodic with the increase of A. It is worth noting that the phenomenon of coexisting attractor is not observed in the integer-order case, where the states of our system come in the form of individual trajectories. By changing the order μ from 1 to 0.6, the bifurcation diagrams become the ones depicted in brown and green colors. In this case, coexisting periodic orbits appear within the interval $[0.1323, 0.1723] \cup [0.489, 0.517]$, along with a symmetry breaking bifurcation.

Meanwhile, the region of chaotic motion increases with the value of A. Finally, the bifurcation diagrams with $\mu = 0.2$ are considered and plotted in red and blue colors for different initial conditions. Specifically, the states colored in blue are those starting from the positive initial condition, whereas the states colored in red are those starting from the

negative initial condition. In this case, the fractional map (8) displays symmetric separate coexisting diagrams. Figure 5 shows some coexisting chaotic and periodic attractors for different values of the system parameter A. Specifically, when we select the parameter $A = 0.04$, the fractional map (8) highlights the coexistence of two symmetric chaotic attractors corresponding to the positive and negative initial conditions, respectively. Similarly, when we choose the parameter $A = 0.2$, the phase plot in Figure 5 shows the coexistence of two periodic symmetric attractors corresponding to the positive and negative initial conditions, respectively. The analysis conducted so far clearly highlights that the dynamics of the fractional map (8) become very complex when the value of the order μ is significantly decreased.

(b) In order to deeply investigate the properties of coexisting attractors in the fractional map (8), bifurcation diagrams and computations of maximum Lyapunov exponents (LE) with respect to the fractional order are carried out. Various dynamic behaviors can be observed by changing the value of μ at the interval $[0, 1]$. By considering the values $B = 0$, $A = 0.5$ and $C = 3$, Figure 5(a) displays the bifurcation diagram of the state variable x_n corresponding to the positive initial condition (blue diagram) and the negative initial condition (red diagram). For $C = 3$, the trajectories of the fractional map change from chaos to coexisting chaotic attractors with some periodic orbits through period doubling route to chaos. When $\mu \leq 0.31$ the chaotic behavior disappears and separate coexisting periodic orbits appear. This indicates that the dynamics of system (8) for $C = 3$ become simpler as the value of μ decreases. This result is also confirmed by the maximum Lyapunov exponents reported in Figure 5(b). Now the bifurcation diagram and the MLE of the fractional map (8) are illustrated in Figure 7 for $A = 0.05$, $B = 0$ and $C = 1$. Similarly, the dynamic behavior of the map (8) depends on the initial condition and the value of μ. The computation of the MLE shows that the states of the fractional map (8) go from chaotic to periodic with the decrease of order μ. From both the Figures 6 and 7 it can be deduced that the property of having coexisting attractors is observed when the fractional order assumes small values. In order to further investigate this property, we choose to plot the phase portraits of the fractional map (8) for multiple initial conditions and for the same parameters used in Figure 6. The obtained results are plotted in Figure 8. When $\mu = 0.9$, a chaotic attractor is observed. When $\mu = 0.6$, there are two symmetric separate chaotic attractors and a chaotic attractor in magenta color. On the other hand, four coexisting attractors are obtained when $\mu = 0.3$, as depicted in Figure 8(c). Suppose now that $A = 0.05$, $B = 0$, $C = 1$ and $\mu = 0.3$, then the corresponding phase diagram for the map (8) is shown in Figure 9 using different initial conditions. In particular, Figure 9 reveals the presence of four coexisting chaotic attractors, i.e., the blue attractor for $x_0 = 0.1$, the red attractor for $x_0 = -0.1$, the green attractor for $x_0 = 2$ and the magenta attractor for $x_0 = -2$. Figure 9 confirms the rich dynamics of the conceived fractional map, indicating that a number of different coexisting chaotic attractors could be found by taking other suitable values of the fractional order as well as other proper initial conditions.

3.2. 0-1 Test. Another tool that can be used to study the influence of the fractional order on the dynamic of a fractional map is "0-1 test." This test, proposed in [50] for fractional-order systems, is able to check the presence of chaos in a series of data that originates from a deterministic system. For the fractional-order model, consider a set of data $x(n)$ where $n = 1, \ldots N$. Using the approach in [50], we transform the trajectories of the fractional-order map into $p - q$ plots. Generally, unbounded $p - q$ trajectories imply chaotic behavior, whereas bounded trajectories implies regular behavior. Herein, we apply the $0 - 1$ test method directly to the solution x_n that is obtained from the discrete formula (9). Herein, we simulate the translation components of the system (8) in the $p - q$ plane. By taking $A = 0.5$, $B = 0$, $C = 3$ and by varying the value of μ, the results of the application of the 0-1 test to the fractional map (8) are reported in Figure 10. In particular, Figure 10(a) depicts the Brownian–like trajectories for all initial conditions, indicating that the suggested map is chaotic for $\mu = 0.9$. On the other hand, Figure 10(b) depicts the Brownian–like trajectories for two different initial conditions, confirming the coexistence of chaotic attractors for $\mu = 0.6$. Finally, when $\mu = 0.3$ the coexistence of chaotic attractors and periodic orbits is confirmed by the plot in Figure 10(c), which depicts bounded–like trajectories for the initial state $x_0 = 0.1$ and Brownian–like trajectories for the initial state $x_0 = 2$. It is concluded that the 0-1 test proves to be a valuable tool for checking the coexistence of different chaotic attractors as well as the coexistence of periodic one in the proposed fractional map (8).

3.3. Approximate Entropy. The approximate entropy (ApEn) [51] is the measurement of the degree of complexity of a series of data from multi-dimensional perspective. This method estimates the regularity by assigning a non-negative number, where higher values indicate higher complexity. By applying the technique in [52], we consider a set of points $x(1), \ldots, x(N)$ that are obtained from the discrete formula (9). The value of the approximate entropy depends on two important parameters, i.e., m and r, where the input r is the similar tolerance whereas m is the embedding dimension. Here, to calculate ApEn values we set $m = 2$ and $r = 0.2\text{std}(x)$ where $\text{std}(x)$ presents the standard deviation of the data x. Those values are preferred values according to similar previous studies. We reconstruct a subsequence of x such that $X(i) = [x(i), \ldots, x(i + m - 1)]$, where m presents the points from $x(i)$ to $x(i + m - 1)$. Let K be the number of $x(i)$ such that the maximum absolute difference of two vectors $x(i)$ and $X(j)$ is lower or equal to the tolerance r. The relative frequency of $x(i)$ being similar to $X(j)$ is given by

$$\phi^m(r) = \frac{1}{n - m - 1} \sum_{i=1}^{n-m+1} \log C_i^m(r). \tag{11}$$

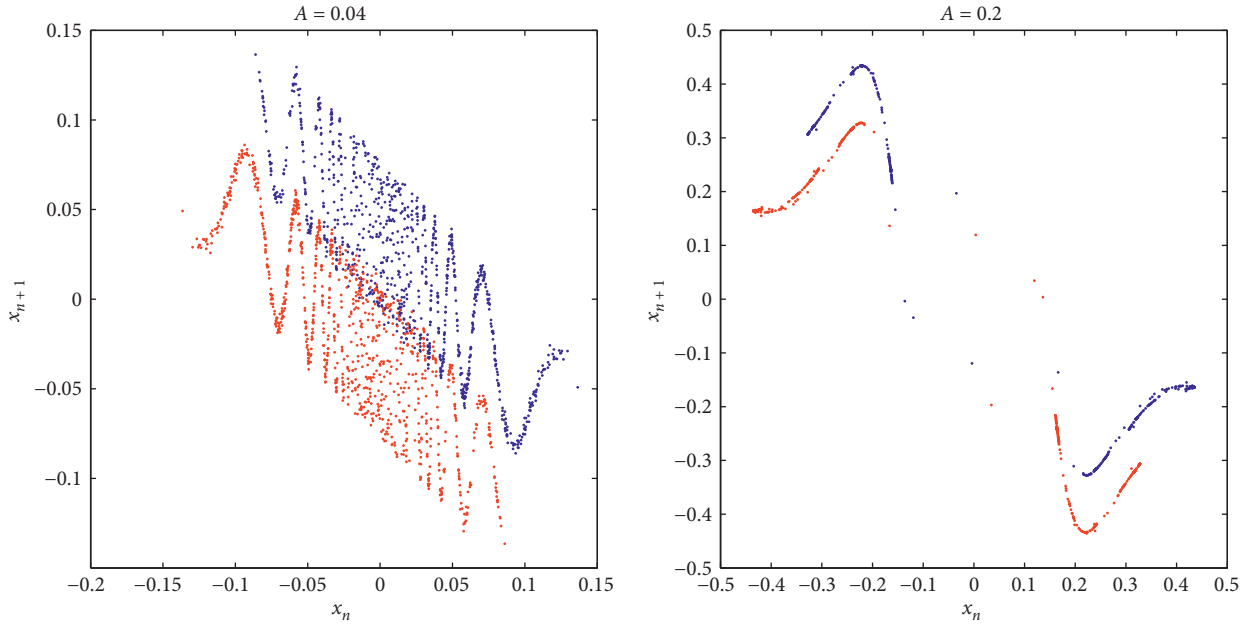

FIGURE 5: Two coexisting chaotic attractors for $A = 0.04$ and $\mu = 0.2$ (a); two coexisting periodic attractors for $A = 0.2$ and $\mu = 0.2$ (b).

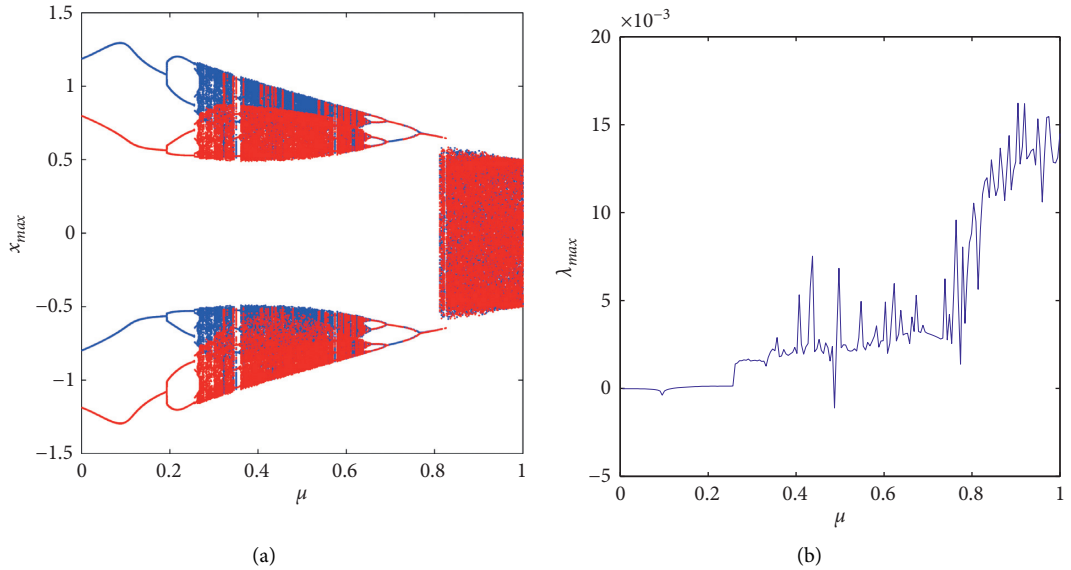

FIGURE 6: Bifurcation and maximum LE of system (8) versus μ depicted in (a) and (b), respectively, for parameters $A = 0.5$, $B = 0$, $C = 3$, and two symmetric initial conditions ($x_0 = 0.1$ for the blue diagram and $x_0 = -0.1$ for the red diagram).

The ApEn is calculated as following

$$b_{8n:\,8n+7} = \mathrm{de2bi}\left(\mathrm{mod}\left(\left\lfloor 10^{15}\left|x_n\right|\right\rfloor, 256\right)\right), \tag{12}$$

where $\phi^m(r)$ is denoted to be

$$x_n = x_0 + \frac{1}{\Gamma(\mu)} \sum_{i=1}^{m} \frac{\Gamma(m-i+\mu)}{\Gamma(m-i+1)} \cdot \left(A \sin\left(\frac{C}{x_{n-m+i-1}}\right) - x_{n-m+i-1} + B\right), \tag{13}$$

We apply the ApEn method to simulated complexity of the fractional map (8) by varying the fractional order and control parameter from 0 to 10. For each value of order μ, we analyze a series of points of length 3500 with different values of C. Figure 11 presents the 3D plots of the approximate entropy for fractional map (8). It is observed that, the fractional map (8) can have a higher complexity with relatively larger parameters values C and fractional order μ; which consist with the previous results. The analysis results in Figure 11 indicate that the change of system parameter C has little effect on the complexity. Thus, in real applications,

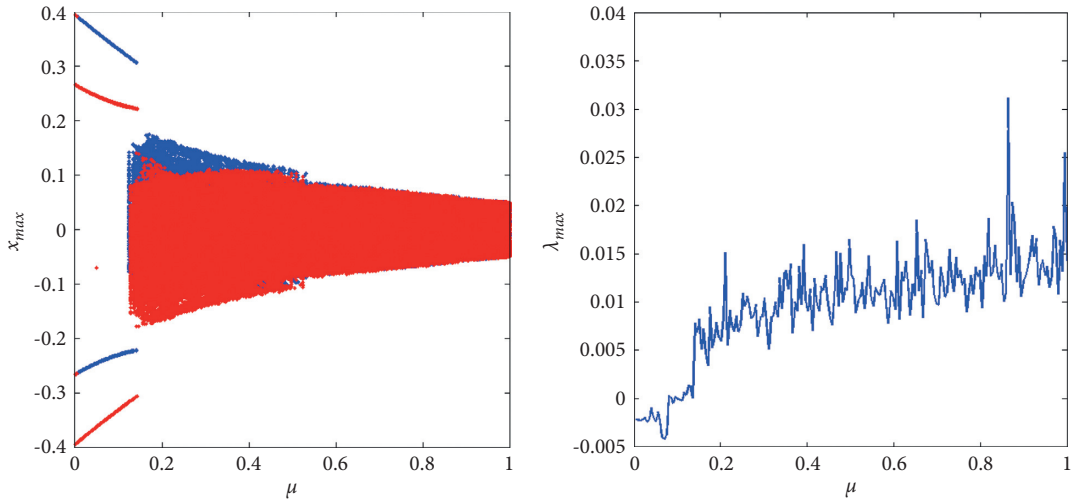

FIGURE 7: Bifurcation and maximum LE of system (8) versus μ depicted in (a) and (b), respectively, for parameters $A = 0.05$, $B = 0$, $C = 1$, and two symmetric initial conditions ($x_0 = 0.1$ for the blue diagram and $x_0 = -0.1$ for the red diagram).

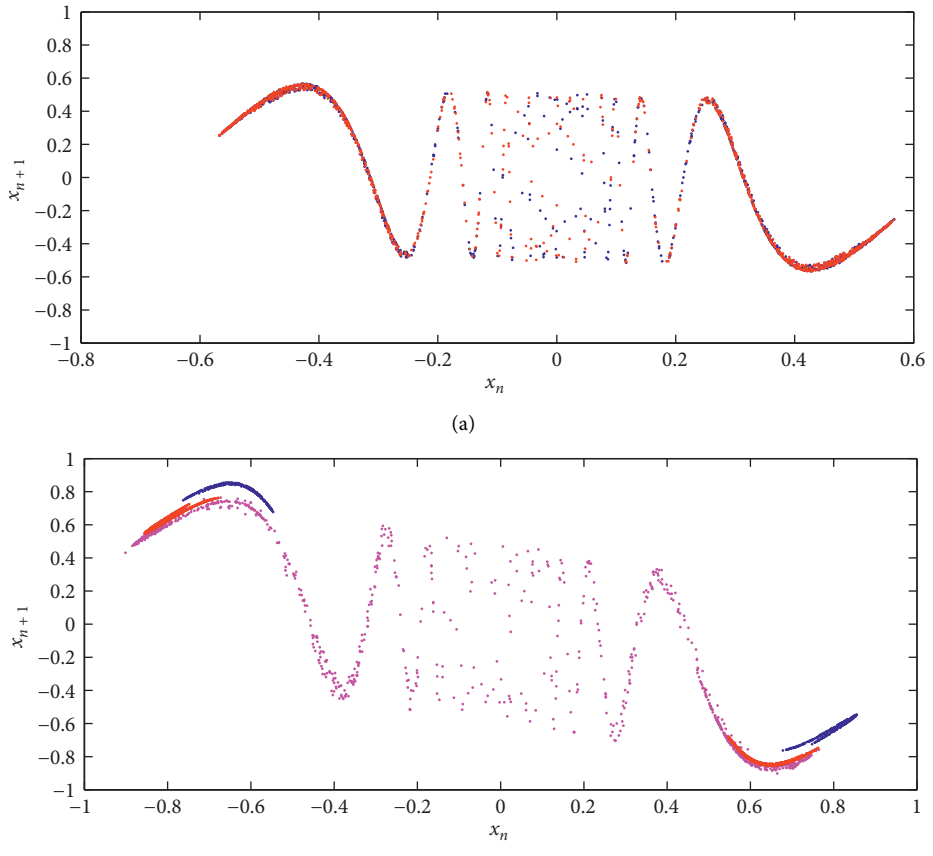

FIGURE 8: Continued.

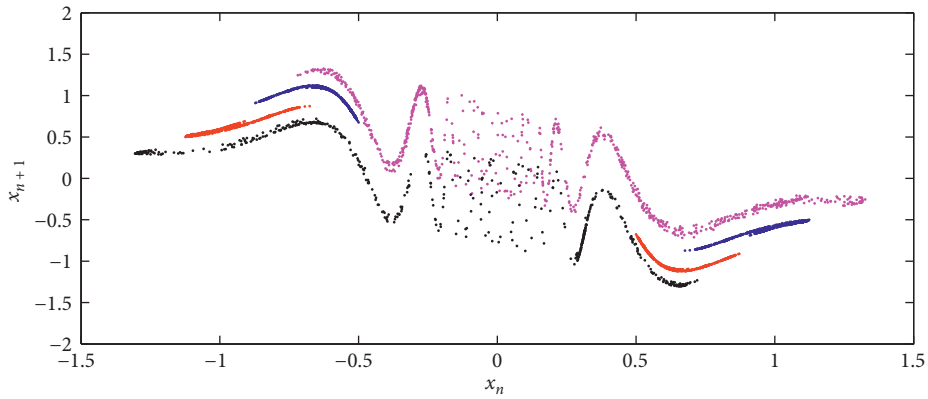

(c)

FIGURE 8: The coexisting attractors of the fractional-order map (8) with parameters $A = 0.5$, $B = 0$, $C = 3$ and with the initial condition $x_0 = -0.1$ for the red attractor and $x_0 = 0.1$ for the blue attractor; (a) chaotic attractor for $\mu = 0.9$, (b) three coexisting chaotic attractors for $\mu = 0.6$ with initial condition $x_0 = 10$ for the magenta attractor; (c) four coexisting chaotic attractors for $\mu = 0.3$ with initial condition $x_0 = 10$ for the magenta attractor and $x_0 = -10$ for the black attractor.

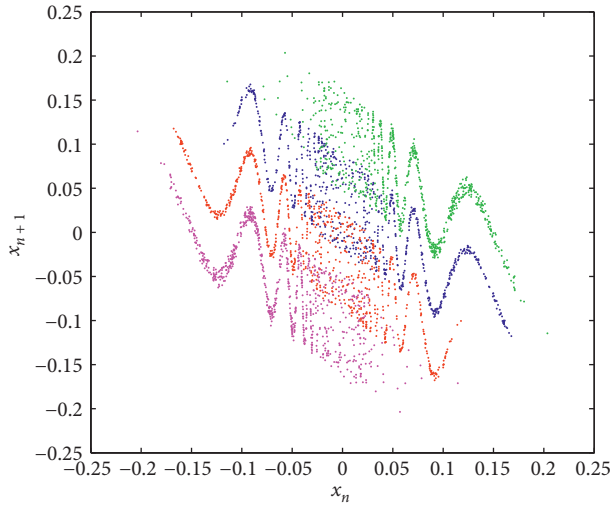

FIGURE 9: Four coexisting chaotic attractors for different initial conditions and system parameters $A = 0.05$, $B = 0$, $C = 1$ and $\mu = 0.3$: blue attractor for $x_0 = 0.1$, red attractor for $x_0 = -0.1$, green attractor for $x_0 = 2$ and magenta attractor for $x_0 = -2$.

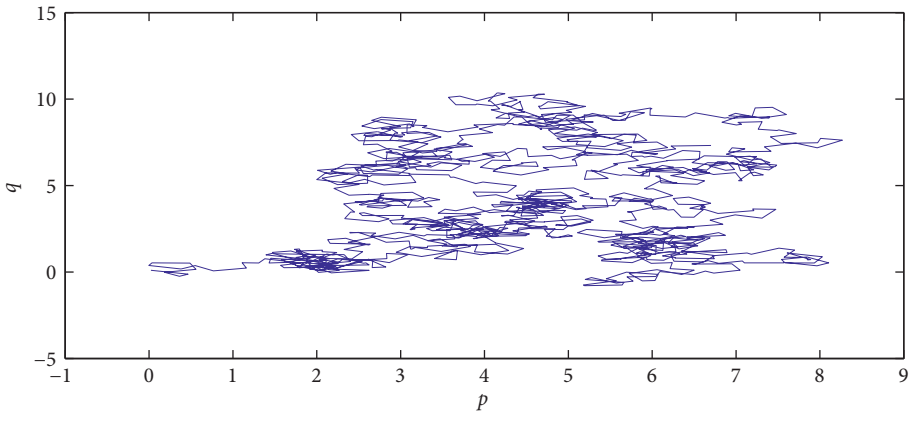

(a)

FIGURE 10: Continued.

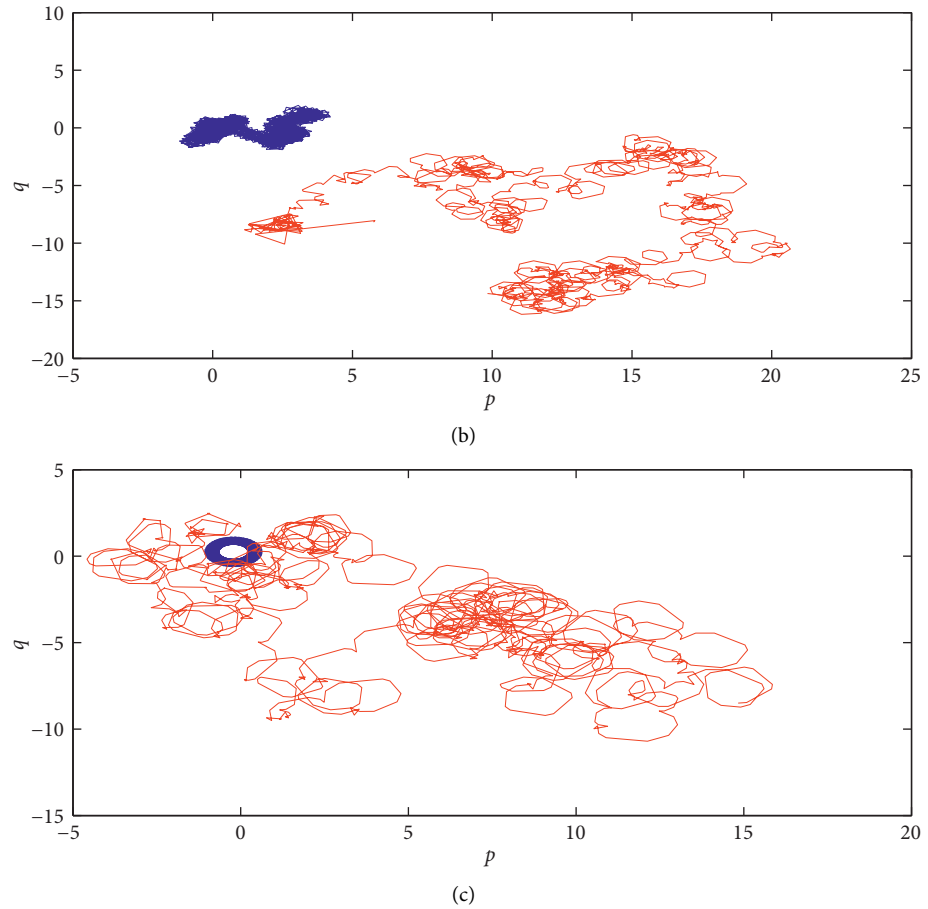

FIGURE 10: 0-1 test of the fractional map (8) for system parameters $A = 0.5$, $B = 0$ and $C = 3$: (a) Brownian-like trajectories for $\mu = 0.9$; (b) Brownian-like trajectories for $\mu = 0.6$ and for two different initial condition (red color for $x_0 = 10$ and blue color for $x_0 = 0.1$); (c) Brownian-like trajectories for $\mu = 0.3$ and initial condition $x_0 = 10$ (in red), along with bounded like trajectories for $x_0 = 0.1$ (in blue).

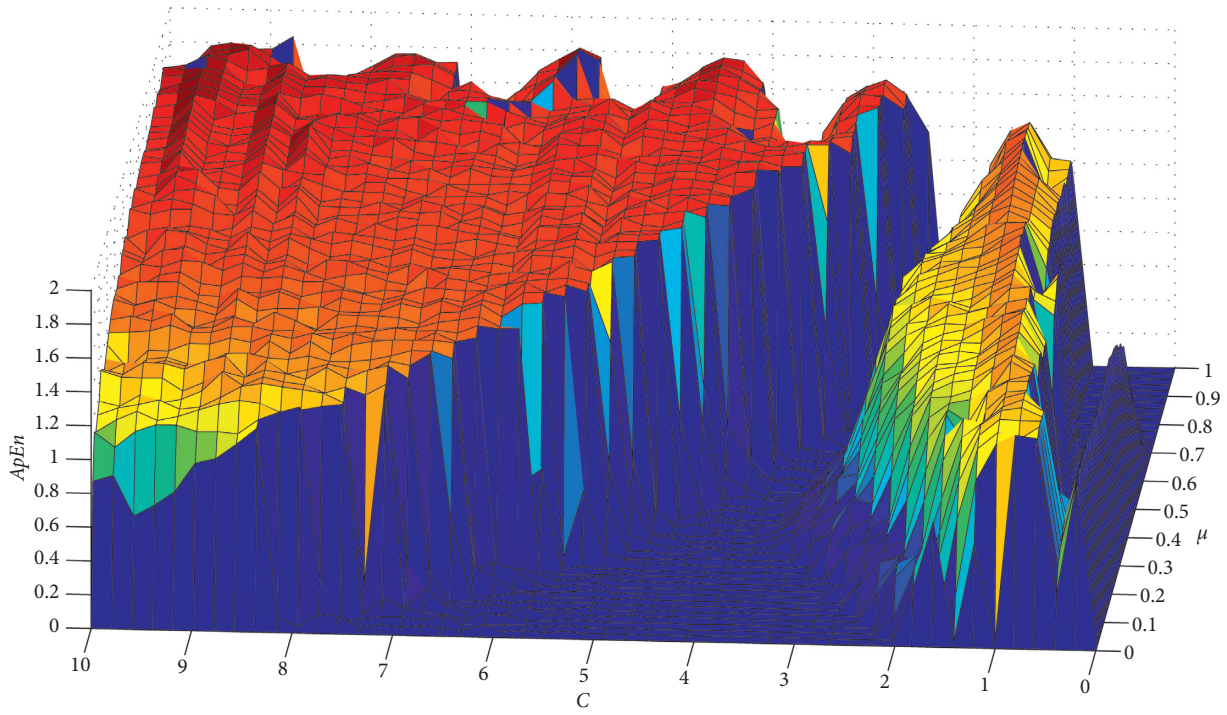

FIGURE 11: The approximate entropy ApEn of the fractional map (8) in three-dimensional space with the variation of system parameter C and fractional order μ, for $A = 0.5$ and $B = 0$.

we should be careful for the range of parameters and fractional order μ.

4. Encryption of Electrophysiological Signals

In this section, an electrophysiological signal will be encrypted using the proposed chaotic map. Here, the signal that will be considered as a sample is a 10 second EEG (electroencephalogram) recording (fp_1) of a subject during arithmetic tasks. More details on the other types of EEG signals can be found in the PhysioBank database [53, 54].

4.1. Design a PRBG. The first step in the encryption scheme is to design a chaotic pseudo-random bit generator. Since the main computational drawback of fractional order systems is their memory effect, the system will be implemented using a finite memory. Thus, its finite form is given as

$$\mathscr{M}_i = \varepsilon_i + \frac{\lfloor 10^5 x_i \rfloor}{10^3}, i = 1, \ldots, \ell, \tag{14}$$

where m denotes the memory used. As one can see from (14), when $i = 1, \ldots, m$ the fractional map states depends on the past m variable, i.e, $x_1(1), \ldots, x_1(m)$. After some trial and error, the memory is chosen as $m = 50$, which satisfyingly models the dynamical behavior of the system, as can be seen in Figure 12. Although the diagram is not identical to the one of the fractional map shown in Figure 4, it accurately showcases chaotic behavior in the range of around 0.2 to 0.8. Implementing fractional systems using finite memory is a standard approach in reducing computational cost and avoiding overflow, and it is used in most microcontroller implementations of fractional chaotic systems [41, 42, 55].

In order to take advantage of the fractional nature of the proposed map, each individual term inside the finite sum (14) is used in the bit generation. So in each iteration of the map, the PRBG generates bits using the following rules:

$$\varepsilon_{enc-bin} = \mathscr{M}_{bin} \oplus \mathscr{B}, \tag{15}$$

where $\lfloor \cdot \rfloor$ denotes the floor operation. So in each iteration, each individual term of the sum in (14), as well as the value x_n of the map are multiplied by 10^{15} and the integer part of this product is taken modulo 512. The result of this operation is then transformed to binary representation. Since the outcome of the modulo is an integer from 0 to 511, transforming it to binary generates nine bits per iteration. Thus, each of the terms $b_{n,1}, \ldots, b_{n,51}$ corresponds to nine bits. The resulting bitstream is taken by concatenating the bits as

$$\mathscr{B} = \left\{ b_{n-1,1}, \ldots, b_{n-1,51}, b_{n,1}, \ldots, b_{n,51}, \ldots \right\}. \tag{16}$$

With the algorithm, there are 459 bits generated in each iteration. So this approach brings an advantage over classic techniques that generate only one bit per iteration, takes advantage of the fractional nature of the map, and also reduces bit generation speed, since fewer iterations of the map are required to reach the required bitstream length.

As noted above, since the sum in (14) is limited from $i = 1$ to $i = n$ when $n < 50$, for $n = 0$ there are 9 bits generated, for $n = 1$ there are 18 bits, and so on, until $n = 49$ where 450 bits are generated. Thus, to reach a bitstream of length N, there are $\left\lceil N/459 + 9\sum_{i=0}^{49} i/459 \right\rceil$ iterations required.

To test the PRBG, a set of $100 \cdot 10^6$ bitstreams is generated and tested through the National Institute of Standards and Technology (NIST) statistical test package SP 800-22 [56]. The test suite consists of 15 statistical tests that are used to verify if a bit sequence is indistinguishable from a random sequence. Each test returns a P value and if the value is higher than a significance level, chosen as the default value 0.01 here, the test is successful. For a PRBG to be classified as random, it should pass all 15 tests. This is verified from Table 1.

4.2. Encryption of Electrophysiological Signal. After the appropriate design of the PRBG, the encryption process is presented. The process consists of two rounds, and a different chaotic map of the form (14) is used in each round, each with parameters x_0, A_1, B_1, C_1 and y_0, A_2, B_2, C_2. In the first round, the source signal is modulated by adding to it the values of the first chaotic map, in order to mask its structure. Then, the modulated signal is transformed into its binary representation, and encrypted using the PRBG of the previous section, generated using the second chaotic map. The encryption is performed using the bitwise XOR operator between the information bitstream and the chaotic bitstream. The complete process is outlined in Algorithm 1.

The transformation of the modulated signal into its binary representation in Step 2 of Algorithm 1 is performed as follows. The modulated signal takes values in the range $[-127.999, 127.999]$. In order to sustain a low run time execution we chose to convert the sampled values by mixing a fixed-point-format with a two's complement representation. So each sample is split into its sign, integer and a decimal parts. The first bit of the binary representation is used to denote the sign. Then, seven bits are used to represent the integer part and ten bits to represent the decimal part. Hence, there are 18 bits overall for each sample, resulting in a bitstream of length $18 \times \ell$. This transformation is outlined in Figure 13.

For the decryption process, the original EEG signal can be reconstructed at the receiver end by following the reverse procedure, that is, performing an XOR between the encrypted binary signal and the same bitstream from the PRBG, generated using the same parameter values, transforming the result back to its decimal format, and then performing the demodulation process, as described in Algorithm 2.

Note that the only information that the receiver needs to know in order to decrypt the signal is the parameter values for the two chaotic maps used to modulate the signal and generate the PRBG. These parameters constitute the key values of the encryption design. Since each chaotic map has four parameters and one initial condition, there are overall ten key values, $x_0, A_1, B_1, C_1, \mu_1, y_0, A_2, B_2, C_2, \mu_2$. Assuming

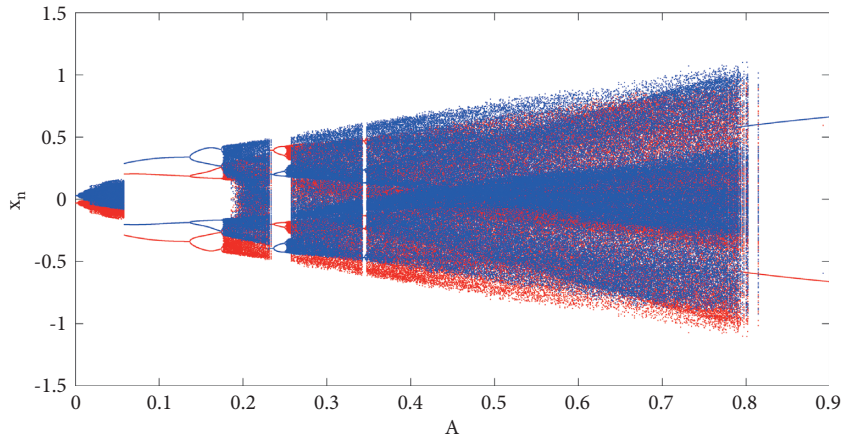

Figure 12: Bifurcation diagram of (14) with respect to parameter A, for $B = 0$, $C = 1$, $\mu = 0.2$, $m = 50$, and $x_0 = 0.1$ (blue), $x_0 = -0.1$ (red).

Table 1: NIST test results ($x_0 = 0.1$, $A = 0.7$, $B = 0$, $C = 1$, $\mu = 0.2$, $m = 50$).

No.	Test	Chi-square P-value	Rate
1	Frequency	0.971 699	100/100
2	BlockFrequency	0.437 274	100/100
3	CumulativeSums	0.213 309	100/100
4	Runs	0.494 392	96/100
5	LongestRun	0.319 084	99/100
6	Rank	0.275 709	99/100
7	FFT	0.366 918	99/100
8	NonOverlappingTemplate	0.554 420	100/100
9	OverlappingTemplate	0.897 763	99/100
10	Universal	0.897 763	100/100
11	ApproximateEntropy	0.455 937	98/100
12	RandomExcursions	0.031 497	63/64
13	RandomExcursionsVariant	0.834 308	61/64
14	Serial	0.051 942	99/100
15	LinearComplexity	0.657 933	99/100

Input: An EEC signal $\mathscr{E}$ of length ℓ. The key values of two chaotic maps of the form (14), $x_0, A_1, B_1, C_1, \mu_1$ and $y_0, A_2, B_2, C_2, \mu_2$.
Output: An encrypted signal $\mathscr{E}_{enc}$ of the same length.
Step 1. Generate ℓ values of the first chaotic map x_i, $i = 1, \ldots, \ell$. Modulate the EEG signal to mask its structure, as $\mathscr{M}_i = \mathscr{E}_i + \lfloor 10^5 x_i \rfloor / 10^3$, $i = 1, \ldots, \ell$.
Step 2. Transform the modulated signal $\mathscr{M}$ into its binary representation $\mathscr{M}_{\text{bin}}$ of length $18 \times \ell$.
Step 3. Generate a bitstream $\mathscr{B}$ of length $16 \times \ell$ using the map y_i as a basis for the PRBG of the previous section (15). Since 8 bits are generated per iteration, the map y_i needs to be iterated $\lceil 2.25 \times \ell \rceil$ times.
Step 4. Encrypt the information bitstream $\mathscr{M}_{\text{bin}}$ by combining it with the chaotic bistream as $\mathscr{E}_{\text{enc-bin}} = \mathscr{M}_{\text{bin}} \oplus \mathscr{B}$.
Step 5. Transform the binary encrypted signal $\mathscr{E}_{\text{enc-bin}}$ to decimal form, to obtain the encrypted signal $\mathscr{E}_{\text{enc}}$.

Algorithm 1: Chaotic Encryption of EEG signal.

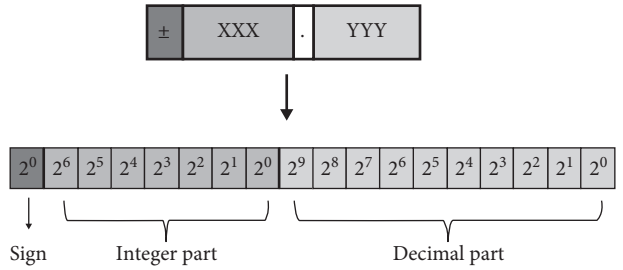

Figure 13: Binary representation of the modulated samples using 18 bits.

Input: An encrypted signal $\mathscr{E}_{\text{enc}}$ of length ℓ. The key values of two chaotic maps of the form (14), x_0, A_1, B_1, C_1 and y_0, A_2, B_2, C_2.
Output: A decrypted signal $\mathscr{E}$ of the same length.
Step 1. Transform the encrypted signal $\mathscr{E}_{\text{enc}}$ to its binary form, to obtain the encrypted bitstream $\mathscr{E}_{\text{enc–bin}}$ of length $18 \times \ell$.
Step 2. Generate a bitstream $\mathscr{B}$ of length $18 \times \ell$ using the map y_i as a basis for the PRBG of the previous section (15). Since 8 bits are generated per iteration, the map y_i needs to be iterated $\lceil 2.25 \times \ell \rceil$ times.
Step 3. Decrypt the bitstream $\mathscr{E}_{\text{enc–bin}}$ by combining it with the chaotic bistream as.
$\mathscr{M}_{\text{bin}} = \mathscr{B} \oplus \mathscr{E}_{\text{enc–bin}}$
Step 4. Transform the modulated binary signal $\mathscr{M}_{\text{bin}}$ into its decimal representation $\mathscr{M}$ of length ℓ.
Step 5. Generate ℓ values of the chaotic map x_i, $i = 1, \ldots, \ell$. Demodulate the signal $\mathscr{M}$ as to obtain the original signal $\mathscr{E}$.
$\mathscr{E}_i = \mathscr{M}_i - \lfloor 10^5 x_i \rfloor / 10^3$, $i = 1, \ldots, \ell$

Algorithm 2: Chaotic Decryption of EEG signal.

a 16-digit accuracy, an upper bound for the key space is $10^{8 \cdot 16} = 10^{128} \approx (10^3)^{42.6} \approx 2^{426}$. This is higher than the bound of 2^{100} required to resist brute force attacks [57]. Note though, that since the system is not chaotic for all parameter values, the real key space is lower than 2^{426}.

4.3. Microcontroller Implementation. The encryption and decryption process was simulated in a microcontroller. For this, an STM32F103 nucleo development board is used, which incorporates a high-performance ARM M3 32-bit RISC core operating at 72 MHz, depicted at Figure 14.

Since an embedded system usually has low ram storage, the modulated signal was saved at the flash memory of the STM32F103RB which embeds an 128 K Byte of flash memory.

The simulation results are shown in Figure 15, where the original (plaintext), modulated, and encrypted signals are shown. Clearly, there is visually no relation between these signals, something that is verified in the next section, through a series of measures. The signals are plotted in Matlab, where the data are loaded from the txt files resulting from the microcontroller simulation. The numerical simulations for the encryption performed in Matlab yield similar results and are thus omitted.

Note that the computation time for the complete procedure of modulating the signal, transforming it to binary format and encrypting it, takes around 8.5 seconds. To reduce computational load and increase speed, the terms $\Gamma(m - i + \mu)/\Gamma(m - i + 1)$ where precomputed and saved in the memory before execution begins. Additionally, further experimentation could lead to reduction in the execution time. For example, in the modulation step the fractional map could be implemented using a shorter memory.

4.4. Encryption Performance. To test the performance of the encryption algorithm, a series of tests are performed on the original, modulated and encrypted signals. The results are gathered on Table 2, for the simulation performed in Matlab R2018b, as well as the microcontroller implementation. The key values of the maps are $x_0 = 0.111$, $A_1 = 0.7$, $B_1 = 0$, $C_1 = 1$, $\mu_1 = 0.2$ and $y_0 = 0.1$, $A_2 = 0.7$, $B_2 = 0$, $C_2 = 1$, $\mu_2 = 0.2$.

Note that apart from the Approximate Entropy measure that is computed for each individual signal, the rest of the measures are computed in each case between the original and modulated signal, and between the original and encrypted signal, and shown in their respective columns.

In all cases, it can be seen that the measures for the Matlab and microcontroller implementations are very close to each other. This means that the microcontroller encryption performs equally well compared to Matlab.

4.4.1. Histogram. Initially, the histogram of the original, modulated and encrypted signals are plotted in Figure 16 for the microcontroller simulation. An encrypted signal should have a uniform histogram, so that no information on the distribution of the signal's values are revealed. Indeed it can be seen that the histogram of the encrypted signal is much more uniform compared to the original signal and modulated ones, that have a shape closer to a normal distribution. The simulation performed in Matlab yields similar histograms, so both simulations perform the same.

4.4.2. Structural Similarity Index (SSIM). The SSIM is a measure of the structural similarity between two signals [29], initially considered for images [58]. It is given by

$$\text{SSIM} = \frac{\left(2\mu_x\mu_y + S_1\right)\left(2\delta_{xy} + S_2\right)}{\left(\mu_x^2 + \mu_y^2 + S_1\right)\left(\delta_x^2 + \delta_y^2 + S_2\right)}, \tag{17}$$

where μ_x, μ_y the mean values of the original and encrypted (or modulated) signals respectively, δ_x^2, δ_y^2 their variances, and δ_{xy} their cross-covariance. The parameters S_1, S_2 take small values, to avoid unstable results when the denominator is close to zero.

The SSIM value is between $[-1, 1]$, with 1 for identical signals, and 0 for signals with no similarity. So, the closest the measure is to zero, the better the encryption. Indeed, the SSIM between the original and modulated signal performed in Matlab is equal to -0.1160, and between the original and encrypted signal is 0.001 6, which is indeed very close to zero.

4.4.3. Log-Likelihood Ratio (LLR). The LLR gives an estimation on the quality of encryption [29, 59–61]. It is based on the assumption that the segment can be represented by a p-th order all-pole linear predictive coding model

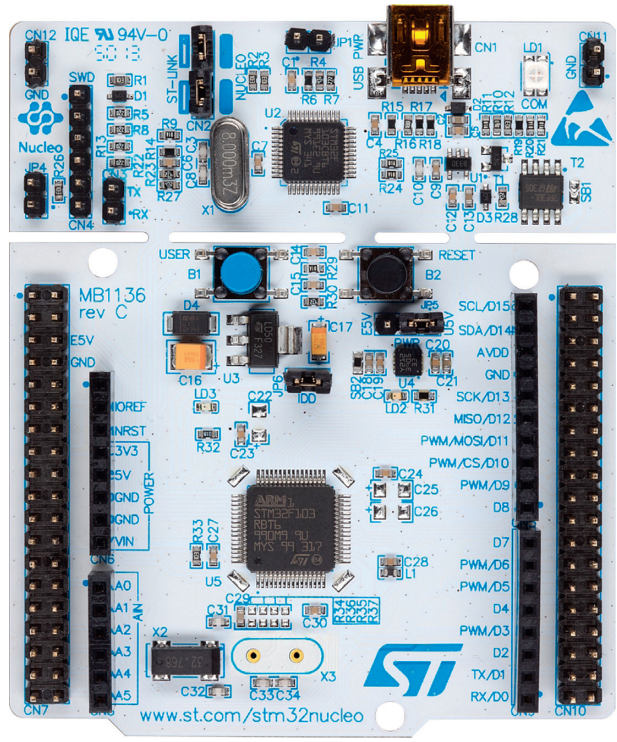

Figure 14: STM32F103 nucleo board with a 32bit RISC processor.

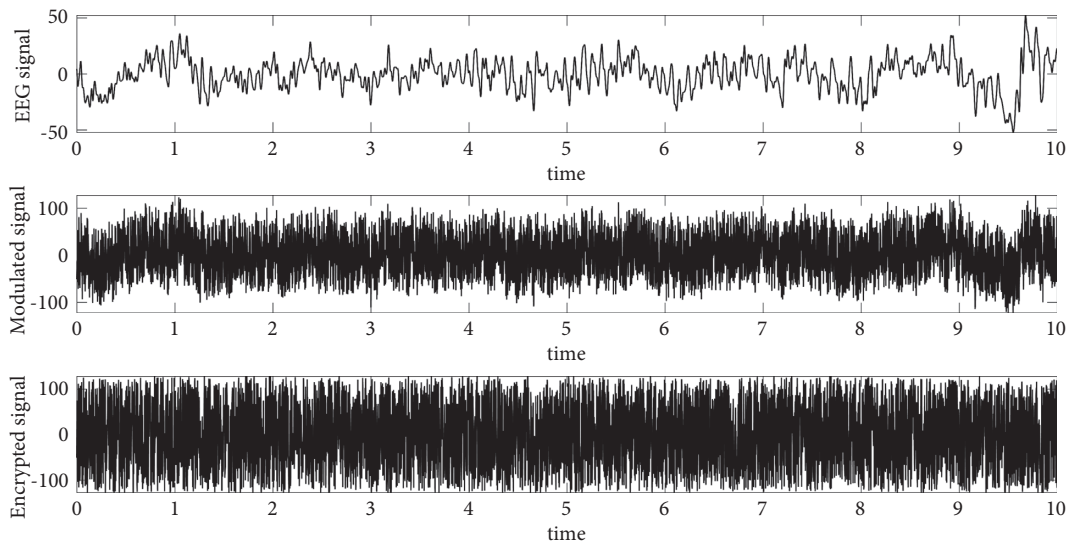

Figure 15: Original EEG signal, modulated signal, and encrypted signal.

Table 2: Performance measures of the encryption design.

Signals	EEC	Matlab		Microcontroller	
		Modulated	Encrypted	Modulated	Encrypted
SSIM	—	−0.1160	0.001 6	−0.0894	0.006 8
LLR	—	1.995 5	1.993 7	1.973 3	2.045 6
SNR	—	−9.7873	−14.6874	−9.8402	−14.6757
r_{xy}	—	0.307 6	−0.0126	0.303 7	0.021 0
SD	—	39.494 9	44.053 6	39.652 1	43.864 9
ApEn	0.497 0	1.577 4	2.270 2	1.579 8	2.228 2

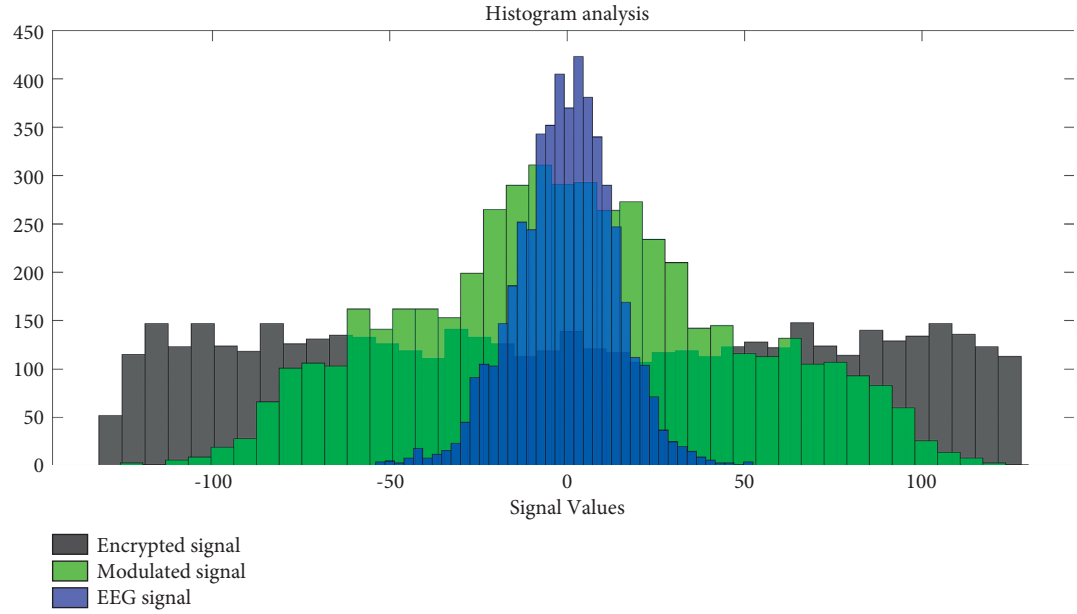

Figure 16: Histograms of the encrypted, modulated, and encrypted signals.

$$x_i = \sum_{m=1}^{p} a_m x_{i-m} + G_x u_i, \tag{18}$$

where x_i is the ith signal sample, a_m, $m = 1, \ldots, p$ the coefficients of the all-pole filter, G_x the gain of the filter and u_i an appropriate excitation input to the signal. The LLR is then defined as:

$$\text{LLR} = \left| \log \left(\frac{a_x R_y a_x^T}{a_y R_z a_y^T} \right) \right|, \tag{19}$$

where a_x the vector of Linear Prediction Coefficients (LPCs) $[1, a_1, a_2, \ldots, a_m]$ of the original signal, a_z the LPCs of the encrypted (or modulated) signal, and R_y the autocorrelation matrix of the encrypted (or modulated) signal. A higher LLR value indicates a good encryption. The LLR between the original and modulated signal is 1.995 5 and between the original and encrypted signals is 1.993 7. The values are both high, which indicates a good encryption.

4.4.4. Signal to Noise Ratio (SNR). The SNR is defined as [29, 60]:

$$\text{SNR} = 10 \log_{10} \frac{\sum_{i=1}^{N} x_i^2}{\sum_{i=1}^{N} (x_i - y_i)^2}, \tag{20}$$

where x, y the encrypted and decrypted (or modulated) signals respectively, and N the number of samples. A low SNR indicates a good encryption. The SNR between the original and modulated signal is −9.7873, while the SNR between the original and encrypted signal is −14.6874. Both values are very low and indicate a good encryption.

4.4.5. Correlation Coefficient. The correlation coefficient [29] between the original and encrypted (or modulated) signals is computed as:

$$r_{xy} = \frac{c_v(x, y)}{\sqrt{\delta_x^2} \sqrt{\delta_y^2}}, \tag{21}$$

where $c_v(x, y)$ the covariance of the two signals and δ^2 their variances. For uncorrelated signals, the correlation coefficient should be close to zero. The correlation coefficient between original and modulated signal is 0.307 6, while the coefficient between original and encrypted is −0.0126.

4.4.6. Spectral Distortion (SD). The SD measures the difference between the spectrum of the original and encrypted (or modulated) signals [29, 60–62]. It is computed as:

$$\text{SD} = \frac{1}{M} \sum_{i=0}^{M-1} \left| V_{x,i} - V_{y,i} \right|, \tag{22}$$

where $V_{x,i}, V_{y,i}$ the spectrum of the original and encrypted (or modulated) signal in decibel at instance i. A higher value of SD indicates a better encryption. The SD between the original and moculated signals is 39.494 9, and the SD between the original and encrypted signals is 44.053 6, so both values are high.

4.4.7. Approximate Entropy (ApEn). The ApEn is applied to measure the complexity of the serie of data [51]. A series with a higher ApEn is considered as being more complex, so for the proposed scheme, the encrypted signal should have a higher value of ApEn compared to the original signal. Indeed the ApEn of the original signal is 0.497 0, for the modulated signal is 1.577 4, and for the encrypted signal is 2.270 2, so the encrypted signal has the highest ApEn.

Overall, each of the measures computed indicates a good encryption performance. Moreover, the design can be accurately replicated on a microcontroller board.

5. Conclusions

Referring to fractional-order discrete-time systems with special features, this paper has introduced the first example of a fractional map with infinite number of equilibria in a bounded domain. The conceived map has also shown coexistence of different types of periodic and chaotic attractors. Dynamics and complexity of the conceived map have been analyzed in details via bifurcation diagrams, maximum Lyapunov exponents, 0-1 test and approximate entropy. Compared with the integer order map, the fractional map has more complexity when the fractional order values is smaller. That is the integer-order map do not have the property of coexisting attractors, while fractional map have it. Afterwards, the proposed map was applied to the problem of encrypting an electrophysiological signal. A PRBG was designed based on the values of the chaotic map, and two rounds of modulation and encryption were performed on the signal. A set of measures were then computed for the original and encrypted signals to verify the performance of the encryption. The design was realised in a microcontroller board, so to increase speed, the fractional map was implemented with finite memory. Future extensions of this work can consider modifications of the encryption design, for example different methods to modulate the signal.

Also, in order to improve execution time, the use of a higher frequency CPU combined with hardware accelerators, such as CORDIC (COordinate Rotation DIgital Computer), will allow faster sinusoidal calculations and floating point arithmetic operations.

Finally, FPGA based realizations of the encryption design are among the future goals set by the authors, since they have been proven an efficient low cost option for implementing fractional [45] and integer order maps [63].

Data Availability

The data used to support the findings of this study are included within the article.

Conflicts of Interest

The authors declare no conflict of interest.

Acknowledgments

The author L.Moysis is thankful to Diego Renza Torres of the Universidad Militar Nueva Granada, Bogotá, Colombia, for his help regarding the SD measure. The authors are also thankful to the anonymous reviewers for their insightful comments that helped improve the manuscript significantly. This research received no external funding.

References

[1] C. Goodrich and A. C. Peterson, *Discrete Fractional Calculus*, Springer, Berlin, Germany, 2015.

[2] B. Yan, S. He, and S. Wang, "Multistability and formation of spiral waves in a fractional-order memristor-based hyperchaotic Lu system with No equilibrium points," *Mathematical Problems in Engineering*, vol. 2020, Article ID 2468134, 12 pages, 2020.

[3] P. Ostalczyk, *Discrete fractional calculus: applications in control and image processing*, World Scientific, vol. 4, Singapore, , 2015.

[4] M. Edelman, E. E. Macau, and M. A. Sanjuan, *Chaotic, fractional, and complex dynamics: new insights and perspectives*, Springer International Publishing, New York, NY, USA, 2018.

[5] G. C. Wu and D. Baleanu, "Discrete fractional logistic map and its chaos," *Nonlinear Dynamics*, vol. 75, no. 1, pp. 283–287, 2014.

[6] G. C. Wu, D. Baleanu, and S. D. Zeng, "Discrete chaos in fractional sine and standard maps," *Physics Letters A*, vol. 378, no. 5-6, pp. 484–487, 2014.

[7] A. Ouannas, A.-A. Khennaoui, G. Grassi, and S. Bendoukha, "On chaos in the fractional-order Grassi-Miller map and its control," *Journal of Computational and Applied Mathematics*, vol. 358, pp. 293–305, 2019.

[8] T. Hu, "Discrete chaos in fractional Hénon map," *Applied Mathematics*, vol. 5, no. 15, 2014.

[9] A.-A. Khennaoui, A. Ouannas, S. Bendoukha, X. Wang, and V.-T. Pham, "On chaos in the fractional-order discrete-time unified system and its control synchronization," *Entropy*, vol. 20, no. 7, p. 530, 2018.

[10] M. K. Shukla and B. B. Sharma, "Investigation of chaos in fractional order generalized hyperchaotic Henon map," *AEU - International Journal of Electronics and Communications*, vol. 78, pp. 265–273, 2017.

[11] Y. Peng, S. He, and K. Sun, "Chaos in the discrete memristor-based system with fractional-order difference," *Results in Physics*, vol. 24, Article ID 104106, 2021.

[12] A.-A. Khennaoui, A. Ouannas, S. Bendoukha, G. Grassi, R. P. Lozi, and V.-T. Pham, "On fractional-order discrete-time systems: chaos, stabilization and synchronization," *Chaos, Solitons & Fractals*, vol. 119, pp. 150–162, 2019.

[13] A. Ouannas, A.-A. Khennaoui, S. Bendoukha, T. Vo, V.-T. Pham, and V. Huynh, "The fractional form of the Tinkerbell map is chaotic," *Applied Sciences*, vol. 8, no. 12, p. 2640, 2018.

[14] A. Ouannas, A. A. Khennaoui, S. Momani, V. T. Pham, and R. El-Khazali, "Hidden attractors in a new fractional–order discrete system: chaos, complexity, entropy, and control," *Chinese Physics B*, vol. 29, no. 5, Article ID 50504, 2020.

[15] E. Zambrano-Serrano, S. Bekiros, M. A. Platas-Garza, C. Posadas-Castillo, and P. Agarwal, H. Jahanshahi and A. A. Aly, On and projective synchronization of a fractional difference map with no equilibria using a fuzzy-based state feedback control," *Physica A: Statistical Mechanics and Its Applications*, vol. 578, Article ID 126100, 2021.

[16] A. O. Almatroud, A. A. Khennaoui, A. Ouannas, and V. T. Pham, "Infinite line of Equilibriums in a novel fractional map with coexisting infinitely many attractors and initial offset boosting," *International Journal of Nonlinear Science and Numerical Simulation*, vol. 2021, 2021.

[17] Y. Peng, K. Sun, and S. He, "A discrete memristor model and its application in Hénon map," *Chaos, Solitons & Fractals*, vol. 137, Article ID 109873, 2020.

[18] H. Li, K. Li, M. Chen, and B. Bao, "Coexisting infinite orbits in an area-preserving Lozi map," *Entropy*, vol. 22, no. 10, p. 1119, 2020.

[19] H. Li, Z. Hua, H. Bao, L. Zhu, M. Chen, and B. Bao, "Two-dimensional memristive hyperchaotic maps and application in secure communication," *IEEE transactions on industrial electronics*, vol. 68, no. 10, 2020.

[20] H. Bao, Z. Hua, N. Wang, L. Zhu, M. Chen, and B. Bao, "Initials-Boosted Coexisting Chaos in 2D Sine Map and Its Hardware Implementation," *IEEE Transactions on Industrial Informatics*, vol. 17, no. 2, pp. 1132–1140, 2020.

[21] A. A. Khennaoui, A. O. Almatroud, A. Ouannas et al., "An unprecedented 2-dimensional discrete-time fractional-order system and its hidden chaotic attractors," *Mathematical Problems in Engineering*, vol. 2021, Article ID 6768215, 10 pages, 2021.

[22] Y. Li, X. He, and W. Zhang, "The fractional difference form of sine chaotification model," *Chaos, Solitons & Fractals*, vol. 137, Article ID 109774, 2020.

[23] Y.-R. Bai, D. Baleanu, and G.-C. Wu, "A novel shuffling technique based on fractional chaotic maps," *Optik*, vol. 168, pp. 553–562, 2018.

[24] G.-C. Wu, D. Baleanu, and Z.-X. Lin, "Image encryption technique based on fractional chaotic time series," *Journal of Vibration and Control*, vol. 22, no. 8, pp. 2092–2099, 2016.

[25] L. Ding and Q. Ding, "A novel image encryption scheme based on 2D fractional chaotic map, dwt and 4D hyper-chaos," *Electronics*, vol. 9, no. 8, p. 1280, 2020.

[26] A. Akgül, C. Arslan, and B. Aricioğlu, "Design of an interface for random number generators based on integer and fractional order chaotic systems," *Chaos Theory and Applications*, vol. 1, no. 1, pp. 1–18, 2019.

[27] C. Yang, I. Taralova, J. J. Loiseau, and S. El-Assad, "A Stream Cipher Based on Fractional Pseudo Chaotic Random Number Generator," in *Proceedings of the 2020 15th International Conference for Internet Technology and Secured Transactions (ICITST)*, pp. 1–6, IEEE, London, UK, December 2020.

[28] A. Akgul, O. F. Boyraz, K. Rajagopal, E. Guleryuz, M. Z. Yildiz, and M. Kutlu, "An unforced megastable chaotic oscillator and its application on protecting electrophysiological signals," *Zeitschrift für Naturforschung A*, vol. 75, no. 12, pp. 1025–1037, 2020.

[29] A. D. Algarni, N. F. Soliman, H. A. Abdallah, and F. E. Abd El-Samie, "Encryption of ecg signals for telemedicine applications," *Multimedia Tools and Applications*, vol. 80, pp. 1–25, 2020.

[30] C.-F. Lin, C.-H. Chung, and J.-H. Lin, "A chaos-based visual encryption mechanism for clinical EEG signals," *Medical, & Biological Engineering & Computing*, vol. 47, no. 7, pp. 757–762, 2009.

[31] C. F. Lin, S. H. Shih, and J. D. Zhu, "Chaos based encryption system for encrypting electroencephalogram signals," *Journal of Medical Systems*, vol. 38, no. 5, pp. 49–10, 2014.

[32] C. F. Lin, "Chaotic visual cryptosystem using empirical mode decomposition algorithm for clinical EEG signals," *Journal of Medical Systems*, vol. 40, no. 3, pp. 1–10, 2016.

[33] M. A. Murillo-Escobar, L. Cardoza-Avendaño, R. M. López-Gutiérrez, and C. Cruz-Hernández, "A double chaotic layer encryption algorithm for clinical signals in telemedicine," *Journal of Medical Systems*, vol. 41, no. 4, p. 59, 2017.

[34] M. Irfan, A. Ali, M. A. Khan, M. Ehatisham-ul-Haq, S. N. M. Shah, and W. Ahmad, "Pseudorandom number generator (prng) design using hyper-chaotic modified robust logistic map (hc-mrlm)," *Electronics*, vol. 9, no. 1, p. 104, 2020.

[35] P. Ayubi, S. Setayeshi, and A. M. Rahmani, "Deterministic chaos game: a new fractal based pseudo-random number generator and its cryptographic application," *Journal of Information Security and Applications*, vol. 52, Article ID 102472, 2020.

[36] B. Stoyanov and T. Ivanova, "CHAOSA: chaotic map based random number generator on Arduino platform," *AIP Conference Proceedings*, AIP Publishing LLC, vol. 2172, no. 1, , Article ID 90001, 2019.

[37] M. A. Murillo-Escobar, C. Cruz-Hernández, L. Cardoza-Avendaño, and R. Méndez-Ramírez, "A novel pseudorandom number generator based on pseudorandomly enhanced logistic map," *Nonlinear Dynamics*, vol. 87, no. 1, pp. 407–425, 2017.

[38] L. Liu, S. Miao, M. Cheng, and X. Gao, "A pseudorandom bit generator based on new multi-delayed Chebyshev map," *Information Processing Letters*, vol. 116, no. 11, pp. 674–681, 2016.

[39] X. Tang and S. Mandal, "Encrypted physical layer communications using synchronized hyperchaotic maps," *IEEE Access*, vol. 9, Article ID 13286, 2021.

[40] C. Meshram, R. W. Ibrahim, A. J. Obaid, S. G. Meshram, A. Meshram, and A. M. Abd El-Latif, "Fractional chaotic maps based short signature scheme under human-centered iot environments," *Journal of Advanced Research*, vol. 32, 2020.

[41] Y.-M. Chu, S. Bekiros, E. Zambrano-Serrano et al., "Artificial macro-economics: a chaotic discrete-time fractional-order laboratory model," *Chaos, Solitons & Fractals*, vol. 145, Article ID 110776, 2021.

[42] O. Megherbi, H. Hamiche, S. Djennoune, and M. Bettayeb, "A new contribution for the impulsive synchronization of fractional-order discrete-time chaotic systems," *Nonlinear Dynamics*, vol. 90, no. 3, pp. 1519–1533, 2017.

[43] A. M. A. El-Sayed, A. Elsonbaty, A. A. Elsadany, and A. E. Matouk, "Dynamical analysis and circuit simulation of a new fractional-order hyperchaotic system and its discretization," *International Journal of Bifurcation and Chaos*, vol. 26, no. 13, Article ID 1650222, 2016.

[44] J. Wang, L. Xiao, K. Rajagopal, A. Akgul, S. Cicek, and B. Aricioglu, "Fractional-order analysis of modified chua's circuit system with the smooth degree of 3 and its microcontroller-based implementation with analog circuit design," *Symmetry*, vol. 13, no. 2, 2021.

[45] S. M. Ismail, L. A. Said, A. A. Rezk et al., "Generalized fractional logistic map encryption system based on fpga," *AEU - International Journal of Electronics and Communications*, vol. 80, pp. 114–126, 2017.

[46] F. Atici and P. Eloe, "Initial value problems in discrete fractional calculus," *Proceedings of the American Mathematical Society*, vol. 137, no. 3, pp. 981–989, 2009.

[47] T. Abdeljawad, "On Riemann and Caputo fractional differences," *Computers & Mathematics with Applications*, vol. 62, no. 3, pp. 1602–1611, 2011.

[48] G. A. Anastassiou, "Principles of delta fractional calculus on time scales and inequalities," *Mathematical and Computer Modelling*, vol. 52, no. 3-4, pp. 556–566, 2010.

[49] Z. Wang, A. J. M. Khalaf, H. Tian, A. Alsaedi, and T. Hayat, "A chaotic map with infinite number of equilibria in a bounded domain," *The European Physical Journal - Special Topics*, vol. 229, no. 6-7, pp. 1109–1116, 2020.

[50] D. Cafagna and G. Grassi, "An effective method for detecting chaos in fractional-order systems," *International Journal of Bifurcation and Chaos*, vol. 20, no. 3, pp. 669–678, 2010.

[51] L. Liu, H. Xiang, and X. Li, "A novel perturbation method to reduce the dynamical degradation of digital chaotic maps," *Nonlinear Dynamics*, vol. 103, no. 1, pp. 1–17, 2021.

[52] S. M. Pincus, "Approximate entropy as a measure of system complexity," *Proceedings of the National Academy of Sciences*, vol. 88, no. 6, pp. 2297–2301, 1991.

[53] I. Zyma, S. Tukaev, I. Seleznov et al., "Electroencephalograms during mental arithmetic task performance," *Data*, vol. 4, no. 1, p. 14, 2019.

[54] A. L. Goldberger, L. A. Amaral, L. Glass et al., "PhysioBank, PhysioToolkit, and PhysioNet: components of a new research resource for complex physiologic signals," *Circulation*, vol. 101, no. 23, pp. e215–20, 2000.

[55] X. Liao, Z. Gao, and H. Huang, "Synchronization Control of Fractional-Order Discrete-Time Chaotic Systems," in *Proceedings of the 2013 European control conference (ECC)*, pp. 2214–2219, IEEE, Zurich, Switzerland, July 2013.

[56] A. Rukhin, J. Soto, J. Nechvatal, M. Smid, and E. Barker, "A statistical test suite for random and pseudorandom number generators for cryptographic applications," *Booz-allen and hamilton inc mclean va*, 2001.

[57] G. Alvarez and S. Li, "Some basic cryptographic requirements for chaos-based cryptosystems," *International journal of bifurcation and chaos*, vol. 16, no. 8, pp. 2129–2151, 2006.

[58] Z. Wang, A. C. Bovik, H. R. Sheikh, and E. P. Simoncelli, "Image quality assessment: from error visibility to structural similarity," *IEEE Transactions on Image Processing*, vol. 13, no. 4, pp. 600–612, 2004.

[59] G. Manjunath and G. V. Anand, "Speech Encryption Using Circulant Transformations," *Proceedings. IEEE International Conference on Multimedia and Expo*, vol. 1pp. 553–556, IEEE, Lausanne, Switzerland, August 2002.

[60] E. Mosa, N. W. Messiha, O. Zahran, and F. E. Abd El-Samie, "Chaotic encryption of speech signals," *International Journal of Speech Technology*, vol. 14, no. 4, pp. 285–296, 2011.

[61] E. M. Elshamy, E.-S. M. El-Rabaie, O. S. Faragallah, O. A. Elshakankiry, F. E. A. El-Samie, and S. F. El-Zoghdy, "Efficient audio cryptosystem based on chaotic maps and double random phase encoding," *International Journal of Speech Technology*, vol. 18, no. 4, pp. 619–631, 2015.

[62] D. Renza, S. Mendoza, and D. M. Ballesteros, "High-uncertainty audio signal encryption based on the Collatz conjecture," *Journal of Information Security and Applications*, vol. 46, pp. 62–69, 2019.

[63] L. Gerardo, D. L. Fraga, E. T. Pérez, E. Tlelo-Cuautle, and C. Mancillas-López, ".Hardware implementation of pseudo-random number generators based on chaotic maps," *Nonlinear Dynamics*, vol. 90, no. 3, pp. 1661–1670, 2017.

Hindawi
Complexity
Volume 2021, Article ID 7242253, 12 pages
https://doi.org/10.1155/2021/7242253

Research Article

Synchronization in Dynamically Coupled Fractional-Order Chaotic Systems: Studying the Effects of Fractional Derivatives

J. L. Echenausía-Monroy,[1] **C. A. Rodríguez-Martíne**,[1] **L. J. Ontañón-García**,[2] **J. Alvarez**,[1] **and J. Pena Ramirez**[1]

[1]*Applied Physics Division, Center for Scientific Research and Higher Education at Ensenada, CICESE. Carr. Ensenada-Tijuana, 3918 Zona Playitas, Ensenada, 22860 BC, Mexico*
[2]*Coordinación Académica Región Altiplano Oeste, Universidad Autónoma de San Luis Potosí, Carretera a Santo Domingo 200, 78 600, Salinas de Hidalgo, S.L.P, Mexico*

Correspondence should be addressed to J. L. Echenausía-Monroy; jose.luis.echenausia@gmail.com and J. Pena Ramirez; jpena@cicese.mx

Received 27 August 2021; Revised 23 October 2021; Accepted 4 December 2021; Published 24 December 2021

Academic Editor: Atila Bueno

This study presents the effectiveness of dynamic coupling as a synchronization strategy for fractional chaotic systems. Using an auxiliary system as a link between the oscillators, we investigate the onset of synchronization in the coupled systems and we analytically determine the regions where both systems achieve complete synchronization. In the analysis, the integration order is considered as a key parameter affecting the onset of full synchronization, considering the stability conditions for fractional systems. The local stability of the synchronous solution is studied using the linearized error dynamics. Moreover, some statistical metrics such as the average synchronization error and Pearson's correlation are used to numerically identify the synchronous behavior. Two particular examples are considered, namely, the fractional-order Rössler and Chua systems. By using bifurcation diagrams, it is also shown that the integration order has a strong influence not only on the onset of full synchronization but also on the individual dynamic behavior of the uncoupled systems.

1. Introduction

Synchronization is an emergent physical phenomenon caused by the interaction of two or more dynamic entities that pervade the natural world [1–4]. In the case of oscillating units, the synchronization phenomenon can be defined as the adjustment of temporal evolution to a common rhythm.

For the case of integer-order systems, there exists a vast and mature literature where we can find different interconnection schemes for synchronizing dynamic systems, like, for example, master-slave synchronization scheme, adaptive synchronization, and synchronization based on state observers, to name a few [5–10]. Although each of these strategies is effective, there are limitations in their applications, e.g., there are cases where these schemes have marginal ranges for which the synchronous response is achieved or have poor robustness to maintain a stable synchronous state under the influence of external disturbances. This is one of the reasons why dynamic interconnections have emerged as an alternative to the classical static schemes. In this case, the interaction between agents is indirectly achieved through a suitably designed dynamic coupling [11–13]. This type of synchronization strategy has shown better performance than static couplings. In particular, dynamic coupling increases the intervals of coupling strength values for which it is possible to achieve synchronized behavior, and it may also be possible to synchronize systems that cannot be synchronized with static coupling [11].

On the other hand, the use of fractional calculus has been extensively studied in nonlinear systems (see, e.g., [14–18]) and also, there exist notable contributions related to the study of synchronization in fractional-order systems (see,

e.g., [16, 19–23]). For example, there is work based on applying sliding modes to fractional-order models to achieve synchronization [24–29]. The modeling and analytical study of fractional-order systems is also a fruitful field, e.g., the use of the Razumikhin approximation for fractional-order systems with delay [30, 31], the extrapolation of Lyapunov theory to fractional systems [32, 33], and the existence and uniqueness of equilibrium points of the Mittag–Leffler criteria [34, 35]. However, the use of dynamic couplings in the context of fractional-order systems seems to be unexplored so far.

Consequently, in this study we present a synchronization scheme of fractional order based on dynamic coupling. In particular, a master-slave interconnection is considered, in which the systems have an indirect interaction via a fractional-order linear system. In the analysis, the Rössler equation [36] and the Chua double-scroll oscillator [37] are considered. Among the questions to be addressed is whether a dynamic coupling designed for integer-order systems is also effective in its fractional-order version? If so, how does the derivative order influence the occurrence of synchronization in the coupled systems? The local stability of the synchronous solution in the coupled systems is investigated by analyzing the error dynamics, and furthermore, the onset of synchronization is also numerically investigated by computing some statistical metrics like Pearson's correlation between time series. Additionally, using bifurcation diagrams, we have investigated the dynamic behavior of the uncoupled systems. The obtained results show that the integration order has a strong influence on the stability of the synchronous solution, and interestingly, it also produces a period-doubling cascade route to chaos in the uncoupled systems.

The rest of the study is organized as follows: Section 2 describes the basics of fractional calculus and gives a brief introduction to fractional-order systems. Then, Section 3 describes the proposed synchronization scheme and the local stability of the synchronous solution in the coupled systems is discussed. Subsequently, in Section 4, the performance of the dynamic coupling is investigated using the Rössler and Chua systems as application examples. Finally, Sections 6 and 7 are dedicated to the discussion and conclusions, respectively.

2. Preliminaries

This section presents a brief overview of some basic concepts about fractional-order systems. In particular, the Caputo derivative, the general representation of a fractional-order system, and the stability of linear time-invariant fractional-order systems are revisited.

2.1. Fractional Caputo Derivative. In the literature, there are various definitions of fractional-order derivatives, the most common being the Riemann–Liouville and Caputo operators [38, 39]. The fractional Caputo derivative for a time-invariant system described by the vector field $f(x)$ is defined as

$$ {}_aD_0^q f(x) = \frac{1}{\Gamma(n-q)} \int_a^x \frac{f^{(n)}(t)}{(x-t)^{q-n+1}} \mathrm{d}t, \tag{1} $$

with $n = \lceil q \rceil$ for the integration order $0 < q < 1$, being Γ the gamma function defined as follows:

$$ \Gamma(z) = \int_0^\infty t^{z-1} e^{-t} \mathrm{d}t. \tag{2} $$

2.2. Fractional-Order Dynamic System. A commensurate fractional-order time-invariant system can be described, in general, as follows:

$$ D_0^{n_k} x(t) = f\left(t, x(t), D_0^{n_1} x(t), D_0^{n_2} x(t), \ldots, D_0^{n_{k-1}} x(t)\right), \tag{3} $$

subject to initial conditions

$$ x^{(j)}(0) = x_0^{(j)}, \text{ with } j = 0, 1, \ldots, \lceil n_k \rceil - 1, \tag{4} $$

where $n_1, n_2, \ldots, n_k$ are rational numbers, such that $n_k > n_{k-1} > \cdots > n_1 > 0$, $n_j - n_{j-1} \leq 1$ for all $j = 2, 3, \ldots, k$, and $0 < n_1 \leq 1$. The least common multiple of the denominator of $n_1, n_2, \ldots, n_k$ is defined by M and set $q = 1/M$ and $N = Mn_k$. Then, equation (3) can be expressed as follows [38]:

$$ \begin{aligned} D_0^q x_0(t) &= x_1(t), \\ D_0^q x_1(t) &= x_2(t), \\ &\vdots \\ D_0^q x_{N-2}(t) &= x_{N-1}(t), \\ D_0^q x_{N-1}(t) &= f\left(t, x_0(t), x_{n_1/q}(t), \ldots, x_{n_{k-1}/q}(t)\right). \end{aligned} \tag{5} $$

2.3. Stability of Time-Invariant Fractional-Order System. A linear time-invariant fractional-order system is described by

$$ \frac{\mathrm{d}^q x(t)}{\mathrm{d}t^q} = Ax, \tag{6} $$

where $x \in \mathbb{R}^n$ is the state vector, $A \in \mathbb{R}^{n \times n}$ is a constant matrix, and $0 < q < 1$ is the fractional commensurate derivative order. Then, the stability of the system described by equation (6) is determined as follows [38]:

(i) System (6) is stable, if and only if $|\arg\lambda_j| \geq q\pi/2$, $\forall j = 1, 2, \ldots, n$

(ii) System (6) is asymptotically stable, if and only if $|\arg\lambda_j| > q\pi/2$, $\forall j = 1, 2, \ldots, n$

(iii) System (6) is unstable, if and only if $|\arg\lambda_j| < q\pi/2$, for at least one λ_j, $j = 1, 2, \ldots, n$

From these conditions, it is clear that the local stability of fractional-order systems depends on the integration order q, so that the stability of an equilibrium point can be modified by the fractional order, and therefore, the stability region at the complex plane is as in Figure 1 [40].

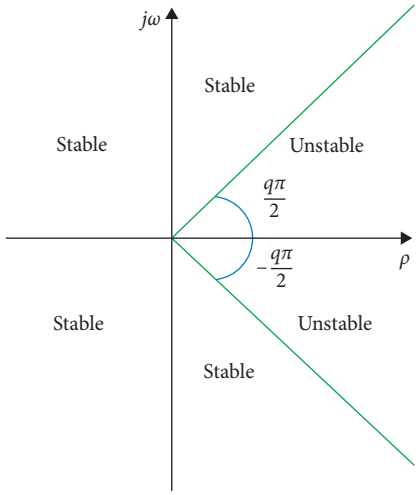

Figure 1: Stability region in a fractional-order linear time-invariant system for $0 < q < 1$.

3. Proposed Synchronization Scheme Based on Dynamic Coupling

The dynamic interconnection considered in this study has been presented in [11] for integer-order systems and is adapted here to the fractional-order case. The scheme, where the interaction between the systems is indirect via a dynamical system (Figure 2) is described by the following set of equations:

$$\begin{aligned} D^q x_m &= F(x_m), \\ D^q x_s &= F(x_s) - B_1 h, \\ D^q h &= Gh - kB_2(x_m - x_s), \end{aligned} \tag{7}$$

where $x_m, x_s \in \mathbb{R}^n$ represents the state vectors of both the master and slave systems and $h = (h_1, h_2)^T$ for $h_i \in \mathbb{R}$, $i = 1, 2$ is the state variables of the dynamic coupling. It is assumed that the vector field F is smooth enough, which can be either linear or nonlinear, and the coupling force between the systems is denoted by k.

On the other hand, the design of a dynamic coupling involves two coupling matrices, denoted $B_1 \in \mathbb{R}^{n\times 2}$ and $B_2 \in \mathbb{R}^{2\times n}$. These matrices are generated under the premise that only one of the elements of each of these matrices is equal to 1, and the other entries are zero, which means that the coupling is applied only in one state variable of the slave system and that the coupling considers only one measured variable.

Finally, the matrix G from equation (7) is given by

$$G = \begin{bmatrix} -\alpha_c & 1 \\ -\gamma_1 & -\gamma_2 \end{bmatrix}, \tag{8}$$

where γ_1, γ_2, and α_c are design parameters of the dynamic coupling. The construction of the coupling system, for the integer-order case, is inspired by the so-called Huygen's coupling [11, 41], which in its simplest form can be interpreted as a damped oscillator.

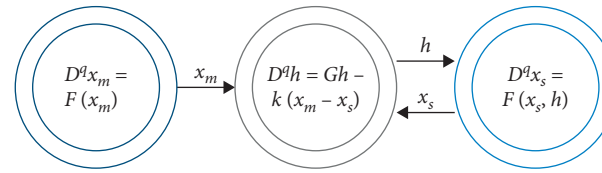

Figure 2: Schematic representation of unidirectionally coupled fractional-order systems interacting via fractional-order dynamic coupling.

Since in this study the focus is on synchronization, it is necessary to give the following definition.

Definition 1. The coupled systems, equation (7), are said to be asymptotically synchronized if

$$\lim_{t\longrightarrow\infty} |x_m - x_s| = 0, \lim_{t\longrightarrow\infty} h = 0. \tag{9}$$

3.1. Local Stability Analysis. In order to investigate the stability of the synchronous solution defined in equation (9), we proceed as follows. First, it is assumed that function F in equation (7) can be written as the sum of linear and nonlinear components, i.e., it is assumed that

$$F(x_i) = Px_i + E(x_i), \tag{10}$$

where $P \in \mathbb{R}^{n\times n}$ is a constant matrix and $E(x_i) \in \mathbb{R}^n$ is a vector containing nonlinear terms.

Next, the synchronization error is defined as $e_p := (x_m - x_s, h)^T$. Note that in the definition of the error, we have included the state h of the dynamic coupling. The reason is because the parameters in the dynamic coupling should be chosen such that, when the systems synchronize, the coupling vanishes. Then, by replacing equations (10) into (7), and computing the corresponding synchronization error dynamics, we obtain

$$D^q e_p = \tilde{A} e_p + g_p(t, e_p), \tag{11}$$

where

$$\begin{aligned} \tilde{A} &= \begin{bmatrix} P & B_1 \\ -KB_2 & G \end{bmatrix}, \\ g_p(t, e_p) &= \begin{bmatrix} f(x_m) - f(x_s) \\ O \end{bmatrix}, \end{aligned} \tag{12}$$

where $O = (0, 0)^T$. Furthermore, note that the term $g_p(t, e_p)$ is a vanishing perturbation [42] because $g_p(t, 0) = 0$. Then, the stability properties of system equation (11) are fully determined by the eigenvalues of the matrix $\tilde{A}$. In particular, following the results presented in Section 2.3, we have that the synchronization error dynamics (equation (11)) is locally asymptotically stable if

$$\left|\arg\lambda_j\right| > \frac{q\pi}{2}, \forall j = 1, 2, \ldots, n. \tag{13}$$

Thus, if it is possible to find values of k, γ_1, γ_2, and α_c such that the above condition is satisfied, then the coupled systems described by equation (7) will achieve complete synchronization, according to Definition 1.

3.2. Statistical Metrics Used for Detecting Complete Synchronization. In this study, the onset of synchronization in the coupled systems (equation (7)) is also numerically studied by computing the following synchronization index.

$$S = \left[\sum_{i=1}^{n} |e_i| + \sum_{i=1}^{n} C_i\right], \tag{14}$$

where n is the dimension of the systems to be synchronized, $|e_i|$ is the absolute value of the synchronization error between the i-th state variable of the master and slave systems, i.e.,

$$\langle e_i \rangle = |x_{mi} - x_{si}|, \tag{15}$$

and C_i is the Pearson correlation [43], computed from the i-th state variable of the master and slave systems described by

$$C_i = \frac{\sigma_{N_{mi}N_{si}}}{\sigma_{N_{mi}}\sigma_{N_{si}}}, \tag{16}$$

where $\sigma_{N_{mi}N_{si}}$ is the covariance between the data obtained from the time series of the state variables of the master and slave systems, and $\sigma_{N_{mi}}\sigma_{N_{si}}$ is the standard deviation obtained from the i-th state variable of the master (slave) oscillator. Finally, when $S = n$, the systems are synchronized.

In the next section, the onset of synchronization with dynamical coupling is studied for two particular fractional-order chaotic systems, namely the Rössler and the Chua oscillators.

4. Application Example 1: Rössler System

The fractional-order version of the well-known Rössler system [44] is given by

$$\begin{aligned} D^q x_1 &= -x_2 - x_3, \\ D^q x_2 &= x_1 + a x_2, \\ D^q x_3 &= b + x_1 x_3 - c x_3, \end{aligned} \tag{17}$$

where x_i, $i = 1, 2, 3$ denotes the state variables and a, b, c are constants.

It has been reported that every system has a limit of integration order for which it is possible to use a fractional-order derivative without stabilizing its dynamics [16, 17, 45]. This could be interpreted to mean that the dynamics described in equation (17) are restricted to have at least one eigenvalue in the unstable region, and this being true only if $|\arg(\lambda)| < q\pi/2$ for at least one of its eigenvalues (λ). With $a = 0.2$, $b = 0.2$, $c = 5.7$, the eigenvalues obtained by the Jacobian matrix evaluated at the equilibrium point $E_1 = (0.007, -0.0351, 0.0351)$ are $\lambda = [0.0970 \pm 0.9952i; -5.6870]$. Since $|\min(\arg(\lambda))| = 1.4736$, the critical order of integration is defined as $q_c = |\min(\arg(\lambda))|(2/\pi)$ (Section 2), and by substitution it is obtained as $q_c = 0.9381$. This result is confirmed by the bifurcation diagram as shown in Figure 3, where the local maxima in x_1 are plotted as a function of the variation of the integration order. Note that the derivative order is the same for all state variables of the system. The inset shows the attractors and the corresponding integration order considered for the developed analysis.

It is worth noting that the bifurcation diagram shown in Figure 3 was numerically calculated using the Adams–Bashforth–Moulton (ABM) method [46] and following the guides for plotting a proper bifurcation diagram [47].

4.1. Dynamically Coupled Fractional-Order Rössler Systems. Now, we consider a pair of identical Rössler systems [44] described by

$$\text{master system} \begin{cases} D^{q_m} x_{1m} = -x_{2m} - x_{3m}, \\ D^{q_m} x_{2m} = x_{1m} + a x_{2m}, \\ D^{q_m} x_{3m} = b + x_{1m} x_{3m} - c x_{3m}, \end{cases} \tag{18}$$

$$\text{slave system} \begin{cases} D^{q_s} x_{1s} = -x_{2s} - x_{3s} - h_2, \\ D^{q_s} x_{2s} = x_{1s} + a x_{2s}, \\ D^{q_s} x_{3s} = b + x_{1s} x_{3s} - c x_{3s}, \end{cases} \tag{19}$$

$$\text{dynamic coupling} \begin{cases} D^{q_d} h_1 = -\alpha_c h_1 + h_2, \\ D^{q_d} h_2 = -\gamma_1 h_1 - \gamma_2 h_2 - k(x_{2m} - x_{2s}), \end{cases} \tag{20}$$

where $x_{m,s}$ denotes the state variables of the master and slave systems, respectively, $h_{1,2}$ denotes the states of the dynamic coupling, k indicates the coupling force between the oscillators, a, b, c are constants of the Rössler model, and q_j, $j = m, s, d$ denotes the integration order of the master, slave, and dynamic coupling, respectively.

Here, we consider the case in which all orders of integration are equal, i.e., $q_m = q_s = q_d$. Then, the dynamic behavior of system equations (18)–(20) is numerically studied as a function of the coupling strength k and the integration order q. For this purpose, equations (18)–(20) are numerically integrated with the following parameter values cf. [11]: $\alpha_c = a$, $\gamma_1 = k$, $\gamma_2 = k$, $a = 0, 2$, $b = 0, 2$, $c = 5, 7$ and initial conditions $[x_{im}, x_{is}, h_i] = [0.1, 0.1, 0.1, -0.2, -0.1, -0.1, 0, 0]$. On the other hand, the coupling strength is varied in the interval $0 \le k \le 20$ with a test size $\Delta_k = 0.2$ and the integration order is varied in the interval $0.96 \le q \le 1$ at $\Delta_q = 2e^{-4}$.

The obtained results are shown in Figure 4(a), where the colors indicate the value of the synchronization index S (see equation (14)). Synchronous behavior is indicated by the dark blue color ($S = 3$), while the remaining colors indicate unsynchronized dynamics.

Moreover, it is evident from Figure 4(a) that there are regions where, for a fixed coupling strength, the limit behavior is completely determined by the integration order. For example, for a fixed coupling strength of $k = 10$, the synchronization index S abruptly changes when the

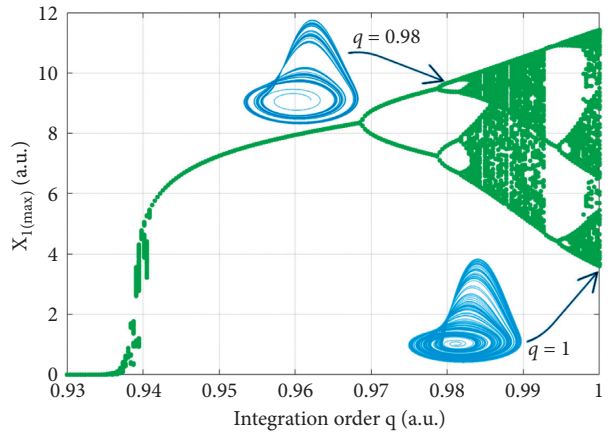

Figure 3: Bifurcation diagram of the Rössler system by modifying the integration order, equation (16). The abscissa axis indicates that the three oscillator state variables have the same integration order.

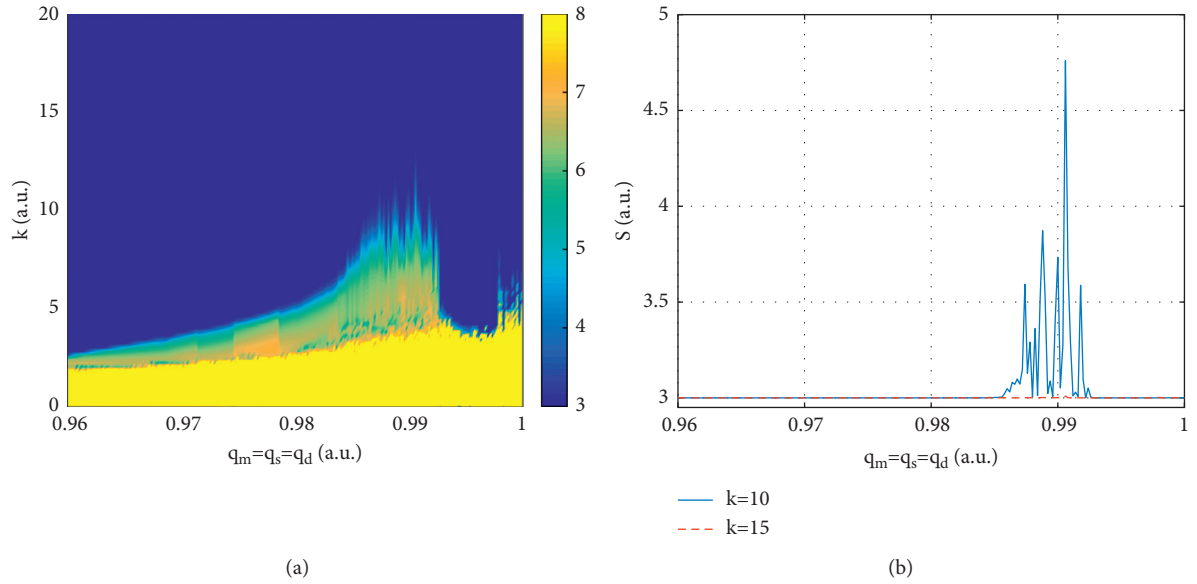

Figure 4: Numerical results for equations (18)–(20). (a) Limit behavior of the system as a function of coupling strength k and integration order q. (b) Synchronization index equation (14) as a function of integration order, for a fixed $k = 10$ and $k = 15$. A value of $S = 3$ indicates complete synchronization.

integration order q is within the interval $0.988 < q < 0.995$, as can be seen in Figure 4(b), but if the coupling strength is increased up to $k = 15$, the systems always achieve complete synchronization.

To validate the synchronization regions obtained by the time series analysis, we conduct a stability analysis following the results presented in Section 3.1. First, let the following synchronization errors be defined as follows: $e_j = x_{jm} - x_{js}$, for $j = 1, 2, 3$, and $e_4 = h_1$, $e_5 = h_2$. Then, the resulting error dynamics are given by

$$\begin{aligned} D^q e_1 &= -e_2 - e_3 + e_5, \\ D^q e_2 &= e_1 + a e_2, \\ D^q e_3 &= x_{1m} x_{3m} - x_{1s} x_{3s} - c e_3, \\ D^q e_4 &= -\alpha_c e_4 + e_5, \\ D^q e_5 &= -\gamma_1 e_4 - \gamma_2 e_5 - k e_2. \end{aligned} \tag{21}$$

Note that the error dynamics in equation (21) can be written in the form of equation (11) with

$$\widetilde{A} = \begin{bmatrix} 0 & -1 & -1 & 0 & 1 \\ 1 & a & 0 & 0 & 0 \\ 0 & 0 & -c & 0 & 0 \\ 0 & 0 & 0 & -\alpha_c & 1 \\ 0 & -k & 0 & -\gamma_1 & -\gamma_2 \end{bmatrix},$$
$$g_p(t, e_p) = \begin{bmatrix} 0 \\ 0 \\ x_{1m}x_{3m} - x_{1s}x_{3s} \\ 0 \\ 0 \end{bmatrix}. \quad (22)$$

Note that the term $g_p(t, e_p)$ in equation (21) is indeed a vanishing perturbation since when the systems synchronize it follows that $x_{1m} = x_{1s}, x_{2m} = x_{2s}$, and $x_{3m} = x_{3s}$ and therefore $g_p(t, 0) = 0$. Consequently, the local stability of the synchronous solution in the coupled systems described by equations (18)–(20) can be determined from the condition in equation (13). In particular, we compute condition equation (13) as a function of the integration order q and the coupling strength k. The obtained results are shown in Figure 5(a), where the blue region corresponds to values of k and q for which condition (13) is not satisfied and thus the synchronous solution is unstable, whereas on the white region, condition (13) is satisfied and then the synchronous solution is expected to be stable. For the sake of comparison, Figure 5(b) shows the overlap of Figure 4 with Figure 5(a). It can be seen that there is a good agreement between the numerical and the analytical results.

Remark 1. In the previous analysis, we have considered the case where the integration order of the systems and the dynamic coupling are the same. However, we also have conducted a numerical study in which the integration orders are different. In particular, we have numerically integrated equations (18)–(20) using the parameter values considered before, as a function of the integration orders of the master and slave systems, while the integration order of the dynamic coupling remains fixed. The integration orders q_m, q_s are varied in the interval $0.98 \leq q_j < 1$, $j = m, s$, and considering the integration order $q_d = 0.985$. The obtained results are shown in Figure 6(a) where the blue areas correspond to synchronization ($S = 3$). From the obtained results, it is clear to see that the integration order of the master and slave systems should be almost the same to observe a synchronized behavior and that larger differences are tolerated as long as the integration order of both systems approaches to one.

On the other hand, Figure 6(b) shows the obtained results for the case that only the integration order of the dynamic coupling is varied, while the oscillators are assumed to have integer order, i.e., $q_m = q_s = 1$. In this case, equations (18)–(20) are numerically integrated by varying the integration order q_d of the dynamic coupling in the interval $0.8 < q_d < 1$ and the corresponding synchronization index, given by equation (14), is calculated. The obtained results are shown in Figure 6(b) for two different coupling forces, where the choice of these k values corresponds to those reported in [11] and those obtained in Figure 4(b).

5. Application Example 2: Chua System

If the Chua system described in [37] is modeled with derivatives of fractional order, then the system described in equation (23) is analyzed.

$$\begin{aligned} D^q x_1 &= \sigma(x_2 - x_1 - \phi(x_1)), \\ D^q x_2 &= x_1 - x_2 + x_3, \\ D^q x_3 &= -\beta x_2, \end{aligned} \quad (23)$$

where D^q is the fractional-order derivative by Caputo's definition, x_i, $i = 1, 2, 3$ denotes the system state variables, σ, β are constants of the Chua circuit, and $\phi(x_1)$ is a nonlinear function defined in equation (24), with constant values a, b.

$$\phi(x_1) = bx_1 + \frac{1}{2}(a - b)\left(|x_1 + 1| - |x_1 - 1|\right). \quad (24)$$

In the same way as for the Rössler fractional-order model, the system described in (23) is analyzed to identify the minimum fractional order that can be modeled without stabilizing the dynamics, namely, $q_c = 0.9541$, since $\sigma = 10, \beta = 14.87, a = -1.27, b = 0.68$. This result is confirmed by the bifurcation diagram as shown in Figure 7, where the local maxima in x_1 are plotted as a function of the integration order variation. The inset shows the attractors and the corresponding integration order.

5.1. Dynamically Coupled Fractional-Order Chua Systems. In the same way as for the Rössler system described above, a pair of Chua oscillators [48] coupled by dynamical connections and defined by the system of equations (25)–(27) is considered.

$$\text{master system} \begin{cases} D^{q_m} x_{1m} = \sigma(x_{2m} - x_{1m} - \phi(x_{1m})), \\ D^{q_m} x_{2m} = x_{1m} - x_{2m} + x_{3m}, \\ D^{q_m} x_{3m} = -\beta x_{2m}, \end{cases} \quad (25)$$

$$\text{slave system} \begin{cases} D^{q_s} x_{1s} = \sigma(x_{2s} - x_{1s} - \phi(x_{1s})), \\ D^{q_s} x_{2s} = x_{1s} - x_{2s} + x_{3s}, \\ D^{q_s} x_{3s} = -\beta x_{2s} - h_1, \end{cases} \quad (26)$$

$$\text{dynamic coupling} \begin{cases} D^{q_d} h_1 = -\alpha_c h_1 + h_2, \\ D^{q_d} h_2 = -\gamma_1 h_1 - \gamma_2 h_2 - k(x_{3m} - x_{3s}), \end{cases} \quad (27)$$

where $x_{m,s}$ denotes the state variables of the master and slave systems, respectively, $h_{1,2}$ is the states of the dynamic coupling, $\phi(x_{1m,s})$ is the nonlinear function defined in equation (28), and k is the coupling force between the systems.

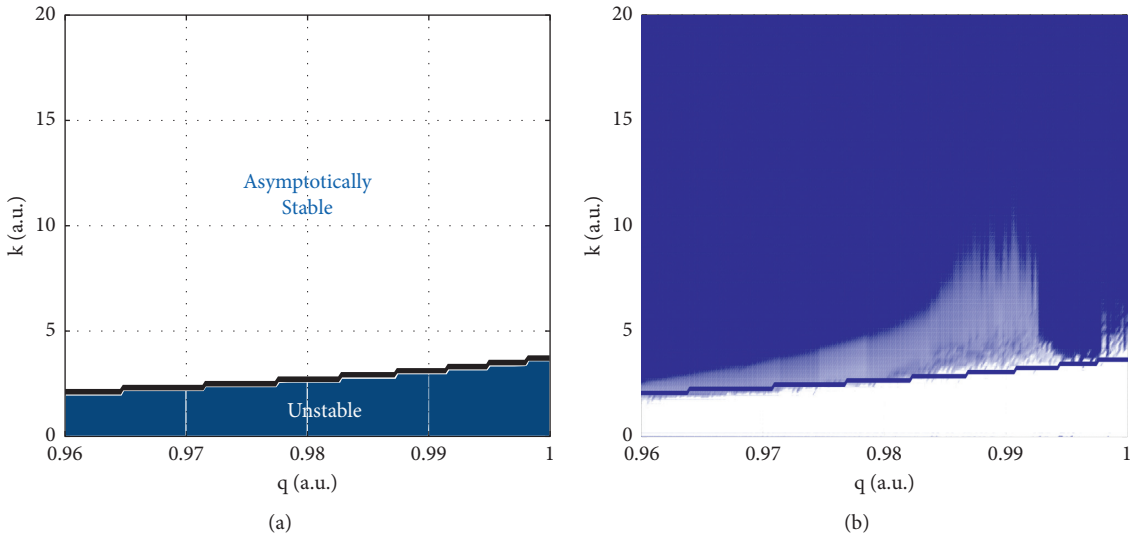

Figure 5: (a) Stability analysis from linear error dynamics for the coupled Rössler system shown in equation (21). (b) Overlap of the analytical result in the synchronization map shown in Figure 4(a).

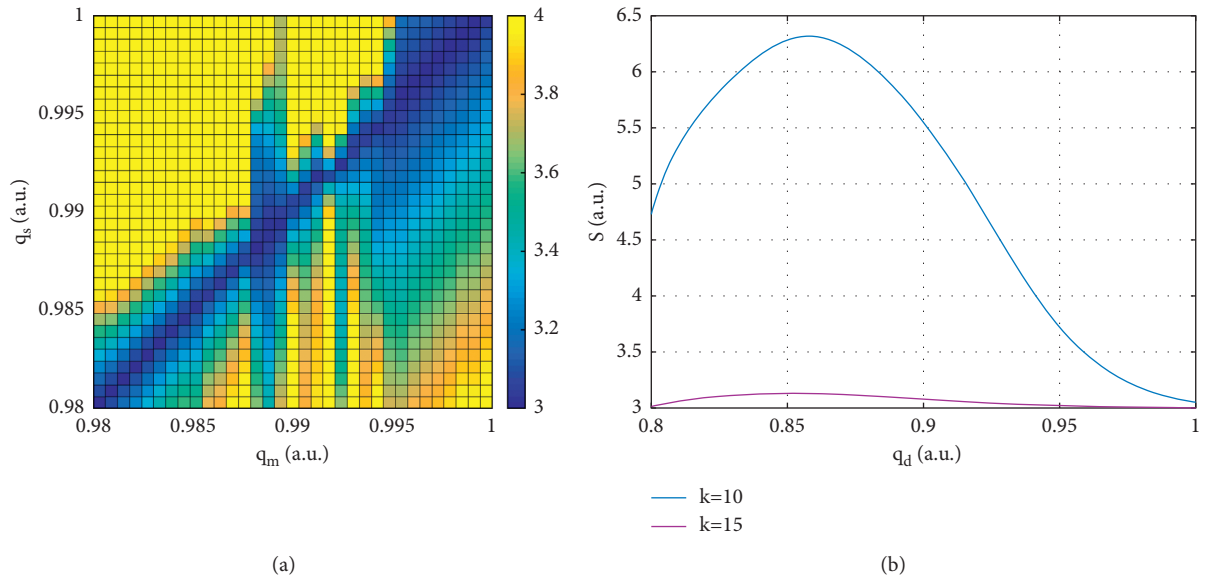

Figure 6: (a) Synchronization map as a function of integration orders q_m and q_s of master and slave Rössler systems, equations (18)–(20), and considering a fixed integration order of $q_d = 0.985$ in the dynamic coupling. (b) Synchronization map for system equations (18)–(20) as a function of the integration order q_d of the dynamic coupling, while considering that the master and slave oscillators have fixed integer order, i.e., $q = 1$.

$$\phi(x_{1i}) = bx_{1i} + \frac{1}{2}(a-b)\left(\left|x_{1i}+1\right| - \left|x_{1i}-1\right|\right), \text{for } i = m, s. \tag{28}$$

As reported in [11], the following values are used in this study for all analyzes developed; $\sigma = 10, \beta = 14.87, a = -1.27, b = -0.68$ for $\alpha_c = 1, \gamma_1 = k, \gamma_2 = k/5$, and initial conditions $[x_{im}, x_{is}, h_i] = [0.1, 0.1, 0.1, -0.2, -0.1, -0.1, 0, 0]$. On the other hand, the coupling strength is varied in the interval $0 \le k \le 60$ with $\Delta_k = 0.5941$ and the integration order is varied in the interval $0.965 \le q \le 1$ for step size.

To identify synchronization regions in the coupled Chua systems of fractional order, an analysis of the coupling force as a function of the integration order is developed. The obtained results are shown in Figure 8. Note that the color map represents the value of the metric S and that the darkest shade of blue represents $S = 3$, which means that the systems have reached full synchronization.

Analogous to the stability analysis performed for the coupled Rössler system, the dynamic error model of the coupled pair of Chua oscillators described in equations (25)–(27) is described by

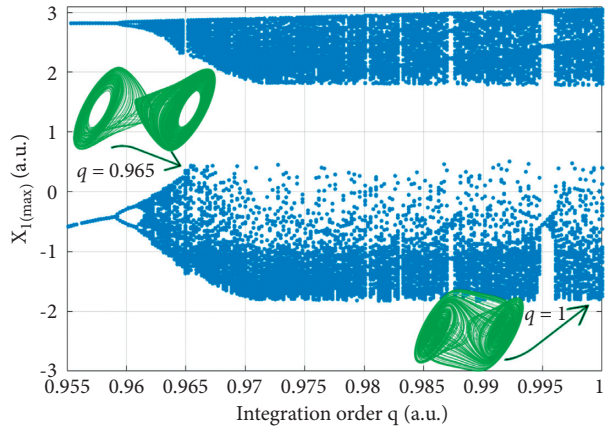

Figure 7: Bifurcation diagram of the Chua system by modifying the integration order, equation (23). The abscissa axis indicates that the three oscillator state variables have the same integration order.

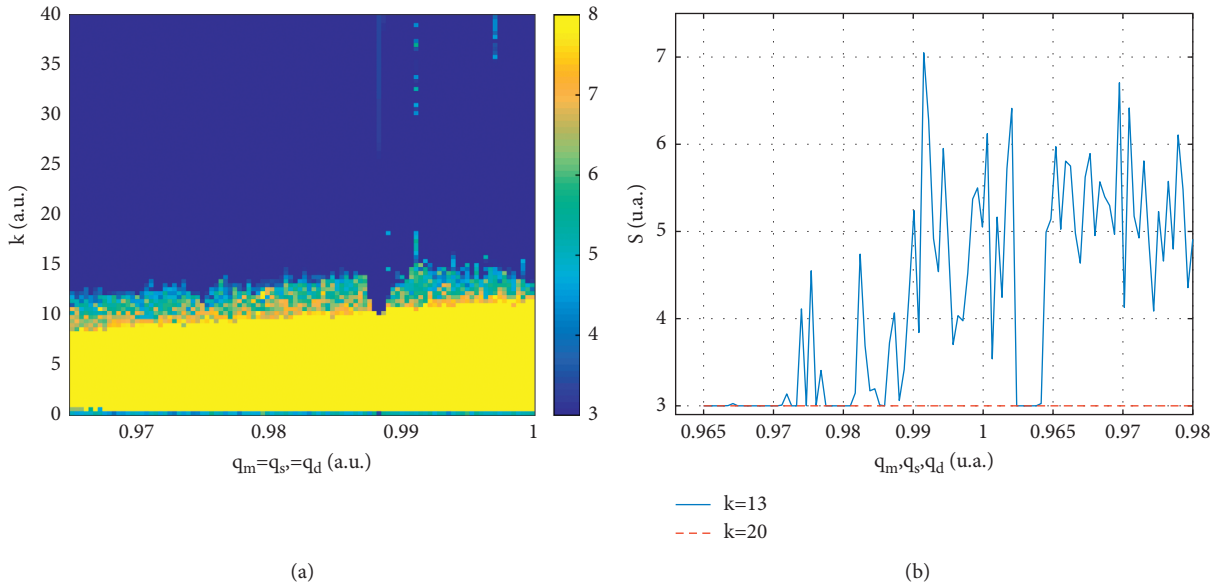

Figure 8: Numerical result equations (25)–(27). (a) Limit behavior of the system as a function of coupling strength k and integration order q. (b) Synchronization index equation (14) as a function of integration order, for a fixed $k = 13$ and $k = 20$. A value of $S = 3$ indicates complete synchronization.

$$\begin{aligned} D^q e_1 &= \sigma\left(e_2 - e_1 - \left[\phi\left(x_{1m}\right) - \phi\left(x_{1s}\right)\right]\right), \\ D^q e_2 &= e_1 - e_2 + e_3, \\ D^q e_3 &= -\beta e_2 - h_1, \\ D^q e_4 &= -\alpha e_4 + e_5, \\ D^q e_5 &= -\gamma_1 e_4 - \gamma_2 e_5 - k e_3. \end{aligned} \tag{29}$$

Due to the nature of the nonlinearity of the Chua circuit, it is not possible to perform the same analysis as in the Rössler system; instead, it is necessary to use the Jacobian of the error model, equation (30), evaluated in one of the equilibrium points of the system. Since the Chua circuit has symmetric equilibrium points located at $E_1 = (-1.841, 0.0004474, 2.179)$ for the previously defined values, the choice of one of these points does not affect the analysis.

$$\tilde{J} = \begin{bmatrix} -\sigma - \sigma p(x) & \sigma & 0 & 0 & 0 \\ 1 & -1 & 1 & 0 & 0 \\ 0 & -\beta & 0 & 1 & 0 \\ 0 & 0 & 0 & -\alpha_c & 1 \\ 0 & 0 & 0 & -\gamma_1 & -\gamma_2 \end{bmatrix}, \tag{30}$$

where $p(x) = 1/2\,(b\,\mathrm{sign}\,(|x| - 1) + b) - 1/2\,(a\,\mathrm{sign}\,(|x| - 1) - a))$.

After defining the system shown in equation (30), it is possible to perform the stability system analysis, where the stability of the dynamic model of the Chua coupling error is sought by modifying the integration order and the coupling force. The analytical result is shown in Figure 9(a) and then compared with the map obtained from the time series

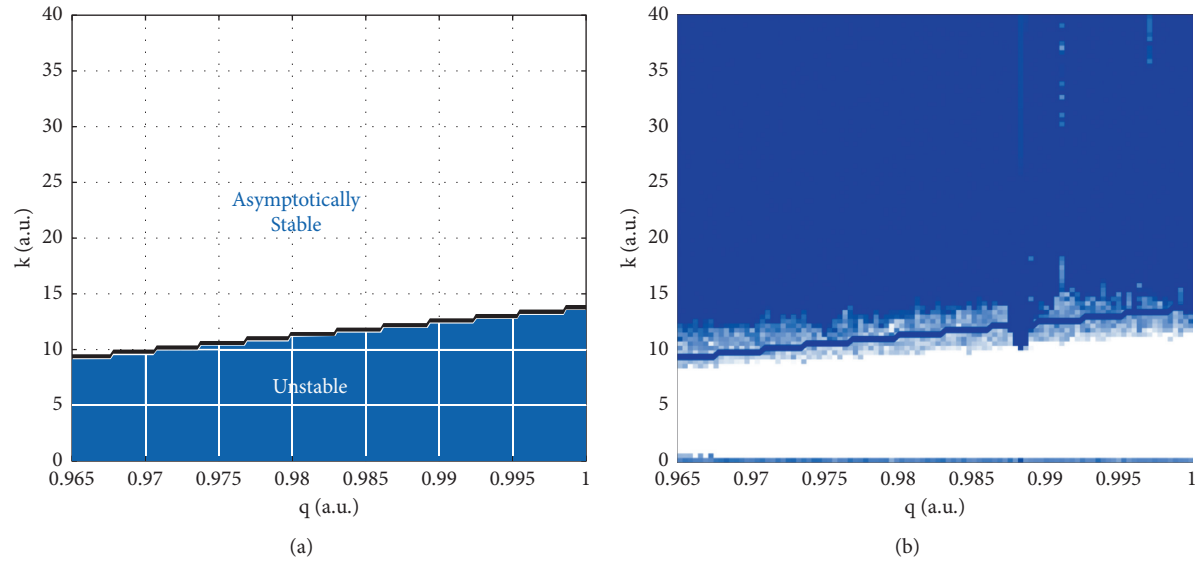

Figure 9: (a) Stability analysis from linear error dynamics for the coupled Chua system as shown in equation (29). (b) Overlay of the analytical result in the synchronization map as shown in Figure 8(a).

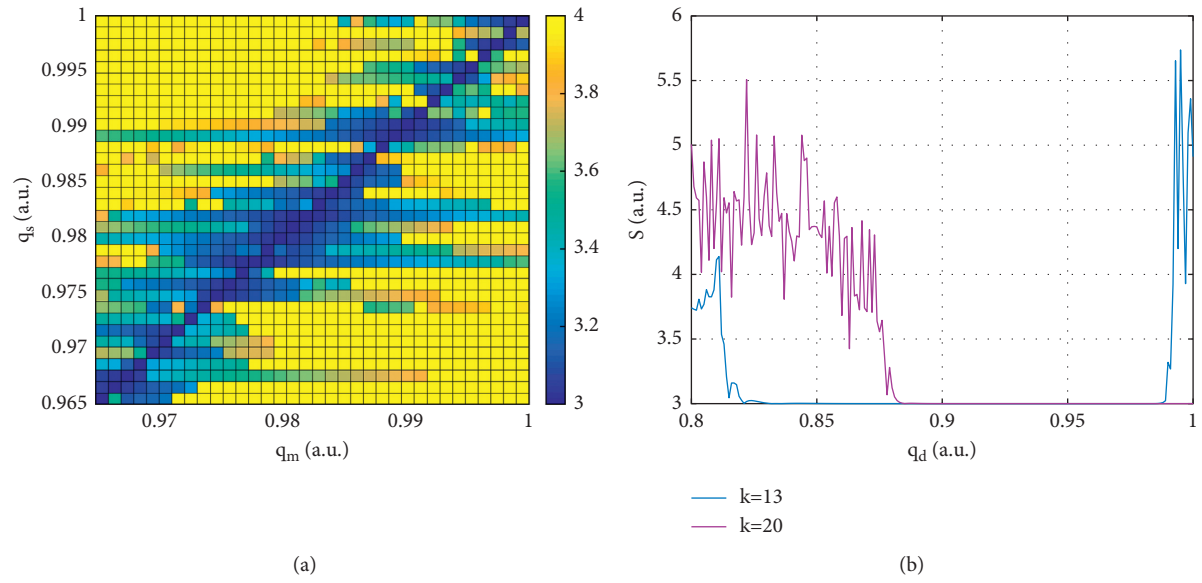

Figure 10: Synchronization map as a function of integration orders for the Chua systems, equations (25)–(27). (a) The integration order of the master and slave is varied, whereas the integration order of the dynamic coupling remains fixed. (b) The order of the dynamic coupling is varied, while the master and slave systems have fixed integer order $q = 1$.

analysis in Figure 8(b). As with the Rössler case, the analytical result is able to describe the boundary at which the system is unstable.

Remark 2. Similarly, to the case of the Rössler systems, we have also investigated the onset of synchronization in the fractional-order Chua oscillators as a function of the derivative orders in the oscillators while keeping the coupling system at fixed q_d, resulting in the map as shown in Figure 10(a). The results from the analysis of the behavior of the Chua systems under the dynamic coupling integration order variation are shown in Figure 10(b), where the integration orders of the oscillators remain fixed at $q_{m,s} = 1$.

6. Discussion

From the results presented in this study, it is possible to confirm the research question formulated in the introduction of this study, according to which the use of dynamic couplings in chaotic systems of fractional order is able to induce complete synchronization, as it has been reported in their counterparts of integer order. Likewise, it is noteworthy

to mention that the transition from unsynchronized behavior to synchronization is not abrupt, since there exists a region where the coupled systems may exhibit some sort of intermittency phenomenon. These areas are indicated by the blurred areas in Figures 4 and 8.

If the oscillators are modeled with fractional derivatives but a fixed integration order is maintained in the coupling system, the desired synchronous behavior is achieved only under the condition that both oscillators have the same integration order. Small variations in the integration order in some of the models cause the systems to lose their synchrony, as shown in Figures 6(a) and 10(a). In contrast, the synchronization seems to have some robustness against variations in the integration order of the dynamic coupling, provided that the oscillators have the same integration order, as shown in the numerical results presented in Figures 6(b) and 10(b).

It is also noteworthy that in the (q, k) plane there exist regions where the systems are easier to synchronize. This is explained by the bifurcation diagrams of the isolated oscillators, given in Figures 3 and 7, where the modification in the integration order causes important qualitative changes in the dynamics of the system, where both models are able to present chaotic or periodic behavior, for a set of parameters where the integer-order dynamics is always chaotic, only due to the modification of the derivative order. This is not only an indication that the synchronization between the systems requires lower coupling forces for periodic and quasiperiodic behaviors but also a clear indication that the change in the integration order can be associated with a modification of the vector field, which can also be achieved in the integer-order system by modifying the system parameters [17].

The local stability analysis is in good agreement with the numerical analysis, as shown in Figures 5 and 9. It should be noted, however, that the stability conditions are only necessary conditions. This result is similar when talking about the stability of the equilibrium points in a chaotic system, where obtaining unstable saddle points with index 2 favors the occurrence of chaotic behavior but does not guarantee the occurrence of a strange attractor in the system [49].

It is worth mentioning that in the cases of analysis where the equations to solve do not have the same derivative order, the algorithm proposed by Petráš is implemented [50]; otherwise, the Adams–Bashforth–Moulton (ABM) method is used [46], which is a generalization of the classical ABM integrator that is well known in the resolution of first-order switching system problems [40, 51].

Notice that the results presented here have been obtained under the assumption of identical oscillators. It is still necessary to determine the robustness of the dynamic coupling against parameter mismatches or external disturbances in the oscillators.

7. Conclusions

We have analyzed the onset of synchronization in fractional-order chaotic systems interacting via a linear time-invariant dynamic coupling, which also is described by fractional derivatives. The obtained results have shown the ability of the dynamic coupling to induce synchronization in the systems, and the strong influence of the integration order on the onset of synchronized behavior has been demonstrated.

Among the observed limitations is that dynamic coupling is sensitive to variations in the integration order of the systems. Therefore, the master and slave systems should have the same integration order. Furthermore, it has been shown that the linearization approach used here to study the local stability of the synchronous solution only provides necessary conditions. Further investigation is needed to derive stronger stability conditions. Perhaps the use of transverse Lyapunov exponents can solve this problem. It remains as future work to extend these results to the bidirectional case and also to the case of networks. Also, it would be interesting to investigate whether any emergent behavior or other types of synchronous behaviors can occur in the coupled systems depending on the integration order of both the systems and the coupling.

Finally, we would like to point out that the results presented here apply to the Caputo definition of fractional derivative. Moreover, these results were obtained using two different numerical approaches, namely, the ABM and the Petráš integrator method. As future work, we plan to compare these results with different fractional operators, such as the Riemann–Liouville operator or the Atangana–Baleanu operator, to name a few.

Data Availability

The data used to support the findings of the study are included within the article.

Conflicts of Interest

The authors declare that they have no conflicts of interest.

Acknowledgments

J. L. E. M. thanks CONACYT for financial support (CVU-706850, project: A1-S-26123), J. P. R. for the opportunity to realize a postdoctoral stay at CICESE, and P. A. M. R. for all his teachings and fruitful discussion.

References

[1] A. Pikovsky, J. Kurths, M. Rosenblum, and J. Kurths, *Synchronization: A Universal Concept in Nonlinear Sciences*, Cambridge University Press, Cambridge ,UK, 2003.

[2] A. Arenas, A. Díaz-Guilera, J. Kurths, Y. Moreno, and C. Zhou, "Synchronization in complex networks," *Physics Reports*, vol. 469, no. 3, pp. 93–153, 2008.

[3] G. V. Osipov, J. Kurths, and C. Zhou, *Synchronization in Oscillatory Networks*, Springer Science & Business Media, Berlin, Germany, 2007.

[4] O. Boubaker and S. Jafari, *Recent Advances in Chaotic Systems and Synchronization: From Theory to Real World Applications*, Elsevier, Amsterdam, Netherland, 2018.

[5] A. L. Fradkov, B. Andrievsky, and R. J. Evans, "Controlled synchronization under information constraints," *Physical Review E*, vol. 78, no. 3, Article ID 036210, 2008.

[6] H. Nijmeijer and A. Rodriguez-Angeles, *Synchronization of Mechanical Systems*, World Scientific, Singapore, 2003.

[7] A. L. Fradkov and A. Y. Markov, "Adaptive synchronization of chaotic systems based on speed gradient method and passification," *IEEE Transactions on Circuits and Systems I: Fundamental Theory and Applications*, vol. 44, no. 10, pp. 905–912, 1997.

[8] A. Ruiz-Silva and J. G. Barajas-Ramírez, "Cluster synchronization in networks of structured communities," *Chaos, Solitons & Fractals*, vol. 113, pp. 169–177, 2018.

[9] A. Ruiz-Silva, "Synchronization patterns on networks of pancreatic β-cell models," *Physica D: Nonlinear Phenomena*, vol. 416, Article ID 132783, 2021.

[10] A. Ruiz-Silva, H. E. Gilardi-Velázquez, and E. Campos, "Emergence of synchronous behavior in a network with chaotic multistable systems," *Chaos, Solitons & Fractals*, vol. 151, Article ID 111263, 2021.

[11] J. Ramirez, A. Arellano-Delgado, and H. Nijmeijer, "Enhancing master-slave synchronization: the effect of using a dynamic coupling," *Physical Review E*, vol. 98, no. 1, Article ID 012208, 2018.

[12] W. d. Jonge, J. P. Ramirez, and H. Nijmeijer, "Dynamic coupling enhances network synchronization," *IFAC-PapersOnLine*, vol. 52, no. 16, pp. 610–615, 2019.

[13] J. Pena Ramirez, E. Garcia, and J. Alvarez, "Master-slave synchronization via dynamic control," *Communications in Nonlinear Science and Numerical Simulation*, vol. 80, Article ID 104977, 2020.

[14] J. M. Munoz-Pacheco, L. C. Lujano-Hernández, C. Muñiz-Montero et al., "Active realization of fractional-order integrators and their application in multiscroll chaotic systems," *Complexity*, vol. 2021, Article ID 6623855, 16 pages, 2021.

[15] M. A. Platas-Garza, E. Zambrano-Serrano, J. R. Rodríguez-Cruz, and C. Posadas-Castillo, "Implementation of an encrypted-compressed image wireless transmission scheme based on chaotic fractional-order systems," *Chinese Journal of Physics*, vol. 71, pp. 22–37, 2021.

[16] X.-Y. Wang and M.-J. Wang, "Dynamic analysis of the fractional-order Liu system and its synchronization," *Chaos: An Interdisciplinary Journal of Nonlinear Science*, vol. 17, no. 3, Article ID 033106, 2007.

[17] J. L. Echenausía-Monroy, H. E. Gilardi-Velázquez, R. Jaimes-Reátegui, V. Aboites, and G. Huerta-Cuellar, "A physical interpretation of fractional-order-derivatives in a jerk system: electronic approach," *Communications in Nonlinear Science and Numerical Simulation*, vol. 90, Article ID 105413, 2020.

[18] J. L. Echenausía-Monroy, G. Huerta-Cuellar, R. Jaimes-Reátegui et al., "Multistability emergence through fractional-order-derivatives in a pwl multi-scroll system," *Electronics*, vol. 9, no. 6, p. 880, 2020.

[19] C. Wang, "Fractional-order sliding mode synchronization for fractional-order chaotic systems," *Advances in Mathematical Physics*, vol. 2018, no. 1, 9 pages, Article ID 3545083, 2018.

[20] J. M. Munoz-Pacheco, C. Posadas-Castillo, and E. Zambrano-Serrano, "The effect of a non-local fractional operator in an asymmetrical glucose-insulin regulatory system: analysis, synchronization and electronic implementation," *Symmetry*, vol. 12, no. 9, Article ID 1395, 2020.

[21] S. Yang, C. Hu, J. Yu, and H. Jiang, "Finite-time cluster synchronization in complex-variable networks with fractional-order and nonlinear coupling," *Neural Networks*, vol. 135, pp. 212–224, 2021.

[22] P.-Y. Xiong, H. Jahanshahi, R. Alcaraz, Y.-M. Chu, J. F. Gómez-Aguilar, and F. E. Alsaadi, "Spectral entropy analysis and synchronization of a multi-stable fractional-order chaotic system using a novel neural network-based chattering-free sliding mode technique," *Chaos, Solitons & Fractals*, vol. 144, Article ID 110576, 2021.

[23] X. Wu, H. Bao, and J. Cao, "Finite-time inter-layer projective synchronization of caputo fractional-order two-layer networks by sliding mode control," *Journal of the Franklin Institute*, vol. 358, no. 1, pp. 1002–1020, 2021.

[24] A. Sambas, S. Vaidyanathan, I. M. Moroz et al., "A simple multi-stable chaotic jerk system with two saddle-foci equilibrium points: analysis, synchronization via backstepping technique and multisim circuit design," *International Journal of Electrical and Computer Engineering*, vol. 11, no. 4, pp. 2088–8708, 2021.

[25] M. Tabasi and S. Balochian, "Synchronization of the chaotic fractional-order genesio-tesi systems using the adaptive sliding mode fractional-order controller," *Journal of Control, Automation and Electrical Systems*, vol. 29, no. 1, pp. 15–21, 2018.

[26] A. Nourian and S. Balochian, "The adaptive synchronization of fractional-order liu chaotic system with unknown parameters," *Pramana*, vol. 86, no. 6, pp. 1401–1407, 2016.

[27] P. Y. Dousseh, C. Ainamon, C. H. Miwadinou, A. V. Monwanou, and J. B. Chabi Orou, "Chaos in a financial system with fractional order and its control via sliding mode," *Complexity*, vol. 2021, Article ID 4636658, 15 pages, 2021.

[28] M. Tabasi and S. Balochian, "Synchronization of fractional order chaotic system of sprott circuit using fractional active fault tolerant controller," *International Journal of Dynamics and Control*, vol. 9, pp. 1–8, 2021.

[29] G. Li, X. Zhang, and H. Yang, "Complexity analysis and synchronization control of fractional-order Jafari-Sprott chaotic system," *IEEE Access*, vol. 8, pp. 53360–53373, 2020.

[30] P. Anbalagan, E. Hincal, E. Hincal et al., "A Razumikhin approach to stability and synchronization criteria for fractional order time delayed gene regulatory networks," *AIMS Mathematics*, vol. 6, no. 5, pp. 4526–4555, 2021.

[31] B. Chen and J. Chen, "Razumikhin-type stability theorems for functional fractional-order differential systems and applications," *Applied Mathematics and Computation*, vol. 254, pp. 63–69, 2015.

[32] J. A. Gallegos and M. A. Duarte-Mermoud, "On the Lyapunov theory for fractional order systems," *Applied Mathematics and Computation*, vol. 287-288, pp. 161–170, 2016.

[33] S. Liu, W. Jiang, X. Li, and X.-F. Zhou, "Lyapunov stability analysis of fractional nonlinear systems," *Applied Mathematics Letters*, vol. 51, pp. 13–19, 2016.

[34] Y. Li, Y. Chen, and I. Podlubny, "Stability of fractional-order nonlinear dynamic systems: Lyapunov direct method and generalized Mittag-Leffler stability," *Computers & Mathematics with Applications*, vol. 59, no. 5, pp. 1810–1821, 2010.

[35] Y. Li, Y. Chen, and I. Podlubny, "Mittag–Leffler stability of fractional order nonlinear dynamic systems," *Automatica*, vol. 45, no. 8, pp. 1965–1969, 2009.

[36] E. Ott, "Strange attractors and chaotic motions of dynamical systems," *Reviews of Modern Physics*, vol. 53, no. 4, pp. 655–671, 1981.

[37] L. Chua, *The Genesis of Chua's circuit, Electronics Research Laboratory, College of Engineering*, University of California, Berkeley, CA, USA, 1992.

[38] K. Diethelm, *The Analysis of Fractional Differential Equations: An Application-Oriented Exposition Using Differential Operators of Caputo Type*, Springer Science & Business Media, Berlin, Germany, 2010.

[39] I. Podlubny, *Fractional Differential Equations: An Introduction to Fractional Derivatives, Fractional Differential Equations, to Methods of their Solution and Some of their Applications*, Elsevier, Amsterdam, Netherland, 1998.
[40] E. Zambrano-Serrano, E. Campos-Cantón, and J. M. Muñoz-Pacheco, "Strange attractors generated by a fractional order switching system and its topological horseshoe," *Nonlinear Dynamics*, vol. 83, no. 3, pp. 1629–1641, 2016.
[41] J. Ramirez, L. Olvera, H. Nijmeijer, and J. Alvarez, "The sympathy of two pendulum clocks: beyond Huygens' observations," *Scientific Reports*, vol. 6, no. 1, pp. 1–16, 2016.
[42] H. Khalil, *Nonlinear Systems*, Prentice-Hall, Englewood Cliffs, NJ, USA, 3rd edition, 2002.
[43] I. Echegoyen, V. Vera-Ávila, R. Sevilla-Escoboza, J. H. Martínez, and J. M. Buldú, "Ordinal synchronization: using ordinal patterns to capture interdependencies between time series," *Chaos, Solitons & Fractals*, vol. 119, pp. 8–18, 2019.
[44] O. Rössler, "An equation for continuous chaos," *Physics Letters A*, vol. 57, no. 5, pp. 397-398, 1976.
[45] S. Bhalekar and M. Patil, "Singular points in the solution trajectories of fractional order dynamical systems," *Chaos: An Interdisciplinary Journal of Nonlinear Science*, vol. 28, no. 11, Article ID 113123, 2018.
[46] K. Diethelm, N. J. Ford, and A. D. Freed, "A predictor-corrector approach for the numerical solution of fractional differential equations," *Nonlinear Dynamics*, vol. 29, no. 1/4, pp. 3–22, 2002.
[47] A. Jafari, I. Hussain, F. Nazarimehr, S. M. R. H. Golpayegani, and S. Jafari, "A simple guide for plotting a proper bifurcation diagram," *International Journal of Bifurcation and Chaos*, vol. 31, no. 1, Article ID 2150011, 2021.
[48] L. Chua, M. Komuro, and T. Matsumoto, "The double scroll family," *IEEE Transactions on Circuits and Systems*, vol. 33, no. 11, pp. 1072–1118, 1986.
[49] R. Hilborn, *Chaos and Nonlinear Dynamics: An Introduction for Scientists and Engineers*, Oxford University Press on Demand, Oxford, UK, 2000.
[50] I. Petráš, "Fractional-order chaotic systems," in *Fractional-Order Nonlinear Systems*, pp. 103–184, Springer, Berlin, Germany, 2011.
[51] H. E. Gilardi-Velázquez and E. Campos-Cantón, "Nonclassical point of view of the Brownian motion generation via fractional deterministic model," *International Journal of Modern Physics C*, vol. 29, no. 3, Article ID 1850020, 2018.

Hindawi
Complexity
Volume 2021, Article ID 9789470, 16 pages
https://doi.org/10.1155/2021/9789470

Corrigendum

Corrigendum to "Chaos in a Financial System with Fractional Order and Its Control via Sliding Mode"

Paul Yaovi Dousseh,[1] Cyrille Ainamon,[1] Clément Hodévèwan Miwadinou,[1,2,3] Adjimon Vincent Monwanou,[1] and Jean Bio Chabi Orou[1]

[1]*Laboratoire de Mécaniques des fluides,de la Dynamique Non-linéaire et de la Modélisation des Systèmes Biologiques (LMFDNMSB), Institut de Mathématiques et de Sciences Physiques (IMSP), Porto-Novo, Benin*
[2]*Département de Physique, ENS-Natitingou, Université des Sciences Technologies,Ingénierie et Mathématiques (UNSTIM), Abomey, Benin*
[3]*Laboratoire de Physique et Applications du Centre Universitaire de Natitingou, Université Nationale des Sciences,Technologiques,Ingénierie et Mathématiques (UNSTIM), Abomey, Benin*

Correspondence should be addressed to Clément Hodévèwan Miwadinou; clement.miwadinou@imsp-uac.org

Received 21 August 2021; Accepted 21 August 2021; Published 20 November 2021

In the article titled "Chaos in a Financial System with Fractional Order and Its Control via Sliding Mode" [1], the authors identified errors in the code related to the minimum effective dimension of the derivation order q_3. The authors have corrected this error, which has resulted in a number of changes to the numerical results and to Figures 4 and 7. The authors confirm that this change does not affect the conclusions of the article, and with the agreement of the editorial board, the corrected article is as follows.

Abstract

In this paper, the dynamical behaviors and chaos control of a fractional-order financial system are discussed. The lowest fractional order found from which the system generates chaos is 2.49 for the commensurate order case and 2.57 for the incommensurate order case. Also, the period-doubling route to chaos was found in this system. The results of this study were validated by the existence of a positive Lyapunov exponent. Besides, in order to control chaos in this fractional-order financial system with uncertain dynamics, a sliding mode controller is derived. The proposed controller stabilizes the commensurate and incommensurate fractional-order systems. Numerical simulations are carried out to verify the analytical results.

1. Introduction

Investigating chaos in dynamical systems is one of the most interesting topics which have been carried out extensively in different scientific fields such as medicine [1], biology [2], mathematics [3], and many others. In the literature, several dynamical systems presenting chaotic behaviors have been proposed such as the Lorenz system [4], the Chen system [5], the Lü system [6], and the Newton–Leipnik system [7]. During the last decades, many researchers have taken a great interest in the subject of chaotic systems' control. In [8], the authors used the sliding mode controller to eliminate chaos in a new uncertain chaotic dynamical system (Liu system). In [9], a robust adaptive sliding mode controller is used to remove chaos in a novel class of chaotic systems. Chaos control in the Lorenz, Chen, and Lü systems using the backstepping technique is performed in [10]. Chaos control in the Newton–Leipnik system is carried out using linear feedback controllers in [11].

Fractional calculus involving fractional-order derivatives, i.e., derivatives of noninteger order, has a history of over 300 years [12]. During those years, this theory was considered a purely mathematical concept. Recently, fractional-order derivatives have been widely applied to several systems in many areas of research to better understand these

systems [13–19]. Indeed, fractional-order derivatives, possessing memory, can describe more accurately different nonlinear phenomena than integer-order derivatives [20, 21]. Very recently, some interesting developments and results in the theory and applications of fractional calculus have been obtained in the literature. For example, see [22], in which the authors used Lie symmetry analysis to obtain an exact solution of the conformable heat equation. In [23], useful properties of the Lie group method with the invariance subspace method are combined to obtain a large family of exact solutions for the fractional Black–Scholes equation. Also, in [24], the necessary optimality conditions of the Euler–Lagrange type of variational problems in which variational functional depends on Atangana–Baleanu derivative are proved. Finally, the Hydon method to determine discrete symmetries for a differential equation is employed to construct discrete symmetries for a family of ordinary, partial, and fractional differential equations in [25]. In fractional-order systems, it was found that the systems with derivation orders q_1, q_2, and q_3 generate chaotic behaviors when $q = q_1 + q_2 + q_3 < 3$ [13–19]; in other words, chaos continues to exist in these systems for derivation orders less than 3.

Since the discovery of chaos by Strotz et al. [26] in an economical model, various financial and economical models have been proposed in the literature to better understand these complex dynamics of these systems. Among others, we have the forced van der Pol model [27], the IS-LM model (Investment Saving-Liquidity Money) [28], the new hyperchaotic finance model [29], and many others [30–33]. In 2001, Ma and Chen [34] proposed a very interesting model to represent the dynamics of financial systems. The analysis of this model revealed interesting dynamics and also an extreme sensitivity to the initial conditions of the variables and parameters of the system. Financial variables such as the exchange rate, gross domestic product, interest rate, and production, to name a few, have a long memory [35, 36], i.e., all future fluctuations of these financial variables are influenced by past and present fluctuations. Thus, fractional-order derivatives, possessing memory effect, can describe more accurately the dynamics of financial systems than integer-order derivatives. In 2008, Chen [14] studied the generalization of Ma and Chen system [34], i.e., considered this system with fractional order. Two routes to chaos were found in this fractional-order system, namely, the route to chaos via intermittency and period-doubling. The lowest derivation order found for which the system generates chaotic behavior was 2.55 in the commensurate fractional-order case and 2.35 in the incommensurate fractional-order case.

Also, to better understand the dynamics of financial systems, a new model was presented by Liao et al. [37] in 2020. Compared to the model proposed by Ma and Chen [34], this new model takes into account the fact that the price index is affected by investment demand. The study of this model was carried out numerically by the authors. It was found that the interaction between three factors in this financial system results in a complex behavior of the system. Complex dynamics behaviors such as period-doubling and chaos were found in this system [37]. Chaotic behavior is undesirable in financial systems because it makes predictions in finance and economics impossible and, therefore, constitutes a risk for investments. Thus, its control in the presence of uncertainties related to the parameters of the system and external disturbances turned out to be necessary.

Chaos control in financial systems has been widely studied in the literature. Several techniques have been designed for the control of financial chaotic systems [38, 39]. One of these techniques is the sliding mode control. Indeed, as a mathematical model cannot represent a physical situation perfectly, it is necessary to consider the uncertainties linked to the values of the system parameters and also any external disturbances to which a model may be subjected. Therefore, it is better to design a robust controller, i.e., insensitive to uncertainties and external disturbances. The sliding mode control is a powerful technique to robustly control uncertain dynamical systems subject to uncertainties and external disturbances [40–42]. The design of the sliding mode controller has been widely discussed in the literature [43–46]. These different criteria make the sliding mode control the right technique for controlling financial systems with uncertain dynamics. For example, in [38], a fractional-order sliding mode controller was designed to eliminate the chaotic behavior in an economical system in the presence of model uncertainties and external disturbances.

Motivated by the above discussions, in this paper, chaos in the financial system presented by Liao et al. [37] with fractional order and robust control of this chaotic behavior are investigated. The study of chaos in this system with fractional order is carried out for the commensurate and the incommensurate fractional order to find the minimum effective dimension, i.e., the lowest sum of derivation orders from which chaos arises in the system using analytical methods and numerical simulations. Finally, a sliding mode control law is designed to control the chaos in this fractional-order financial system with or without uncertainties and external disturbances. Numerical simulations are carried out to show that the controller can suppress chaos in the system and also can stabilize and maintain the system states on the sliding surface.

The remaining part of this paper is structured as follows: In Section 2, some definitions and analytical conditions for the existence of chaos in fractional-order systems are given. The fractional-order financial system is presented in Section 3. The dynamics study of this fractional-order financial system is carried out in Section 4. In Section 5, a simple but robust fractional-order sliding mode controller is designed to globally and asymptotically stabilize the system. Numerical simulations are performed in Section 6 to verify the analytical results obtained. This work ends with a conclusion in Section 7.

2. Definitions and Lemma

Fractional calculus is a generalization of ordinary calculus. Some definitions of fractional derivatives are given in [12]. The most commonly used definitions in the literature are the Grunwald–Letnikov, the Riemann–Liouville, and the Caputo definitions [12].

During this work, we will only use the Caputo fractional derivative, because unlike the Riemann–Liouville definition of fractional derivative which involves initial conditions of fractional order, this fractional derivative involves initial conditions which take the same form as the case of the integer order, which has a physical interpretation. The Caputo (C) fractional derivative of order q is given by

$$ {}_a^C D_t^q f(t) = \frac{1}{\Gamma(n-q)} \int_a^t (t-\tau)^{n-q-1} f^{(n)}(\tau) \mathrm{d}\tau, \quad n-1 < q < n, \tag{1} $$

with a and t which are numbers representing the limits of the operator ${}_a^c D_t^q$. The symbol $\Gamma(.)$ is the gamma function.

Definition 1 (see [47–49]). A saddle equilibrium point is a fixed point at which the equivalent linearized model has at least one eigenvalue in the stable region (eigenvalue with the negative real part) and one in the unstable region (eigenvalue with the positive real part).

Definition 2 (see [47–50]). In a three-dimensional (3D) dynamical system, a saddle fixed point is called a saddle equilibrium point of index 1 if one of its eigenvalues is unstable (positive) and the other two are stable (negative). However, a saddle fixed point is called saddle equilibrium point of index 2 if two of its eigenvalues are unstable and the other is stable.

To analyze the stability of fixed points in a fractional-order system, the following lemma can be used [47, 48, 51].

Lemma 1 (see [47]). *For an incommensurate fractional-order system, i.e., a fractional-order system in which derivation orders are not the same, an equilibrium point E^* of the system is asymptotically stable if the condition*

$$ |\arg(\lambda)| > \frac{\pi}{2M}, \tag{2} $$

is satisfied for all roots λ of the following equation:

$$ \det(\Delta(\lambda)) = \det\left(\mathrm{diag}\left(\left[\lambda^{Mq_1}, \lambda^{Mq_2}, \cdots, \lambda^{Mq_n}\right]\right) - \mathbf{J}\right) = 0, \tag{3} $$

in which $\mathbf{J}$ is the Jacobian matrix of the system evaluated at the equilibrium point E^* and M represents the least common multiple (LCM) of the denominators u_i's of q_i's, where $q_i = v_i/u_i$, v_i and $u_i \in Z^+$, for $i = 1, 2, \ldots, n$.

Condition (2) can be rewritten as follows:

$$ \frac{\pi}{2M} - \min_i\left\{\left|\arg(\lambda_i)\right|\right\} < 0. \tag{4} $$

Hence, an equilibrium point E^* will be asymptotically stable if its roots λ_i satisfy condition (4).

The term $\pi/2M - \min_i\{|\arg(\lambda_i)|\}$ is called the instability measure for equilibrium points in fractional-order systems (IMFOS). This measure is a necessary [47] but not a sufficient condition for the presence of chaos in a fractional-order system [52–54].

3. The Chaotic Financial System with Fractional Order

Recently, as reported in the literature [37], the financial model takes into account the interaction between the interest rate x, the investment demand y, and the price index z. The system is described as follows:

$$ \begin{cases} \dfrac{\mathrm{d}x}{\mathrm{d}t} = \mathrm{d}z + (y-e)x, \\ \dfrac{\mathrm{d}y}{\mathrm{d}t} = -ky^2 - lx^2 + m, \\ \dfrac{\mathrm{d}z}{\mathrm{d}t} = -\gamma z - \delta x - \rho y, \end{cases} \tag{5} $$

in which the parameters e, k, γ, m, l, ρ, and δ are constants. The authors numerically investigated the chaotic behaviors in this system. In [37], system (5) exhibits chaotic behavior when $e = 0.3$, $k = 0.02$, $\gamma = 1$, $m = 1$, $l = 0.1$, $\rho = 0.05$, $d = 1.2$, and $\delta = 1$ and initial conditions (1.2, 1.5, 1.6) are considered (see Figure 1).

In this paper, we consider system (5) with fractional order. Standard derivatives are replaced by fractional-order derivatives as follows:

$$ \begin{cases} D^{q_1} x = \mathrm{d}z + (y-e)x, \\ D^{q_2} y = -ky^2 - lx^2 + m, \\ D^{q_3} z = -\gamma z - \delta x - \rho y, \end{cases} \tag{6} $$

where $q_i \in (0, 1)$ and $D^{q_i} = d^{q_i}/\mathrm{d}t^{q_i}$ $(i = 1, 2, 3)$. If $q_1 = q_2 = q_3 = q$, then system (6) is called a commensurate fractional-order system; otherwise, it is called an incommensurate order system [47].

The Jacobian matrix of system (6) is evaluated at one of its equilibrium points $E^* = (x^*, y^*, z^*)$ and is given by

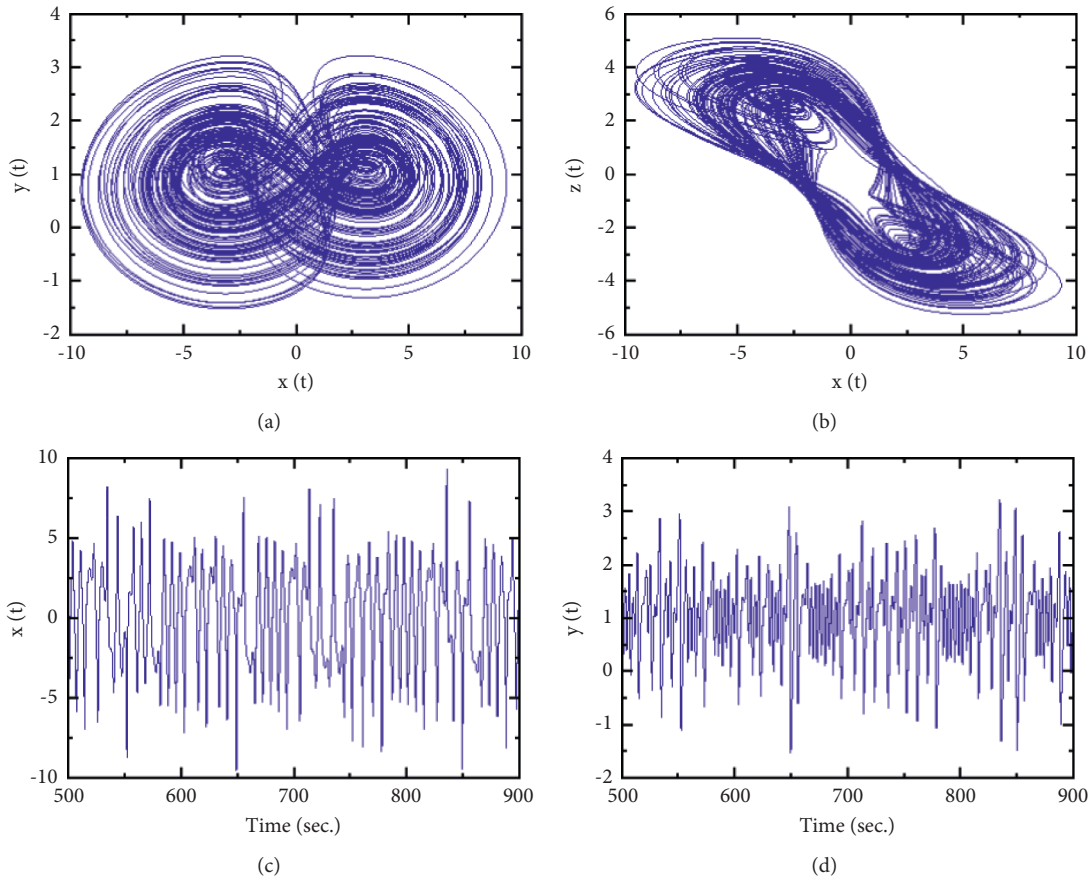

FIGURE 1: Phase diagrams and time series of system (5): (a) projected onto the $x - y$ phase plane, (b) projected onto the $x - z$ phase plane, (c) time series of x, and (d) time series of y.

$$J = \begin{pmatrix} y^* - e & x^* & d \\ -2lx^* & -2ky^* & 0 \\ -\delta & -\rho & -\gamma \end{pmatrix}. \tag{7}$$

When the values of the system parameters are chosen as above, the equilibrium points of system (6) can be calculated by solving the equations $D^{q_1}x = 0$, $D^{q_2}y = 0$, and $D^{q_3}z = 0$. The system has four equilibrium points which are given by

$$\begin{aligned} E_1 &= (0.049498497,\ -7.070201517,\ 0.304011579), \\ E_2 &= (0.076160842,\ 7.069016737,\ -0.429611679), \\ E_3 &= (3.087391472,\ 1.529728564,\ -3.163877901), \\ E_4 &= (-3.093050811,\ 1.471456216,\ 3.019478000). \end{aligned} \tag{8}$$

The corresponding eigenvalues and their nature are given in Table 1.

Taking into account Definition 2 and from Table 1, it can be seen that fixed points E_1 and E_2 are saddle equilibrium points of index 1 and the others are saddle equilibrium points of index 2.

Using the Adams–Bashforth–Moulton predictor-corrector method proposed by Diethelm et al. [55], the numerical solution of system (6) can be written as follows:

$$\begin{cases} x_{n+1} = x_0 + \dfrac{h^{q_1}}{\Gamma(q_1+2)}\left[\mathrm{d}z^p_{n+1} + \left(y^p_{n+1} - e\right)x^p_{n+1}\right] \\ \quad + \dfrac{h^{q_1}}{\Gamma(q_1+2)}\displaystyle\sum_{j=0}^{n}\chi_{1,j,n+1}\left(\mathrm{d}z_j + \left(y_j - e\right)x_j\right), \\ y_{n+1} = y_0 + \dfrac{h^{q_2}}{\Gamma(q_2+2)}\left[-k\left(y^p_{n+1}\right)^2 - l\left(x^p_{n+1}\right)^2 + m\right] \\ \quad + \dfrac{h^{q_2}}{\Gamma(q_2+2)}\displaystyle\sum_{j=0}^{n}\chi_{2,j,n+1}\left(-ky_j^2 - lx_j^2 + m\right), \\ z_{n+1} = z_0 + \dfrac{h^{q_3}}{\Gamma(q_3+2)}\left[-\gamma z^p_{n+1} - \delta x^p_{n+1} - \rho y^p_{n+1}\right] \\ \quad + \dfrac{h^{q_3}}{\Gamma(q_3+2)}\displaystyle\sum_{j=0}^{n}\chi_{3,j,n+1}\left(-\gamma z_j - \delta x_j - \rho y_j\right), \end{cases} \tag{9}$$

where

Table 1: Equilibrium points, corresponding eigenvalues, and their nature.

Equilibrium points	Eigenvalues	Nature
E_1	$\lambda_1 = -7.1758, \lambda_2 = -1.1944, \lambda_3 = 0.2828$	Saddle equilibrium point
E_2	$\lambda_1 = 6.6418, \lambda_2 = -0.8428, \lambda_3 = -0.2828$	Saddle equilibrium point
E_3	$\lambda_1 = -0.7378,\ \lambda_{2,3} = 0.4532 \pm 1.5251i$	Saddle equilibrium point
E_4	$\lambda_1 = -0.7548, \lambda_{2,3} = 0.4337 \pm 1.5487i$	Saddle equilibrium point

$$
\begin{cases}
x_{n+1}^{p} = x_0 + \dfrac{1}{\Gamma(q_1)} \displaystyle\sum_{j=0}^{n} \theta_{1,j,n+1}\left(\mathrm{d}z_j + \left(y_j - e\right)x_j\right), \\
y_{n+1}^{p} = y_0 + \dfrac{1}{\Gamma(q_2)} \displaystyle\sum_{j=0}^{n} \theta_{2,j,n+1}\left(-ky_j^2 - lx_j^2 + m\right), \\
z_{n+1}^{p} = z_0 + \dfrac{1}{\Gamma(q_3)} \displaystyle\sum_{j=0}^{n} \theta_{3,j,n+1}\left(-\gamma z_j - \delta x_j - \rho y_j\right), \\
\chi_{i,j,n+1} = \begin{cases}
n^{q_i+1} - (n - q_i)(n+1)^{q_i}, & j = 0, \\
(n-j+2)^{q_i+1} + (n-j)^{q_i+1} & \\
\qquad -2(n-j+1)^{q_i+1}, & 1 \le j \le n, \\
1, & j = n+1,
\end{cases} \\
\theta_{i,j,n+1} = \dfrac{h^{q_i}}{q_i}\left[(n-j+1)^{q_i} - (n-j)^{q_i}\right], \\
1 \le j \le n, \quad i = 1, 2, 3.
\end{cases}
\tag{10}
$$

4. Dynamics Analysis of the Financial System with Fractional Order

In this section, the numerical method proposed by Diethelm et al. [55] and presented in the previous section is used to solve numerically system (6) in the commensurate and incommensurate fractional-order cases. The parameters' values defined in Section 3 and initial conditions $(x_0, y_0, z_0) = (1.2, 1.5, 1.6)$ will be considered in this part. Using the well-known tools for studying dynamical systems such as phase diagrams, time series, bifurcation diagram, and largest Lyapunov exponent, the dynamics of the financial system with fractional order will be investigated.

4.1. Dynamics for the Commensurate Fractional-Order System. Here, we consider system (6) when $q_1 = q_2 = q_3 = q$ (commensurate order). System (6) does not exhibit chaotic behavior if it satisfies the inequality $q < 2/\pi \min_i\{|\arg(\lambda_i)|\}$ [47, 48, 51] with λ_i being the eigenvalues of the Jacobian matrix of system (6) evaluated at one of its fixed points. For the equilibrium points E_3 and E_4, we have $\min_i\{|\arg(\lambda_i)|\} = 1.2819$; hence,

$$
q < \frac{2}{\pi} \min_i\left\{\left|\arg(\lambda_i)\right|\right\} \approx 0.816. \tag{11}
$$

Figure 2 shows that the largest Lyapunov exponent of system (6) with commensurate fractional order is positive only if $q > 0.82$. Therefore, the system does not show chaotic behavior when $q < 0.82$. It is found using numerical simulations that the system exhibits a chaotic attractor for $q \ge 0.83$. For $q = 0.83$, phase diagrams are shown in Figure 3(a) for the $x - y$ phase plane and in Figure 3(b) for the $x - z$ phase plane. Figures 3(c) and 3(d) show the time series of state variables x and y, respectively, for $q = 0.83$. As it can be seen, the system exhibits chaotic behavior, and this is confirmed by a positive Lyapunov exponent for $q = 0.83$.

Therefore, the minimum effective dimension of system (6) for the commensurate fractional order is $0.83 \times 3 = 2.49$. Thus, simulation results show that chaos exists in this fractional-order financial system with a derivation order less than 3. For numerical simulations, the step size $h = 0.01$ is used.

4.2. Dynamics for the Incommensurate Fractional-Order System. When one of the system's derivation orders has a different value from the other two, we get an incommensurate fractional-order system [47].

By observing Figure 4, we can see that the largest Lyapunov exponent of system (6) is positive for $q_1 \ge 0.57$ with $q_2 = q_3 = 1$ (see Figure 4(a)), for $q_2 \ge 0.87$ with $q_1 = q_3 = 1$ (see Figure 4(b)), and for $q_3 \ge 0.89$ with $q_1 = q_2 = 1$ (see Figure 4(c)). For example, we consider the following cases.

Case 1. Fix $\mathbf{q}_2 = \mathbf{q}_3 = 1$, and let us take different values of $\mathbf{q}_1$:

(i) $q_1 = 0.55$ and $q_2 = q_3 = 1$. In this case, we have $\nu_1 = 11$, $u_1 = 20$, and $\nu_2 = \nu_3 = u_2 = u_3 = 1$, so $M = \mathrm{LCM}(20, 1, 1) = 20$ and

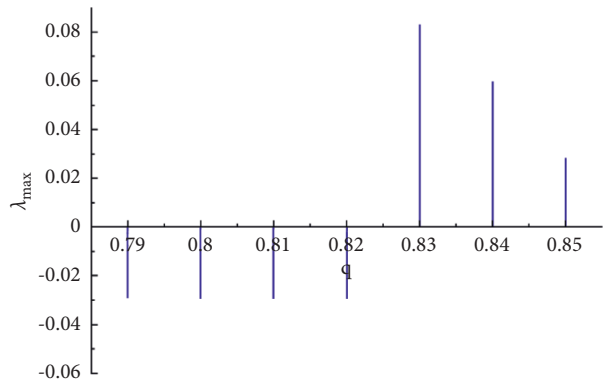

Figure 2: The largest Lyapunov exponent with the variation of derivation order q.

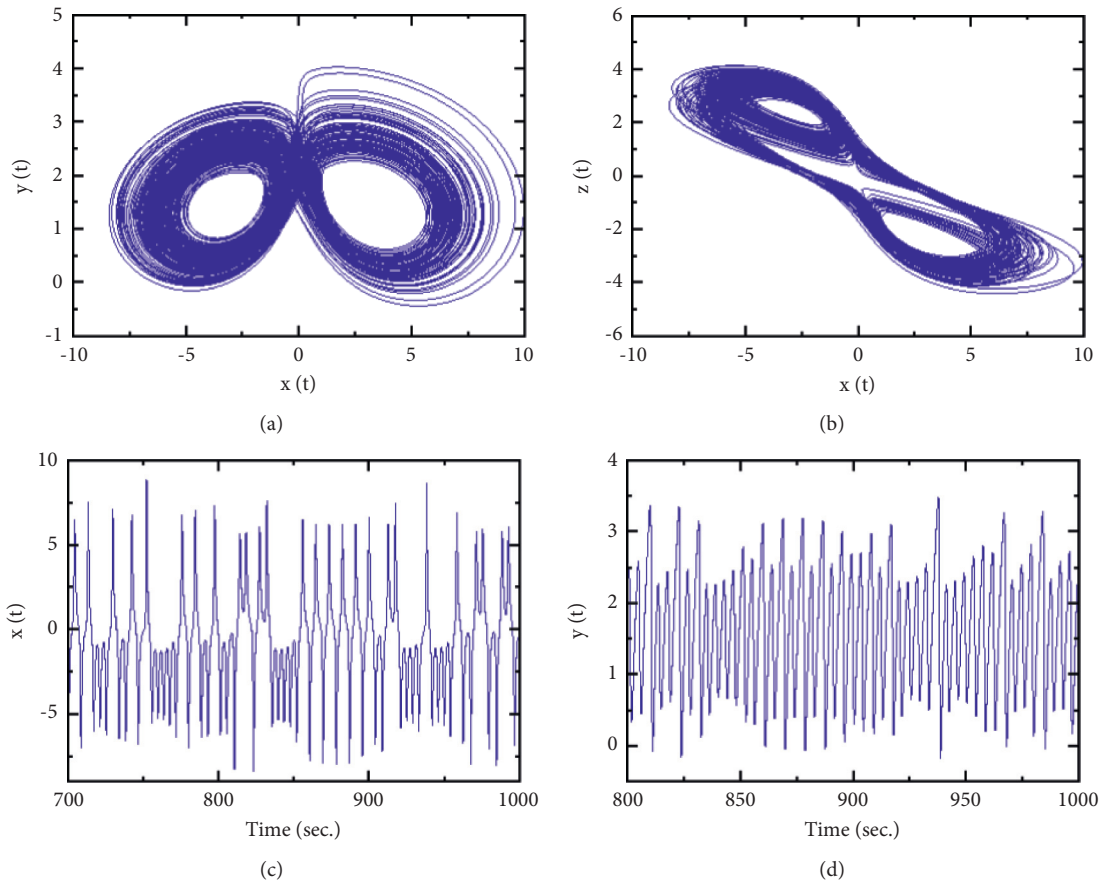

Figure 3: Phase diagrams and time series of system (6) with fractional order $q = 0.83$: (a) projected onto the $x - y$ phase plane, (b) projected onto the $x - z$ phase plane, (c) time series of x, and (d) times series of y.

$$\Delta(\lambda) = \operatorname{diag}\left(\lambda^{Mq_1}, \lambda^{Mq_2}, \lambda^{Mq_3}\right) - J(E_3) = \operatorname{diag}\left(\lambda^{11}, \lambda^{20}, \lambda^{20}\right) - J(E_3), \tag{12}$$

$$\det(\Delta(\lambda)) = \lambda^{51} - 1.22972856\lambda^{40} + 1.061189142\lambda^{31} + 1.801422624\lambda^{20} + 0.061189142\lambda^{11} + 1.867529457 = 0. \tag{13}$$

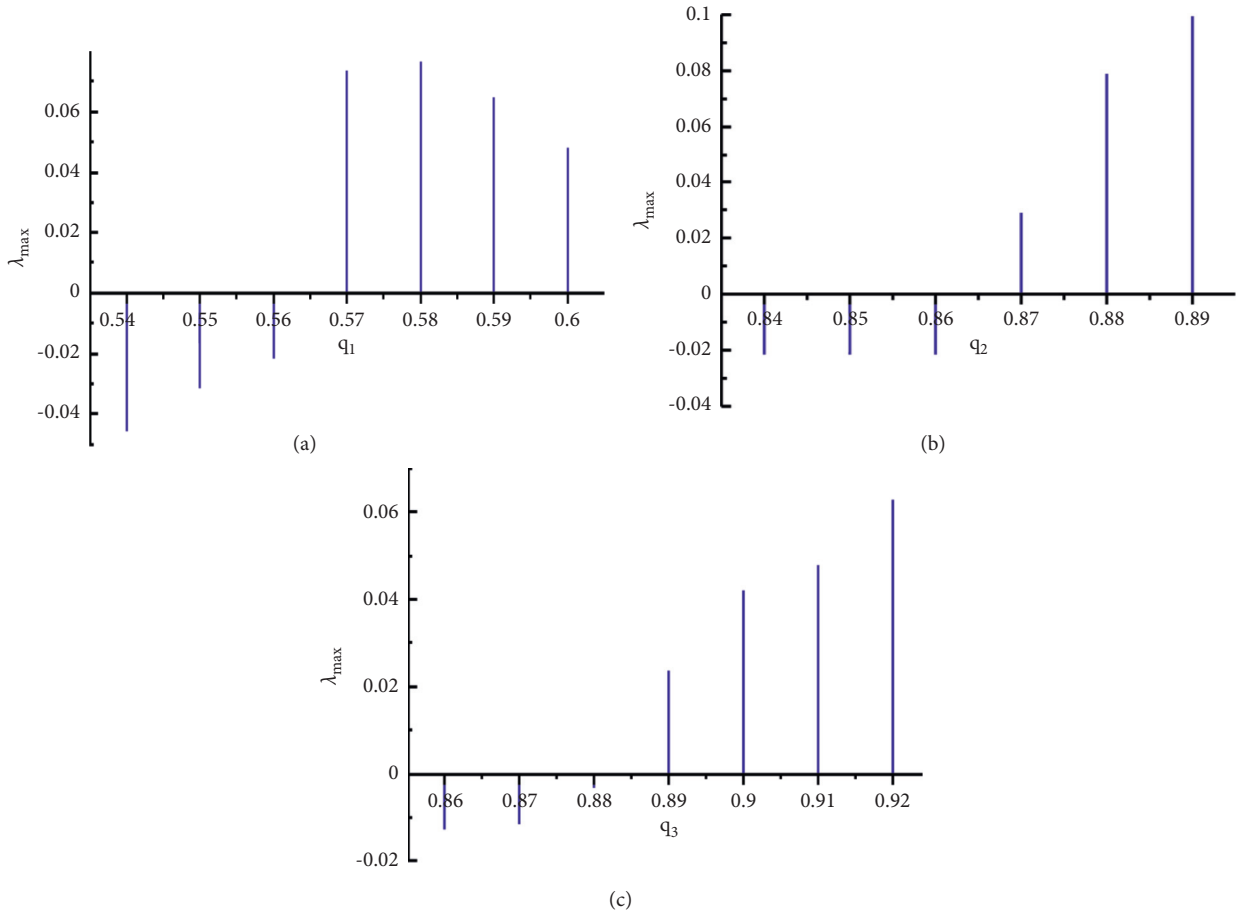

Figure 4: Largest Lyapunov exponents with variation of derivation orders: (a) q_1, when $q_2 = q_3 = 1$, (b) q_2, when $q_1 = q_3 = 1$, and (c) q_3, when $q_1 = q_2 = 1$.

By solving equation (13), we have

$$\begin{aligned}\text{IMFOS} &= \frac{\pi}{2M} - \min_i \left|\arg\left(\lambda_i\right)\right| = \frac{\pi}{40} - 0.079176 \\ &= -0.00064 < 0.\end{aligned} \tag{14}$$

In this case, IMFOS < 0; therefore, for the derivation orders $q = (0.55, 1, 1)$, system (6) does not exhibit a chaotic behavior.

(ii) Consider now $q_1 = 0.57$ and $q_2 = q_3 = 1$; by the same procedure as the above case, we have $M = 100$ and

$$\begin{aligned}\det\left(\Delta\left(\lambda\right)\right) = {} & \lambda^{257} - 1.22972856\lambda^{200} \\ & + 1.061189142\lambda^{157} + 1.801422624\lambda^{100} \\ & + 0.061189142\lambda^{57} + 1.867529457 = 0.\end{aligned} \tag{15}$$

By solving equation (15), we have

$$\begin{aligned}\text{IMFOS} &= \frac{\pi}{2M} - \min_i \left|\arg\left(\lambda_i\right)\right| = \frac{\pi}{200} - 0.015682 \\ &= 0.000026 > 0.\end{aligned} \tag{16}$$

IMFOS > 0; therefore, for the given derivation orders, the system satisfies the necessary condition to present a chaotic attractor. Numerical simulations confirm this conclusion in Figure 5. Hence, the lowest value for which q_1 in this case generates a chaotic behavior is 0.57, where $\lambda_{max} > 0$.

Case 2. Fix $\mathbf{q}_1 = \mathbf{q}_3 = 1$, and let us take different values of $\mathbf{q}_2$:

(i) Consider $q_1 = 1$, $q_2 = 0.86$, and $q_3 = 1$; by the same procedure as the above case, we get $M = \text{LCM}(1, 50, 1) = 50$ and

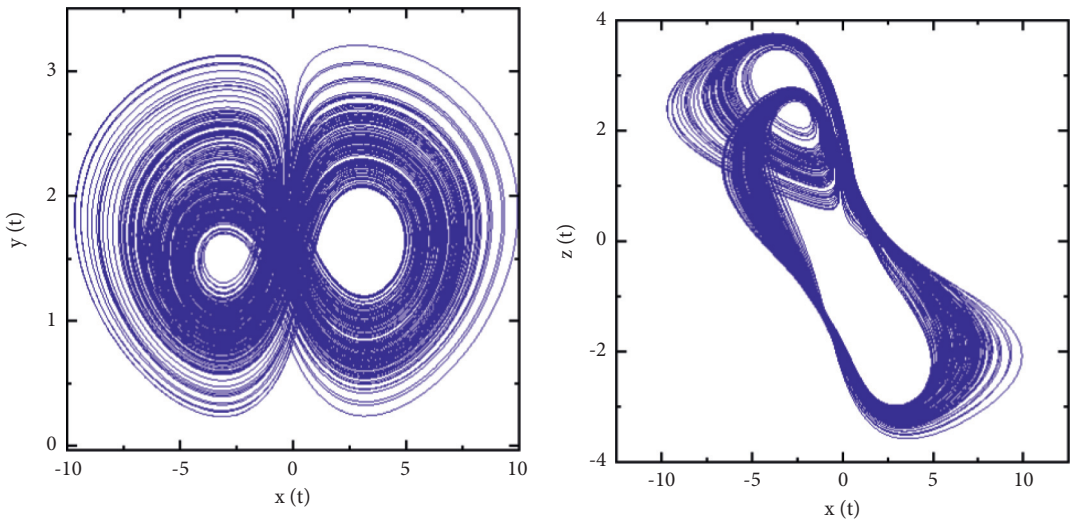

FIGURE 5: Phase diagrams of system (6) with fractional orders $q_1 = 0.57$ and $q_2 = q_3 = 1$ projected onto (a) the $x - y$ phase plane and (b) the $x - z$ phase plane.

$$\det(\Delta(\lambda)) = \lambda^{143} + 0.061189142\lambda^{100} - 0.22972856\lambda^{93} + 1.892340326\lambda^{50} - 0.02972856\lambda^{43} + 1.867529457 = 0. \tag{17}$$

By solving equation (17), the IMFOS of the system is

$$\text{IMFOS} = \frac{\pi}{2M} - \min_i \left|\arg(\lambda_i)\right| = \frac{\pi}{100} - 0.027339 = 0.004077 > 0. \tag{18}$$

In this case, IMFOS > 0 but system (6) does not exhibit chaotic behavior ($\lambda_{\max} < 0$). This shows that the condition IMFOS ≥ 0 is a necessary condition for chaos to exist and not the sufficient one.

(ii) Consider now $q_1 = 1$, $q_2 = 0.87$, and $q_3 = 1$; by the same procedure as the above case, we have $M = 100$ and

$$\det(\Delta(\lambda)) = \lambda^{287} + 0.061189142\lambda^{200} - 0.22972856\lambda^{187} + 1.892340326\lambda^{100} - 0.02972856\lambda^{87} + 1.867529457 = 0. \tag{19}$$

The system's IMFOS is

$$\text{IMFOS} = \frac{\pi}{2M} - \min_i \left|\arg(\lambda_i)\right| = \frac{\pi}{200} - 0.013605 = 0.002103 > 0. \tag{20}$$

In this case, the system exhibits a chaotic behavior as it can be seen in Figure 6, where we can observe the chaotic attractor of the system.

Therefore, the lowest value for which q_2 in this case generates chaotic behavior is 0.87, where $\lambda_{\max} > 0$.

Case 3. Fix $\mathbf{q}_1 = \mathbf{q}_2 = 1$, and let us take different values of $\mathbf{q}_3$:

(i) Consider $q_1 = 1$, $q_2 = 1$, and $q_3 = 0.88$; then, $M = \text{LCM}(1, 1, 25) = 25$ and

$$\det(\Delta(\lambda)) = \lambda^{72} + \lambda^{50} - 1.168539418\lambda^{47} + 0.031460582\lambda^{25} + 1.831151184\lambda^{22} + 1.867529457 = 0. \tag{21}$$

By solving equation (21), we get

$$\text{IMFOS} = \frac{\pi}{2M} - \min_i \left|\arg(\lambda_i)\right| = \frac{\pi}{50} - 0.051947 = 0.010885 > 0. \tag{22}$$

In this case, IMFOS > 0 but the system does not exhibit chaotic behavior ($\lambda_{\max} < 0$).

(ii) Consider now $q_1 = 1$, $q_2 = 1$, and $q_3 = 0.89$; then, we have $M = 100$ and

$$\det(\Delta(\lambda)) = \lambda^{289} + \lambda^{200} - 1.168539418\lambda^{189} + 0.031460582\lambda^{100} + 1.831151184\lambda^{89} + 1.867529457 = 0. \tag{23}$$

From equation (23), we get

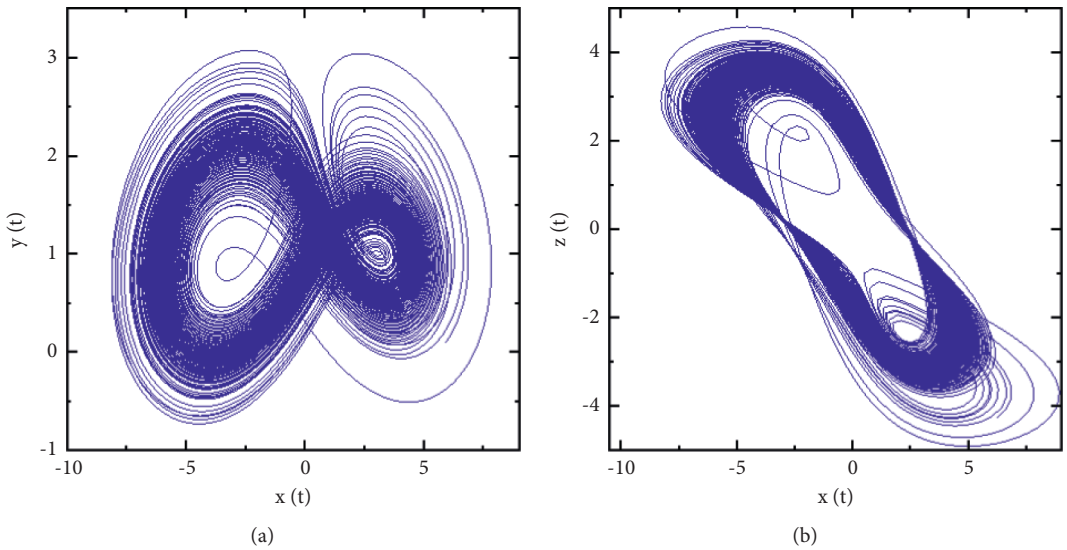

Figure 6: Phase diagrams of system (6) with fractional orders $q_1 = 1$, $q_2 = 0.87$, and $q_3 = 1$ projected onto (a) the $x - y$ phase plane and (b) the $x - z$ phase plane.

$$\text{IMFOS} = \frac{\pi}{2M} - \min_i \left|\arg(\lambda_i)\right| = \frac{\pi}{200} - 0.012974 = 0.002734 > 0. \tag{24}$$

Hence, for the derivation orders $q = (1, 1, 0.89)$, system (6) satisfies the necessary condition for the existence of chaos in the system. In this case, this is confirmed numerically in Figure 7.

Therefore, the lowest value from which q_3 in this case generates chaotic behavior is $q_3 = 0.89$, where. $\lambda_{\max} > 0$.

When the value of q_3 increases from 0.85 to 0.90, the route to chaos via period-doubling is found. The bifurcation diagram and largest Lyapunov exponent when the derivation order q_3 varies on the closed interval [0.85, 0.90] are plotted in Figure 8. Clearly, from the bifurcation diagram, the period-doubling route to chaos can be seen. Figures 9(a)–9(d) show that the system has period-1, period-2, and period-4 and chaotic attractors for $q_3 = 0.85$, 0.87, 0.878, and 0.89, respectively. Note that the step size used for the numerical simulations in this section is $h = 0.01$.

From these three cases, we deduce that the minimum effective dimension of system (6) in the incommensurate fractional-order case is 2.57.

In the next section, a simple but robust fractional-order sliding mode control law will be designed to control chaos in system (6).

5. The Sliding Mode Controller Design

According to the sliding mode control theory, to design a sliding mode controller, we have two steps:

(i) Build a sliding surface, which represents the desired dynamics of the system such as stability

(ii) Develop a control law in a way that the system states are brought towards the sliding surface in a finite time and are maintained in a neighborhood of the sliding surface when time evolves [38]

The sliding mode control law is itself composed of two parts; the first, which is continuous, is called equivalent control law and the second is discontinuous. The equivalent control law describes the behavior of the system to be controlled when its trajectories are on the sliding surface. The discontinuous reaching law ensures the convergence of all the system states towards the sliding surface.

To control chaos in fractional-order financial system (6), the controller $u(t)$ is added at the level of the second state equation as follows:

$$\begin{cases} D^{q_1} x = \mathrm{d}z + (y - e)x, \\ D^{q_2} y = -ky^2 - lx^2 + m + u, \\ D^{q_3} z = -\gamma z - \delta x - \rho y. \end{cases} \tag{25}$$

Motivated by the literature [38, 43], as a choice for the sliding surface, we choose the following fractional-order sliding surface:

$$\sigma(t) = D^{q_2 - 1} y(t) + D^{-1}\left(ky^2(t) + lx^2(t) + \eta y(t)\right) = D^{q_2 - 1} y(t) + \int_0^t \left(ky^2(\tau) + lx^2(\tau) + \eta y(\tau)\right)\mathrm{d}\tau, \tag{26}$$

where η is an arbitrary positive constant. In the sliding mode, the invariance conditions of the surface must be satisfied and are defined as follows (i.e., the sliding surface and its derivative must satisfy the relations which appear in the following equation):

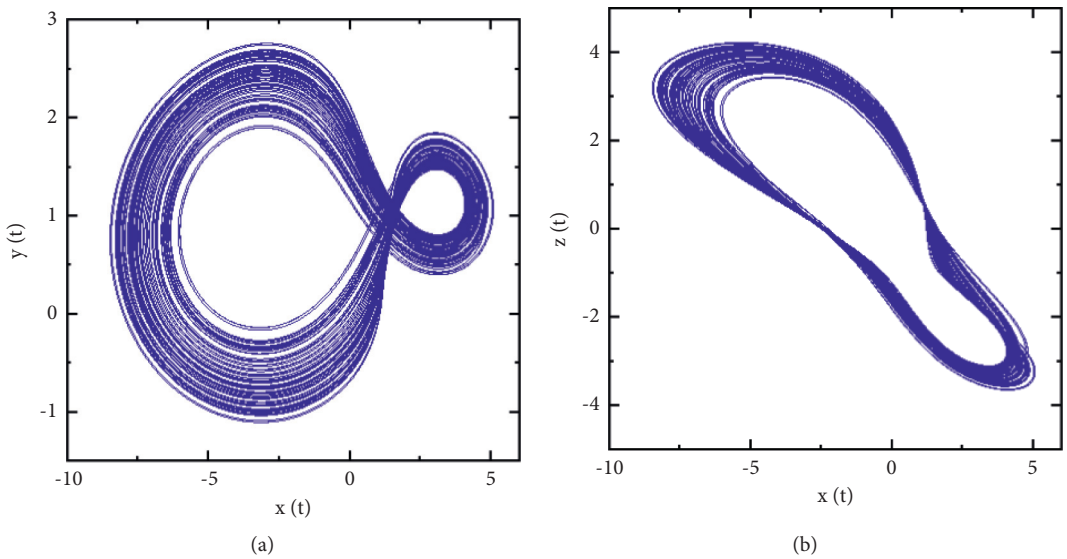

Figure 7: Phase diagrams of system (6) with fractional orders $q_1 = 1$, $q_2 = 1$, and $q_3 = 0.89$ projected onto (a) the $x - y$ phase plane and (b) the $x - z$ phase plane.

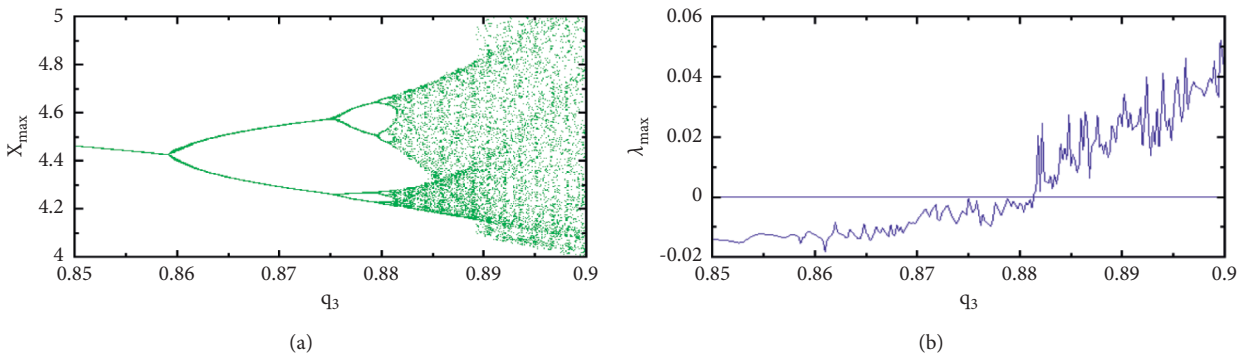

Figure 8: Bifurcation diagram and largest Lyapunov exponent (λ_{max}) of system (6) with order q_3: (a) bifurcation diagram and (b) largest Lyapunov exponent (λ_{max}).

$$\sigma(t) = 0,$$
$$\frac{d}{dt}\sigma(t) = \dot{\sigma}(t) = 0. \tag{27}$$

From equations (26) and (27), we get

$$D^{q_2} y(t) = -\left(ky^2(t) + lx^2(t) + \eta y(t)\right). \tag{28}$$

From system (25) and equation (28), we obtain the equivalent control law as follows:

$$\begin{aligned} u_{eq} &= \frac{d^{q_2} y}{dt^{q_2}} + ky^2 + lx^2 - m, \\ &= -\left(ky^2 + lx^2 + \eta y\right) + ky^2 + lx^2 \\ &\quad - m \\ &= -\eta y - m. \end{aligned} \tag{29}$$

Regarding the discontinuous reaching law, it is chosen as follows:

$$u_r = G_r \operatorname{sign}(\sigma), \tag{30}$$

in which

$$\operatorname{sign}(\sigma) = \begin{cases} +1, & \text{if } \sigma > 0, \\ 0, & \text{if } \sigma = 0, \\ -1, & \text{if } \sigma < 0, \end{cases} \tag{31}$$

and G_r is the gain of the controller.

Finally, the total control law has the following form:

$$u(t) = u_{eq}(t) + u_r(t) = -\eta y - m + G_r \operatorname{sign}(\sigma). \tag{32}$$

Theorem 1. *System (6) with control law (32), i.e., system (25) is globally and asymptotically stable if the controller gain $G_r < 0$.*

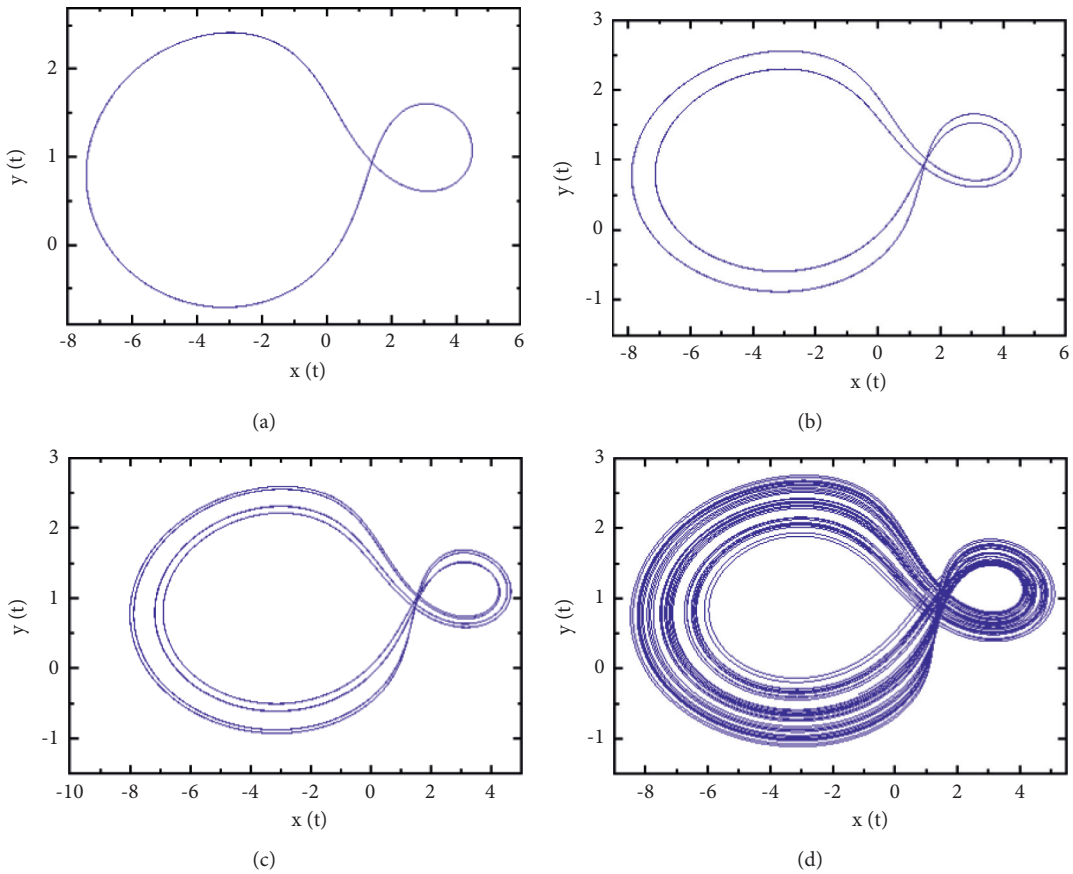

Figure 9: Phase diagrams showing the period-doubling route to chaos for system (6) with $q_1 = q_2 = 1$ and fractional order: (a) $q_3 = 0.85$, (b) $q_3 = 0.87$, (c) $q_3 = 0.878$, and (d) $q_3 = 0.89$.

Proof. For this, let us choose the Lyapunov quadratic function as follows:

$$V = \frac{1}{2}\sigma^2, \tag{33}$$

and its derivative gives

$$\begin{aligned}\dot{V} &= \sigma\dot{\sigma} = \sigma\left[D^{q_2}y + ky^2 + lx^2 + \eta y\right] \\ &= \sigma\left[-ky^2 - lx^2 + m + u + ky^2 + lx^2 + \eta y\right] \\ &= \sigma\left[-ky^2 - lx^2 + m - \eta y - m + G_r\operatorname{sign}(\sigma)\right. \\ &\quad \left. + ky^2 + lx^2 + \eta y\right] \\ &= \sigma\left[G_r\operatorname{sign}(\sigma)\right] \\ &= G_r|\sigma| < 0.\end{aligned} \tag{34}$$

Therefore, we have found a Lyapunov function which satisfies the conditions of Lyapunov theorem, i.e., $V > 0$ and $\dot{V} < 0$. Thus, system (25) with sliding mode control law (32) is globally and asymptotically stable. □

Theorem 2. *Suppose that system (25) is perturbed by uncertainties and an external disturbance. Thus, the system has the following form:*

$$\begin{cases} D^{q_1}x = \mathrm{d}z + (y - e)x, \\ D^{q_2}y = -ky^2 - lx^2 + m \\ \quad + \Delta g(x, y, z) + p(t) + u, \\ D^{q_3}z = -\gamma z - \delta x - \rho y, \end{cases} \tag{35}$$

in which $\Delta g(x, y, z)$ and $p(t)$ are supposed to be bounded, i.e., $|\Delta g(x, y, z)| \le \mu_1$ and $|p(t)| \le \mu_2$, where μ_1 and μ_2 are positive constants. System (35) with sliding mode control law (32) is globally and asymptotically stable if $G_r < -(\mu_1 + \mu_2)$.

Proof. For this, let us choose Lyapunov quadratic function (33); thus, we have

$$\begin{aligned}\dot{V} &= \sigma\dot{\sigma} = \sigma\left[D^{q_2}y + ky^2 + lx^2 + \eta y\right] \\ &= \sigma\left[-ky^2 - lx^2 + m + \Delta g(x, y, z) + p(t)\right. \\ &\quad \left. + u + ky^2 + lx^2 + \eta y\right] \\ &= \sigma\left[\Delta g(x, y, z) + p(t) + G_r\operatorname{sign}(\sigma)\right] \\ &\le (G_r + \mu_1 + \mu_1)|\sigma| < 0.\end{aligned} \tag{36}$$

Thus, the proof is achieved. □

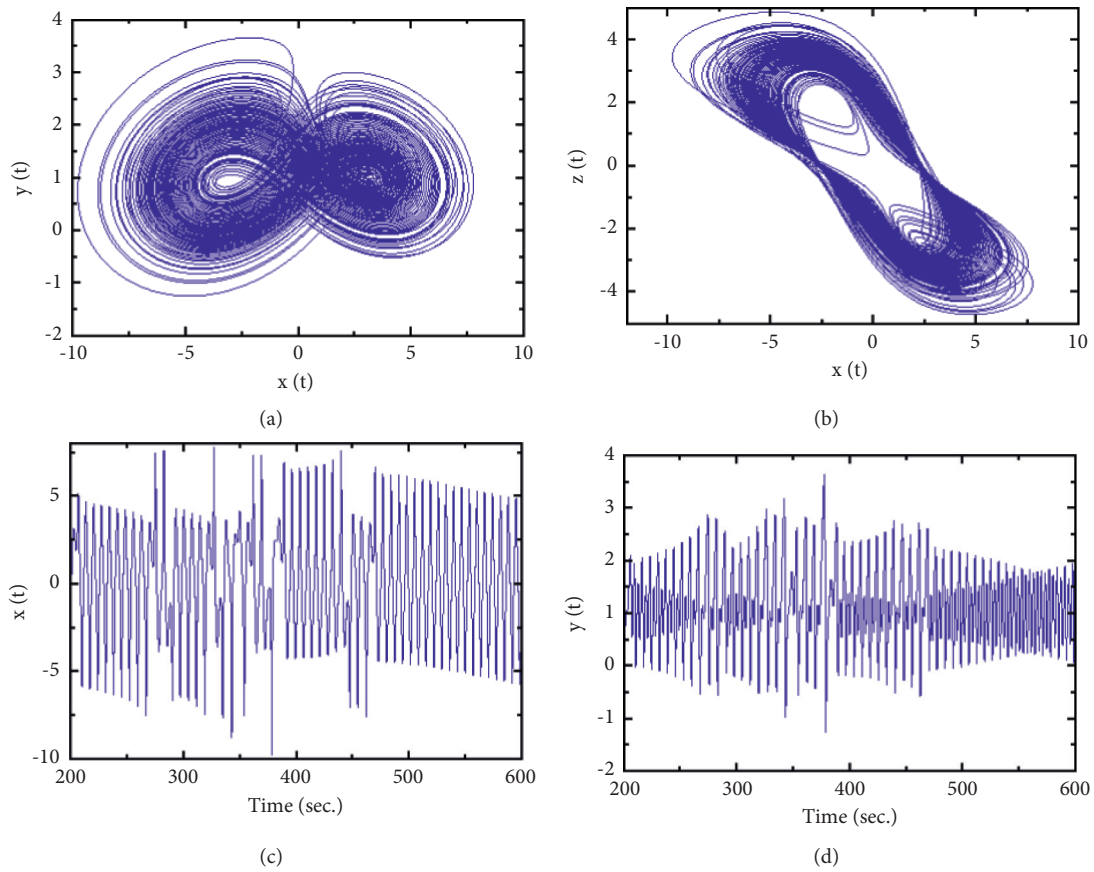

FIGURE 10: Phase diagrams and time series of system (6) with $q_1 = 1$, $q_2 = 0.88$, and $q_3 = 1$: (a) projected onto the $x - y$ phase plane, (b) projected onto the $x - z$ phase plane, (c) time series of x, and (d) time series of y.

6. Numerical Simulations

This part of the paper presents three illustrative examples to verify the effectiveness of the proposed control technique. Numerical simulations are carried out with initial conditions $(x_0, y_0, z_0) = (1.2, 1.5, 1.6)$, $\eta = 0.5$, and $G_r = -2$. For the commensurate fractional-order case, $q_1 = q_2 = q_3 = q = 0.83$ is chosen for which the system is chaotic (see Figure 3). For the incommensurate fractional-order case, $q_1 = 1$, $q_2 = 0.88$, and $q_3 = 1$ are chosen. For this choice, the largest Lyapunov exponent is positive (see Figure 4(b)). The corresponding phase diagrams and time series are shown in Figure 10. Note that the controller can be activated in the system at any time. In this part, it is activated at $t = 20$ sec.

Case 1: commensurate order without uncertainty and an external disturbance

As it was shown above, system (25) without the controller $u(t)$ is chaotic for$q_1 = q_2 = q_3 = q = 0.83$. Now, applying controller (32) to the system, simulation results can be seen in Figure 11. From this figure, it is observed that control law (32) can effectively asymptotically stabilize the state variables of system (25) (see Figures 11(a)–11(c)). Besides, the time series of the sliding surface $\sigma(t)$ is plotted in Figure 11(d). From this figure, it can be observed that the controller stabilizes the trajectories of the system on the sliding surface and maintains them on this surface when time evolves.

Case 2: commensurate order with uncertainty and an external disturbance

In this part, we disturb the fractional-order financial system by an uncertainty defined by $\Delta g(x, y, z) = 0.2 \sin(\sqrt{x^2 + y^2 + z^2})$ and an external disturbance $p(t) = 0.5 \sin(2t)$, where $|\Delta g(x, y, z)| \leq \mu_1 = 0.2$ and $|p(t)| \leq \mu_2 = 0.5$. The time series of system (25) state variables (see Figures 12(a)–12(c)) and the time series of sliding surface (26) (see Figure 12(d)) in the presence of control law (32) can be seen through Figure 12. From this figure, we can see that the controller stabilizes the system in the presence of uncertainty and external disturbance.

Case 3: incommensurate order with uncertainty and an external disturbance

In this case, we disturb financial system (25) with the incommensurate fractional order by the same uncertainty and external disturbance as Case 2.

The time series of system (25) state variables and the time series of the sliding surface in the presence of control law

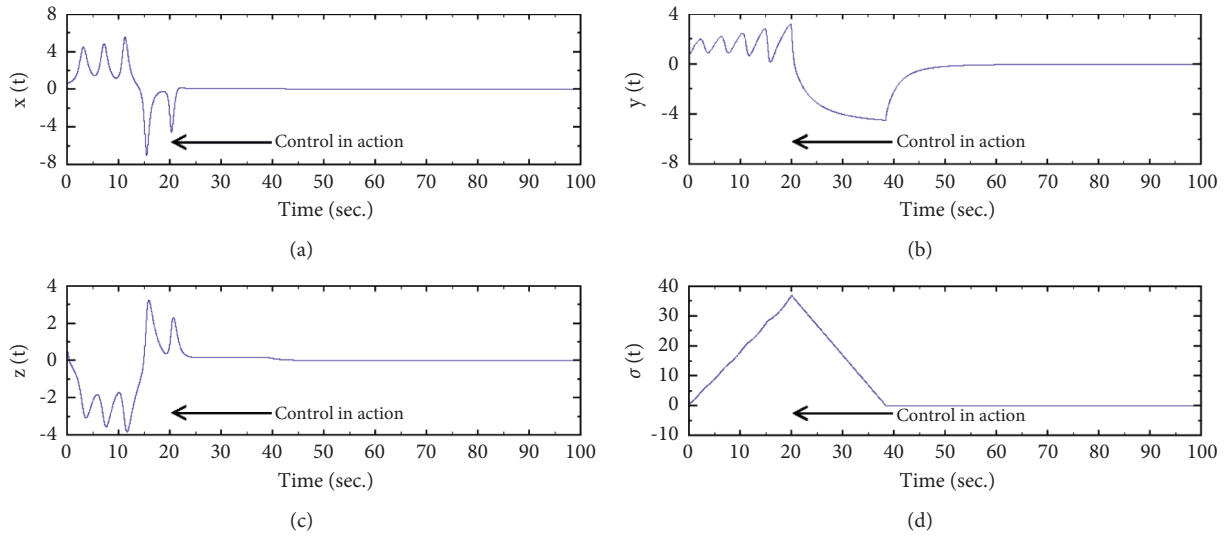

Figure 11: The time series of the controlled commensurate fractional-order system state variables and corresponding time series of the sliding surface without uncertainty and external disturbance (the control input is activated at $t = 20$ sec).

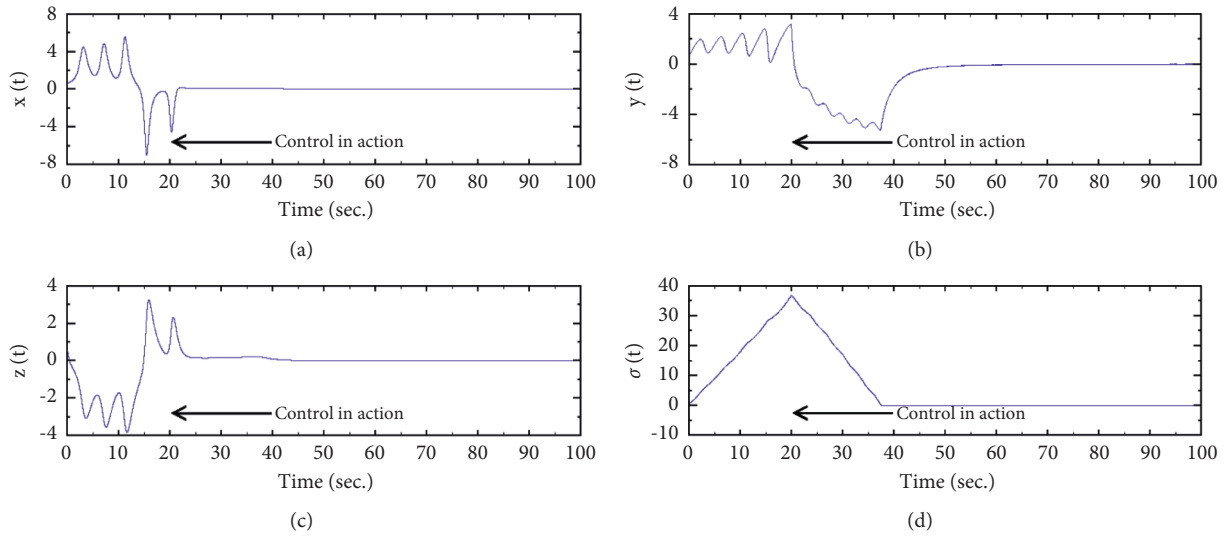

Figure 12: The time series of the controlled commensurate fractional-order system state variables and corresponding time series of the sliding surface with uncertainty and external disturbance (the control input is activated at $t = 20$ sec).

(32) are shown in Figure 13. From this figure, it can be observed that the state variables of the system are stabilized.

In each figure, the time series of the sliding surface is plotted to show the ability of the controller to bring back all the system states onto the sliding surface and to maintain them on this surface when time evolves. Simulation results show that controller (32) is able to stabilize systems (25) and (35) in commensurate and incommensurate fractional-order cases. Therefore, the designed control law can suppress chaos in this fractional-order financial system in the presence or absence of uncertainty and external disturbance.

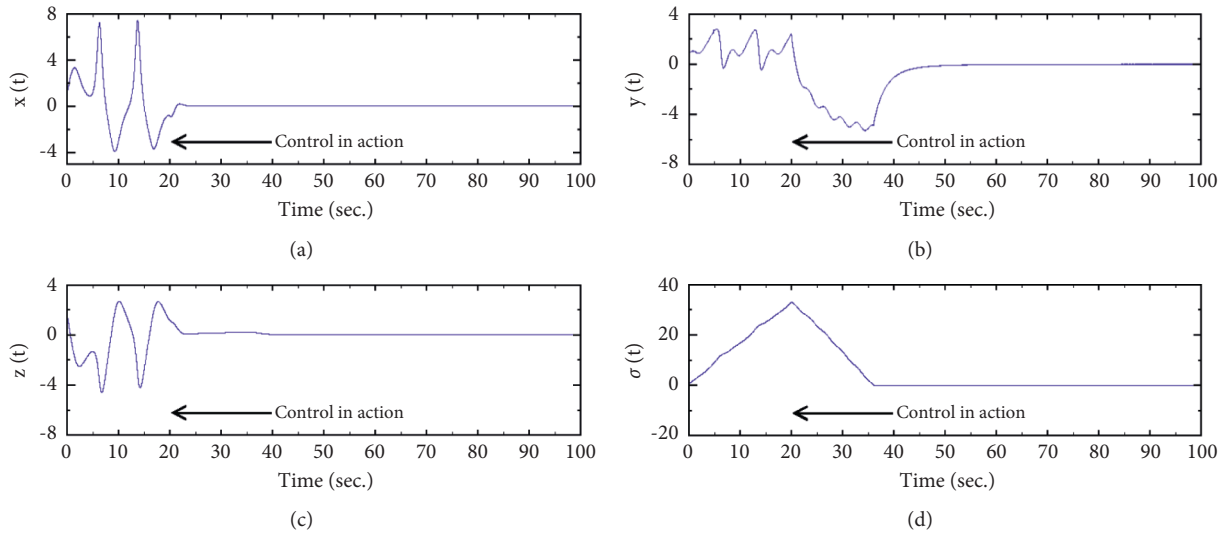

Figure 13: The time series of the controlled incommensurate fractional-order system state variables and corresponding time series of the sliding surface with uncertainty and external disturbance (the control input is activated at $t = 20$ sec).

7. Conclusions

In this paper, the dynamics of a financial system with fractional order as well as the robust chaos control in this system are studied analytically and numerical simulations are performed to confirm the analytical results. The existence of chaos in this study is validated by a positive Lyapunov exponent and by an analytical condition existing in the literature. The fractional-order system exhibits rich dynamics behaviors such as periodic and chaotic behaviors. A period-doubling route to chaos is found in this system. Numerical simulations revealed that chaos exists in this fractional-order system for derivation orders less than 3. The lowest derivation order found to have chaos in the commensurate fractional-order case is 2.49 and 2.57 for the incommensurate fractional-order case. Regarding the robust control of chaos in the system, by using Lyapunov's stability theorem, a simple but robust fractional-order sliding mode control law has been designed to stabilize the chaotic trajectories of the fractional-order financial system in the presence or absence of uncertainty and external disturbance. It should be noted that the controller has been applied only at the investment demand state equation to fully control the system. Numerical simulations show that this controller is effective and can control the financial system with commensurate and incommensurate fractional orders. In [14], Chen studied the fractional-order version of the financial system proposed by Ma and Chen [34]. The lowest derivation order obtained in [14] for chaos to exist is 2.55 in the commensurate order case and 2.35 in the incommensurate order case. Compared to the fractional-order version of Liao et al. [37] proposed in this paper, the emergence of chaos is enhanced in the commensurate order case and suppressed in the incommensurate order case. It is well known that time delay can affect the behavior of dynamical systems. For future works, chaotic dynamics analysis of this fractional-order financial system with time delay can be considered.

8. Data Availability

All data are included in the text directly.

9. Conflicts of Interest

The authors declare that they have no conflicts of interest.

10. References

[1] W. L. Ditto, "Applications of chaos in biology and medicine," *AIP Conference Proceedings*, vol. 376, no. 1, pp. 175–201, 1996.

[2] J. Ma, C. N. Wang, J. Tang, and Y. F. Xia, "Suppression of the spiral wave and turbulence in the excitability-modulated media," *International Journal of Theoretical Physics*, vol. 48, no. 1, pp. 150–157, 2009.

[3] Y. J. Liu and Q. G. Yang, "Dynamics of a new Lorenz-like chaotic system," *Nonlinear Analysis: Real World Applications*, vol. 11, no. 4, pp. 2563–2572, 2010.

[4] E. N. Lorenz, "Deterministic nonperiodic flow," *Journal of atmospheric sciences*, vol. 20, no. 2, pp. 130–141, 1963.

[5] G. Chen and T. Ueta, "Yet another chaotic attractor," *International Journal of Bifurcation and chaos*, vol. 9, no. 07, pp. 1465–1466, 1999.

[6] J. Lü, G. Chen, and S. Zhang, "Dynamical analysis of a new chaotic attractor," *International Journal of Bifurcation and chaos*, vol. 12, no. 05, pp. 1001–1015, 2002.

[7] R. B. Leipnik and T. A. Newton, "Double strange attractors in rigid body motion with linear feedback control," *Physics Letters A*, vol. 86, no. 2, pp. 63–67, 1981.

[8] S. Dadras, H. R. Momeni, and V. J. Majd, "Sliding mode control for uncertain new chaotic dynamical

system," *Chaos, Solitons and Fractals*, vol. 41, no. 4, pp. 1857–1862, 2009.

[9] M. Roopaei, B. R. Sahraei, and T. C. Lin, "Adaptive sliding mode control in a novel class of chaotic systems," *Communications in Nonlinear Science and Numerical Simulation*, vol. 15, no. 12, pp. 4158–4170, 2010.

[10] M. T. Yassen, "Chaos control of chaotic dynamical system using backstepping design," *Chaos, Solitons and Fractals*, vol. 27, no. 2, pp. 537–548, 2006.

[11] Q. Jia, "Chaos control and synchronization of the Newton-Leipnik chaotic system," *Chaos, Solitons and Fractals*, vol. 35, no. 4, pp. 814–824, 2008.

[12] I. Podlubny, *Fractional Differential Equations*, Academic Press, New York, 1999.

[13] C. Li and G. Peng, "Chaos in Chen's system with a fractional order," *Chaos, Solitons and Fractals*, vol. 22, no. 2, pp. 443–450, 2004.

[14] W-C. Chen, "Nonlinear dynamics and chaos in a fractional-order financial system," *Chaos, Solitons and Fractals*, vol. 36, no. 5, pp. 1305–1314, 2008.

[15] V. Daftardar-Gejji and S. Bhalekar, "Chaos in fractional ordered Liu system," *Computer and Mathematics with Applications*, vol. 59, no. 3, pp. 1117–1127, 2010.

[16] X. Wang, Y. He, and M. Wang, "Chaos control of a fractional order modified coupled dynamos system," *Nonlinear Analysis*, vol. 71, no. 12, pp. 6126–6134, 2009.

[17] T. T. Harley, C. F. Lorenzo, and H. K. Qammar, "Chaos in a fractional order Chua's system," *IEEE Transactions on Circuits and Systems I*, vol. 42, no. 8, pp. 485–490, 1995.

[18] I. Grigorenko and E. Grigorenko, "Chaotic dynamics of the fractional Lorenz system," *Physical review letters*, vol. 91, no. 3, pp. 034101, 2003.

[19] W. M. Ahmad and J. C. Sprott, "Chaos in fractional-order autonomous nonlinear systems," *Chaos, Solitons and Fractals*, vol.16, no. 2, pp. 339–351, 2003.

[20] I. Petrás, *Fractional-order nonlinear systems: modeling, analysis and simulation*, Springer Science and Bussiness Media, 2011.

[21] C. Li and W. Deng, "Remarks on fractional derivatives," *Applied Mathematics and Computation*, vol. 187, no. 2, pp. 777–784, 2007.

[22] Y. Chatibi and A. Ouhadan, "Lie symmetry analysis of conformable differential equations," *AIMS Mathematics*, vol. 4, no. 4, pp. 1133–1144, 2019.

[23] Y. Chatibi, E. H. El kinani, and A. Ouhadan, "Lie symmetry analysis and conservation laws for the time fractional Black-Scholes equation," *International Journal of Geometric Methods in Modern Physics*, vol. 17, no. 01, 14 pages, 2020.

[24] Y. Chatibi, E. H. El Kinani, and A. Ouhadan, "Variational calculus involving nonlocal fractional derivative with Mittag-Leffler kernel," *Chaos, Solitons and Fractals*, vol. 118, pp. 117–121, 2019.

[25] Y. Chatibi, E. H. El kinani, and A. Ouhadan, "On the discrete symmetry analysis of some classical and fractional differential equations," *Mathematical Methods in the Applied Sciences*, vol. 44, no. 4, pp. 2868–2878, 2019.

[26] R. H. Strotz, J. C. McAnulty, and J. B. Naines, "Goodwin's nonlinear theory of the business cycle: an electro-analog solution," *Econometrica, Journal of Econometric Society*, vol. 21, pp. 390–411, 1953.

[27] A. C. L. Chian, "Nonlinear dynamics and chaos in macroeconomics," *International Journal of Theoretical and Applied Finance*, vol. 3, no. 3, pp. 601, 2000.

[28] L. De Cesare and M. Sportelli, "A dynamic IS-LM model with delayed taxation revenues," *Chaos, Solitons & Fractals*, vol. 25, no. 1, pp. 233–244, 2005.

[29] H. Yu, G. Cai, and Y. Li, "Dynamic analysis and control of a new hyperchaotic finance system," *Nonlinear Dynamics*, vol. 67, no. 3, pp. 2171–2182, 2012.

[30] L. Chen and G. Chen, "Controlling chaos in an economic model," *Physica A: Statistical Mechanics and its Applications*, vol. 374, no. 1, pp. 349–358, 2007.

[31] W. Wu, Z. Chen, and W. H. Ip, "Complex nonlinear dynamics and controlling chaos in a Cournot duopoly economic model," *Nonlinear Analysis: Real World Applications*, vol. 11, no. 5, pp. 4363–4377, 2010.

[32] S. Invernizzi and A. Medio, "On lags and chaos in economic dynamic models," *Journal of mathematical economics*, vol. 20, no. 6, pp. 521–550, 1991.

[33] D. A. Hsieh, "Chaos and nonlinear dynamic: application to financial markets," *The Journal of Finance*, vol. 46, no. 5, pp. 1839–1877, 1991.

[34] J. H. Ma and Y. S. Chen, "Study for the bifurcation topological structure and the global complicated character of a kind of nonlinear finance system, I," *Applied Mathematics and Mechanics*, vol. 22, no. 11, pp. 1240–1251, 2001.

[35] E. Panas, "Long memory and chaotic models of price on the London metal exchange," *Resources Policy*, vol. 27, no. 4, pp. 235–246, 2001.

[36] B. J. West and S. Picozzi, "Fractional langevin model of memory in financial time series," *Physical Review E*, vol. 65, no. 3, pp. 037106-1-3, 2002.

[37] Y. Liao, Y. Zhou, F. Xu, and X-B. Shu, "A Study on the Complexity of a New Chaotic Financial System," *Complexity*, vol. 2020, Article ID 8821156, 5 pages, 2020.

[38] S. Dadras and H. R. Momeni, "Control of a fractional-order economical system via sliding mode," *Physica A*, vol. 389, no. 12, pp. 2434–2442, 2010.

[39] M. S. Abd-Elouahab, N. E. Hamri, and J. Wang, "Chaos control of a fractional order financial System,"

Mathematical Problems in Engineering, vol. 2010, Article ID 270646, 18 pages, 2010.

[40] W. Perruquetti and J. P. Barbot, *Sliding Mode Control in Engineering*, Marcel Dekker Inc., New York, NY, 2002.

[41] J. E. Slotine and W. Li, *Applied Nonlinear Control*, Englewood Cliffs NJ: Prentice Hall, 1991.

[42] H. K. Khalil, *Nonlinear Systems*, Englewood Cliffs, NJ: Prentice Hall, 1996.

[43] M. R. Faieghi, H. Delavari, and D. Baleanu, "Control of an uncertain fractional-order Liu system via fuzzy fractional-order sliding mode control," *Journal of Vibration and control*, vol. 18, no. 9, pp. 1366–1374, 2012.

[44] D. Chen, Y. Liu, X. Ma, and R. Zhang, "Control of a class of fractional-order chaotic systems via sliding mode," *Nonlinear Dynamics*, vol. 67, no. 1, pp. 893–901, 2012.

[45] C. Yin, S. Zhong, and W. Chen, "Design of sliding mode controller for a class of fractional-order chaotic systems," *Communications in Nonlinear Science and Numerical Simulation*, vol. 17, no. 1, pp. 356–366, 2012.

[46] A.-J. Muñoz-Vázquez, V. Parra-Vega, and A. Sánchez-Orta, "Fractional integral sliding modes for robust tracking of nonlinear systems," *Nonlinear Dynamics*, vol. 87, no. 2, pp. 895–901, 2017.

[47] M. S. Tavazoei and M. Haeri, "Chaotic attractors in incommensurate fractional order systems," *Physica D*, vol. 237, no. 20, pp. 2628–2637, 2008.

[48] M. S. Tavazoei and M. Haeri, "A necessary condition for double scroll attractor existence in fractional order systems," *Physics Letters A*, vol. 367, no. 1–2, pp. 102–113, 2007.

[49] E. Campos-Cantón, J. G. Barajas-Ramirez, G. Solis-Perales, and R. Femat, "Multiscroll attractors by switching systems," *Chaos: An Interdisciplinary Journal of Nonlinear Science*, vol. 20, no. 1, pp. 013116, 2010.

[50] L. O. Chua., M. Komuro, and T. Matsumoto, "The double scroll family," *IEEE Transactions on circuits and Systems*, vol. 33, no. 11, pp. 1072–1118, 1986.

[51] D. Matignon, "Stability results for fractional differential equations with applications to control Processing," *Computational engineering in systems applications*, vol. 2, no. 1, pp. 963–968, 1996.

[52] S. Bhalekar and M. Patil, "Singular points in the solution trajectories of fractional order dynamical systems," *Chaos: An Interdisciplinary Journal of Nonlinear Science*, vol. 28, no. 11, pp. 113123, 2018.

[53] J. L. Echenausía-Monroy, G. Huerta-Cuellar, R. Jaimes-Reátegui, J. H. García-López, V. Aboites, B. B. Cassal-Quiroga, and H. E. Gilardi-Velázquez, "Multistability Emergence through Fractional-Order-Derivatives in a PWL Multi-Scroll System," *Electronics*, vol. 9, no. 6, pp. 880, 2020.

[54] J. L. Echenausía-Monroy, H. E. Gilardi-Velázquez, R. Jaimes-Reátegui, V. Aboites, and G. Huerta-Cuellar, "A physical interpretation of fractional-order-derivatives in a jerk system: Electronic approach," *Communications in Nonlinear Science and Numerical Simulation*, vol. 90, pp. 105413, 2020.

[55] K. Diethelm, N. J. Ford, and A. D. Freed, "A predictor-corrector approach for the numerical solution of fractional differential equations," *Nonlinear Dynamics*, vol. 29, no. 1, pp. 3–22, 2002.

References

[1] P. Y. Dousseh, C. Ainamon, C. H. Miwadinou, A. V. Monwanou, and J. B. Chabi Orou, "Chaos in a Financial System with Fractional Order and Its Control via Sliding Mode," *Complexity*, vol. 2021, Article ID 4636658, 15 pages, 2021.

Hindawi
Complexity
Volume 2021, Article ID 8490695, 10 pages
https://doi.org/10.1155/2021/8490695

WILEY | Hindawi

Research Article

Diverse Dynamic Behaviors and Firing Activities of the Modified Fractional-Order Hindmarsh–Rose Neuronal Model Induced by Fractional-Order

Xin Yang,[1] **GuangJun Zhang**,[2] **XueRen Li**,[1] **and Dong Wang**[1]

[1]*Aeronautics Engineering College, Air Force Engineering University, Xi'an 710038, China*
[2]*Department of Basic Sciences, Air Force Engineering University, Xi'an 710058, China*

Correspondence should be addressed to GuangJun Zhang; 1418008562@qq.com

Received 28 June 2021; Revised 9 August 2021; Accepted 24 October 2021; Published 12 November 2021

Academic Editor: Guillermo Huerta Cuellar

It is important to investigate the firing activities of neurons, and previous experimental works have shown that fractional-order neuronal models depict the firing rate of neurons more verifiably. In this study, a modified fractional-order Hindmarsh–Rose neuronal model is proposed, and the dynamics and firing activities are investigated. Some novel phenomenon can be found. First, by analyzing numerically and theoretically, the Hopf bifurcation is found to occur when the external direct current stimulus is chosen appropriately. The effects of fractional-order on the bifurcation are also studied. Second, when injecting a direct current stimulus, compared with the integer-order model, the system has more varying dynamic behaviors and firing pattern transitions. Under different external current stimulus, periodic firing patterns and chaotic firing patterns occur when fractional-order changes, but the regions of chaotic firing patterns are different. In other words, the transition mode of periodic firing and chaotic firing induced by fractional-order is different under different external current stimulus. The two-dimensional colored diagram of firing patterns is also investigated. Finally, when injecting periodic current stimulus, regular/irregular bursting, multiple spiking, regular\irregular square wave bursting, and mixed firing mods are found by setting the appropriate fractional-order, amplitude, and frequency of the external current stimulus. Some firing patterns cannot be found in integer-order models. When the amplitude is chosen at appropriate values, the region of frequency when the system displays the mixed firing modes decreases with increasing fractional-order.

1. Introduction

The neuron was modeled and analyzed by a large amount of experimental data, and the results show that the firing behaviors of neurons are nonlinear processes. In 1952, Hodgkin and Huxley used equivalent circuits and large amounts of data from experiments to model and analyze the data. They constructed the Hodgkin–Huxley (HH) neuron model through theoretical derivation [1]. In 1961, FitzHugh simplified the variables in the HH model and constructed a low-dimensional model, the two-dimensional Fitz-Hugh–Nagumo (FHN) model [2]. Morris and Lecar summarized the new neuron model (Morris–Lecar (ML) model) from the experimental data of the arctic goose muscle fiber, which is a further simplification of the HH model. In 1982, based on voltage clamp experiment data of snail nerve cells, Hindmarsh and Rose proposed the Hindmarsh–Rose (HR) model [3]. The modified HR model is called the polynomial model, which is the modified HR-type model [4]. This is also an important model for neurons, but research on this model's firing activities is limited. The modified HR model has many dynamic characteristics and depicts bursting and spiking behaviors successfully. It is significant to investigate the dynamic behavior of the modified HR model. Firing activities are important phenomena in the neuronal system. A number of researchers have used different neuronal models to try to explain some of the phenomena observed in experiments. Studying the motor mechanism of the

neuronal dynamical system helps us to understand relevant phenomena in the brain and contribute to the development of artificial intelligence.

Neuronal models have been studied numerically and theoretically [5, 6]. In [7], the HR neuronal model was used to develop a new type of a central pattern generator. Neuronal models describe the firing patterns in real neurons, for example [8]. For neuronal model firing, the effects of electromagnetic radiation [9, 10] and extracellular alternating-current feld [11] have been investigated. In [9], chaotic bursting and periodic firing were found in the HR model under an electric field, and Hopf bifurcation was verified in this system. In [10], the mode transition of electrical activities induced by electromagnetic radiation was studied. The two-dimensional discrete HR model was investigated in [12]. Diverse bifurcation points and dynamic behaviors were found. The neuronal system's synchronization behaviors were investigated in [9, 13]. For collective behaviors in neuronal networks, [14] depicted the dynamics of the neurons and neuronal network, such as the mode transition in electrical activity, pattern formation, and selection in networks of neurons. In recent years, some researchers have investigated modified HR models by analyzing bifurcation points theoretically and firing pattern transitions [15–17]. Reference [15] analyzed the dynamic behaviors of a modified HR model with induced electromagnetic radiation and injected current stimulus, and diverse bifurcation points and firing activities were found. The firing pattern transitions with direct current stimulus and without current stimulus were investigated in [16, 17], respectively. At present, there are few studies on the modified HR model, but this model's dynamic behaviors can be important to understand the experimental results.

The above studies studied the integer-order model only. In results of [18], after analyzing the dynamics of the firing rate with a range of stimulus dynamics, showed that the multiple time scale adaptation is consistent with fractional-order differentiation. Fractional computation is related to the intrinsic properties of dynamical systems [19]. Local memory, nonuniform diffusion effects, and many other aspects require fractional computation [19, 20]. Fractional-order differentiation is a fundamental and general computation that can contribute to efficient information processing, stimulus anticipation, and assessment of frequency-independent phase shifts of oscillatory neuronal firing. In this way, fractional-order differentiation has advantages over integer-order differentiation in the depiction of the firing characteristics of some types of neurons. The fractional-order model can give a more complete picture of neurons' dynamic characteristics than the integer-order model. In the past, scholars have performed much research on fraction-order dynamical systems and applied them in many fields, such as financial systems [21], biomedicine [22, 23], and the spread of infectious diseases [24]. In terms of the fractional-order neuronal model, the single fractional-order HR neuronal model [25] was investigated, and the transitions of chaotic firing and periodical firing, spike firing, and bursting firing were observed. Other fractional-order models such as the fractional-order Lorenz [26, 27], piecewise-linear (PWL) hyperchaotic system [28], and Rossler system [27, 29] were also investigated, and diverse dynamic behaviors were found. The firing activities of neuronal models need to be further investigated, and modified fractional-order HR model may have more diverse firing patterns. However, there is no research studying the modified fractional-order HR model under external direct and periodic current stimulus. Like [21, 23], the Adomian decomposition methods (ADM) algorithm is used in the present study because of its great computational efficiency.

From this perspective, this study is organized as follows: first, the modified fractional-order HR model under an external current stimulus is proposed. The bifurcation analysis and influence of fractional-order on the bifurcation are studied numerically and theoretically. Then, the firing patterns, firing pattern transition, and bifurcation diagrams with a bifurcation parameter of fractional-order when injected with a direct current stimulus were investigated. Finally, when a periodic current stimulus is injected, diverse firing activities are studied.

2. Model Description and Bifurcation Analysis

2.1. Model Description. After Hindmarsh and Rose proposed the Hindmarsh–Rose model [3], a large number of studies have been constructed on the HR neuronal model. The HR neuronal model is described as follows:

$$\begin{cases} \dot{x} = y - ax^3 + bx^2 - z + I, \\ \dot{y} = c - dx^2 - y, \\ \dot{z} = r[s(x - \overline{x}) - z], \end{cases} \tag{1}$$

where x is the membrane action potential, y is a recovery variable, z is a slow adaption current, and I is the external stimulus current. $a, b, c, d, r, s, \overline{x}$ are the parameters in the system, and they are usually set as $a = 1, b = 3, c = 1, d = 5, r = 0.006, s = 4, \overline{x} = -1.56$. From previous studies [15–17], the integer-order modified HR model under a current stimulus is described as follows:

$$\begin{cases} \dot{x} = -s\left(-ax^3 + x^2\right) - y - bz + I, \\ \dot{y} = \varphi\left(x^2 - y\right), \\ \dot{z} = \varepsilon[sa_1 x + b_1 - kz], \end{cases} \tag{2}$$

where x represents the membrane voltage of the model; y and z measure the gating dynamics of the ion channels and the dynamics of the cytosolic channels, respectively; $a, b, a_1, b_1, k, s, \varphi$ are the parameters of the modified HR model, and in this study, they are set as $a = 0.5, b = 1$, $\varphi = 1, \varepsilon = 0.02, s = -1.61, a_1 = -0.1, b_1 = -0.045, k = 0.2$. I is a variable.

There are many definitions of fractional derivatives, and in practice, the most frequently used definitions are three: the Grunwald–Letnikov derivative, Riemann–Liouville derivative, and Caputo derivative. According to [25], under some conditions, the three definitions are equivalent and can be intertranslated. The Caputo derivative makes the Laplace transformation more concise, so it is simpler to solve the

fractional-order derivative. Similar to most literature, the Caputo derivative is adopted in this study.

Definition 1. The Caputo derivative of function $f(x)$ is defined as

$$ {}_0^C D_t^q f(x) = \frac{1}{\Gamma(n-q)} \int_0^t \frac{f^{(n)}(\tau)}{(t-\tau)^{q-n+1}} \mathrm{d}\tau, \tag{3} $$

where $n-1 < q < n$, $\Gamma(\bullet)$ is the gamma function which is defined as

$$ \Gamma(z) = \int_0^{\infty} t^{z-1} e^{-1} \mathrm{d}t. \tag{4} $$

Especially, when $0 < q < 1$,

$$ {}_0^C D_t^q f(x) = \frac{1}{\Gamma(1-q)} \int_0^t \frac{f'(\tau)}{(t-\tau)^q} \mathrm{d}\tau. \tag{5} $$

The fractional-order modified HR neuronal model can be proposed as

$$ \begin{cases} D_t^q x = -s\left(-ax^3 + x^2\right) - y - bz + I, \\ D_t^q y = \varphi\left(x^2 - y\right), \\ D_t^q z = \varepsilon\left[sa_1 x + b_1 - kz\right], \end{cases} \tag{6} $$

where D_t^q is the differential operator defined by Caputo, q is the fractional-order operator, and the other variables and parameters are the same as in the integer-order model. In this study, similar to the integer-order model, the parameters are set as follows: $a = 0.5, b = 1, \varphi = 1, \varepsilon = 0.02, s = -1.61$, $a_1 = -0.1, b_1 = -0.045, k = 0.2$. I and q are the variables.

2.2. Bifurcation Analysis. The equilibrium point can be obtained by solving the equation system $\dot{x} = \dot{y} = \dot{z} = 0$, which is

$$ \begin{cases} \dot{x} = -s\left(-ax^3 + x^2\right) - y - bz + I = 0, \\ \dot{y} = \varphi\left(x^2 - y\right) = 0, \\ \dot{z} = \varepsilon\left[sa_1 x + b_1 - kz\right] = 0. \end{cases} \tag{7} $$

In this part, similar to the integer-order model in the above part, I is variable, and the other parameters are set as $a = 0.5, b = 1, \varphi = 1, \varepsilon = 0.02, s = -1.61$, $a_1 = -0.1, b_1 = -0.045, k = 0.2$. The equilibrium point $S_e(x_e, y_e, z_e)$ can be described as follows after calculation:

$$ S_e\left(x_e, x_e^2, \frac{1}{k}\left(sa_1 x_e + b_1\right)\right). \tag{8} $$

From equation system (7) and the equilibrium point $S_e(x_e, y_e, z_e)$, the equation with one unknown quantity is as follows:

$$ -sax_e^3 + (s+1)x_e^2 + \frac{bsa_1}{k} x_e + \left(\frac{bb_1}{k} - I\right) = 0. \tag{9} $$

To solve the equation, the Cardan formula [5] is introduced. Now, the conversions are $m_1 = -sa$, $m_2 = (s+1)$, $m_3 = bsa_1/k$, $m_4 = ((bb_1/k) - I)$, $x_e = y_e - (m_2/3m_1)$. Equation (9) can be simplified as follows:

$$ y_e^3 + py_e + q = 0, \tag{10} $$

where $p = 3m_1m_3 - m_2^2/3m_1^2$, $q = 27m_1^2m_4 - 9m_1m_2m_3 + 3m_2^3/27m_1^3$, and the Cardan discriminant is $\Delta = (q/2)^2 + (p/3)^2$. After calculation, the Cardan discriminant $\Delta > 0$, so there exists a single real root which is defined by

$$ x_e = \sqrt[3]{-\frac{q}{2} + \sqrt{\Delta}} + \sqrt[3]{-\frac{q}{2} - \sqrt{\Delta}} - \frac{m_2}{3m_1}. \tag{11} $$

Now, we consider the existence of Hopf bifurcation. Suppose that the system $\dot{x} = f_\mu(x)$, $x \in \mathbb{R}^n, \mu \in \mathbb{R}$ has an equilibrium (x_0, μ_0) at which the following properties are satisfied:

(1) $D_x f_{\mu_0}(x_0)$ has a simple pair of purely imaginary eigenvalues and other eigenvalues with negative real parts

(2) $\mathrm{d}/\mathrm{d}\mu\,(R(\lambda(\mu)))|_{\mu=\mu_0} \neq 0$

Then, the system has a Hopf bifurcation at the equilibrium (x_0, μ_0). The eigenvalues can be analyzed by determining the Jacobian matrix associated with system (7), and the characteristic equation $\det(J_e - \lambda L) = 0$ can be obtained as equation (12), where L is an identity matrix of the same size as J_e.

$$ J_e = \begin{pmatrix} 3sax_e^2 - 2sx_e & -1 & -b \\ 2\varphi x_e & -\varphi & 0 \\ \varepsilon sa_1 & 0 & -k\varepsilon \end{pmatrix}, \tag{12} $$

$$ P(\lambda) = \lambda^3 + F_1\lambda^2 + F_2\lambda + F_3, $$

in which

$$ \begin{aligned} F_1 &= \varphi - G + k\varepsilon, \\ F_2 &= 2\varphi x_e - \varphi G + k\varepsilon(\varphi - G) + b\varepsilon sa_1, \\ F_3 &= k\varepsilon\left(2\varphi x_e - \varphi G\right) + b\varepsilon sa_1\varphi, \\ G &= 3sax_e^2 - 2sx_e. \end{aligned} \tag{13} $$

Using the same method as in equation (9), equation (9) can be simplified as follows:

$$ \lambda'^3 + p\lambda'^2 + q = 0, \tag{14} $$

in which $p_1 = 3F_2 - F_1^2/3$, $q_1 = 27F_3 - 9F_1F_2 + 3F_1^3/27$. The three roots of equation (12) are

$$\lambda_1 = \sqrt[3]{-\frac{q_1}{2} + \sqrt{\Delta}} + \sqrt[3]{-\frac{q_1}{2} - \sqrt{\Delta}} - \frac{F_1}{3},$$

$$\lambda_2 = \frac{-1 + j\sqrt{3}}{2} \sqrt[3]{-\frac{q_1}{2} + \sqrt{\Delta}} + \frac{-1 - j\sqrt{3}}{2} \sqrt[3]{-\frac{q_1}{2} - \sqrt{\Delta}} - \frac{F_1}{3},$$

$$\lambda_3 = \frac{-1 - j\sqrt{3}}{2} \sqrt[3]{-\frac{q_1}{2} + \sqrt{\Delta}} + \frac{-1 + j\sqrt{3}}{2} \sqrt[3]{-\frac{q_1}{2} - \sqrt{\Delta}} - \frac{F_1}{3}. \tag{15}$$

From the above analysis, when $I = I_{cr} = -0.253$, there exists a simple pair of purely imaginary eigenvalues and a negative real root at equilibrium (x_0, μ_0). Then, the results can be calculated as

$$\frac{d\lambda_1}{dI}|_{I=I_{cr}} \neq 0. \tag{16}$$

The conclusion that there exists a Hopf bifurcation when $I = I_{cr}$ can be drawn. For the fractional-order system, the stability can be studied using the following lemma:

Lemma 1. *Consider the linear autonomous system* $D^q X = AX$, $X(0) = X_0$, *where* $X \in R^n (n \in N)$ *and* $A \in R^{n\times n}$. *The system is asymptotically stable when and only when* $|\arg(\lambda)| > q\pi/2$ *is satisfied for an arbitrary eigenvalue* λ. *The system is stable when and only when* $|\arg(\lambda)| > q\pi/2$ *is satisfied for an arbitrary eigenvalue* λ. *The stable area of the q-order linear system is shown in Figure 1.*

According to Lemma 1, the critical values of the external current stimulus I_{cr} for the fractional-order model to start firing at different fractional-orders can be calculated, and the results are shown in Figure 2.

2.3. Firing Behavior under Different Direct Current Stimulus and Fractional-Orders. In this section, the parameters are also set as $a = 0.5, b = 1, \varphi = 1, \varepsilon = 0.02, s = -1.61, a_1 = -0.1, b_1 = -0.045, k = 0.2$. I and q are the variables. In [17], the firing activity of integer-order and the influence of parameters on the firing patterns were studied. In this section, the influence of fractional-order and direct current stimulus are investigated. In [17], when $I = 0.06$, the integer-order modified HR model shows a spiking firing pattern. Figure 3 shows the bifurcation diagram varying with the fractional-order when $I = 0.06$. Figure 3 shows that the firing patterns change with varying fractional-order.

Figure 4 shows the corresponding time series of x and the phase diagram of (x, y). When $q = 0.2$, as shown in Figures 4(a) and 4(b), the neuronal model displays periodic-6 bursting. From Figures 4(c) and 4(d), the neuronal model displays periodic-5 bursting when $q = 0.25$. When $q = 0.3$ and $q = 0.39$, the neuronal model displays chaotic bursting (Figures 4(e), 4(f), 4(i), and 4(j)). The neuronal model displays periodic-4 bursting when $q = 0.35$ (Figures 4(g) and 4(h)), periodic-2 bursting when $q = 0.415$ (Figures 4(k) and 4(l)), and spiking when $q = 0.55$ (Figures 4(m) and 4(n)). From the above analysis, under the influence of the fractional-order, more complex dynamic behaviors occur. The

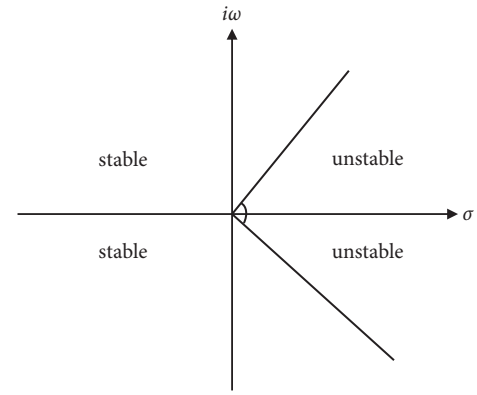

Figure 1: Stable area of the q-order linear system.

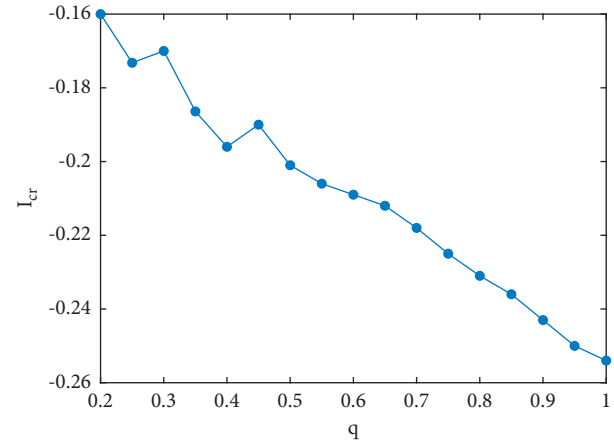

Figure 2: The $I_{cr} \sim q$ curve.

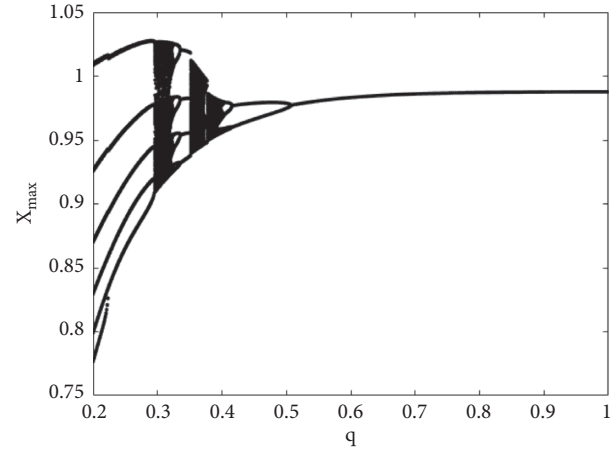

Figure 3: Bifurcation diagram with a bifurcation parameter of fractional-order when $I = 0.06$.

fractional-order can induce a periodic firing pattern for the integer-order model transiting to the chaotic firing pattern.

To prove that if fractional-order can induce a chaotic firing pattern for an integer-order model transitioning to a periodic firing pattern, the firing pattern varies with fractional-order when $I = 0.015$ is set as an example. In [17], the integer-order neuronal model displays chaotic firing. As shown in Figure 5 (the bifurcation diagram when $I = 0.015$),

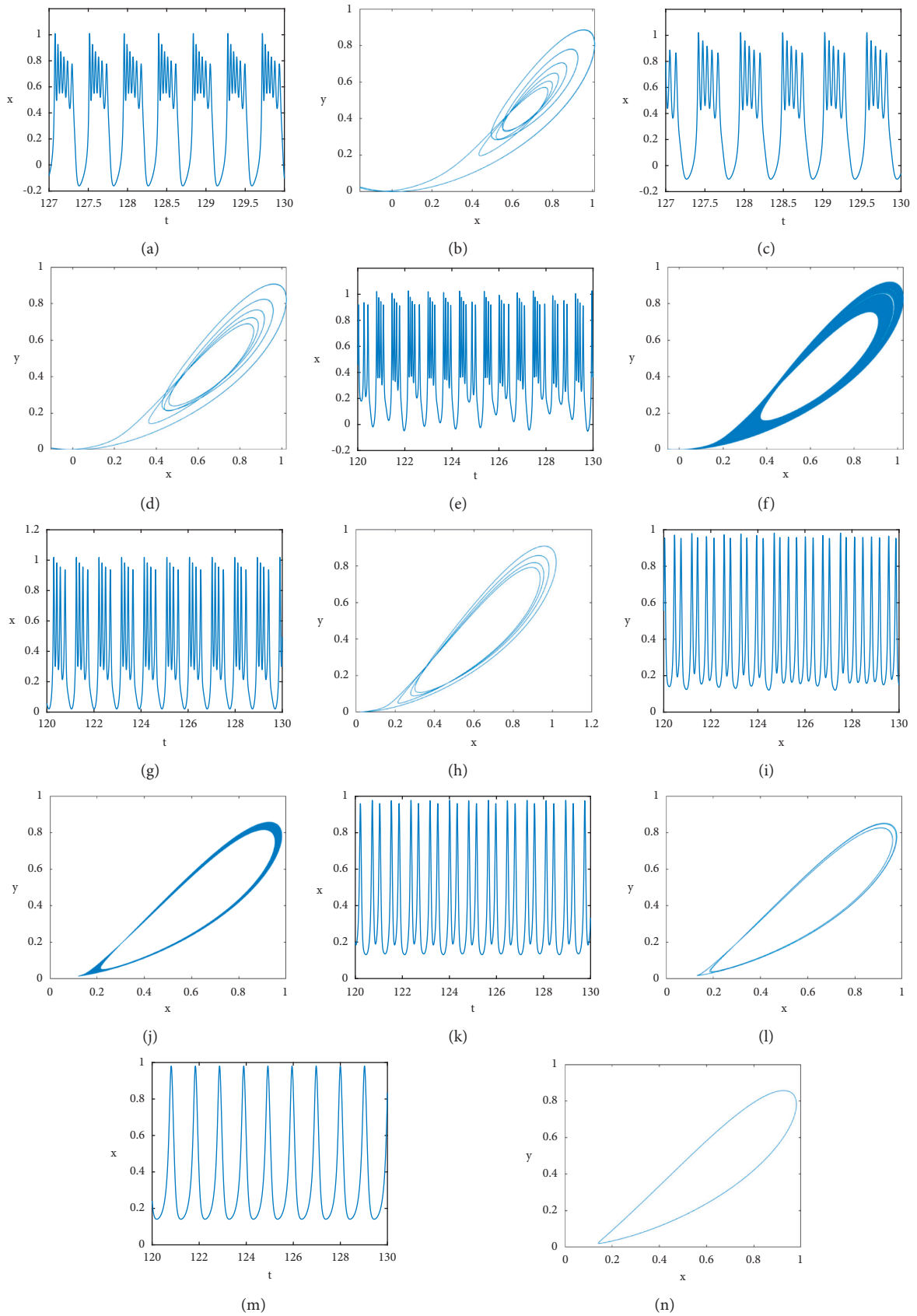

FIGURE 4: Corresponding time series of x and the phase diagram of (x, y) when (a)-(b) $q = 0.2$, (c)-(d) $q = 0.25$, (e)-(f) $q = 0.3$, (g)-(h) $q = 0.35$, (i)-(j) $q = 0.39$, (k)-(l) $q = 0.415$, and (m)-(n) $q = 0.55$.

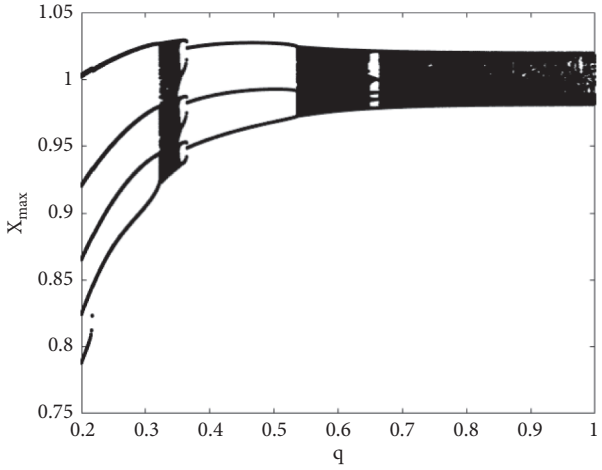

Figure 5: Bifurcation diagram with a bifurcation parameter of fractional-order when $I = 0.015$.

periodic bursting occurs when the fractional-order decreases. There exists a periodic window around $q = 0.65$.

When $I = 0.015$, the corresponding time series of x and the phase diagram of (x, y) are shown in Figure 6. When $q = 0.8$, as shown in Figures 6(a) and 6(b), the neuronal model displays chaotic firing. When $q = 0.4$, $q = 0.3$, $q = 0.2$, the neuronal model displays periodic-3, periodic-4, and periodic-5 bursting (Figures 6(c)–6(h)). Meanwhile, fractional-order can induce the chaotic firing pattern to transition to a periodic firing pattern.

From Figure 7, the two-dimensional colored diagram of firing patterns, we can easily find the chaotic firing range and periodic firing range. We find that the chaotic range is larger when the direct current stimulus is smaller.

2.4. Firing Behavior under External Periodic Current Stimulus. In the above analysis, various firing activities are investigated when the modified fractional-order HR model is under direct external current. When the direct external current is replaced by a periodic external current stimulus, there are various firing activities. New firing patterns are found when the fractional-order changes. Spiking, bursting, and other firing patterns can occur at an appropriate fractional-order and by injecting a periodic current stimulus. The modified fractional-order HR model under periodic external current stimulus is as follows:

$$\begin{cases} D_t^q x = -s\left(-ax^3 + x^2\right) - y - bz + A\sin(\eta t), \\ D_t^q y = \varphi\left(x^2 - y\right), \\ D_t^q z = \varepsilon\left[sa_1 x + b_1 - kz\right], \end{cases} \tag{17}$$

where A is the amplitude of the external current stimulus and η is the angular frequency. In this section, similar to the above section, the parameters are set as $a = 0.5, b = 1, \varphi = 1, \varepsilon = 0.02, s = -1.61, a_1 = -0.1, b_1 = -0.045, k = 0.2$, and the fractional-order q, the amplitude A, and angular frequency η are considered as variables.

We set $A = 0.01$, and regular bursting and irregular bursting can be found. When $q = 0.3, \eta = 0.01$, the system is in regular bursting, as shown in Figure 8(a). Irregular bursting can be found when $q = 0.6, \eta = 0.01$ (Figure 8(b)). After further investigating the firing activities, the critical value of fractional-order exists between regular bursting and irregular bursting. When the frequency η is changed, we can also find irregular bursting and regular bursting. For example, when $\eta = 0.1$, the system is in regular bursting when $q = 0.3$ (Figure 8(c)) and irregular bursting when $q = 0.6$ (Figure 8(d)).

The amplitude of the external current stimulus is increased as $A = 0.05$. Multiple spiking consisting of different spiking frequencies, spiking, and square wave bursting can be found. Set $\eta = 0.01$, and the system is in regular bursting for $q = 0.3$ (Figure 9(a)), multiple spiking when $q = 0.7$ (Figure 9(b)), and square wave bursting when $q = 0.9$ (Figure 9(c)). Setting $\eta = 0.05$, the system displays mixed firing modes that include bursting and spiking when $q = 0.4$ (Figure 9(d)), irregular bursting when $q = 0.8$ (Figure 9(e)), and another irregular bursting that is different from the above bursting activities when $q = 0.95$ (Figure 9(f)). Furthermore, setting $\eta = 0.1$, the system displays regular spiking when $q = 0.9$ (Figure 9(g)), mixed mode oscillations that consist of multiple numbers of spiking and subthreshold oscillations when $q = 0.95$ (Figure 9(h)), and the system can also display regular bursting and mixed firing modes when $q = 0.4$ (Figure 9(i)).

When $A = 0.1$, the firing activities are similar to the above firing patterns. However, a novel phenomenon can be found. First, setting $q = 0.5$, the system is in mixed firing modes when $\eta = 0.01$ (Figure 10(a)), irregular square wave bursting when $\eta = 0.05$ (Figure 10(b)), and regular square wave bursting when $\eta = 0.1$ (Figure 10(c)). Then, setting $q = 0.4$, the system is in mixed firing modes when $\eta = 0.01$ and $\eta = 0.05$ (Figures 10(d) and 10(e)), and regular square wave bursting when $\eta = 0.1$ (Figure 10(f)). When $q = 0.3$, we can find that the system displays mixed firing modes when $\eta = 0.01$, $\eta = 0.05$, and $\eta = 0.1$. From the above analysis, we can conclude that the region of frequency η when the system displays the mixed firing modes decreases with increasing fractional-order.

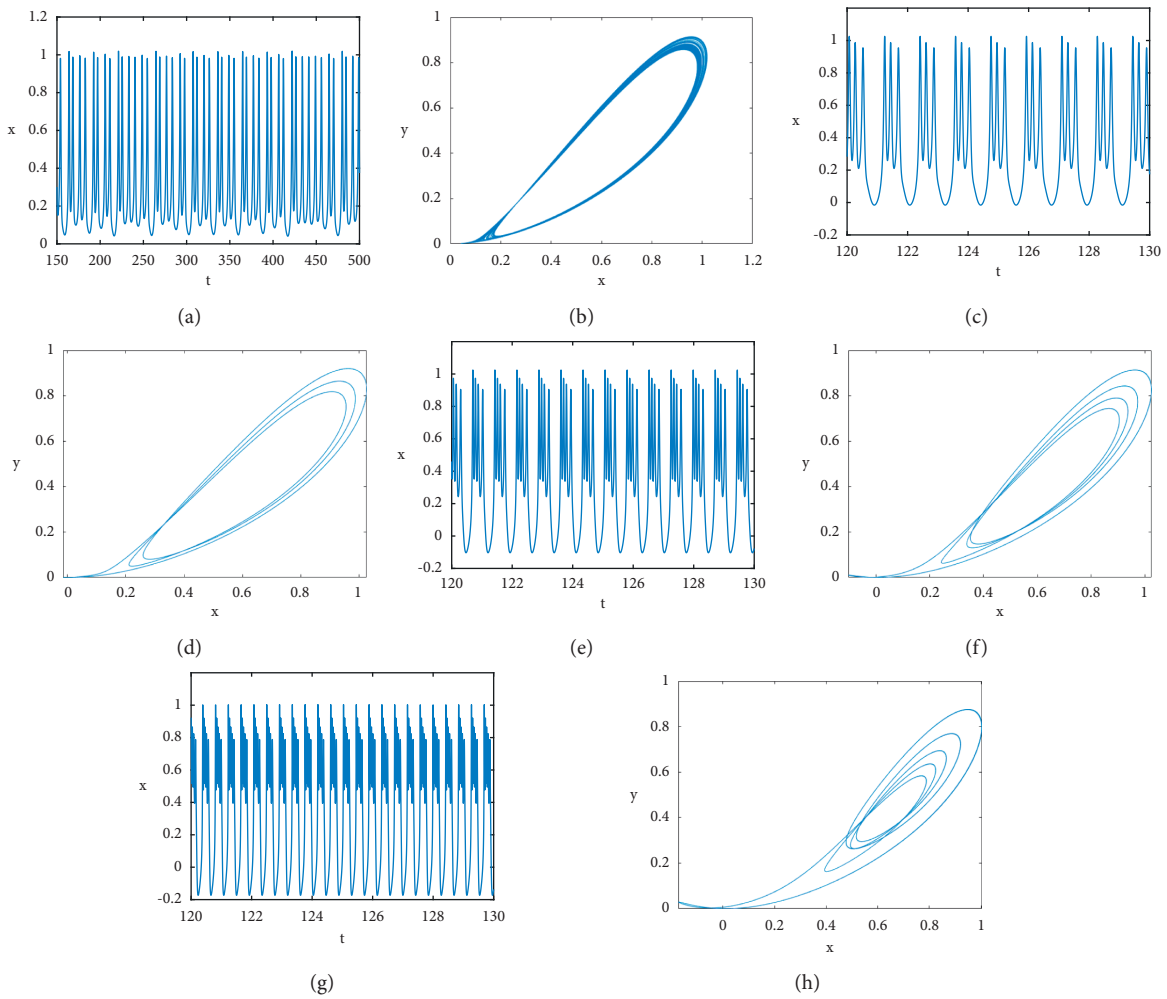

Figure 6: Corresponding time series of x and the phase diagram of (x, y) when (a)-(b) $q = 0.8$, (c)-(d) $q = 0.4$, (e)-(f) $q = 0.3$, and (g)-(h) $q = 0.2$.

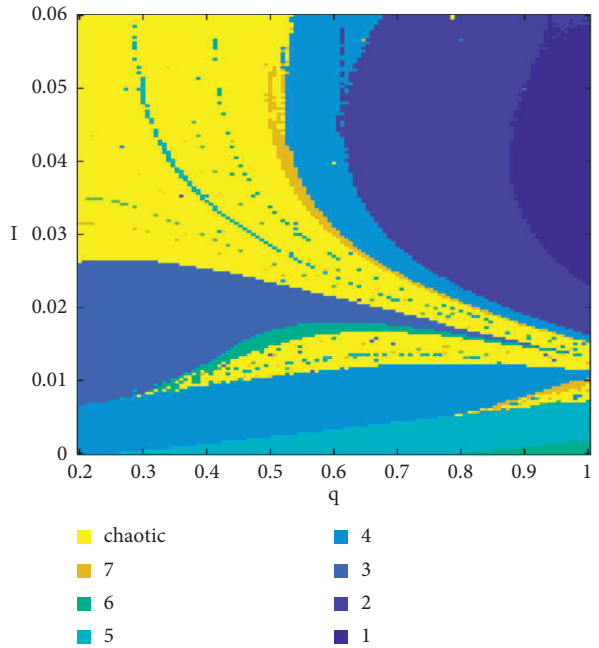

Figure 7: Two-dimensional colored diagram of firing patterns.

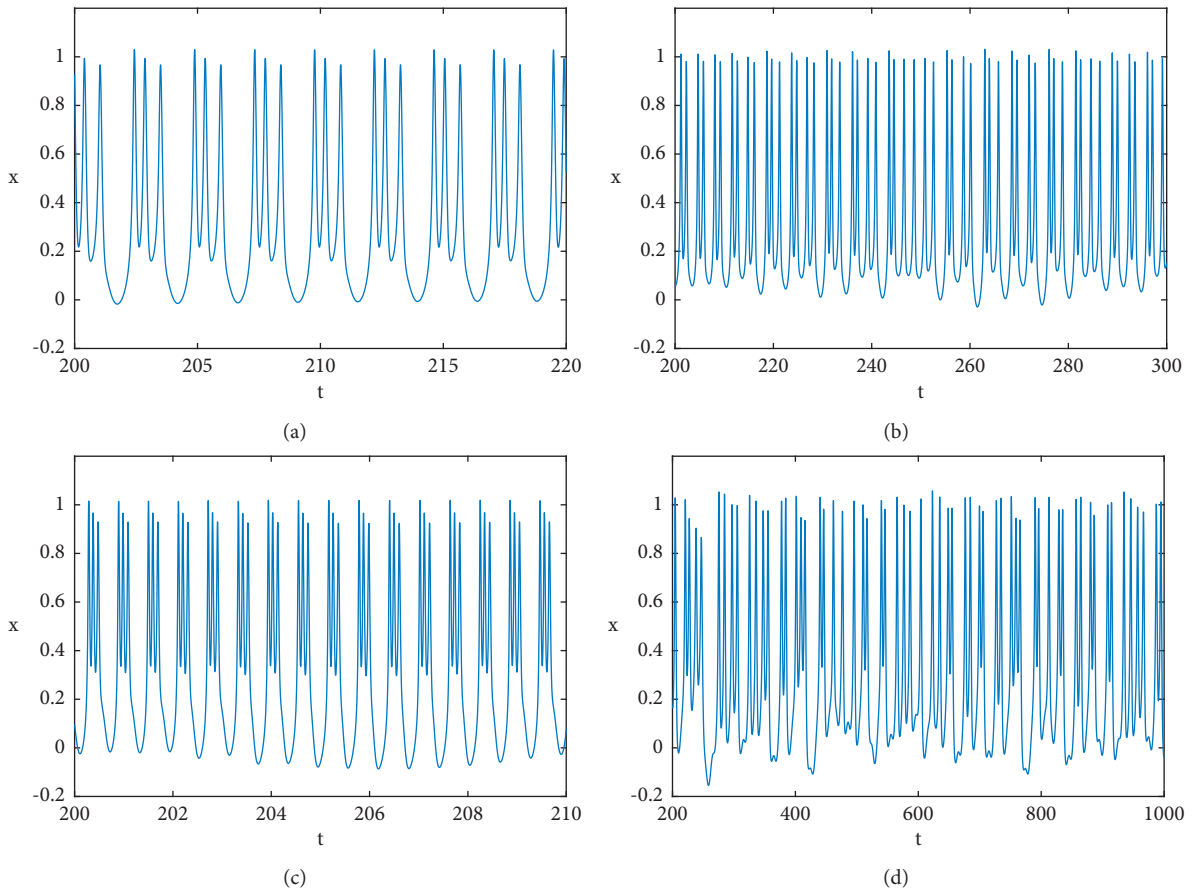

Figure 8: Firing patterns when $A = 0.01$, $\eta = 0.01$, (a) $q = 0.3$, (b) $q = 0.6$, $\eta = 0.1$, (c) $q = 0.3$, and (d) $q = 0.6$.

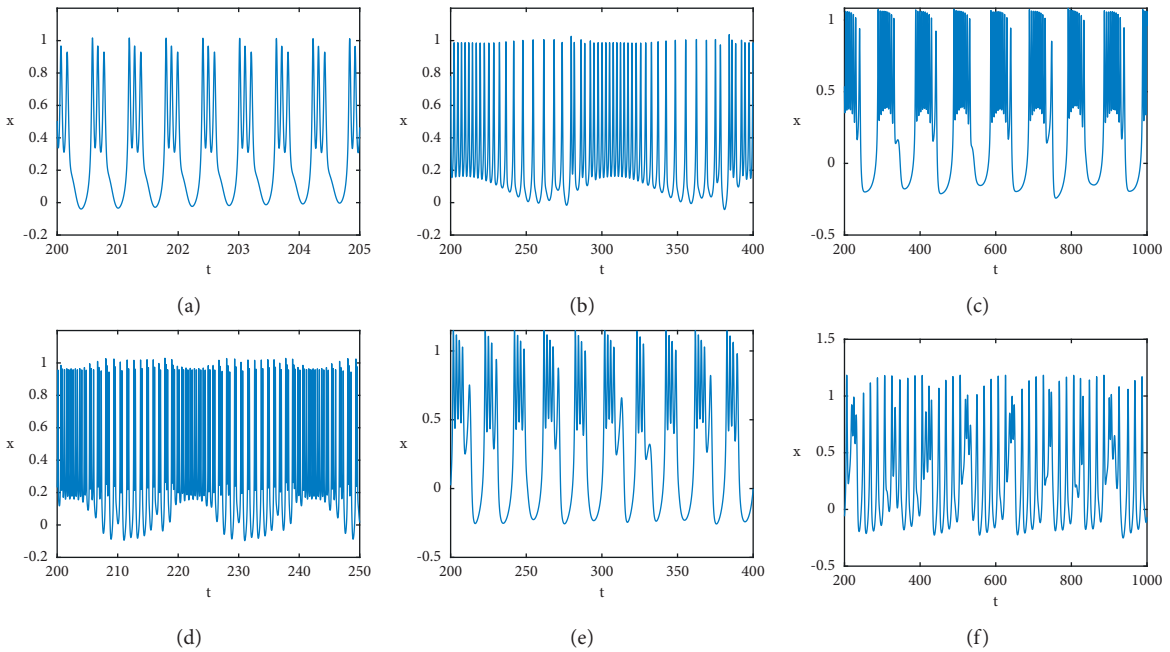

Figure 9: Continued.

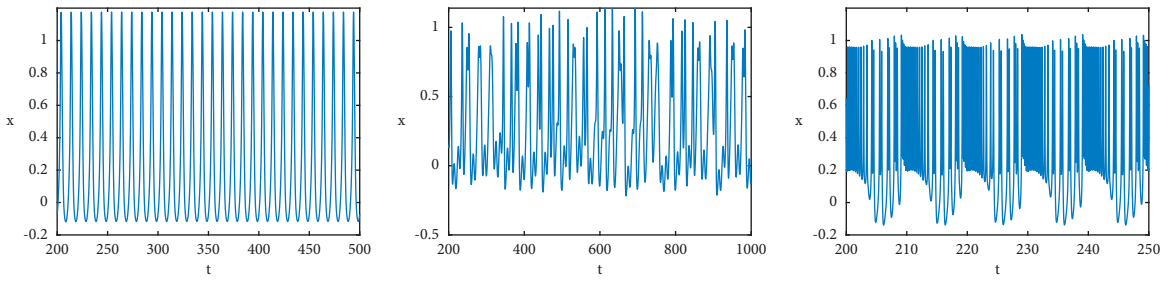

Figure 9: Firing patterns when $A = 0.05$, $\eta = 0.01$, (a) $q = 0.3$, (b) $q = 0.7$, and (c) $q = 0.9$; $A = 0.05$, $\eta = 0.05$, (d) $q = 0.4$, (e) $q = 0.8$, and (f) $q = 0.95$; $A = 0.05$, $\eta = 0.1$ (g) $q = 0.9$, (h) $q = 0.95$, and (i) $q = 0.4$.

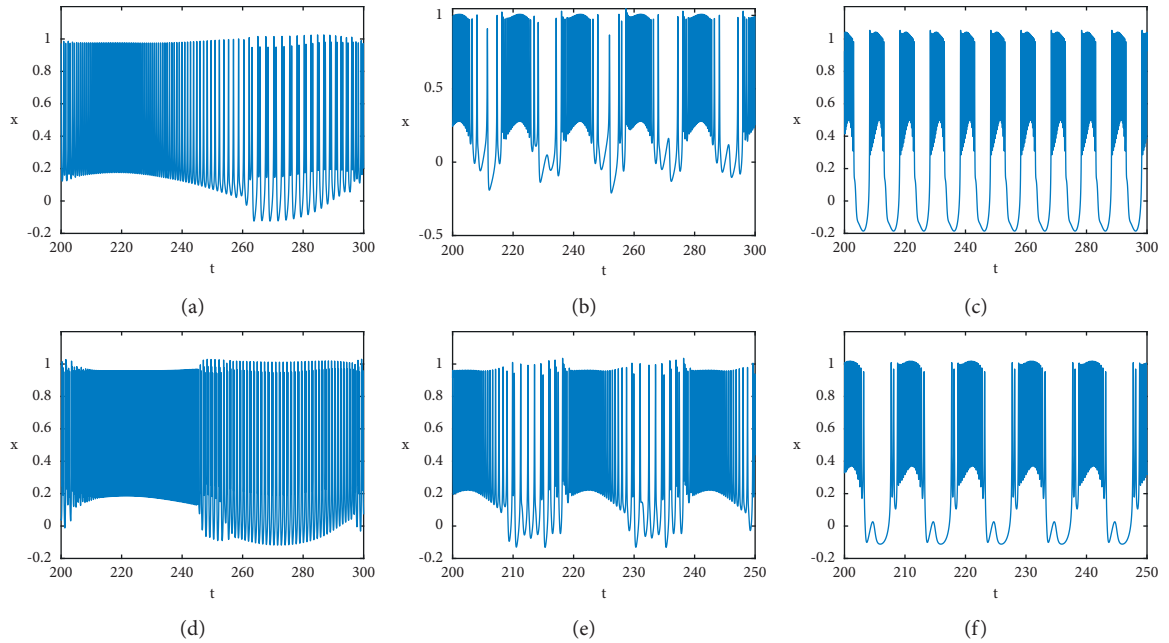

Figure 10: Firing patterns when $A = 0.1$, $q = 0.5$ (a) $\eta = 0.01$, (b) $\eta = 0.05$, and (c) $\eta = 0.1$; $A = 0.1$, $q = 0.4$, (d) $\eta = 0.01$, (e) $\eta = 0.05$, and (f) $\eta = 0.1$.

3. Conclusion

In this study, the dynamic behaviors of the modified HR model were investigated, and diverse firing activities and some novel phenomena were found. First, according to the integer-order model and Cardan formula, the existence of Hopf bifurcation can be proven. The critical values of the direct external current stimulus for each fractional-order are also obtained. Then, when direct current stimulus is injected, the fractional-order model exhibits more complex dynamic behaviors compared with the integer-order model. In some direct current stimulus, the fractional-order can induce periodic firing for the integer-order model transitioning to chaotic firing, vice versa. In an appropriate direct current stimulus, from the bifurcation diagram with a bifurcation parameter of fractional-order, there is some transition of firing patterns such as chaotic bursting, periodic bursting (including different bursting modes), and periodic spiking. In addition, from the two-dimensional colored diagram, we can clearly find the chaotic firing range and periodic range. Finally, when periodic current stimulus is injected, at some appropriate fractional-order and parameters of periodic current stimulus, the fractional-order model can display regular/irregular bursting, regular/irregular spiking, multiple spiking, regular/irregular square wave bursting, and mixed firing modes. The region of frequency when the system displays the mixed firing modes decreases with the increasing fractional-order at some amplitude values of the external current stimulus.

Data Availability

The data used to support the findings of this study are included within the article, and other data used can be obtained from the corresponding author upon request.

Conflicts of Interest

The authors declare that they have no conflicts of interest.

References

[1] A. L. Hodgkin and A. F. Huxley, "A quantitative description of membrane current and its application to conduction and excitation in nerve," *The Journal of Physiology*, vol. 117, no. 4, pp. 500–544, 1952.

[2] R. FitzHugh, "Impulses and physiological states in theoretical models of nerve membrane," *Biophysical Journal*, vol. 1, no. 6, pp. 445–466, 1961.

[3] C. Morris and H. Lecar, "Voltage oscillations in the barnacle giant muscle fiber," *Biophysical Journal*, vol. 35, no. 1, pp. 193–213, 1981.

[4] T. A. Krasimira, M. O. Hinke, R. Thorsten, and A. Sherman, "Full system bifurcation analysis of endocrine bursting models," *Journal of Theoretical Biology*, vol. 264, no. 4, pp. 1133–1146, 2010.

[5] C. S. Herrmann and A. Klaus, "Autapse turns neuron into oscillator," *International Journal of Bifurcation and Chaos*, vol. 14, no. 2, pp. 623–633, 2004.

[6] A. Shilnikov and M. Kolomiets, "Methods of the qualitative theory for the Hindmarsh-Rose model: a case study-a tutorial," *International Journal of Bifurcation and Chaos*, vol. 18, no. 8, pp. 2141–2168, 2008.

[7] D. G. Zhang, Q. Zhang, and X. Y. Zhu, "Exploring a type of central pattern generator based on Hindmarsh–Rose model: from theory to application," *International Journal of Neural Systems*, vol. 25, no. 1, Article ID 1450028, 2015.

[8] H. Gu and B. Pan, "A four-dimensional neuronal model to describe the complex nonlinear dynamics observed in the firing patterns of a sciatic nerve chronic constriction injury model," *Nonlinear Dynamics*, vol. 81, no. 4, pp. 2107–2126, 2015.

[9] K. M. Wouapi, B. H. Fotsin, F. P. Louodop, K. F. Feudjio, Z. T. Njitacke, and T. H. Djeudjo, "Various firing activities and finite-time synchronization of an improved Hindmarsh-Rose neuron model under electric field effect," *Cognitive Neurodynamics*, vol. 14, no. 3, pp. 375–397, 2020.

[10] M. Lv and J. Ma, "Multiple modes of electrical activities in a new neuron model under electromagnetic radiation," *Neurocomputing*, vol. 205, pp. 375–381, 2016.

[11] H. Yu, J. Wang, B. Deng, and X. Wei, "Firing patterns of map-based neuron under extracellular alternating-current feld," *Acta Biochimica et Biophysica Sinica*, vol. 26, no. 10, pp. 907–918, 2010.

[12] B. Li and Z. He, "Bifurcations and chaos in a two-dimensional discrete Hindmarsh-Rose model," *Nonlinear Dynamics*, vol. 76, no. 1, pp. 697–715, 2014.

[13] H. Wang, Q. Wang, and Q. Lu, "Bursting oscillations, bifurcation and synchronization in neuronal systems," *Chaos, Solitons & Fractals*, vol. 44, no. 8, pp. 667–675, 2011.

[14] B. Bao, Q. Yang, D. Zhu, Y. Zhang, Q. Xu, and M. Chen, "Initial-induced coexisting and synchronous firing activities in memristor synapse-coupled Morris-Lecar bi-neuron network," *Nonlinear Dynamics*, vol. 99, no. 3, pp. 2339–2354, 2020.

[15] A. Mondal, R. K. Upadhyay, and J. Ma, "Bifurcation analysis and diverse firing activities of a modified excitable neuron model," *Cognitive Neurodynamics*, vol. 13, no. 4, pp. 393–407, 2019.

[16] K. J. Wu, T. Q. Luo, H. W. Lu, and Y. Wang, "Bifurcation study of neuron firing activity of the modified Hindmarsh-Rose model," *Neural Computing & Applications*, vol. 27, no. 3, pp. 739–747, 2016.

[17] K. J. Wu, W. Q. Li, and D. C. Wang, "Bifurcation of modified HR neural model under direct current," *Journal of Ambient Intelligence and Humanized Computing*, vol. 11, no. 12, pp. 6211–6221, 2020.

[18] B. N. Lundstrom, M. H. Higgs, W. J. Spain, and A. L. Fairhall, "Fractional differentiation by neocortical pyramidal neurons," *Nature Neuroscience*, vol. 1, no. 11, pp. 1335–1342, 2008.

[19] J. Ma, "Chaos theory and applications: the physical evidence, mechanism are important in chaotic systems," *Chaos Theory and Applications*, vol. 4, no. 1, pp. 1–3, 2022.

[20] J. A. T. Machado, V. Kiryakova, and F. Mainardi, "Recent history of fractional calculus," *Communications in Nonlinear Science and Numerical Simulation*, vol. 16, pp. 1140–1153, 2011.

[21] Z. Wang, X. Huang, and G. D. Shi, "Analysis of nonlinear dynamics and chaos in a fractional order financial system with time delay," *Computers & Mathematics With Applications*, vol. 62, no. 3, pp. 1531–1539, 2011.

[22] Y. X. Fu, Y. M. Kang, and G. R. Chen, "Stochastic resonance based visual perception using spiking neural networks," *Frontiers in Computational Neuroscience*, vol. 14, 2020.

[23] T. J. Anastasio, "The fractional-order dynamics OF brainstem vestibulooculomotor neurons," *Biological Cybernetics*, vol. 72, no. 1, pp. 69–79, 1994.

[24] K. Rajagopal, N. Hasanzadeh, F. Parastesh, I. Hamarash, S. Jafari, and I. Hussain, "A fractional-order model for the novel coronavirus (COVID-19) outbreak," *Nonlinear Dynamics*, vol. 101, no. 1, pp. 711–718, 2020.

[25] J. Dong, G. J. Zhang, Y. Xie, and Y. Hong, "Dynamic behavior analysis of fractional-order Hindmarsh-Rose neuronal model," *Cognitive Neurodynamics*, vol. 8, no. 2, pp. 167–175, 2014.

[26] S. B. He, K. H. Sun, X. Mei, B. Yan, and S. Xu, "Numerical analysis of a fractional-order chaotic system based on conformable fractional-order derivative," *European Physical Journal Plus*, vol. 132, no. 1, p. 36, 2017.

[27] C. Letellier and L. A. Aguirre, "Dynamical analysis of fractional-order Rössler and modified Lorenz systems," *Physics Letters A*, vol. 377, no. 28, pp. 1707–1719, 2013.

[28] L. M. Zhang, K. H. Sun, W. H. Liu, and S. B. He, "A novel color image encryption scheme using fractional-order hyperchaotic system and DNA sequence operations," *Chinese Physics B*, vol. 26, no. 10, pp. 98–106, 2017.

[29] D. Cafagna and G. Grassi, "Hyperchaos in the fractional-order Rossler system with lowest-order," *International Journal of Bifurcation and Chaos*, vol. 19, no. 1, pp. 339–347, 2009.

Hindawi
Complexity
Volume 2021, Article ID 1097505, 14 pages
https://doi.org/10.1155/2021/1097505

Research Article

Extremal Solutions for Caputo Conformable Differential Equations with *p*-Laplacian Operator and Integral Boundary Condition

Zhongqi Peng,[1] **Yuan Li**,[1] **Qi Zhang**,[1] **and Yimin Xue**[2]

[1]*School of Science, Shenyang University of Technology, Shenyang 110870, China*
[2]*School of Mathematics and Statistics, Xuzhou University of Technology, Xuzhou 221018, China*

Correspondence should be addressed to Yuan Li; syliyy@163.com

Received 16 August 2021; Accepted 6 October 2021; Published 25 October 2021

Academic Editor: Ning Wang

The Caputo conformable derivative is a new Caputo-type fractional differential operator generated by conformable derivatives. In this paper, using Banach fixed point theorem, we obtain the uniqueness of the solution of nonlinear and linear Cauchy problem with the conformable derivatives in the Caputo setting, respectively. We also establish two comparison principles and prove the extremal solutions for nonlinear fractional *p*-Laplacian differential system with Caputo conformable derivatives by utilizing the monotone iterative technique. An example is given to verify the validity of the results.

1. Introduction

In recent years, fractional calculus has been widely developed in pure mathematics and applied mathematics [1–7]. The characteristic of fractional calculus is that there are many different fractional derivatives or integrals, like Riemann–Liouville (RL), Caputo, Hadamard, Caputo–Hadamard types, and so on [1, 2, 8, 9]. So, the scholars have the opportunity to choose the most appropriate operators to describe complex problems in the real world. We recall some definitions from the traditional fractional calculus [1, 2].

The left RL fractional integral of order $\beta > 0$ is given by

$$ {}_a^R I^\beta f(t) = \frac{1}{\Gamma(\beta)} \int_a^b (t-s)^{\beta-1} f(s) \mathrm{d}s. \tag{1} $$

The left RL fractional derivative of order $\beta > 0$ is defined as

$$ {}_a D^\beta f(t) = \left(\frac{\mathrm{d}}{\mathrm{d}t}\right)^n {}_a I^{n-\beta} f(t) = \frac{(\mathrm{d}/\mathrm{d}t)^n}{\Gamma(n-\beta)} \int_a^t (t-s)^{n-\beta-1} f(s) \mathrm{d}s. \tag{2} $$

The left Caputo fractional derivative of order $\beta > 0$ is given by

$$ {}_a^C D^\beta f(t) = {}_a I^{n-\beta} f^{(n)}(t) = \frac{1}{\Gamma(n-\beta)} \int_a^t (t-s)^{n-\beta-1} f^{(n)}(s) \mathrm{d}s. \tag{3} $$

However, some basic properties such as product rule and chain rule are not valid for the RL and Caputo-type fractional derivatives. In 2014, Khalil et al. [10] defined a new fractional differential operator named the conformable derivative which satisfies the product rule and some other properties. In 2015, Abdeljawad [11] defined the left conformable integral ${}_a I^\alpha$ and derivative ${}_a T^\alpha$ as

$$ \begin{aligned} {}_a I^\alpha f(t) &= \frac{1}{\Gamma(\alpha)} \int_a^b (s-a)^{\alpha-1} f(s) \mathrm{d}s, \\ {}_a T^\alpha f(t) &= \lim_{\varepsilon \longrightarrow 0} \frac{f\left(t + \varepsilon (t-a)^{1-\alpha}\right) - f(t)}{\varepsilon}, \end{aligned} \tag{4} $$

where $\alpha \in (0, 1], t > 0, f\colon [a, +\infty) \longrightarrow \mathbb{R}$. If f is differentiable, then ${}_a T^\alpha f(t) = (t-a)^{1-\alpha} f'(t)$.

In 2017, Jarad et al. [12] established the conformable calculus in both RL and Caputo setting based on the work of Abdeljawad.

The left RL conformable integral of order $\beta \in \mathbb{C}, \mathrm{Re}(\beta) > 0$, is given by

$$ {}_a^{\beta}I^{\alpha} f(t) = \frac{1}{\Gamma(\beta)} \int_a^t \left(\frac{(t-a)^{\alpha} - (s-a)^{\alpha}}{\alpha} \right)^{\beta-1} f(s) \frac{\mathrm{d}s}{(s-a)^{1-\alpha}}. \tag{5} $$

The fractional integral (5) coincides with the traditional RL fractional integral (1) if $\alpha = 1$.

Let $I_{\alpha}([a,b]) = \{f\colon [a,b] \longrightarrow \mathbb{R}; f(t) = {}_aI^{\alpha}\psi(t) + f(a)$ for some $\psi \in L_{\alpha}(a)\}$, where $L_{\alpha}(a) = \{\psi\colon [a,b] \longrightarrow \mathbb{R};$ ${}_aI^{\alpha}\psi(t)$ exists for any $t \in [a,b]\}$. If $n \in \mathbb{N}^+$, $f \in C_{\alpha,a}^n [a,b] = \{f\colon [a,b] \longrightarrow \mathbb{R}; {}_a^{n-1}T^{\alpha} f \in I_{\alpha}([a,b])\}$, the left conformable derivative of order $\beta \in \mathbb{C}, \mathrm{Re}(\beta) > 0$, in the Caputo setting is defined by

$$ \begin{aligned} {}_a^{C\beta}D^{\alpha} f(t) &= {}_a^{n-\beta}I^{\alpha}\left({}_a^nT^{\alpha} f(t)\right) \\ &= \frac{1}{\Gamma(n-\beta)} \int_a^t \left(\frac{(t-a)^{\alpha} - (s-a)^{\alpha}}{\alpha} \right)^{n-\beta-1} \\ &\quad \frac{{}_a^nT^{\alpha} f(s)}{(s-a)^{1-\alpha}} \mathrm{d}s, \end{aligned} \tag{6} $$

where $n = [\beta] + 1$, ${}_a^nT^{\alpha} = \underbrace{{}_aT^{\alpha}\,{}_aT^{\alpha} \cdots {}_aT^{\alpha}}_{n \text{ times}}$ and ${}_aT^{\alpha} f(t) = (t-a)^{1-\alpha} f'(t)$. The fractional derivative (6) coincides with the traditional Caputo fractional derivative (3) if $\alpha = 1$. Readers can see [13, 14] for more details.

It is well known that the monotone iterative technique coupled with the method of upper and lower solutions is an effective mechanism to obtain extremal solutions for nonlinear problems [15]. By using this method, scholars have studied the periodic boundary value problems (BVPs) [16–24], anti-periodic BVPs [25–27], and integral BVPs [28, 29] of integer-order differential equations. Later, this method was widely used to study the initial value problems, periodic BVPs or integral BVPs of RL and Caputo fractional differential equations [30–35].

Mathematical modeling of the real world in physics and mechanical and dynamical systems often involves the p-Laplacian operator. In order to study the turbulent flow in a porous medium, Lejbenson [36] introduced the model of differential equation with the p-Laplacian operator. Many results about the fractional differential equations with the p-Laplacian operator were also studied [37–39]. However, the Caputo conformable fractional differential equations with the p-Laplacian operator have not been considered.

In [37], Liu et al. studied the following problem:

$$ \begin{cases} D_{0^+}^{\beta}\left(\phi_p\left({}^CD_{0^+}^{\alpha} x(t)\right)\right) = h\left(t, x(t), {}^CD_{0^+}^{\alpha} x(t)\right), \quad t \in (0,1), \\ {}^CD_{0^+}^{\alpha} x(0) = x'(0) = 0, \\ x(1) = r_1 x(\eta), {}^CD_{0^+}^{\alpha} x(1) = r_2\, {}^CD_{0^+}^{\alpha} x(\xi), \end{cases} \tag{7} $$

where $1 < \alpha, \beta \le 2, r_1, r_2 \ge 0$, $h \in C([0,1] \times t[0,+\infty) n \times q$ $(-\infty, 0] h, [0,+\infty))$, and $\phi_p(s)$ is the p-Laplacian operator. The extremal solutions were obtained under the assumption that

$$ h(t, w_1, z_1) \le h(t, w_2, z_2), \quad \text{for } 0 \le w_1 < w_2, z_1 > z_2 \ge 0. \tag{8} $$

Inspired by the above work, we study the nonlinear fractional p-Laplacian differential system involving the Caputo conformable derivatives as follows:

$$ \begin{cases} {}_a^{C\beta}D^{\alpha}\left(\phi_p\left({}_a^{C\gamma}D^{\alpha} x(t)\right)\right) = h\left(t, x(t), {}_a^{C\gamma}D^{\alpha} x(t)\right), \quad t \in [a,b], \\ {}_a^kT^{\alpha}\phi_p\left({}_a^{C\gamma}D^{\alpha} x(a)\right) = b_k, x(a) = \int_a^b w(s, x(s))\mathrm{d}s + \rho, \end{cases} \tag{9} $$

where $n-1 < \beta \le n, n = [\beta] + 1, 0 < \gamma, \alpha \le 1$, $\rho \ge 0$, $h \in C([a,b] \times \mathbb{R}^2, \mathbb{R})$, $w \in C([a,b] \times \mathbb{R}, \mathbb{R})$, $b_k (k = 0, 1, \ldots, n-1)$ are real numbers, $\phi_p(s) = |s|^{p-2}s (p > 1)$ is the p-Laplacian operator, $(\phi_p)^{-1} = \phi_q$, $(1/p) + (1/q) = 1$, and ${}_a^{C\delta}D^{\alpha}$ is Caputo conformable derivative with order $\delta (= \beta, \gamma)$.

To obtain the extremal solutions of problem (9), we need consider the nonlinear Cauchy problem

$$ \begin{aligned} {}_a^{C\beta}D^{\alpha} z(t) &= g(t, z(t)), \\ {}_a^kT^{\alpha} z(a) &= b_k, \quad t \in (a,b], \end{aligned} \tag{10} $$

and the linear Cauchy problem

$$ \begin{aligned} {}_a^{C\beta}D^{\alpha} z(t) &= \sigma(t) - \lambda z(t), \\ {}_a^kT^{\alpha} z(a) &= b_k, \quad t \in [a,b]. \end{aligned} \tag{11} $$

The main contributions of this paper are as follows:

(i) We obtain the unique solution to problem (10) and construct the approximate solutions to problem (11) in terms of Mittag-Leffler function. The corresponding results of problem (10) and problem (11) can be seen as a generalization of Theorem 3.25 and Theorem 4.3 in [1], respectively.

(ii) Based on two comparison principles, we obtain the extremal solutions to problem (9) by using the monotone iterative technique. Different from [37], the restrictive condition of function h is no longer needed in this paper.

The remainder of this paper is organized as follows. In Section 2, we give some preliminaries and define some special spaces. In Section 3, we show the uniqueness of the solution for linear and nonlinear Cauchy problems. In Section 4, two comparison principles are established. In Section 5, the extremal solutions for problem (9) are obtained. In Section 6, a numerical example is given.

2. Preliminaries

In this section, we introduce some definitions and lemmas to be used in the sequel.

Let $C^n(J, \mathbb{R})$ be a Banach space of all n-order continuously differentiable functions on $J = [a,b]$. For $n-1 < \beta \le n, 0 < \gamma, \alpha \le 1$, and $0 \le \tau < 1$ such that $\tau \le \beta - k$, we define the spaces $C_{\gamma}(J), C_{\alpha,\tau}(J), C_T^n(J), C_{T,\tau}^n(J)$, and $C_{T,\tau}^{\beta,n}(J)$ as follows:

$$C_\gamma(J)=\left\{f:\ f(t)\in C(J),{}_a^{C\gamma}D^\alpha f(J)\in C(J)\right\},\tag{12}$$

under the norm $\|f\|_\gamma=\|f\|_C+\|{}_a^{C\gamma}D^\alpha f\|_C$, where $\|f\|_C=\max_{t\in J}|f(t)|$ and $\|{}_a^{C\gamma}D^\alpha f\|_C=\max_{t\in J}|{}_a^{C\gamma}D^\alpha f(t)|$.

$$C_{\alpha,\tau}(J)=\left\{f(t)\in C(a,b]:\left(\frac{(t-a)^\alpha}{\alpha}\right)^\tau f(t)\in C(J)\right\},$$

$$C_{\alpha,0}(J)=C(J),\tag{13}$$

under the norm

$$\|f\|_{C_{\alpha,\tau}}=\left\|\left(\frac{(t-a)^\alpha}{\alpha}\right)^\tau f\right\|_C=\max_{t\in J}\left|\left(\frac{(t-a)^\alpha}{\alpha}\right)^\tau f(t)\right|,$$

$$C_T^n(J)=\left\{f(t)\in C(J):{}_a^nT^\alpha f(t)\in C(J)\right\},\tag{14}$$

under the norm

$$\begin{aligned}\|f\|_{C_T^n}&=\sum_{k=0}^n\left\|{}_a^nT^\alpha f\right\|_C=\sum_{k=0}^n\max_{t\in J}\left|{}_a^nT^\alpha f(t)\right|,\\ C_{T,\tau}^n(J)&=\left\{f(t)\in C(J):{}_a^{n-1}T^\alpha f(t)\in C(J),{}_a^nT^\alpha f(t)\in C_{\alpha,\tau}(J)\right\},\\ C_{T,\tau}^{\beta,n}(J)&=\left\{f(t)\in C_T^{n-1}(J):{}_a^{C\beta}D^\alpha f(t)\in C_{\alpha,\tau}(J)\right\}.\end{aligned}\tag{15}$$

For convenience, we present the following assumptions:

($\mathbf{H}_1$) For $t\in(a,b]$, $z_1,z_2\in C_T^{n-1}(J)$, assume that function g satisfies

$$\left|g(t,z_1(t))-g(t,z_2(t))\right|\le M\left|z_1(t)-z_2(t)\right|,\quad M\ge 0.\tag{16}$$

($\mathbf{H}_2$) Assume that $x_0(t)\le y_0(t), t\in J$, where $x_0(t), y_0(t)\in C_\gamma(J)$ are lower and upper solutions of (9), respectively.

($\mathbf{H}_3$) Assume that a constant $\lambda\le 0$ such that

$$\begin{aligned}&h\left(t,y(t),{}_a^{C\gamma}D^\alpha y(t)\right)-h\left(t,x(t),{}_a^{C\gamma}D^\alpha x(t)\right)\\&\quad\ge-\lambda\left(\phi_p\left({}_a^{C\gamma}D^\alpha y(t)\right)-\phi_p\left({}_a^{C\gamma}D^\alpha x(t)\right)\right),\end{aligned}\tag{17}$$

where $x_0(t)\le x(t)\le y(t)\le y_0(t)$, $t\in J$.

($\mathbf{H}_4$) Assume that a constant $0\le\eta<(1/(b-a))$ such that

$$w(t,y(t))-w(t,x(t))\ge\eta(y(t)-x(t)),\tag{18}$$

where $x_0(t)\le x(t)\le y(t)\le y_0(t)$, $t\in J$.

Definition 1. The function $x_0(t)\in C_\gamma(J)$ satisfying $\phi_p({}_a^{C\gamma}D^\alpha x_0(t))\in C_T^n(J)$ is a lower solution of problem (9) if it satisfies

$$\begin{cases}{}_a^{C\beta}D^\alpha\left(\phi_p\left({}_a^{C\gamma}D^\alpha x_0(t)\right)\right)\le h\left(t,x_0(t),{}_a^{C\gamma}D^\alpha x_0(t)\right),\quad t\in J,\\ {}_a^kT^\alpha\phi_p\left({}_a^{C\gamma}D^\alpha x_0(a)\right)\le b_k,\\ x(a)\le\int_a^b w(s,x_0(s))\mathrm{d}s+\rho.\end{cases}\tag{19}$$

The function $y_0(t)\in C_\gamma(J)$ satisfying $\phi_p({}_a^{C\gamma}D^\alpha y_0(t))\in C_T^n(J)$ is an upper solution of problem (9) if the above inequalities are reversed.

Lemma 1 (see [12]). *For $\alpha>0$, the space $C_{\alpha,a}^n(J)$ consists of those and only those functions which are represented in the form*

$$\begin{aligned}f(t)=&\frac{1}{(n-1)!}\int_a^t\left(\frac{(t-a)^\alpha-(s-a)^\alpha}{\alpha}\right)^{n-1}\frac{\psi(s)\mathrm{d}s}{(s-a)^{1-\alpha}}\\&+\sum_{k=0}^{n-1}\frac{{}_a^kT^\alpha f(a)}{k!}\frac{(x-a)^{\alpha k}}{\alpha^k},\end{aligned}\tag{20}$$

where $\psi(t)={}_a^nT^\alpha f(t)$ and $\psi(t)\in L_\alpha(a)$.

Lemma 2 (see [12]). *Let $f\in C_{\alpha,a}^n(J)$, $\beta\in\mathbb{C}$. Then,*

$${}_a^\beta I^\alpha\left({}_a^{C\beta}D^\alpha f(t)\right)=f(t)-\sum_{k=0}^{n-1}\frac{{}_a^kT^\alpha f(a)(t-a)^{\alpha k}}{\alpha^k k!}.\tag{21}$$

Remark 1. Lemma 1 still holds if we replace the space $C^n_{\alpha,a}(J)$ with $C^n_{T,\tau}(J)$. In such case, $\psi(t) = {}^{n}_{a}T^{\alpha} f(t)$ and $\psi(t) \in C_{\alpha,\tau}(J)$. In particular, $\psi(t) \in C(J)$ when $\tau = 0$. Lemma 2 is also valid for $f \in C^n_T(J)$.

Lemma 3 (see [12]). *Let* $\mathrm{Re}(\beta) > 0$, $\mathrm{Re}(\gamma) > 0$, $0 < m < Re(\beta)$, $m \in \mathbb{N}$. *Then,*

(a) ${}^{\beta}_{a}I^{\alpha}({}^{\gamma}_{a}I^{\alpha}) f(t) = {}^{\beta+\gamma}_{a}I^{\alpha} f(t)$.
(b) ${}^{\beta}_{a}I^{\alpha}(t-a)^{\alpha(\gamma-1)} = (1/\alpha^{\beta})(\Gamma(\gamma)/\Gamma(\beta+\gamma))$ $(t-a)^{\alpha(\beta+\gamma-1)}$.
(c) ${}^{m}_{a}T^{\alpha}({}^{\beta}_{a}I^{\alpha} f(t)) = {}^{\beta-m}_{a}I^{\alpha} f(t)$.

Lemma 4 (see [1]) (Banach fixed point theorem). *Let* (U, d) *be a nonempty complete metric space, let* $0 \le \rho < 1$, *and let* $A: U \longrightarrow U$ *be the map such that, for every* $x, y \in U$, *the relation*

$$d(Ax, Ay) \le \rho d(x, y), \tag{22}$$

holds. Then, the operator A *has a unique fixed point* $x^* \in U$. *Moreover, if* A^k $(k \in \mathbb{N})$ *is the sequence of operators defined by*

$$\begin{aligned} A^1 &= A, \\ A^k &= AA^{k-1} \quad (k \in \mathbb{N}\backslash\{1\}), \end{aligned} \tag{23}$$

then for any $x_0 \in U$, *the sequence* $\{A^k x_0\}_{k=1}^{\infty}$ *converges to the above fixed point* x^*.

3. The Unique Solution to the Nonlinear and Linear Cauchy Problems

In this section, we first consider the unique solution of nonlinear Cauchy problem (10) and linear Cauchy problem (11), where the function g: $(a, b] \times \mathbb{R} \longrightarrow \mathbb{R}$ such that $g \in C_{\alpha,\tau}(J)$.

Let $z(t) \in C^{n-1}_T(J)$, and by Lemma 2 and the initial value condition ${}^{k}_{a}T^{\alpha} z(t) = b_k$, problem (10) can be reduced to the Volterra-type integral equation

$$z(t) = \sum_{j=0}^{n-1} \frac{b_j (t-a)^{\alpha j}}{\alpha^j j!} + \frac{1}{\Gamma(\beta)} \int_a^t K^{\beta-1}(t, s) g(s, z(s)) \frac{\mathrm{d}s}{(s-a)^{1-\alpha}}, \tag{24}$$

where $K(t, s) = (((t-a)^{\alpha} - (s-a)^{\alpha})/\alpha), a \le s \le t \le b$. Denoting $z_0 = \sum_{j=0}^{n-1} (b_j (t-a)^{\alpha j}/\alpha^j j!)$, equation (24) can be rewritten as $z(t) = (Az)(t)$, where

$$(Az)(t) = z_0(t) + \frac{1}{\Gamma(\beta)} \int_a^t K^{\beta-1}(t, s) g(s, z(s)) \frac{\mathrm{d}s}{(s-a)^{1-\alpha}}. \tag{25}$$

Theorem 1. *If* (H_1) *holds, there exists a unique solution* $z(t) \in C^{\beta,n-1}_{T,\tau}(J)$ *for problem (10).*

Proof. First, we choose t_1 $(a < t_1 < b)$ such that

$$\sum_{k=0}^{n-1} \frac{M}{\Gamma(\beta-k+1)} \left(\frac{(t_1-a)^{\alpha}}{\alpha}\right)^{\beta-k} < 1, \tag{26}$$

and prove that (10) has a unique solution $z(t) \in C^{n-1}_T[a, t_1]$.

Applying the operator ${}^{k}_{a}T^{\alpha}$ to both sides of (25), by Lemma 3 (c), we can get

$${}^{k}_{a}T^{\alpha}(Az(t)) = {}^{k}_{a}T^{\alpha} z_0(t) + \frac{1}{\Gamma(\beta-k)} \int_a^t K^{\beta-k-1}(t, s) \frac{g(s, z(s))\mathrm{d}s}{(s-a)^{1-\alpha}}, \tag{27}$$

where ${}^{k}_{a}T^{\alpha} z_0(t) = \sum_{j=k}^{n-1} (b_j (t-a)^{(j-k)}/\alpha^{j-k}(j-k)!)$. It is obvious that ${}^{k}_{a}T^{\alpha} z_0(t)$ is continuous on $[a, t_1]$. Furthermore, for $0 \le \tau < \beta - k$ and $g \in C_{\alpha,\tau}(J)$, we get by (14) that

$$\begin{aligned} \left|{}^{\beta-k}_{a}I^{\alpha} g\right| &= \left|\frac{1}{\Gamma(\beta-k)} \int_a^t K^{\beta-k-1}(t, s) g(s, z(s)) \frac{\mathrm{d}s}{(s-a)^{1-\alpha}}\right| \\ &\le \frac{1}{\Gamma(\beta-k)} \int_a^t \left(\frac{(t-a)^{\alpha} - (s-a)^{\alpha}}{\alpha}\right)^{\beta-k-1} |g(s, z(s))| \frac{\mathrm{d}s}{(s-a)^{1-\alpha}} \\ &\le \frac{\|g\|_{C_{\alpha,\tau}[a,t_1]}}{\Gamma(\beta-k)} \int_a^t \left(\frac{(t-a)^{\alpha} - (s-a)^{\alpha}}{\alpha}\right)^{\beta-k-1} \left(\frac{(s-a)^{\alpha}}{\alpha}\right)^{-\tau} \frac{\mathrm{d}s}{(s-a)^{1-\alpha}} \\ &\le \frac{\Gamma(1-\tau)\|g\|_{C_{\alpha,\tau}[a,t_1]}}{\Gamma(\beta-k+1-\tau)} \left(\frac{(t_1-a)^{\alpha}}{\alpha}\right)^{\beta-k-\tau}, \end{aligned} \tag{28}$$

that is,

$$\left\|{}_a^{\beta-k}I^{\alpha}g\right\|_{C[a,t_1]} \leq \frac{\Gamma(1-\tau)\|g\|_{C_{\alpha,\tau}[a,t_1]}}{\Gamma(\beta-k+1-\tau)}\left(\frac{(t_1-a)^{\alpha}}{\alpha}\right)^{\beta-k-\tau}. \tag{29}$$

Inequality (29) implies that the operator ${}_a^{\beta-k}I^{\alpha}$ is bounded from $C_{\alpha,\tau}[a,t_1]$ to $C[a,t_1]$. In particular, if $\tau = 0$, then $g \in C(J)$ and ${}_a^{\beta-k}I^{\alpha}$ is bounded from $C[a,t_1]$ to $C[a,t_1]$ such that

$$\left\|{}_a^{\beta-k}I^{\alpha}g\right\|_{C[a,t_1]} \leq \frac{\|g\|_{C[a,t_1]}}{\Gamma(\beta-k+1)}\left(\frac{(t_1-a)^{\alpha}}{\alpha}\right)^{\beta-k}. \tag{30}$$

It follows from (29) and (30) that ${}_a^kT^{\alpha}(Az(t))$ is continuous on $[a,t_1]$, that is, $(Az)(t) \in C_T^{n-1}[a,t_1]$. By (14), (15), and (H_1), we have

$$\begin{aligned}
&\sum_{k=0}^{n-1}\left|{}_a^kT^{\alpha}(Az_1(t)) - {}_a^kT^{\alpha}(Az_2(t))\right| \\
&= \sum_{k=0}^{n-1}\left|\frac{1}{\Gamma(\beta-k)}\int_a^t K^{\beta-k-1}(t,s)\left[g(s,z_1(s)) - g(s,z_2(s))\right]\frac{\mathrm{d}s}{(s-a)^{1-\alpha}}\right| \\
&\leq \sum_{k=0}^{n-1}\frac{1}{\Gamma(\beta-k)}\int_a^t K^{\beta-k-1}(t,s)\left|g(s,z_1(s)) - g(s,z_2(s))\right|\frac{\mathrm{d}s}{(s-a)^{1-\alpha}} \\
&\leq \sum_{k=0}^{n-1}\frac{M}{\Gamma(\beta-k)}\int_a^t\left(\frac{(t-a)^{\alpha}-(s-a)^{\alpha}}{\alpha}\right)^{\beta-k-1}\left|z_1(s)-z_2(s)\right|\frac{\mathrm{d}s}{(s-a)^{1-\alpha}} \\
&\leq \sum_{k=0}^{n-1}\frac{M\|z_1-z_2\|_{C[a,t_1]}}{\Gamma(\beta-k+1)}\left(\frac{(t_1-a)^{\alpha}}{\alpha}\right)^{\beta-k} \\
&\leq \sum_{k=0}^{n-1}\frac{M\|z_1-z_2\|_{C_T^{n-1}[a,t_1]}}{\Gamma(\beta-k+1)}\left(\frac{(t_1-a)^{\alpha}}{\alpha}\right)^{\beta-k},
\end{aligned} \tag{31}$$

that is,

$$\begin{aligned}
\|Az_1 - Az_2\|_{C_T^{n-1}[a,t_1]} &= \sum_{k=0}^{n-1}\left\|{}_a^kT^{\alpha}(Az_1(t)) - {}_a^kT^{\alpha}(Az_2(t))\right\|_{C[a,t_1]} \\
&\leq \sum_{k=0}^{n-1}\frac{M\|z_1-z_2\|_{C_T^{n-1}[a,t_1]}}{\Gamma(\beta-k+1)}\left(\frac{(t_1-a)^{\alpha}}{\alpha}\right)^{\beta-k}.
\end{aligned} \tag{32}$$

From Lemma 4 and (26), we get that there exists a unique solution $z_1^* \in C_T^{n-1}[a,t_1]$ to problem (10). Moreover, $z_1^*(t)$ satisfies

$$\lim_{i\longrightarrow\infty}\left\|A^iz_g - z_1^*\right\|_{C_T^{n-1}[a,t_1]} = 0, \tag{33}$$

where $z_g(t)$ is any function in $C_T^{n-1}[a,t_1]$ and $A^iz_g(t) = AA^{i-1}z_g(t)$. Let $z_i(t) = A^iz_g(t)$; then,

$$\lim_{i\longrightarrow\infty}\left\|z_i(t) - z_1^*\right\|_{C_T^{n-1}[a,t_1]} = 0. \tag{34}$$

Next, choose $t_2, t_3, \ldots, t_R$ such that $a = t_0 < t_1 < t_2 < \cdots < t_R = b$. Using the same arguments as above, we get that problem (10) has a unique solution $z_r^* \in C_T^{n-1}[t_{r-1}, t_r]$ $(r = 1, 2, \ldots, R)$. Therefore, (10) has a unique solution $z^* = z_r^* \in C_T^{n-1}(J)$.

Finally, we show that the unique solution $z^*(t)$ belongs to $C_{T,\tau}^{\beta,n-1}(J)$. By (15) and (H_1), we have

$$\begin{aligned}
\left\|{}_a^{C\beta}D^{\alpha}z_i - {}_a^{C\beta}D^{\alpha}z^*\right\|_{C_{\alpha,\tau}(J)} &= \left\|g(t,z_i(t)) - g(t,z^*(t))\right\|_{C_{\alpha,\tau}(J)} \\
&\leq M\left(\frac{(t_1-a)^{\alpha}}{\alpha}\right)^{\tau}\left\|z_i - z^*\right\|_{C(J)} \\
&\leq M\left(\frac{(t_1-a)^{\alpha}}{\alpha}\right)^{\tau}\left\|z_i - z^*\right\|_{C_T^{n-1}(J)}.
\end{aligned} \tag{35}$$

Taking the limit as $i \longrightarrow \infty$, we obtain

$$\lim_{i\longrightarrow\infty} \left\| {}_a^{C\beta}D^{\alpha} z_i - {}_a^{C\beta}D^{\alpha} z^* \right\|_{C_{\alpha,\tau}(J)} = 0, \tag{36}$$

which implies that $z^*(t) \in C_{T,\tau}^{\beta,n-1}(J)$. This ends the proof. □

Remark 2. When $\alpha = 1$, the RL conformable integral and Caputo conformable derivative coincide with the traditional RL fractional integral and Caputo derivative, respectively. Hence, the results of Theorem 3.25 in [1] can be seen as the special case of Theorem 1.

Corollary 1. *If (H_1) holds and the function g: $J \times \mathbb{R} \longrightarrow \mathbb{R}$ satisfies $g \in C(J)$, then Cauchy problem (10) has a unique solution $z(t)$ belonging to $C_T^{n-1}(J)$.*

Proof. Corollary 1 can be proven by replacing τ with 0 and using the same argument in Theorem 1. □

Theorem 2. *If $\sigma(t) \in C(J)$ and λ is a constant, then problem (11) has a unique solution $z(t) \in C_T^{n-1}(J)$ which is given by*

$$\begin{aligned} z(t) = &\sum_{j=0}^{n-1} \frac{b_j (t-a)^{j\alpha}}{\alpha^j} E_{\beta,j+1}\left[\frac{-\lambda (t-a)^{\alpha\beta}}{\alpha^{\beta}}\right] \\ &+ \int_a^t K^{\beta-1}(t,s) E_{\beta,\beta}\left(-\lambda K^{\beta}(t,s)\right) \frac{\sigma(s)\mathrm{d}s}{(s-a)^{1-\alpha}}, \end{aligned} \tag{37}$$

where $E_{p,q}(\rho) = \sum_{k=0}^{\infty} (\rho^k / \Gamma(pk+q))$ is the Mittag-Leffler function.

Proof. Clearly $g(t, z(t)) = \sigma(t) - \lambda z(t)$ satisfies (H_1). By Corollary 1, there exists a unique solution $z(t) \in C_T^{n-1}(J)$ to problem (11).

Next, we prove that this unique solution is given by (18). By Lemma 2 and the initial value condition ${}_a^k T^{\alpha} z(t) = b_k$, problem (11) can be reduced to the equation

$$z(t) = \sum_{j=0}^{n-1} \frac{b_j (t-a)^{\alpha j}}{\alpha^j j!} + (-\lambda)_a^{\beta} I^{\alpha} z(t) + {}_a^{\beta} I^{\alpha} \sigma(t). \tag{38}$$

We apply the successive approximations method to solve equation (38) by taking $z_0(t) = \sum_{j=0}^{n-1} b_j (t-a)^{\alpha j} / \alpha^j j!$ and

$$z_m(t) = z_0(t) + (-\lambda)_a^{\beta} I^{\alpha} z_{m-1}(t) + {}_a^{\beta} I^{\alpha} \sigma(t), \quad m = 1, 2, \ldots. \tag{39}$$

By Lemma 3 (b), for $m = 1$, we have

$$\begin{aligned} z_1(t) &= z_0(t) + (-\lambda)_a^{\beta} I^{\alpha} z_0(t) + {}_a^{\beta} I^{\alpha} \sigma(t) \\ &= z_0(t) + \sum_{j=0}^{n-1} \frac{(-\lambda) b_j}{\alpha^j j!} {}_a^{\beta} I^{\alpha} (t-a)^{\alpha j} + {}_a^{\beta} I^{\alpha} \sigma(t) \\ &= z_0(t) + \sum_{j=0}^{n-1} \frac{(-\lambda) b_j (t-a)^{\alpha(\beta+j)}}{\alpha^{\beta+j} \Gamma(\beta+j+1)} + {}_a^{\beta} I^{\alpha} \sigma(t). \end{aligned} \tag{40}$$

By (a) and (b) of Lemma 3, for $m = 2$,

$$\begin{aligned} z_2(t) &= z_0(t) + (-\lambda)_a^{\beta} I^{\alpha} z_1(t) + {}_a^{\beta} I^{\alpha} \sigma(t) \\ &= z_0(t) + (-\lambda)_a^{\beta} I^{\alpha} \left[z_0(t) + (-\lambda)_a^{\beta} I^{\alpha} z_0(t) + {}_a^{\beta} I^{\alpha} \sigma(t) \right] + {}_a^{\beta} I^{\alpha} \sigma(t) \\ &= z_0(t) + (-\lambda)_a^{\beta} I^{\alpha} z_0(t) + (-\lambda)_a^{2\beta} I^{\alpha} z_0(t) + (-\lambda)_a^{2\beta} I^{\alpha} \sigma(t) + {}_a^{\beta} I^{\alpha} \sigma(t) \\ &= z_0(t) + \sum_{j=0}^{n-1} \frac{(-\lambda) b_j (t-a)^{\alpha(\beta+j)}}{\alpha^{\beta+j} \Gamma(\beta+j+1)} + \sum_{j=0}^{n-1} \frac{(-\lambda)^2 b_j (t-a)^{\alpha(2\beta+j)}}{\alpha^{2\beta+j} \Gamma(2\beta+j+1)} \\ &\quad + (-\lambda)_a^{2\beta} I^{\alpha} \sigma(t) + {}_a^{\beta} I^{\alpha} \sigma(t). \end{aligned} \tag{41}$$

Continuing this process, we have

$$\begin{aligned} z_m(t) &= \sum_{j=0}^{n-1} \frac{b_j (t-a)^{j\alpha}}{\alpha^j} \sum_{r=0}^{m} \frac{(-\lambda)^r (t-a)^{r\alpha\beta}}{\alpha^{r\beta} \Gamma(r\beta+j+1)} + \sum_{r=1}^{m} (-\lambda)^{r-1} {}_a^{r\beta} I^{\alpha} \sigma(t) \\ &= \sum_{j=0}^{n-1} \frac{b_j (t-a)^{j\alpha}}{\alpha^j} \sum_{r=0}^{m} \frac{(-\lambda)^r (t-a)^{r\alpha\beta}}{\alpha^{r\beta} \Gamma(r\beta+j+1)} \\ &\quad + \int_a^t K^{\beta-1}(t,s) \sum_{r=0}^{m} \frac{(-\lambda)^r K^{r\beta}(t,s)}{\Gamma((r+1)\beta)} \frac{\sigma(s)\mathrm{d}s}{(s-a)^{1-\alpha}}. \end{aligned} \tag{42}$$

Taking the limit as $m \longrightarrow \infty$ and according to the definition of Mittag-Leffler function, we get formula (37). This ends the proof. □

Remark 3. If $\alpha = 1$, we can get the results of Theorem 4.3 in [1].

4. Comparison Principles

In this section, two comparison principles which will be used in the next section are established.

Lemma 5. *Let $\eta \neq (1/b-a)$ and $y(t) \in C(J)$. Then, the following problem:*

$$\begin{cases} {}_{a}^{C\gamma}D^{\alpha}x(t) = y(t), & t \in J, \\ x(a) = \eta \int_{a}^{b} x(s)\mathrm{d}s + \rho, \end{cases} \tag{43}$$

is equivalent to

$$x(t) = \int_{a}^{b} G(t,s)y(s)\frac{\mathrm{d}s}{(s-a)^{1-\alpha}} + \frac{\rho}{1-\eta(b-a)}, \tag{44}$$

where

$$G(t,s) = \frac{1}{\xi}\begin{cases} \dfrac{[1-\eta(b-a)]\gamma(b-a)^{\alpha-1}K^{\gamma-1}(t,s) + \eta K^{\gamma}(b,s)}{1-\eta(b-a)}, & a \le s \le t \le b, \\ \dfrac{\eta K^{\gamma}(b,s)}{1-\eta(b-a)}, & a \le t \le s \le b, \end{cases} \tag{45}$$

$$\xi = (b-a)^{\alpha-1}\Gamma(\gamma+1).$$

Proof. For $0 < \gamma \le 1$, by Lemma 2, equation ${}_{a}^{C\gamma}D^{\alpha}x(t) = y(t)$ can be reduced to

$$x(t) = {}_{a}^{\gamma}I^{\alpha}y(t)c_0, \tag{46}$$

where c_0 is a constant. By the boundary condition, we easily get $c_0 = \eta\int_{a}^{b} x(s)\mathrm{d}s + \rho$. Hence,

$$x(t) = {}_{a}^{\gamma}I^{\alpha}y(t) + \eta\int_{a}^{b} x(s)\mathrm{d}s + \rho. \tag{47}$$

Let $\Delta = \int_{a}^{b} x(t)\mathrm{d}t$, and we can deduce from (47) that

$$\begin{aligned} \Delta &= \int_{a}^{b}\frac{1}{\Gamma(\gamma)}\int_{a}^{t}\left(\frac{(t-a)^{\alpha}-(s-a)^{\alpha}}{\alpha}\right)^{\gamma-1} y(s)\frac{\mathrm{d}s}{(s-a)^{1-\alpha}}\mathrm{d}t + \int_{a}^{b}(\eta\Delta+\rho)\mathrm{d}t \\ &= \int_{a}^{b}\frac{1}{\Gamma(\gamma+1)(b-a)^{\alpha-1}}\left(\frac{(b-a)^{\alpha}-(s-a)^{\alpha}}{\alpha}\right)^{\gamma} y(s)\mathrm{d}s + (\eta\Delta+\rho)(b-a) \\ &= \int_{a}^{b}\frac{K^{\gamma}(b,s)y(s)}{\Gamma(\gamma+1)(b-a)^{\alpha-1}}\frac{\mathrm{d}s}{(s-a)^{1-\alpha}} + (\eta\Delta+\rho)(b-a). \end{aligned} \tag{48}$$

Therefore,

$$\Delta = \int_{a}^{b}\frac{K^{\gamma}(b,s)y(s)}{[1-\eta(b-a)]\Gamma(\gamma+1)(b-a)^{\alpha-1}}\frac{\mathrm{d}s}{(s-a)^{1-\alpha}} + \frac{\rho(b-a)}{1-\eta(b-a)}. \tag{49}$$

Substituting (49) into (47), we have

$$\begin{aligned} x(t) &= \frac{1}{\Gamma(\gamma)} \int_a^t K^{\gamma-1}(t,s) y(s) \frac{\mathrm{d}s}{(s-a)^{1-\alpha}} + \frac{\eta\rho(b-a)}{1-\eta(b-a)} + \rho \\ &\quad + \int_a^b \frac{\eta K^{\gamma}(b,s) y(s)}{[1-\eta(b-a)]\Gamma(\gamma+1)(b-a)^{\alpha-1}} \frac{\mathrm{d}s}{(s-a)^{1-\alpha}} \\ &= \frac{1}{\xi} \int_a^t \frac{[1-\eta(b-a)]\gamma(b-a)^{\alpha-1}K^{\gamma-1}(t,s) + \eta K^{\gamma}(b,s)}{1-\eta(b-a)} y(s) \frac{\mathrm{d}s}{(s-a)^{1-\alpha}} \\ &\quad + \frac{1}{\xi} \int_t^b \frac{\eta K^{\gamma}(b,s)}{1-\eta(b-a)} y(s) \frac{\mathrm{d}s}{(s-a)^{1-\alpha}} + \frac{\rho}{1-\eta(b-a)} \\ &= \int_a^b G(t,s) y(s) \frac{\mathrm{d}s}{(s-a)^{1-\alpha}} + \frac{\rho}{1-\eta(b-a)}. \end{aligned} \tag{50}$$

This ends the proof. □

Remark 4. For $a \le t, s \le b$, $0 \le \eta < (1/(b-a))$, the function $G(t,s)$ is continuous and nonnegative.

Lemma 6. *For $x(t) \in C_\gamma(J)$, the following linear problem:*

$$\begin{cases} {}_a^{C\beta}D^{\alpha}\left(\phi_p\left({}_a^{C\gamma}D^{\alpha}(t)\right)\right) = \sigma(t) - \lambda\phi_p\left({}_a^{C\gamma}D^{\alpha}x(t)\right), \quad t \in J, \\ {}_a^{k}T^{\alpha}\phi_p\left({}_a^{C\gamma}D^{\alpha}x(a)\right) = b_k, \\ x(a) = \eta\int_a^b x(s)\mathrm{d}s + \rho, \end{cases} \tag{51}$$

has a unique solution.

Proof. Let $z(t) = \phi_p({}_a^{C\gamma}D^{\alpha}x(t))$. By Theorem 2, the problem

$$\begin{aligned} {}_a^{C\beta}D^{\alpha}z(t) &= \sigma(t) - \lambda z(t), \\ {}_a^{k}T^{\alpha}z(t) &= b_k, \quad t \in J \end{aligned} \tag{52}$$

has a unique solution $z(t) \in C_T^{n-1}(J)$, that is, ${}_a^{C\gamma}D^{\alpha}x(t) = \phi_q(z(t)) \in C_T^{n-1}(J)$. Hence, ${}_a^{C\gamma}D^{\alpha}x(t) \in C(J)$.

By Lemma 5, the following problem

$$\begin{aligned} {}_a^{C\gamma}D^{\alpha}x(t) &= \phi_q(z(t)), \\ x(a) &= \eta\int_a^b x(s)\mathrm{d}s + \rho, \quad t \in J, \end{aligned} \tag{53}$$

is equivalent to

$$x(t) = \int_a^b G(t,s)\phi_q(z(s)) \frac{\mathrm{d}s}{(s-a)^{1-\alpha}} + \frac{\rho}{1-\eta(b-a)}. \tag{54}$$

Considering (52) and (53), we obtain the conclusion that problem (51) has a unique solution which is given by (54). □

Based on the above work, we can get the following comparison principles.

Lemma 7. *If $\lambda \le 0$ and $z(t) \in C_T^{n-1}(J)$ satisfy the following relation:*

$$\left\{ {}_a^{C\beta}D^{\alpha}z(t) \ge -\lambda z(t), {}_a^{k}T^{\alpha}z(a) \ge 0, \right. \tag{55}$$

then for $t \in J, z(t) \ge 0$.

Proof. Let ${}_a^{C\beta}D^{\alpha}z(t) = p(t) - \lambda z(t), {}_a^{k}T^{\alpha}z(a) = a_k$; then, $p(t) \ge 0, a_k \ge 0$. From (37), we can see that $z(t) \ge 0$. This ends the proof. □

Lemma 8. *If $0 \le \eta < (1/(b-a))$ and $x(t) \in C_\gamma(J)$ satisfy the following relation:*

$$\left\{ {}_a^{C\gamma}D^{\alpha}x(t) \ge 0, x(a) \ge \eta\int_a^b x(s)\mathrm{d}s, \right. \tag{56}$$

then for $t \in J, x(t) \ge 0$.

Proof. Let ${}_a^{C\gamma}D^{\alpha}x(t) = q(t), x(a) = \int_a^b \eta x(s)\mathrm{d}s + d$; then, $q(t) \ge 0, d \ge 0$. From (53) and (54), we have that

$$x(t) = \int_a^b G(t,s)q(s) \frac{\mathrm{d}s}{(s-a)^{1-\alpha}} + \frac{d}{1-\eta(b-a)}, \tag{57}$$

which implies that $x(t) \ge 0$ due to $G(t,s) \ge 0$. This ends the proof. □

5. Extremal Solutions for Nonlinear System

The extremal solutions of problem (9) are obtained in this section.

Theorem 3. *If (H_2)–(H_4) hold, then problem (9) has extremal solutions $x^*(t), y^*(t)$ in the sector $[x_0, y_0] = \{x(t) \in C_\gamma(J): x_0(t) \le x(t) \le y_0(t), t \in J\}$. Moreover,*

$$\begin{aligned} &x_0(t) \le x^*(t) \le y^*(t) \le y_0(t), \\ &{}_a^{C\gamma}D^{\alpha} x_0(t) \le {}_a^{C\gamma}D^{\alpha} x^*(t) \le {}_a^{C\gamma}D^{\alpha} y^*(t) \le {}_a^{C\gamma}D^{\alpha} y_0(t). \end{aligned} \tag{58}$$

Proof. For $t \in J, n = 1, 2, \ldots$, define

$$\begin{cases} {}_a^{C\beta}D^{\alpha}\left(\phi_p\left({}_a^{C\gamma}D^{\alpha} x_n(t)\right)\right) = h\left(t, x_{n-1}(t), {}_a^{C\gamma}D^{\alpha} x_{n-1}(t)\right) - \lambda\left[\phi_p\left({}_a^{C\gamma}D^{\alpha} x_n(t)\right) - \phi_p\left({}_a^{C\gamma}D^{\alpha} x_{n-1}(t)\right)\right], \\ {}_a^{k}T^{\alpha}\phi_p\left({}_a^{C\gamma}D^{\alpha} x_n(a)\right) = b_k, \\ x_n(a) = \int_a^b \left[w\left(s, x_{n-1}(s)\right) + \eta\left(x_n(s) - x_{n-1}(s)\right)\right]\mathrm{d}s + \rho, \end{cases} \tag{59}$$

$$\begin{cases} {}_a^{C\beta}D^{\alpha}\left(\phi_p\left({}_a^{C\gamma}D^{\alpha} y_n(t)\right)\right) = h\left(t, y_{n-1}(t), {}_a^{C\gamma}D^{\alpha} y_{n-1}(t)\right) - \lambda\left[\phi_p\left({}_a^{C\gamma}D^{\alpha} y_n(t)\right) - \phi_p\left({}_a^{C\gamma}D^{\alpha} y_{n-1}(t)\right)\right], \\ {}_a^{k}T^{\alpha}\phi_p\left({}_a^{C\gamma}D^{\alpha} y_n(a)\right) = b_k, \\ y_n(a) = \int_a^b \left[w\left(s, y_{n-1}(s)\right) + \eta\left(y_n(s) - y_{n-1}(s)\right)\right]\mathrm{d}s + \rho. \end{cases} \tag{60}$$

By Lemma 6, x_n, y_n are well defined. The proof includes three steps. □

Step 1. We prove the monotone property of $\{x_n\}$ and $\{y_n\}$.

Let $r(t) = \phi_p({}_a^{C\gamma}D^{\alpha} x_1(t)) - \phi_p({}_a^{C\gamma}D^{\alpha} x_0(t))$, and by (H_2) and (59), we get

$$\left\{ {}_a^{C\beta}D^{\alpha} r(t) \ge -\lambda r(t), \quad t \in J, {}_a^{k}T^{\alpha} r(a) \ge 0. \right. \tag{61}$$

From Lemma 7, we have $r(t) \ge 0$, i.e., $\phi_p({}_a^{C\gamma}D^{\alpha} x_1(t)) \ge \phi_p({}_a^{C\gamma}D^{\alpha} x_0(t))$. Moreover,

$${}_a^{C\gamma}D^{\alpha} x_1(t) \ge {}_a^{C\gamma}D^{\alpha} x_0(t) \tag{62}$$

holds because of the monotone increasing property of $\phi_p(s)$.

Let $\tilde{r}(t) = x_1(t) - x_0(t)$. From (H_2), (H_4), (59), and (62), we have

$$\begin{cases} {}_a^{C\gamma}D^{\alpha}\tilde{r}(t) = {}_a^{C\gamma}D^{\alpha} x_1(t) - {}_a^{C\gamma}D^{\alpha} x_0(t) \ge 0, \\ \tilde{r}(a) \ge \int_a^b \eta\tilde{r}(s)\mathrm{d}s. \end{cases} \tag{63}$$

From Lemma 8, we have $\tilde{r}(t) \ge 0$, i.e., $x_1(t) \ge x_0(t)$. The same argument holds that ${}_a^{C\gamma}D^{\alpha} y_0(t) \ge {}_a^{C\gamma}D^{\alpha} y_1(t)$, $y_0(t) \ge y_1(t)$. Let $m(t) = \phi_p({}_a^{C\gamma}D^{\alpha} y_1(t)) - \phi_p({}_a^{C\gamma}D^{\alpha} x_1(t))$, and from (H_3), (59), and (60), we get

$$\begin{aligned} {}_a^{C\beta}D^{\alpha} m(t) &= h\left(t, y_0(t) {}_a^{C\gamma}D^{\alpha} y_0(t)\right) - h\left(t, x_0(t), {}_a^{C\gamma}D^{\alpha} x_0(t)\right) \\ &\quad - \lambda\left[\phi_p\left({}_a^{C\gamma}D^{\alpha} y_1(t)\right) - \phi_p\left({}_a^{C\gamma}D^{\alpha} y_0(t)\right)\right] \\ &\quad + \lambda\left[\phi_p\left({}_a^{C\gamma}D^{\alpha} x_1(t)\right) - \phi_p\left({}_a^{C\gamma}D^{\alpha} x_0(t)\right)\right] \\ &\ge -\lambda m(t), \\ {}_a^{k}T^{\alpha} m(a) &= 0. \end{aligned} \tag{64}$$

From Lemma 7, we have $m(t) \ge 0$, i.e., $\phi_p({}_a^{C\gamma}D^{\alpha} y_1(t)) \ge \phi_p({}_a^{C\gamma}D^{\alpha} x_1(t))$. Hence,

$${}_a^{C\gamma}D^{\alpha} y_1(t) \ge {}_a^{C\gamma}D^{\alpha} x_1(t). \tag{65}$$

Let $\tilde{m}(t) = y_1 - x_1$. We get from (65) and (H_4) that

$$\begin{cases} {}_a^{C\gamma}D^{\alpha}\tilde{m}(t) = {}_a^{C\gamma}D^{\alpha} y_1(t) - {}_a^{C\gamma}D^{\alpha} x_1(t) \ge 0, \\ \tilde{m}(a) = \int_a^b \left[w\left(s, y_0(s)\right) + \eta\left(y_1(s) - y_0(s)\right) - w\left(s, x_0(s)\right) - \eta\left(x_1(s) - x_0(s)\right)\right]\mathrm{d}s \ge \int_a^b \eta\tilde{m}(s)\mathrm{d}s. \end{cases} \tag{66}$$

From Lemma 8, we have $\tilde{m}(t) \ge 0$, i.e. $y_1 \ge x_1$. Therefore, $x_0 \le x_1 \le y_1 \le y_0$ and ${}_a^{C\gamma}D^{\alpha} x_0 \le {}_a^{C\gamma}D^{\alpha} x_1 \le {}_a^{C\gamma}D^{\alpha} y_1 \le {}_a^{C\gamma}D^{\alpha} y_0$.

Next we prove $x_1(t)$, $y_1(t)$ are lower and upper solutions of (9), respectively. From (H_3), (H_4), and (59), we have

$$
\begin{aligned}
{}_a^{C\beta}D^{\alpha}\left(\phi_p\left({}_a^{C\gamma}D^{\alpha}x_1(t)\right)\right) &= h\left(t,x_0(t),{}_a^{C\gamma}D^{\alpha}x_0(t)\right)-h\left(t,x_1(t),{}_a^{C\gamma}D^{\alpha}x_1(t)\right)\\
&\quad+h\left(t,x_1(t),{}_a^{C\gamma}D^{\alpha}x_1(t)\right)-\lambda\left[\phi_p\left({}_a^{C\gamma}D^{\alpha}x_1(t)\right)-\phi_p\left({}_a^{C\gamma}D^{\alpha}x_0(t)\right)\right]\\
&\le -\lambda\left[\phi_p\left({}_a^{C\gamma}D^{\alpha}x_0(t)\right)-\phi_p\left({}_a^{C\gamma}D^{\alpha}x_1(t)\right)\right]+h\left(t,x_1(t),{}_a^{C\gamma}D^{\alpha}x_1(t)\right)\\
&\quad-\lambda\left[\phi_p\left({}_a^{C\gamma}D^{\alpha}x_1(t)\right)-\phi_p\left({}_a^{C\gamma}D^{\alpha}x_0(t)\right)\right]=h\left(t,x_1(t),{}_a^{C\gamma}D^{\alpha}x_1(t)\right),\\
{}_a^{k}T^{\alpha}\phi_p\left({}_a^{C\gamma}D^{\alpha}x_1(a)\right) &= b_k,\\
x_1(a) &= \int_a^b\left[w\left(s,x_0(s)\right)-w\left(s,x_1(s)\right)+w\left(s,x_1(s)\right)+\eta\left(x_1(s)-x_0(s)\right)\right]\mathrm{d}s+\rho\\
&\le \int_a^b\left[\eta\left(x_0(s)-x_1(s)\right)+\eta\left(x_1(s)-x_0(s)\right)+w\left(s,x_1(s)\right)\right]\mathrm{d}s+\rho\\
&= \int_a^b w\left(s,x_1(s)\right)\mathrm{d}s+\rho.
\end{aligned}
\tag{67}
$$

Clearly, $x_1(t)$ is a lower solution of (9). Similarly, $y_1(t)$ is an upper solution of (9). We obtain by applying mathematical induction that

$$
\begin{aligned}
&x_0(t)\le x_1(t)\le\cdots\le x_n(t)\le\cdots\le y_n(t)\le\cdots\le y_1(t)\le y_0(t),\\
&{}_a^{C\gamma}D^{\alpha}x_0(t){}_a^{C\gamma}D^{\alpha}x_1(t)\le\cdots\le{}_a^{C\gamma}D^{\alpha}x_n(t)\le\cdots{}_a^{C\gamma}D^{\alpha}y_n(t)\\
&\qquad\le\cdots\le{}_a^{C\gamma}D^{\alpha}y_1(t)\le{}_a^{C\gamma}D^{\alpha}y_0(t).
\end{aligned}
\tag{68}
$$

Step 2. We conclude that the sequences $\{x_n\}$ and $\{y_n\}$ satisfy the relations:

$$
\begin{aligned}
\lim_{n\longrightarrow\infty}x_n(t) &= x^*(t),\\
\lim_{n\longrightarrow\infty}{}_a^{C\gamma}D^{\alpha}x_n(t) &= {}_a^{C\gamma}D^{\alpha}x^*(t),
\end{aligned}
\tag{69}
$$

$$
\begin{aligned}
\lim_{n\longrightarrow\infty}y_n(t) &= y^*(t),\\
\lim_{n\longrightarrow\infty}{}_a^{C\gamma}D^{\alpha}y_n(t) &= {}_a^{C\gamma}D^{\alpha}y^*(t).
\end{aligned}
\tag{70}
$$

Let $F(x_n)(t)=h(t,x_n(t),{}_a^{C\gamma}D^{\alpha}x_n(t))+\lambda\phi_p({}_a^{C\gamma}D^{\alpha}x_n(t))$. We can see that the function F is continuous and nondecreasing from the assumption of h. By (37) and (54), equation (59) can be reduced to the equation

$$
\begin{aligned}
x_n(t)) \int_a^b G(t,s)\phi_q\Bigg[&\sum_{j=0}^{n-1}\frac{b_j(s-a)^{j\alpha}}{\alpha^j}E_{\beta,j+1}\left(\frac{-\lambda(s-a)^{\alpha\beta}}{\alpha^{\beta}}\right)\\
&+\int_a^s K^{\beta-1}(s,\theta)E_{\beta,\beta}\left(-\lambda K^{\beta}(s,\theta)\right)\frac{F\left(x_{n-1}(\theta)\right)\mathrm{d}\theta}{(\theta-a)^{1-\alpha}}\Bigg]\frac{\mathrm{d}s}{(s-a)^{1-\alpha}}\\
&+\frac{\int_a^b\left[w\left(s,x_{n-1}(s)\right)-\eta x_{n-1}(s)\right]\mathrm{d}s+\rho}{1-\eta(b-a)}.
\end{aligned}
\tag{71}
$$

Clearly, $\{x_n\}$ is uniformly bounded in $C_\gamma(J)$. By the continuity of F, G, ϕ_q, and K, we can easily get that $\{x_n\}$ is equicontinuous. By the Arzelà–Ascoli theorem, we have that $\{x_n\}$ satisfies (69). In the same way, we get that $\{y_n\}$ satisfies (70). Moreover, $x^*(t)$ and $y^*(t)$ are solutions of (9).

Step 3. We prove that x^* and y^* are extremal solutions of problem (9).

Assume that any solution $x(t)$ of problem (9) satisfies $x_n(t)\le x(t)\le y_n(t)$. Let $u(t)=\phi_p({}_a^{C\gamma}D^{\alpha}x(t))-\phi_p({}_a^{C\gamma}D^{\alpha}x_{n+1}(t))$, and by (H_3), we have

$$\begin{aligned} {}_{a}^{C\beta}D^{\alpha}u(t) &= h\left(t, x(t), {}_{a}^{C\gamma}D^{\alpha}x(t)\right) - h\left(t, x_n(t), {}_{a}^{C\gamma}D^{\alpha}x_n(t)\right) \\ &\quad + \lambda\left[\phi_p\left({}_{a}^{C\gamma}D^{\alpha}x_{n+1}(t)\right) - \phi_p\left({}_{a}^{C\gamma}D^{\alpha}x_n(t)\right)\right] \\ &\geq -\lambda u(t), \\ {}_{a}^{k}T^{\alpha}u(a) &= 0. \end{aligned} \tag{72}$$

From Lemma 7, we have $u(t) \geq 0$, i.e., $\phi_p({}_{a}^{C\gamma}D^{\alpha}x(t)) \geq \phi_p({}_{a}^{C\gamma}D^{\alpha}x_{n+1}(t))$. Hence,

$${}_{a}^{C\gamma}D^{\alpha}x(t) \geq {}_{a}^{C\gamma}D^{\alpha}x_{n+1}(t). \tag{73}$$

Let $\tilde{u}(t) = x(t) - x_{n+1}(t)$, and by (H_4), (59), and (73), we have

$$\begin{cases} {}_{a}^{C\gamma}D^{\alpha}\tilde{u}(t) \geq 0, \\ \tilde{u}(a) = \int_a^b \left[w(s, x(s)) - w\left(s, x_n(s)\right) - \eta\left(x_{n+1}(s) - x_n(s)\right)\right]\mathrm{d}s \geq \eta\int_a^b \tilde{u}(s)\mathrm{d}s. \end{cases} \tag{74}$$

We get $\tilde{u}(t) \geq 0$ from Lemma 8, i.e., $x(t) \geq x_{m+1}(t)$. Similarly, ${}_{a}^{C\gamma}D^{\alpha}y_{n+1}(t) \geq {}_{a}^{C\gamma}D^{\alpha}x(t)$, $y_{n+1}(t) \geq x(t)$. Hence, $x_{n+1}(t) \leq x(t) \leq y_{n+1}(t)$ holds. Therefore, $x^*(t) \leq x(t) \leq y^*(t)$ as $n \longrightarrow \infty$, $\forall t \in J$. This ends the proof.

Remark 5. In [37], the authors assume that $h \in C([0,1] \times t[0,+\infty)n \times q(-\infty, 0]h, [0,+\infty))$, $h(t, w_1, z_1) \leq h(t, w_2, z_2)$ for $0 \leq w_1 < w_2, z_1 > z_2 \geq 0$, $t \in [0,1]$. The nonlinear term h in this paper satisfies the weaker conditions.

6. Example

We present a numerical example as follows:

$$\begin{cases} {}_{0}^{(1/2)}D^{(1/2)}\phi_2\left({}_{0}^{(1/2)}D^{(1/2)}x(t)\right) = t^{(3/4)} + \dfrac{x(t)}{3\left(t^{(1/4)} + t^{-(3/4)}\right)} + \dfrac{1}{4^0}{}^{(1/2)}D^{(1/2)}x(t), \quad t \in [0,1], \\ \phi_2\left({}_{0}^{(1/2)}D^{(1/2)}x(0)\right) = 0, \\ x(0) = \displaystyle\int_0^1 \left[\frac{1}{7}(s+1)x(s) + s\right]\mathrm{d}s + 1, \end{cases} \tag{75}$$

where $k = 0, b_0 = 0, p = 2, a = 0, b = 1, \rho = 1, \beta = \gamma = \alpha = (1/2)$ and

$$\begin{cases} h\left(t, x(t), {}_{a}^{(1/2)}D^{(1/2)}x(t)\right) = t^{(3/4)} + \dfrac{x(t)}{3\left(t^{(1/4)} + t^{-(3/4)}\right)} + \dfrac{1}{4^0}{}^{(1/2)}D^{(1/2)}x(t), \\ w(t, x(t)) = \dfrac{1}{7}(t+1)x(t) + t. \end{cases} \tag{76}$$

Taking $x_0(t) = 0, y_0(t) = 3t + 3$, we can get

$$\begin{cases} {}_0^{(1/2)}D^{(1/2)}\phi_2\left({}_0^{(1/2)}D^{(1/2)}x_0(t)\right) = 0 \le t^{(3/4)} + \dfrac{x(t)}{3\left(t^{(1/4)} + t^{-(3/4)}\right)} + \dfrac{1}{4^0}{}_0^{(1/2)}D^{(1/2)}x_0(t), & t \in [0,1], \\ \phi_2\left({}_0^{(1/2)}D^{(1/2)}x_0(0)\right) = 0, & x_0(0) < \dfrac{3}{2}, \end{cases}$$

$$\begin{cases} {}_0^{(1/2)}D^{(1/2)}\phi_2\left({}_0^{(1/2)}D^{(1/2)}y_0(t)\right) = {}_0^{(1/2)}D^{(1/2)}\left(\dfrac{4\sqrt{2}}{\sqrt{\pi}}t^{(3/4)}\right) = 3t^{(1/2)} \ge \left(2 + \dfrac{\sqrt{2}}{\sqrt{\pi}}\right)t^{(3/4)}, & t \in [0,1], \\ \phi_2\left({}_0^{(1/2)}D^{(1/2)}y_0(0)\right) = 0, & y_0(0) = 3 > \dfrac{5}{2}. \end{cases} \tag{77}$$

Hence, x_0 and y_0 are lower and upper solutions of (75), respectively. Therefore, (H_2) is satisfied. For $x_0(t) \le x \le y \le y_0(t)$,

$$\begin{aligned} &h\left(t, y(t), {}_0^{(1/2)}D^{(1/2)}y(t)\right) - h\left(t, x(t), {}_0^{(1/2)}D^{(1/2)}x(t)\right) \\ &= \frac{y(t) - x(t)}{3\left(t^{(1/4)} + t^{-(3/4)}\right)} + \frac{1}{4^0}{}_0^{(1/2)}D^{(1/2)}(y(t) - x(t)) \\ &\ge \frac{1}{4^0}{}_0^{(1/2)}D^{(1/2)}(y(t) - x(t)) \\ &= \frac{1}{4}\left[\phi_2\left({}_0^{(1/2)}D^{(1/2)}y(t)\right) - \phi_2\left({}_0^{(1/2)}D^{(1/2)}x(t)\right)\right], \\ &w(t, y(t)) - w(t, x(t)) \ge \frac{1}{7}(y(t) - x(t)). \end{aligned} \tag{78}$$

We can see that $\lambda = -(1/4) < 0, \eta = (1/7)$. Therefore, (H_3) and (H_4) hold. In light of Theorem 1, the extremal solutions of (75) can be obtained in $[x_0, y_0]$.

7. Conclusions

In this paper, we mainly use the montone iterative technique to study the Caputo conformable differential equations with p-Laplacian operator and integral boundary condition. A minimal and a maximal solution between the lower and the upper solutions are obtained. This method provides a constructive procedure for the solutions, and it is also useful for the investigation of qualitative properties of solutions. Since the Caputo conformable derivative can be reduced to the traditional Caputo derivative, some results produced from the traditional Caputo differential system can be seen as special cases of this paper. Moreover, the Caputo conformable derivative depends on two parameters naturally and the one coming from conformable operator can better describe long-memory processes. We believe that the Caputo and RL conformable fractional operators will play a key role in studying new types of fractional variational problems, Sturm–Liouville problems, optimal control problems, and modeling of complex systems.

Abbreviations

RL: Riemann–Liouville
BVP: Boundary value condition.

Data Availability

No data were used to support this study.

Conflicts of Interest

The authors declare that they have no conflicts of interest.

Authors' Contributions

All authors contributed equally to this study and read and approved the final manuscript.

Acknowledgments

We would like to thank Professor Desheng Li for many helpful conversations. This study was supported by the National Natural Science and Mathematics Foundation of China (grant no. 11526177).

References

[1] A. A. Kilbas, H. M. Srivastava, and J. J. Trujillo, *Theory and Applications of Fractional Differential Equatuins*, Elsevier, Amsterdam, Netherlands, 2006.

[2] I. Podlubny, *Fractional Differential Equations*, Academic Press, New York, NY, USA, 1999.

[3] K. S. Miller and B. Ross, *An Introduction to the Fractional Calculus and Fractional Differential Equation*, Wiley, New York, NY, USA, 1993.

[4] R. Hilfer, *Applications of Fractional Calculus in Physics*, Word Scientific, Singapore, 2015.

[5] J. T. Machado, V. Kiryakova, and F. Mainardi, "Recent history of fractional calculus," *Communications in Nonlinear Science and Numerical Simulation*, vol. 16, no. 3, pp. 1140–1153, 2011.

[6] C. F. Lorenzo and T. T. Hartley, "Variable order and distributed order fractional operators," *Nonlinear Dynamics*, vol. 29, no. 1, pp. 57–98, 2002.

[7] B. Ahmad, A. Alsaedi, S. K. Ntouyas, and J. Tariboon, *Hadamard-Type Fractional Differential Equations, Inclusions and Inequalities*, Springer, Berlin, Germany, 2017.

[8] S. G. Samko, A. A. Kilbas, and O. I. Marichev, *Fractional Integrals and Derivatives: Theory and Applications*, Gordon & Breach, Yverdon, Switzerland, 1993.

[9] F. Jarad, T. Abdeljawad, and D. Baleanu, "Caputo-type modification of the hadamard fractional derivatives," *Advances in Difference Equations*, vol. 2012, no. 1, p. 142, 2012.

[10] R. Khalil, M. Al Horani, A. Yousef, and M. Sababheh, "A new definition of fractional derivative," *Journal of Computational and Applied Mathematics*, vol. 264, pp. 65–70, 2014.

[11] T. Abdeljawad, "On conformable fractional calculus," *Journal of Computational and Applied Mathematics*, vol. 279, pp. 57–66, 2015.

[12] F. Jarad, E. Uğurlu, T. Abdeljawad, and D. Baleanu, "On a new class of fractional operators," *Advances in Difference Equations*, vol. 2017, no. 1, p. 247, 2017.

[13] T. Abdeljawad, Q. M. Al-Mdallal, and F. Jarad, "Fractional logistic models in the frame of fractional operators generated by conformable derivatives," *Chaos, Solitons & Fractals*, vol. 119, pp. 94–101, 2019.

[14] T. Abdeljawad, "Fractional operators with boundary points dependent kernels and integration by parts," *Discrete & Continuous Dynamical Systems - S*, vol. 13, no. 3, pp. 351–375, 2020.

[15] G. S. Ladde, V. Lakshmikantham, and A. S. Vatsala, *Monotone Iterative Technique for Nonlinear Differential Equations*, Pitman, Boston, MA, USA, 1985.

[16] H.-K. Xu and J. J. Nieto, "Extremal solutions of a class of nonlinear integro-differential equations in banach spaces," *Proceedings of the American Mathematical Society*, vol. 125, no. 9, pp. 2605–2614, 1997.

[17] B. Ahmad and J. J. Nieto, "The monotone iterative technique for three-point second-order integrodifferential boundary value problems with p-laplacian," *Boundary Value Problems*, vol. 2007, no. 7, pp. 1–9, 2007.

[18] J. J. Nieto and R. Rodríguez-López, "New comparison results for impulsive integro-differential equations and applications," *Journal of Mathematical Analysis and Applications*, vol. 328, no. 2, pp. 1343–1368, 2007.

[19] W. Wang, J. Shen, and Z. Luo, "Multi-point boundary value problems for second-order functional differential equations," *Computers & Mathematics with Applications*, vol. 56, no. 8, pp. 2065–2072, 2008.

[20] J. J. Nieto and N. Alvarez-Noriega, "Periodic boundary value problems for nonlinear first order ordinary differential equations," *Acta Mathematica Hungarica*, vol. 71, no. 1-2, pp. 49–58, 1996.

[21] Z. Luo and J. J. Nieto, "New results for the periodic boundary value problem for impulsive integro-differential equations," *Nonlinear Analysis: Theory, Methods & Applications*, vol. 70, no. 6, pp. 2248–2260, 2009.

[22] Z. He and J. Yu, "Periodic boundary value problem for first-order impulsive ordinary differential equations," *Journal of Mathematical Analysis and Applications*, vol. 272, no. 1, pp. 67–78, 2002.

[23] Z. Luo and Z. Jing, "Periodic boundary value problem for first-order impulsive functional differential equations," *Computers & Mathematics with Applications*, vol. 55, no. 9, pp. 2094–2107, 2008.

[24] J. J. Nieto and R. Rodríguez-López, "Periodic boundary value problem for non-lipschitzian impulsive functional differential equations," *Journal of Mathematical Analysis and Applications*, vol. 318, no. 2, pp. 593–610, 2006.

[25] W. Ding, Y. Xing, and M. Han, "Anti-periodic boundary value problems for first order impulsive functional differential equations," *Applied Mathematics and Computation*, vol. 186, no. 1, pp. 45–53, 2007.

[26] M. Yao, A. Zhao, and J. Yan, "Anti-periodic boundary value problems of second order impulsive differential equations," *Computers & Mathematics with Applications*, vol. 59, no. 12, pp. 3617–3629, 2010.

[27] Z. Luo, J. Shen, and J. J. Nieto, "Antiperiodic boundary value problem for first-order impulsive ordinary differential equations," *Computers & Mathematics with Applications*, vol. 49, no. 2-3, pp. 253–261, 2005.

[28] T. Jankowski, "Positive solutions for second order impulsive differential equations involving stieltjes integral conditions," *Nonlinear Analysis: Theory, Methods & Applications*, vol. 74, no. 11, pp. 3775–3785, 2011.

[29] G. Song, Y. Zhao, and X. Sun, "Integral boundary value problems for first order impulsive integro-differential equations of mixed type," *Journal of Computational and Applied Mathematics*, vol. 235, no. 9, pp. 2928–2935, 2011.

[30] S. Zhang, "Monotone iterative method for initial value problem involving Riemann-Liouville fractional derivatives," *Nonlinear Analysis: Theory, Methods & Applications*, vol. 71, no. 5-6, pp. 2087–2093, 2009.

[31] Z. Wei, W. Dong, and J. Che, "Periodic boundary value problems for fractional differential equations involving a Riemann-Liouville fractional derivative," *Nonlinear Analysis: Theory, Methods & Applications*, vol. 73, no. 10, pp. 3232–3238, 2010.

[32] T. Jankowski, "Boundary problems for fractional differential equations," *Applied Mathematics Letters*, vol. 28, pp. 14–19, 2014.

[33] L. Zhang, B. Ahmad, and G. Wang, "The existence of an extremal solution to a nonlinear system with the right-handed Riemann-Liouville fractional derivative," *Applied Mathematics Letters*, vol. 31, pp. 1–6, 2014.

[34] G. Wang, "Monotone iterative technique for boundary value problems of a nonlinear fractional differential equation with deviating arguments," *Journal of Computational and Applied Mathematics*, vol. 236, no. 9, pp. 2425–2430, 2012.

[35] L. Zhang, B. Ahmad, and G. Wang, "Explicit iterations and extremal solutions for fractional differential equations with nonlinear integral boundary conditions," *Applied Mathematics and Computation*, vol. 268, pp. 388–392, 2015.

[36] L. S. Lejbenson, "General problem of the movement of a compressible fluid in a porous medium," *Izv Akad Nauk SSSR, Ser Geogr Geofiz.*vol. 9, pp. 7–10, 1983.

[37] X. Liu, M. Jia, and W. Ge, "The method of lower and upper solutions for mixed fractional four-point boundary value problem with p-Laplacian operator," *Applied Mathematics Letters*, vol. 65, pp. 56–62, 2017.

[38] J. Qin, G. Wang, L. Zhang, and B. Ahmad, "Monotone iterative method for a p-Laplacian boundary value problem with fractional conformable derivatives," *Boundary Value Problems*, vol. 2019, no. 1, p. 145, 2019.

[39] Y. Liu and X. Yang, "Resonant boundary value problems for singular multi-term fractional differential equations," *Differential Equations & Applications*, vol. 5, no. 3, pp. 409–472, 2013.

Hindawi
Complexity
Volume 2021, Article ID 9096727, 20 pages
https://doi.org/10.1155/2021/9096727

Research Article

Further Exploration on Bifurcation for Fractional-Order Bidirectional Associative Memory (BAM) Neural Networks concerning Time Delay*

Nengfa Wang,[1] Changjin Xu ,[2] and Zixin Liu[1]

[1]*School of Mathematics and Statistics, Guizhou University of Finance and Economics, Guiyang 550025, China*
[2]*Guizhou Key Laboratory of Economics System Simulation, Guizhou University of Finance and Economics, Guiyang 550025, China*

Correspondence should be addressed to Changjin Xu; xcj403@126.com

Received 25 May 2021; Revised 16 July 2021; Accepted 8 October 2021; Published 22 October 2021

Academic Editor: Eric Campos

This work principally considers the stability issue and the emergence of Hopf bifurcation for a class of fractional-order BAM neural network models concerning time delays. Through the detailed analysis on the distribution of the roots of the characteristic equation of the involved fractional-order delayed BAM neural network systems, we set up a new delay-independent condition to guarantee the stability and the emergence of Hopf bifurcation for the investigated fractional-order delayed BAM neural network systems. The work indicates that delay is a significant element that has a vital impact on the stability and the emergence of Hopf bifurcation in fractional-order delayed BAM neural network systems. The simulation figures and bifurcation plots are clearly presented to verify the derived key research results. The established conclusions of this work have significant guiding value in regulating and optimizing neural networks.

1. Introduction

Neural networks have been found to have immense application prospect in a lot of subject areas such as modeling human brain, remote sensing, biological science, pattern recognition, artificial intelligence, and control technique [1, 2]. Usually, time delay often occurs in neural network systems due to the lag of the response of signal transmission of the neurons in neural networks. Thus, it is necessary for us to establish the delayed neural networks to describe the real situation of neural networks. Generally speaking, time delay often gives rise to the disappearance of stability, periodic oscillation, chaotic behavior, and so on [3, 4]. In order to grasp the effect of time delay on various dynamical properties of neural networks, miscellaneous delayed neural networks have been built and studied. Up to now, a great deal of valuable publications has been achieved. For instance, Aouiti et al. [5] investigated the existence and global exponential stability of pseudo almost periodic solution to delayed BAM neural networks involving leakage delays by virtue of fixed point theory and mathematical inequality skills. Yang et al. [6] studied the almost automorphic solution to high-order delayed BAM neural networks by means of the exponential dichotomy theory, Banach contraction mapping law, and differential inequality strategy. Maharajan et al. [7] set up a new global robust exponential stability condition for a class of uncertain BAM neural network systems involving mixed time delays. Popa [8] focused on the global μ-stability for impulsive complex-valued BAM neural networks concerning mixed delays. Sowmiya et al. [9] made a detailed analysis on mean-square asymptotic stability for impulsive discrete-time stochastic BAM neural networks involving Markovian jumping and multiple delays. For details, we refer the readers to [10, 11].

The general BAM networks are given by

$$\begin{cases} \dot{p}_i(t) = -\alpha_i p_i(t) + \sum_{j=1}^{m} a_{ji} h_i\left(q_j\left(t-\eta_{ji}\right)\right) + \mathscr{P}_i, \\ \dot{q}_j(t) = -\beta_j q_j(t) + \sum_{i=1}^{n} b_{ij} k_j\left(p_i\left(t-\zeta_{ij}\right)\right) + \mathscr{Q}_j, \end{cases} \tag{1}$$

where $i = 1, 2, \ldots, n$; $j = 1, 2, \ldots, m$, α_i and β_j describe the stability of internal neuron processes on $\mathscr{P}$-layer and $\mathscr{Q}$-layer, respectively; a_{ji}, b_{ij} represent the connection weights; $p_i(t)$ and $q_j(t)$ denote the states of the neurons on $\mathscr{P}$-layer and $\mathscr{Q}$-layer, respectively; h_i and k_j are activation functions; $\mathscr{P}_i, \mathscr{Q}_j$ denote the inputs; η_{ji} and ζ_{ij} are time delays. The model (1) describes the change law of different neurons which lie in two layers. For details, please see [12, 13].

System (1) is a large-scale nonlinear dynamical model. It owns very complicated dynamical properties. In order to have a good command of the internal law of network system (1), many researchers pay much attention to some simplified versions of delayed neural network models. By the investigation on various dynamical peculiarities of the simplified neural network systems, we are able to grasp the potential dynamical properties for large-scale delayed neural network systems. During the past several years, a lot of works on the simplified neural network models have been published. For example, Hajihosseini et al. [14] discussed the bifurcation problem for recurrent neural networks involving three neurons. Kaslik and Balint [15] investigated the Neimark–Sacker bifurcation of a discrete-time delayed neural network system involving two neurons. Ge and Xu [16] obtained the sufficient condition to ensure the stability and the onset of Hopf bifurcation for delayed neural networks involving four neurons. Yang and Ye [17] dealt with the stability and bifurcation behavior for delayed BAM neural network involving five neurons. As to more concrete literatures on this theme, one can see [4, 18].

All above publications are only restricted to the integer-order dynamical equations. In recent years, fractional calculus has displayed wide application value in a lot of fields such as heat and mass transfer, electromagnetic and electrodynamics, control science, population systems, biophysics, and neural networks [19–27]. The study shows that fractional calculus can be regarded as a very useful tool to describe the object issues in the real world because it owns the memory property and hereditary function during the dynamic change process [28, 29]. Recently, fractional calculus has become the biggest concern of the present day world. In particular, fractional-order neural networks have also become one of the key hot issues in neural network area. Delay-induced Hopf bifurcation is a significant dynamical property in delayed dynamical models. However, it is a pity that a great deal of works is only concerned with delay-induced Hopf bifurcation for integer-order dynamical system concerning delays and few publications focus on the fractional-order case (see [30, 31]). In fractional-order neural networks, what is the effect of time delay and fractional-order on the stability and bifurcation? The solution of this problem is beneficial to the design of neural networks. Up to now, there are many bifurcation problems that are expected to be solved. This viewpoint stimulates us to deal with the delay-induced Hopf bifurcation of delayed neural networks involving multiple neurons.

Based on the neural networks (1), we consider the following fractional-order simplified delayed neural networks:

$$\begin{cases} \frac{d^{\xi}u_1(t)}{dt^{\xi}} = -ku_1(t) + a_{11}h\left(u_4(t-\zeta)\right) + a_{12}l\left(u_5(t-\zeta)\right) + a_{13}l\left(u_6(t-\zeta)\right), \\ \frac{d^{\xi}u_2(t)}{dt^{\xi}} = -ku_2(t) + a_{21}h\left(u_5(t-\zeta)\right) + a_{22}l\left(u_6(t-\zeta)\right) + a_{23}l\left(u_4(t-\zeta)\right), \\ \frac{d^{\xi}u_3(t)}{dt^{\xi}} = -ku_3(t) + a_{31}h\left(u_6(t-\zeta)\right) + a_{32}l\left(u_4(t-\zeta)\right) + a_{33}l\left(u_5(t-\zeta)\right), \\ \frac{d^{\xi}u_4(t)}{dt^{\xi}} = -ku_4(t) + a_{41}h\left(u_1(t-\zeta)\right) + a_{42}l\left(u_2(t-\zeta)\right) + a_{43}l\left(u_3(t-\zeta)\right), \\ \frac{d^{\xi}u_5(t)}{dt^{\xi}} = -ku_5(t) + a_{51}h\left(u_2(t-\zeta)\right) + a_{52}l\left(u_3(t-\zeta)\right) + a_{53}l\left(u_1(t-\zeta)\right), \\ \frac{d^{\xi}u_6(t)}{dt^{\xi}} = -ku_6(t) + a_{61}h\left(u_3(t-\zeta)\right) + a_{62}l\left(u_1(t-\zeta)\right) + a_{63}l\left(u_2(t-\zeta)\right), \end{cases} \tag{2}$$

where $\xi \in (0,1]$ is a real number; k describes the stability of internal neuron processes on $\mathscr{P}$-layer and $\mathscr{Q}$-layer; $a_{ij}(i = 1,2,3,4,5,6; j = 1,2,3)$ represents the connection weights; $u_i(t)(i = 1,2,3)$ denotes the state of the i-neuron on $\mathscr{P}$-layer; $u_j(t)(j = 4,5,6)$ denotes the state of the j-neuron on $\mathscr{Q}$-layer; h and l are activation functions. In order to establish the key results of this work, we make the following hypothesis:

$$\begin{aligned} &(H1)\, h, \\ &l \in C^1, \\ &h(0) = l(0) = 0. \end{aligned} \tag{3}$$

The remainder of this article is planned as follows. Section 2 presents the key theories on fractional calculus. Section 3 displays the main conclusions on stability and Hopf bifurcation for neural networks (2). Section 4 executes software simulations to illustrate the key conclusions of this article. Section 5 ends this work with a simple conclusion.

2. Indispensable Definitions and Lemmas

In this part, we give several necessary definitions and lemmas about fractional calculus which will be used in the next part.

Definition 1 (see [32]). Define Caputo fractional-order derivative as follows:

$$\mathscr{D}^{\xi}u(\varrho) = \frac{1}{\Gamma(l-\xi)}\int_{\varrho_0}^{\varrho}\frac{u^{(l)}(s)}{(\varrho - s)^{\xi-l+1}}ds, \tag{4}$$

where $u(\varrho) \in ([\varrho_0, \infty), R), \Gamma(s) = \int_0^{\infty}\varrho^{s-1}e^{-\varrho}d\varrho, \quad \varrho \geq \varrho_0$, and$l \in Z^+, \xi \in [l-1, l)$.

Lemma 1 (see [33, 34]). *Consider the following model:*

$$\frac{d^{\xi}u(t)}{dt^{\xi}} = w(t, u(t)), u(0) = u_0, \tag{5}$$

where $\xi \in (0,1]$ and $w(t,u(t))$: $R^+ \times R^n \longrightarrow R^n, n \in Z^+$. Let u_* be the equilibrium point of system (5). If every eigenvalue (denoted by ς) of $(\partial w(t,u)/\partial u)|_{u=u_*}$ obeys $|arg(\varsigma)| > (\xi\pi/2)$, then we say that u_* is locally asymptotically stable.

Lemma 2 (see [35]). *Consider the following model:*

$$\begin{cases} \dfrac{d^{\xi_1}\mathscr{H}_1(t)}{dt^{\xi_1}} = e_{11}\mathscr{H}_1(t-\zeta_{11}) + e_{12}\mathscr{H}_2(t-\zeta_{12}) + \cdots + e_{1l}\mathscr{H}_l(t-\zeta_{1l}), \\ \dfrac{d^{\xi_2}\mathscr{H}_2(t)}{dt^{\xi_2}} = e_{21}\mathscr{H}_1(t-\zeta_{21}) + e_{22}\mathscr{H}_2(t-\zeta_{22}) + \cdots + e_{2l}\mathscr{H}_l(t-\zeta_{2l}), \\ \vdots \\ \dfrac{d^{\xi_l}\mathscr{H}(t)}{dt^{\xi_l}} = e_{l1}\mathscr{H}_1(t-\zeta_{l1}) + e_{l2}\mathscr{H}_2(t-\zeta_{l2}) + \cdots + e_{ll}\mathscr{H}_l(t-\zeta_{ll}), \end{cases} \tag{6}$$

where $\xi_i \in (0,1)(i = 1,2,...,l)$, the initial value $\mathscr{H}_i(t) = \omega_i(t) \in C[-\max_{i,h}\zeta_{ih}, 0]$, $t \in [-\max_{i,h}\zeta_{il}, 0]$, and $i,h = 1,2,...,l$. Denote

$$\Delta(\eta) = \begin{bmatrix} \eta^{\xi_1} - e_{11}e^{-\eta\zeta_{11}} & -e_{12}e^{-\eta\zeta_{12}} & \cdots & -e_{1l}e^{-\eta\zeta_{1l}} \\ -e_{21}e^{-\eta\zeta_{12}} & \eta^{\xi_2} - e_{22}e^{-\eta\zeta_{22}} & \cdots & -e_{2l}e^{-\eta\zeta_{2l}} \\ \vdots & \vdots & \ddots & \vdots \\ -e_{l1}e^{-\eta\zeta_{l1}} & -e_{l2}e^{-\eta\zeta_{l2}} & \cdots & \eta^{\xi_l} - e_{ll}e^{-\eta\zeta_{ll}} \end{bmatrix}. \tag{7}$$

Then, the zero solution of system (6) is said to be asymptotically stable in Lyapunov sense provided that every root of $det(\Delta(\eta)) = 0$ owns negative real parts.

3. Exploration on Delay-Induced Hopf Bifurcation

In this part, by discussing the characteristic equation of system (2) and setting the time delay as bifurcation parameter, we will establish the delay-independent sufficient

condition to guarantee the stability and the onset of Hopf bifurcation for system (2).

In view of $(H1)$, one can easily know that system (2) owns the unique equilibrium $\mathscr{U}(0,0,0,0,0,0)$. The linear system of system (2) at the zero equilibrium $\mathscr{U}(0,0,0,0,0,0)$ owns the expression:

$$\begin{cases} \dfrac{d^{\xi}u_1(t)}{dt^{\xi}} = -ku_1(t) + b_{11}\left(u_4(t-\zeta)\right) + b_{12}\left(u_5(t-\zeta)\right) + b_{13}\left(u_6(t-\zeta)\right), \\ \dfrac{d^{\xi}u_2(t)}{dt^{\xi}} = -ku_2(t) + b_{21}\left(u_5(t-\zeta)\right) + b_{22}\left(u_6(t-\zeta)\right) + b_{23}\left(u_4(t-\zeta)\right), \\ \dfrac{d^{\xi}u_3(t)}{dt^{\xi}} = -ku_3(t) + b_{31}\left(u_6(t-\zeta)\right) + b_{32}\left(u_4(t-\zeta)\right) + b_{33}\left(u_5(t-\zeta)\right), \\ \dfrac{d^{\xi}u_4(t)}{dt^{\xi}} = -ku_4(t) + b_{41}\left(u_1(t-\zeta)\right) + b_{42}\left(u_2(t-\zeta)\right) + b_{43}\left(u_3(t-\zeta)\right), \\ \dfrac{d^{\xi}u_5(t)}{dt^{\xi}} = -ku_5(t) + b_{51}\left(u_2(t-\zeta)\right) + b_{52}\left(u_3(t-\zeta)\right) + b_{53}\left(u_1(t-\zeta)\right), \\ \dfrac{d^{\xi}u_6(t)}{dt^{\xi}} = -ku_6(t) + b_{61}\left(u_3(t-\zeta)\right) + b_{62}\left(u_1(t-\zeta)\right) + b_{63}\left(u_2(t-\zeta)\right), \end{cases} \tag{8}$$

where $b_{i1} = a_{i1}h'_{i1}(0), b_{i2} = a_{i2}l'(0), b_{i3} = a_{i3}l'(0)$, $i = 1,2,3,4,5,6$. The characteristic equation for equation (8) owns the expression:

$$\det\begin{bmatrix} s^{\xi}+k & 0 & 0 & -b_{11}e^{-s\zeta} & -b_{12}e^{-s\zeta} & -b_{13}e^{-s\zeta} \\ 0 & s^{\xi}+k & 0 & -b_{23}e^{-s\eta} & -b_{21}e^{-s\zeta} & -b_{22}e^{-s\zeta} \\ 0 & 0 & s^{\xi}+k & -b_{32}e^{-s\eta} & -b_{33}e^{-s\zeta} & -b_{31}e^{-s\zeta} \\ -b_{41}e^{-s\zeta} & -b_{42}e^{-s\zeta} & -b_{43}e^{-s\zeta} & s^{\xi}+k & 0 & 0 \\ -b_{53}e^{-s\zeta} & -b_{51}e^{-s\zeta} & -b_{52}e^{-s\zeta} & 0 & s^{\xi}+k & 0 \\ -b_{62}e^{-s\zeta} & -b_{63}e^{-s\zeta} & -b_{61}e^{-s\zeta} & 0 & 0 & s^{\xi}+k \end{bmatrix} = 0. \tag{9}$$

By equation (9), we get

$$\mathscr{U}_1(s) + \mathscr{U}_2(s)e^{-2s\zeta} + \mathscr{U}_3(s)e^{-4s\zeta} + \mathscr{U}_4(s)e^{-6s\zeta} = 0, \tag{10}$$

where

$$\begin{cases} \mathcal{U}_1(s) = s^{6\xi} + \mu_5 s^{5\xi} + \mu_4 s^{4\xi} + \mu_3 s^{3\xi} + \mu_2 s^{2\xi} + \mu_1 s^{\xi} + \mu_0, \\ \mathcal{U}_2(s) = \nu_4 s^{4\xi} + \nu_3 s^{3\xi} + \nu_2 s^{2\xi} + \nu_1 s^{\xi} + \nu_0, \\ \mathcal{U}_3(s) = \chi_2 s^{2\xi} + \chi_1 s^{\xi} + \chi_0, \\ \mathcal{U}_4(s) = \rho_0 = -c_{11}c_{22}c_{33}, \end{cases} \tag{11}$$

where

$$\begin{cases} \mu_0 = k^6 - k^4(c_{13}c_{31} + c_{12}c_{21} + c_{23}c_{32}) - k^3(c_{11}c_{23}c_{31} + c_{13}c_{21}c_{32}), \\ \mu_1 = 6k^2 - 4k^3(c_{13}c_{31} + c_{12}c_{21} + c_{23}c_{32}) - 3k^2(c_{11}c_{23}c_{31} + c_{13}c_{21}c_{32}) \\ +2k[c_{33}(c_{11} + c_{22}) + c_{11}c_{22}], \\ \mu_2 = 9k^4 - 6k^2(c_{13}c_{31} + c_{12}c_{21} + c_{23}c_{32}) - 3k(c_{11}c_{23}c_{31} + c_{13}c_{21}c_{32}) \\ +c_{33}(c_{11} + c_{22}) + c_{11}c_{22}, \\ \mu_3 = 26k^3 - 4k(c_{13}c_{31} + c_{12}c_{21} + c_{23}c_{32}) - (c_{11}c_{23}c_{31} + c_{13}c_{21}c_{32}), \\ \mu_4 = 15k^2 - (c_{13}c_{31} + c_{12}c_{21} + c_{23}c_{32}), \\ \mu_5 = 6k, \\ \nu_0 = k^2(c_{11}c_{31}c_{22} + c_{12}c_{21}c_{33} + c_{11}c_{23}c_{32}) - k^4(c_{11} + c_{22} + c_{33}), \\ \nu_1 = 2k(c_{11}c_{31}c_{22} + c_{12}c_{21}c_{33} + c_{11}c_{23}c_{32}) - 4k^3(c_{11} + c_{22} + c_{33}), \\ \nu_2 = c_{11}c_{31}c_{22} + c_{12}c_{21}c_{33} + c_{11}c_{23}c_{32} - 6k^2, \\ \nu_3 = -4k(c_{11} + c_{22} + c_{33}), \\ \nu_4 = -(c_{11} + c_{22} + c_{33}), \\ \chi_0 = k^2[c_{33}(c_{11} + c_{22}) + c_{11}c_{22}], \\ \chi_1 = 2k[c_{33}(c_{11} + c_{22}) + c_{11}c_{22}], \\ \chi_2 = c_{33}(c_{11} + c_{22}) + c_{11}c_{22}, \end{cases} \tag{12}$$

where

$$\begin{cases} c_{11} = b_{41}b_{11} + b_{42}b_{23} + b_{43}b_{32}, \\ c_{12} = b_{41}b_{12} + b_{42}b_{21} + b_{43}b_{33}, \\ c_{13} = b_{41}b_{13} + b_{42}b_{22} + b_{43}b_{31}, \\ c_{21} = b_{53}b_{11} + b_{51}b_{23} + b_{52}b_{32}, \\ c_{22} = b_{53}b_{12} + b_{51}b_{21} + b_{52}b_{33}, \\ c_{23} = b_{53}b_{13} + b_{51}b_{22} + b_{52}b_{31}, \\ c_{31} = b_{62}b_{11} + b_{63}b_{23} + b_{61}b_{32}, \\ c_{32} = b_{62}b_{12} + b_{63}b_{21} + b_{61}b_{33}, \\ c_{33} = b_{62}b_{13} + b_{63}b_{22} + b_{61}b_{31}. \end{cases} \tag{13}$$

By virtue of (10), we get

$$\mathcal{U}_1(s)e^{4s\zeta} + \mathcal{U}_2(s)e^{2s\zeta} + \mathcal{U}_3(s) + \mathcal{U}_4(s)e^{-2s\zeta} = 0. \tag{14}$$

Assume that $s = i\vartheta = \vartheta(\cos(\pi/2) + i\sin(\pi/2))$ is the root of (14) and denote the real parts and imaginary parts of $\mathcal{U}_j(s)(j = 1, 2, 3, 4)$ by $\mathcal{U}_{jR}(s)$ and $\mathcal{U}_{jI}(s)(j = 1, 2, 3, 4)$, respectively. It follows from (14) that

$$\begin{cases} \mathcal{U}_{1R}(\vartheta)\cos 4\vartheta\zeta - \mathcal{U}_{1I}(\vartheta)\sin 4\vartheta\zeta + [\mathcal{U}_{2R}(\vartheta) + \mathcal{U}_{4R}(\vartheta)]\cos 2\vartheta\zeta \\ +[\mathcal{U}_{4I}(\vartheta) - \mathcal{U}_{2I}(\vartheta)]\sin 2\vartheta\zeta = -\mathcal{U}_{3R}(\vartheta), \\ \mathcal{U}_{1I}(\vartheta)\cos 4\vartheta\zeta + \mathcal{U}_{1R}(\vartheta)\sin 4\vartheta\zeta + [\mathcal{U}_{2I}(\vartheta) + \mathcal{U}_{4I}(\vartheta)]\cos 2\vartheta\zeta \\ +[\mathcal{U}_{2R}(\vartheta) - \mathcal{U}_{4R}(\vartheta)]\sin 2\ \vartheta\zeta = -\mathcal{U}_{3I}(\vartheta), \end{cases} \tag{15}$$

where

$$\begin{cases} \mathcal{U}_{1R}(\vartheta) = \vartheta^{6\xi}\cos\ 3\ \xi\pi + \mu_5\vartheta^{5\xi}\cos\frac{5\xi\pi}{2} + \mu_4\vartheta^{4\xi}\cos\ 2\ \xi\pi \\ + \mu_3\vartheta^{3\xi}\cos\frac{3\xi\pi}{2} + \mu_2\vartheta^{2\xi}\cos\ \xi\pi + \mu_1\vartheta^{\xi}\cos\frac{\xi\pi}{2} + \mu_0, \\ \mathcal{U}_{1I}(\vartheta) = \vartheta^{6\xi}\sin\ 3\ \xi\pi + \mu_5\vartheta^{5\xi}\sin\frac{5\xi\pi}{2} + \mu_4\vartheta^{4\xi}\sin\ 2\ \xi\pi \\ + \mu_3\vartheta^{3\xi}\sin\frac{3\xi\pi}{2} + \mu_2\vartheta^{2\xi}\sin\ \xi\pi + \mu_1\vartheta^{\xi}\sin\frac{\xi\pi}{2}, \\ \mathcal{U}_{2R}(\vartheta) = \nu_4\vartheta^{4\xi}\cos\ 2\ \xi\pi + \nu_3\vartheta^{3\xi}\cos\frac{3\xi\pi}{2} + \nu_2\vartheta^{2\xi}\cos\ \xi\pi + \nu_1\vartheta^{\xi}\cos\frac{\xi\pi}{2} + \nu_0, \\ \mathcal{U}_{2I}(\vartheta) = \nu_4\vartheta^{4\xi}\sin\ 2\ \xi\pi + \nu_3\vartheta^{3\xi}\sin\frac{3\xi\pi}{2} + \nu_2\vartheta^{2\xi}\sin\ \xi\pi + \nu_1\vartheta^{\xi}\sin\frac{\xi\pi}{2}, \\ \mathcal{U}_{3R}(\vartheta) = \chi_2\vartheta^{2\xi}\cos\ \xi\pi + \chi_1\vartheta^{\xi}\cos\frac{\xi\pi}{2} + \chi_0, \\ \mathcal{U}_{3I}(\vartheta) = \chi_2\vartheta^{2\xi}\sin\ \xi\pi + \chi_1\vartheta^{\xi}\sin\frac{\xi\pi}{2}, \\ \mathcal{U}_{4R}(\vartheta) = \rho_0, \\ \mathcal{U}_{4I}(\vartheta) = 0. \end{cases} \tag{16}$$

In view of (16), we can rewrite (15) as

$$\begin{cases} \mathcal{U}_{1R}(\vartheta)\cos\ 4\ \vartheta\zeta - \mathcal{U}_{1I}(\vartheta)\sin\ 4\ \vartheta\zeta + [\mathcal{U}_{2R}(\vartheta) + \mathcal{U}_{4R}(\vartheta)]\cos\ 2\ \vartheta\zeta - \mathcal{U}_{2I}(\vartheta)\sin\ 2\ \vartheta\zeta = -\mathcal{U}_{3R}(\vartheta), \\ \mathcal{U}_{1I}(\vartheta)\cos\ 4\ \vartheta\zeta + \mathcal{U}_{1R}(\vartheta)\sin\ 4\ \vartheta\zeta + \mathcal{U}_{2I}(\vartheta) + \cos\ 2\ \vartheta\zeta + [\mathcal{U}_{2R}(\vartheta) - \mathcal{U}_{4R}(\vartheta)]\sin\ 2\ \vartheta\zeta = -\mathcal{U}_{3I}(\vartheta), \end{cases} \tag{17}$$

According to $\sin\ 2\ \vartheta\zeta = \pm\sqrt{1 - \cos^2 2\vartheta\zeta}$, we are to deal with two cases.

(i) If $\sin\ 2\ \vartheta\zeta = \sqrt{1 - \cos^2 2\vartheta\zeta}$, it follows from the first equation of (17) that

$$2\mathcal{U}_{1R}(\vartheta)\left(2\cos^2 2\vartheta\zeta - 1\right) - 2\mathcal{U}_{1I}(\vartheta)\cos\ 2\ \vartheta\zeta\sqrt{1 - \cos^2 2\vartheta\zeta} + [\mathcal{U}_{2R}(\vartheta) + \mathcal{U}_{4R}(\vartheta)]\cos\ 2\ \vartheta\zeta - \mathcal{U}_{2I}(\vartheta)\sqrt{1 - \cos^2 2\vartheta\zeta} = -\mathcal{U}_{3R}(\vartheta), \tag{18}$$

which leads to

$$\left[2\mathcal{U}_{1R}(\vartheta)\left(2\cos^2 2\vartheta\zeta - 1\right) + \left[\mathcal{U}_{2R}(\vartheta) + \mathcal{U}_{4R}(\vartheta)\right]\cos 2\vartheta\zeta + \mathcal{U}_{3R}(\vartheta)\right]^2 - \left[2\mathcal{U}_{1I}(\vartheta)\cos 2\vartheta\zeta - \mathcal{U}_{2I}(\vartheta)\right]^2\left(1 - \cos^2 2\vartheta\zeta\right). \tag{19}$$

Then, one gets

$$\rho_1\cos^4 2\vartheta\zeta + \rho_2\cos^3 2\vartheta\zeta + \rho_3\cos^2 2\vartheta\zeta + \rho_4\cos 2\vartheta\zeta + \rho_5 = 0, \tag{20}$$

where

$$\begin{cases} \rho_1 = 16\mathcal{U}_{1R}^2(\vartheta) + 4\mathcal{U}_{1I}^2(\vartheta), \\ \rho_2 = 8\mathcal{U}_{1R}(\vartheta)\left(\mathcal{U}_{2R}(\vartheta) + \mathcal{U}_{4R}(\vartheta)\right) + 4\mathcal{U}_{1I}(\vartheta)\mathcal{U}_{2I}(\vartheta), \\ \rho_3 = \left(\mathcal{U}_{2R}(\vartheta) + \mathcal{U}_{4R}(\vartheta)\right)^2 + 8\mathcal{U}_{1R}(\vartheta)\left(\mathcal{U}_{3R}(\vartheta) - 2\mathcal{U}_{1R}(\vartheta)\right) + \mathcal{U}_{2I}^2(\vartheta) - 4\mathcal{U}_{1R}^2(\vartheta), \\ \rho_4 = 2\left(\mathcal{U}_{2R}(\vartheta) + \mathcal{U}_{4R}(\vartheta)\right)\left(\mathcal{U}_{3R}(\vartheta) - \mathcal{U}_{1R}(\vartheta)\right) - 4\mathcal{U}_{1I}(\vartheta)\mathcal{U}_{2I}(\vartheta), \\ \rho_5 = \left(\mathcal{U}_{3R}(\vartheta) - 2\mathcal{U}_{1R}(\vartheta)\right)^2 - \mathcal{U}_{2I}^2(\vartheta). \end{cases} \tag{21}$$

Suppose that $\cos 2\vartheta\zeta = \eta$ and set

$$h(\eta) = \eta^4 + \frac{\rho_2}{\rho_1}\eta^3 + \frac{\rho_3}{\rho_1}\eta^2 + \frac{\rho_4}{\rho_1}\eta + \frac{\rho_5}{\rho_1}, \tag{22}$$

then

$$\frac{dh(\eta)}{d\eta} = 4\eta^3 + \frac{3\rho_2}{\rho_1}\eta^2 + \frac{2\rho_3}{\rho_1}\eta + \frac{\rho_4}{\rho_1}. \tag{23}$$

Let

$$4\eta^3 + \frac{3\rho_2}{\rho_1}\eta^2 + \frac{2\rho_3}{\rho_1}\eta + \frac{\rho_4}{\rho_1} = 0. \tag{24}$$

Assume that $y = \eta + (\rho_2/4\rho_1)$, then (24) can be expressed as

$$y^3 + r_1 y + r_2 = 0, \tag{25}$$

where

$$\begin{aligned} r_1 &= \frac{\rho_3}{2\rho_1} - \frac{3\rho_2^2}{16\rho_1^2}, \\ r_2 &= \frac{\rho_2^3}{32\rho_1^3} - \frac{\rho_2\rho_3}{8\rho_1^2} + \frac{\rho_4}{4\rho_1}. \end{aligned} \tag{26}$$

Denote

$$\begin{aligned} \delta_1 &= \left(\frac{r_2}{2}\right)^2 + \left(\frac{r_1}{3}\right)^3, \\ \delta_2 &= \frac{-1 + i\sqrt{3}}{2}. \end{aligned} \tag{27}$$

By (25), one gets

$$\begin{cases} y_1 = \sqrt[3]{-\frac{r_2}{2} + \sqrt{\delta_1}} + \sqrt[3]{-\frac{r_2}{2} - \sqrt{\delta_1}}, \\ y_2 = \sqrt[3]{-\frac{r_2}{2} + \sqrt{\delta_1}}\,\delta_2 + \sqrt[3]{-\frac{r_2}{2} - \sqrt{\delta_1}}\,\delta_2^2, \\ y_3 = \sqrt[3]{-\frac{r_2}{2} + \sqrt{\delta_1}}\,\delta_2^2 + \sqrt[3]{-\frac{r_2}{2} - \sqrt{\delta_1}}\,\delta_2. \end{cases} \tag{28}$$

According to the analysis above, one can obtain the expression of $\cos 2\vartheta\zeta$. Then, one can derive the expression of $\sin 2\vartheta\zeta$. Here, we suppose that

$$\begin{aligned} \cos 2\vartheta\zeta &= \varphi_1(\vartheta), \\ \sin 2\vartheta\zeta &= \varphi_2(\vartheta). \end{aligned} \tag{29}$$

Hence,

$$\varphi_1^2(\vartheta) + \varphi_2^2(\vartheta) = 1. \tag{30}$$

By virtue of computer software, one can easily derive the root (say ϑ) of (30). Thus, one has

$$\zeta^{1l} = \frac{1}{2\vartheta}\left[\arccos\varphi_1(\vartheta) + 2l\pi\right], \quad l = 0, 1, 2, \ldots. \tag{31}$$

(ii) If $\sin 2\vartheta\zeta = -\sqrt{1 - \cos^2 2\vartheta\zeta}$, by means of the same method, one can also derive

$$\begin{aligned} \cos 2\vartheta\zeta &= \psi_1(\vartheta), \\ \sin 2\vartheta\zeta &= \psi_2(\vartheta). \end{aligned} \tag{32}$$

Then,

$$\psi_1^2(\vartheta)+\psi_2^2(\vartheta)=1. \tag{33}$$

By virtue of computer software, we can derive the root (say ϑ) of (33). Then,

$$\zeta^{2k}=\frac{1}{2\vartheta}\left[\arccos\ \psi_1(\vartheta)+2k\pi\right],\quad k=0,1,2,\ldots. \tag{34}$$

Define

$$\zeta_0=\min\left\{\zeta^{1l},\zeta^{2l}\right\},\quad l=0,1,2,\ldots. \tag{35}$$

In the sequel, we are to verify the transversality condition to ensure the onset of Hopf bifurcation. The following hypothesis is needed. $(H2)$ $\mathscr{A}_R^*\mathscr{B}_R^*+\mathscr{A}_I^*\mathscr{B}_I^*>0$, where

$$\begin{aligned}
\mathscr{A}_R^*=&\left[6\xi\vartheta_0^{6\xi-1}\cos\frac{(6\xi-1)\pi}{2}+5\xi\mu_5\vartheta_0^{5\xi-1}\cos\frac{(5\xi-1)\pi}{2}+4\xi\mu_4\vartheta_0^{4\xi-1}\times\ \cos\frac{(4\xi-1)\pi}{2}+3\xi\mu_3\vartheta_0^{3\xi-1}\cos\frac{(3\xi-1)\pi}{2}\right.\\
&\left.+2\xi\mu_2\vartheta_0^{2\xi-1}\cos\frac{(2\xi-1)\pi}{2}+\xi\mu_1\vartheta_0^{\xi-1}\cos\frac{(\xi-1)\pi}{2}\right]\\
&+\left[4\xi\nu_4\vartheta_0^{4\xi-1}\cos\frac{(4\xi-1)\pi}{2}+3\xi\nu_3\vartheta_0^{3\xi-1}\cos\frac{(3\xi-1)\pi}{2}+2\xi\nu_2\vartheta_0^{2\xi-1}\cos\frac{(2\xi-1)\pi}{2}+\xi\nu_1\vartheta_0^{\xi-1}\cos\frac{(\xi-1)\pi}{2}\right]\cos\ 2\vartheta_0\zeta_0\\
&+\left[4\xi\nu_4\vartheta_0^{4\xi-1}\sin\frac{(4\xi-1)\pi}{2}+3\xi\nu_3\vartheta_0^{3\xi-1}\sin\frac{(3\xi-1)\pi}{2}+2\xi\nu_2\vartheta_0^{2\xi-1}\sin\frac{(2\xi-1)\pi}{2}+\xi\nu_1\vartheta_0^{\xi-1}\sin\frac{(\xi-1)\pi}{2}\right]\sin\ 2\vartheta_0\zeta_0\\
&+\left[2\xi\chi_2\vartheta_0^{2\xi-1}\cos\frac{(2\xi-1)\pi}{2}+\xi\chi_1\vartheta_0^{\xi-1}\cos\frac{(\xi-1)\pi}{2}\right]\cos\ 4\vartheta_0\zeta_0+\left[2\xi\chi_2\vartheta_0^{2\xi-1}\sin\frac{(2\xi-1)\pi}{2}+\xi\chi_1\vartheta_0^{\xi-1}\sin\frac{(\xi-1)\pi}{2}\right]\sin\ 4\vartheta_0\zeta_0,\\
\mathscr{A}_I^*=&\left[6\xi\vartheta_0^{6\xi-1}\sin\frac{(6\xi-1)\pi}{2}+5\xi\mu_5\vartheta_0^{5\xi-1}\sin\frac{(5\xi-1)\pi}{2}+4\xi\mu_4\vartheta_0^{4\xi-1}\times\ \sin\frac{(4\xi-1)\pi}{2}+3\xi\mu_3\vartheta_0^{3\xi-1}\sin\frac{(3\xi-1)\pi}{2}\right.\\
&\left.+2\xi\mu_2\vartheta_0^{2\xi-1}\sin\frac{(2\xi-1)\pi}{2}+\xi\mu_1\vartheta_0^{\xi-1}\sin\frac{(\xi-1)\pi}{2}\right]\\
&+\left[4\xi\nu_4\vartheta_0^{4\xi-1}\cos\frac{(4\xi-1)\pi}{2}+3\xi\nu_3\vartheta_0^{3\xi-1}\cos\frac{(3\xi-1)\pi}{2}+2\xi\nu_2\vartheta_0^{2\xi-1}\cos\frac{(2\xi-1)\pi}{2}+\xi\nu_1\vartheta_0^{\xi-1}\cos\frac{(\xi-1)\pi}{2}\right]\sin\ 2\vartheta_0\zeta_0\\
&-\left[4\xi\nu_4\vartheta_0^{4\xi-1}\sin\frac{(4\xi-1)\pi}{2}+3\xi\nu_3\vartheta_0^{3\xi-1}\sin\frac{(3\xi-1)\pi}{2}+2\xi\nu_2\vartheta_0^{2\xi-1}\sin\frac{(2\xi-1)\pi}{2}+\xi\nu_1\vartheta_0^{\xi-1}\sin\frac{(\xi-1)\pi}{2}\right]\cos\ 2\vartheta_0\zeta_0\\
&-\left[2\xi\chi_2\vartheta_0^{2\xi-1}\cos\frac{(2\xi-1)\pi}{2}+\xi\chi_1\vartheta_0^{\xi-1}\cos\frac{(\xi-1)\pi}{2}\right]\sin\ 4\vartheta_0\zeta_0+\left[2\xi\chi_2\vartheta_0^{2\xi-1}\sin\frac{(2\xi-1)\pi}{2}+\xi\chi_1\vartheta_0^{\xi-1}\sin\frac{(\xi-1)\pi}{2}\right]\cos\ 4\vartheta_0\zeta_0,\\
\mathscr{B}_R^*=&2\vartheta_0\left(\nu_4\vartheta_0^{4\xi}\cos\ 2\ \xi\pi+\nu_3\vartheta_0^{3\xi}\cos\frac{3\xi\pi}{2}+\nu_2\vartheta_0^{2\xi}\cos\ \xi\pi+\nu_1\vartheta_0^{\xi}\cos\frac{\xi\pi}{2}+\nu_0\right)\sin\ 2\vartheta_0\zeta_0\\
&+2\vartheta_0\left(\nu_4\vartheta_0^{4\xi}\sin\ 2\ \xi\pi+\nu_3\vartheta_0^{3\xi}\sin\frac{3\xi\pi}{2}+\nu_2\vartheta_0^{2\xi}\sin\ \xi\pi+\nu_1\vartheta_0^{\xi}\sin\frac{\xi\pi}{2}+\nu_0\right)\cos\ 2\vartheta_0\zeta_0,\\
\mathscr{B}_I^*=&2\vartheta_0\left(\nu_4\vartheta_0^{4\xi}\cos\ 2\ \xi\pi+\nu_3\vartheta_0^{3\xi}\cos\frac{3\xi\pi}{2}+\nu_2\vartheta_0^{2\xi}\cos\ \xi\pi+\nu_1\vartheta_0^{\xi}\cos\frac{\xi\pi}{2}+\nu_0\right)\cos\ 2\vartheta_0\zeta_0\\
&+2\vartheta_0\left(\nu_4\vartheta_0^{4\xi}\sin\ 2\ \xi\pi+\nu_3\vartheta_0^{3\xi}\sin\frac{3\xi\pi}{2}+\nu_2\vartheta_0^{2\xi}\sin\ \xi\pi+\nu_1\vartheta_0^{\xi}\sin\frac{\xi\pi}{2}+\nu_0\right)\sin\ 2\vartheta_0\zeta_0.
\end{aligned} \tag{36}$$

Lemma 3. *Assume that $s(\zeta) = \phi_1(\zeta) + i\phi_2(\zeta)$ is the root of (10) at $\zeta = \zeta_0$ and $\phi_1(\zeta_0) = 0, \phi_2(\zeta_0) = \vartheta_0$, then $Re[(ds/d\zeta)]_{\zeta=\zeta_0,\vartheta=\vartheta_0} > 0$.*

Proof. By virtue of (10), we get

$$\begin{aligned}&\frac{d\mathcal{U}_1(s)}{d\zeta} + \frac{d\mathcal{U}_2(s)}{d\zeta}e^{-2s\zeta} - 2e^{-2s\zeta}\left(\frac{ds}{d\zeta}\zeta + s\right)\mathcal{U}_2(s) + \frac{d\mathcal{U}_3(s)}{d\zeta}e^{-4s\zeta},\\ &-4e^{-4s\zeta}\left(\frac{ds}{d\zeta}\zeta + s\right)\mathcal{U}_3(s) + \frac{d\mathcal{U}_4(s)}{d\zeta}e^{-6s\zeta} - 6e^{-6s\zeta}\left(\frac{ds}{d\zeta}\zeta + s\right)\mathcal{U}_4(s) = 0.\end{aligned} \tag{37}$$

Since

$$\begin{cases}\dfrac{d\mathcal{U}_1(s)}{d\zeta} = \left[6\xi s^{6\xi-1} + 5\xi\mu_5 s^{5\xi-1} + 4\xi\mu_4 s^{4\xi-1} + 3\xi\mu_3 s^{3\xi-1} + 2\xi\mu_2 s^{2\xi-1} + \xi\mu_1 s^{\xi-1}\right]\dfrac{ds}{d\zeta},\\ \dfrac{d\mathcal{U}_2(s)}{d\zeta} = \left[4\xi\nu_4 s^{4\xi-1} + 3\xi\nu_3 s^{3\xi-1} + 2\xi\nu_2 s^{2\xi-1} + \xi\nu_1 s^{\xi-1}\right]\dfrac{ds}{d\xi},\\ \dfrac{d\mathcal{U}_3(s)}{d\zeta} = \left[2\xi\chi_2 s^{2\xi-1} + \xi\chi_1 s^{\xi-1}\right]\dfrac{ds}{d\zeta},\\ \dfrac{d\mathcal{U}_4(s)}{d\zeta} = 0,\end{cases} \tag{38}$$

then by (37) and (38), one gets

$$\left[\frac{ds}{d\zeta}\right]^{-1} = \frac{\mathcal{A}(s)}{\mathcal{B}(s)} - \frac{\zeta}{s}, \tag{39}$$

where

$$\begin{cases}\mathcal{A}(s) = 6\xi s^{6\xi-1} + 5\xi\mu_5 s^{5\xi-1} + 4\xi\mu_4 s^{4\xi-1} + 3\xi\mu_3 s^{3\xi-1} + 2\xi\mu_2 s^{2\xi-1}\\ + \xi\mu_1 s^{\xi-1} + \left(4\xi\nu_4 s^{4\xi-1} + 3\xi\nu_3 s^{3\xi-1} + 2\xi\nu_2 s^{2\xi-1} + \xi\nu_1 s^{\xi-1}\right)e^{-2s\zeta} + \left[2\xi\chi_2 s^{2\xi-1} + \xi\chi_1 s^{\xi-1}\right]e^{-4s\zeta},\\ \mathcal{B}(s) = 2se^{-2s\zeta}\left(\nu_4 s^{4\xi} + \nu_3 s^{3\xi} + \nu_2 s^{2\xi} + \nu_1 s^{\xi} + \nu_0\right)\\ + 4s\left(\chi_2 s^{2\xi} + \chi_1 s^{\xi} + \chi_0\right)e^{-4s\zeta} + 6s\rho_0 e^{-6s\zeta}.\end{cases} \tag{40}$$

It follows from $(H2)$ that

$$\mathrm{Re}\left\{\left[\frac{ds}{d\zeta}\right]^{-1}\right\}|_{\zeta=\zeta_0,\vartheta=\vartheta_0}=\frac{\mathscr{A}_R^*\mathscr{B}_R^*+\mathscr{A}_I^*\mathscr{B}_I^*}{\left(\mathscr{A}_R^*\right)^2+\left(\mathscr{B}_I^*\right)^2}>0. \tag{41}$$

This completes the proof.
Let

$$\begin{cases}\tau_1=\mu_5,\\ \tau_2=\mu_4+\nu_4,\\ \tau_3=\mu 3+\nu_3,\\ \tau_4=\mu_2+\nu_2+\chi_2,\\ \tau_5=\mu_1+\nu_1+\chi_1,\\ \tau_6=\mu_0+\nu_0+\chi_0+\rho_0.\end{cases} \tag{42}$$

Next, the following assumption is needed:
$(H3)$ the following inequalities are true:

$$\begin{cases}\mathscr{G}_1=\tau_1>0,\\ \mathscr{G}_2=\det\begin{bmatrix}\tau_1 & 1\\ \tau_3 & \tau_2\end{bmatrix}>0,\\ \mathscr{G}_3=\det\begin{bmatrix}\tau_1 & 1 & 0\\ \tau_3 & \tau_2 & \tau_1\\ \tau_5 & \tau_4 & \tau_3\end{bmatrix}>0,\\ \mathscr{G}_4=\det\begin{bmatrix}\tau_1 & 1 & 0 & 0\\ \tau_3 & \tau_2 & \tau_1 & 1\\ \tau_5 & \tau_4 & \tau_3 & \tau_2\\ 0 & \tau_6 & \tau_5 & \tau_4\end{bmatrix}>0,\\ \mathscr{G}_5=\det\begin{bmatrix}\tau_1 & 1 & 0 & 0 & 0\\ \tau_3 & \tau_2 & \tau_1 & 1 & 0\\ \tau_5 & \tau_4 & \tau_3 & \tau_2 & \tau_1\\ 0 & \tau_6 & \tau_5 & \tau_4 & \tau_3\\ 0 & 0 & 0 & \tau_6 & \tau_5\end{bmatrix}>0,\\ \mathscr{G}_6=\tau_6>0.\end{cases} \tag{43}$$

Lemma 4. *If $\zeta=0$ and $(\mathscr{H}3)$ is fulfilled, then system (2) is locally asymptotically stable.*

Proof. Obviously, (10) with $\zeta=0$ owns the following expression:

$$\mathscr{U}_1(s)+\mathscr{U}_2(s)+\mathscr{U}_3(s)+\mathscr{U}_4(s)=0. \tag{44}$$

Namely,

$$\lambda^6+\tau_1\lambda^5+\tau_2\lambda^4+\tau_3\lambda^3+\tau_4\lambda^2+\tau_5\lambda+\tau_6=0. \tag{45}$$

By means of $(H3)$, one knows that every root λ_i of (45) satisfies $|\arg(\lambda_i)|>(\xi\pi/2)(i=1,2,\ldots,6)$. So, we can obtain that Lemma 3 holds. This ends the proof.

According to the study above, the following result is built.

Theorem 1. *If $(H1)$–$(H3)$ hold true, then the equilibrium point $\mathscr{U}(0,0,0,0,0,0)$ of system (2) is locally asymptotically stable proved that $\zeta\in[0,\zeta_0)$ and a Hopf bifurcation is to arise around $\mathscr{U}(0,0,0,0,0,0)$ if $\zeta=\zeta_0$.*

Remark 1. Theorem 1 shows that ζ_0 is a critical value which determines whether system (2) is stable or unstable. If $\zeta<\zeta_0$, then system (2) is stable, and if $\zeta>\zeta_0$, then system (2) becomes unstable and a family of periodic solutions will appear near $\mathscr{U}(0,0,0,0,0,0)$.

Remark 2. In [3, 4], Cheng et al. studied the stability and Hopf bifurcation of integer-order delayed neural networks. They obtain the characteristic equation by applying integer-order differential equation theory and determinant knowledge. In this work, we investigate the stability and Hopf bifurcation of fractional-order delayed neural networks. We obtain the characteristic equation by applying fractional-order differential equation theory, Laplace transform, and determinant knowledge. The investigation on the distribution of the characteristic roots for characteristic equation of fractional-order neural networks is more difficult that of integer-order case. From this viewpoint, we think that our work replenishes and improves the earlier works of Cheng et al. [3, 4].

4. Software Simulation Plots

Give the fractional-order neural network system:

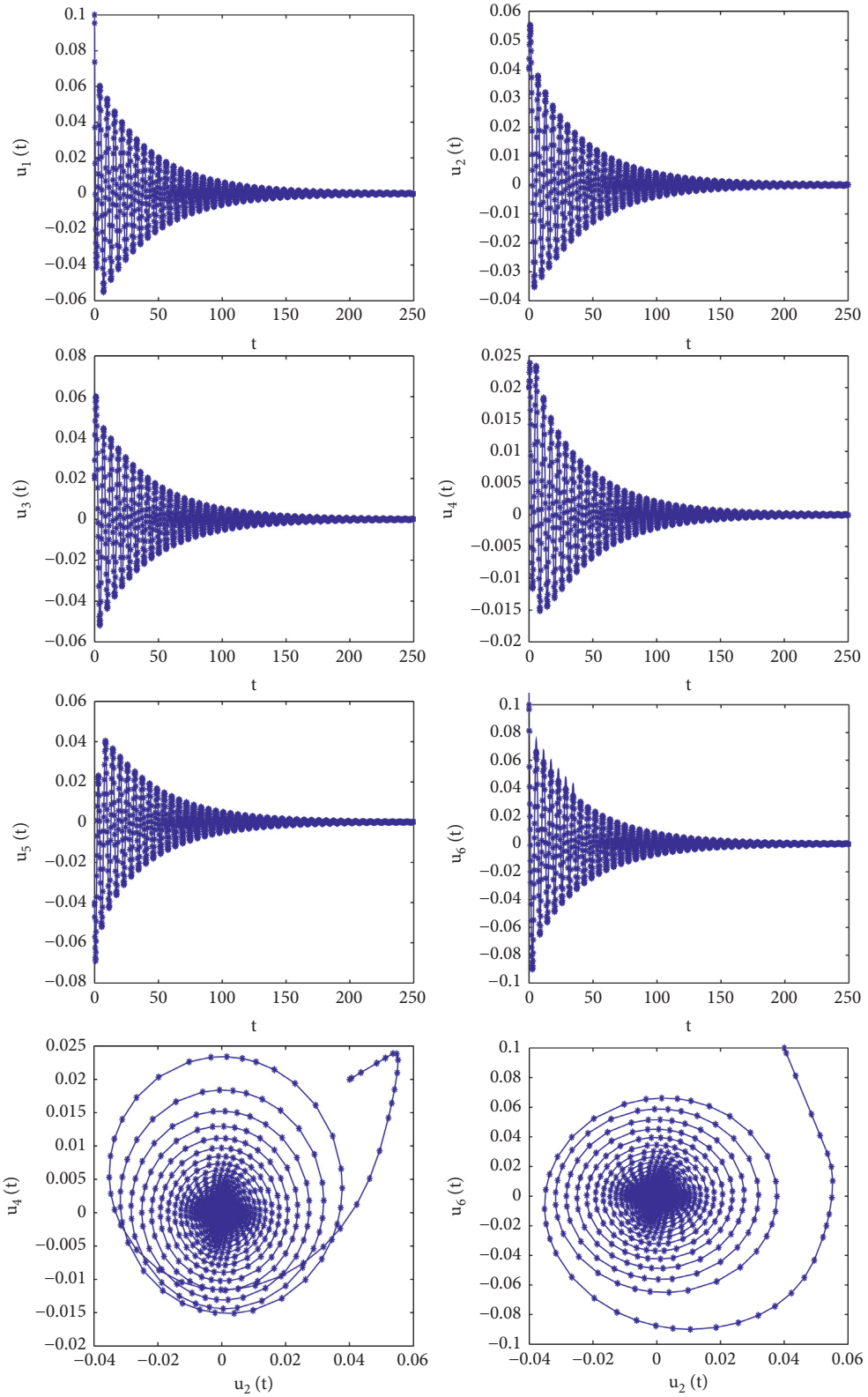

(a)

Figure 1: Continued.

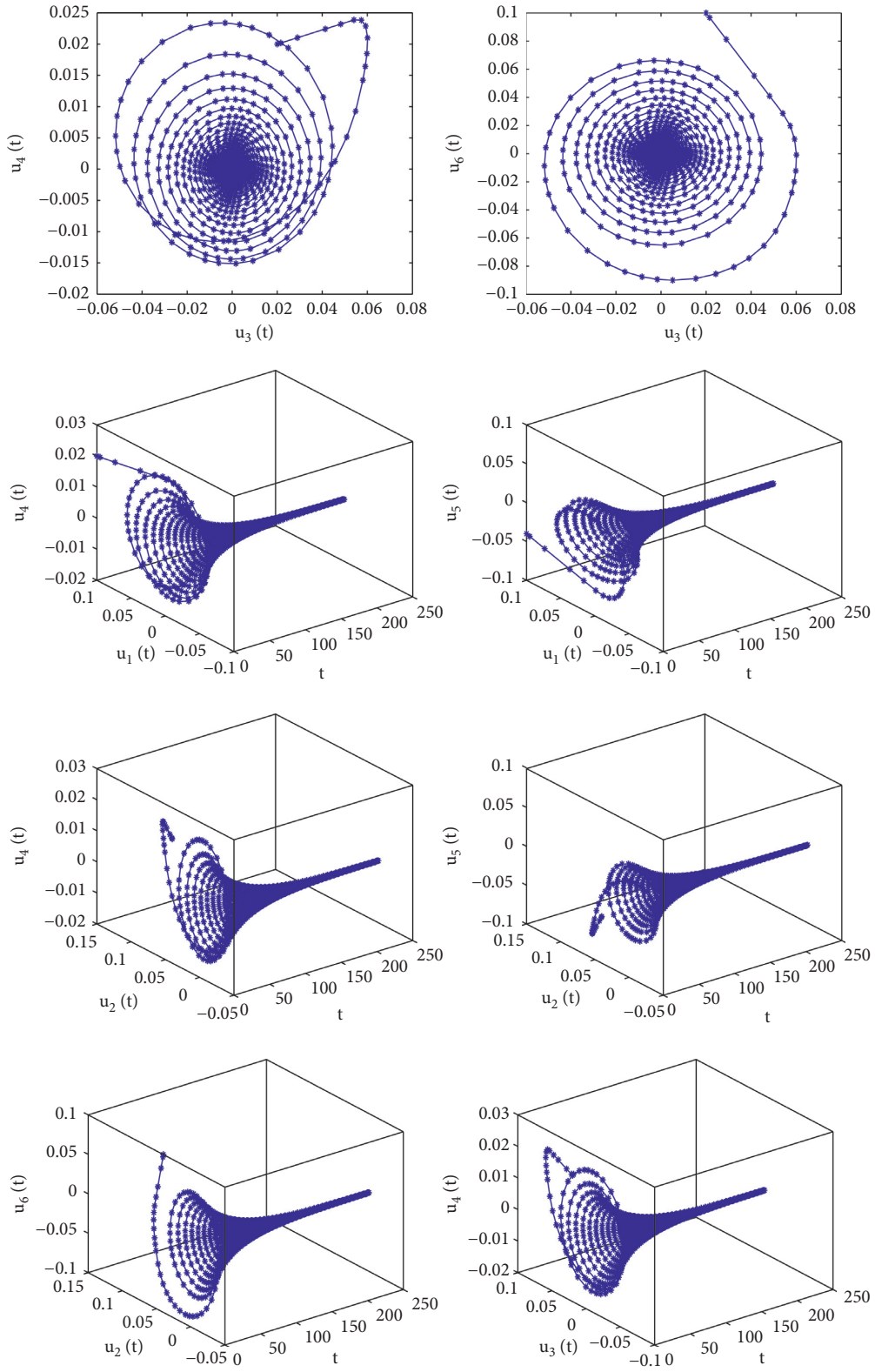

(b)

Figure 1: Continued.

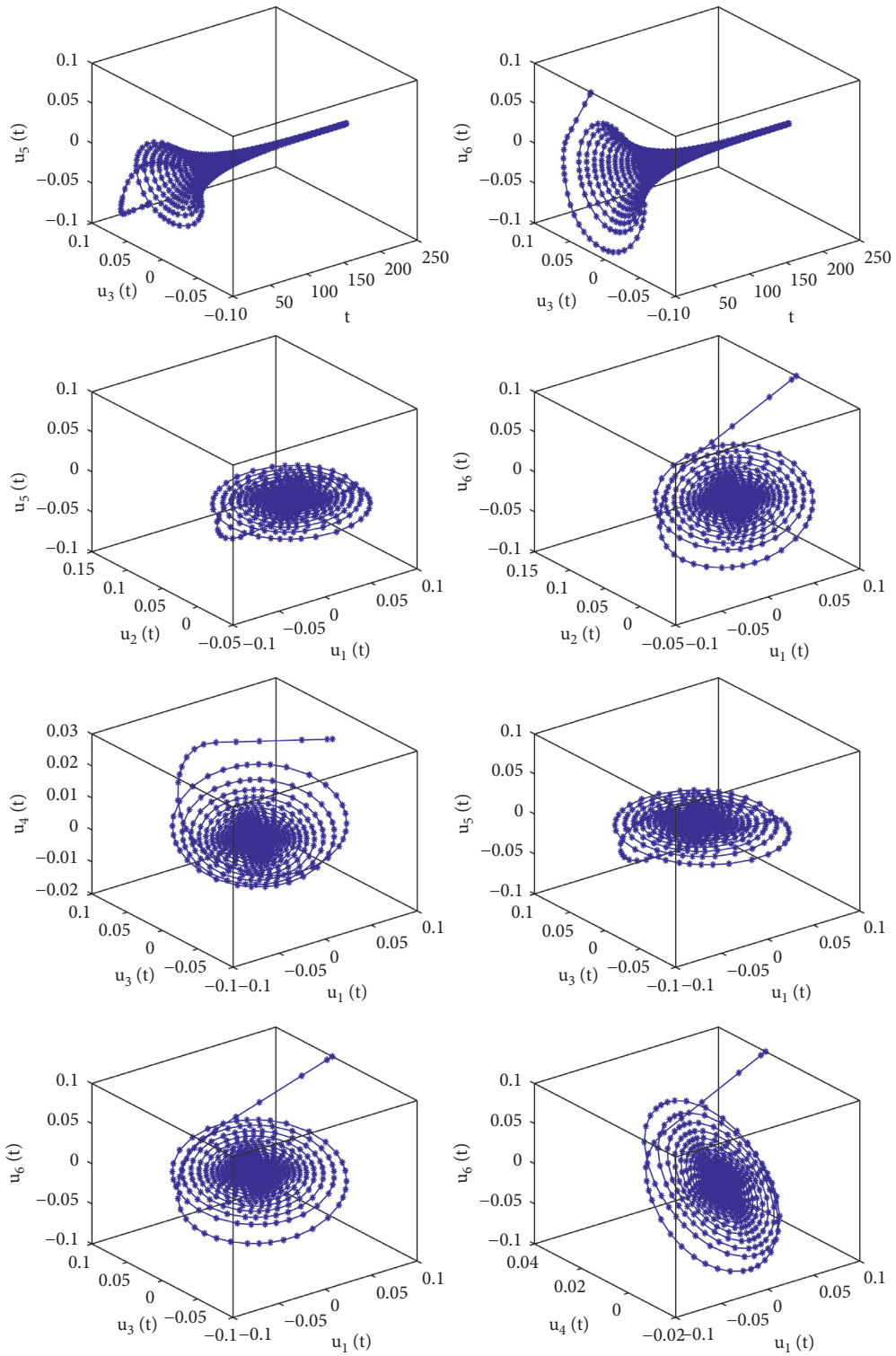

(c)

Figure 1: Continued.

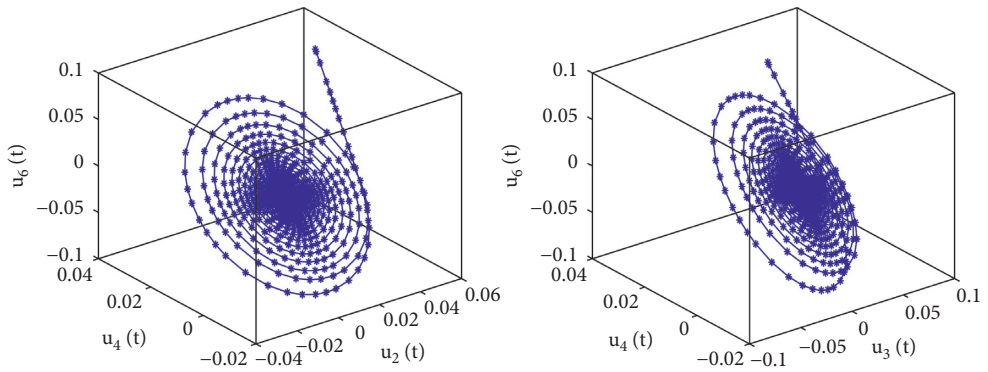

(d)

Figure 1: Stability property for neural network model (46) involving $\zeta = 0.65 < \zeta_0 = 0.75$.

$$\begin{cases} \dfrac{d^{\xi}u_1(t)}{dt^{\xi}} = -u_1(t) + 0.8\tanh\left(u_4(t-\zeta)\right) + 0.8\tanh\left(u_5(t-\zeta)\right) - 0.9\tanh\left(u_6(t-\zeta)\right), \\ \dfrac{d^{\xi}u_2(t)}{dt^{\xi}} = -u_2(t) + 0.5\tanh\left(u_5(t-\zeta)\right) - 0.2\tanh\left(u_6(t-\zeta)\right) + 0.5\tanh\left(u_4(t-\zeta)\right), \\ \dfrac{d^{\xi}u_3(t)}{dt^{\xi}} = -u_3(t) - 0.5\tanh\left(u_6(t-\zeta)\right) - 0.5\tanh\left(u_4(t-\zeta)\right) + 0.8\tanh\left(u_5(t-\zeta)\right), \\ \dfrac{d^{\xi}u_4(t)}{dt^{\xi}} = -u_4(t) + 0.2\tanh\left(u_1(t-\zeta)\right) + 0.6\tanh\left(u_2(t-\zeta)\right) - 0.8\tanh\left(u_3(t-\zeta)\right), \\ \dfrac{d^{\xi}u_5(t)}{dt^{\xi}} = -u_5(t) - 0.9\tanh\left(u_2(t-\zeta)\right) - 0.5\tanh\left(u_3(t-\zeta)\right) + 0.7\tanh\left(u_1(t-\zeta)\right), \\ \dfrac{d^{\xi}u_6(t)}{dt^{\xi}} = -u_6(t) + 0.2\tanh\left(u_3(t-\zeta)\right) - 1.2\tanh\left(u_1(t-\zeta)\right) - 0.9\tanh\left(u_2(t-\zeta)\right). \end{cases} \tag{46}$$

Apparently, neural network system (46) owns the unique zero equilibrium point $\mathscr{U}(0,0,0,0,0,0)$. Let $\xi = 0.94$. By means of computer software, one can derive $\zeta_0 = 0.75$ and $\vartheta_0 = 2.0922$. By virtue of algebraic computation with computer, one can verify that the assumptions $(H1)$–$(H3)$ of Theorem 1 hold. Then, one can conclude that the zero equilibrium point $\mathscr{U}(0,0,0,0,0,0)$ of neural network system (46) is locally asymptotically stable provided that $\zeta \in [0, 0.75)$. To illustrate this fact, we carry out computer simulations. We carry out numerical discretizations of model (46) by Adams–Bashforth–Moulton numerical algorithm. The integration algorithm starts with the solutions of system (46) in terms of R-L integral. The implicit discretization approach is applied to construct the tactics. We select $\zeta = 0.67 < \zeta_0 = 0.75$. The computer simulation figures are presented in Figure 1 which shows the locally asymptotically stable behavior of the neural network system (46). When ζ passes through the critical value $\zeta_0 = 0.75$, then the delay-induced Hopf bifurcation of neural network system (46) will arise in the vicinity of $\mathscr{U}(0,0,0,0,0,0)$. To explain this fact, we select $\zeta = 0.9 > \zeta_0 = 0.75$. The computer simulation figures are presented in Figure 2 which shows the Hopf bifurcation phenomenon of neural network system (46). The initial conditions are $(0.09, 0.038, 0.02, 0.02, -0.039, 0.08)$ and the time step is 0.0035 and the time of simulation is 250 seconds. To display the Hopf bifurcation phenomenon of neural network system (46) intuitively, we also draw the bifurcation plots which can be seen in Figures 3–8. From Figures 3–8, one can easily know that the bifurcation value of neural network system is 0.75.

Remark 3. In Figure 1, the subfigures 1–10 stand for the relation of the variable in horizontal axis and vertical axis. The subfigures 11–26 stand for the relation of the variable in horizontal axis, vertical axis, and vertical axis. In Figure 2, the subfigures 1–10 stand for the relation of the variable in horizontal axis and vertical axis. The subfigures 11–26 stand

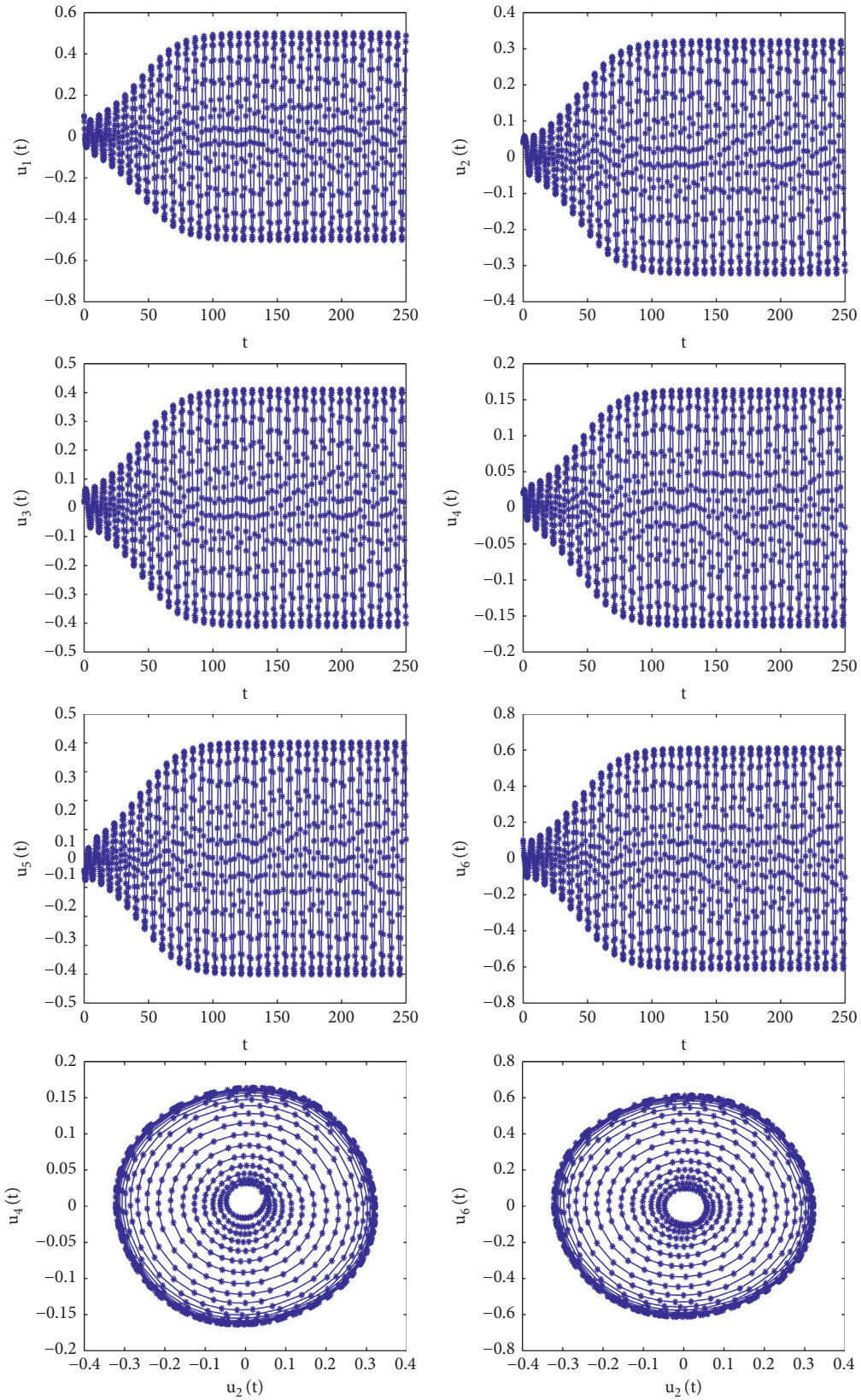

(a)

Figure 2: Continued.

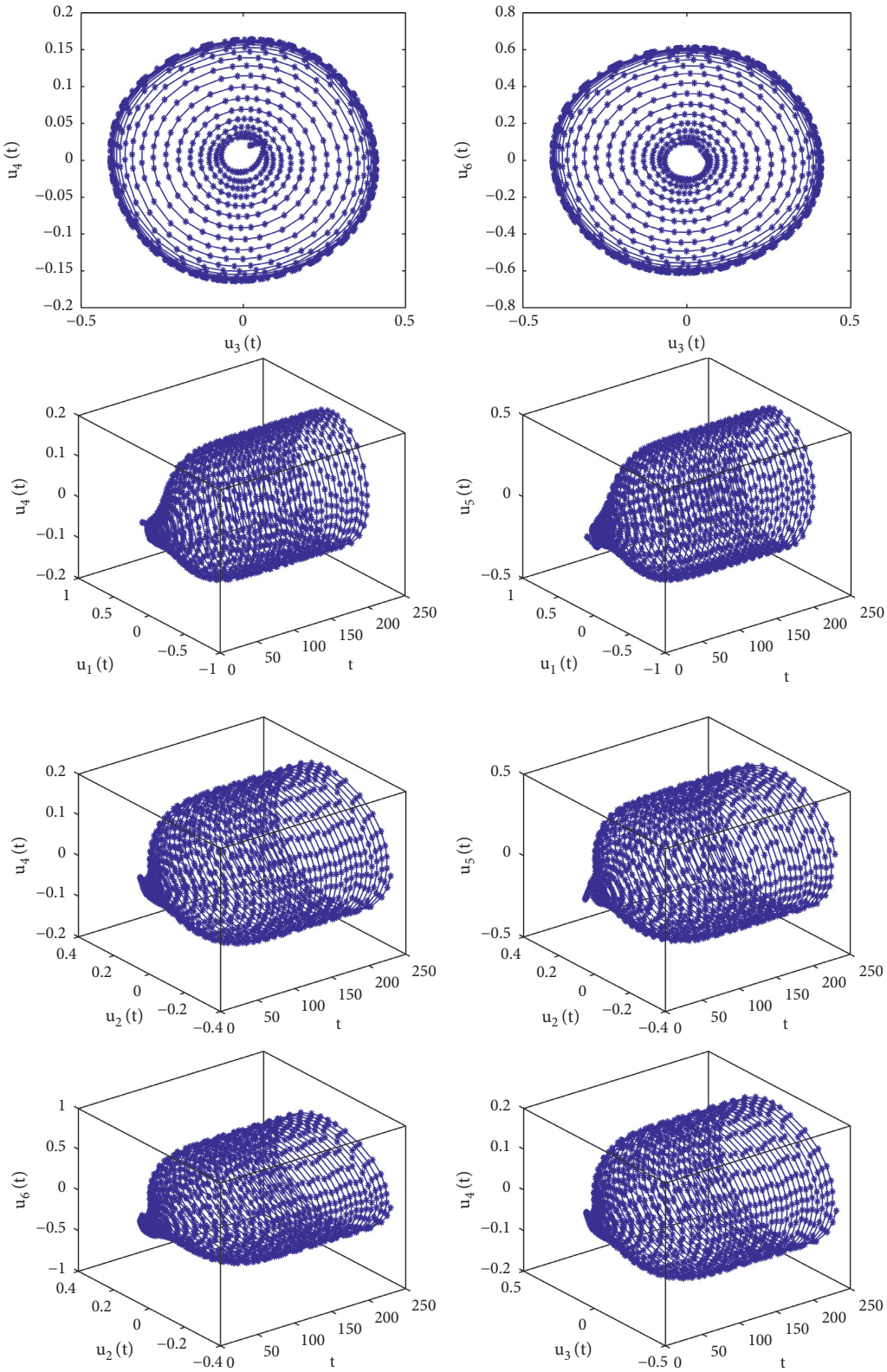

(b)

Figure 2: Continued.

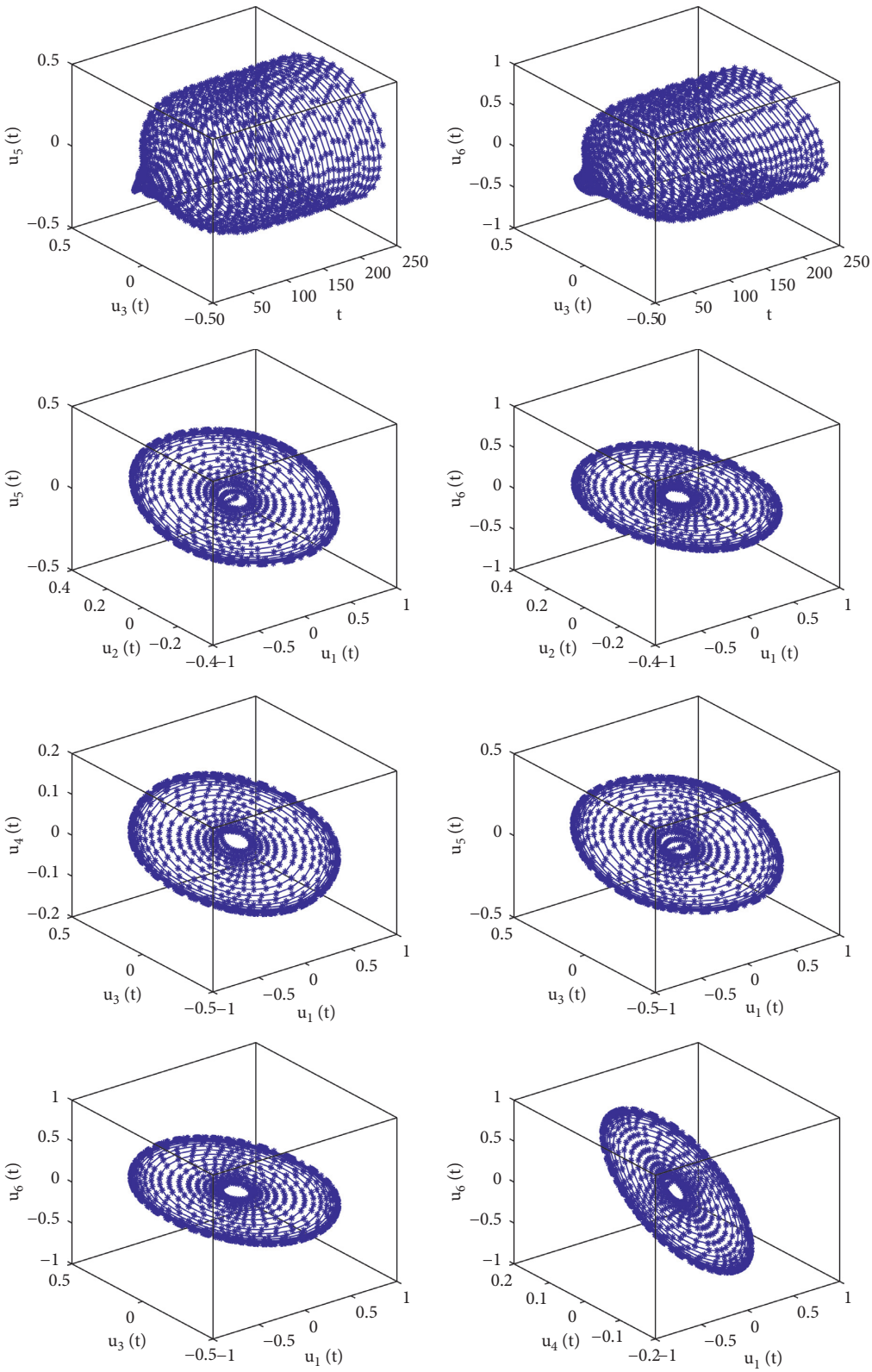

(c)

Figure 2: Continued.

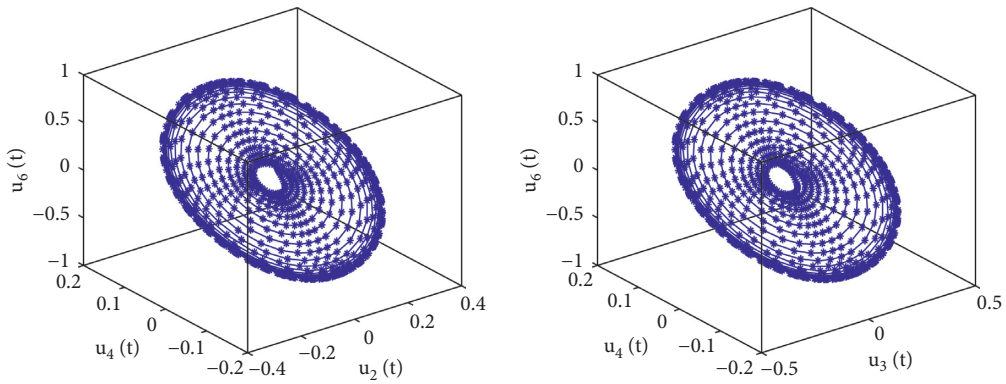

(d)

Figure 2: Hopf bifurcation for neural network model (46) involving $\zeta = 0.9 > \zeta_0 = 0.75$.

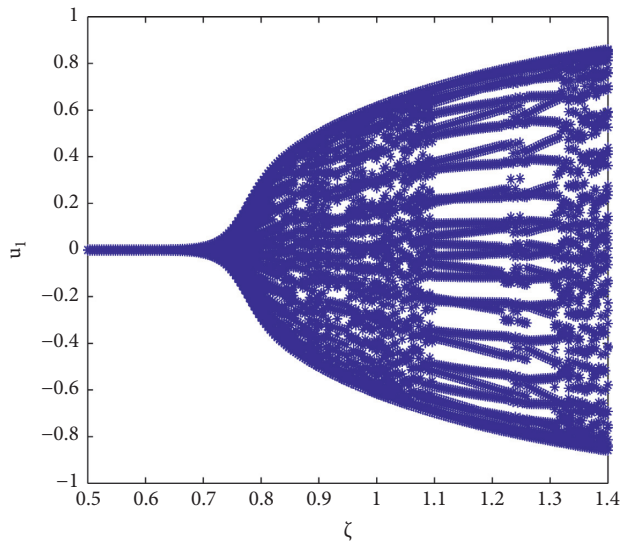

Figure 3: Bifurcation figure of neural network model (46): ζ-u_1.

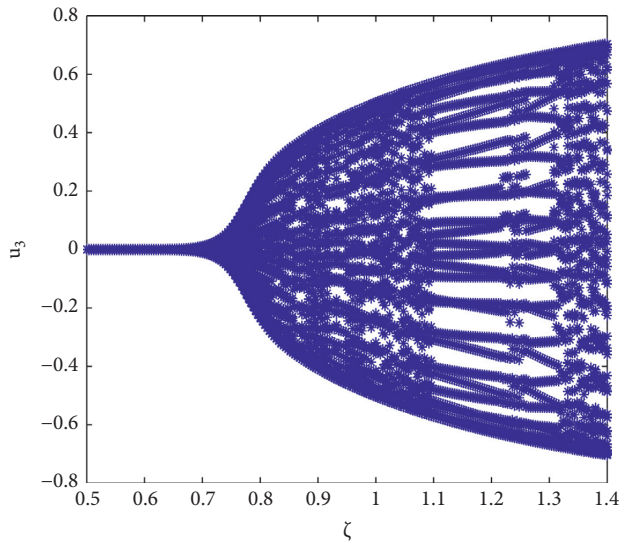

Figure 5: Bifurcation figure of neural network model (4.2): ζ-u_3.

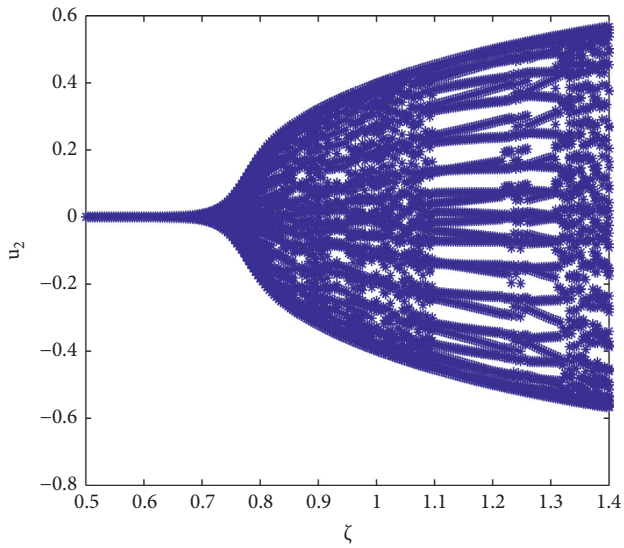

Figure 4: Bifurcation figure of neural network model (46): ζ-u_2.

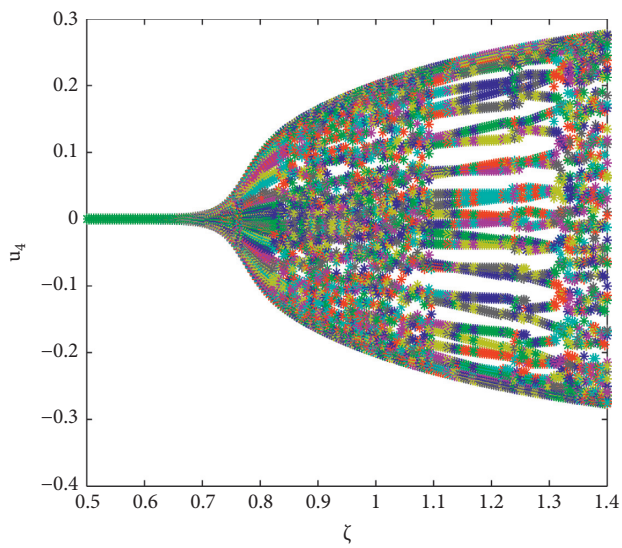

Figure 6: Bifurcation figure of neural network model (4.2): ζ-u_4.

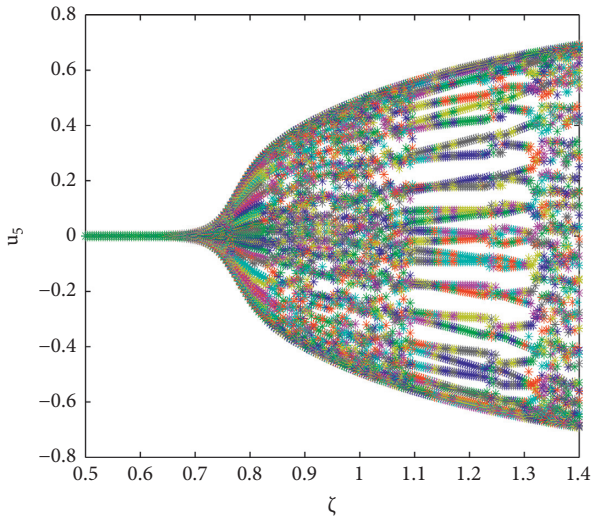

Figure 7: Bifurcation figure of neural network model (46): ζ-u_5.

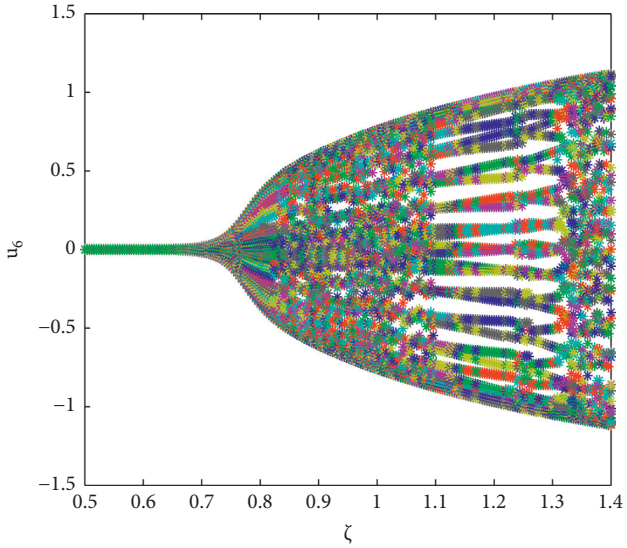

Figure 8: Bifurcation figure of neural network model (46): ζ-u_6.

for the relation of the variable in horizontal axis, vertical axis, and vertical axis.

5. Conclusions

Delay-induced Hopf bifurcation phenomenon is a significant dynamical behavior in delayed dynamical models. In particular, delay-induced Hopf bifurcation in neural network area has attracted much attention from good many scholars in the whole world. During the past decades, some researchers have investigated the Hopf bifurcation problem of fractional-order delayed neural networks. However, the major works are only concerned with the low-dimensional delayed fractional-order delayed neural networks; few works focus on the high-dimensional fractional-order ones. In this work, we mainly focus on the stability problem and the appearance of Hopf bifurcation of high-dimensional fractional-order delayed BAM neural network systems. The study shows that when the time delay keeps in a suitable range, the neural network systems will remain a stable state and if the time delay passes the critical value, then a Hopf bifurcation will take place around the equilibrium point of the involved neural networks. Thus, the time delay is a momentous factor that affects the stability and Hopf bifurcation for the investigated neural networks. In the end, the software simulation results and bifurcation diagrams efficaciously illustrate the effectiveness of the crucial analytical conclusions.

Data Availability

No data were used to support this study.

Conflicts of Interest

The authors declare that they have no conflicts of interest.

Acknowledgments

This work was supported by the Innovation Exploration and Academic New Seedling Project of Guizhou University of Finance and Economics ([2017]5736-025) and National Natural Science Foundation of China (No. 62062018).

References

[1] B. Wróbel, A. Abdelmotaleb, N. Davey, and V. Steuber, "Evolving small spiking neural networks to work as state machines for temporal pattern recognition," *BMC Neuroscience*, vol. 16, 2015 Article number: P238.

[2] I. Rojas, J. Cabestany, and A. Catala, "Advances in artificial neural networks and computational intelligence," *Neural Processing Letters*, vol. 42, no. 1, pp. 1–3, 2015.

[3] Z. Cheng, K. Xie, T. Wang, and J. Cao, "Stability and Hopf bifurcation of three-triangle neural networks with delays," *Neurocomputing*, vol. 322, pp. 206–215, 2018.

[4] Z. Cheng, D. Li, and J. Cao, "Stability and Hopf bifurcation of a three-layer neural network model with delays," *Neurocomputing*, vol. 175, pp. 355–370, 2016.

[5] C. Aouiti, I. Ben Gharbia, J. Cao, M. Salah M'hamdi, and A. Alsaedi, "Existence and global exponential stability of pseudo almost periodic solution for neutral delay BAM neural networks with time-varying delay in leakage terms," *Chaos, Solitons & Fractals*, vol. 107, pp. 111–127, 2018.

[6] W. Yang, W. Yu, J. Cao, F. E. Alsaadi, and T. Hayat, "Almost automorphic solution for neutral type high-order Hopfield BAM neural networks with time-varying leakage delays on time scales," *Neurocomputing*, vol. 267, pp. 241–260, 2017.

[7] C. Maharajan, R. Raja, J. Cao, and G. Rajchakit, "Novel global robust exponential stability criterion for uncertain inertial-type BAM neural networks with discrete and distributed time-varying delays via Lagrange sense," *Journal of the Franklin Institute*, vol. 355, no. 11, pp. 4727–4754, 2018.

[8] C.-A. Popa, "Global μ-stability of neutral-type impulsive complex-valued BAM neural networks with leakage delay and unbounded time-varying delays," *Neurocomputing*, vol. 376, pp. 73–94, 2020.

[9] C. Sowmiya, R. Raja, Q. Zhu, and G. Rajchakit, "Further mean-square asymptotic stability of impulsive discrete-time stochastic BAM neural networks with Markovian jumping

and multiple time-varying delays," *Journal of the Franklin Institute*, vol. 356, no. 1, pp. 561–591, 2019.

[10] F. Lin and Z. Zhang, "Global asymptotic synchronization of a class of BAM neural networks with time delays via integrating inequality techniques," *Journal of Systems Science and Complexity*, vol. 33, no. 2, pp. 366–382, 2020.

[11] N. Belmahi and N. Shawagfeh, "A new mathematical model for the glycolysis phenomenon involving Caputo fractional derivative: well posedness, stability and bifurcation," *Chaos, Solitons & Fractals*, vol. 142, Article ID 110520, 2021.

[12] M. Liu, X. Xu, and C. Zhang, "Stability and global Hopf bifurcation for neutral BAM neural network," *Neurocomputing*, vol. 145, pp. 122–130, 2014.

[13] K. Gopalsamy and X. Xue-Zhong He, "Delay-independent stability in bidirectional associative memory networks," *IEEE Transactions on Neural Networks*, vol. 5, no. 6, pp. 998–1002, 1994.

[14] A. Hajihosseini, F. Maleki, and G. R. Rokni Lamooki, "Bifurcation analysis on a generalized recurrent neural network with two interconnected three-neuron components," *Chaos, Solitons & Fractals*, vol. 44, no. 11, pp. 1004–1019, 2011.

[15] E. Kaslik and S. Balint, "Bifurcation analysis for a discrete-time Hopfield neural network of two neurons with two delays and self-connections," *Chaos, Solitons & Fractals*, vol. 39, no. 1, pp. 83–91, 2009.

[16] J. Ge and J. Xu, "Stability and Hopf bifurcation on four-neuron neural networks with inertia and multiple delays," *Neurocomputing*, vol. 287, pp. 34–44, 2018.

[17] Y. Yang and J. Ye, "Stability and bifurcation in a simplified five-neuron BAM neural network with delays," *Chaos, Solitons & Fractals*, vol. 42, no. 4, pp. 2357–2363, 2009.

[18] B. Wang and J. Jian, "Stability and Hopf bifurcation analysis on a four-neuron BAM neural network with distributed delays," *Communications in Nonlinear Science and Numerical Simulation*, vol. 15, no. 2, pp. 189–204, 2010.

[19] R. Amin, K. Shah, M. Asif, and I. Khan, "A computational algorithm for the numerical solution of fractional order delay differential equations," *Applied Mathematics and Computation*, vol. 402, Article ID 125863, 2021.

[20] A. Si-Ammour, S. Djennoune, and M. Bettayeb, "A sliding mode control for linear fractional systems with input and state delays," *Communications in Nonlinear Science and Numerical Simulation*, vol. 14, no. 5, pp. 2310–2318, 2009.

[21] C. Xu, Z. Liu, L. Yao, and C. Aouiti, "Further exploration on bifurcation of fractional-order six-neuron bi-directional associative memory neural networks with multi-delays," *Applied Mathematics and Computation*, vol. 410, Article ID 126458, 2021.

[22] P. Mani, R. Rajan, L. Shanmugam, and Y. Hoon Joo, "Adaptive control for fractional order induced chaotic fuzzy cellular neural networks and its application to image encryption," *Information Sciences*, vol. 491, pp. 74–89, 2019.

[23] L. Li, X. Liu, M. Tang, S. Zhang, and X.-M. Zhang, "Asymptotical synchronization analysis of fractional-order complex neural networks with non-delayed and delayed couplings," *Neurocomputing*, vol. 445, pp. 180–193, 2021.

[24] C. Xu, M. Liao, P. Li, and S. Yuan, "Impact of leakage delay on bifurcation in fractional-order complex-valued neural networks," *Chaos, Solitons & Fractals*, vol. 142, Article ID 110535, 2021.

[25] B. Cao and X. Nie, "Event-triggered adaptive neural networks control for fractional-order nonstrict-feedback nonlinear systems with unmodeled dynamics and input saturation," *Neural Networks*, vol. 142, pp. 288–302, 2021.

[26] C. J. Xu, W. Zhang, C. Aouiti, Z. X. Liu, M. X. Liao, and P. L. Li, "Further investigation on bifurcation and their control of fractional-order BAM neural networks involving four neurons and multiple delays," *Mathematical Methods in the Applied Sciences*, vol. 75. , 2021 in press.

[27] C. Xu, Z. Liu, M. Liao, P. Li, Q. Xiao, and S. Yuan, "Fractional-order bidirectional associate memory (BAM) neural networks with multiple delays: the case of Hopf bifurcation," *Mathematics and Computers in Simulation*, vol. 182, pp. 471–494, 2021.

[28] T. Kan, Z. Gao, C. Yang, and J. Jian, "Convolutional neural networks based on fractional-order momentum for parameter training," *Neurocomputing*, vol. 449, pp. 85–99, 2021.

[29] M. Xiao, W. X. Zheng, J. Lin, G. Jiang, L. Zhao, and J. Cao, "Fractional-order PD control at Hopf bifurcations in delayed fractional-order small-world networks," *Journal of the Franklin Institute*, vol. 354, no. 17, pp. 7643–7667, 2017.

[30] B. Tao, M. Xiao, Q. Sun, and J. Cao, "Hopf bifurcation analysis of a delayed fractional-order genetic regulatory network model," *Neurocomputing*, vol. 275, pp. 677–686, 2018.

[31] W. Hu, D. Ding, Y. Zhang, N. Wang, and D. Liang, "Hopf bifurcation and chaos in a fractional order delayed memristor-based chaotic circuit system," *Optik*, vol. 130, pp. 189–200, 2017.

[32] I. Podlubny, *Fractional Differential Equations*, Academic Press, New York, NY, USA, 1999.

[33] D. Matignon, "Stability results for fractional differential equations with applications to control processing," *Computational Engineering in Systems Applications*, vol. 2, pp. 963–968, 1996.

[34] X. Wang, Z. Wang, and J. Xia, "Stability and bifurcation control of a delayed fractional-order eco-epidemiological model with incommensurate orders," *Journal of the Franklin Institute*, vol. 356, no. 15, pp. 8278–8295, 2019.

[35] W. Deng, C. Li, and J. Lü, "Stability analysis of linear fractional differential system with multiple time delays," *Nonlinear Dynamics*, vol. 48, no. 4, pp. 409–416, 2007.

Hindawi
Complexity
Volume 2021, Article ID 9162259, 13 pages
https://doi.org/10.1155/2021/9162259

Research Article

Fast Simulation and Chaos Investigation of a DC-DC Boost Inverter

Rachid Dhifaou[1] **and Houda Brahmi**[2]

[1]*Unit of Research (ERCO), INSAT Tunisia, Centre Urbain Nord, B.P. N 676, 1080 Tunis Cedex, Tunisia*
[2]*University of Tunis el Manar, Higher Institute of Medicals Technologies of Tunis (ISTMT), Unit of Research ERCO-INSAT, 9 Rue Zouhair Essafi, 1006 Tunis, Tunisia*

Correspondence should be addressed to Houda Brahmi; houda.brahmi@istmt.utm.tn

Received 24 May 2021; Accepted 29 July 2021; Published 14 August 2021

Academic Editor: Guillermo Huerta Cuellar

Intensive and repetitive simulations are required to study static and dynamic behaviours of systems. Particular phenomena such as bifurcation and chaos require long simulation times and analysis. To check the existence of bifurcations and chaos in a dynamic system, a fine-tuning procedure of a bifurcation parameter is to be carried out. This increases considerably the computing time, and a great amount of patience is needed to obtain adequate results. Because of the high switching frequency of a boost inverter, the integration process of the dynamic model used to describe it uses an integration step that is in general less than one microsecond. This makes the integration process time consuming even for a short simulation. Thus, a fast, but accurate, method is suitable to analyse the dynamic behaviour of the converter. This work contains two topics. First, we develop a like-discrete integration process that permits precise results in a very fast manner. For one switching period, we compute only two or a maximum of three breaking points depending on whether we treat a continuous conduction mode (CCM) or a discontinuous conduction mode (DCM) of the inductor current. Furthermore, with each segment of the dynamic trajectory, an exact analytic formula is associated. The second goal is to use this result to develop a discrete iterative map formulated as in standard discrete time series models. The Jacobian matrix of the found iterative map is defined and used to compute Lyapunov exponents to prove existence of chaos. Performance of the developed study is positively evaluated by using classical simulations and fine-tuning a bifurcation parameter to detect chaos. This parameter is the desired reference of the inductor current peak. Results show that the proposed scheme is very fast and accurate. The study can be easily extended to other switching topologies of DC-DC inverters.

1. Introduction

DC-DC boost inverter, also known as a step up inverters, are largely studied in literature [1–3]. These power electronic devices transfer electric energy from a DC input voltage source to an output load that requires a higher voltage. The efficiency of DC-DC boost inverter is good in general which makes them largely employed in various applications. Battery chargers, photovoltaic energy-based systems, and DC motor drives are typical examples [4,5]. As for all DC-DC power converter topologies, energy transfer in this device is achieved by switching the state of a power transistor at high frequencies. Output voltage or current is varied by adjusting the control variable, commonly named the duty cycle. The operating steady-state regime can be done with an open loop or closed loop configuration, by using the appropriate controller. Important advances are reached in the field of both voltage control and current control [6–8].

To perform successful and reliable practical control, numerical simulations are of great importance. Intensive and repetitive simulations are also needed to study particular phenomena such as bifurcations [9,10] and chaos [10,11]. It is shown in the literature that a lot of piecewise dynamic systems exhibit chaotic behaviour [12,13]. DC-DC converters are nonlinear periodically controlled systems that operate under practically piecewise dynamic trajectories. Chaotic regimes are confirmed for various switching power converters.

To check the existence of bifurcations and chaos in a dynamic system, a fine-tuning procedure of a bifurcation parameter is required. This increases considerably the computing time, and a great amount of patience is required to establish adequate results. Because of the high switching frequency of the PWM technique [14], to solve the model of a DC-DC boost inverter, an integration step smaller than one microsecond is required. This makes the integration process time consuming even for short simulations. Thus, a fast, but accurate, method is required to analyse the dynamic behaviour of the converter.

The first goal of this work is to develop a type-like discrete integration process with precise and fast results. For one switching period, we compute only two or a maximum of three breaking points depending on whether we treat a continuous conduction mode (CCM) or a discontinuous conduction mode (DCM) of the inductor current [1,2]. Furthermore, with each segment of the dynamic trajectory, an exact analytic formula is associated.

The second goal of the paper is to use these results in developing a discrete iterative map formulated as in standard discrete time series models [15,16]. A Jacobian matrix as found with an iterative map is defined and used to compute Lyapunov exponents [12,13] via the QR factorisation technique.

In switching inverter topologies, a current peak control (CPC) is frequently used [3] to impose an adequate operating point. In such case, the feedback control block is composed of a saw tooth generator, a comparator, and a latch. A drive circuit uses latch output to generate the gating pulses. The switch is turned on at the beginning of each switching period and turned off if the inductor current becomes greater than a reference value and remains in the off state until the beginning of the next cycle. Simulations of this control system are frequently done in Matlab/Simulink environment. In this paper, we will demonstrate that there is no need for this control block. Only a simple relation is needed to compute transient duty cycle. Furthermore, the program is realised in terms of a simple and fast Matlab m-file.

According to these goals, the paper is organised as follows. Section 2 develops fundamentals of the inverter. It includes the equivalent electrical circuit modelling the DC-DC boost inverter, commutation equations, properties of DCM and CCM regimes, and dynamical submodels associated with ON and OFF states. Section 3 develops exact and analytical relations of dynamic variables for both ON and OFF states. This section proposes, in particular, a simple correction of the time interval associated with DCM regime. Section 4 deals with fundamental steady-state equations. For both DCM regime and CCM regime, mean values of inductor current and output voltage are detailed and expressed. Effect of inductor inductance, output load resistance, and switching period on the boundary between DCM and CCM is graphically explained. Section 5 presents the main steps of the dynamic simulation algorithm and discusses how to implement the current peak control. In Section 6, we develop the procedure of obtaining a discrete map model and discuss how to conduct the computation of Lyapunov exponents. Finally, Section 7 presents various simulation cases. Results obtained in open-loop and closed-loop control are presented and commented. The discussion is particularly focused on tuning the bifurcation parameter and analysing chaos. Computing time is also considered in the scheme evaluation.

2. Fundamentals of a DC-DC boost inverter

Figure 1 shows an equivalent circuit diagram of a boost DC-DC inverter supplying a pure resistive loadR_o. Parameters$E$, L, and C denote, respectively, the input voltage source, the inductance of the inductor, and the output filtering capacitor. In this work, we consider the most widely used model [2, 8] characterised by ideal components. This means that the power transistor is an ideal switch; the inductor, filtering capacitor, and diode are lossless. In the conduction mode, the voltage across the diode is zero. The power transistor works as short circuit or as an open circuit depending on whenever the signal command $u(t)$ equals 1 or0. Along switching time, boost inverter equivalent circuit shown by Figure 1 takes two forms as shown by Figures 2(a) and Figure 2(b) [14]. During the ON state, the transistor behaves like a short and no current flows through the diode. Therefore, the inductor becomes in fact disconnected from the parallel part $(R_o - C)$ and the positive voltage of the capacitor biases the diode. The current flowing through the inductor increases; as a result, the electromagnetic energy in the inductance L increases. At the same time, the filtering capacitor discharges into the load resistance R_o, and therefore the voltage across the capacitor decreases. During the OFF state, the power transistor behaves like an open circuit, and the diode is conducting. Therefore, the input voltage supplies directly to the load. The voltage across the capacitor increases and the current through the inductor decreases because the electromagnetic energy is transformed into electrostatic energy.

Command $u(t)$ is a PWM signal characterised by a switching period T and a duty cycleα. In the following, this period will be divided into three time intervals t_1, t_2, and t_3 as indicated by equations (1) and (2). The first interval corresponds to the ON state given by $(u(t) = 1)$. The second and third intervals are associated with the OFF state corresponding to $(u(t) = 0)$. In these equations, coefficients (α, β, γ) correspond, respectively, to ratios of (t_1, t_2, t_3) with respect to the switching period$T$. Coefficient $\alpha$is known by duty cycle. Coefficient β is the complement of α in the case of continuous conduction mode (CCM). Coefficient γ is the complement of $(\alpha + \beta)$ in the case of discontinuous conduction mode (DCM).

$$\begin{aligned} t_1 &= \alpha T, \\ t_2 &= \beta T, \\ t_3 &= \gamma T, \end{aligned} \tag{1}$$

$$\begin{aligned} t_1 + t_2 + t_3 &= T, \\ \alpha + \beta + \gamma &= 1. \end{aligned} \tag{2}$$

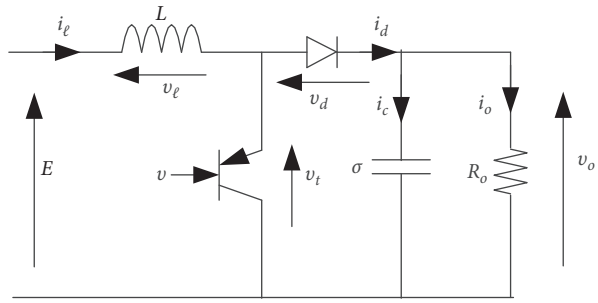

Figure 1: Boost inverter equivalent circuit.

This organisation aims to take into account continuous conduction mode (CCM) and discontinuous conduction mode (DCM) of inductor current. As previously indicated, inductor current $i_\ell(t)$ increases during the ON state and decreases during the OFF state. Let us consider that the switching period T begins with an inductor current $I_{\ell 0}$ and a capacitor voltage V_{c0}, and just when the OFF state takes place, these variables are, respectively, $I_{\ell 1}$and V_{c1}. If $i_\ell(t)$ in the OFF state remains positive until the end of the period, we have the CCM case and $(t_3 = 0)$; therefore, $(t_2 = \beta T = (1-\alpha)T)$. At the end of the period T, the current through the inductor and voltage across the capacitor are denoted $I_{\ell 2}$ and V_{c2}, respectively. If $i_\ell(t)$reaches zero before the period finishes, we have the DCM case, $(t_3 > 0)$ and $(t_2 = \beta T < (1-\alpha)T)$. In this case, the current through the inductor remains null during t_3 because the diode is biased. However, the voltage across the capacitor decreases exponentially from the value V_{c2} to a third value V_{c3}. Figures 3(a) and 3(b) sketch this scenario in terms of inductor current $i_\ell(t)$ and capacitor voltage $v_c(t)$. These figures correspond to the transient regime and report the possible breaking points for a DCM case. For both DCM and CCM regimes, we establish the following commutation equation:

$$\begin{aligned} v_\ell &= E - (1-u)v_o, \\ v_o &= v_c. \end{aligned} \tag{3}$$

Thus, without any particular difficulty, the following dynamic model is derived:

$$\begin{cases} \dfrac{\mathrm{d}i_\ell}{\mathrm{d}t} = \dfrac{E-(1-u)v_c}{L}, \\ \dfrac{\mathrm{d}v_c}{\mathrm{d}t} = \dfrac{(1-u)R_o i_\ell - v_c}{R_o C}. \end{cases} \tag{4}$$

Depending on whether we are dealing with an ON state or an OFF state, we have to treat two different models. In the ON state, the model becomes equivalent to two independent submodels as given by systems (5) and (6). In the OFF state, we have the model given by systems (7) and (8).

$$\begin{cases} \dfrac{\mathrm{d}i_\ell}{\mathrm{d}t} = \dfrac{E}{L}, \end{cases} \tag{5}$$

$$\begin{cases} \dfrac{\mathrm{d}v_c}{\mathrm{d}t} = -\dfrac{v_c}{R_o C}, \end{cases} \tag{6}$$

$$\begin{cases} \dfrac{\mathrm{d}i_\ell}{\mathrm{d}t} = \dfrac{E-v_c}{L}, \end{cases} \tag{7}$$

$$\begin{cases} \dfrac{\mathrm{d}v_c}{\mathrm{d}t} = \dfrac{R_o i_\ell - v_c}{R_o C} \end{cases} \tag{8}$$

For the OFF state case, isolating $v_c$from (7) and establishing its time derivative yields

$$v_c = E - L\frac{\mathrm{d}i_\ell}{\mathrm{d}t}, \tag{9}$$

$$\frac{\mathrm{d}v_c}{\mathrm{d}t} = -L\frac{\mathrm{d}^2 i_\ell}{\mathrm{d}t^2}. \tag{10}$$

Thus, for the OFF state case, equations (9) and (10), combined with equation (8), result in

$$\frac{\mathrm{d}^2 i_\ell}{\mathrm{d}t^2} + \frac{1}{\tau_c}\frac{\mathrm{d}i_\ell}{\mathrm{d}t} + \frac{i_\ell}{\tau_\ell \tau_c} - \frac{I_{er}}{\tau_\ell \tau_c} = 0, \tag{11}$$

$$\begin{aligned} \tau_c &= R_o C, \\ \tau_\ell &= \frac{L}{R_o}, \\ I_{er} &= \frac{E}{R_o}. \end{aligned} \tag{12}$$

The second-order linear ODE (11) furnishes the following characteristic polynomial:

$$s^2 + \frac{s}{\tau_c} + \frac{1}{\tau_\ell \tau_c} = 0. \tag{13}$$

With the condition $(L < 4R_o^2 C)$, this polynomial admits two complex conjugate poles which means that we have a damped oscillating system. The time constant (τ) and the pulsation (ω) are expressed by

$$\begin{aligned} s &= -\frac{1}{\tau} \pm j\omega, \\ \tau &= 2\tau_c = 2R_o C, \\ \omega &= \frac{1}{\tau}\sqrt{\frac{2\tau}{\tau_\ell} - 1}. \end{aligned} \tag{14}$$

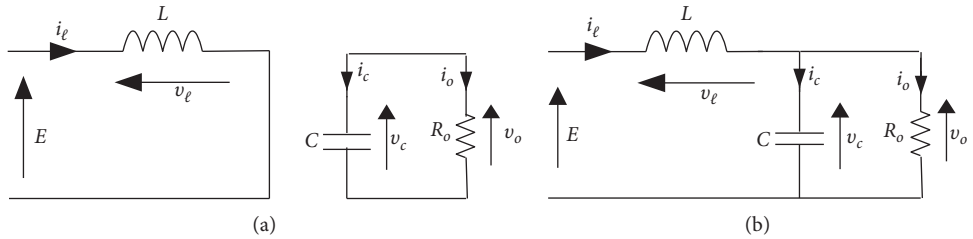

Figure 2: (a) Equivalent circuit in ON state case. (b) Equivalent circuit in OFF state case.

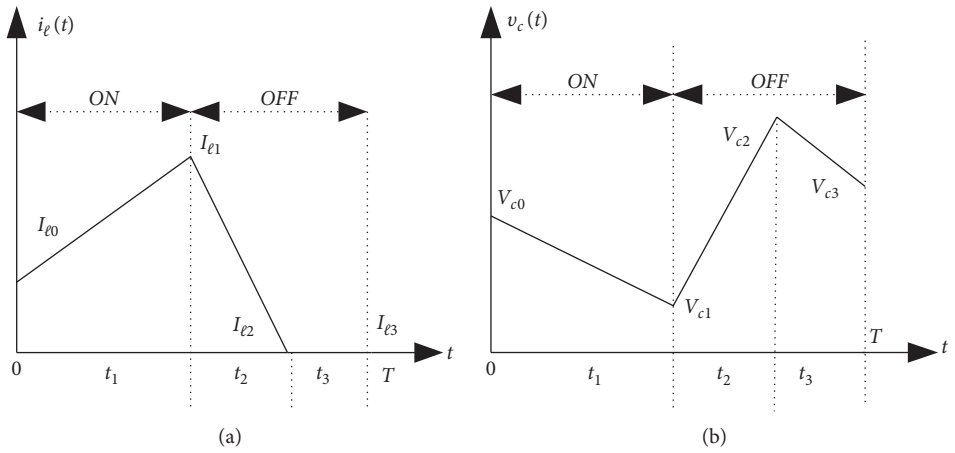

Figure 3: (a) Illustrative evolution of inductor current. (b) Illustrative evolution of capacitor voltage.

3. Temporal Solution of the Mathematical Model

3.1. Analytical Solution of ON State Case. Here, we have to solve a simple dynamic system ((5) and (6)) which is completely decoupled into two independent subsystems. The inductor current and capacitor voltage of the boost inverter are of the form

$$\begin{aligned} i_\ell(t) &= I_{\ell 0} + \frac{E}{L}t, \\ v_c(t) &= V_{c0}e^{-(t/\tau_c)}. \end{aligned} \tag{15}$$

This solution is verified by the construction of $(i_\ell(0) = I_{\ell 0})$ and $(v_c(0) = V_{c0})$. $I_{\ell 1}$ and V_{c1} of $i_\ell(t)$ and $v_c(t)$ at $(t_1 = \alpha T)$ are expressed by

$$\begin{aligned} I_{\ell 1} &= i_\ell(t_1) = I_{\ell 0} + \frac{E\alpha T}{L}, \\ V_{c1} &= v_c(t_1) = V_{c0}e^{-(\alpha T/\tau_c)}. \end{aligned} \tag{16}$$

3.2. Analytical Solution of OFF State Case. Solution $i_\ell(t)$ of (11) is naturally composed of two terms. The first term is the particular solution corresponding to the case where $i_\ell(t)$is constant. The second one is the homogeneous solution which is a sinusoidal damped variable. Thus, we get

$$i_\ell(t) = I_{er} + [\eta_1 \sin(\theta) + \eta_2 \cos(\theta)]e^{-(t/\tau)}, \tag{17}$$

$$\theta = \omega t. \tag{18}$$

For $(t = 0)$, we have $(i_\ell(0) = I_{\ell 1})$ which implies

$$\eta_2 = I_{\ell 1} - I_{er}. \tag{19}$$

To identify parameter η_1, we obtain the derivative with respect to time of equation (17) and make it equal to equation (7). Therefore, we obtain

$$\frac{di_\ell}{dt} = -\left\{\left[\omega\eta_2 + \frac{\eta_1}{\tau}\right]\sin(\theta) + \left[\frac{\eta_2}{\tau} - \omega\eta_1\right]\cos(\theta)\right\}e^{-(t/\tau)} = \frac{E - v_c}{L}. \tag{20}$$

By applying this expression at $(t = 0)$, one deduces

$$\eta_1 = \frac{I_{\ell 1} - I_{er}}{\omega\tau} + \frac{E - V_{c1}}{L\omega}. \tag{21}$$

The behaviour of the voltage across the capacitor is derived from equation (20). This results in

$$v_c(t) = E + [\eta_3 \sin(\theta) + \eta_4 \cos(\theta)]e^{-(t/\tau)}, \tag{22}$$

$$\begin{aligned} \eta_3 &= L\omega\left[\eta_2 + \frac{\eta_1}{\omega\tau}\right], \\ \eta_4 &= L\omega\left[\frac{\eta_2}{\omega\tau} - \eta_1\right]. \end{aligned} \tag{23}$$

To compute values $I_{\ell 2}$ of $i_\ell(t)$ and V_{c2} of $v_c(t)$ at t_2, let us first assume that we are in the CCM regime by setting $(\gamma =$

0) and $(\beta = (1-\alpha))$ or equivalently by setting $(t_3 = 0)$ and $(t_2 = (1-\alpha)T)$. The following equations are obtained. Note that all coefficients $(\eta_1, \eta_3, \eta_4, \eta_5)$are functions of $(\delta = \omega\beta T)$.

$$I_{\ell 2} = I_{er} + \eta_5\left[\eta_1 \sin(\delta) + \eta_2 \cos(\delta)\right], \tag{24}$$

$$V_{c2} = E + \eta_5\left[\eta_3 \sin(\delta) + \eta_4 \cos(\delta)\right], \tag{25}$$

$$\begin{aligned} \eta_5 &= e^{-(\delta/\omega\tau)}, \\ \delta &= \omega\beta T, \\ \beta &= (1-\alpha). \end{aligned} \tag{26}$$

If $I_{\ell 2}$ computed by equation (24) is positive, the assumption of CCM holds and the computed values of $I_{\ell 2}$ and V_{c2} are valid. If $I_{\ell 2}$ is negative, this means that the assumption is false and we are in DCM case. Consequently, coefficient β is less than $(1-\alpha)$ and must be equal to the solution satisfying

$$I_{\ell 2} = I_{er} + \eta_5(\delta)\left[\eta_1(\delta)\sin(\delta) + \eta_2 \cos(\delta)\right] = 0. \tag{27}$$

This relation is nonlinear in terms of β and needs to be solved iteratively by the Newton–Raphson method. To ovoid additional computing time, we propose to compute β by linearizing $i_\ell(t)$ around $(t = 0)$ and setting the result to zero. This approach is based on the fact that the damping time constant (τ) is big enough when compared with the switching period, which is true in the real world. So, applying a first-order Taylor expansion to equation (20) yields

$$\begin{aligned} i_\ell(t) &= I_{\ell 1} + \frac{\mathrm{d}i_\ell}{\mathrm{d}t}\Big|_{t=0}, \\ t &= I_{\ell 1} - \left[\frac{V_{c1} - E}{L}\right]t. \end{aligned} \tag{28}$$

Thus, we obtain

$$\beta = \frac{LI_{\ell 1}}{(V_{c1} - E)T}. \tag{29}$$

The voltage of the capacitor V_{c2} at $(t_2 = \beta T)$ is recomputed by using equation (25) that continues to be valid with the new value of $(\beta < (1-\alpha))$. During the remaining time interval $(t \in [(\alpha+\beta)TT])$, the inductor current is kept null; $(i_\ell(t) = I_{\ell 2} = 0)$. However, the voltage across the capacitor decreases exponentially from the value V_{c2} to a third valueV_{c3}. At the end of the switching period, this voltage takes the value of

$$\begin{aligned} V_{c3} &= V_{c2}e^{-(\gamma T/\tau)}, \\ \gamma &= 1 - \alpha - \beta. \end{aligned} \tag{30}$$

Note finally that according to Figures 3(a) and 3(b), the mean values of the current through the inductor and the voltage of the capacitor are calculated at each switching period by the following equations. In the case of CCM, the third term in equation (31) must be removed because $\gamma$is null in this situation.

$$I_\ell = \frac{\alpha(I_{\ell 0} + I_{\ell 1}) + \beta(I_{\ell 1} + I_{\ell 2})}{2}, \tag{31}$$

$$V_c = \frac{\alpha(V_{c0} + V_{c1}) + \beta(V_{c1} + V_{c2}) + \gamma(V_{c2} + V_{c3})}{2}. \tag{32}$$

4. Fundamental Steady-State Equations

As previously outlined, there are two possible modes for the boost converter: CCM and DCM. In CCM, the inductor current flows continuously above zero during the totality of the switching period. The output voltage can be described by a relatively simple expression making control reliable via the duty cycleα. In addition, the inductor voltage waveform is almost a constant signal that results in an inductor current ripple close to a triangular signal. In the DCM, the inductor current reaches zero before the end of the switching period. The output voltage is described by a high nonlinear equation in terms of the duty cycle making it difficult to control. Figures 4(a) and 4(b) sketch general shapes of the inductor and diode current in the case of DCM regime.

To evaluate the input current and the output voltage in steady operating conditions, we use the small ripple approximation hypothesis that permits to replace instantaneous variables in minor time intervals by their mean values. Figures 5(a) and 5(b) report waveforms of inductor voltage $v_\ell(t)$ and capacitor current $i_c(t)$ during one switching period. During the three possible time intervals forming the switching period as defined by Figures 3(a) and 3(b), from Figures 5(a) and 5(b), we establish

$$\begin{aligned} &t \in t_1 = \alpha T\colon V_\ell = E, I_c = -\frac{V_o}{R_o} = -I_o, \\ &t \in t_2 = \beta T\colon V_\ell = E - V_o, I_c = I_\ell - I_o, \\ &t \in t_3 = \gamma T\colon V_\ell = 0, I_c = -I_o. \end{aligned} \tag{33}$$

By applying the principle of charge-discharge balance of inductor electromagnetic energy and capacitor electrostatic energy, mean values $V_\ell$and I_c of $v_\ell(t)$ and $i_c(t)$ must be zero. So, we deduce

$$\begin{aligned} \alpha E + \beta(E - V_o) &= 0, \\ -(1-\beta)I_o + \beta(I_\ell - I_o) &= 0. \end{aligned} \tag{34}$$

Solving these equations for unknown V_o andI_ℓ, we generate the steady-state solution:

$$V_o = \frac{(\alpha+\beta)E}{\beta}, \tag{35}$$

$$I_\ell = \frac{I_o}{\beta} = \frac{(\alpha+\beta)I_{er}}{\beta^2}. \tag{36}$$

Also, note that equations (35) and (36) established above for steady state of CCM case can be found from models (5) and (6) if we substitute variable $(1-u)$ by its mean value

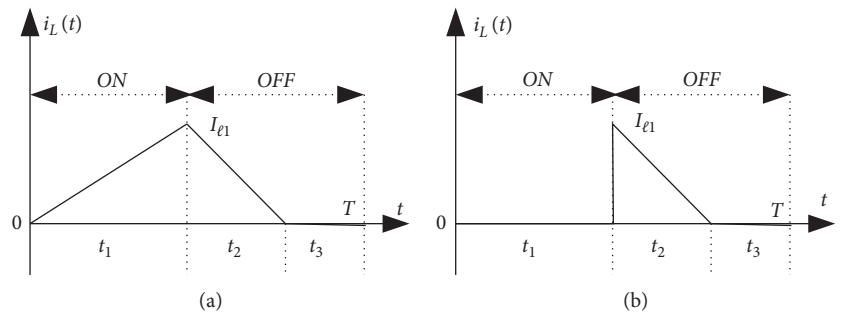

Figure 4: (a) General shape of inductor current in DCM. (b) General shape of diode current in DCM.

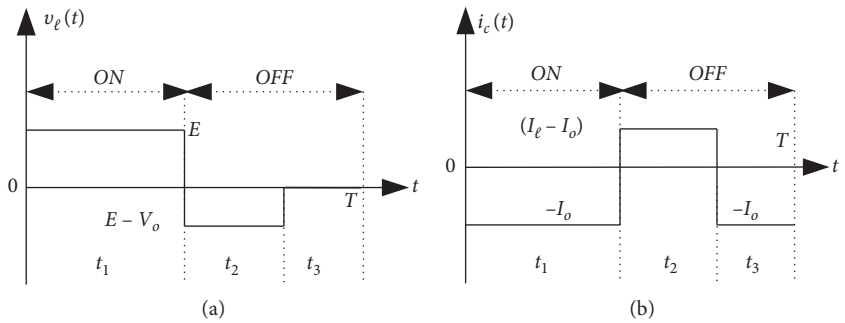

Figure 5: (a) Simplified waveform of inductor voltage. (b) Simplified waveform of capacitor current.

$\beta$and we set time derivatives to zero as in classical continuous dynamic systems.

4.1. Continuous Conduction Mode. In the CCM case, we have $(\beta = (1 - \alpha))$, and consequently equations (35) and (36) become

$$V_o = \frac{E}{1-\alpha}, \tag{37}$$

$$I_\ell = \frac{I_{er}}{(1-\alpha)^2}. \tag{38}$$

With this assumption, the peak-to-peak ripple of the inductor current and capacitor voltage is approximated by the following equations:

$$\Delta i_\ell \simeq \frac{E\alpha T}{L}, \tag{39}$$

$$\Delta v_C \simeq \frac{I_{er}\alpha T}{C(1-\alpha)}. \tag{40}$$

4.2. Discontinuous Conduction Mode. In the DCM case, the initial inductor current $I_{\ell 0}$ is zero and peak current $I_{\ell 1}$ is such that

$$I_{\ell 1} = \frac{E\alpha T}{L}. \tag{41}$$

The inductor peak current $I_{\ell 1}$ and diode average current I_d are defined by

$$I_d = I_o = \frac{\beta I_{\ell 1}}{2} = \frac{\beta E\alpha T}{2L}. \tag{42}$$

This allows us to deduce

$$\beta = \frac{KV_o}{\alpha E}, \qquad K = \frac{2L}{R_o T}. \tag{43}$$

Substituting β into equation (35) results in

$$KV_o(V_o - E) - (\alpha E)^2 = 0. \tag{44}$$

Solving equation (44) in terms of V_o allows us to define the output voltage and input current:

$$V_o = \frac{E}{2}\left[1 + \sqrt{1 + \frac{4\alpha^2}{K}}\right], \tag{45}$$

$$I_\ell = \frac{\left(E\alpha^2 + KV_o\right)}{R_o K}. \tag{46}$$

Just when the steady-state operating point passes from the CCM to the DCM regime, i.e., just at the boundary separating these regimes, the voltage solution given by equation (45) becomes greater than that of equation (35). That is:

$$1+\sqrt{1+\frac{4\alpha^2}{K}}>\frac{2}{1-\alpha}. \quad (47)$$

Arranging this, one concludes that DCM is characterised by the following inequality:

$$f(\alpha)=\alpha(1-\alpha)^2>K. \quad (48)$$

Function $f(\alpha)$ of inequality (48) passes by a maximum point defined by $(f_{\max}=4/27)$ for $(\alpha=1/3)$ as illustrated by Figure 6. If $(K\geq f_{\max})$, the inductor current is continuous over the complete range of the switching period and relations (37) and (38) hold for $(\alpha\in[\,0\ \ 1\,])$. If $(K<f_{\max})$, the inductor current has a discontinuous mode in the interval $(\alpha\in[\,\alpha_1\ \ \alpha_1\,])$ and a continuous mode in the remaining intervals $(\alpha\in[\,0\ \ \alpha_1\,])$ and $(\alpha\in[\,\alpha_2\ \ 1\,])$. Parameters $\alpha_1$and α_2 are the solutions of equation $(f(\alpha)=K)$. In the central region where we have DCM, the output voltage and input current are given by equations (45) and (46).

5. Dynamic Simulation Algorithm and Control

Now that all necessary relations to realise the dynamic simulation of the boost converter are available, it is of importance to note that an integration step that corresponds to a one switching period is needed. We will first present how the integration process works. Second, we will discuss the possibility of implementation of the classical switching controller.

5.1. Dynamic Simulation Algorithm. The dynamic simulation algorithm is simple. It is based on the following main steps:

(i) Set the initial inductor current and capacitor voltage $(i_\ell=I_{\ell0}=0)$ and $(v_c=V_{c0}=0)$ and save these values as a first point.

(ii) Compute $(I_{\ell1},V_{c1})$ and save this point.

(iii) Compute $(I_{\ell2},V_{c2})$ using $(\beta=1-\alpha)$. If $(I_{\ell2}\geq0)$, save this point and go to step (iv); otherwise, go to step (v).

(iv) Reinitialise with $(I_{\ell0}=I_{\ell2})$ and $(V_{c0}=V_{c2})$ and go to step (ii).

(v) Recompute β and V_{c2} as previously explained and save the new point $(0,V_{c2})$. Then, compute V_{c3}, set $(I_{\ell3}=0)$, and save this point.

(vi) Reinitialise with $(I_{\ell0}=0)$ and $(V_{c0}=V_{c3})$ and go to step (ii).

It is obvious that for one period, we have to save two or three points depending on whether we are in the CCM or DCM case. Furthermore, if we zoom in a plotted curve illustrating the result, we find a linear piecewise trajectory. The reason is evident.

5.2. Dynamic Control. Various interesting works in the field of control design of DC-DC boost inverter, such as classical control [8], sliding mode control [17], fuzzy control [18], and so on, can be found in the literature. Widely used approaches develop a second-order controller based on transfer functions for small signals. Here, the main goal is to implement the classical switching controller, which is by nature a current peak controller (CPC). The feedback control block is composed of a saw tooth generator, a comparator, and a latch. The output of the latch is used by the drive circuit that generates the gating pulses. The switch is turned on at the beginning of each switching period and turned off if the inductor current becomes greater than a programmed reference value I_{ref} and remains in the OFF state until the beginning of the next cycle. During simulation, this is equivalent to computing the PWM duty cycle α from the initial current $I_{\ell0}$ and reference current I_{ref}. Thus, at the beginning of the period, duty cycle α is computed by equation (49) which is equivalent to equation (41) where $I_{\ell1}$ is set equal to I_{ref}. The simulation algorithm previously presented remains practically the same.

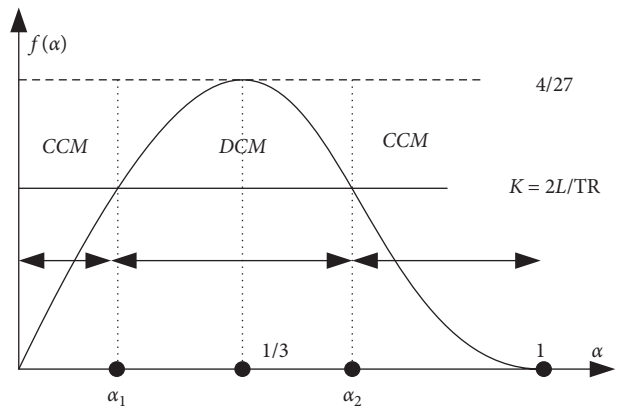

Figure 6: DCM-CCM boost inverter curve.

$$\alpha=\frac{(I_{\text{ref}}-I_{\ell0})L}{TE}. \quad (49)$$

6. Discrete Map and Lyapunov Exponents of DC-DC boost inverter

In this section of the paper, the load resistance is chosen to ensure that the circuit operates theoretically in the continuous mode. The sequence of the braking points computed for a set of some consecutive switching periods is used to define a discrete iterative map process. The obtained time series added to the Jacobian matrix of the map permits the computation of Lyapunov exponents. If the largest Lyapunov exponent (LLE) is positive, the system enters in a chaotic behaviour. Points corresponding to the minimum peak current form the selected discrete time series. In this sense, let us indicate two successive switching periods by $(k,k+1)$ and denote the couple $(I_{\ell0},I_{\ell2})$ of inductor current and the corresponding couple (V_{c0},V_{c2}) of voltage capacitor as follows:

$$\begin{aligned} I_{\ell 0} &= x_k, \\ I_{\ell 2} &= x_{k+1}, \\ V_{c0} &= y_k, \\ V_{c2} &= y_{k+1}. \end{aligned} \tag{50}$$

In this way, equation (50) of the duty cycle and equations (21), (23), and (26) of coefficients $(\eta_1, \eta_3, \eta_4, \eta_5)$ are reformulated as functions of the discrete iterative variables.

$$\begin{aligned} \delta &= \delta(x_k) = \omega T - \frac{L\omega}{E}(I_{\text{ref}} - x_k), \\ \eta_0 &= \eta_0(x_k) = e^{-(2(\omega T - \delta(x_k))/\omega\tau)}, \\ \eta_1 &= \eta_1(x_k, y_k) = \frac{\eta_2}{\omega\tau} + \frac{E - \eta_0(x_k) y_k}{L\omega}, \\ \eta_3 &= \eta_3(x_k, y_k) = L\omega\left[\eta_2 + \frac{\eta_1(x_k, y_k)}{\omega\tau}\right], \\ \eta_4 &= \eta_4(x_k, y_k) = L\omega\left[\frac{\eta_2}{\omega\tau} - \eta_1(x_k, y_k)\right], \\ \eta_5 &= \eta_5(x_k) = e^{-(\delta(x_k)/\omega\tau)}. \end{aligned} \tag{51}$$

This leads to the iterative process defined by

$$\delta(x_k) = \omega T - \frac{L\omega}{E}(I_{\text{ref}} - x_k), \tag{52}$$

$$\begin{aligned} f_x(x_k, y_k) = I_{er} + \eta_5(x_k)[\eta_1(x_k, y_k)\sin(\delta(x_k)) \\ + \eta_2 \cos(\delta(x_k))], \end{aligned} \tag{53}$$

$$\begin{aligned} f_y(x_k, y_k) &= E + \eta_5(x_k)[\eta_3(x_k, y_k)\sin(\delta(x_k)) \\ &\quad + \eta_4(x_k, y_k)\cos(\delta(x_k))], \\ x_{k+1} &= f_x(x_k, y_k), \\ y_{k+1} &= f_y(x_k, y_k). \end{aligned} \tag{54}$$

Let $J(x, y)$ denote the Jacobian matrix associated with the system above. The computation of this matrix at each iteration furnishes the possibility to compute Lyapunov exponents λ via the QR factorisation method. This is the most suitable method to compute these exponents for a time series process with known Jacobian. At each iteration k, the Lyapunov exponents are computed as follows:

$$\lambda(k) = \frac{1}{k}\sum_{k} \text{Log}(|\text{Diag}(R)|). \tag{55}$$

In this relation, $\text{Diag}(R)$ denotes the diagonal of matrix R computed in Matlab environment by the following syntax. In this process, matrix Q is initialised by the identity matrix. Note also that because $J(x, y)$ is space consuming, the development of its elements is reported in the Appendix.

$$[Q, R]_{k+1} = qr(J_k Q_k). \tag{56}$$

Kaplan–Yorke dimension [19] is a powerful tool that describes the complexity of chaotic attractors. This dimension is also known by the Kaplan–Yorke conjecture. First, Lyapunov exponents are arranged in decreasing order $(\lambda_1 > \lambda_2 > \cdots \lambda_n)$, and index j corresponding to inequality (57) is determined. Then, the conjecture is that the dimension of the attractor is given by (53). For the studied case, equation (58) is equivalent to equation (59).

$$\begin{aligned} \sum_{i=1}^{j} \lambda_j \geq 0, \\ \sum_{i=1}^{j+1} \lambda_j < 0, \end{aligned} \tag{57}$$

$$D_{ky} = j + \frac{1}{|\lambda_{j+1}|}\sum_{i=1}^{j} \lambda_i, \tag{58}$$

$$D_{ky} = 1 + \frac{\lambda_1}{|\lambda_2|}. \tag{59}$$

Reference peak current I_{ref} will be considered a bifurcation parameter. By varying I_{ref}, we will observe how the circuit changes its behaviour from a stable system to a chaotic system via the period-doubling mechanism.

7. Results and Comments

The boost inverter parameters used to illustrate this study are reported in Table 1. Results are carried out in Matlab environment. Necessary software is written in a m-file code. For all simulations, the initial inductor current and capacitor voltage are set to zero.

According to these parameters, the frequency and time constant characterising dynamic inverter behaviour in the OFF state are $(f = 1.415\,\text{kHz})$ and $(\tau = 480\,\mu\text{s})$, respectively. This time constant is 4.8 times greater than the switching period. Equation (48) implies that the DCM boundary coefficient is $(K = 1 > 4/27)$. That is, the inverter works in CCM for full range of the duty cycle because the used rated resistance load is less than the critical load resistance whose value is $(R_o = 135\,\Omega)$. To simulate a DCM case, we use $(R_o = 200\,\Omega)$. In this case, we have $(K = 0.1 < 4/27)$ that results in a DCM in the range $(\alpha \in [\,0.1330 \;\; 0.5874\,])$.

7.1. Simulation No. 1. Two simulation tests are carried out. The first test corresponds to $(\alpha = 0.5)$ and $(R_o = 20\,\Omega)$. A CCM regime is expected. Using equation (38), we found $(I_\ell = 1.967\,\text{A})$. The second simulation is realised with $(\alpha = 0.3)$ and $(R_o = 200\,\Omega)$ and a DCM regime is expected. Using equation (46), we found $(I_\ell = 0.1237\,\text{A})$. Figures 7(a) and 7(b) show steady-state evolution of inductor current for these tests, respectively, and confirm the predicted $I_\ell$values.

Table 1: System parameters.

Parameter	Notation	Value
Rated input voltage	E	10 V
Rated resistance of the load	R_o	20 Ω
Rated switching period	T	100 μs
Inductor inductance	L	1000 μH
Filtering capacitor	C	12 μF

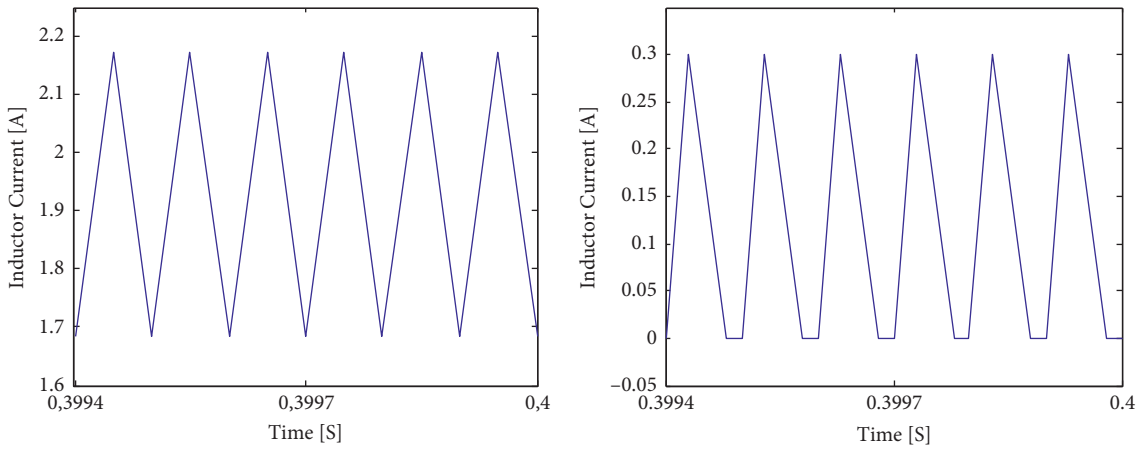

Figure 7: (a) CCM steady state of inductor current in open-loop case. (b) DCM steady state of inductor current in open-loop case.

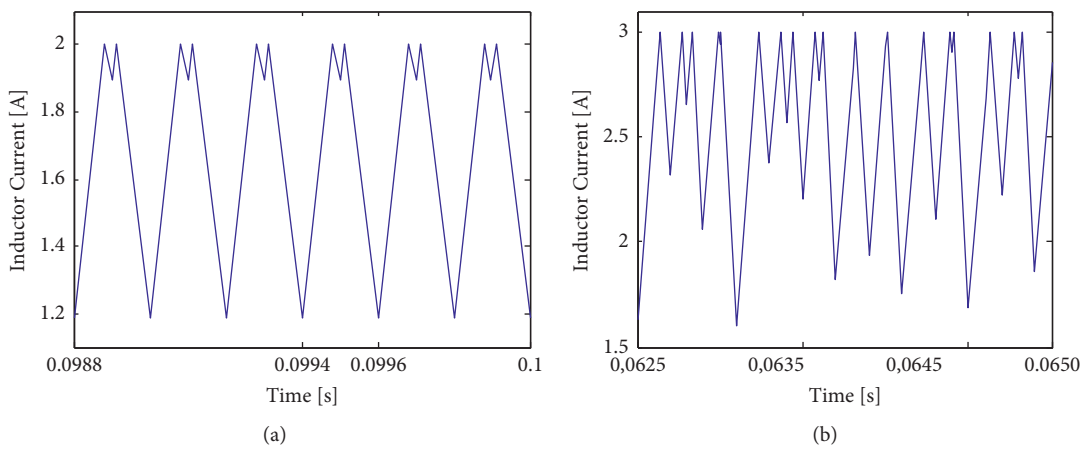

Figure 8: (a) CCM chaotic steady state of inductor current in closed-loop test with ($I_{\text{ref}} = 2$ A). (b) CCM chaotic steady state of inductor current in closed-loop test with ($I_{\text{ref}} = 3$ A).

7.2. Simulation No. 2. We consider a load resistance ($R_o = 20\,\Omega$), and we simulate two tests of inductor current peak: ($I_{\text{ref}1} = 2$ A) and ($I_{\text{ref}2} = 3$ A). Figures 8(a) and 8(b) show steady-state evolution of inductor current for these two tests, respectively. $I_{\ell 2}$ and V_{c2} of inductor current and capacitor voltage at the end of the switching period are saved. Figures 9(a) and 9(b) show phase portraits of $I_{\ell 2}$ and V_{c2} in dot plot form. Figures 10(a) and 10(b) show the dot plot of ($I_{\ell 2} = f(\alpha)$) and ($V_{c2} = f(\alpha)$), respectively. All these figures show without ambiguity the existence of chaos phenomenon in boost DC-DC dynamics when controlled in CPC type. To show areas with period doubling and those of intermittence, a fine variation of bifurcation parameter is required.

7.3. Simulation No. 3. The load resistance ($R_o = 20\,\Omega$) is used. We tune the bifurcation parameter I_{ref} with a small variation in the range of 1 A to 5 A. For each value of I_{ref}, we discard the transient part of the trajectory and save the remaining steady-state part. At the end, all results are plotted in dot plot form. Lyapunov exponents are calculated at the same time of dynamic trajectories. Figures 11(a) and 11(b) show bifurcation diagrams of inductor current and capacitor

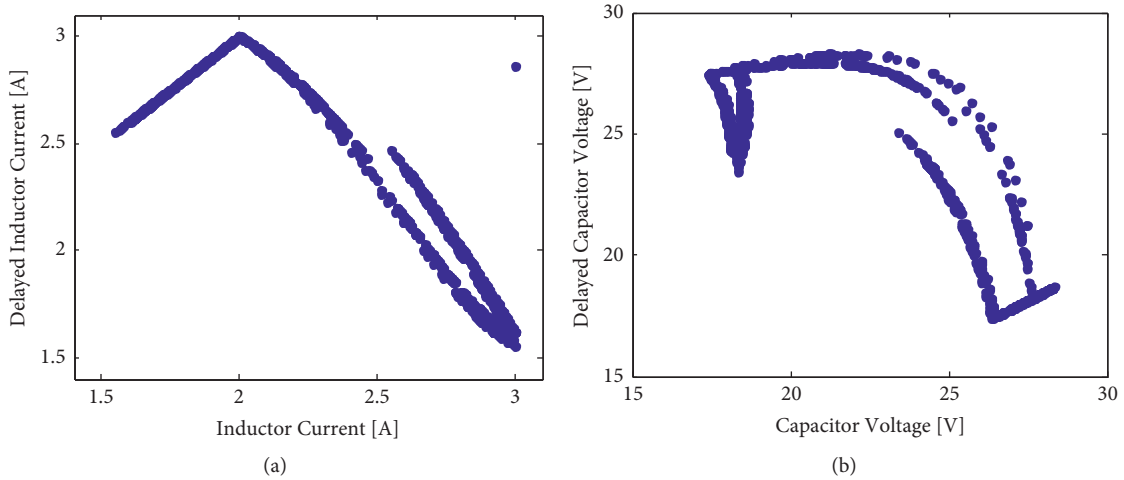

FIGURE 9: (a) Phase portrait of CCM chaotic steady state of inductor current in closed-loop test with (I_{ref} = 3 A). (b) Phase portrait of CCM chaotic steady state of voltage capacitor in closed-loop test with (I_{ref} = 3 A).

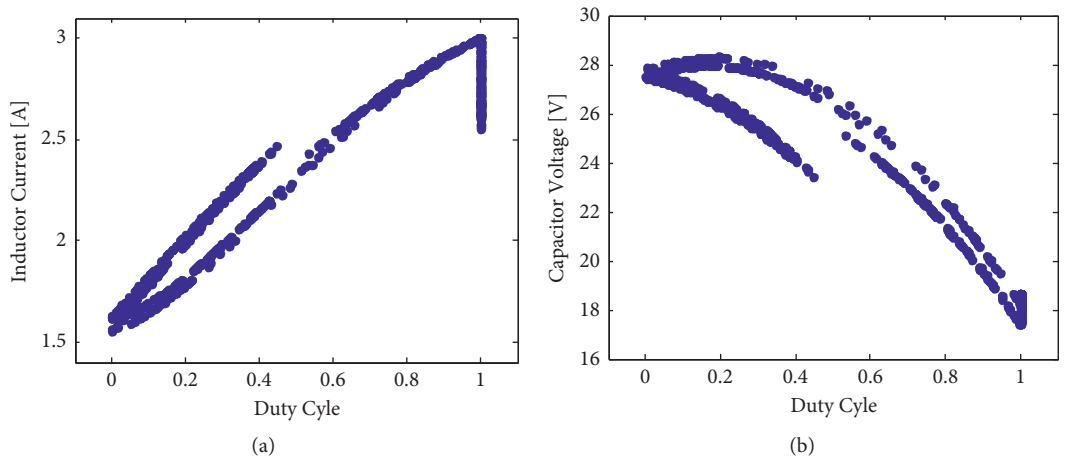

FIGURE 10: (a) Closed-loop CCM chaotic steady state of inductor current versus duty cycle (I_{ref} = 3 A). (b) Closed-loop CCM chaotic steady state of capacitor voltage versus duty cycle (I_{ref} = 3 A).

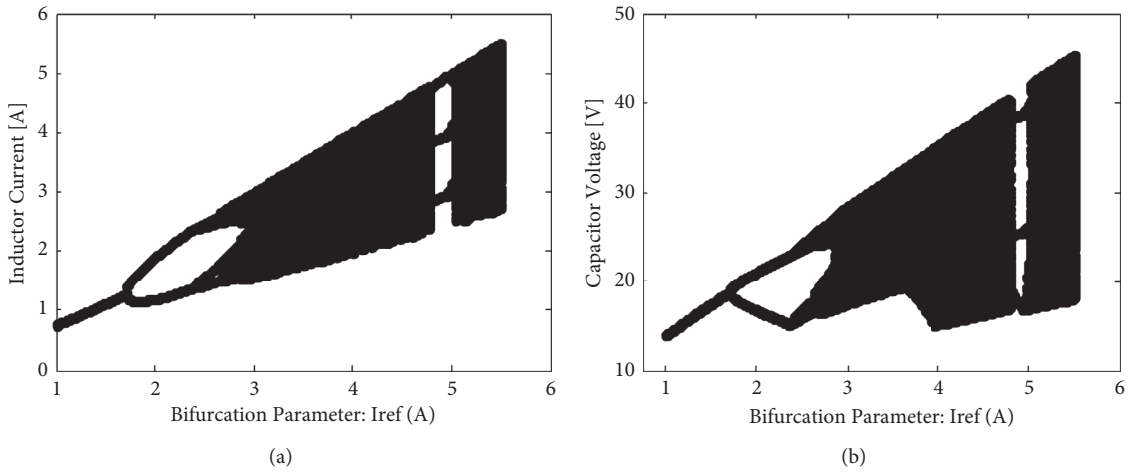

FIGURE 11: (a) Bifurcation diagram of inductor current. (b) Bifurcation diagram of capacitor voltage.

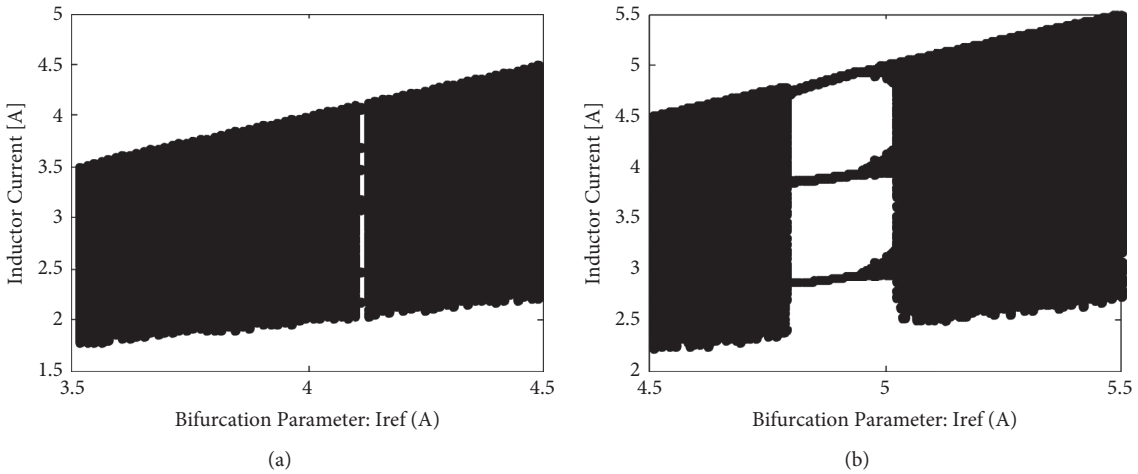

FIGURE 12: (a) First zoom on bifurcation diagram of inductor current. (b) Second zoom on bifurcation diagram of inductor current.

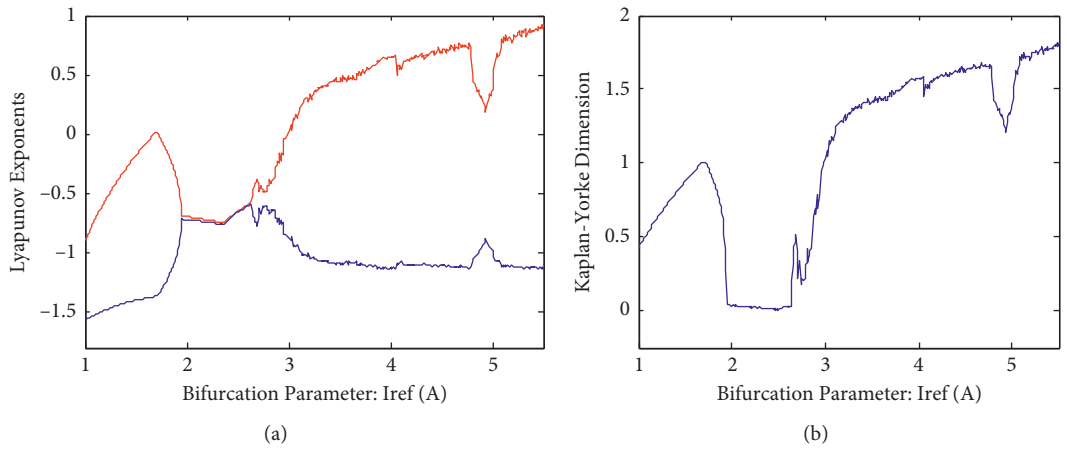

FIGURE 13: (a) Effect of bifurcation parameter on Lyapunov exponents. (b) Effect of bifurcation parameter on Kaplan–Yorke dimension.

voltage, respectively. We observe the phenomenon of period doubling and then the entrance of the system in a chaotic behaviour. Figures 12(a) and 12(b) furnish more details on this behaviour. It is observed that period doubling begins with ($I_{\text{ref}} = 1.69$ A). Then, at ($I_{\text{ref}} = 2.37$ A), ($I_{\text{ref}} = 2.63$ A), and ($I_{\text{ref}} = 2.7$ A), the system enters in $4T$, $8T$, and $16T$ type orbits, respectively. Two intermittence [20] areas are observed around ($I_{\text{ref}} = 4.1$ A) and ($I_{\text{ref}} = 4.9$ A). Figures 13(a) and 13(b) show Lyapunov exponents and Kaplan–Yorke dimension evolution versus the bifurcation parameter. As the system is of dimension 2, we generate two Lyapunov exponents. It is found that one (LLE) becomes positive for a bifurcation parameter ($I_{\text{ref}} > 2.8$ A). This indicates the beginning of a chaotic region. The second exponent is negative. The largest exponent is red colored while the other is blue colored. Note that LLE detects intermittence areas. Kaplan–Yorke dimension evolution is similar to LLE because LLE here is dominant. In the chaotic region, this dimension increases but remains inferior to 2, the physical dimension of the system.

8. Conclusion

We have developed in this paper a study on DC-DC boost inverter based on two levels. The first level of the paper develops a like-discrete integration process based on determination of precise analytical relations of breaking points characterising the switching behaviour of DC-DC boost inverter. The presented scheme gives good results in a very fast manner because for one switching period, we compute only two three breaking points depending on whether we have a continuous conduction mode (CCM) or a discontinuous conduction mode (DCM) of the inductor current. Performance of the developed analytical solution is thus successfully proved. The second level of the paper develops a discrete iterative map as in standard discrete time series models. Jacobian matrix of the found iterative map is defined and used to compute Lyapunov exponents. These exponents confirm the existence of chaos in the system behaviour when varying the reference value of the controlled inductor current. This level of the study is limited to CCM regime. On

the other hand, it is obvious that established iterative map can be easily extended to other inverter topologies such as interleaved configurations [21].

Appendix

A. Jacobian Matrix of the Discrete Iterative Map

First, compute these preliminary coefficients:

$$\begin{aligned}
\frac{\partial \delta}{\partial x} &= \frac{L\omega}{E},\\
\frac{\partial \eta_0}{\partial \delta} &= \frac{2\eta_0}{\omega T},\\
\frac{\partial \eta_1}{\partial \delta} &= -\frac{Y}{L\omega}\frac{\partial \eta_0}{\partial \delta},\\
\frac{\partial \eta_1}{\partial x} &= \frac{\partial \eta_1}{\partial \delta}\frac{\partial \delta}{\partial x},\\
\frac{\partial \eta_1}{\partial y} &= -\frac{\eta_0}{L\omega},\\
\frac{\partial \eta_3}{\partial x} &= \frac{L}{\tau}\frac{\partial \eta_1}{\partial x},\\
\frac{\partial \eta_3}{\partial y} &= \frac{L}{\tau}\frac{\partial \eta_1}{\partial y},\\
\frac{\partial \eta_4}{\partial x} &= -\omega L\frac{\partial \eta_1}{\partial x},\\
\frac{\partial \eta_4}{\partial y} &= -\omega L\frac{\partial \eta_1}{\partial y},\\
\frac{\partial \eta_5}{\partial \delta} &= -\frac{\eta_5}{\omega \tau},\\
\frac{\partial \eta_5}{\partial x} &= \frac{\partial \eta_5}{\partial \delta}\frac{\partial \delta}{\partial x}.
\end{aligned} \tag{A.1}$$

Secondly, compute the Jacobian matrix by

$$J(x,y) = \begin{bmatrix} \frac{\partial f_x}{\partial x} & \frac{\partial f_x}{\partial y} \\ \frac{\partial f_y}{\partial x} & \frac{\partial f_y}{\partial y} \end{bmatrix} = \begin{bmatrix} J_{11} & J_{12} \\ J_{21} & J_{22} \end{bmatrix},$$

$$\begin{aligned}
J_{11} &= \frac{\partial F_x}{\partial x} = \left[\eta_1 \sin(\delta) + \eta_2 \cos(\delta)\right]\frac{\partial \eta_5}{\partial x} + \eta_5\frac{\partial \eta_1}{\partial x}\sin(\delta)\\
&\quad + \eta_5\left[\eta_1 \cos(\delta) - \eta_2 \sin(\delta)\right]\frac{\partial \delta}{\partial x},\\
J_{12} &= \frac{\partial F_x}{\partial y} = \eta_5\frac{\partial \eta_1}{\partial y}\sin(\delta),\\
J_{21} &= \frac{\partial F_y}{\partial x} = \left[\eta_3 \sin(\delta) + \eta_4 \cos(\delta)\right]\frac{\partial \eta_5}{\partial x}\\
&\quad + \eta_5\left[\eta_3 \cos(\delta) - \eta_4 \sin(\delta)\right]\frac{\partial \delta}{\partial x}\\
&\quad + \eta_5\left[\frac{\partial \eta_3}{\partial x}\sin(\delta) + \frac{\partial \eta_4}{\partial x}\cos(\delta)\right],\\
J_{22} &= \frac{\partial F_y}{\partial y} = \eta_5\left[\frac{\partial \eta_3}{\partial y}\sin(\delta) + \frac{\partial \eta_4}{\partial y}\cos(\delta)\right].
\end{aligned} \tag{A.2}$$

Data Availability

The parameters of DC-DC boost converter used to support the findings of this study are included within the article.

Conflicts of Interest

The authors declare that they have no conflicts of interest.

References

[1] K. De Gusseme, M. David, S. Van de, P. Alex, B. Van den, and A. M. Jan, "Digital control of boost PFC converters operating in both continuous and discontinuous conduction mode," in *Proceedings of the 35th Annual IEEE Power Electronics Specialists Conference Aachen*, Aachen, Germany, June 2004.

[2] W. Jiang, Y.-f. Zhou, and J.-n. Chen, "Modelling and simulation of boost converter in CCM and DCM," in *Proceedings of the 2nd International Conference on Power Electronics and Intelligent Transportation System*, Shenzhen, China, November 2009.

[3] T. Suntio, "Modelling and analysis of a PCM-controlled boost converter designed to operate in," *DCM' Energies*, vol. 12, p. 4, 2019.

[4] E. N. Chaves, G. P. Viajante, M. A. A. Freitas et al., "Design based on internal model applied in a quadratic boost converter with P&O MPPT," in *Proceedings of the International Conference on Renewable Energies and Power Quality (ICREPQ'18)*, Salamanca, Spain, March 2018.

[5] V. García-Rodríguez, R. Silva-Ortigoza, E. Hernández-Márquez, J. García-Sánchez, and H. Taud, "DC/DC boost converter-inverter as driver for a DC motor: modeling and experimental verification," *Energies*, vol. 11, no. 8, p. 2044, 2018.

[6] P. Karamanakos, T. Geyer, and S. Manias, "Direct voltage control of DC-DC boost converters using model predictive control based on enumeration," in *Proceedings of the 15th International Power Electronics and Motion Control Conference, EPE-PEMC 2012 ECCE Europe*, Novi Sad, Serbia, September 2012.

[7] J. Moreno-Valenzuela and O. Garcia-Alarcon, "On control of a boost DC-DC power converter under constrained input," *Complexity*, vol. 2017, Article ID 4143901, , 2019.

[8] R. De Keyser, J. Bonilla, and C. Ionescu, "A comparative study of several control techniques applied to a boost converter," in *Proceedings of the IEEE 10th International Conference on*

Optimisation of Electrical and Electronic Equipment OPTIM, Brasov, Romania, December 2006.

[9] F. H. Qi and Y. Sun, "Study of bifurcation and chaos in the current-mode controlled boost DC-DC converter," *Applied Mechanics and Materials*, vol. 733, pp. 635–638, 2015.

[10] M. Jayakumar and V. Vanitha, "Investigation of chaos and bifurcation in boost converter," *International Journal of Pure and Applied Mathematics*, vol. 18, no. 11, pp. 171–177, 2018.

[11] B.-C. Bao, J.-P. Xu, and Y. Liang, "Inductor current sampled feedback control of chaos in current-mode boost converter," *Journal of Electronic Science and Technology of China*, vol. 6, no. 1, 2008.

[12] O. Boubaker and R. Dhifaoui, "Robust chaos synchronisation for Chua's circuits via active sliding mode control," in *Chaos, Complexity and Leadership*, S. Banerjee and S. S. Ercetin, Eds., Springer, Berlin, Germany, 2012.

[13] A. Lassoued, O. Boubaker, R. Dhifaoui, and S. Safari, "Experimental observations and circuit realization of a Jerk chaotic system with piecewise nonlinear function," *Recent Advances in Chaotic Systems and Synchronization*, Elsevier Inc, Amsterdam, Netherlands, 2019.

[14] D. Tannir, Y. Wang, and P. Li, "Accurate modelling of non ideal low-power PWM DC-DC converters operating in CCM and DCM using enhanced circuit-averaging techniques," *ACM Transactions on Design Automation of Electronic Systems*, vol. 21, no. 4, Article ID 61, 2016.

[15] W. Alan, B. Jack, L. S. Harry, and A.V. John, "Determining Lyapunov exponents from a time series," *Physica 16D*, pp. 285–317, North-Holland, Amsterdam, Netherlands, 1985.

[16] L. A. Dmitrieva, Y. A. Kuperin, N. M. Smetanin, and A.C. German, "Method of calculating Lyapunov exponents for time series using artificial neural networks committees," in *Proceedings of the International Conference Days on Diffraction*, pp. 127–132, St. Petersburg, Russia, July 2016.

[17] H. Guldemir, "Modelling and sliding mode control of Dc-Dc buck-boost converter," in *Proceedings of the 6th International Advanced Technologies Symposium (IATS'11)*, Elazıg, Turkey, May 2011.

[18] R. Bazdaric, M. Drago, A. Leban, D. Voncina, and I. Skrjanc, "Fuzzy model predictive control of a DC-DC boost converter based on non-linear model identification," *Mathematical and Computer Modelling of Dynamical Systems*, vol. 23, 2016.

[19] J. L. Kaplan and J. A. Yorke, "Chaotic behavior of multidimensional difference equations," in *Functional Differential Equations and Approximations of Fixed Points*, H.-O. Peitgen and H.-O. Walther, Eds., Springer-Verlag, Berlin, Germany, 1979.

[20] Y. Zhou, J. Ning, H. C. Herbert, and K. Chi, "Complex intermittency in switching converters," *International Journal of Bifurcation and Chaos*, vol. 18, no. 1, pp. 121–140, 2008.

[21] M. Kabalo, D. Paire, B. Blunier, D. Bouquain, M. Godoy Simões, and A. Miraoui, "Experimental evaluation of four-phase floating interleaved boost converter design and control for fuel cell applications," *IET Power Electronics*, vol. 6, no. 2, pp. 215–226, 2013.

Hindawi
Complexity
Volume 2021, Article ID 4636658, 15 pages
https://doi.org/10.1155/2021/4636658

Research Article

Chaos in a Financial System with Fractional Order and Its Control via Sliding Mode

Paul Yaovi Dousseh,[1] Cyrille Ainamon,[1] Clément Hodévèwan Miwadinou,[1,2,3] Adjimon Vincent Monwanou,[1] and Jean Bio Chabi Orou[1]

[1]*Laboratoire de Mécaniques des fluides, de la Dynamique Non-linéaire et de la Modélisation des Systèmes Biologiques (LMFDNMSB), Institut de Mathématiques et de Sciences Physiques (IMSP), Porto-Novo, Benin*
[2]*Département de Physique, ENS-Natitingou, Université des Sciences, Technologies, Ingénierie et Mathématiques (UNSTIM), Abomey, Benin*
[3]*Laboratoire de Physique et Applications du Centre Universitaire de Natitingou, Université Nationale des Sciences, Technologiques, Ingénierie et Mathématiques (UNSTIM), Abomey, Benin*

Correspondence should be addressed to Clément Hodévèwan Miwadinou; clement.miwadinou@imsp-uac.org

Received 15 April 2021; Revised 26 May 2021; Accepted 3 July 2021; Published 19 July 2021

Academic Editor: Guillermo Huerta Cuellar

In this paper, the dynamical behaviors and chaos control of a fractional-order financial system are discussed. The lowest fractional order found from which the system generates chaos is 2.49 for the commensurate order case and 2.13 for the incommensurate order case. Also, period-doubling route to chaos was found in this system. The results of this study were validated by the existence of a positive Lyapunov exponent. Besides, in order to control chaos in this fractional-order financial system with uncertain dynamics, a sliding mode controller is derived. The proposed controller stabilizes the commensurate and incommensurate fractional-order systems. Numerical simulations are carried out to verify the analytical results.

1. Introduction

Investigating chaos in dynamical systems is one of the most interesting topics which has been carried out extensively in different scientific fields such as medicine [1], biology [2], mathematics [3], and many others. In the literature, several dynamical systems presenting chaotic behaviors have been proposed such as the Lorenz system [4], the Chen system [5], the Lü system [6], and the Newton–Leipnik system [7]. During the last decades, many researchers have taken a great interest in the subject of chaotic systems' control. In [8], the authors used the sliding mode controller to eliminate chaos in a new uncertain chaotic dynamical system (Liu system). In [9], a robust adaptive sliding mode controller is used to remove chaos in a novel class of chaotic systems. Chaos control in the Lorenz, Chen, and Lü systems using the backstepping technique is performed in [10]. Chaos control in the Newton–Leipnik system is carried out using linear feedback controllers in [11].

Fractional calculus involving fractional order derivatives, i.e., derivatives of noninteger order, has a history of over 300 years [12]. During those years, this theory was considered a purely mathematical concept. Recently, fractional order derivatives have been widely applied to several systems in many areas of research to better understand these systems [13–19]. Indeed, fractional order derivatives, possessing memory, can describe more accurately different nonlinear phenomena than integer order derivatives [20, 21]. Very recently, some interesting developments and results in the theory and applications of fractional calculus have been obtained in the literature. For example, see [22], in which authors used Lie symmetry analysis to obtain an exact solution of the conformable heat equation. In [23], useful properties of the Lie group method with the invariance subspace method are combined to obtain a large family of

exact solutions for the fractional Black–Scholes equation. Also, in [24], the necessary optimality conditions of Euler–Lagrange type of variational problems in which variational functional depends on the Atangana–Baleanu derivative are proved. Finally, the Hydon method to determine discrete symmetries for a differential equation is employed to construct discrete symmetries for a family of ordinary, partial, and fractional differential equations in [25]. In fractional order systems, it was found that the systems with derivation orders q_1, q_2, and q_3 generate chaotic behaviors when $q = q_1 + q_2 + q_3 < 3$ [13–19]; in other words, chaos continues to exist in these systems for derivation orders less than 3.

Since the discovery by Strotz et al. [26] of chaos in an economical model, various financial and economical models have been proposed in the literature to better understand this complex dynamic of these systems. Among others, we have the forced Van der Pol model [27], the IS-LM model (Investment Saving-Liquidity Money) [28], the new hyperchaotic finance model [29], and many others [30–33]. In 2001, Ma and Chen [34] proposed a very interesting model to represent the dynamics of financial systems. The analysis of this model revealed interesting dynamics and also an extreme sensitivity to the initial conditions of the variables and parameters of the system. Financial variables such as the exchange rate, gross domestic product, interest rate, and production, to name a few, have a long memory [35, 36], i.e., all future fluctuations of these financial variables are influenced by past and present fluctuations. Thus, fractional order derivatives, possessing memory effect, can describe more accurately the dynamics of financial systems than integer order derivatives. In 2008, Chen [14] studied the generalization of the Ma and Chen system [34], i.e., considered this system with fractional order. Two routes to chaos were found in this fractional order system, namely, the route to chaos via intermittency and period doubling. The lowest derivation order found for which the system generates chaotic behavior was 2.55 in the commensurate fractional-order case and 2.35 in the incommensurate fractional-order case.

Also, to better understand the dynamics of financial systems, a new model was presented by Liao et al. [37] in 2020. Compared to the model proposed by Ma and Chen [34], this new model takes into account the fact that the price index is affected by investment demand. The study of this model was carried out numerically by the authors. It was found that the interaction between three factors in this financial system results in a complex behavior of the system. Complex dynamics behaviors such as period doubling and chaos were found in this system [37]. Chaotic behavior is undesirable in financial systems because it makes predictions in finance and economics impossible and, therefore, constitutes a risk for investments. Then, its control in the presence of uncertainties related to the parameters of the system and external disturbances turned out to be necessary.

Chaos control in financial systems has been widely studied in the literature. Several techniques have been designed for the control of financial chaotic systems [38, 39]. One of these techniques is the sliding mode control. Indeed, as a mathematical model cannot represent a physical situation perfectly, it is necessary to consider the uncertainties linked to the values of the system parameters and also any external disturbances to which a model may be subjected. Therefore, it is better to design a robust controller, i.e., insensitive to uncertainties and external disturbances. The sliding mode control is a powerful technique to robustly control uncertain dynamical systems subject to uncertainties and external disturbances [40–42]. The design of the sliding mode controller has been widely discussed in the literature [43–46]. These different criteria make the sliding mode control the right technique for controlling financial systems with uncertain dynamics. For example, in [38], a fractional-order sliding mode controller was designed to eliminate the chaotic behavior in an economical system in the presence of model uncertainties and external disturbances.

Motivated by the above discussions, in this paper, chaos in the financial system presented by Liao et al. [37] with fractional order and robust control of this chaotic behavior are investigated. The study of chaos in this system with fractional order is carried out for the commensurate and the incommensurate fractional order to find the minimum effective dimension, i.e., the lowest sum of derivation orders from which chaos arise in the system using analytical methods and numerical simulations. Finally, a sliding mode control law is designed to control the chaos in this fractional-order financial system with or without uncertainties and external disturbances. Numerical simulations are carried out to show that the controller can suppress chaos in the system and also can stabilize and maintain the system states on the sliding surface.

The remaining part of this paper is structured as follows. In Section 2, some definitions and analytical condition for the existence of chaos in fractional order systems are given. The fractional-order financial system is presented in Section 3. The dynamics study of this fractional-order financial system is carried out in Section 4. In Section 5, a simple but robust fractional-order sliding mode controller is designed to globally and asymptotically stabilize the system. Numerical simulations are performed in Section 6 to verify the analytical results obtained. This work ends with a conclusion in Section 7.

2. Definitions and Lemma

Fractional calculus is a generalization of ordinary calculus. Some definitions of fractional derivatives are given in [12]. The most commonly used definitions in the literature are the Grunwald–Letnikov, the Riemann–Liouville, and the Caputo definitions [12].

During this work, we will only use the Caputo fractional derivative because unlike the Riemann–Liouville definition of the fractional derivative which involves initial conditions of the fractional order, this fractional derivative involves initial conditions which take the same form as the case of the integer order, which has a physical interpretation. The Caputo (C) fractional derivative of order q is given by

$$ {}_{a}^{C}D_{t}^{q} f(t) = \frac{1}{\Gamma(n-1)} \int_{a}^{t} (t-\tau)^{n-q-1} f^{(n)}(\tau) \mathrm{d}\tau, \quad n-1 < q < n, \tag{1} $$

with a and t which are numbers representing the limits of the operator ${}_{a}^{C}D_{t}^{q}$. The symbol $\Gamma(\cdot)$ is the gamma function.

Definition 1 (see [47–49]). A saddle equilibrium point is a fixed point at which the equivalent linearized model has at least one eigenvalue in the stable region (eigenvalue with the negative real part) and one in the unstable region (eigenvalue with the positive real part).

Definition 2 (see [47–50]). In a three-dimensional (3D) dynamical system, a saddle fixed point is called a saddle equilibrium point of index 1 if one of its eigenvalues is unstable (positive) and the other two are stable (negative), whereas a saddle fixed point is called a saddle equilibrium point of index 2 if two of its eigenvalues are unstable and the other is stable.

To analyze the stability of a fractional-order system fixed points, the following lemma can be used [47, 48, 51].

Lemma 1 (see [47]). *For an incommensurate fractional-order system, i.e., a fractional order system in which derivation orders are not the same, an equilibrium point E^* of the system is asymptotically stable if the following condition*

$$ |\arg(\lambda)| > \frac{\pi}{2M}, \tag{2} $$

is satisfied for all roots λ of the following equation:

$$ \det(\Delta(\lambda)) = \det\left(\mathrm{diag}\left(\left[\lambda^{Mq_1}, \lambda^{Mq_2}, \ldots, \lambda^{M_{q_n}}\right]\right) - J\right) = 0, \tag{3} $$

in which J is the Jacobian matrix of the system evaluated at the equilibrium point E^* and M represents the Least Common Multiple (LCM) of the denominators u_i's of q_i's where $q_i = (v_i/u_i)$, v_i and $u_i \in Z+$, for $i = 1, 2, \ldots, n$.

Condition (2) can be rewritten as follows:

$$ \frac{\pi}{2M} - \min_i\left\{\left|\arg(\lambda_i)\right|\right\} < 0. \tag{4} $$

So, an equilibrium point E will be asymptotically stable if its roots λ_i satisfy condition (4).

The term $(\pi/2M) - \min_i\{|\arg(\lambda_i)|\}$ is called the Instability Measure for equilibrium points in Fractional Order Systems (IMFOS). This measure is a necessary [47], but not a sufficient condition for the presence of chaos in a fractional order system [52–54].

3. The Chaotic Financial System with Fractional Order

Recently, as reported in the literature [37], the financial model takes into account the interaction between the interest rate x, the investment demand y, and the price index z. The system is described as follows:

$$ \begin{cases} \dfrac{\mathrm{d}x}{\mathrm{d}t} = \mathrm{d}z + (y-e)x, \\ \dfrac{\mathrm{d}y}{\mathrm{d}t} = -ky^2 - lx^2 + m, \\ \dfrac{\mathrm{d}z}{\mathrm{d}t} = -\gamma z - \delta x - \rho y, \end{cases} \tag{5} $$

in which the parameters e, k, γ, m, l, ρ, and δ are constants. The authors numerically investigated the chaotic behaviors in this system. In [37], system (5) exhibits chaotic behavior when $e = 0.3, k = 0.02, \gamma = 1, m = 1, l = 0.1, \rho = 0.05, d = 1.2, \delta = 1$, and initial conditions $(1.2, 1.5, 1.6)$ are considered (see Figure 1).

In this paper, we consider system (5) with the fractional order. Standard derivatives are replaced by fractional order derivatives as follows:

$$ \begin{cases} D^{q_1}x = \mathrm{d}z + (y-e)x, \\ D^{q_2}y = -ky^2 - lx^2 + m, \\ D^{q_3}z = -\gamma z - \delta x - \rho y, \end{cases} \tag{6} $$

where $q_i \in (0, 1)$ and $D^{q_i} = (\mathrm{d}^{q_i}/\mathrm{d}t^{q_i})$ $(i = 1, 2, \text{and } 3)$. If $q_1 = q_2 = q_3 = q$, then system (6) is called a commensurate fractional-order system; otherwise, it is called an incommensurate order system [47].

The Jacobian matrix of system (6) evaluated at one of its equilibrium points $E^* = (x^*, y^*, z^*)$ is given by

$$ J = \begin{pmatrix} y^* - e & x^* & d \\ -2lx^* & -2ky^* & 0 \\ -\delta & -\rho & -\gamma \end{pmatrix}. \tag{7} $$

When the values of the system parameters are chosen as above, the equilibrium points of system (6) can be calculated by solving the equations $D^{q_1}x = 0, D^{q_2}y = 0$, and $D^{q_3}z = 0$. The system has four equilibrium points which are given by

$$ \begin{aligned} E_1 &= (0.049498497, -7.070201517, 0.304011579), \\ E_2 &= (0.076160842, 7.069016737, -0.429611679), \\ E_3 &= (3.087391472, 1.529728564, -3.163877901), \\ E_4 &= (-3.093050811, 1.471456216, 3.019478000). \end{aligned} \tag{8} $$

The corresponding eigenvalues and their nature are given in Table 1.

Taking into account Definition 2 and from Table 1, it can be seen that fixed points E_1 and E_2 are saddle equilibrium points of index 1 and the others are saddle equilibrium points of index 2.

Using the Adams–Bashforth–Moulton predictor-corrector method proposed by Diethelm et al. [55], the numerical solution of system (6) can be written as follows:

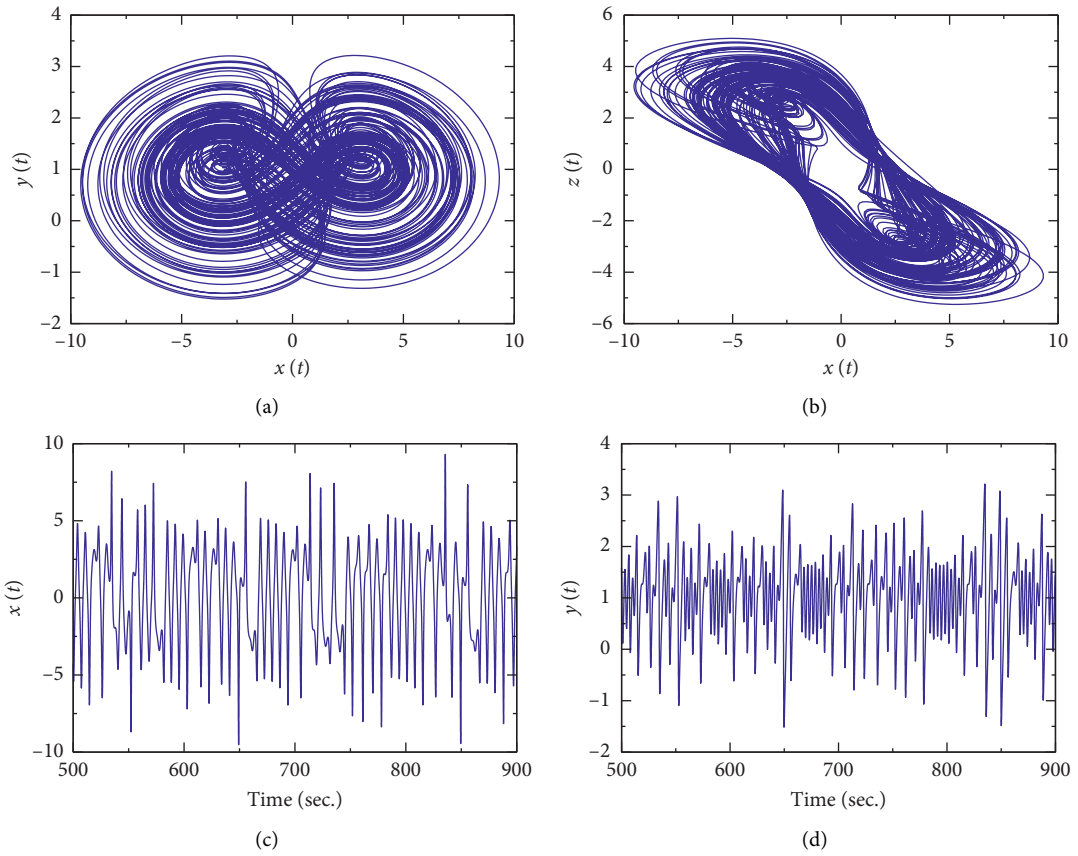

Figure 1: Phase diagrams and time series of system (5). (a) Projected onto the $x - y$ phase plane. (b) Projected onto the $x - z$ phase plane. (c) Time series of x. (d) Time series of y.

$$
\begin{cases}
x_{n+1} = x_0 + \dfrac{h^{q_1}}{\Gamma(q_1+2)}\left[\mathrm{d}z^p_{n+1} + \left(y^p_{n+1} - e\right)x^p_{n+1}\right], \\
\dfrac{+h^{q_1}}{\Gamma(q_1+2)}\displaystyle\sum_{j=0}^{n}\chi_{1,j,n+1}\left(\mathrm{d}z_j + \left(y_j - e\right)x_j\right), \\
y_{n+1} = y_0 + \dfrac{h^{q_2}}{\Gamma(q_2+2)}\left[-k\left(y^p_{n+1}\right)^2 - l\left(x^p_{n+1}\right)^2 + m\right], \\
\dfrac{+h^{q_2}}{\Gamma(q_2+2)}\displaystyle\sum_{j=0}^{n}\chi_{2,j,n+1}\left(-ky_j^2 - lx_j^2 + m\right), \\
z_{n+1} = z_0 + \dfrac{h^{q_3}}{\Gamma(q_3+2)}\left[-\gamma z^p_{n+1} - \delta x^p_{n+1} - \rho y^p_{n+1}\right], \\
\dfrac{+h^{q_3}}{\Gamma(q_3+2)}\displaystyle\sum_{j=0}^{n}\chi_{3,j,n+1}\left(-\gamma z_j - \delta x_j - \rho y_j\right),
\end{cases}
\tag{9}
$$

where

Table 1: Equilibrium points, corresponding eigenvalues, and their nature.

Equilibrium points	Eigenvalues	Nature
E_1	$\lambda_1 = -7.1758, \lambda_2 = -1.1944, \lambda_3 = 0.2828$	Saddle equilibrium point
E_2	$\lambda_1 = 6.6418, \lambda_2 = -0.8428, \lambda_3 = -0.2828$	Saddle equilibrium point
E_3	$\lambda_1 = -0.7378, \lambda_{2,3} = 0.4532 \pm 1.5251i$	Saddle equilibrium point
E_4	$\lambda_1 = -0.7548, \lambda_{2,3} = 0.4337 \pm 1.5487i$	Saddle equilibrium point

$$\begin{cases} x_{n+1}^{p} = x_0 + \dfrac{1}{\Gamma(q_1)} \displaystyle\sum_{j=0}^{n} \theta_{1,j,n+1}\left(\mathrm{d}z_j + \left(y_j - e\right)x_j\right), \\ y_{n+1}^{p} = y_0 + \dfrac{1}{\Gamma(q_2)} \displaystyle\sum_{j=0}^{n} \theta_{2,j,n+1}\left(-ky_j^2 - lx_j^2 + m\right), \\ z_{n+1}^{p} = z_0 + \dfrac{1}{\Gamma(q_3)} \displaystyle\sum_{j=0}^{n} \theta_{3,j,n+1}\left(-\gamma z_j - \delta x_j - \rho y_j\right), \end{cases} \tag{10}$$

$$\begin{cases} \chi_{i,j,n+1} = \begin{cases} n^{q_i+1} - (n - q_i)(n+1)^{q_i}, & j = 0, \\ (n-j+2)^{q_i+1} + (n-j)^{q_i+1} - 2(n-j+1)^{q_i+1}, & 1 \le j \le n, \\ 1, & j = n+1, \end{cases} \\ \theta_{i,j,n+1} = \dfrac{h^{q_i}}{q_i}\left[(n-j+1)^{q_i} - (n-j)^{q_i}\right], \quad 1 \le j \le n, i = 1, 2, 3. \end{cases}$$

4. Dynamics Analysis of the Financial System with Fractional Order

In this section, the numerical method proposed by Diethelm et al. [55] and presented in the previous section is used to solve numerically system (6) in the commensurate and incommensurate fractional-order cases. The parameters' values defined in Section 3 and initial conditions $(x_0, y_0, z_0) = (1.2, 1.5, 1.6)$ will be considered in this part. Using the well-known tools for studying dynamical systems such as phase diagrams, time series, bifurcation diagram, and largest Lyapunov exponent, the dynamics of the financial system with the fractional order will be investigated.

4.1. Dynamics for Commensurate Fractional-Order System. Here, we consider system (6) when $q_1 = q_2 = q_3 = q$ (commensurate order). System (6) does not exhibit chaotic behavior if it satisfies the inequality $q < (2/\pi)\min_i\{|\arg(\lambda_i)|\}$ [47, 48, 51] with λ_i being the eigenvalue of the Jacobian matrix of system (6) evaluated at one of its fixed points. For the equilibrium points E_3 and E_4, we have $\min_i\{|\arg(\lambda_i)|\} = 1.2819$; so,

$$q < \frac{2}{\pi} \min_i\{|\arg(\lambda_i)|\} \approx 0.816. \tag{11}$$

Figure 2 shows that the largest Lyapunov exponent of system (6) with the commensurate fractional order is positive only if $q > 0.82$. Therefore, the system does not show chaotic behavior when $q < 0.82$. It is found using numerical simulations that the system exhibits a chaotic attractor for $q \ge 0.83$. For $q = 0.83$, phase diagrams are shown in Figure 3(a) for the $x - y$ phase plane and in Figure 3(b) for the $x - z$ phase plane. Figures 3(c) and 3(d) show the time series of state variables x and y, respectively, for $q = 0.83$. As it can be seen, the system exhibits chaotic behavior, and this is confirmed by a positive Lyapunov exponent for $q = 0.83$.

Therefore, the minimum effective dimension of system (6) for the commensurate fractional order is $0.83 \times 3 = 2.49$. Thus, simulation results show that chaos exists in this fractional-order financial system with the derivation order less than 3. For numerical simulations, the step size $h = 0.01$ is used.

4.2. Dynamics for Incommensurate Fractional-Order System. When one of the system's derivation orders has a different value from the other two, we get an incommensurate fractional-order system [47].

By observing Figure 4, we can see that the largest Lyapunov exponent of system (6) is positive for $q_1 \ge 0.57$ with $q_2 = q_3 = 1$ (see Figure 4(a)), for $q_2 \ge 0.87$ with $q_1 = q_3 = 1$ (see Figure 4(b)), and for $q_3 \ge 0.13$ with $q_1 = q_2 = 1$ (see Figure 4(c)). For the examples, we consider the following cases:

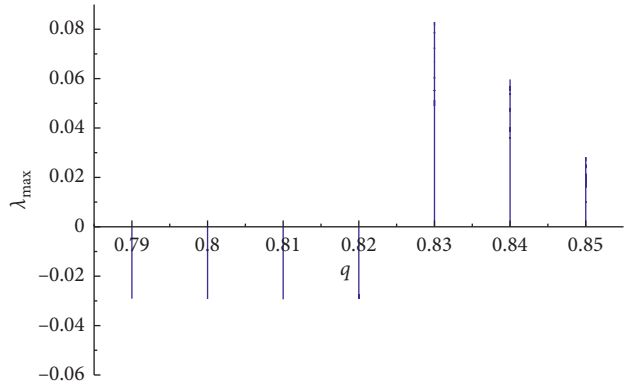

Figure 2: The largest Lyapunov exponent with the variation of derivation order q.

Case 1: fix $q_2 = q_3 = 1$, and let us take different values of q_1.

(i) $q_1 = 0.55$ and $q_2 = q_3 = 1$. In this case, we have $v_1 = 11, u_1 = 20$, and $v_2 = v_3 = u_2 = u_3 = 1$, so $M = \mathrm{LCM}(20, 1, 1) = 20$ and

$$\Delta(\lambda) = \mathrm{diag}\left(\lambda^{Mq_1}, \lambda^{Mq_2}, \lambda^{Mq_3}\right) - J(E_3) = \mathrm{diag}\left(\lambda^{11}, \lambda^{20}, \lambda^{20}\right) - J(E_3), \tag{12}$$

$$\begin{aligned}\det(\Delta(\lambda)) = {} & \lambda^{51} - 1.22972856\lambda^{40} \\ & + 1.061189142\lambda^{31} + 1.801422624\lambda^{20} \\ & + 0.061189142\lambda^{11} + 1.867529457 = 0.\end{aligned} \tag{13}$$

By solving equation (13), we have

$$\begin{aligned}\mathrm{IMFOS} &= \frac{\pi}{2M} - \min_i |\arg(\lambda_i)| = \frac{\pi}{40} - 0.079176 \\ &= -0.00064 < 0.\end{aligned} \tag{14}$$

In this case, IMFOS < 0; therefore, for the derivation orders $q = (0.55, 1, 1)$, system (6) does not exhibit a chaotic behavior.

(ii) Consider now $q_1 = 0.57$ and $q_2 = q_3 = 1$; by the same procedure as the above case, we have $M = 100$, and

$$\det(\Delta(\lambda)) = \lambda^{257} - 1.22972856\lambda^{200} + 1.061189142\lambda^{157} + 1.801422624\lambda^{100} + 0.061189142\lambda^{57} + 1.867529457 = 0. \tag{15}$$

By solving equation (15), we have

$$\begin{aligned}\mathrm{IMFOS} &= \frac{\pi}{2M} - \min_i |\arg(\lambda_i)| = \frac{\pi}{200} - 0.015682 \\ &= 0.000026 > 0.\end{aligned} \tag{16}$$

IMFOS > 0; therefore, for the given derivation orders, the system satisfies the necessary condition to present a chaotic attractor. Numerical simulations confirm this conclusion in Figure 5. So, the lowest value for which q_1 in this case generates a chaotic behavior is 0.57, where $\lambda_{max} > 0$.

Case 2: fix $q_1 = q_3 = 1$, and let us take different values of q_2.

(i) Consider $q_1 = 1, q_2 = 0.86$, and $q_3 = 1$; by the same procedure as the above case, we get $M = \mathrm{LCM}(1, 50, 1) = 50$, and

$$\begin{aligned}\det(\Delta(\lambda)) = {} & \lambda^{143} + 0.061189142\lambda^{100} \\ & - 0.22972856\lambda^{93} + 1.892340326\lambda^{50} \\ & - 0.02972856\lambda^{43} + 1.867529457 = 0.\end{aligned} \tag{17}$$

By solving equation (17), the IMFOS of the system is

$$\begin{aligned}\mathrm{IMFOS} &= \frac{\pi}{2M} - \min_i |\arg(\lambda_i)| \frac{\pi}{100} - 0.027339 \\ &= 0.004077 > 0.\end{aligned} \tag{18}$$

In this case, IMFOS > 0 but system (6) does not exhibit chaotic behavior ($\lambda_{max} < 0$). This shows that the condition IMFOS ≥ 0 is a necessary condition for chaos to exist and not the sufficient one.

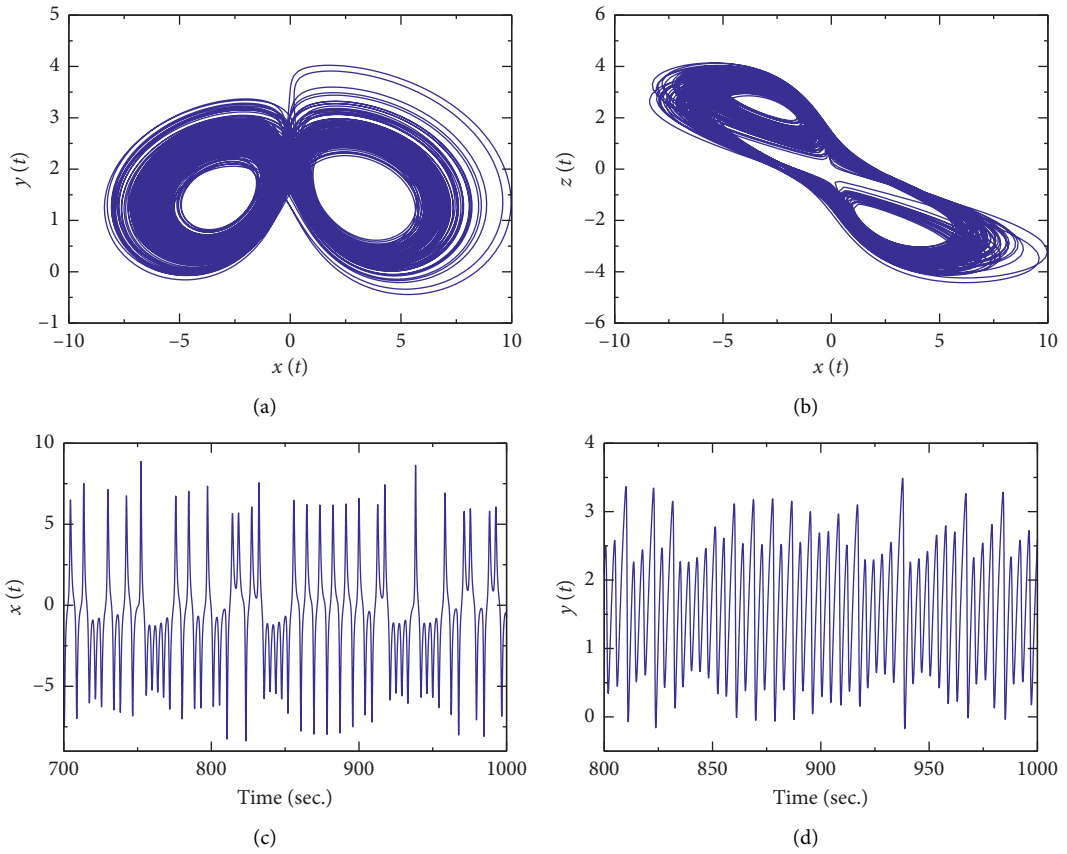

FIGURE 3: Phase diagrams and time series of system (6) with fractional order $q = 0.83$. (a) Projected onto the $x - y$ phase plane. (b) Projected onto the $x - z$ phase plane. (c) Time series of x. (d) Times series of y.

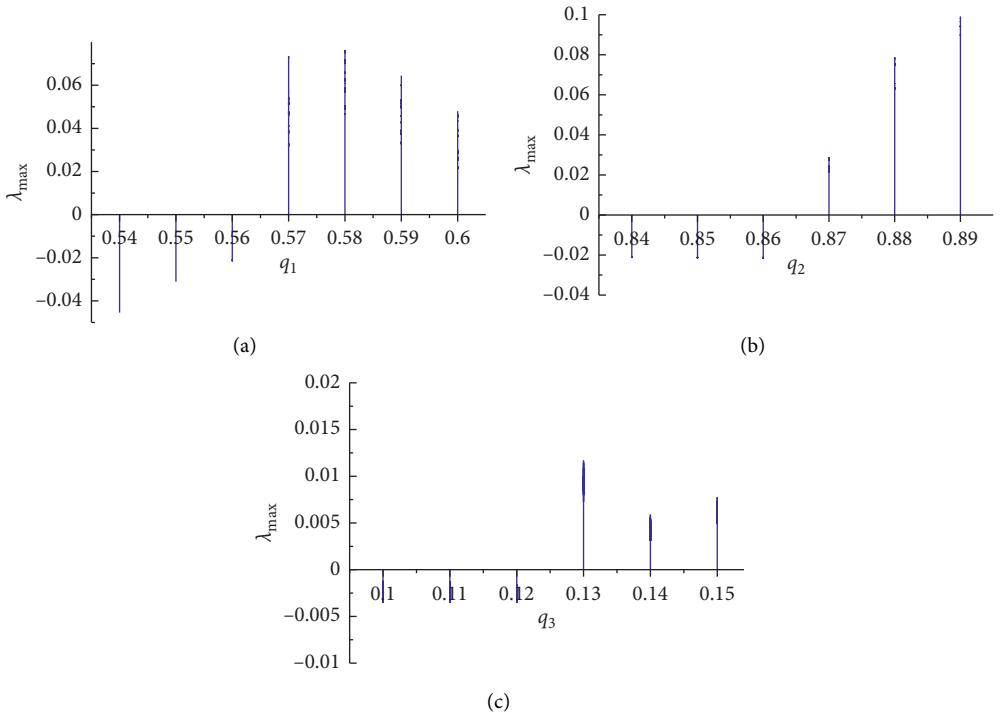

FIGURE 4: Largest Lyapunov exponents with variation of derivation orders. (a) q_1, when $q_2 = q_3 = 1$. (b) q_2, when $q_1 = q_3 = 1$. (c) q_3, when $q_1 = q_2 = 1$.

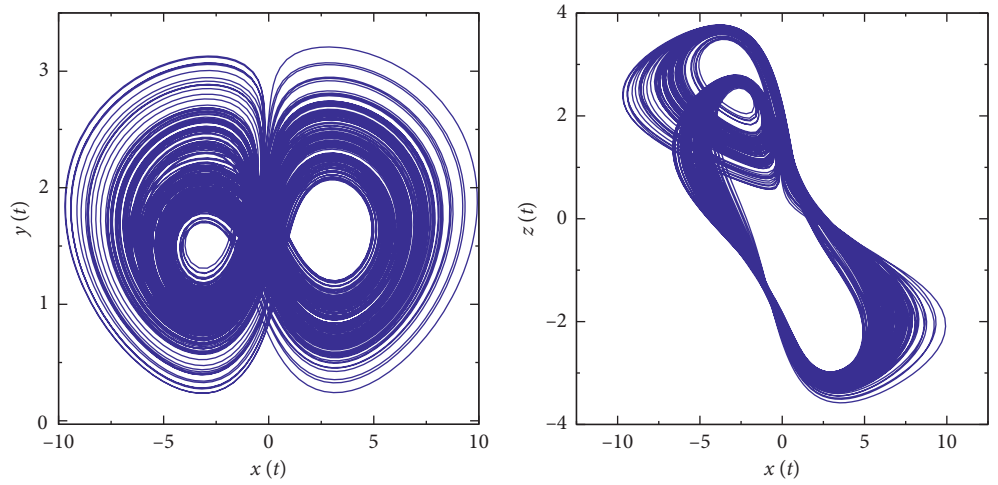

FIGURE 5: Phase diagrams of system (6) with fractional orders $q_1 = 0.57$ and $q_2 = q_3 = 1$ projected onto (a) the $x - y$ phase plane and (b) the $x - z$ phase plane.

(ii) Consider now $q_1 = 1, q_2 = 0.87$, and $q_3 = 1$; by the same procedure as the above case, we have $M = 100$, and

$$\begin{aligned}\det(\Delta(\lambda)) &= \lambda^{287} + 0.061189142\lambda^{200} \\ &-0.22972856\lambda^{187} + 1.892340326\lambda^{100} \\ &-0.02972856\lambda^{87} + 1.867529457 = 0.\end{aligned} \tag{19}$$

The system's IMFOS is

$$\begin{aligned}\text{IMFOS} &= \frac{\pi}{2M} - \min_i |\arg(\lambda_i)| \frac{\pi}{200} - 0.013605 \\ &= 0.002103 > 0.\end{aligned} \tag{20}$$

In this case, the system exhibits a chaotic behavior as it can be seen in Figure 6, where we can observe the chaotic attractor of the system.

Therefore, the lowest value for which q_2 in this case generates chaotic behavior is 0.87, where $\lambda_{\max} > 0$.

Case 3: fix $q_1 = q_2 = 1$, and let us take different values of q_3.

(i) Consider $q_1 = 1, q_2 = 1$, and $q_3 = 0.10$; then, $M = \text{LCM}(1, 1, 10) = 10$, and

$$\begin{aligned}\det(\Delta(\lambda)) &= \lambda^{21} + \lambda^{20} - 1.168539418\lambda^{11} \\ &+ 0.031460582\lambda^{10} + 1.831151184\lambda \\ &+ 1.867529457 = 0.\end{aligned} \tag{21}$$

By solving equation (21), we get

$$\begin{aligned}\text{IMFOS} &= \frac{\pi}{2M} - \min_i |\arg(\lambda_i)| \frac{\pi}{20} - 0.135623 \\ &= 0.021457 > 0.\end{aligned} \tag{22}$$

In this case, IMFOS > 0 but the system does not exhibit chaotic behavior ($\lambda_{\max} < 0$).

(ii) Consider now $q_1 = 1, q_2 = 1$, and $q_3 = 0.13$; then, we have $M = 100$, and

$$\begin{aligned}\det(\Delta(\lambda)) &= \lambda^{213} + \lambda^{200} - 1.168539418\lambda^{113} \\ &+ 0.031460582\lambda^{100} + 1.831151184\lambda^{13} \\ &+ 1.867529457 = 0.\end{aligned} \tag{23}$$

From equation (23), we get

$$\begin{aligned}\text{IMFOS} &= \frac{\pi}{2M} - \min_i |\arg(\lambda_i)| \frac{\pi}{200} - 0.013550 \\ &= 0.002158 > 0.\end{aligned} \tag{24}$$

So, for the derivation orders $q = (1, 1, 0.13)$, system (6) satisfies the necessary condition for the existence of chaos in the system. In this case, this is confirmed numerically in Figure 7.

Therefore, the lowest value from which q_3 in this case generates chaotic behavior is $q_3 = 0.13$, where $\lambda_{\max} > 0$.

When the value of q_3 increases from 0.85 to 0.90, the route to chaos via period doubling is found. The bifurcation diagram and largest Lyapunov exponent when the derivation order q_3 varies on the closed interval $[0.85, 0.90]$ are plotted in Figure 8. Clearly, from the bifurcation diagram, the period-doubling route to chaos can be seen. Figures 9(a)–9(d) show that the system has period-1, period-2, period-4, and chaotic attractors for $q_3 = 0.85, 0.87, 0.878$, and 0.89, respectively. Note that the step size used for the numerical simulations in this section is $h = 0.01$.

From these three cases, we deduce that the minimum effective dimension of system (6) in the incommensurate fractional-order case is 2.13.

In the next section, a simple but robust fractional-order sliding mode control law will be designed to control chaos in system (6).

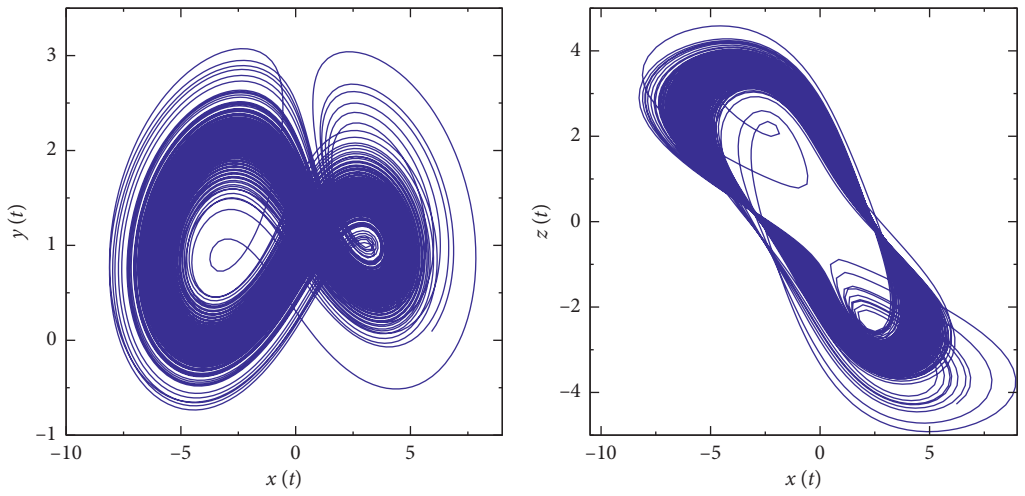

FIGURE 6: Phase diagrams of system (6) with fractional orders $q_1 = 1, q_2 = 0.87$, and $q_3 = 1$ projected onto (a) the $x - y$ phase plane and (b) the $x - z$ phase plane.

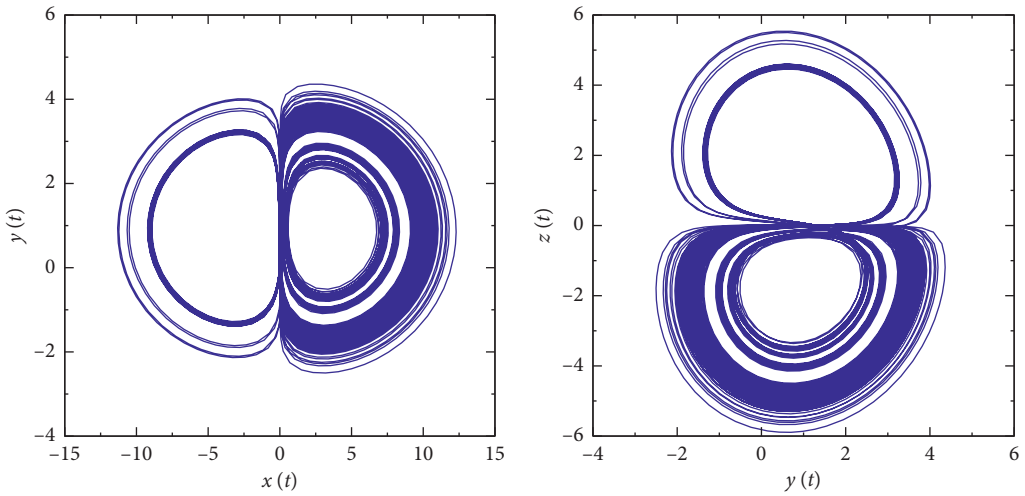

FIGURE 7: Phase diagrams of system (6) with fractional orders $q_1 = 1, q_2 = 1$, and $q_3 = 0.13$ projected onto (a) the $x - y$ phase plane and (b) the $x - z$ phase plane.

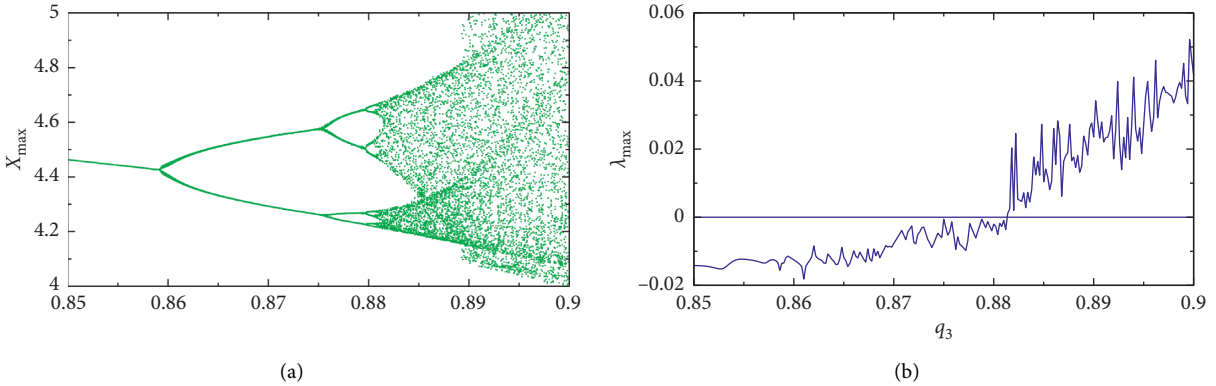

FIGURE 8: Bifurcation diagram and largest Lyapunov exponent ($\lambda_{\max}$) of system (6) with order q_3. (a) Bifurcation diagram. (b) Largest Lyapunov exponent ($\lambda_{\max}$).

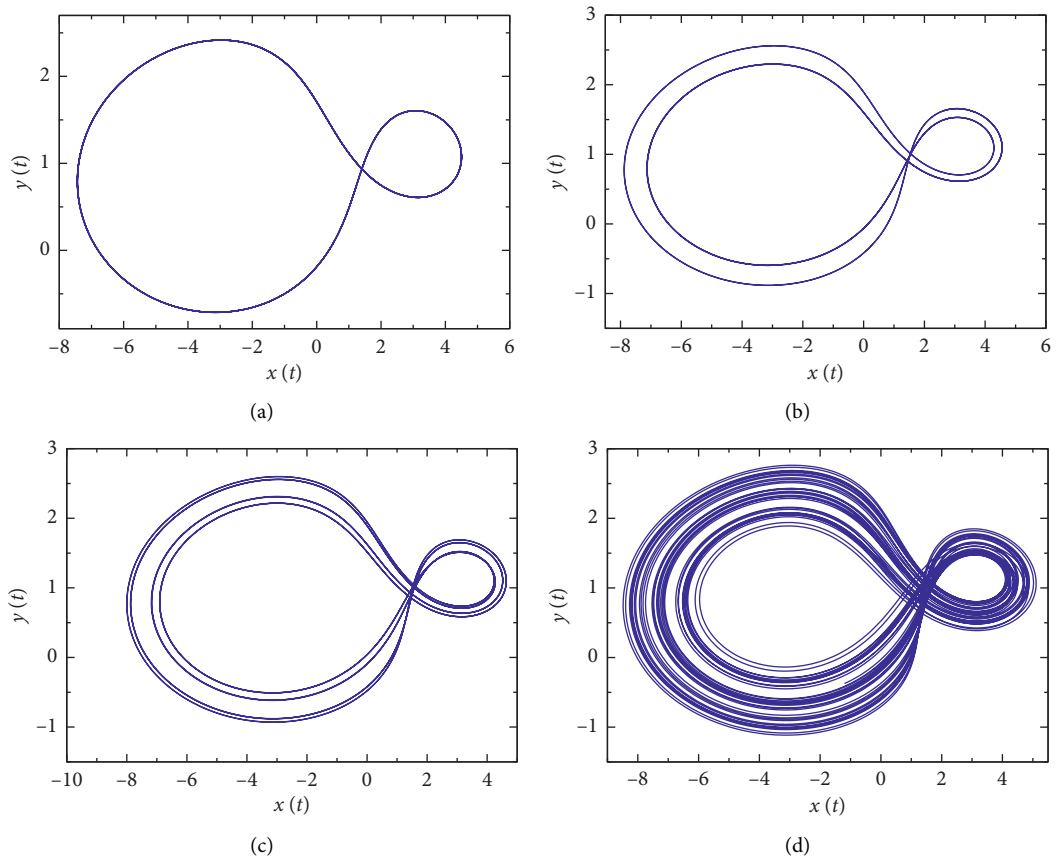

FIGURE 9: Phase diagrams showing the period-doubling route to chaos for system (6) with $q_1 = q_2 = 1$ and fractional order: (a) $q_3 = 0.85$, (b) $q_3 = 0.87$, (c) $q_3 = 0.878$, and (d) $q_3 = 0.89$.

5. The Sliding Mode Controller Design

According to the sliding mode control theory, to design a sliding mode controller, we have two steps:

(i) Build a sliding surface, which represents the desired dynamics of the system such as stability

(ii) Develop a control law in a way that the system states are brought towards the sliding surface in a finite time and are maintained in a neighborhood of the sliding surface when time evolves [38]

The sliding mode control law is itself composed of two parts; the first, which is continuous, is called the equivalent control law, and the second is discontinuous. The equivalent control law describes the behavior of the system to be controlled when its trajectories are on the sliding surface. The discontinuous reaching law ensures the convergence of all the system states towards the sliding surface.

To control chaos in fractional-order financial system (6), the controller $u(t)$ is added at the level of the second state equation as follows:

$$\begin{cases} D^{q_1}x = \mathrm{d}z + (y - e)x, \\ D^{q_2}y = -ky^2 - lx^2 + m + u, \\ D^{q_3}z = -\gamma z - \delta x - \rho y. \end{cases} \tag{25}$$

Motivated by literature [38, 43], as a choice for the sliding surface, we choose the following fractional-order sliding surface:

$$\begin{aligned} \sigma(t) &= D^{q_2-1}y(t) + D^{-1}\left(ky^2(t) + lx^2(t) + ny(t)\right) \\ &= D^{q_2-1}y(t) + \int_0^t \left(ky^2(\tau) + lx^2(\tau) + \eta y(\tau)\right)\mathrm{d}\tau, \end{aligned} \tag{26}$$

where η is an arbitrary positive constant. In the sliding mode, the invariance conditions of the surface must be satisfied and are defined as follows (i.e., the sliding surface and its derivative must satisfy the relations which appear in the following equation):

$$\begin{aligned} \sigma(t) &= 0, \\ \frac{\mathrm{d}}{\mathrm{d}t}\sigma(t) &= \sigma'(t) = 0. \end{aligned} \tag{27}$$

From equations (26) and (27), we get

$$D^{q_2}y(t) = -\left(ky^2(t) + lx^2(t)\right) + \eta y(t). \tag{28}$$

From system (25) and equation (28), we obtain the equivalent control law as follows:

$$\begin{aligned} u_{\text{eq}} &= \frac{\mathrm{d}^{q_2} y}{\mathrm{d}t^{q_2}} + ky^2 + lx^2 - m \\ &= -\left(ky^2 + lx^2 + \eta y\right) + ky^2 + lx^2 - m \\ &= -\eta y - m. \end{aligned} \tag{29}$$

Regarding the discontinuous reaching law, it is chosen as follows:

$$u_r = G_r \operatorname{sign}(\sigma), \tag{30}$$

in which

$$\operatorname{sign}(\sigma) = \begin{cases} +1, & \text{if } \sigma > 0, \\ 0, & \text{if } \sigma = 0, \\ -1, & \text{if } \sigma < 0, \end{cases} \tag{31}$$

and G_r is the gain of the controller. Finally, the total control law has the following form:

$$u(t) = u_{\text{eq}}(t) + u_r(t) = -\eta y - m + G_r \operatorname{sign}(\sigma). \tag{32}$$

Theorem 1. *System (6) with control law (32), i.e., system (25) is globally and asymptotically stable if the controller gain $G_r < 0$.*

Proof. For this, let us choose the Lyapunov quadratic function as follows:

$$V = \frac{1}{2}\sigma^2, \tag{33}$$

and its derivative gives

$$\begin{aligned} \dot{V} &= \sigma\dot{\sigma} = \sigma\left[D^{q_2} y + ky^2 + lx^2 + \eta y\right] \\ &= \sigma\left[-ky^2 - lx^2 + m + u + ky^2 + lx^2 + \eta y\right] \\ &= \sigma\left[-ky^2 - lx^2 + m - ny - m + G_r \operatorname{sign}(\sigma) + ky^2 + lx^2 + \eta y\right] \\ &= \sigma\left[G_r \operatorname{sign}(\sigma)\right] \\ &= G_r|\sigma| < 0. \end{aligned} \tag{34}$$

Therefore, we have found a Lyapunov function which satisfies the conditions of Lyapunov theorem, i.e., $V > 0$ and $V' < 0$. Thus, system (25) with sliding mode control law (32) is globally and asymptotically stable. □

Theorem 2. *Suppose that system (25) is perturbed by uncertainties and an external disturbance. Thus, the system has the following form:*

$$\begin{cases} D^{q_1} x = \mathrm{d}z + (y - e)x, \\ D^{q_2} y = -ky^2 - lx^2 + m + \Delta g(x, y, z) + p(t) + u, \\ D^{q_3} z = -\gamma z - \delta x - \rho y, \end{cases} \tag{35}$$

in which $\Delta g(x, y, z)$ and $p(t)$ are supposed to be bounded, i.e., $|\Delta g(x, y, z)| \le \mu_1$ and $|(t)| \le \mu_2$, where μ_1 and μ_2 are positive constants. System (35) with sliding mode control law (32) is globally and asymptotically stable if $G_r < -(\mu_1 + \mu_2)$.

Proof. For this, let us choose Lyapunov quadratic function (33); thus, we have

$$\begin{aligned} \dot{V} &= \sigma\dot{\sigma} = \sigma\left[D^{q_2} y + ky^2 + lx^2 + \eta y\right] \\ &= \sigma\left[-ky^2 - lx^2 + m + \Delta g(x, y, z) \right. \\ &\quad \left. + p(t) + u + ky^2 + lx^2 + \eta y\right] \\ &= \sigma\left[\Delta g(x, y, z) + p(t) + G_r \operatorname{sign}(\sigma)\right] \\ &\le \left(G_r + \mu_1 + \mu_1\right)|\sigma| < 0. \end{aligned} \tag{36}$$

Thus, the proof is achieved. □

6. Numerical Simulations

This part of the paper presents three illustrative examples to verify the effectiveness of the proposed control technique. Numerical simulations are carried out with initial conditions $(x_0, y_0, z_0) = (1.2, 1.5, 1.6)$, $\eta = 0.5$, and $G_r = -2$. For the commensurate fractional-order case, $q_1 = q_2 = q_3 = q = 0.83$ is chosen and for which the system is chaotic (see Figure 3). For the incommensurate fractional-order case, $q_1 = 1, q_2 = 0.88$, and $q_3 = 1$ are chosen. For this choice, the largest Lyapunov exponent is positive (see Figure 4(b)). The corresponding phase diagrams and time series are shown in Figure 10. Note that the controller can be activated in the system at any time. In this part, it is activated at $t = 20$ sec.

Case 1: commensurate order without uncertainty and an external disturbance.

As it was shown above, system (25) without the controller $u(t)$ is chaotic for $q_1 = q_2 = q_3 = q = 0.83$. Now, applying controller (32) to the system, simulation results can be seen in Figure 11. From this figure, it is observed that control law (32) can effectively asymptotically stabilize the state variables of system (25) (see Figures 11(a)–11(c)). Besides, the time series of the sliding surface $\sigma(t)$ is plotted in Figure 11(d). From this figure, it can be observed that the controller stabilizes the trajectories of the system on the sliding surface and maintains them on this surface when time evolves.

Case 2: commensurate order with uncertainty and an external disturbance.

In this part, we disturb the fractional-order financial system by an uncertainty defined by $\Delta g(x, y, z) = 0.2 \sin(\sqrt{x^2 + y^2 + z^2})$ and an external disturbance $p(t) = 0.5 \sin(2t)$, where $|\Delta g(x, y, z)| \le \mu_1 = 0.2$ and $|p(t)| \le \mu_2 = 0.5$. The time series of system (25) state variables (see Figures 12(a)–12(c)) and the time series of sliding surface (26) (see Figure 12(d)) in the presence of control law (32) can be seen through Figure 12. From this figure, we can see that the controller stabilizes the system in the presence of uncertainty and external disturbance.

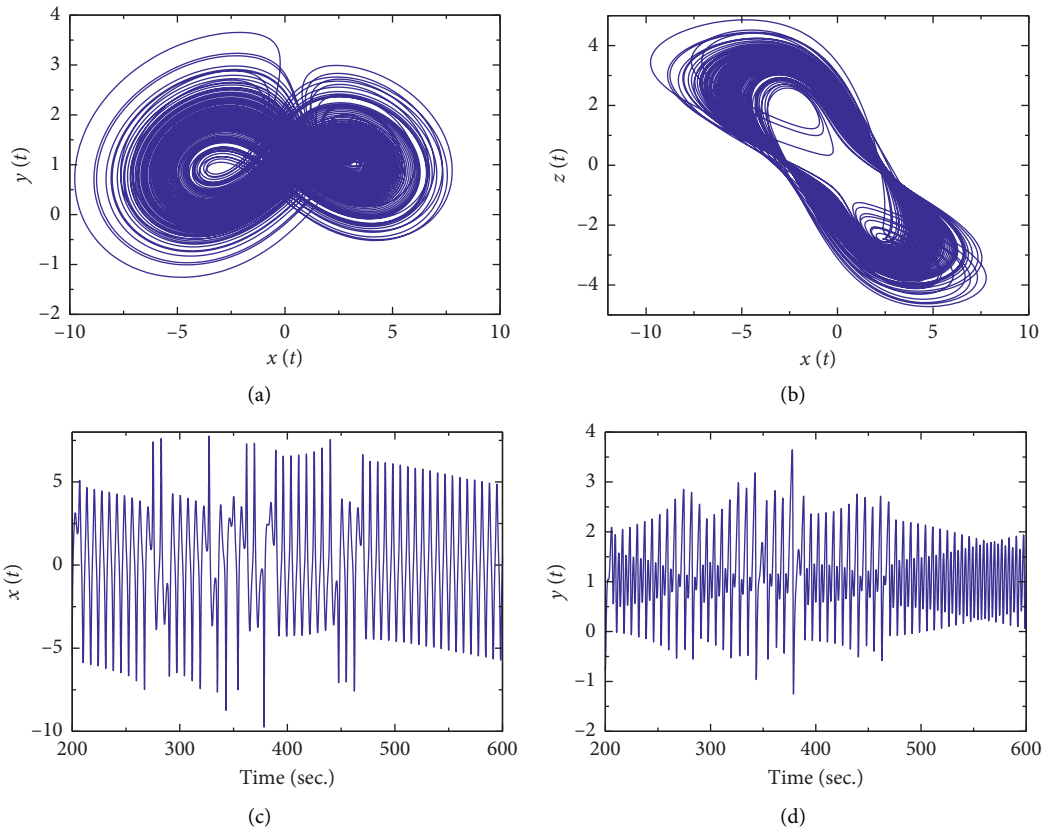

FIGURE 10: Phase diagrams and time series of system (6) with $q_1 = 1, q_2 = 0.88$, and $q_3 = 1$. (a) Projected onto the $x - y$ phase plane. (b) Projected onto the $x - z$ phase plane. (c) Time series of x. (d) Time series of y.

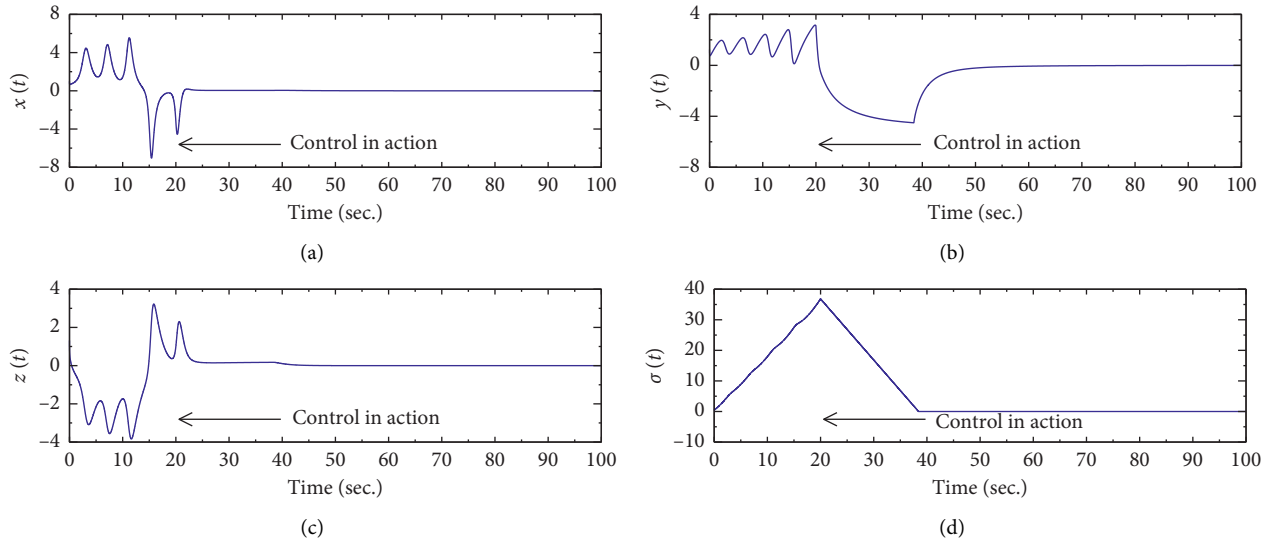

FIGURE 11: The time series of the controlled commensurate fractional-order system state variables and corresponding time series of the sliding surface without uncertainty and external disturbance (the control input is activated at $t = 20$ sec).

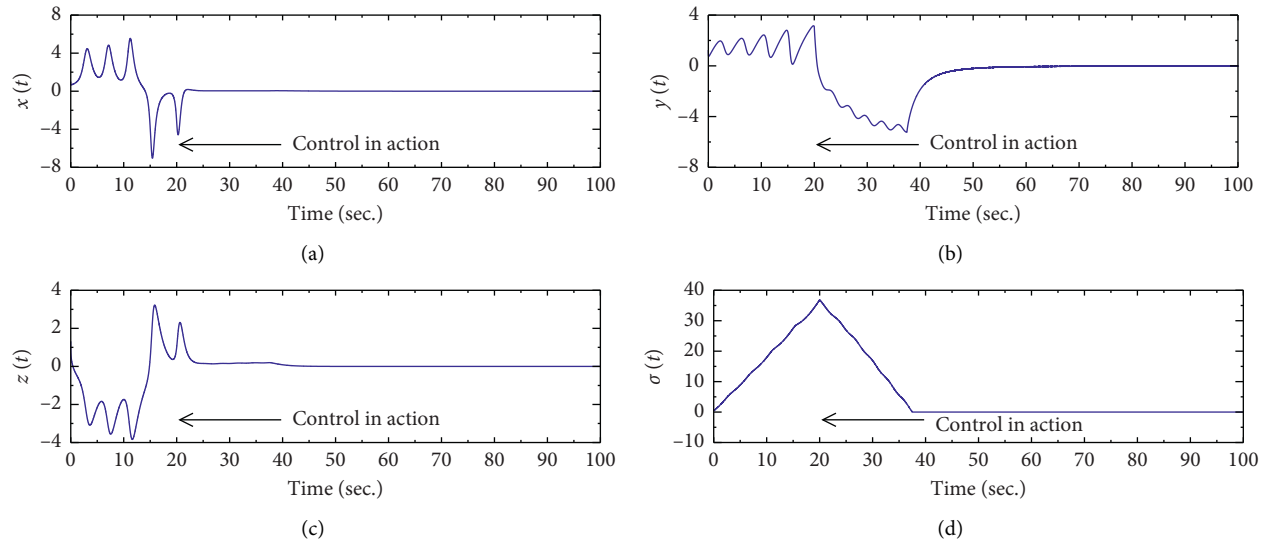

Figure 12: The time series of the controlled commensurate fractional-order system state variables and corresponding time series of the sliding surface with uncertainty and external disturbance (the control input is activated at $t = 20$ sec).

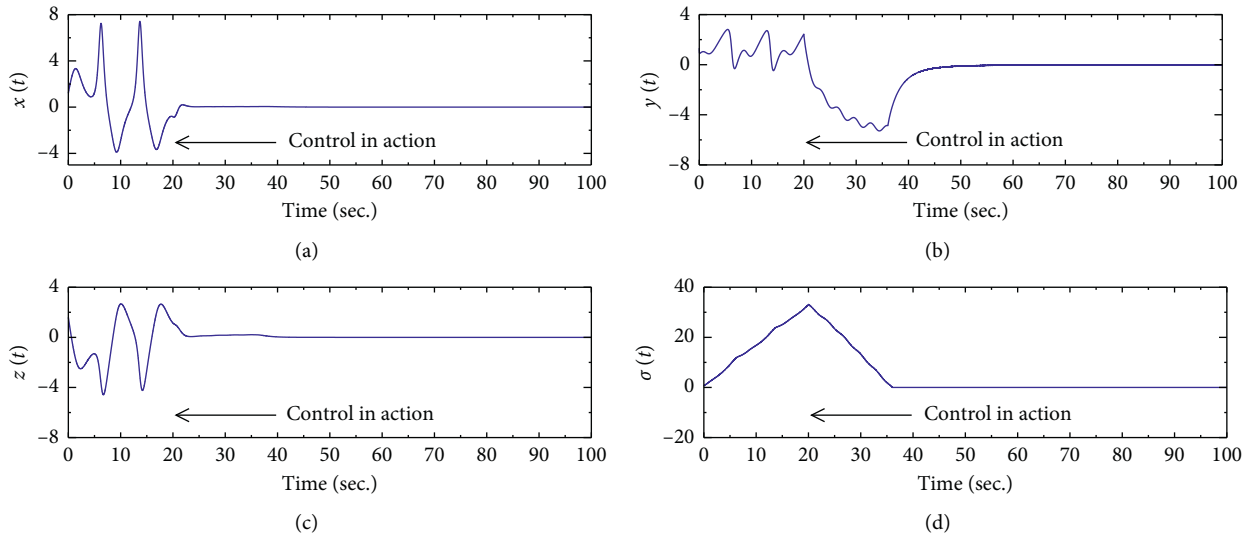

Figure 13: The time series of the controlled incommensurate fractional-order system state variables and corresponding time series of the sliding surface with uncertainty and external disturbance (the control input is activated at $t = 20$ sec).

Case 3: incommensurate order with uncertainty and an external disturbance.

In this case , we disturb financial system (25) with the incommensurate fractional order by the same uncertainty and external disturbance as case 2.

The time series of system (25) state variables and the time series of the sliding surface in the presence of control law (32) are shown in Figure 13. From this figure, it can be observed that the state variables of the system are stabilized.

In each figure, the time series of the sliding surface is plotted to show the ability of the controller to bring back all the system states onto the sliding surface and to maintain them on this surface when time evolves. Simulation results show that controller (32) is able to stabilize systems (25) and (35) in commensurate and incommensurate fractional-order cases. Therefore, the designed control law can suppress chaos in this fractional-order financial system in the presence or not of uncertainty and external disturbance.

7. Conclusions

In this paper, the dynamics of a financial system with the fractional order as well as the robust chaos control in this system are studied analytically, and numerical simulations are performed to confirm the analytical results. The existence of chaos in this study is validated by a positive Lyapunov exponent and by an analytical condition existing in the

literature. The fractional order system exhibits rich dynamics behaviors such as periodic and chaotic behaviors. A period-doubling route to chaos is found in this system. Numerical simulations revealed that chaos exists in this fractional order system for derivation orders less than 3. The lowest derivation order found to have chaos in the commensurate fractional-order case is 2.49 and 2.13 for the incommensurate fractional-order case. Regarding the robust control of chaos in the system, by using Lyapunov's stability theorem, a simple but robust fractional-order sliding mode control law has been designed to stabilize the chaotic trajectories of the fractional-order financial system in the presence or not of uncertainty and external disturbance. It should be noted that the controller has been applied only at the investment demand state equation to fully control the system. Numerical simulations show that this controller is effective and can control the financial system with commensurate and incommensurate fractional orders. In [14], Chen studied the fractional order version of the financial system proposed by Ma and Chen [34]. The lowest derivation order obtained in [14] for chaos to exist is 2.55 in the commensurate order case and 2.35 in the incommensurate order case. Compared to the fractional order version of Liao et al. [37] proposed in this paper, the emergence of chaos is enhanced in both cases. It is well known that time delay can affect the behavior of dynamical systems. For future works, chaotic dynamics analysis of this fractional-order financial system with time delay can be considered.

Data Availability

No data were used to support the findings of this study.

Conflicts of Interest

The authors declare that they have no conflicts of interest.

Acknowledgments

The authors thank IMSP-UAC and German Academic Exchange Service (DAAD) for financial support under the programme "In-Country/In-Region Scholarship Programme" (Funding program no. 57506853).

References

[1] W. L. Ditto, "Applications of chaos in biology and medicine," *AIP Conference Proceedings*, vol. 376, no. 1, pp. 175–201, 1996.

[2] J. Ma, C. N. Wang, J. Tang, and Y. F. Xia, "Suppression of the spiral wave and turbulence in the excitability-modulated media," *International Journal of Theoretical Physics*, vol. 48, no. 1, pp. 150–157, 2009.

[3] Y. Liu and Q. Yang, "Dynamics of a new Lorenz-like chaotic system," *Nonlinear Analysis: Real World Applications*, vol. 11, no. 4, pp. 2563–2572, 2010.

[4] E. N. Lorenz, "Deterministic nonperiodic flow," *Journal of the Atmospheric Sciences*, vol. 20, no. 2, pp. 130–141, 1963.

[5] G. Chen and T. Ueta, "Yet another chaotic attractor," *International Journal of Bifurcation and Chaos*, vol. 9, no. 7, pp. 1465-1466, 1999.

[6] J. Lü, G. Chen, and S. Zhang, "Dynamical analysis of a new chaotic attractor," *International Journal of Bifurcation and Chaos*, vol. 12, no. 5, pp. 1001–1015, 2002.

[7] R. B. Leipnik and T. A. Newton, "Double strange attractors in rigid body motion with linear feedback control," *Physics Letters A*, vol. 86, no. 2, pp. 63–67, 1981.

[8] S. Dadras, H. R. Momeni, and V. J. Majd, "Sliding mode control for uncertain new chaotic dynamical system," *Chaos, Solitons & Fractals*, vol. 41, no. 4, pp. 1857–1862, 2009.

[9] M. Roopaei, B. R. Sahraei, and T. C. Lin, "Adaptive sliding mode control in a novel class of chaotic systems," *Communications in Nonlinear Science and Numerical Simulation*, vol. 15, no. 12, pp. 4158–4170, 2010.

[10] M. T. Yassen, "Chaos control of chaotic dynamical systems using backstepping design," *Chaos, Solitons & Fractals*, vol. 27, no. 2, pp. 537–548, 2006.

[11] Q. Jia, "Chaos control and synchronization of the Newton-leipnik chaotic system," *Chaos, Solitons & Fractals*, vol. 35, no. 4, pp. 814–824, 2008.

[12] I. Podlubny, *Fractional Differential Equations,*Academic Press, Cambridge, MA, USA, 1999.

[13] C. Li and G. Peng, "Chaos in Chen's system with a fractional order," *Chaos, Solitons & Fractals*, vol. 22, no. 2, pp. 443–450, 2004.

[14] W. C. Chen, "Nonlinear dynamics and chaos in a fractional-order financial system," *Chaos, Solitons & Fractals*, vol. 36, no. 5, pp. 1305–1314, 2008.

[15] V. Daftardar-Gejji and S. Bhalekar, "Chaos in fractional ordered Liu system," *Computers & Mathematics with Applications*, vol. 59, no. 3, pp. 1117–1127, 2010.

[16] X. Y. Wang, Y. J. He, and M. J. Wang, "Chaos control of a fractional order modified coupled dynamos system," *Nonlinear Analysis: Theory, Methods & Applications*, vol. 71, no. 12, pp. 6126–6134, 2009.

[17] T. T. Harley, C. F. Lorenzo, and H. K. Qammar, "Chaos in a fractional order Chua's system," *IEEE Transactions on Circuits and Systems I*, vol. 42, no. 8, pp. 485–490, 1995.

[18] I. Grigorenko and E. Grigorenko, "Chaotic dynamics of the fractional Lorenz system," *Physical Review Letters*, vol. 91, no. 3, Article ID 034101, 2003.

[19] W. M. Ahmad and J. C. Sprott, "Chaos in fractional-order autonomous nonlinear systems," *Chaos, Solitons & Fractals*, vol. 16, no. 2, pp. 339–351, 2003.

[20] I. Petrás, *Fractional-Order Nonlinear Systems: Modeling, Analysis and Simulation*, Springer Science and Bussiness Media, Berlin, Germany, 2011.

[21] C. Li and W. Deng, "Remarks on fractional derivatives," *Applied Mathematics and Computation*, vol. 187, no. 2, pp. 777–784, 2007.

[22] Y. Chatibi, A. Ouhadan, E. Hassan El Kinani, and A. Ouhadan, "Lie symmetry analysis of conformable differential equations," *AIMS Mathematics*, vol. 4, no. 4, pp. 1133–1144, 2019.

[23] Y. Chatibi, E. H. El kinani, and A. Ouhadan, "Lie symmetry analysis and conservation laws for the time fractional black-scholes equation," *International Journal of Geometric Methods in Modern Physics*, vol. 17, no. 1, p. 14, 2020.

[24] Y. Chatibi, E. H. El Kinani, and A. Ouhadan, "Variational calculus involving nonlocal fractional derivative with mittag-leffler kernel," *Chaos, Solitons & Fractals*, vol. 118, pp. 117–121, 2019.

[25] Y. Chatibi, E. H. El kinani, and A. Ouhadan, "On the discrete symmetry analysis of some classical and fractional differential

equations," *Mathematical Methods in the Applied Sciences*, vol. 44, no. 4, pp. 2868–2878, 2019.

[26] R. H. Strotz, J. C. McAnulty, and J. B. Naines, "Goodwin's nonlinear theory of the business cycle: an electro-analog solution," *Econometrica*, vol. 21, no. 3, pp. 390–411, 1953.

[27] A. C. L. Chian, "Nonlinear dynamics and chaos in macroeconomics," *International Journal of Theoretical and Applied Finance*, vol. 3, no. 3, p. 601, 2000.

[28] L. De Cesare and M. Sportelli, "A dynamic IS-LM model with delayed taxation revenues," *Chaos, Solitons & Fractals*, vol. 25, no. 1, pp. 233–244, 2005.

[29] H. Yu, G. Cai, and Y. Li, "Dynamic analysis and control of a new hyperchaotic finance system," *Nonlinear Dynamics*, vol. 67, no. 3, pp. 2171–2182, 2012.

[30] L. Chen and G. Chen, "Controlling chaos in an economic model," *Physica A: Statistical Mechanics and Its Applications*, vol. 374, no. 1, pp. 349–358, 2007.

[31] W. Wu, Z. Chen, and W. H. Ip, "Complex nonlinear dynamics and controlling chaos in a cournot duopoly economic model," *Nonlinear Analysis: Real World Applications*, vol. 11, no. 5, pp. 4363–4377, 2010.

[32] S. Invernizzi and A. Medio, "On lags and chaos in economic dynamic models," *Journal of Mathematical Economics*, vol. 20, no. 6, pp. 521–550, 1991.

[33] D. A. Hsieh, "Chaos and nonlinear dynamic: application to financial markets," *The Journal of Finance*, vol. 46, no. 5, pp. 1839–1877, 1991.

[34] J. H. Ma and Y. S. Chen, "Study for the bifurcation topological structure and the global complicated character of a kind of nonlinear finance system, I," *Applied Mathematics and Mechanics*, vol. 22, no. 11, pp. 1240–1251, 2001.

[35] E. Panas, "Long memory and chaotic models of prices on the London metal exchange," *Resources Policy*, vol. 27, no. 4, pp. 235–246, 2001.

[36] B. J. West and S. Picozzi, "Fractional Langevin model of memory in financial time series," *Physical Review E, Statistical, Nonlinear, and Soft Matter Physics*, vol. 65, no. 3, Article ID 037106, 2002.

[37] Y. Liao, Y. Zhou, F. Xu, and X. B. Shu, "A study on the complexity of a new chaotic financial system," *Complexity*, vol. 2020, Article ID 8821156, 5 pages, 2020.

[38] S. Dadras and H. R. Momeni, "Control of a fractional-order economical system via sliding mode," *Physica A: Statistical Mechanics and Its Applications*, vol. 389, no. 12, pp. 2434–2442, 2010.

[39] M. S. Abd-Elouahab, N. E. Hamri, and J. Wang, "Chaos control of a fractional order financial system," *Mathematical Problems in Engineering*, vol. 2010, Article ID 270646, 18 pages, 2010.

[40] W. Perruquetti and J. P. Barbot, *Sliding Mode Control in Engineering*, Marcel Dekker Inc., New York, NY, USA, 2002.

[41] J. E. Slotine and W. Li, *Applied Nonlinear Control*, Prentice Hall, Englewood Cliffs, NJ, USA, 1991.

[42] H. K. Khalil, *Nonlinear Systems*, Prentice Hall, Englewood Cliffs, NJ, USA, 1996.

[43] M. R. Faieghi, H. Delavari, and D. Baleanu, "Control of an uncertain fractional-order Liu system via fuzzy fractional-order sliding mode control," *Journal of Vibration and Control*, vol. 18, no. 9, pp. 1366–1374, 2012.

[44] D. Y. Chen, Y. X. Liu, X. Y. Ma, and R. F. Zhang, "Control of a class of fractional-order chaotic systems via sliding mode," *Nonlinear Dynamics*, vol. 67, no. 1, pp. 893–901, 2012.

[45] C. Yin, S. M. Zhong, and W. F. Chen, "Design of sliding mode controller for a class of fractional-order chaotic systems," *Communications in Nonlinear Science and Numerical Simulation*, vol. 17, no. 1, pp. 356–366, 2012.

[46] A. J. Muñoz-Vázquez, V. Parra-Vega, and A. Sánchez-Orta, "Fractional integral sliding modes for robust tracking of nonlinear systems," *Nonlinear Dynamics*, vol. 87, no. 2, pp. 895–901, 2017.

[47] M. S. Tavazoei and M. Haeri, "Chaotic attractors in incommensurate fractional order systems," *Physica D: Nonlinear Phenomena*, vol. 237, no. 20, pp. 2628–2637, 2008.

[48] M. S. Tavazoei and M. Haeri, "A necessary condition for double scroll attractor existence in fractional order systems," *Physics Letters A*, vol. 367, no. 1-2, pp. 102–113, 2007.

[49] E. Campos-Cantón, J. G. Barajas-Ramirez, G. Solis-Perales, and R. Femat, "Multiscroll attractors by switching systems," *Chaos: An Interdisciplinary Journal of Nonlinear Science*, vol. 20, no. 1, Article ID 013116, 2010.

[50] L. Chua, M. Komuro, and T. Matsumoto, "The double scroll family," *IEEE Transactions on Circuits and Systems*, vol. 33, no. 11, pp. 1072–1118, 1986.

[51] D. Matignon, "Stability results for fractional differential equations with applications to control processing," *Computational Engineering in Systems Applications*, vol. 2, no. 1, pp. 963–968, 1996.

[52] S. Bhalekar and M. Patil, "Singular points in the solution trajectories of fractional order dynamical systems," *Chaos: An Interdisciplinary Journal of Nonlinear Science*, vol. 28, no. 11, Article ID 113123, 2018.

[53] J. L. Echenausía-Monroy, G. Huerta-Cuellar, R. Jaimes-Reátegui, J. H. García-López et al., "Multistability emergence through fractional-order-derivatives in a PWL multi-scroll system," *Electronics*, vol. 9, no. 6, p. 880, 2020.

[54] J. L. Echenausía-Monroy, H. E. Gilardi-Velázquez, R. Jaimes-Reátegui, V. Aboites, and G. Huerta-Cuellar, "A physical interpretation of fractional-order-derivatives in a jerk system: electronic approach," *Communications in Nonlinear Science and Numerical Simulation*, vol. 90, Article ID 105413, 2020.

[55] K. Diethelm, N. J. Ford, and A. D. Freed, "A predictor-corrector approach for the numerical solution of fractional differential equations," *Nonlinear Dynamics*, vol. 29, no. 1, pp. 3–22, 2002.

Hindawi
Complexity
Volume 2021, Article ID 2747174, 18 pages
https://doi.org/10.1155/2021/2747174

WILEY | Hindawi

Review Article

Recent Advances in Dimensionality Reduction Modeling and Multistability Reconstitution of Memristive Circuit

Yunzhen Zhang,[1] **Yuan Ping**,[1] **Zhili Zhang**,[1] **and Guangzhe Zhao**[2]

[1]*School of Information Engineering, Xuchang University, Xuchang 461000, China*
[2]*Academic Administration, Xuchang University, Xuchang 461000, China*

Correspondence should be addressed to Yunzhen Zhang; yunzhenzhang@xcu.edu.cn

Received 20 May 2021; Accepted 23 June 2021; Published 9 July 2021

Academic Editor: Cristiana J. Silva

Due to the introduction of memristors, the memristor-based nonlinear oscillator circuits readily present the state initial-dependent multistability (or extreme multistability), i.e., coexisting multiple attractors (or coexisting infinitely many attractors). The dimensionality reduction modeling for a memristive circuit is carried out to realize accurate prediction, quantitative analysis, and physical control of its multistability, which has become one of the hottest research topics in the field of information science. Based on these considerations, this paper briefly reviews the specific multistability phenomenon generating from the memristive circuit in the voltage-current domain and expounds the multistability control strategy. Then, this paper introduces the accurate flux-charge constitutive relation of memristors. Afterwards, the dimensionality reduction modeling method of the memristive circuits, i.e., the incremental flux-charge analysis method, is emphatically introduced, whose core idea is to implement the explicit expressions of the initial conditions in the flux-charge model and to discuss the feasibility and effectiveness of the multistability reconstitution of the memristive circuits using their flux-charge models. Furthermore, the incremental integral transformation method for modeling of the memristive system is reviewed by following the idea of the incremental flux-charge analysis method. The theory and application promotion of the dimensionality reduction modeling and multistability reconstitution are proceeded, and the application prospect is prospected by taking the synchronization application of the memristor-coupled system as an example.

1. Introduction

The intrinsic memory property [1] of the memristor makes the memristor-based nonlinear circuits and systems easily exhibit the state initial-dependent dynamical behaviors. By keeping the system parameters unchanged and changing the state initials, the trajectories of the memristive circuits and systems can asymptotically approach to different stable states, showing the state initial-dependent multistability [2, 3] or extreme multistability [4–7], i.e., coexisting multiple or infinitely many attractors. On the one hand, these coexisting multistable modes can provide more flexibility for information engineering applications [8–11]; on the other hand, it may also lead the application systems to abnormal working states [12]. These ungovernable problems pose a severe test for realizing the control of multistable modes. In addition, the dynamical behaviors of memristive circuits and systems are highly dependent on the state initials, but the state initials cannot be explicitly expressed in their state equations, which bring great obstacles in mechanical analyses of the state initial-dependent dynamical behaviors. Moreover, the memristive circuits and systems usually have line equilibrium set, plane equilibrium set, no equilibrium, or stable equilibrium, whose stabilities and induced dynamical behaviors are hard to be analyzed by using the traditional stability theory [12]. Therefore, accurate prediction, quantitative analysis, and physical control of such special phenomena have become an important research problem in the field of information science.

Traditional control strategies usually adopted nonfeedback control strategy to convert a multistable system to a mono-stable system [13–17] or adopted feedback control

strategy to stabilize the system in a certain desired state [13, 18, 19]. But these control strategies cannot achieve the multistable control. To solve this problem, researchers proposed different dimensionality reduction modeling schemes based on the memristive circuit and system [20, 21]. In [22], the concept of dimensionality reduction modeling was proposed, which modeled the memristive circuits with two physical quantities of flux and charge as main state variables, and the dimension of the obtained flux-charge model was lower than that of the traditional voltage-current model. Bao et al. [23] built the reduce-ordered flux-charge model of a two-memristor-based circuit and analyzed its dynamical characteristics via the voltage-current and flux-charge models. Bao et al. [24] qualitatively pointed out that the flux-charge model of the memristive circuit can be equivalent to realize its dynamical behavior in the voltage-current model. However, in these early studies, the state initials of the memristive circuit were not explicitly expressed in the dimensionality reduction model [25], resulting in the information loss of state initials of the memristive circuit. Therefore, the established dimensionality reduction model could not reflect the multistability of the memristive circuit. In recent years, Corinto proposed an incremental flux-charge analysis method [26, 27] and applied it to the dimensionality reduction modeling of memristor-based cellular neural networks [28] and memristor-based oscillator array [29]. With this method, the state initials of the memristive circuit can be expressed as standalone system parameters in the flux-charge domain [12], which is conducive to the analyses and measurements of the state initial-dependent dynamical behaviors. Thereafter, this method was applied for reconstituting and analyzing extreme multistability of ideal memristor-based circuits [12, 20, 30, 31]. On this basis, the incremental integral transformation method was proposed for the analyses of memristive systems [21, 32]. Hereto, a complete set of dimensionality reduction reconstruction theory for ideal memristor-based circuits and systems was thereby formed.

It should be noted that, in the original literature, these two methods were called the flux-charge analysis method [26, 27] and the state variable mapping method [21], respectively. But the state variables of the dimensionality reduction model are actually expressed by the incremental integral of the original memristive circuit's and system's state variables, whose core idea is integral transformation. Therefore, in this paper, these two methods are called the incremental flux-charge analysis method and the incremental integral transformation method, respectively. By using these two methods, on the one hand, the implicit state initials in the original memristive circuit and system can be transformed into the explicitly state initial-related system parameters appearing in the dimensionality reduction model. On the other hand, the line or plane equilibrium set in the original memristive circuit and system can be converted into the certain equilibrium, which is beneficial to the elaboration of the dynamic mechanism. In short, the state initial-dependent dynamical behaviors of the original memristive circuit and system are transformed into the parameter-dependent dynamical behaviors of the dimensionality reduction model. In addition, synchronization, as one of the basic nonlinear phenomena, has received extensive attention in the field of basic theory and engineering applications [33]. In the nonmemristor-coupled system, the state initials have significant effect on the synchronization characteristics [34–36]. Based on the above dimensionality reduction methods, in the study of the synchronization on the memristor-coupled system [37], the synchronization effect of the state initial-related system parameters can be studied quantitatively after the state initials are expressed explicitly in the state equation.

The incremental flux-charge analysis method and the incremental integral transformation method realize the mapping transformation of the state variable domain by means of integral transformation and describe and analyze the multistability of the original memristive circuit and system based on the transformed state variable domain, which provides theoretical basis for the precise prediction, quantitative analysis, and physical control of such special phenomena. In this paper, the dimensionality reduction modeling and multistability reconstruction of the memristive circuit and system are summarized to help researchers fully understand the state initial-dependent multistability dimensionality reduction reconstruction strategy of the memristive circuit and system. Then, the reconstruction strategy is applied to the synchronization research of the memristor-coupled system to quantitatively study the influence of state initials on synchronization.

2. Multistability of Memristive Circuit in the Voltage-Current Domain

2.1. Multistability and Coexisting Multiple Attractors. Multistability [13, 38–41] is an inherent phenomenon of the nonlinear dynamical system, in which multiple attractors coexist with the change of state initials under the fixed system parameters. The term "multistability" first appeared in the study of visual perception [42]. Arecchi also found the coexistence attractors' phenomenon in electronic circuits [43] and gas lasers [44]. Later, a large number of theoretical and experimental studies have explored this special phenomenon in different systems [45–55]. In addition, in some special coupled systems [56, 57], the phenomenon of coexisting infinitely many attractors, i.e., extreme multistability [58–61], can also be observed.

In recent years, the hidden attractor [62–76], as a special class of newly defined attractor, has attracted extensive attention from researchers. The attractor that we usually say is also called the self-excited attractor, which is caused by the unstable equilibrium. Unlike the self-excited attractor [67, 77], the attraction basin with the hidden attractor does not intersect any equilibrium [78], and its existence increases the uncertainty of the system. When the system has a stable equilibrium [5] or no equilibrium [3, 79, 80], the induced multistability is called hidden multistability. Note that when the system has a stable equilibrium [5] and can produce dynamical behavior other than the point attractor, it can be confirmed that the system has hidden multistability. However, if the system has no equilibrium and can produce

only one stable oscillation behavior, the system is a hidden system, but it does not have multistability [81].

It has been shown that the hidden attractor is sensitive to the state initial of the system. In the domain of stable equilibrium, the system trajectory will converge to the stable point, but under the special state initial, the system trajectory can form the stable chaotic attractor or periodic limit cycle. Figures 1(a) and 1(b), respectively, show the self-excited and hidden attractors generated by a novel Chua's circuit [67]. Figures 1(c) and 1(d), respectively, show the local plane projection of Figures 1(a) and 1(b), where the red dots are a pair of nonzero equilibria. According to the orbit of the attractor and the position relationship of the equilibrium in the figure, it can be seen that the attraction basin of the self-excited attractor must cover the unstable equilibrium, while the attraction basin of the hidden attractor with the neighborhood of the stable equilibrium does not overlap. Therefore, the self-excited attractor and hidden attractor can be clearly distinguished according to the intersection relationship between the attraction basin and the equilibrium neighborhood in phase space.

In general, coexisting infinitely many attractors can be classified into the following four types:

(a) Different attractor types: hyperchaotic attractor, chaotic attractor, quasi-periodic limit cycle, periodic limit cycle, and stable point

(b) Different attractor topologies: the same type of attractor has completely different topologies, such as spiral and double-scroll attractors, scroll complete and incomplete attractors, and attractors with different dynamic amplitude

(c) Different number of limit cycles: limit cycles with different number of periods

(d) Different attractor positions: attractors are located in different phase space.

2.2. The Difference between Multistability and Chaotic Initial Sensitivity. Since Chua put forward the generalized concept of the memristive system [82], the circuit and system constructed by the memristor have received great attention. In the early memristive circuit [83–87], scholars found that the stability of the equilibrium was closely related to the state initial of the memristor, which meant that the coexistence of multiple attractors was easy to occur in the memristive circuit. Then, in the memristive circuit, Bao found that the state initial-dependent dynamical behavior was a special kind of multistability phenomenon, i.e., extreme multistability. And, in [88], Bao et al. explicitly proposed the extreme multistability in the memristive circuit for the first time, that is, in the memristive circuit with line equilibrium, there was a peculiar coexistence infinitely many attractor phenomenon, which relied on the internal state initial of the memristor. In particular, Jafari et al. [89] pointed out the difference between the state initial-dependent dynamical behavior (extreme multistability) of the memristive system and the chaotic initial sensitivity of the general nonlinear dynamical system. That is, for the general nonlinear dynamical system, the initial sensitivity of system trajectory was only a quantitative change, and the trajectories of the system starting from the different state initials would traversal in the corresponding attraction region along different trajectories, without changing the dynamical properties of the system. However, the extreme multistability of the memristive system was a qualitative change; the change of state initial could cause the trajectory of the memristive system to jump between the attraction domains of different dynamical behaviors. Therefore, the state initial-dependent multistability in the memristive circuit and the chaotic initial sensitivity in the general chaotic circuit are two completely different concepts.

2.3. Multistability in Memristive Circuit and System. Since physical accessibility of memristors has been reported [90], lots of investigations were carried out for various memristor-based application circuits and systems, including cellular nonlinear/neural network [91], spiking and bursting neuron circuit [92], active band-pass filter-based oscillating circuit [93], FitzHugh–Nagumo neuron circuit [94], recurrent neural network [95], hypogenetic jerk chaotic system [21, 96, 97], and hyperchaotic autonomous system [98], from which rich dynamical behaviors have been manifested by theoretical studies, numerical simulations, and experimental measurements. The results showed that the stabilities of the memristive circuit and system, especially the ideal memristor-based nonlinear circuit and system, had a great relationship with the state initial of the memristor [88, 99]. Therefore, the coexisting infinitely many attractors appeared in such memristive circuit and system [12, 20, 100]. Under the fixed system parameters, the solution trajectories of the system can be represented by diverse stable states with the varied state initials, such as point, period, quasi-period, chaos, and hyperchaos [7, 98, 101, 102]. Such a special phenomenon is mostly relevant to no equilibrium [103, 104], limited number equilibria [105], or even infinitely many equilibria [6, 106]. Particularly, when the number of coexisting attractors tends to infinite, the phenomenon is called extreme multistability [39, 56, 89, 107–109].

In principle, the coexisting infinitely many attractors caused by extreme multistability generally has a complete smooth bifurcation route with respect to the state initial, and the bifurcation trajectories are gradual [110], such as period-doubling bifurcation and Hopf bifurcation, as shown in Figure 2. It is important to emphasize that extreme multistability is not the same as coexisting infinitely many attractors. The aforesaid coexisting infinitely many attractors are commonly triggered in the memristive circuit and system with line or plane equilibrium set, entirely different from those generated from the offset-boostable flow by introducing an extra periodic signal [111–113] and also different from those generated from the attractor position offset caused by the state initial [114].

According to the definition of memristor [1, 82, 115, 116], researchers have proposed a variety of physical realizable memristor simulators with the characteristics of memristor ports [117], which can be mainly

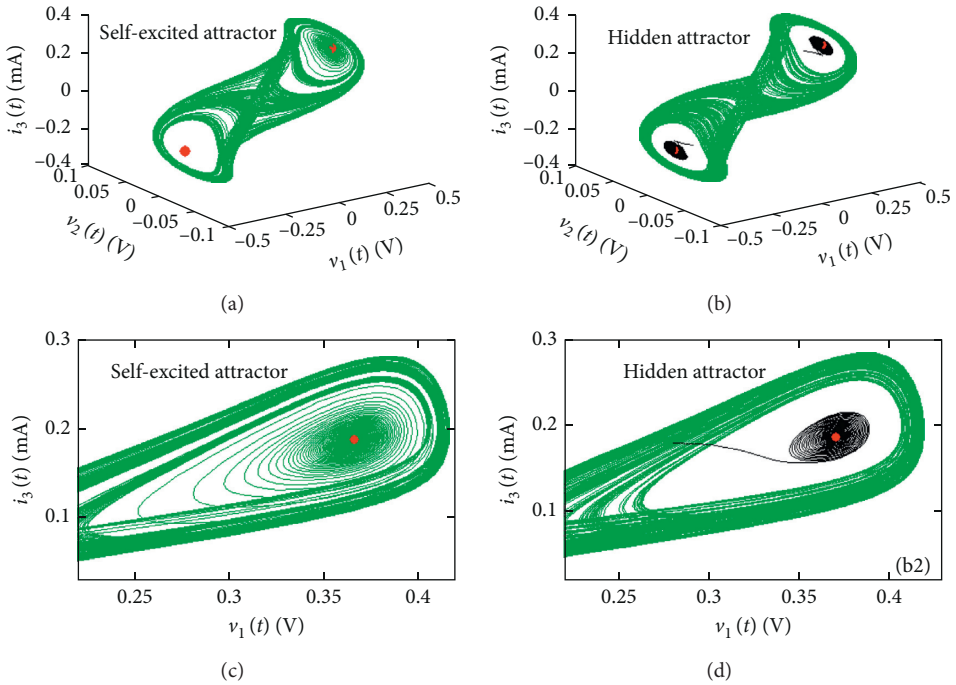

Figure 1: The generated attractors from a novel Chua's circuit (the red points are the nonzero equilibria): (a) self-excited attractor; (b) hidden attractor; (c) local plane projection of a; (d) local plane projection of b.

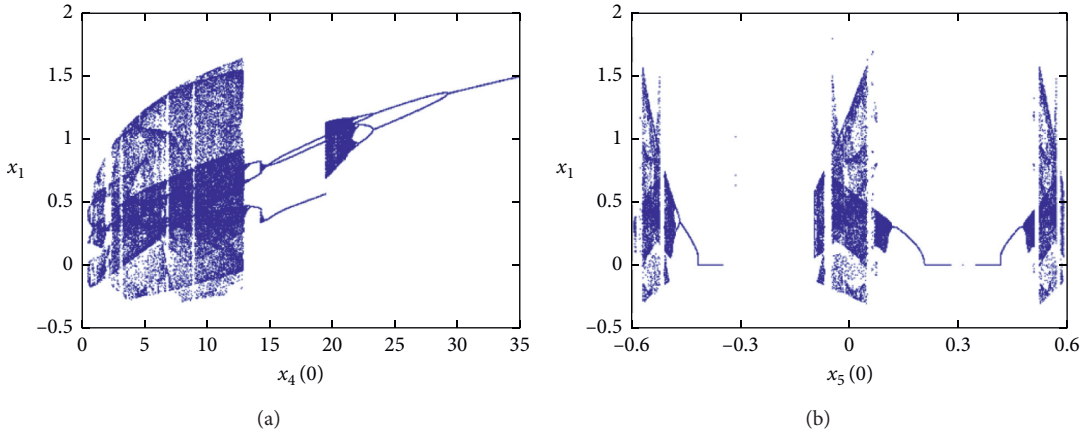

Figure 2: Extreme multistability: (a) with the variation of memristive initial $x_4(0)$; (b) with the variation of memristive initial $x_5(0)$.

divided into two categories: one is the ideal memristor or nonideal memristor based on the equivalent realization of operational amplifier and analog multiplier [62, 101, 118, 119]; the other is the generalized memristor with diode bridge cascade RC, RL, or LC filters [120–124]. From the essential definition of the ideal memristor [116], it can be seen that the memristor is derived from the relationship between flux and charge [115]. The ideal memristor is usually divided into the charge-controlled memristor and flux-controlled memristor. Its voltage-current relation curve has the characteristic of typical italic "8" type pinched hysteresis loop, and the main characteristics are zero crossing [82, 116, 125], double value [115], singular symmetry, tapering [116, 126], self-crossing type [127], and stability [128].

The nonideal memristor-based nonlinear circuit or system usually has certain equilibria [129], and their stability is not affected by the state initials. However, under the fixed system parameters, with the varied state initials, the system will produce the coexistence steady-state mode [2], namely, multistability. And, when a memristive circuit or system has a stable equilibrium or no equilibrium [3, 5], the system will produce hidden multistability.

The ideal memristor-based nonlinear circuit or system usually has infinitely many equilibria, and their positions and stabilities are related to the internal state initials of

memristors, which indicates the extreme multistability of the memristive circuit or system. Bao et al. [88] proposed an ideal flux-controlled memristor-based Chua's circuit with line equilibrium set and revealed the state initial-dependent extreme multistability phenomenon of the memristive circuit. In [93], the ideal flux-controlled memristor was used to replace Chua's diode, and a memristive circuit with line equilibrium set was obtained, and the extreme multistability phenomenon of the circuit was studied. By introducing two ideal memristors into Chua's circuit, a memristive circuit with a plane equilibrium set was obtained in [130] and further revealed the extreme multistability phenomenon. By introducing an ideal flux-controlled memristor into a three-dimensional hypogenertic jerk system, the paper [96] constructed a memristive system with four line equilibria sets, which could produce the extreme multistability phenomenon dependent on the state initial of the memristor and other state initials. Yuan et al. [107] designed a memristor-based multiscroll hyperchaotic system by introducing an ideal flux-controlled memristor and revealed its extreme multistability phenomenon. By introducing a micro-perturbation into the memristive circuit, a memristive circuit with no equilibrium was constructed, which could produce the phenomenon of hidden extreme multistability [131].

3. Multistability Control Strategy

3.1. Multistability Generic Control Strategy. Multistability has been reported in different scientific fields such as physics, chemistry, biology, and economy [13]. Because of its sensitive dependence on state initial, the multistability phenomenon can induce the system to switch between different coexisting states under the fixed system parameters, which provides great flexibility for the engineering application of the multistable system [8, 9, 13, 105, 132–134]. But, at the same time, it is easy to lead the application systems to abnormal working states, which puts forward a severe test to the multistable mode control strategy. For example, in the design of equipment with certain characteristics, it is necessary to avoid multistable or to stabilize it in the desired state, which will cause a lot of inconvenience in practical application. Therefore, it is necessary to control the multistable through appropriate control strategy.

In order to convert a multistable system to a mono-stable system, nonfeedback control strategy was usually adopted. In other words, by adding external disturbance to the system, such as the introduction of short pulse [13], a specific attractor could be selected in a multistable system to achieve multistability control. By introducing pseudoperiodic driving [14, 15] or harmonic disturbance [16, 17], the undesirable attractor types could be eliminated, and then, the system could be controlled in a certain stable state. In order to stabilize the system in a certain desired state, feedback control strategy was usually adopted [18], such as periodic driving [19] and time-delay feedback [13]. Yet these control strategies cannot achieve the multistable control. However, via the special constitutive relation of the memristor, some scholars have proposed appropriate multistability dimensionality reduction reconstitution strategies for specific types of the memristive circuit and system and realized the control of multistable modes. A brief introduction is given below.

3.2. Multistability Dimensionality Reduction Reconstitution Strategy. The multistability of the memristive circuit/system can provide more flexibility for the memristive circuit/system to be applied in engineering application fields of image processing, signal encryption, and so on [8, 9, 105, 132–137]. However, due to the sensitive dependence of the multistability on the state initial, there are two main problems when the traditional analysis method is used to analyze the multistable mode of the memristive circuit/system. On the one hand, the dynamical behaviors of the multistable circuit/system are highly dependent on the state initials, but the state initials cannot be expressed explicitly in the state equation of the multistable circuit/system, which makes it impossible to quantitatively analyze the state initial-dependent dynamical behavior of the memristive circuit/system. On the other hand, since the memristive circuit/system usually has line equilibrium set, plane equilibrium set, space equilibrium set, or no equilibrium, when we use the traditional analysis method to analyze the dynamical behavior, it is very difficult to correctly judge whether the equilibrium of the system is stable or not, or cannot analyze the system equilibrium, which makes it impossible to quantitatively describe the internal mechanism of multistability. These problems make it difficult to accurately predict, quantitatively analyze, and physically control the state initial-dependent dynamical behaviors.

Therefore, in the process of analyzing the multistability of the memristive circuit and system, in order to solve these problems, researchers proposed different dimensionality reduction modeling schemes based on the memristive circuit [20] and memristive system [21]. In fact, a prototype of dimensionality reduction modeling had been developed in the earlier literature [22–24]. In [22], the concept of dimensionality reduction modeling was proposed, which modeled the memristive circuits with two physical quantities of flux and charge as main state variables, and the dimension of the obtained flux-charge model was lower than that of the traditional voltage-current model. Bao et al. [23] built the reduce-ordered flux-charge model of a two-memristor-based memristive circuit and analyzed its dynamical characteristics via the voltage-current and flux-charge models. Bao et al. [24] qualitatively pointed out that the flux-charge model of the memristive circuit could be equivalent to realize its dynamical behavior in the voltage-current model. However, in these early studies, the state initials of the memristive circuits were not explicitly expressed in the dimensionality reduction model [25], resulting in the information loss of state initials of the memristive circuit. Therefore, the established dimensionality reduction model could not reflect the original multistability of the memristive circuits and systems.

In recent years, Corinto proposed an incremental flux-charge analysis method [26], the method was based on the

Kirchhoff flux and charge law and the constitutive relation of the circuit element under the incremental flux and incremental charge. Compared with the circuit equation in the voltage-current domain, the circuit equation in the flux-charge domain established by this method had a simpler equation structure, which could simplify the complexity of dynamical analysis and clearly understand the influence of state initial. To further demonstrate the effectiveness of the method, Corinto applied the method to the analysis of Hopf bifurcation and period-doubling cascade induced by state initial [27]. Subsequently, more scholars applied it to the study of complex memristive circuits such as memristor-based cellular neural network [28] and memristor-based oscillator array [29]. Then, Chen clearly proposed that this method could represent the state initials of all dynamical elements in the circuit as standalone state initial-related system parameters [12], which was conducive to the analysis and measurement of the state initial-dependent dynamical behaviors in the memristive circuit. Moreover, this method was applied to the reconstruction and analysis of extreme multistability for the ideal memristor-based circuit [12, 20, 30, 31]. And, on this basis, the incremental integral transformation method for the memristive system was proposed [21, 32], forming a complete set of dimensionality reduction reconstruction theory for ideal memristor-based circuits and systems. That is, firstly, the integral transformations on all state variables of the original memristive circuit/system are carried out (note that all terms in the system equation must be integrable). Then, the dimensionality reduction modeling is implemented by using the nondynamic property [22] of the memristor in the flux-charge domain. Then, based on the dimensionality reduction model, the state initial-dependent dynamical behaviors of the original memristive circuit/system are reconstructed and analyzed.

4. Flux-Charge Constitutive Relation of Memristor

In the 1970s, Chua proposed the fourth basic circuit element, memristor, to characterize the relationship between flux and charge [115] and deduced the existence the memristor from the symmetry of circuit variables and the characteristics of the electromagnetic field, as shown in Figure 3. As can be seen from Figure 3, there are four basic physical quantities in the circuit: current i, voltage v, charge q, and flux φ. There are six mathematical relations among them; among which the relations between current and charge and voltage and flux are as follows:

$$q(t) = \int_{-\infty}^{t} i(\xi)\mathrm{d}\xi, \tag{1a}$$

$$\varphi(t) = \int_{-\infty}^{t} v(\xi)\mathrm{d}\xi. \tag{1b}$$

Equations (1a) and (1b), respectively, represent that charge is the integral of current with respect to time and flux is the integral of voltage with respect to time. According to

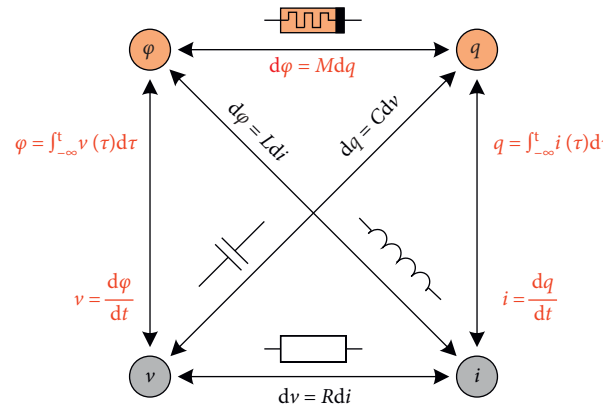

Figure 3: Circuit basic variables and four basic elements.

the incremental flux-charge analysis method, Corinto and Forti [26] gave the definition of incremental charge and incremental flux for any $t \geq t_0$ $(-\infty < t_0 < \infty)$, i.e., $q(t;t_0) = \int_{t_0}^{t} i(\xi)\mathrm{d}\xi$, $\varphi(t;t_0) = \int_{t_0}^{t} v(\xi)\mathrm{d}\xi$, and equation (1) can be further written as

$$q(t) = \int_{-\infty}^{t} i(\xi)\mathrm{d}\xi = \int_{-\infty}^{t_0} i(\xi)\mathrm{d}\xi + \int_{t_0}^{t} i(\xi)\mathrm{d}\xi = q(t_0) + q(t;t_0), \tag{2a}$$

$$\varphi(t) = \int_{-\infty}^{t} v(\xi)\mathrm{d}\xi = \int_{-\infty}^{t_0} v(\xi)\mathrm{d}\xi + \int_{t_0}^{t} v(\xi)\mathrm{d}\xi = \varphi(t_0) + \varphi(t;t_0). \tag{2b}$$

It is well known that charge and flux are internal state variables of the memristor in the voltage-current domain, and the internal state initial represents the memory property of the memristor. However, its state initial cannot appear explicitly in the state equation, so it is naturally impossible to assign its value accurately. Therefore, the memory of the memristor cannot be simulated effectively in the voltage-current domain. Compared with the two basic physical quantities of voltage and current, flux and charge can better represent the basic physical properties of circuit elements [138], which provide a theoretical basis for exploring the intrinsic properties of circuit elements. To this end, it is assumed that the voltage $v(t)$ and the current $i(t)$ on the memristor adopt the associated reference direction, and two different types of memristors are selected to build their flux-charge constitutive relation.

4.1. Flux-Charge Constitutive Relation of Charge-Controlled Memristor. For the charge-controlled memristor in Figure 4(a), the voltage-current relationship between the current $i(t)$ flowing through it and the voltage $v(t)$ at both ends of it in the voltage-current domain can be described as

$$v(t) = M(q_M)i(t), \tag{3}$$

where the memristive function $M(q_M)$ is the nonlinear function about charge $q_M(t)$ and has the same dimension as resistance; the unit is ohms (Ω). In this voltage-current model, $q_M(t)$ is the internal state variable of the memristor,

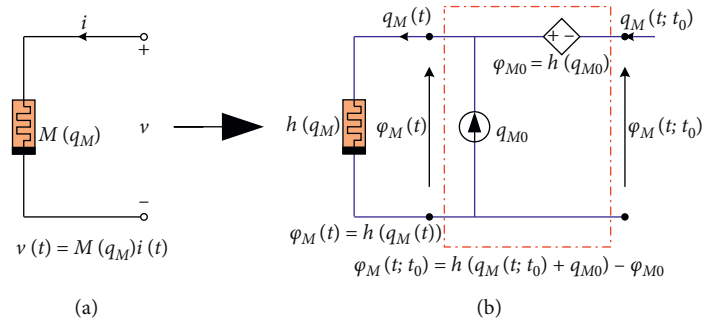

FIGURE 4: Charge-controlled memristor. The constitutive relation transformation from the voltage-current domain to the flux-charge domain: (a) voltage-current constitutive relation; (b) flux-charge constitutive relation.

and its state initial $q_M(t_0)$ represents the memory property of the memristor.

Compared with the voltage-current domain, we take charge and flux as state variables in the flux-charge domain; take the integral from $-\infty$ to t for both sides of equation (3), and combine with equation (1) to obtain the flux-charge constitutive relation of the charge-controlled memristor in the flux-charge domain as follows:

$$\varphi_M(t) = \int_{-\infty}^{t} v(\xi)\mathrm{d}\xi = \int_{-\infty}^{t} M(q_M) i(\xi)\mathrm{d}\xi = h(q_M(t)), \tag{4}$$

where the function $h(\bullet)$ is the nonlinear function about $q_M(t)$.

According to equations (2a) and (2b), equation (4) can be further rewritten as

$$\varphi_M(t;t_0) = h(q_M(t;t_0) + q_{M0}) - \varphi_{M0}, \tag{5}$$

where $\varphi_{M0} = \varphi_M(t_0)$ and $q_{M0} = q_M(t_0)$; equation (5) describes the memristor as a special nonlinear element whose memory is explicitly shown by the internal state initial q_{M0} [27], i.e., the internal state initial of the memristor can be explicitly expressed in the flux-charge domain, which is conducive to the quantitative analysis of state initial-dependent dynamical behavior. By comparing equation (5) with equation (3), it is not difficult to conclude that the state variable in the flux-charge domain is expressed by the incremental integral of the state variable in the voltage-current domain, and its state initial is zero, i.e., when $t = t_0$, $\varphi_M(t_0; t_0) = q_M(t_0; t_0) = 0$. Figure 4 visually shows the transformation of the charge-controlled memristor from voltage-current constitutive relation to flux-charge constitutive relation.

4.2. Flux-Charge Constitutive Relation of Flux-Controlled Memristor. For the flux-controlled memristor in Figure 5(a), the voltage-current relationship between the current flowing through it and the voltage at both ends of it in the voltage-current domain can be described as

$$i(t) = W(\varphi_W) v(t), \tag{6}$$

where φ_W is the internal state variable of the memristor and $W(\varphi_W)$ is the memductance function.

Similar to the charge-controlled memristor, charge and flux are used as state variables in the flux-charge domain. The integral of both sides of equation (6) from $-\infty$ to t is taken, and the flux-charge constitutive relation of the flux-controlled memristor in the flux-charge domain is obtained by combining with equation (1) as follows:

$$q_W(t) = \int_{-\infty}^{t} i(\xi)\mathrm{d}\xi = \int_{-\infty}^{t} W(\varphi_W) v(\xi)\mathrm{d}\xi = f(\varphi_W(t)), \tag{7}$$

where the function $f(\bullet)$ is the nonlinear function about $\varphi_W(t)$.Further, equation (7) can be written as

$$q_W(t;t_0) = f(\varphi_W(t;t_0) + \varphi_{W0}) - q_{W0}, \tag{8}$$

where $\varphi_{W0} = \varphi_W(t_0)$ and $q_{W0} = q_W(t_0)$. Similarly, the flux-controlled memristor can also be expressed as a special nonlinear element in the flux-charge domain, and its memory is reflected by the internal state initial φ_{W0}; and, when $t = t_0$, $\varphi_W(t_0; t_0) = q_W(t_0; t_0) = 0$. Figure 5(b) shows the flux-charge constitutive relation of the flux-controlled memristor.

5. Incremental Flux-Charge Analysis Method for Memristive Circuit

Bao et al. [22] pointed out that, in the voltage-current model, the memristor was a dynamic element, resulting in an increase in the order of the circuit equation. In the flux-charge model, the memristor was a nondynamic element, so the order of the circuit remains the same. Therefore, for the memristive circuit, when flux and charge are taken as state variables rather than voltage and current [25, 139], the memristor is described as a nondynamic element, which can reduce the dimension of the established mathematical model [12, 20, 30], from which the term "dimensionality reduction" is derived. It should be noted that the flux-charge model and the voltage-current model are different from each other in their algebraic equations, but they are equivalent representations in nonlinear dynamical behaviors. And, the implicit state initials of all dynamic components in the voltage-current model can be expressed as the explicit initial-related system parameters in the flux-charge model, which is convenient to realize the mechanism explanation of state initial-dependent dynamical behavior in the

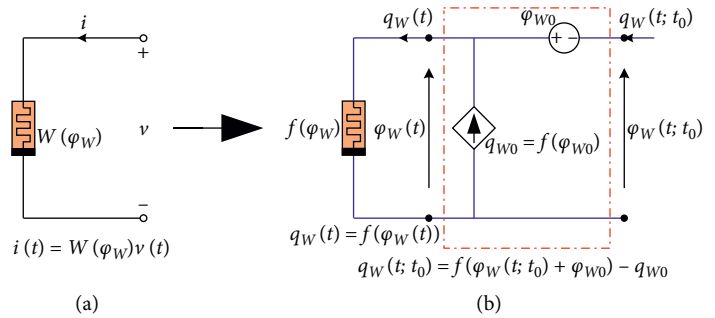

Figure 5: Flux-controlled memristor: the constitutive relation transformation from the voltage-current domain to the flux-charge domain; (a) voltage-current constitutive relation; (b) flux-charge constitutive relation.

memristive circuit, namely, to realize the multistability reconstitution [30]. In addition, dimensionality reduction modeling can reduce the complexity of quantitative analysis and numerical simulation, which has certain theoretical significance and engineering application value.

Bao et al. [130] proposed a two-memristor-based Chua's circuit, as shown in Figure 6, and revealed its state initial-dependent extreme multistability phenomenon. Based on the memristive circuit, Chen adopted the incremental flux-charge analysis method [31] and obtained the dimensionality reduction model in the flux-charge domain, which not only solved the special dynamic characteristics problem of the circuit which could not be quantitatively explained in the voltage-current domain but also made the system model simpler and more conducive to the analysis of its dynamical formation mechanism.

To be specific, this article mainly solved the following five problems:

(a) The 5-order dynamic circuit of the original system was described by a 3-dimensional system model, and the dimensionality reduction modeling was realized.

The two-memristor-based Chua's circuit [130] in the voltage-current domain was

$$\begin{cases} \dfrac{dV_1}{dt} = -\dfrac{1}{RC_1}(V_1 - V_2) + \dfrac{1}{R_bC_1}\left(1 - g_1V_4^2\right)V_1, \\ \dfrac{dV_2}{dt} = -\dfrac{k}{RC_2}(V_1 - V_2) + \dfrac{k}{R_dC_2}\left(1 - g_2V_5^2\right)V_2 - \dfrac{2k+1}{(k+1)R_1C_2}V_3, \\ \dfrac{dV_3}{dt} = -\dfrac{k+1}{RC_3}(V_1 - V_2) + \dfrac{k+1}{R_dC_3}\left(1 - g_2V_5^2\right)V_2 - \dfrac{2}{R_1C_3}V_3, \\ \dfrac{dV_4}{dt} = -\dfrac{1}{R_aC_4}V_1, \\ \dfrac{dV_5}{dt} = -\dfrac{1}{R_cC_5}V_2. \end{cases} \tag{9}$$

Its dimensionality reduction model [31] in the flux-charge domain was

$$\begin{cases} C_1\dfrac{d\varphi_1(t;t_0)}{dt} = \dfrac{1}{R}\left(-\varphi_1(t;t_0) + \varphi_2(t;t_0)\right) - q_4(t;t_0) + C_1V_1(t_0), \\ C_2\dfrac{d\varphi_2(t;t_0)}{dt} = \dfrac{k}{R}\left(-\varphi_1(t;t_0) + \varphi_2(t;t_0)\right) + kq_5(t;t_0) - \dfrac{2k+1}{(k+1)R_1}\varphi_3(t;t_0) + C_2V_2(t_0), \\ C_3\dfrac{d\varphi_3(t;t_0)}{dt} = \dfrac{k+1}{R}\left(-\varphi_1(t;t_0) + \varphi_2(t;t_0)\right) + (k+1)q_5(t;t_0) - \dfrac{2}{R_1}\varphi_3(t;t_0) + C_3V_3(t_0), \end{cases} \tag{10}$$

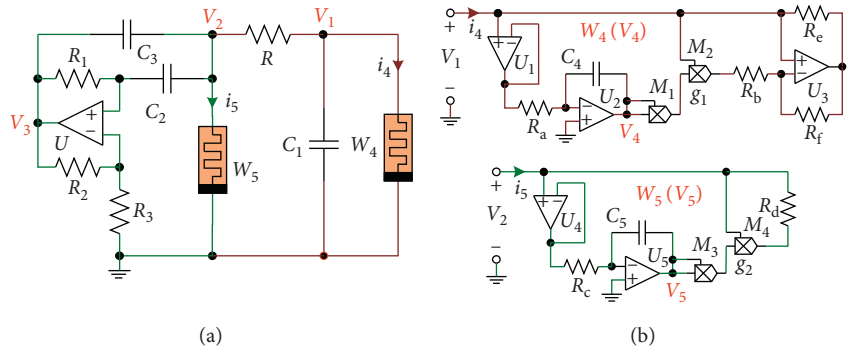

FIGURE 6: Two-memristor-based Chua's circuit: (a) circuit schematic of active BPF-based memristive Chua's circuit; (b) equivalent circuit for the memristors W_4 and W_5.

where

$$q_4(t;t_0) = -\frac{\varphi_1(t;t_0)}{R_b}\left[1 - \frac{g_1\varphi_1^2(t;t_0)}{3(R_aC_4)^2}\right] - \frac{\varphi_1(t;t_0)}{R_b}\left[-g_1V_4^2(t_0) + \frac{g_1V_4(t_0)}{R_aC_4}\varphi_1(t;t_0)\right],$$
$$q_5(t;t_0) = \frac{\varphi_2(t;t_0)}{R_d}\left[1 - \frac{g_2\varphi_2^2(t;t_0)}{3(R_cC_5)^2}\right] + \frac{\varphi_2(t;t_0)}{R_d}\left[-g_2V_5^2(t_0) + \frac{g_2V_5(t_0)}{R_cC_5}\varphi_2(t;t_0)\right]. \quad (11)$$

(b) Converted the plane equilibrium set of the original memristive circuit to three or five determined equilibria.

Original memristive circuit (9) had a plane equilibrium set $P = \{(V_1, V_2, V_3, V_4, V_5) | V_1 = V_2 = V_3 = 0\,\text{V}, V_4 = \mu\text{V}, V_5 = \eta\text{V}\}$, which led to two critical stable zero eigenvalues at the equilibrium set. Therefore, it was impossible to accurately determine the stability of equilibrium set, resulting in local inconsistency between the stability interval divided by the nonzero eigenvalues and the actual observed dynamical behavior. In flux-charge dimensionality reduction model (10), the plane equilibrium set was transformed into three or five determinate equilibria which were related to the initial-related system parameter $V_i(t_0)$ ($i = 1, 2, 3, 4,$ and 5), which eliminated the ill-posed zero eigenvalues of the original memristive circuit. According to the evolution characteristics of the determined equilibria with $V_i(t_0)$, the theoretical explanation of the inconsistency between the stability interval of the equilibrium set and the dynamical behavior of the original memristive circuit was given, and the state initial-dependent dynamical mechanism of the original memristive circuit was quantitatively expounded.

(c) Reasonable reasons for the significant change of dynamical behavior under the change of small state initial were expounded.

The state initial $V_1(t_0)$ of original memristive circuit (9) was fine-tuned from 10^{-9} to -10^{-9} (that is, the initial-related system parameter of dimensionality reduction model (10) was fine-tuned from 10^{-9} to -10^{-9}), and the dynamical behavior changed greatly. This phenomenon could not be reasonably explained in the voltage-current domain, but after dimensionality reduction modeling, it could be explained in the flux-charge domain according to the symmetry of dimensionality reduction model (10).

(d) Extreme multistability reconstitution was implemented.

The implicit state initial $V_i(t_0)$ of system (9) was explicitly expressed in dimensionality reduction model (10) as the initial-related system parameter. When the state initial of system (10) was set as (0, 0, 0), the kinetic map shown in [31] had the same dynamical behavior as the attraction basin shown in [130], intuitively illustrated dimensionality reduction model (10), perfectly reconstructed the state initial-dependent dynamical behavior of original memristive circuit (9), and realized the extreme multistability reconstitution.

(e) In the hardware circuit of the flux-charge model, the multistable mode control of the memristive circuit was realized by changing the initial-related system parameters.

6. Incremental Integral Transformation Method for Memristive System

On the basis of the incremental flux-charge analysis method, for the ideal memristor-based system, the incremental

integral transformation method was proposed in [21] to obtain an equivalent dimensionality reduction model. From the new state variable domain, the state initial-dependent extreme multistability of the original memristive system was studied quantitatively, so as to realize the reconstitution of the extreme multistability, and then, the theoretical basis of the dimensionality reduction reconstitution of the memristive system was given [110]. However, it should be noted that this method only applies to the simple ideal memristor-based system with only memristor nonlinear terms. But for the complex memristive system with other nonlinear terms besides the memristor nonlinear term [32], because it is difficult to obtain an explicit expression of the time integral of complex nonlinear terms, it is necessary to find appropriate intermediate variables and variable substitution to achieve the purpose of equivalent dimensionality reduction modeling. For this reason, the hybrid incremental integral transformation method was proposed in [32].

6.1. Incremental Integral Transformation Method for Simple Memristive System. For the simple ideal memristor-based system with only the memristor nonlinear term, the incremental integral transformation method is used to realize dimensionality reduction modeling and multistability reconstitution. Taking the memristive hyperjerk system as an example, the system has only one memristor nonlinear term with smooth hyperbolic tangent memductance [140], and its mathematical model is

$$\begin{cases} \dot{x}_1 = x_2, \\ \dot{x}_2 = x_3, \\ \dot{x}_3 = x_4, \\ \dot{x}_4 = \tanh(x_1)x_2 - x_3 - 0.5x_4. \end{cases} \tag{12}$$

According to the incremental integral transformation method [21], the dimensionality reduction model can be obtained as

$$\begin{cases} \dot{X}_2 = X_3 + \delta_2, \\ \dot{X}_3 = X_4 + \delta_3, \\ \dot{X}_4 = -X_3 - 0.5X_4 + \ln\ \cosh(X_2 + \delta_1) - \ln\ \cosh(\delta_1) + \delta_4. \end{cases} \tag{13}$$

The corresponding equilibrium is transformed from the line equilibrium set to two determined equilibria, and the state variables between the dimensionality reduction model and the original system have the following corresponding relationship:

$$\begin{aligned} x_1 &= X_2 + \delta_1, \\ x_2 &= X_3 + \delta_2, \\ x_3 &= X_4 + \delta_3, \\ x_4 &= \dot{X}_4. \end{aligned} \tag{14}$$

It should be noted that the system parameter δ_i ($i = 1$, 2, 3, and 4) of the dimensionality reduction model represents the state initial $x_i(0)$ ($i = 1$, 2, 3, and 4) of the original memristive system. Similar to the above incremental flux-charge analysis method, when the initial is set to (0, 0, 0), based on the dimensionality reduction model, the state initial-dependent extreme multistability reconstitution of the original memristive system can be realized.

6.2. Hybrid Incremental Integral Transformation Method for Complex Memristive System. For the ideal memristor-based system with other nonlinear terms besides the memristor nonlinear term, the hybrid incremental integral transformation method was proposed in [32], which successfully solved the dimensionality reduction modeling and multistability reconstitution problems of the memristive system with complex nonmemristor cubic nonlinear terms.

To be specific, this article mainly solved the following three problems:

(a) By introducing a new intermediate variable, the problem that the nonmemristor cubic nonlinear integral term could not be expressed by a simple relation was eliminated.

The mathematical model of a four-dimensional complex memristive system with a nonmemristor cubic nonlinear term [32] is described as

$$\begin{cases} \dot{x}_1 = x_2, \\ \dot{x}_2 = (1 - x_4)x_3, \\ \dot{x}_3 = x_1 - ax_2 - x_3 - bx_1^3, \\ \dot{x}_4 = -x_3. \end{cases} \tag{15}$$

Incremental integral transformation method [21] was adopted to carry out integral transformation on the system. By introducing an intermediate variable $W = b\int_0^t x_1^3 \mathrm{d}\tau$, the problem that this integral term could not be expressed as a simple relational expression was eliminated, and a four-dimensional intermediate transformation system with the same dimension as the original system was obtained, that is,

$$\begin{cases} \dot{X}_1 = X_2 + \delta_1, \\ \dot{X}_2 = 0.5X_3^2 + (1 - \delta_4)X_3 + \delta_2, \\ \dot{X}_3 = X_1 - aX_2 - X_3 - W + \delta_3, \\ \dot{W} = b(X_2 + \delta_1)^3. \end{cases} \tag{16}$$

(b) The variable substitution method was used to eliminate the divergence of state variables in the intermediate transformation system, and then, the dimensionality reduction modeling was realized.

Through variable substitution $Y_1 = X_1 - W$, $Y_2 = X_2$, and $Y_3 = X_3$, the divergence problem of state variables X_1 and W was eliminated, and the equivalent three-dimensional dimensionality reduction model of the system was obtained, i.e.,

$$\begin{cases} \dot{Y}_1 = Y_2 + \delta_1 - b(Y_2 + \delta_1)^3, \\ \dot{Y}_2 = 0.5Y_3^2 + (1 - \delta_4)Y_3 + \delta_2, \\ \dot{Y}_3 = Y_1 - aY_2 - Y_3 + \delta_3. \end{cases} \tag{17}$$

(c) The extreme multistability reconstitution of the memristive system with other nonlinear terms besides memristor nonlinear terms was realized.

The three line equilibria sets of the original system were transformed into six determinated equilibria, and the ill zero eigenvalue of the original system was eliminated. And, the state initial $x_i(t_0)$ ($i = 1, 2, 3,$ and 4), as the initial-related system parameter δ_i ($i = 1, 2, 3,$ and 4), was explicitly expressed in the dimensionality reduction model. When $Y_1(0)$, $Y_2(0)$, and $Y_3(0)$ were set to 0, dimensionality reduction system (17) could reconstruct the extreme multistability of original system (15).

6.3. Hidden Extreme Multistability Reconstitution. Different from the memristive system mentioned above, the nonautonomous FitzHugh–Nagumo (FHN) neuronal circuit was used to solve the problem of critical stability (i.e., hidden attractors) of the system [141]. By using dimensionality reduction modeling, it was proved that the attractors generated by the system were indeed hidden [70, 141]. This article mainly solved the following four problems:

(a) It made up for the gap that the nonautonomous memristive circuit produced extreme multistability.

A memristor with a smooth hyperbolic tangent nonlinear memductance was used to replace the nonsmooth piecewise linear memductance in the FHN neuron circuit in [94]; a nonautonomous memristive FHN neuron model that could produce extreme multistability was obtained.

(b) By using the incremental integral transformation method, the original 3-dimensional system was transformed into 2-dimensional dimensionality reduction. The nonautonomous memristive FHN neuron model is described as

$$\begin{cases} \dot{x}_1 = x_2 + 0.5\left(1 - \tanh\, x_3\right)x_1 + 1.8\, \cos\left(\tau\right), \\ \dot{x}_2 = -x_1 - x_2, \\ \dot{x}_3 = -x_1. \end{cases} \tag{18}$$

After the incremental integral transformation, the model of dimensionality reduction was obtained:

$$\begin{cases} \dot{X}_1 = X_2 + 0.5X_1 + 0.5\, \ln\ \cosh\left(X_1 - \delta_3\right) + 1.8\, \sin\left(\tau\right) + \delta_1 - 0.5\, \ln\ \cosh\left(\delta_3\right), \\ \dot{X}_2 = -X_1 - X_2 + \delta_2. \end{cases} \tag{19}$$

(c) The critical stability of the original system was transformed into the deterministic stability of the dimensionality reduction model.

The original system contained the nonautonomous term, which caused the system's equilibrium to change alternately between stable line equilibrium set and no equilibrium with time. The attractor generated by no equilibrium was hidden. However, due to the existence of zero eigenvalue, the line equilibrium set had critical stability, so it was impossible to determine whether the system produced hidden attractor. After dimensionality reduction modeling, no equilibrium and zero eigenvalue were eliminated, and the dimensionality reduction model only had certain equilibria which changed with time and were always stable, thus the equilibria had certain stability; it was proved that the attractors generated by the original system were indeed hidden.

(d) The hidden extreme multistability reconstitution of the nonautonomous memristive system was realized.

7. Synchronization Application of Memristor-Coupled System

Because of the nano-sized property, memristors are used to mimic biological neuronal synapses [142–145], which play important roles in the process of information transmission among the coupled neurons [146–149]. And, various memristor-coupled systems are studied, such as memristor-coupled Hindmarsh–Rose neurons [150] and memristor-coupled Hopfield neural network [151, 152].

It is all known that abundant collective behaviors appear in the actual neural system due to the interactions in neurons [153, 154]; among them, synchronization is the outstanding collective features in neuroscience [155–157], which is regarded as one of the mechanisms to propagate and to code information in brain [158, 159]. However, there are different kinds of brain disorder diseases, such as Alzheimer's, epilepsy, Parkinson's, and schizophrenia, which are involved with the abnormal activities of synchronization [160]. Therefore, neuron synchrony is a fundamental topic in neuroscience.

Different from the traditional nonlinear elements, the memristor is a special nonlinear element with internal state variables [1]. Therefore, using the memristor to couple the nonlinear system can easily generate special synchronization behaviors that depend on the initials of the memristor, which is completely different from the general nonlinear coupling system [161, 162]. In the general nonlinear coupled system, as long as the coupling strength is large enough, the master system and slave system starting from any state initials will always asymptotically achieve complete synchronization [163]. Naturally, in the nonmemristor-coupled system, some scholars have analyzed the initial influence on synchronization from the qualitative point of view and

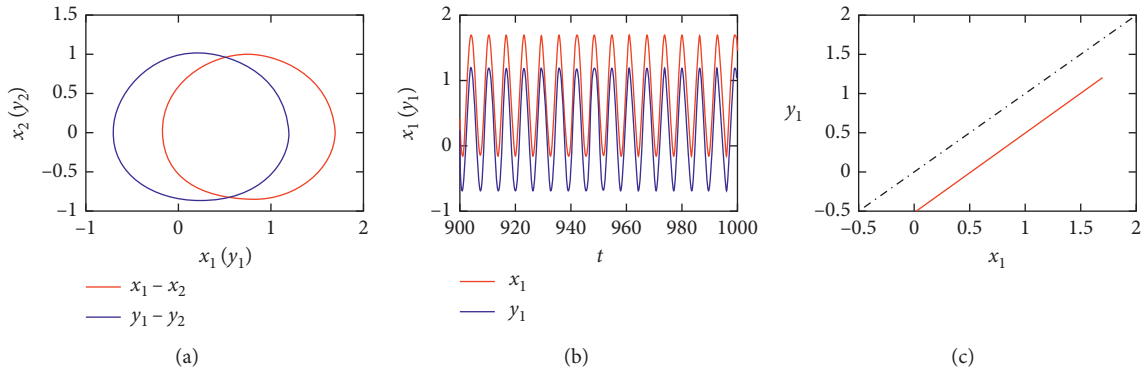

Figure 7: Periodic synchronizations with parallel offsets between the master system and slave system.

found that the synchronization stability depended on the state initial setting to some extent [35]. For memristor-coupled systems, various synchronization research studies have attracted important attention, and different influencing factors on synchronization were proposed. For examples, in [164], the effect of coupling strength on synchronization transition was investigated. In [165], the influence of coupling intensity and induction coefficient on phase synchronization was discussed. In [166], the effect of electromagnetic parameters on synchronization was studied. In [94], the effect of the coupling memristor parameter on synchronization was given. In [147, 167, 168], the robust analysis approach to asymptotic finite-time synchronization and interval matrix method of global exponential synchronization were proposed for investigations of the delayed memristive neural networks.

However, the dynamical effects of the state initials on synchronization in the memristor-coupled systems were rarely concerned in the published literatures [37, 169, 170]. The first reason is that the state initials are implicit parameters and cannot be expressed explicitly in the state equations. Secondly, such a result makes many researchers question it, because according to our previous understanding of synchronization, state initials are irrelevant to synchronization behavior [161, 162, 171]; however, now, it is said that state initials have influence on synchronization behavior, and their influence cannot be ignored; most scholars are doubtful about this conclusion. At the same time, if the conclusion is presented only by numerical analysis and other qualitative means, its credibility is undoubtedly not enough.

Interestingly, these problems can be solved by simplifying the mathematical models via using appropriate state variables or applying reasonable approximation and simplification [21, 37, 172, 173]. In [173], the initial effects on synchronization for the memristor-coupled system were quantitatively analyzed by the incremental flux-charge analysis method. Due to the inherent state initial mismatches between the two identical coupling systems, the two systems could not achieve complete synchronization under a large coupling strength [173], but synchronous motion with parallel offset could be realized, as shown in Figure 7. Based on the above dimensionality reduction reconstitution method, in the study of the synchronization of the memristor-coupled system, the inherent state initial mismatches between two identically coupled systems can be expressed as the initials-related parameter mismatches between two nonidentically coupled dimensionality reduction systems, and then, the quantitative theoretical research on the influence of the state initial on synchronization can be easily realized.

8. Summary and Prospect

The inherent memory property of the memristor makes the memristor-based circuit and system easy to produce the state initial-dependent dynamical behavior. Especially, the state initial-dependent extreme multistability phenomenon has been paid more and more attention by scholars, and abundant results have been obtained. Most of the existing literatures verify this special phenomenon through numerical simulation or circuit simulation, or capture different attractors randomly by closing and disconnecting the power supply in hardware experiments. The dimensionality reduction analysis method proposed in the literature theoretically realizes the precise prediction, quantitative analysis, and physical control of extreme multistability. For the ideal memristor-based circuit and system, the incremental flux-charge analysis method and incremental integral transformation method can effectively realize dimensionality reduction modeling and extreme multistability reconstitution of memristive circuits and systems, and then, physical control and mechanism exposition of extreme multistability can be realized through quantitative analysis. It can be seen from the existing research contents and results that although great progress has been made in the study of the state initial-dependent dynamical behavior of memristive circuits and systems, there are still many problems to be studied, mainly focusing on the following seven aspects: (a) prediction and control of the nonideal memristor-based circuit and system by state initial; (b) how to model the dimensionality reduction of the memristive circuit and system with high order or complex nonlinear terms; (c) study on the influence of state initial on the dynamical behavior of the memristor-coupled circuit and system and neural electrical networks; (d) for different types of complex memristive systems (such

as time-delay memristive system and fractional-order memristive system), how to carry out equivalent transformation and dimensionality reduction modeling, so as to realize the reconstitution of its state initial-dependent dynamical behaviors; (e) the multistability of the original memristive circuit and system can be reconstructed from the dimensionality reduction model constructed by the incremental flux-charge analysis method and incremental integral transformation method, only when the state initial is set as the origin. However, the dimensionality reduction model is usually a nonlinear system, and its state initial will have a great influence on the system. Therefore, when the state initial is set to nonzero, how to predict and control the multistability of the original memristive circuit and system; (f) at present, the dimensionality reduction methods are used to study continuous memristive systems, so how to study the multistability of discrete memristive systems is an urgent scientific problem to be solved; (g) it is also a scientific problem to be solved whether the extreme multistability system can be built with real memristor devices and tested experimentally to make the research method more practical.

Data Availability

The data used to support the findings of this study are available from the corresponding author upon request.

Conflicts of Interest

The authors declare that they have no conflicts of interest.

Acknowledgments

This research issue was supported by the Natural Science Foundation of Henan Province under Grant no. 202300410351, Key Scientific Research of Colleges and Universities in Henan Province under Grant no. 21A120007, and Key Technologies R&D Program of Henan Province under Grant no. 212102210084.

References

[1] L. O. Chua, "The fourth element," *Proceedings of the IEEE*, vol. 100, no. 6, pp. 1920–1927, 2012.

[2] J. Kengne, A. N. Negou, and D. Tchiotsop, "Antimonotonicity, chaos and multiple attractors in a novel autonomous memristor-based jerk circuit," *Nonlinear Dynamics*, vol. 88, no. 4, pp. 2589–2608, 2017.

[3] V. T. Pham, C. Volos, S. Jafari, X. Wang, and S. Vaidyanathan, "Hidden hyperchaotic attractor in a novel simple memristive neural network," *Optoelectronics and Advanced Materials, Rapid Communications*, vol. 8, no. 11-12, pp. 1157–1163, 2014.

[4] L. Zhou, C. H. Wang, and L. L. Zhou, "Generating four-wing hyperchaotic attractor and two-wing, three-wing, and four-wing chaotic attractors in 4D memristive system," *Internatinal Journal of Bifurcation and Chaos*, vol. 27, no. 2, Article ID 1750027, 2017.

[5] Q. Li, H. Zeng, and J. Li, "Hyperchaos in a 4D memristive circuit with infinitely many stable equilibria," *Nonlinear Dynamics*, vol. 79, no. 4, pp. 2295–2308, 2015.

[6] Q. Tan, Y. Zeng, and Z. Li, "A simple inductor-free memristive circuit with three line equilibria," *Nonlinear Dynamics*, vol. 94, no. 3, pp. 1585–1602, 2018.

[7] G. Y. Wang, F. Yuan, G. R. Chen, and Y. Zhang, "Coexisting multiple attractors and riddled basins of a memristive system," *Chaos*, vol. 28, Article ID 013125, 2018.

[8] G. Y. Peng, F. H. Min, and E. R. Wang, "Circuit implementation, synchronization of multistability, and image encryption of a four-wing memristive chaotic system," *Journal of Electrical and Computer Engineering*, vol. 2018, Article ID 8649294, 13 pages, 2018.

[9] B. Hu, Z.-H. Guan, G. Chen, and F. L. Lewis, "Multistability of delayed hybrid impulsive neural networks with application to associative memories," *IEEE Transactions on Neural Networks and Learning Systems*, vol. 30, no. 5, pp. 1537–1551, 2019.

[10] X. Chen, S. Qian, F. Yu et al., "Pseudorandom number generator based on three kinds of four-wing memristive hyperchaotic system and its application in image encryption," *Complexity*, vol. 2020, Article ID 8274685, 17 pages, 2020.

[11] F. Yu, Z. Zhang, H. Shen et al., "Design and FPGA implementation of a pseudo-random number generator based on a Hopfield neural network under electromagnetic radiation," *Frontiers in Physics*, vol. 9, Article ID 690651, 2021.

[12] M. Chen, M. Sun, B. Bao, H. Wu, Q. Xu, and J. Wang, "Controlling extreme multistability of memristor emulator-based dynamical circuit in flux-charge domain," *Nonlinear Dynamics*, vol. 91, no. 2, pp. 1395–1412, 2018.

[13] A. N. Pisarchik and U. Feudel, "Control of multistability," *Physics Reports*, vol. 540, no. 4, pp. 167–218, 2014.

[14] L. M. Pecora and T. L. Carroll, "Pseudoperiodic driving: eliminating multiple domains of attraction using chaos," *Physical Review Letters*, vol. 67, no. 8, pp. 945–948, 1991.

[15] T. L. Carroll and L. M. Pecora, "Using chaos to keep period-multiplied systems in phase," *Physical Review E*, vol. 48, no. 4, pp. 2426–2436, 1993.

[16] B. K. Goswami, "Controlled destruction of chaos in the multistable regime," *Physical Review E*, vol. 76, no. 1, Article ID 016219, 2007.

[17] A. N. Pisarchik and R. Jaimes-Reategui, "Control of basins of attraction in a multistable fiber laser," *Physics Letters A*, vol. 374, no. 2, pp. 228–234, 2009.

[18] S. Gadaleta and G. Dangelmayr, "Learning to control a complex multistable system," *Physical Review E*, vol. 63, no. 3, Article ID 036217, 2001.

[19] Y. Jiang, "Trajectory selection in multistable systems using periodic drivings," *Physics Letters A*, vol. 264, no. 1, pp. 22–29, 1999.

[20] M. Chen, B. C. Bao, T. Jiang et al., "Flux-charge analysis of initial state-dependent dynamical behaviors of a memristor emulator-based Chua's circuit," *International Journal of Bifurcation and Chaos*, vol. 28, no. 10, Article ID 1850120, 2018.

[21] M. Chen, Y. Feng, H. Bao et al., "State variable mapping method for studying initial-dependent dynamics in memristive hyper-jerk system with line equilibrium," *Chaos, Solitons & Fractals*, vol. 115, pp. 313–324, 2018.

[22] B. C. Bao, Z. Liu, and H. Leung, "Is memristor a dynamic element?" *Electronics Letters*, vol. 49, no. 24, pp. 1523–1525, 2013.

[23] B. C. Bao, C. L. Wang, H. G. Wu, and X. H. Qiao, "Dimensionality reduction modeling and characteristic analysis

of memristive circuit," *Acta Physica Sinica*, vol. 63, no. 2, Article ID 020504, 2014.

[24] B. C. Bao, F. W. Hu, Z. Liu, and J. P. Xu, "Mapping equivalent approach to analysis and realization of memristor based dynamical circuit," *Chinese Physics B*, vol. 23, no. 7, pp. 303–310, 2014.

[25] F. Yuan, G. Y. Wang, and X. W. Wang, "Chaotic oscillator containing memcapacitor and meminductor and its dimensionality reduction analysis," *Chaos*, vol. 27, no. 3, Article ID 033103, 2017.

[26] F. Corinto and M. Forti, "Memristor circuits: flux-charge analysis method," *IEEE Transactions on Circuits and Systems I: Regular Papers*, vol. 63, no. 11, pp. 1997–2009, 2016.

[27] F. Corinto and M. Forti, "Memristor circuits: bifurcations without parameters," *IEEE Transactions on Circuits and Systems I: Regular Papers*, vol. 64, no. 6, pp. 1540–1551, 2017.

[28] M. Di Marco, M. Forti, and L. Pancioni, "Memristor standard cellular neural networks computing in the flux-charge domain," *Neural Networks*, vol. 93, pp. 152–164, 2017.

[29] F. Corinto and M. Forti, "Complex dynamics in arrays of memristor oscillators via the flux–charge method," *IEEE Transactions on Circuits and Systems I: Regular Papers*, vol. 65, no. 3, pp. 1040–1050, 2017.

[30] H. Bao, T. Jiang, K. B. Chu, M. Chen, Q. Xu, and B. C. Bao, "Memristor-based canonical Chua's circuit: extreme multistability in voltage-current domain and its controllability in flux-charge domain," *Complexity*, vol. 2018, Article ID 5935637, 13 pages, 2018.

[31] M. Chen, M. X. Sun, H. Bao, Y. H. Hu, and B. C. Bao, "Flux-charge analysis of two-memristor-based Chua's circuit: dimensionality decreasing model for detecting extreme multistability," *IEEE Transactions on Industrial Electronics*, vol. 67, no. 3, pp. 2197–2206, 2019.

[32] M. Chen, Y. Feng, H. Bao, B. C. Bao, H. G. Wu, and Q. Xu, "Hybrid state variable incremental integral for reconstructing extreme multistability in memristive jerk system with cubic nonlinearity," *Complexity*, vol. 2019, Article ID 8549472, , 2019.

[33] A. S. Pikovsky, M. Rosenblum, and J. Kurths, *Synchronization: A Universal Concept in Nonlinear Sciences*, Cambridge University Press, Cambridge, UK, 2003.

[34] H. G. Wu, S. Y. Chen, and B. C. Bao, "Impulsive synchronization and initial value effect for a memristor-based chaotic system," *Acta Physica Sinica*, vol. 64, no. 3, Article ID 030501, 2015.

[35] F. Wu, P. Zhou, A. Alsaedi, T. Hayat, and J. Ma, "Synchronization dependence on initial setting of chaotic systems without equilibria," *Chaos, Solitons & Fractals*, vol. 110, pp. 124–132, 2018.

[36] F.-q. Wu, J. Ma, and G.-d. Ren, "Synchronization stability between initial-dependent oscillators with periodical and chaotic oscillation," *Journal of Zhejiang University-Science A*, vol. 19, no. 12, pp. 889–903, 2018.

[37] J. Zhang and X. Liao, "Effects of initial conditions on the synchronization of the coupled memristor neural circuits," *Nonlinear Dynamics*, vol. 95, no. 2, pp. 1269–1282, 2019.

[38] U. Feudel, "Complex dynamics in multistable systems," *International Journal of Bifurcation and Chaos*, vol. 18, no. 6, pp. 1607–1626, 2008.

[39] S. Jafari, A. Ahmadi, A. J. M. Khalaf, H. R. Abdolmohammadi, V. T. Pham, and F. E. Alsaadi, "A new hidden chaotic attractor with extreme multi-stability," *AEÜ-International Journal of Electronics and Communications*, vol. 89, pp. 131–135, 2018.

[40] F. Yu, L. Liu, H. Shen et al., "Multistability analysis, coexisting multiple attractors, and FPGA implementation of Yu-Wang four-wing chaotic system," *Complexity*, vol. 2020, Article ID 7530976, 16 pages, 2020.

[41] F. Yu, H. Shen, L. Liu et al., "CCII and FPGA realization: a multistable modified fourth-order autonomous Chua's chaotic system with coexisting multiple attractors," *Complexity*, vol. 2020, Article ID 5212601, 17 pages, 2020.

[42] F. Atteneave, "Multistability in perception," *Scientific American*, vol. 225, no. 6, pp. 62–71, 1971.

[43] F. T. Arecchi and F. Lisi, "Hopping mechanism generating 1f noise in nonlinear systems," *Physical Review Letters*, vol. 49, no. 2, pp. 94–98, 1982.

[44] F. T. Arecchi, R. Meucci, G. Puccioni, and J. Tredicce, "Experimental evidence of subharmonic bifurcations, multistability, and turbulence in a Q-switched gas laser," *Physical Review Letters*, vol. 49, no. 17, pp. 1217–1220, 1982.

[45] Q. Hui, W. M. Haddad, and J. M. Bailey, "Multistability, bifurcations, and biological neural networks: a synaptic drive firing model for cerebral cortex transition in the induction of general anesthesia," *Nonlinear Analysis: Hybrid Systems*, vol. 5, no. 3, pp. 554–572, 2011.

[46] A. Geltrude, K. A. Naimee, S. Euzzor, R. Meucci, F. T. Arecchi, and B. K. Goswami, "Feedback control of bursting and multistability in chaotic systems," *Communications in Nonlinear Science and Numerical Simulation*, vol. 17, no. 7, pp. 3031–3039, 2012.

[47] J. C. Sprott, X. Wang, and G. R. Chen, "Coexistence of point, periodic and strange attractors," *Internatinal Journal of Bifurcation and Chaos*, vol. 23, no. 5, Article ID 1350093, 2013.

[48] P. R. Sharma, M. D. Shrimali, A. Prasad, and U. Feudel, "Controlling bistability by linear augmentation," *Physics Letters A*, vol. 377, no. 37, pp. 2329–2332, 2013.

[49] C. B. Li and J. C. Sprott, "Multistability in a butterfly flow," *International Journal of Bifurcation and Chaos*, vol. 23, no. 12, pp. 1294–1296, 2014.

[50] C. B. Li and J. C. Sprott, "Multistability in the Lorenz system: a broken butterfly," *International Journal of Bifurcation and Chaos*, vol. 24, no. 10, Article ID 1450131, 2014.

[51] C. B. Li, W. Hu, J. C. Sprott, and X. Wang, "Multistability in symmetric chaotic systems," *The European Physical Journal Special Topics*, vol. 224, no. 5, pp. 1493–1506, 2015.

[52] A. P. Kuznetsov, S. P. Kuznetsov, E. Mosekilde, and N. V. Stankevich, "Co-existing hidden attractors in a radio-physical oscillator system," *Journal of Physics A: Mathematical and Theoretical*, vol. 48, no. 12, Article ID 125101, 2015.

[53] P. R. Sharma, M. D. Shrimali, A. Prasad, N. V. Kuznetsov, and G. A. Leonov, "Control of multistability in hidden attractors," *The European Physical Journal Special Topics*, vol. 224, no. 8, pp. 1485–1491, 2015.

[54] B. C. Bao, Q. D. Li, N. Wang, and Q. Xu, "Multistability in Chua's circuit with two stable node-foci," *Chaos*, vol. 26, no. 4, Article ID 043111, 2016.

[55] B. C. Bao, A. H. Hu, H. Bao, Q. Xu, M. Chen, and H. G. Wu, "Three-dimensional memristive Hindmarsh–Rose neuron model with hidden coexisting asymmetric behaviors," *Complexity*, vol. 2018, Article ID 3872573, 11 pages, 2018.

[56] M. S. Patel, U. Patel, A. Sen et al., "Experimental observation of extreme multistability in an electronic system of two coupled Rössler oscillators," *Physical Review E*, vol. 89, no. 2, Article ID 022918, 2014.

[57] C. Hens, S. K. Dana, and U. Feudel, "Extreme multistability: attractor manipulation and robustness," *Chaos*, vol. 25, no. 5, Article ID 053112, 2015.

[58] Y. Liu and Z. You, "Multi-stability and almost periodic solutions of a class of recurrent neural networks," *Chaos, Solitons & Fractals*, vol. 33, no. 2, pp. 554–563, 2007.

[59] C. N. Ngonghala, U. Feudel, and K. Showalter, "Extreme multistability in a chemical model system," *Physical Review E*, vol. 83, no. 5, Article ID 056206, 2011.

[60] C. R. Hens, R. Banerjee, U. Feudel, and S. K. Dana, "How to obtain extreme multistability in coupled dynamical systems," *Physical Review E*, vol. 85, no. 3, Article ID 035202, 2012.

[61] Z. T. Zhusubaliyev and E. Mosekilde, "Multistability and hidden attractors in a multilevel DC/DC converter," *Mathematics and Computers in Simulation*, vol. 109, pp. 32–45, 2015.

[62] M. Chen, J. Yu, and B. C. Bao, "Finding hidden attractors in improved memristor-based Chua's circuit," *Electronics Letters*, vol. 51, no. 6, pp. 462–464, 2015.

[63] G. A. Leonov, N. V. Kuznetsov, and V. I. Vagaitsev, "Localization of hidden Chua's attractors," *Physics Letters A*, vol. 375, no. 23, pp. 2230–2233, 2011.

[64] G. A. Leonov and N. V. Kuznetsov, "Hidden attractors in dynamical systems: from hidden oscillations in Hilbert-Kolmogorov, Aizerman, and Kalman problems to hidden chaotic attractor in Chua circuits," *International Journal of Bifurcation and Chaos*, vol. 23, no. 1, Article ID 1330002, 2013.

[65] N. V. Kuznetsov and G. A. Leonov, "Hidden attractors in dynamical systems: systems with no equilibria, multistability and coexisting attractors," *IFAC Proceedings Volumes*, vol. 47, no. 3, pp. 5445–5454, 2014.

[66] Q. D. Li, H. Z. Zeng, and X. S. Yang, "On hidden twin attractors and bifurcation in the Chua's circuit," *Nonlinear Dynamics*, vol. 77, no. 1-2, pp. 255–266, 2014.

[67] B. C. Bao, F. W. Hu, M. Chen, Q. Xu, and Y. J. Yu, "Self-excited and hidden attractors found simultaneously in a modified Chua's circuit," *International Journal of Bifurcation and Chaos*, vol. 25, no. 5, Article ID 1550075, 2015.

[68] V.-T. Pham, C. Volos, S. Jafari, and T. Kapitaniak, "Coexistence of hidden chaotic attractors in a novel no-equilibrium system," *Nonlinear Dynamics*, vol. 87, no. 3, pp. 2001–2010, 2017.

[69] S. Zhang and Y. Zeng, "A simple Jerk-like system without equilibrium: asymmetric coexisting hidden attractors, bursting oscillation and double full Feigenbaum remerging trees," *Chaos, Solitons & Fractals*, vol. 120, pp. 25–40, 2019.

[70] M. Chen, C. Wang, H. Bao, X. Ren, and B. C. Bao, "Reconstitution for interpreting hidden dynamics with stable equilibrium point," *Chaos, Solitons and Fractals*, vol. 140, Article ID 110188, 2020.

[71] H. Chang, Y. X. Li, G. R. Chen, and F. Yuan, "Extreme multistability and complex dynamics of a memristor-based chaotic system," *International Journal of Bifurcation and Chaos*, vol. 30, no. 8, Article ID 2030019, 2020.

[72] Z. Wei, A. Yousefpour, H. Jahanshahi, U. Erkin Kocamaz, and I. Moroz, "Hopf bifurcation and synchronization of a five-dimensional self-exciting homopolar disc dynamo using a new fuzzy disturbance-observer-based terminal sliding mode control," *Journal of the Franklin Institute*, vol. 358, no. 1, pp. 814–833, 2021.

[73] N. Wang, G. S. Zhang, N. V. Kuznetsov, and H. Bao, "Hidden attractors and multistability in a modified Chua's circuit," *Communication in Nonlinear Science and Numerical Simulation*, vol. 92, Article ID 105494, 2021.

[74] C. Du, L. Liu, Z. Zhang, and S. Yu, "A Coupling method of double memristors and analysis of extreme transient behavior," *Nonlinear Dynamics*, vol. 104, no. 1, pp. 765–787, 2021.

[75] X. L. An and S. Qiao, "The hidden, period-adding, mixed-mode oscillations and control in a HR neoron under electromagnetic induction," *Chaos, Solitons and Fractals*, vol. 143, Article ID 110587, 2021.

[76] H. Jahanshahi, O. O. Lopez, J. M. M. Pacheco et al., "Simulation and experimental validation of a non-equilibrium chaotic system," *Chaos, Solitons and Fractals*, vol. 143, Article ID 110539, 2021.

[77] T. M. Liu, H. Z. Yan, S. Banerjee, and J. Mou, "A Fractional-order chaotic system with hidden attractor and self-excited attractor and its DSP implementation," *Chaos, Solitons and Fractals*, vol. 145, Article ID 110791, 2021.

[78] D. Dudkowski, S. Jafari, T. Kapitaniak, N. V. Kuznetsov, G. A. Leonov, and A. Prasad, "Hidden attractors in dynamical systems," *Physics Reports*, vol. 637, pp. 1–50, 2016.

[79] S. Zhang, J. H. Zheng, X. P. Wang, and Z. G. Zeng, "A novel no-equilibrium HR neuron model with hidden homogeneous extreme multistability," *Chaos, Solitons and Fractals*, vol. 145, Article ID 110761, 2021.

[80] Y. Yang, L. L. Huang, J. H. Xiang, H. Bao, and H. Z. Li, "Design of multi-wing 3D chaotic systems with only stable equilibrium or no equilibrium point using rotation symmetry," *AEÜ-International Journal of Electronics and Communications*, vol. 135, Article ID 153710, 2021.

[81] V. T. Pham, S. Jafari, S. Vaidyanathan, C. Volos, and X. Wang, "A novel memristive neural network with hidden attractors and its circuitry implementation," *Science China Technological Sciences*, vol. 59, no. 3, pp. 358–363, 2016.

[82] L. O. Chua and S. M. Sung Mo Kang, "Memristive devices and systems," *Proceedings of the IEEE*, vol. 64, no. 2, pp. 209–223, 1976.

[83] B. C. Bao, J. P. Xu, and Z. Liu, "Initial state dependent dynamical behaviors in memristor based chaotic circuit," *Chinese Physics Letters*, vol. 27, no. 7, Article ID 070504, 2010.

[84] B. C. Bao, Z. H. Ma, J. P. Xu, Z. Liu, and Q. Xu, "A simple memristor chaotic circuit with complex dynamics," *International Journal of Bifurcation and Chaos*, vol. 21, no. 9, pp. 2629–2645, 2011.

[85] B. C. Bao, J. P. Xu, G. H. Zhou, Z. H. Ma, and L. Zou, "Chaotic memristive circuit: equivalent circuit realization and dynamical analysis," *Chinese Physics B*, vol. 20, no. 12, Article ID 120502, 2011.

[86] B. Bao, G. Shi, J. Xu, Z. Liu, and S. Pan, "Dynamics analysis of chaotic circuit with two memristors," *Science China Technological Sciences*, vol. 54, no. 8, pp. 2180–2187, 2011.

[87] B. C. Bao, X. Zhou, Z. Liu, and F. W. Hu, "Generalized memory element and chaotic memory system," *International Journal of Bifurcation and Chaos*, vol. 23, no. 8, Article ID 1350135, 2013.

[88] B. C. Bao, Q. Xu, H. Bao, and M. Chen, "Extreme multistability in a memristive circuit," *Electronics Letters*, vol. 52, no. 12, pp. 1008–1010, 2016.

[89] S. Jafari, A. Ahmadi, S. Panahi, and K. Rajagopal, "Extreme multi-stability: when imperfection changes quality," *Chaos, Solitons & Fractals*, vol. 108, pp. 182–186, 2018.

[90] D. B. Strukov, G. S. Snider, D. R. Stewart, and R. S. Williams, "The missing memristor found," *Nature*, vol. 453, no. 7191, pp. 80–83, 2008.

[91] S. Duan, X. Hu, Z. Dong, L. Wang, and P. Mazumder, "Memristor-based cellular nonlinear/neural network: design, analysis, and applications," *IEEE Transactions on Neural Networks and Learning Systems*, vol. 26, no. 6, pp. 1202–1213, 2015.

[92] Y. Babacan, F. Kaçar, and K. Gürkan, "A spiking and bursting neuron circuit based on memristor," *Neurocomputing*, vol. 203, pp. 86–91, 2016.

[93] B. Bao, T. Jiang, Q. Xu, M. Chen, H. Wu, and Y. Hu, "Coexisting infinitely many attractors in active band-pass filter-based memristive circuit," *Nonlinear Dynamics*, vol. 86, no. 3, pp. 1711–1723, 2016.

[94] J. Zhang and X. Liao, "Synchronization and chaos in coupled memristor-based Fitz Hugh-Nagumo circuits with memristor synapse," *AEU-International Journal of Electronics and Communications*, vol. 75, pp. 82–90, 2017.

[95] G. M. Tornez Xavier, F. Gómez Castañeda, L. M. Flores Nava, and J. A. Moreno Cadenas, "Memristive recurrent neural network," *Neurocomputing*, vol. 273, pp. 281–295, 2018.

[96] H. Bao, N. Wang, B. Bao, M. Chen, P. Jin, and G. Wang, "Initial condition-dependent dynamics and transient period in memristor-based hypogenetic jerk system with four line equilibria," *Communications in Nonlinear Science and Numerical Simulation*, vol. 57, pp. 264–275, 2018.

[97] C. Qin, K. H. Sun, and S. B. He, "Characterstic analysis of fractional-order memristor-based hypogenetic jerk system and its DSP implementation," *Electronics*, vol. 10, no. 7, Article ID 841, 2021.

[98] B. A. Mezatio, M. T. Motchongom, B. R. Wafo Tekam, R. Kengne, R. Tchitnga, and A. Fomethe, "A novel memristive 6D hyperchaotic autonomous system with hidden extreme multistability," *Chaos, Solitons & Fractals*, vol. 120, pp. 100–115, 2019.

[99] W. Wang, Y. C. Zeng, and R. T. Sun, "Research on a six-order chaotic circuit with three memristors," *Acta Physica Sinica*, vol. 66, no. 4, Article ID 040502, 2017.

[100] B. C. Bao, M. A. Peol, H. Bao, M. Chen, H. Z. Li, and B. Chen, "No-argument memristive hyper-jerk system and its coexisting chaotic bubbles boosted by initial conditions," *Chaos, Solitons and Fractals*, vol. 144, Article ID 110744, 2021.

[101] Q. Xu, Y. Lin, B. Bao, and M. Chen, "Multiple attractors in a non-ideal active voltage-controlled memristor based Chua's circuit," *Chaos, Solitons & Fractals*, vol. 83, pp. 186–200, 2016.

[102] M. Chen, Q. Xu, Y. Lin, and B. Bao, "Multistability induced by two symmetric stable node-foci in modified canonical Chua's circuit," *Nonlinear Dynamics*, vol. 87, no. 2, pp. 789–802, 2017.

[103] B. C. Bao, H. Bao, N. Wang, M. Chen, and Q. Xu, "Hidden extreme multistability in memristive hyperchaotic system," *Chaos, Solitons & Fractals*, vol. 94, pp. 102–111, 2017.

[104] Z. Wang, A. Akgul, V.-T. Pham, and S. Jafari, "Chaos-based application of a novel no-equilibrium chaotic system with coexisting attractors," *Nonlinear Dynamics*, vol. 89, no. 3, pp. 1877–1887, 2017.

[105] J. Kengne, Z. N. Tabekoueng, V. K. Tamba, and A. N. Negou, "Periodicity, chaos, and multiple attractors in a memristor-based Shinriki's circuit," *Chaos*, vol. 25, no. 10, Article ID 103126, 2015.

[106] G. Y. Wang, C. B. Shi, X. W. Wang, and F. Yuan, "Coexisting oscillation and extreme multistability for a memcapacitor-based circuit," *Mathematical Problems in Engineering*, vol. 2017, Article ID 6504969, 13 pages, 2017.

[107] F. Yuan, G. Y. Wang, and X. W. Wang, "Extreme multistability in a memristor-based Chua's multi-scroll hyperchaotic system," *Chaos*, vol. 26, no. 7, Article ID 073107, 2016.

[108] Y. M. Lu and F. H. Min, "Dynamic analysis of symmetric behavior in flux-controlled memristor circuit based on field programmable gate array," *Acta Physica Sinica*, vol. 68, no. 13, Article ID 130502, 2019.

[109] H. M. Li, Y. F. Yang, W. Li, S. B. He, and C. L. Li, "Extremely rich dynamics in a memristor-based chaotic system," *European Physical Journal Plus*, vol. 135, no. 7, Article ID 579, 2020.

[110] Y. Zhang, Z. Liu, H. Wu, S. Chen, and B. Bao, "Two-memristor-based chaotic system and its extreme multistability reconstitution via dimensionality reduction analysis," *Chaos, Solitons & Fractals*, vol. 127, pp. 354–363, 2019.

[111] C. Li, J. C. Sprott, and Y. Mei, "An infinite 2-D lattice of strange attractors," *Nonlinear Dynamics*, vol. 89, no. 4, pp. 2629–2639, 2017.

[112] C. Li, W. Joo-Chen Thio, J. C. Sprott, H. H.-C. Iu, and Y. Xu, "Constructing infinitely many attractors in a programmable chaotic circuit," *IEEE Access*, vol. 6, pp. 29003–29012, 2018.

[113] C. Li and J. C. Sprott, "An infinite 3-D quasiperiodic lattice of chaotic attractors," *Physics Letters A*, vol. 382, no. 8, pp. 581–587, 2018.

[114] H. G. Wu, Y. Ye, B. C. Bao, M. Chen, and Q. Xu, "Memristor initial boosting behaviors in a two-memristor-based hyperchaotic system," *Chaos, Solitons & Fractals*, vol. 121, pp. 178–185, 2019.

[115] L. Chua, "Memristor-the missing circuit element," *IEEE Transactions on Circuit Theory*, vol. 18, no. 5, pp. 507–519, 1971.

[116] L. Chua, "Resistance switching memories are memristors," *Applied Physics A*, vol. 102, no. 4, pp. 765–783, 2011.

[117] B. C. Bao, Q. Xu, and H. Bao, *Memristive Circuit and Multistability*, Science Press, Beijing, China, 2018.

[118] B. Muthuswamy, "Implementing memristor based chaotic circuits," *International Journal of Bifurcation and Chaos*, vol. 20, no. 5, pp. 1335–1350, 2010.

[119] H. H. C. Iu, D. S. Yu, A. L. Fitch, V. Sreeram, and H. Chen, "Controlling chaos in a memristor based circuit using a twin-T notch filter," *IEEE Transactions on Circuits and Systems I: Regular Papers*, vol. 58, no. 6, pp. 1337–1344, 2011.

[120] H. G. Wu, B. C. Bao, Z. Liu, Q. Xu, and P. Jiang, "Chaotic and periodic bursting phenomena in a memristive Wien-bridge oscillator," *Nonlinear Dynamics*, vol. 83, no. 1-2, pp. 893–903, 2016.

[121] B. C. Bao, P. Wu, H. Bao, M. Chen, and Q. Xu, "Chaotic bursting in memristive diode bridge-coupled Sallen-key lowpass filter," *Electronics Letters*, vol. 53, no. 16, pp. 1104-1105, 2017.

[122] Q. Quan Xu, N. Wang, B. C. Ning Wang, M. Bocheng Bao, C. D. Mo Chen, and C. Li, "A feasible memristive Chua's circuit via bridging a generalized memristor," *Journal of Applied Analysis & Computation*, vol. 6, no. 4, pp. 1152–1163, 2016.

[123] M. Chen, J. Yu, Q. Yu, C. Li, and B. Bao, "A memristive diode bridge-based canonical Chua's circuit," *Entropy*, vol. 16, no. 12, pp. 6464–6476, 2014.

[124] B. C. Bao, P. Y. Wu, H. Bao, Q. Xu, and M. Chen, "Numerical and experimental confirmations of quasi-periodic behavior and chaotic bursting in third-order autonomous memristive oscillator," *Chaos, Solitons & Fractals*, vol. 106, pp. 161–170, 2018.

[125] L. O. Chua, "Nonlinear circuit foundations for nanodevices, part I: the four-element torus," *Proceedings of the IEEE*, vol. 9, no. 11, pp. 1830–1859, 2003.

[126] R. Williams, "How we found the missing memristor," *IEEE Spectrum*, vol. 45, no. 12, pp. 28–35, 2008.

[127] D. Biolek, V. Biolkova, and Z. Biolek, "Pinched hysteretic loops of ideal memristors, memcapacitors and meminductors must be "self-crossing"" *Electronics Letters*, vol. 47, no. 25, pp. 1385–1387, 2011.

[128] S. P. Adhikari, M. P. Sah, H. Kim, and L. O. Chua, "Three fingerprints of memristor," *IEEE Transactions on Circuits and Systems I: Regular Papers*, vol. 60, no. 11, pp. 3008–3021, 2013.

[129] Y. Lin, W. B. Liu, and Q. Shen, "Bi-stability in a fifth-order voltage-controlled memristor-based Chua's chaotic circuit," *Acta Physica Sinica*, vol. 67, no. 23, Article ID 230502, 2018.

[130] B. Bao, T. Jiang, G. Wang, P. Jin, H. Bao, and M. Chen, "Two-memristor-based Chua's hyperchaotic circuit with plane equilibrium and its extreme multistability," *Nonlinear Dynamics*, vol. 89, no. 2, pp. 1157–1171, 2017.

[131] L. Wang, S. Zhang, Y. C. Zeng, and Z. J. Li, "Generating hidden extreme multistability in memristive chaotic oscillator via micro-perturbation," *Electronics Letters*, vol. 54, no. 13, pp. 808–810, 2018.

[132] T. Fozin Fonzin, J. Kengne, and F. B. Pelap, "Dynamical analysis and multistability in autonomous hyperchaotic oscillator with experimental verification," *Nonlinear Dynamics*, vol. 93, no. 2, pp. 653–669, 2018.

[133] S. Morfu, B. Nofiele, and P. Marquié, "On the use of multistability for image processing," *Physics Letters A*, vol. 367, no. 3, pp. 192–198, 2007.

[134] G. Peng and F. Min, "Multistability analysis, circuit implementations and application in image encryption of a novel memristive chaotic circuit," *Nonlinear Dynamics*, vol. 90, no. 3, pp. 1607–1625, 2017.

[135] J. Sun, Q. Yang, and Y. Wang, "Dynamical analysis of novel memristor chaotic system and DNA encryption application," *Iranian Journal of Science and Technology, Transactions of Electrical Engineering*, vol. 44, no. 1, pp. 449–460, 2020.

[136] S. Zhang, J. H. Zheng, X. P. Wang, and Z. G. Zeng, "Multi-scroll hidden attractor in memristive HR neuron model under electromagnetic radiation and its applications," *Chaos*, vol. 31, no. 1, Article ID 011101, 2021.

[137] Q. Lai, Z. Wan, A. Akgul, O. F. Boyraz, and M. Z. Yildiz, "Design and implementation of a new memristive chaotic system with application in touchless fingerprint encryption," *Chinese Journal of Physics*, vol. 67, pp. 615–630, 2020.

[138] F. Z. Wang, "A triangular periodic table of elementary circuit elements," *IEEE Transactions on Circuits and Systems I: Regular Papers*, vol. 60, no. 3, pp. 616–623, 2013.

[139] J. Mou, K. Sun, J. Ruan, and S. He, "A nonlinear circuit with two memcapacitors," *Nonlinear Dynamics*, vol. 86, no. 3, pp. 1735–1744, 2016.

[140] Y. Z. Zhang, Z. Liu, H. G. Wu, S. Y. Chen, and B. C. Bao, "Extreme multistability in memristive hyper-jerk system and stability mechanism analysis using dimensionality reduction model," *European Physical Journal Special Topic*, vol. 228, no. 10, pp. 1995–2009, 2019.

[141] H. Bao, W. Liu, and M. Chen, "Hidden extreme multistability and dimensionality reduction analysis for an improved non-autonomous memristive FitzHugh-Nagumo circuit," *Nonlinear Dynamics*, vol. 96, no. 3, pp. 1879–1894, 2019.

[142] C. K. Volos, I. M. Kyprianidis, I. M. Kyprianidis, I. N. Stouboulos, E. Tlelo-Cuautle, and S. Vaidyanathan, "Memristor: a new concept in synchronization of coupled neuromorphic circuits," *Journal of Engineering Science and Technology Review*, vol. 8, no. 2, pp. 157–173, 2015.

[143] Y. Xu, Y. Jia, J. Ma, T. Hayat, and A. Alsaedi, "Collective response in electrical activities of neurons under field coupling," *Scientific Reports*, vol. 8, no. 1, Article ID 1349, 2018.

[144] M. Ge, Y. Jia, Y. Xu, and L. Yang, "Mode transition in electrical activities of neuron driven by high and low frequency stimulus in the presence of electromagnetic induction and radiation," *Nonlinear Dynamics*, vol. 91, no. 1, pp. 515–523, 2018.

[145] Z. Wang, S. Joshi, S. E. Savel'ev et al., "Memristors with diffusive dynamics as synaptic emulators for neuromorphic computing," *Nature Materials*, vol. 16, no. 1, pp. 101–108, 2017.

[146] H. Kim, M. P. Sah, C. Yang, T. Roska, and L. O. Chua, "Memristor bridge synapses," *Proceedings of the IEEE*, vol. 100, no. 6, pp. 2061–2070, 2012.

[147] X. S. Yang, J. D. Cao, and J. L. Liang, "Exponential synchronization of memristive neural networks with delays: interval matrix method," *IEEE Transactions on Neural Networks and Learning Systems*, vol. 28, no. 8, pp. 1878–1888, 2016.

[148] C. H. Wang, H. R. Lin, J. R. Sun, L. Zhou, C. Zhou, and Q. L. Deng, "Research progress on chaos, memory and neural network circuits based on memristor," *Journal of Electronics and Information Technology*, vol. 42, no. 4, pp. 795–810, 2020.

[149] D. Ma, G. Wang, C. Han, Y. Shen, and Y. Liang, "A memristive neural network model with associative memory for modeling affections," *IEEE Access*, vol. 6, pp. 61614–61622, 2018.

[150] H. Bao, W. Liu, and A. Hu, "Coexisting multiple firing patterns in two adjacent neurons coupled by memristive electromagnetic induction," *Nonlinear Dynamics*, vol. 95, no. 1, pp. 43–56, 2019.

[151] C. Chen, J. Chen, H. Bao, M. Chen, and B. Bao, "Coexisting multi-stable patterns in memristor synapse-coupled Hopfield neural network with two neurons," *Nonlinear Dynamics*, vol. 95, no. 4, pp. 3385–3399, 2019.

[152] M. Chen, C. J. Chen, B. C. Bao, and Q. Xu, "Initial sensitive dynamics in memristor synapse-coupled Hopfield neural network," *Journal of Electronics and Information Technology*, vol. 42, no. 4, pp. 870–877, 2020.

[153] S. Mostaghimi, F. Nazarimehr, S. Jafari, and J. Ma, "Chemical and electrical synapse-modulated dynamical properties of coupled neurons under magnetic flow," *Applied Mathematics and Computation*, vol. 348, pp. 42–56, 2019.

[154] K. Wu, T. Wang, C. Wang, T. Du, and H. Lu, "Study on electrical synapse coupling synchronization of Hindmarsh-Rose neurons under Gaussian white noise," *Neural Computing and Applications*, vol. 30, no. 2, pp. 551–561, 2018.

[155] M. Ge, Y. Jia, J. B. Kirunda et al., "Propagation of firing rate by synchronization in a feed-forward multilayer Hindmarsh-Rose neural network," *Neurocomputing*, vol. 320, pp. 60–68, 2018.

[156] G. Ren, Y. Xu, and C. Wang, "Synchronization behavior of coupled neuron circuits composed of memristors," *Nonlinear Dynamics*, vol. 88, no. 2, pp. 893–901, 2017.

[157] W. Yao, C. Wang, J. Cao, Y. Sun, and C. Zhou, "Hybrid multisynchronization of coupled multistable memristive neural networks with time delays," *Neurocomputing*, vol. 363, pp. 281–294, 2019.

[158] R. Eckhorn, "Neural mechanisms of scene segmentation: recordings from the visual cortex suggest basic circuits for linking field models," *IEEE Transactions on Neural Networks*, vol. 10, no. 3, pp. 464–479, 1999.

[159] R. Bartsch, J. W. Kantelhardt, T. Penzel, and S. Havlin, "Experimental evidence for phase synchronization transitions in the human cardiorespiratory system," *Physical Review Letters*, vol. 98, Article ID 54102, 2007.

[160] P. J. Uhlhaas and W. Singer, "Neural synchrony in brain disorders: relevance for cognitive dysfunctions and pathophysiology," *Neuron*, vol. 52, no. 1, pp. 155–168, 2006.

[161] F. Yu, L. Liu, B. Y. He et al., "Analysis and FPGA realization of a novel 5D hyperchaotic four-wing memristive system, active control synchronization, and secure communication application," *Complexity*, vol. 2019, Article ID 4047957, 18 pages, 2019.

[162] F. Yu, L. Liu, H. Shen et al., "Dynamic analysis, circuit design and synchronization of a novel 6D memristive four-wing hyperchaotic system with multiple coexisting attractors," *Complexity*, vol. 2020, Article ID 5904607, 17 pages, 2020.

[163] S. Boccaletti, J. Kurths, G. Osipov, D. L. Valladares, and C. S. Zhou, "The synchronization of chaotic systems," *Physical Reports*, vol. 366, no. 1, pp. 1–101, 2002.

[164] Q. Y. Wang, Z. S. Duan, Z. S. Feng, G. R. Chen, and Q. S. Lu, "Synchronization transition in gap-junction-coupled leech neurons," *Physica A*, vol. 387, no. 16-17, pp. 4404–4410, 2008.

[165] Y. Xu, Y. Jia, J. Ma, A. Alsaedi, and B. Ahmad, "Synchronization between neurons coupled by memristor," *Chaos, Solitons & Fractals*, vol. 104, pp. 435–442, 2017.

[166] F. Xu, J. Zhang, T. Fang, S. Huang, and M. Wang, "Synchronous dynamics in neural system coupled with memristive synapse," *Nonlinear Dynamics*, vol. 92, no. 3, pp. 1395–1402, 2018.

[167] X. S. Yang and D. W. C. Ho, "Synchronization of delayed memristive neural networks: robust analysis approach," *IEEE Transactions on Cybernetics*, vol. 46, no. 12, pp. 3377–3387, 2015.

[168] X. Xiong, R. Tang, and X. Yang, "Finite-time synchronization of memristive neural networks with proportional delay," *Neural Processing Letters*, vol. 50, no. 2, pp. 1139–1152, 2018.

[169] H. Bao, Y. Zhang, W. Liu, and B. Bao, "Memristor synapse-coupled memristive neuron network: synchronization transition and occurrence of chimera," *Nonlinear Dynamics*, vol. 100, no. 1, pp. 937–950, 2020.

[170] B. Bao, Q. Yang, D. Zhu, Y. Zhang, Q. Xu, and M. Chen, "Initial-induced coexisting and synchronous firing activities in memristor synapse-coupled Morris-Lecar bi-neuron network," *Nonlinear Dynamics*, vol. 99, no. 3, pp. 2339–2354, 2020.

[171] Q. Lai, Z. Q. Wan, P. D. K. Kuate, and H. Fotsin, "Coexisting attractors, circuit implementation and synchronization control of a new chaotic system evolved from the simplest memristor chaotic circuit," *Communications in Nonlinear Science and Numerical Simulation*, vol. 89, Article ID 105341, 2020.

[172] F. Min, C. Li, L. Zhang, and C. Li, "Initial value-related dynamical analysis of the memristor-based system with reduced dimensions and its chaotic synchronization via adaptive sliding mode control method," *Chinese Journal of Physics*, vol. 58, pp. 117–131, 2019.

[173] Y. Zhang, Z. Liu, H. Wu, S. Chen, and B. Bao, "Dimensionality reduction analysis for detecting initial effects on synchronization of memristor-coupled system," *IEEE Access*, vol. 7, no. 1, pp. 109689–109698, 2019.

Hindawi
Complexity
Volume 2021, Article ID 2437737, 9 pages
https://doi.org/10.1155/2021/2437737

Research Article

Chimera State in the Network of Fractional-Order FitzHugh–Nagumo Neurons

Janarthanan Ramadoss,[1] Sajedeh Aghababaei,[2] Fatemeh Parastesh,[2] Karthikeyan Rajagopal,[3] Sajad Jafari,[2,4] and Iqtadar Hussain[5]

[1]*Centre for Artificial Intelligence, Chennai Institute of Technology, Malayambakkam, India*
[2]*Department of Biomedical Engineering, Amirkabir University of Technology, No. 350, Hafez Ave, Valiasr Square, Tehran 159163-4311, Iran*
[3]*Centre for Nonlinear Systems, Chennai Institute of Technology, Malayambakkam, India*
[4]*Health Technology Research Institute, Amirkabir University of Technology, No. 350, Hafez Ave, Valiasr Square, Tehran 159163-4311, Iran*
[5]*Department of Mathematics, Statistics and Physics, Qatar University, Doha 2713, Qatar*

Correspondence should be addressed to Karthikeyan Rajagopal; rkarthiekeyan@gmail.com

Received 13 May 2021; Accepted 21 June 2021; Published 30 June 2021

Academic Editor: Guillermo Huerta Cuellar

The fractional calculus in the neuronal models provides the memory properties. In the fractional-order neuronal model, the dynamics of the neuron depends on the derivative order, which can produce various types of memory-dependent dynamics. In this paper, the behaviors of the coupled fractional-order FitzHugh–Nagumo neurons are investigated. The effects of the coupling strength and the derivative order are under consideration. It is revealed that the level of the synchronization is decreased by decreasing the derivative order, and the chimera state emerges for stronger couplings. Furthermore, the patterns of the formed chimeras rely on the order of the derivatives.

1. Introduction

Fractional-order models have attracted much attention from scientists in different fields such as physics and electronics [1–5]. Considering the fractional derivative, a memory feature is added to the systems. Therefore, the fractional-order model can provide a more precise description of the real phenomena than the integer-order [6]. Furthermore, the fractional calculus has found wide applications in controlling the integer-order systems [7]. The fractional derivative also plays important role in demonstrating different firing patterns of the neurons [8]. Consequently, several fractional neuron models have been presented [9–11].

The complicated interactions among the neurons cause the neural system to act as a complex network [12]. The emergence of collective behaviors is an important characteristic of complex networks [13]. Some examples of collective behaviors are synchronization [14], chimera state [15], and solitary state [16]. Synchronization is an important phenomenon in many applications [17]. Many studies have focused on the synchronization of chaotic systems [18–23]. Furthermore, synchronization manages many neural functions and participates in many brain disorders [24]. In special cases, synchrony and asynchrony are observed simultaneously in a specific region of the brain. For example, the unihemispheric sleep, the neural bump state, and the epileptic seizure disease can be mentioned [25]. This particular condition is called the chimera state [26]. After the foundation of chimera state in 2002 [27], it became the focus of many researchers in a variety of dynamical systems such as the mechanical [28], optical [29], and chemical [30] oscillators and neuronal models [25, 31, 32]. Furthermore, these studies have represented the chimeras with different

spatiotemporal patterns and properties, including the amplitude chimera [33] and traveling chimera [34].

In neuronal studies, the chimeras were under consideration from different perspectives such as the neurons' dynamics, network topology, and coupling scheme. Santos et al. [35] investigated the chimera in 2D networks with regular and fractal topologies and found the spiral chimeras with multiple asynchronous cores. Wang et al. [36] reported the existence of chimera state in the hyperchaotic neurons with hyperchaotic dynamics. Blondeau Soh et al. [37] represented that shifting the neighbors in the coupling leads the network towards the chimera state. Provata and Venetis [38] studied a neuronal network with power-law coupling and showed that the chimera exists in the weak couplings with large exponents. Li et al. [39] considered two unidirectionally coupled layers of neurons and showed different collective behaviors in the master layer and the induced imperfect chimera state in the slave layer.

Among the chimera studies in neuronal networks, a few have considered the fractional models. Vázquez-Guerrero et al. [40] showed that the network of fractional Hindmarsh–Rose neurons is capable of representing chimera state. They also presented a fractional adaptive controller to obtain the synchronization. In another study, they designed an observer to synchronize the chimera state in coupled fractional neurons [41]. He [42] investigated the magnetic Hindmarsh–Rose model with fractional derivative and showed that analyzing the complexity of the network can help in recognition of its dynamical behavior. In this paper, we study the dynamical behaviors of a network of fractional-order FitzHugh–Nagumo systems. The effects of the order of derivatives and the coupling strength on the chimera state are under consideration.

2. The Model

Recently, the scientists have focused on proposing new models for describing the neural behaviors with considering different aspects of neurons [43, 44]. Here, we use the FitzHugh–Nagumo (FHN) model with considering the fractional derivative as follows [45]:

$$\begin{aligned}\frac{\mathrm{d}^q u}{\mathrm{d}t^q} &= u - \frac{u^3}{3} - v + I,\\ \frac{\mathrm{d}^q v}{\mathrm{d}t^q} &= 0.08\,(u + 0.7 - 0.8v),\end{aligned} \tag{1}$$

where u and v are the membrane voltage and the recovery variable and I is the external excitation current fixed at 0.5. The fractional derivative order is denoted by q, and $\mathrm{d}^q/\mathrm{d}t^q$ is the Caputo–Fabrizio (CF) fractional operator defined by

$$\frac{\mathrm{d}^q}{\mathrm{d}t^q} u(t) = \frac{1}{\Gamma(1-q)} \int_{t_0}^{t} \frac{\dot{x}(\tau)}{(t-\tau)^q}\,\mathrm{d}\tau, \quad 0 < q < 1, \tag{2}$$

where Γ is the Gamma function. The dynamics of the model relies on the values of the derivative order. Figure 1(a) represents the bifurcation of the model according to q. To consider the spiking firing for the model, the range of $0.7 < q < 1$ is selected in all simulations. The time series and phase spaces of the model for $q = 1$, 0.9, 0.8, and 0.7 are shown in Figures 1(b)–1(e). It is observed that by decreasing q, the amplitude of the oscillations decreases and the period increases.

We consider the network of fractional FHN neurons with the following equations:

$$\begin{aligned}\frac{\mathrm{d}^q u_i}{\mathrm{d}t^q} &= u_i - \frac{u_i^3}{3} - v_i + I + d\sum_{j=1}^{N} G_{ij}\left[b_{uu}\left(u_j - u_i\right) + b_{uv}\left(v_j - v_i\right)\right],\\ \frac{\mathrm{d}^q v_i}{\mathrm{d}t^q} &= 0.08\left(u_i + 0.7 - 0.8v_i\right) + d\sum_{j=1}^{N} G_{ij}\left[b_{vu}\left(u_j - u_i\right) + b_{vv}\left(v_j - v_i\right)\right],\end{aligned} \tag{3}$$

where d is the coupling strength and G is the Laplacian matrix of connections. The network has a ring structure with nonlocal coupling as shown in Figure 2 (each neuron is connected to its 40 nearest neighbors, and $N = 100$). The coupling between variables is through a rotational matrix as follows [46]:

$$B = \begin{pmatrix} b_{uu} & b_{uv} \\ b_{vu} & b_{vv} \end{pmatrix} = \begin{pmatrix} \cos\phi & \sin\phi \\ -\sin\phi & \cos\phi \end{pmatrix}, \tag{4}$$

with $\phi = (\pi/2) - 0.1$ being the coupling phase.

3. Results

The network is solved numerically by using the Adam–Bashforth method based on the algorithm proposed in [47] with random initial conditions. To identify different behaviors, the strength of incoherence (SI) is used [48]. To find this measure, at first, the variables are transformed into new ones as $x_i = u_i - u_{i+1}$, $i = 1, \ldots, N$. Then, the network is divided into $M = N/n$ groups of n neurons, and the local standard deviation is computed as follows:

$$\sigma(m) = \left\langle \sqrt{\frac{1}{n}\sum_{j=n(m-1)+1}^{mn} \left[x_i - \langle x\rangle\right]^2} \right\rangle_t, \quad m = 1, \ldots, M, \tag{5}$$

where $\langle x\rangle = 1/N\sum_{i=1}^{N} x_i(t)$. Finally, the SI is computed by

$$\begin{aligned} s_m &= \theta(\delta - \sigma(m)),\\ \mathrm{SI} &= 1 - \frac{\sum_{m=1}^{M} s_m}{M}, \end{aligned} \tag{6}$$

where θ is the Heaviside function and δ is a threshold set at 0.23, here, and $n = 4$. The value of SI determines the behavior of the network by SI = 0, $0 < \mathrm{SI} < 1$, and SI = 1 for synchronization, chimera, and asynchronization, respectively.

The network of equation (3) with integer-order ($q = 1$) represents different dynamical behaviors with varying the coupling strength (d). However, the dynamical changes occur in very small coupling strengths. The patterns of the neurons by varying d values are demonstrated in Figure 3. The left panel represents the space-time plots, and the right

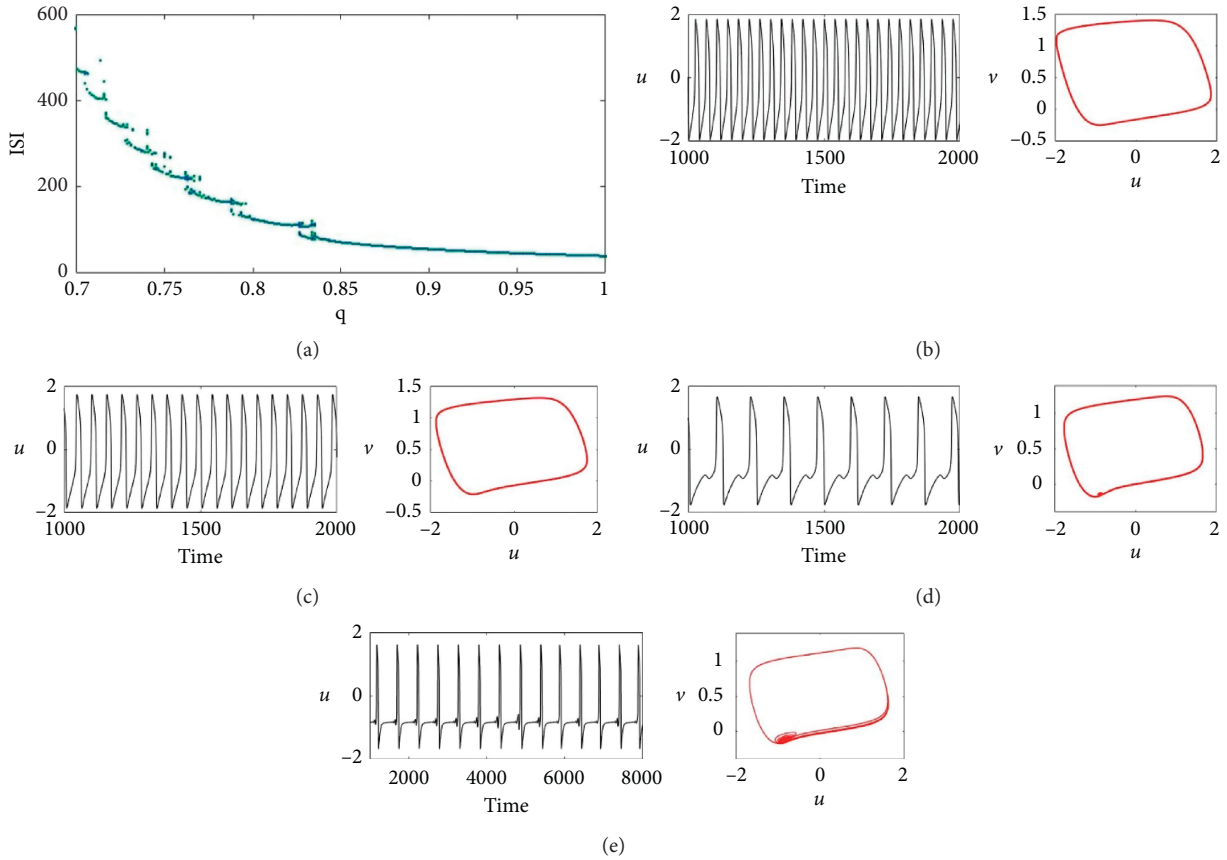

Figure 1: (a) The bifurcation diagram of the model; inter spike intervals (ISI) versus the derivative order (q). (b–e) The time series and phase spaces of the model for different q values: (b) $q = 1$; (c) $q = 0.9$; (d) $q = 0.8$; (e) $q = 0.7$.

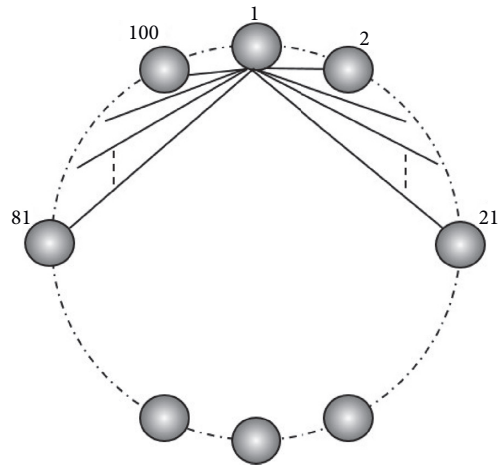

Figure 2: The ring structure of the $N = 100$ neurons with nonlocal coupling. Each neuron is connected to its 40 nearest neighbors. The connections for $i = 1$ are illustrated.

panel represents the time snapshots of the neurons. By increasing the coupling strength, the initial asynchronous pattern of the neurons changes to the chimera state. For $d = 10^{-7}$, a chimera state is created (shown in Figure 3(a)), and it can be seen that there are synchronous and asynchronous neurons in the network. With an increment in the coupling strength, more neurons locate in the synchronous group. The behavior of the network for $d = 1.7 \times 10^{-5}$ is illustrated in Figure 3(b). In this case, most neurons are synchronous, while a few oscillate differently. This behavior is called the solitary state [49, 50]. As the coupling becomes stronger, different neurons are attracted to the synchronous group and a complete synchronization is observed (Figure 3(c)).

The behavior of the neurons is considerably influenced when the derivative of the network's equations changes to the fractional. To investigate this, the coupling strength is considered to be fixed at $d = 2 \times 10^{-5}$, where the integer-order network shows the solitary state (similar to Figure 3(b)) and the fractional order is changed. With decreasing the fractional order (q), firstly, the network synchronization is enhanced. This is shown in Figure 4(a) for $q = 0.9$. However, more decrement of q disturbs the synchronous behavior of the network. Figure 4(b) represents the chimera state for $q = 0.8$ with a similar coupling strength value. When q decreases to $q = 0.7$, the network becomes completely asynchronous (Figure 4(c)). The waveforms of the neurons in each case are depicted in the right panel of Figure 4.

For different fractional orders, the range of the coupling strength for the appearance of different dynamical behaviors is different. As the fractional order decreases, the chimera

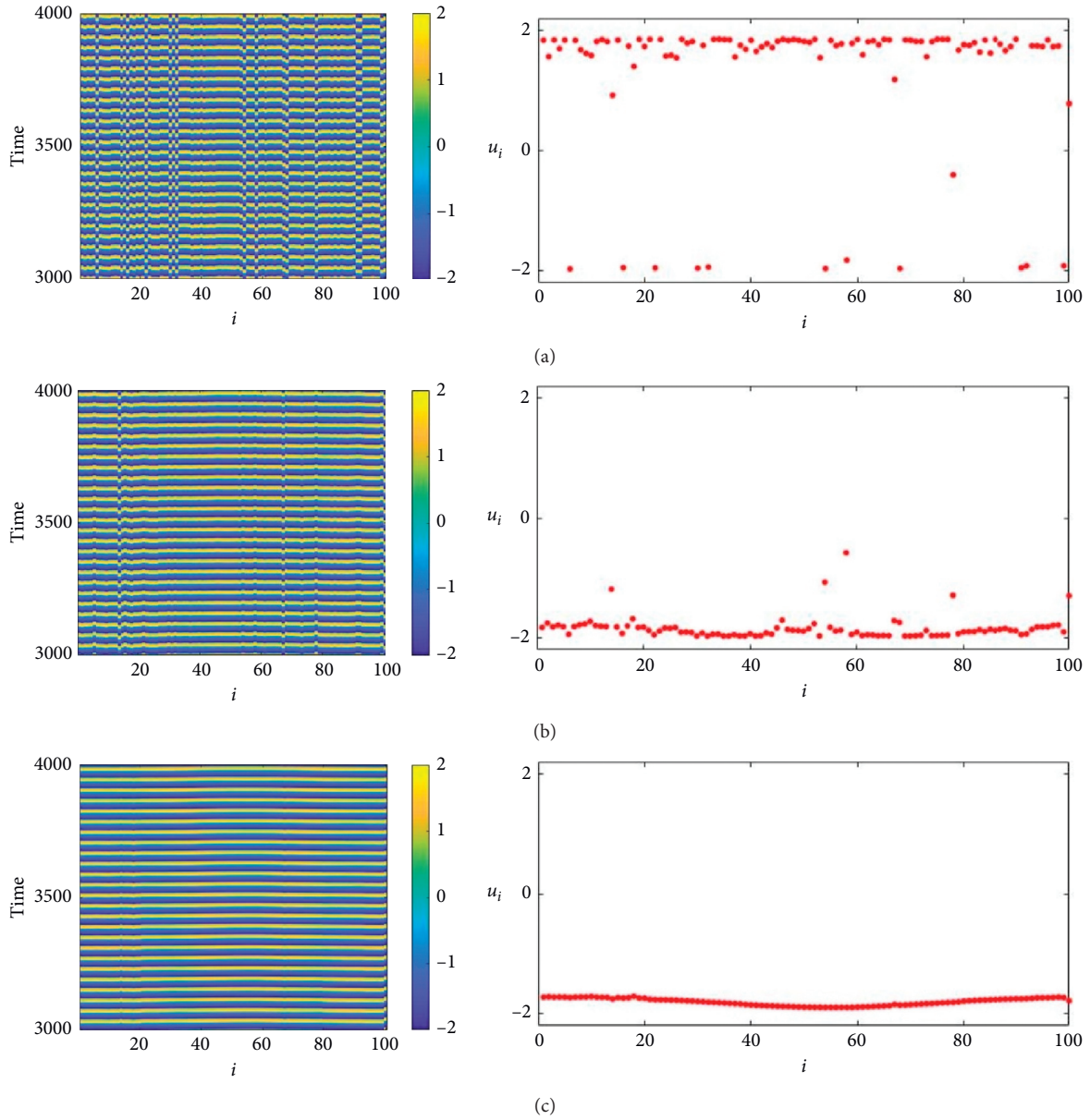

FIGURE 3: The patterns of the network (left panel) and time snapshots (right panel) with integer-order derivative: (a) chimera state for $d = 10^{-7}$ (SI = 0.74); (b) solitary state for $d = 1.7 \times 10^{-5}$ (SI = 0.39); (c) synchronization for $d = 5 \times 10^{-5}$ (SI = 0).

state is formed in higher coupling strengths. Figure 5(a) shows the chimera state in $q = 0.9$ for $d = 4.6 \times 10^{-6}$. In this case, there are several groups containing a few synchronous neurons. For$q = 0.8$, the chimera is observed for $d = 3 \times 10^{-5}$ and more neurons are involved in the synchronous cluster (Figure 5(b)). When q decreases to $q = 0.7$, in some time intervals, some neurons become synchronous. Therefore, the chimera for this derivative is nonstationary. The chimera for $q = 0.7$ is shown in Figure 5(c). To illustrate the coherent and incoherent clusters better, the local order parameter is computed and shown in the right column of Figure 5. This parameter can be obtained as $L_k = |1/2p \sum_{|k-l| \le p} \exp(j\phi_l)|$, $k = 1, \ldots, N$, where ϕ_l is the geometric phase of lth oscillator calculated by $\phi_l = a \tan(y_l/x_l)$. The size of the spatial window is denoted by p. When $L_k = 1$, the kth oscillator belongs to a coherent group.

Figure 6 represents the strength of incoherence of the network for different fractional orders. For $q = 1$, the network is in chimera state until $d = 5 \times 10^{-5}$ and becomes synchronous for larger coupling strengths (Figure 6(a)). A similar pattern is observed for $q = 0.95$ (Figure 6(b)). When q decreases to $q = 0.9$, the synchronization occurs for very smaller coupling strengths ($d = 2.2 \times 10^{-5}$). For $q = 0.85$, the network's dynamical behavior returns to the $q = 1$ manner. With more decrement of q, a stronger coupling is needed for the synchronization. Figure 6(e) shows that $q = 0.8$ has the larger chimera region. For $q = 0.7$ and $q = 0.75$, a large asynchronization region is

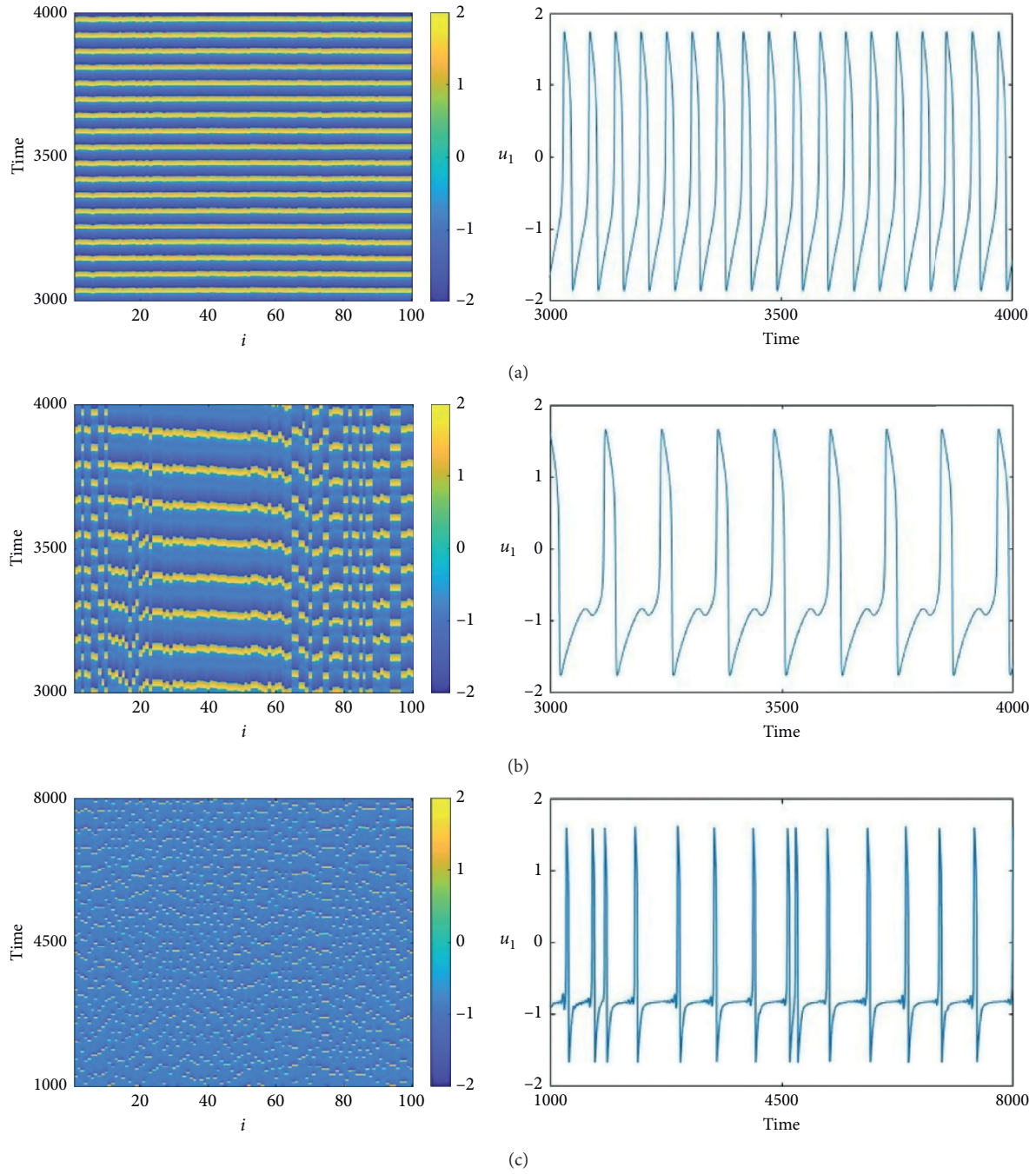

FIGURE 4: Upper panel: the patterns of the network for $d = 2 \times 10^{-5}$ and different derivative orders. The integer-order network exhibits a solitary state at this coupling. (a) Synchronization for $q = 0.9$ (SI = 0). (b) Chimera for $q = 0.8$ (SI = 0.8). (c) Asynchronization for $q = 0.7$ (SI = 0).

observed. The variation of SI according to q is illustrated in Figure 7. It is observed that for low coupling strength, the integer network is in a chimera state. The chimera state is preserved until $q = 0.835$, and then all neurons become asynchronous. For strong couplings, the integer-order network is synchronous. With decreasing q, the synchronization remains until $q = 0.84$. For $q < 0.84$, the chimera state is formed. However, in the range $0.8 < q < 0.823$, the synchronization may appear in the network determined by the initial conditions.

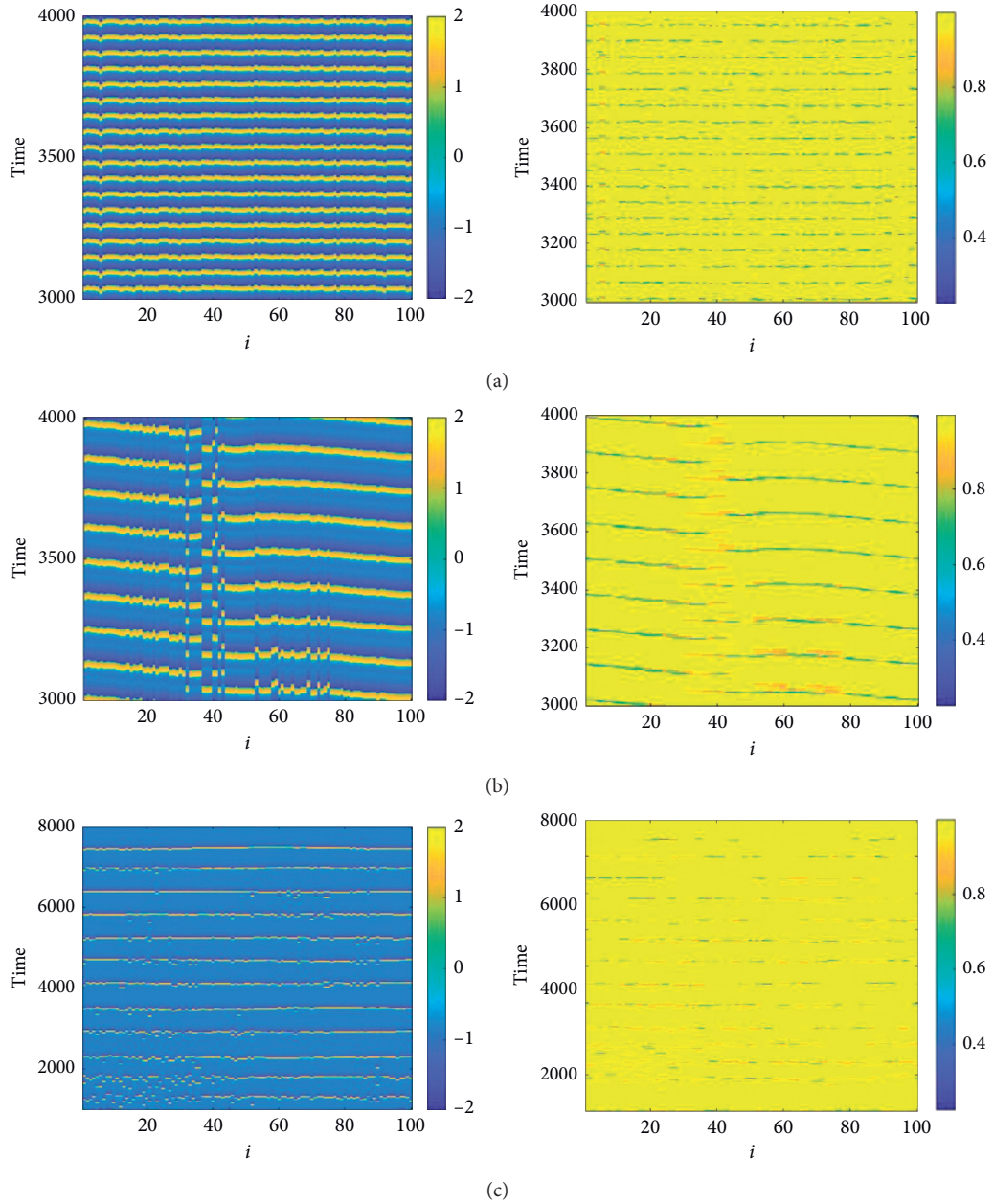

Figure 5: The chimera patterns in the fractional-order network. The left and right columns show the spatiotemporal patterns and the local order parameters ($p = 2$), respectively: (a) $q = 0.9$ and $d = 4.6 \times 10^{-6}$ (SI =); (b) $q = 0.8$ and $d = 3 \times 10^{-5}$ (SI = 0.48); (c) $q = 0.7$ and $d = 10^{-4}$ (SI = 0.42). By varying the derivative order, the chimera is formed with different patterns.

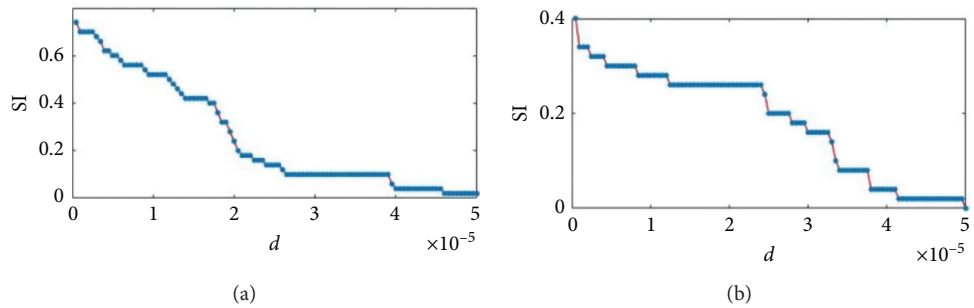

Figure 6: Continued.

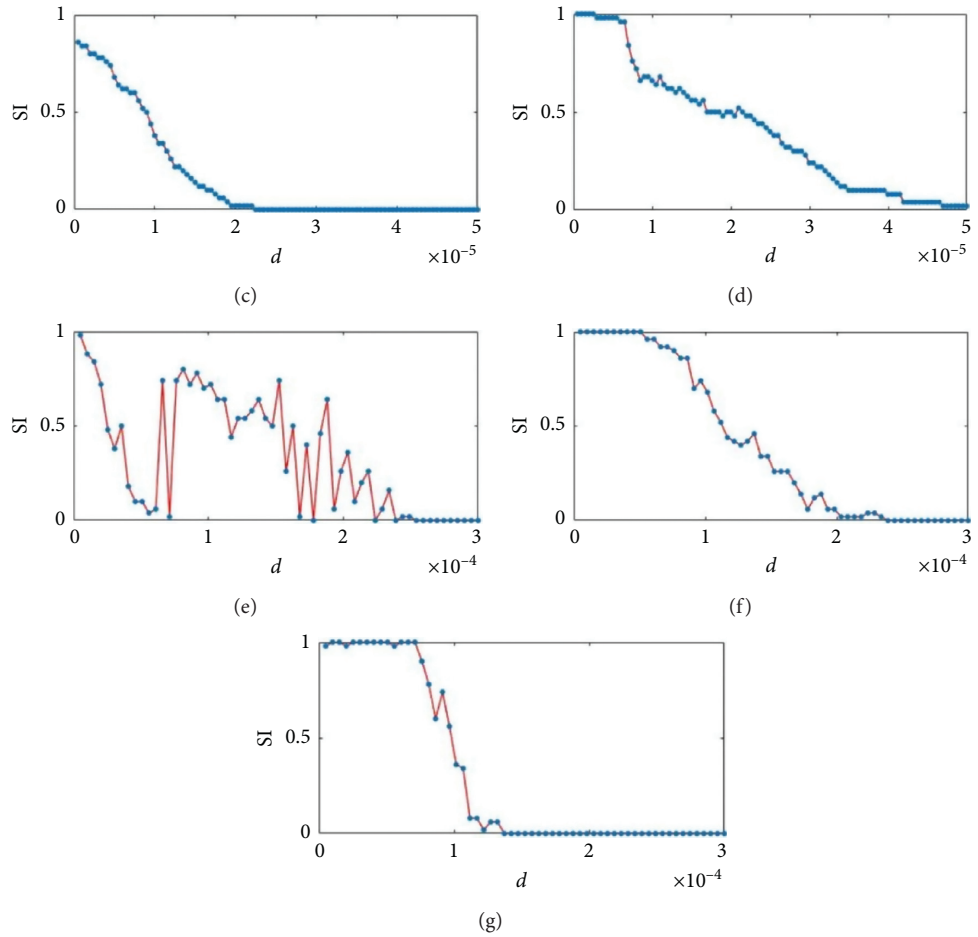

Figure 6: The strength of incoherence according to coupling strength for various values of derivative order: (a) $q = 1$; (b) $q = 0.95$; (c) $q = 0.9$; (d) $q = 0.85$; (e) $q = 0.8$; (f) $q = 0.75$; (g) $q = 0.7$.

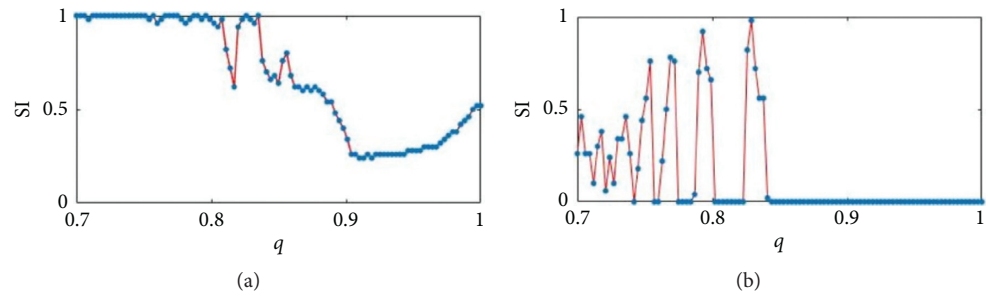

Figure 7: The strength of incoherence according to derivative order (q) for weak and strong coupling strengths: (a) $d = 10^{-5}$; (b) $d = 10^{-4}$.

4. Conclusion

In this paper, a network of coupled fractional-order Fitz-Hugh–Nagumo neurons was studied. The dynamical behavior of the network was investigated under the variation of the coupling strength and the derivative order. The bifurcation diagram of the fractional system with respect to the derivative order revealed that the dynamics of the model is dependent on the fractional order. Consequently, by changing the value of the derivative order, various collective behaviors of the neurons can be found. The integer-order neurons experience asynchronization, chimera, and synchronization with increasing the coupling strength, respectively. In the fractional-order network, decreasing the derivative order for the constant coupling strength, resulted in the lower synchrony level in the network. Therefore, the fractional-order network has the same state transition; however, it occurs in higher coupling strengths. Thus, the chimera or synchronous states appear for stronger couplings. Furthermore, the pattern of the chimera was changed with varying the derivative order. For $q = 0.9$, some small synchronous clusters were formed, while in $q = 0.8$, a large

cluster of synchronous neurons was observed. For lower q values ($q = 0.7$), the position of the synchronous cluster was time-dependent and the nonstationary chimera state appeared.

Data Availability

The data used to support the findings of the study are included within the article.

Conflicts of Interest

The authors declare that there are no conflicts of interest.

Acknowledgments

This work was funded by the Center for Nonlinear Systems, Chennai Institute of Technology, India, with funding number CIT/CNS/2021/RP-015.

References

[1] J. L. Echenausía-Monroy, G. Huerta-Cuellar, R. Jaimes-Reátegui et al., "Multistability emergence through fractional-order-derivatives in a PWL multi-scroll system," *Electronics*, vol. 9, no. 6, p. 880, 2020.

[2] Y. Peng, S. He, and K. Sun, "Chaos in the discrete memristor-based system with fractional-order difference," *Results in Physics*, vol. 24, Article ID 104106, 2021.

[3] E. Zambrano-Serrano, E. Campos-Cantón, and J. M. Muñoz-Pacheco, "Strange attractors generated by a fractional order switching system and its topological horseshoe," *Nonlinear Dynamics*, vol. 83, no. 3, pp. 1629–1641, 2016.

[4] E. Zambrano-Serrano, J. M. Muñoz-Pacheco, and E. Campos-Cantón, "Chaos generation in fractional-order switched systems and its digital implementation," *AEU-International Journal of Electronics and Communications*, vol. 79, pp. 43–52, 2017.

[5] S. He, H. Natiq, S. Banerjee, and K. Sun, "Complexity and chimera states in a network of fractional-order laser systems," *Symmetry*, vol. 13, no. 2, p. 341, 2021.

[6] J.-M. He and F.-Q. Chen, "A new fractional order hyper-chaotic Rabinovich system and its dynamical behaviors," *International Journal of Non-linear Mechanics*, vol. 95, pp. 73–81, 2017.

[7] H. Chen and Y. Chen, "Fractional-order generalized principle of self-support (FOGPSS) in control system design," *IEEE/CAA Journal of Automatica Sinica*, vol. 3, no. 4, pp. 430–441, 2016.

[8] S. A. Malik and A. H. Mir, "FPGA realization of fractional order neuron," *Applied Mathematical Modelling*, vol. 81, pp. 372–385, 2020.

[9] M. Shi and Z. Wang, "Abundant bursting patterns of a fractional-order Morris-Lecar neuron model," *Communications in Nonlinear Science and Numerical Simulation*, vol. 19, no. 6, pp. 1956–1969, 2014.

[10] A. Mondal, S. K. Sharma, R. K. Upadhyay, and A. Mondal, "Firing activities of a fractional-order FitzHugh-Rinzel bursting neuron model and its coupled dynamics," *Scientific Report*, vol. 9, pp. 1–11, 2019.

[11] Y. Yu, M. Shi, H. Kang, M. Chen, and B. Bao, "Hidden dynamics in a fractional-order memristive Hindmarsh-Rose model," *Nonlinear Dynamics*, vol. 100, no. 1, pp. 891–906, 2020.

[12] O. Sporns, "The human connectome: a complex network," *Annals of the New York Academy of Sciences*, vol. 1224, no. 1, pp. 109–125, 2011.

[13] S. Boccaletti, V. Latora, Y. Moreno, M. Chavez, and D. Hwang, "Complex networks: structure and dynamics," *Physics Reports*, vol. 424, no. 4-5, pp. 175–308, 2006.

[14] A. Arenas, A. Díaz-Guilera, J. Kurths, Y. Moreno, and C. Zhou, "Synchronization in complex networks," *Physics Reports*, vol. 469, no. 3, pp. 93–153, 2008.

[15] F. Parastesh, S. Jafari, H. Azarnoush et al., "Chimeras," *Physics Report*, vol. 898, pp. 1–114, 2020.

[16] E. Rybalova, V. S. Anishchenko, G. I. Strelkova, and A. Zakharova, "Solitary states and solitary state chimera in neural networks," *Chaos: An Interdisciplinary Journal of Nonlinear Science*, vol. 29, no. 7, Article ID 71106, 2019.

[17] A. Anzo-Hernández, E. Campos-Cantón, and M. Nicol, "Itinerary synchronization between PWL systems coupled with unidirectional links," *Communications in Nonlinear Science and Numerical Simulation*, vol. 70, pp. 102–124, 2019.

[18] M. Zanin, J. R. Sevilla-Escoboza, R. Jaimes-Reátegui, J. H. Garcıa-Lopez, G. Huerta-Cuellar, and A. N. Pisarchik, "Synchronization attack to chaotic communication systems," *The Interdisciplinary Journal of Discontinuity, Nonlinearity, and Complexity*, vol. 2, no. 4, pp. 333–343, 2013.

[19] D. Lopez Mancilla, E. Villafana Rauda, J. H. Garcia Lopez, R. Jaimes Reategui, G. Huerta Cuellar, and R. Chiu, "Analysis of perturbed synchronization of piecewise rössler using sliding modes control," *IEEE Latin America Transactions*, vol. 13, no. 8, pp. 2482–2487, 2015.

[20] R. Jaimes-Reátegui, V. P. Vera-Ávila, R. Sevilla-Escoboza et al., "Synchronization of unidirectionally delay-coupled chaotic oscillators with memory," *The European Physical Journal Special Topics*, vol. 225, no. 13-14, pp. 2707–2715, 2016.

[21] G. Minero-Ramales, D. López-Mancilla, C. E. Castañeda et al., "A discrete-time chaos synchronization system for electronic locking devices," *The European Physical Journal Special Topics*, vol. 225, no. 13-14, pp. 2655–2667, 2016.

[22] E. Campos, J. Urías, and N. F. Rulkov, "Multimodal synchronization of chaos," *Chaos: An Interdisciplinary Journal of Nonlinear Science*, vol. 14, no. 1, pp. 48–54, 2004.

[23] J. S. González Salas, E. Campos Cantón, F. C. Ordaz Salazar, and I. Campos Cantón, "Forced synchronization of a self-sustained chaotic oscillator," *Chaos: An Interdisciplinary Journal of Nonlinear Science*, vol. 18, no. 2, Article ID 23136, 2008.

[24] S. Petkoski and V. K. Jirsa, "Transmission time delays organize the brain network synchronization," *Philosophical Transactions of the Royal Society A: Mathematical, Physical and Engineering Sciences*, vol. 377, no. 2153, Article ID 20180132, 2019.

[25] S. Majhi, B. K. Bera, D. Ghosh, and M. Perc, "Chimera states in neuronal networks: a review," *Physics of Life Reviews*, vol. 28, pp. 100–121, 2019.

[26] D. M. Abrams and S. H. Strogatz, "Chimera states for coupled oscillators," *Physical Review Letters*, vol. 93, no. 17, Article ID 174102, 2004.

[27] Y. Kuramoto and D. Battogtokh, "Coexistence of coherence and incoherence in nonlocally coupled phase oscillators," *Nonlinear Phenomena in Complex Systems*, vol. 5, pp. 380–385, 2002.

[28] P. R. Carvalho and M. A. Savi, "Synchronization and chimera state in a mechanical system," *Nonlinear Dynamics*, vol. 102, pp. 907–925, 2020.

[29] E. A. Viktorov, T. Habruseva, S. P. Hegarty, G. Huyet, and B. Kelleher, "Coherence and incoherence in an optical comb," *Physical Review Letters*, vol. 112, no. 22, Article ID 224101, 2014.

[30] N. M. Awal, D. Bullara, and I. R. Epstein, "The smallest chimera: periodicity and chaos in a pair of coupled chemical oscillators," *Chaos: An Interdisciplinary Journal of Nonlinear Science*, vol. 29, no. 1, Article ID 13131, 2019.

[31] S. Majhi, M. Perc, and D. Ghosh, "Chimera states in a multilayer network of coupled and uncoupled neurons," *Chaos: An Interdisciplinary Journal of Nonlinear Science*, vol. 27, no. 7, Article ID 73109, 2017.

[32] Z. Wang, S. Baruni, F. Parastesh et al., "Chimeras in an adaptive neuronal network with burst-timing-dependent plasticity," *Neurocomputing*, vol. 406, pp. 117–126, 2020.

[33] T. Banerjee, D. Biswas, D. Ghosh, E. Schöll, and A. Zakharova, "Networks of coupled oscillators: from phase to amplitude chimeras," *Chaos: An Interdisciplinary Journal of Nonlinear Science*, vol. 28, no. 11, pp. 113–124, 2018.

[34] A. J. Alvarez-Socorro, M. G. Clerc, and N. Verschueren, "Traveling chimera states in continuous media," *Communications in Nonlinear Science and Numerical Simulation*, vol. 94, Article ID 105559, 2021.

[35] M. S. Santos, P. R. Protachevicz, I. L. Caldas et al., "Spiral wave chimera states in regular and fractal neuronal networks," *Journal of Physics: Complexity*, vol. 2, no. 1, Article ID 15006, 2020.

[36] S. Wang, S. He, K. Rajagopal, A. Karthikeyan, and K. Sun, "Route to hyperchaos and chimera states in a network of modified Hindmarsh-Rose neuron model with electromagnetic flux and external excitation," *The European Physical Journal Special Topics*, vol. 229, no. 6-7, pp. 929–942, 2020.

[37] G. Blondeau Soh, P. Louodop, R. Kengne, and R. Tchitnga, "Chimera dynamics in an array of coupled FitzHugh-Nagumo system with shift of close neighbors," *Heliyon*, vol. 6, no. 4, Article ID e03739, 2020.

[38] A. Provata and I. E. Venetis, "Chimera states in Leaky integrate-and-fire dynamics with power law coupling," *European Physical Journal B*, vol. 93, pp. 1–9, 2020.

[39] X. Li, T. Xu, and J. Li, "Synchronization and chimera states in a multilayer neuronal network with unidirectional interlayer links," *The European Physical Journal Special Topics*, vol. 228, no. 11, pp. 2419–2427, 2019.

[40] P. Vázquez-Guerrero, J. F. Gómez-Aguilar, F. Santamaria, and R. F. Escobar-Jiménez, "Synchronization patterns with strong memory adaptive control in networks of coupled neurons with chimera states dynamics," *Chaos, Solitons & Fractals*, vol. 128, pp. 167–175, 2019.

[41] P. Vázquez-Guerrero, J. F. Gómez-Aguilar, F. Santamaria, and R. F. Escobar-Jiménez, "Design of a high-gain observer for the synchronization of chimera states in neurons coupled with fractional dynamics," *Physica A: Statistical Mechanics and Its Applications*, vol. 539, Article ID 122896, 2020.

[42] S. He, "Complexity and chimera states in a ring-coupled fractional-order memristor neural network," *Frontiers in Applied Mathematics and Statistics*, vol. 6, p. 24, 2020.

[43] N. Wang, G. Zhang, and H. Bao, "Bursting oscillations and coexisting attractors in a simple memristor-capacitor-based chaotic circuit," *Nonlinear Dynamics*, vol. 97, no. 2, pp. 1477–1494, 2019.

[44] Y. Liu, W.-j. Xu, J. Ma, F. Alzahrani, and A. Hobiny, "A new photosensitive neuron model and its dynamics," *Frontiers of Information Technology & Electronic Engineering*, vol. 21, no. 9, pp. 1387–1396, 2020.

[45] M. Armanyos and A. G. Radwan, "Fractional-order fitzhugh-nagumo and izhikevich neuron models," in *Proceedings of the 2016 13th International Conference on Electrical Engineering/Electronics, Computer, Telecommunications and Information Technology (ECTI-CON)*, pp. 1–5, Chiang Mai, Thailand, June 2016.

[46] I. Omelchenko, O. E. Omel'chenko, P. Hövel, and E. Schöll, "When nonlocal coupling between oscillators becomes stronger: patched synchrony or multichimera states," *Physical Review Letters*, vol. 11022, 224101.

[47] K. Diethelm and A. D. Freed, "The FracPECE subroutine for the numerical solution of differential equations of fractional order," *Forschung und wissenschaftliches Rechnen*, vol. 1999, pp. 57–71, 1998.

[48] R. Gopal, V. Chandrasekar, A. Venkatesan, and M. Lakshmanan, "Observation and characterization of chimera states in coupled dynamical systems with nonlocal coupling," *Physical Review E*, vol. 89, Article ID 52914, 2014.

[49] M. Mikhaylenko, L. Ramlow, S. Jalan, and A. Zakharova, "Weak multiplexing in neural networks: switching between chimera and solitary states," *Chaos: An Interdisciplinary Journal of Nonlinear Science*, vol. 29, no. 2, Article ID 23122, 2019.

[50] S. Majhi, T. Kapitaniak, and D. Ghosh, "Solitary states in multiplex networks owing to competing interactions," *Chaos: An Interdisciplinary Journal of Nonlinear Science*, vol. 29, no. 1, Article ID 13108, 2019.

Hindawi
Complexity
Volume 2021, Article ID 5534872, 20 pages
https://doi.org/10.1155/2021/5534872

Research Article

Study of a Fractional-Order Chaotic System Represented by the Caputo Operator

Ndolane Sene

Département de Mathématiques de la Décision, Université Cheikh Anta Diop de Dakar, Faculté des Sciences Economiques et Gestion, BP 5683 Dakar Fann, Senegal

Correspondence should be addressed to Ndolane Sene; ndolanesene@yahoo.fr

Received 19 January 2021; Revised 5 April 2021; Accepted 3 June 2021; Published 14 June 2021

Academic Editor: Guillermo Huerta Cuellar

This paper is presented on the theory and applications of the fractional-order chaotic system described by the Caputo fractional derivative. Considering the new fractional model, it is important to establish the presence or absence of chaotic behaviors. The Lyapunov exponents in the fractional context will be our fundamental tool to arrive at our conclusions. The variations of the model's parameters will generate chaotic behavior, in general, which will be established using the Lyapunov exponents and bifurcation diagrams. For the system's phase portrait, we will present and apply an interesting fractional numerical discretization. For confirmation of the results provided in this paper, the circuit schematic is drawn and simulated. As it will be observed, the results obtained after the simulation of the numerical scheme and with the Multisim are in good agreement.

1. Introduction

In the last decade, chaos theory has attracted many researchers. Chaos theory is a field of mathematics that can be applied in many domains: from modeling chaotic financial systems [1], in representing circuit schematics [2, 3], and others. The chaotic systems and their circuit schematics have received many investigations in the literature, see, for example, [2–4]. With the new development of fractional calculus, some researchers were interested in modeling chaotic systems using the new and old fractional operators. The impact of the fractional derivatives is an interesting question which merits investigations. Many problems are opened in fractional calculus. The first question is how to construct the numerical scheme to obtain the phase portraits of chaotic systems. Many numerical techniques are used in fractional differential equations that can be applied naturally to solve chaotic systems. In [5], Danca finds interesting remarks that the characterization of the hyperchaotic system using two positive Lyapunov exponents is not an adequate definition in a fractional context. Therefore, modeling chaos using fractional operators is an open problem that admits some interesting interrogations which are not solved yet. Fractional calculus finds many recent advancements in fractional operators and their applicability in real-world problems. For recent advances of fractional calculus and its applications, see the following investigations [1, 6–10].

The chaos literature in integer version and fractional context is very long, but we recall the investigations we find essential for our study. In [11], Pacheco et al. study a new analysis of a new chaotic system with different families of hidden and self-excited attractors by using the fractional operator. In [12], Rajagopal et al. analyze using fractional-order derivative a memristor no equilibrium chaotic system; they proposed synchronizing their introduced model. In other words, they try to find adequate control to synchronize slave and master chaotic systems. In [2], Avalos-Ruiz et al. propose a control implementation on an FPGA for a class of fractional chaotic systems in the context of fractional variable order derivative with Mittag-Leffler kernel. In [13], Perez et al. propose the fractional-order chaotic system in the context of conformable Liouville–Caputo operator. At the same time, they present a novel numerical scheme for the used fractional operator to depict the phase portraits of their proposed chaotic system. In [14], Gomez et al. investigate the chaos in a calcium oscillation model using the Mittag-Leffler

fractional derivative operator. In [15], Atangana and Gomez offer a new hyperchaotic system in the context of the Mittag-Leffler fractional operator. They provided a numerical scheme to depict the considered model's phase portrait in the fractional operators' context. They mainly apply their numerical procedure to the fractional Chua model. In [16], Li et al. introduce a new four-wing model with integer-order derivative, which will be subject to investigations in the fractional context. In [3], Akgul gives a chaotic system for modeling the memcapacitor model using a fractional-order derivative. In [17], Rajagopal et al. continue their exciting investigation of the fractional-order chaotic system in the fractional calculus field. They propose a work on the multiscroll chaotic system and give an application to the synchronization of their proposed model. In [18], Akgul et al. address a user interface for the generation of random numbers based on fractional and integer-order chaotic systems. For more investigations in chaos, see in the following investigations [4, 12–14, 19].

The novelties of the present paper are described in the following lines. This paper focuses on the phase space, the bifurcation diagrams, and the chaos's characterization using the Lyapunov exponents for a fractional version of the Li et al. chaotic system. We analyze the impact of the fractional-order derivative on the dynamics of a fractional version of the system in [16] with Lyapunov exponents and bifurcation diagram aids. Its possible implementation in terms of electrical modeling has been proposed as well. One of the novelties of the present work is the Lyapunov exponents in the fractional context, which is an open problem. Note that the Lyapunov exponents' properties in the integer context for hyperchaotic and chaotic behaviors are not adequate definitions in the fractional version. This remark was first discussed in [5]. Furthermore, the slight variation of the model's parameters in the dynamics has been investigated using bifurcation diagrams. We provide in this paper that the initial conditions impact the chaotic behaviors in the fractional context. The circuit schematic of the fractional chaotic system and the results after simulation in Multisim confirm the theoretical findings obtained via the numerical scheme.

The paper is structured in the following form. In Section 2, we define the fractional operators' necessaries for our work. In Section 3, we present the fractional-order chaotic system described by the Caputo derivative. Section 4 offers the numerical scheme used to obtain the considered fractional system's phase portraits. In Section 5, we illustrate the numerical method by depicting the supposed system's phase portraits with different fractional-order of the Caputo derivative. We also characterize the nature of the chaos using the Lyapunov exponents. In Section 6, we present the bifurcation diagrams and phase space according to the variation of the considered fractional-order chaotic system's parameters. In Section 7, we give the possible implementation of the fractional-order chaotic system in modeling electrical circuits; this section will confirm the paper's theoretical findings. Section 8 provides the stability analysis of the fractional-order chaotic system's equilibrium points with the Matignon criterion used in fractional calculus. In Section 9, we analyze the sensitivity of the initial conditions in the fractional-order chaotic system. We finish with the final remarks and future perspectives of research.

2. On Fractional Operators in Fractional Calculus

In this paper, we study a fractional differential system; before, it was indispensable to recall the fractional operators used in this work. Many fractional derivatives exist, those with singularities as the Caputo and Riemann–Liouville derivatives, those with nonsingularities as the exponential derivative, and the Mittag-Leffler fractional derivative. Due to space limitations, we provide the Caputo derivative and the Riemann–Liouville derivative and their generalizations.

Definition 1 (see [20, 21]). The integral defined by Riemann and Liouville called Riemann–Liouville integral of a given function z: $[0, +\infty[\longrightarrow \mathbb{R}$ is

$$\left(I^{\alpha} z\right)(t) = \frac{1}{\Gamma(\alpha)} \int_0^t (t-s)^{\alpha-1} z(s) \mathrm{d}s, \tag{1}$$

with the function $\Gamma(\ldots)$ symbolizing the Gamma Euler function and under the order $\alpha > 0$.

There exists a generalization of the Riemann–Liouville operator recently proposed in the literature; we have the following definition.

Definition 2 (see [22]). The generalized Riemann–Liouville fractional integral of a given function z: $[0, +\infty[\longrightarrow \mathbb{R}$ is

$$I^{\alpha,\rho} z(t) = \frac{1}{\Gamma(\alpha)} \int_0^t \left(\frac{t^{\rho} - s^{\rho}}{\rho}\right)^{\alpha-1} z(s) \frac{\mathrm{d}s}{s^{1-\rho}}, \tag{2}$$

where the orders α and ρ satisfy the following relationship α and $\rho > 0$ and the function gamma is $\Gamma(\ldots)$, for all $t > 0$.

We can observe that when the order $\rho = 1$, we get the classical Riemann–Liouville integral operator. Furthermore, when $\alpha = \rho = 1$, we have the integer version of the integral.

Caputo proposed another derivative due to the inconvenience of the Riemann–Liouville operator. We recall the Caputo derivative in the following definitions and its generalization.

Definition 3 (see [20, 21]). The Caputo fractional derivative of order $\alpha \in (0, 1)$ can be represented as the form of the function z: $[0, +\infty[\longrightarrow \mathbb{R}$:

$$D_c^{\alpha} z(t) = \frac{1}{\Gamma(1-\alpha)} \int_0^t (t-s)^{-\alpha} z'(s) \mathrm{d}s, \tag{3}$$

with the Gamma Euler function denoted by $\Gamma(\ldots)$.

Definition 4 (see [22]). The generalized Caputo derivative of order $\alpha \in (0, 1)$ is described as the form of the function z: $[0, +\infty[\longrightarrow \mathbb{R}$:

$$D^{\alpha,\rho}z(t) = \frac{1}{\Gamma(1-\alpha)}\int_0^t \left(\frac{t^\rho - s^\rho}{\rho}\right)^{-\alpha} z'(s)\mathrm{d}s, \quad (4)$$

with the orders α and ρ satisfying the relations $\alpha \in (0.1)$ and $\rho > 0$ and the Gamma function is denoted by $\Gamma(\ldots)$, for all $t > 0$.

There exist many fractional operators, and all of them have their advantages. The use of the Caputo derivative in the present work has many motivations. Firstly, all fractional operators take into account the memory effect. Secondly, our main motivation is the initial conditions because the Riemann–Liouville derivative cannot consider them. In the Riemann–Liouville derivative case, the starting condition should be an integral form known in physics to be unrealistic. It cannot be satisfied in many real-world problems. Another basic motivation is in the context of Riemann–Liouville; the derivative of a constant is not null, contrary to the context of the Caputo derivative where the derivative of a constant is null.

3. Fractional-Order Chaotic System

This section provides a fractional version of the chaotic model based on the system presented by Li et al. [16]. Before the investigation, we recall Li et al. chaotic equations represented with the integer-order derivative by the following equation:

$$\begin{aligned} x' &= ax + y + yz, \\ y' &= -xz + yz, \\ z' &= -bz - cxy + m, \end{aligned} \quad (5)$$

with initial conditions

$$\begin{aligned} x(0) &= 1, \\ y(0) &= -1, \\ z(0) &= 1. \end{aligned} \quad (6)$$

The strange attractor is obtained at $a = 1, b = 1$, and $m = 1$ according to Li et al. work. The Lyapunov exponents of the model presented in system (5) are $\mathrm{LYE}_1 = 0.409$, $\mathrm{LYE}_2 = 0$, and $\mathrm{LYE}_3 = -1.773$. In the original paper, the system presented in equation (5) is called a four-wing chaotic equation and admits three real equilibrium points, which are unstable and have two other complex equilibrium points. For more explanations related to the system in equation (5), see [16]. In our present work, we consider the memory effect generated by the fractional operators. Therefore, we investigate the following modified fractional-order chaotic system:

$$\begin{aligned} D_c^\kappa x &= ax + y + yz, \\ D_c^\beta y &= -xz + yz, \\ D_c^\alpha z &= -bz - cxy + m, \end{aligned} \quad (7)$$

with the initial condition defined by the following relation:

$$\begin{aligned} x(0) &= x_0 = 0.2, \\ y(0) &= y_0 = 0.2, \\ z(0) &= z_0 = 0.2. \end{aligned} \quad (8)$$

Our objective is to give a new fractional-order system; therefore, we set the following values for the parameters of model (7); there are $a = 1$, $b = 1$, $c = 1$, and $m = 0$. In terms of comparison, we can observe that equation (7) is a fractional version of equation (5). Furthermore, we can observe when the order of the Caputo derivative is $\kappa = \beta = \alpha = 1$ in equation (7); we recover the constructive equation of original equation (5) presented in [16]. The difference is in the initial conditions. This paper will be to focus on detecting the chaotic behavior when the fractional-order derivative is utilized. The fractional-order operator impact will be analyzed and proved by the comparison of the attractors' geometries. The variation of the model's parameters such as a and c generate strange actuators and will be confirmed using the bifurcation diagrams. We will also establish via the stability analysis of the equilibrium points of our considered chaotic system; there exists a chaotic region according to the variation of the order of the Caputo derivative. Equation (7) is said the system with commensurate fractional-order when $\kappa = \beta = \alpha$; else, it is said the equation with incommensurate fractional-order.

4. Numerical Scheme for the Fractional-Order Chaotic System

In this section, we apply the numerical scheme proposed by Garrapa [23] for our proposed fractional-order equation (7) necessary to depict the phase portraits. This numerical discretization uses the numerical approach of the Riemann–Liouville integral. In this section, we consider equation (7) with commensurate fractional-order. The first step will be to determine the analytical solution of fractional differential equation (7) using Riemann–Liouville integral:

$$x(t) = x(0) + I^\alpha u(t, x_1), \quad (9)$$

$$y(t) = y(0) + I^\alpha v(t, x_1), \quad (10)$$

$$z(t) = z(0) + I^\alpha w(t, x_1). \quad (11)$$

We set the following function obtained from model (7):

$$\begin{aligned} u(t, x_1) &= ax + y + yz, \\ v(t, x_1) &= -xz + yz, \\ w(t, x_1) &= -bz - cxy. \end{aligned} \quad (12)$$

For the graphical representations, we introduce the discretization at the point t_n; then, equations (9)–(11) can be written in the following form:

$$x(t_n) = x(0) + I^\alpha u(t_n, x_1), \quad (13)$$

$$y(t_n) = y(0) + I^\alpha v(t_n, x_1), \quad (14)$$

$$z(t_n) = z(0) + I^{\alpha} w(t_n, x_1). \tag{15}$$

Introducing the step-size h and $t_n = nh$, the discretization of the fractional integrals can be represented for the functions u, v, and w as the following:

$$I^{\alpha} u(t_n, x_1) = h^{\alpha} \sum_{j=1}^{n} d_{n-j} u(t_j, x_{1j}), \tag{16}$$

$$I^{\alpha} v(t_n, x_1) = h^{\alpha} \sum_{j=1}^{n} d_{n-j} v(t_j, x_{1j}), \tag{17}$$

$$I^{\alpha} w(t_n, x_1) = h^{\alpha} \sum_{j=1}^{n} d_{n-j} w(t_j, x_{1j}), \tag{18}$$

where the parameters are given by

$$\begin{aligned} d_{n-j} &= \frac{\left((n-j+1)^{\alpha} - (n-j)^{\alpha}\right)}{1/(\Gamma(1+\alpha))}, \\ d_n &= \frac{\left((n+1)^{\alpha} - (n)^{\alpha}\right)}{1/(\Gamma(1+\alpha))}. \end{aligned} \tag{19}$$

For the simplification of the numerical scheme of the Riemann–Liouville integral, we introduce the first-order interpolant polynomial of the functions $u(\tau)$, $v(\tau)$, and $w(\tau)$ given by the following relations [23]:

$$u(\tau) = u\left(t_{j+1}, x_{1j+1}\right) + \frac{\tau - t_{j+1}}{h}\left[u(t_{j+1}, x_{1j+1}) - u(t_j, x_{1j})\right], \tag{20}$$

$$v(\tau) = v\left(t_{j+1}, x_{1j+1}\right) + \frac{\tau - t_{j+1}}{h}\left[v(t_{j+1}, x_{1j+1}) - v(t_j, x_{1j})\right], \tag{21}$$

$$w(\tau) = w(t_{j+1}, x_{1j+1}) + \frac{\tau - t_{j+1}}{h}\left[w(t_{j+1}, x_{1j+1}) - w(t_j, x_{1j})\right]. \tag{22}$$

Replacing equations (20)–(22) into equations (16)–(18), we get, after recursive summation, more simple formulas for the numerical approach of the fractional integrals:

$$I^{\alpha} u(t_n, x_1) = h^{\alpha}\left[\overline{d}_n^{(\alpha)} u(0) + \sum_{j=1}^{n} d_{n-j}^{(\alpha)} u(t_j, x_{1j})\right], \tag{23}$$

$$I^{\alpha} v(t_n, x_1) = h^{\alpha}\left[\overline{d}_n^{(\alpha)} v(0) + \sum_{j=1}^{n} d_{n-j}^{(\alpha)} v(t_j, x_{1j})\right], \tag{24}$$

$$I^{\alpha} w(t_n, x_1) = h^{\alpha}\left[\overline{d}_n^{(\alpha)} w(0) + \sum_{j=1}^{n} d_{n-j}^{(\alpha)} w(t_j, x_{1j})\right], \tag{25}$$

where the parameters are given explicitly as the following form:

$$\overline{d}_n^{(\alpha)} = \frac{(n-1)^{\alpha} - n^{\alpha}(n-\alpha-1)}{\Gamma(2+\alpha)}, \tag{26}$$

and furthermore, when $n = 1, 2, \ldots$, then the parameter d can be expressed as the following forms:

$$\begin{aligned} d_0^{(\alpha)} &= \frac{1}{\Gamma(2+\alpha)}, \\ d_n^{(\alpha)} &= \frac{(n-1)^{\alpha+1} - 2n^{\alpha+1} + (n+1)^{\alpha+1}}{\Gamma(2+\alpha)}. \end{aligned} \tag{27}$$

For the numerical schemes which are used to represent the graphics, it is obtained after plugging equations (23)–(27) into equations (13)–(15); we have the following expressions:

$$\begin{aligned} x(t_n) &= x(0) + h^{\alpha}\left[\overline{d}_n^{(\alpha)} u(0) + \sum_{j=1}^{n} \kappa_{n-j}^{(\alpha)} u(t_j, x_{1j})\right], \\ y(t_n) &= y(0) + h^{\alpha}\left[\overline{d}_n^{(\alpha)} v(0) + \sum_{j=1}^{n} \kappa_{n-j}^{(\alpha)} v(t_j, x_{1j})\right], \\ z(t_n) &= z(0) + h^{\alpha}\left[\overline{d}_n^{(\alpha)} w(0) + \sum_{j=1}^{n} \kappa_{n-j}^{(\alpha)} w(t_j, x_{1j})\right]. \end{aligned} \tag{28}$$

For the previous representations, it is necessary to recall the numerical discretization for our functions u, v, and w; we have the following:

$$\begin{aligned} u(t_j, x_{1j}) &= a x_j + y_j + y_j z_j, \\ v(t_j, x_{1j}) &= -x_j z_j + y_j z_j, \\ w(t_j, x_{1j}) &= -b z_j - c x_j y_j. \end{aligned} \tag{29}$$

The convergence and stability are not detailed in this section, see [23]; here, we just give information related to these two properties. We assume that $x(t_n)$, $y(t_n)$, and $z(t_n)$ are the approximate numerical solutions of the fractional system represented in equation (7), and x_n, y_n, and z_n are the exact solutions; the residual function with the Caputo derivative is given by the following expression:

$$\begin{aligned} |x(t_n) - x_n| &= \mathcal{O}\left(h^{\min\{\alpha+1,2\}}\right), \\ |y(t_n) - y_n| &= \mathcal{O}\left(h^{\min\{\alpha+1,2\}}\right), \\ |z(t_n) - z_n| &= \mathcal{O}\left(h^{\min\{\alpha+1,2\}}\right). \end{aligned} \tag{30}$$

We can notice that the convergence of the numerical scheme presented in this section is obtained when the step-size h converges to 0 [23]. The stability of our numerical scheme is obtained from the Lipchitz criterion of the functions u, v, and w.

5. Illustration of the Numerical Scheme

This section presents the phase portraits of fractional-order system (7) with commensurate and incommensurate fractional orders. The main objective is to illustrate the numerical scheme presented in previous Section 4. We set the

following values for the parameters of the model $a = 1$, $b = 1$, and $c = 1$ and the initial conditions given by equation (9). For Figure 1, the considered order is $\alpha = 0.95$.

For more illustrations, we consider system (7) with commensurate order $\alpha = 0.90$. The phase portraits are presented in Figure 2.

An interesting procedure of comparison between the geometry of the attractors can be found in [24]. The method consists of comparing the amplitude of the attractors in different orders of the Caputo derivative. The comparison of the attractors' geometry at the orders $\alpha = 0.9$ and $\alpha = 0.95$ can be analyzed for model (7). We adopt the sketch presented in [24]. We consider the phase portraits in plane (x, y) in Figures 1 and 2 and construct polygons, calculate their areas, and compare them. We have following Figures 3 and 4.

In Figure 3, amplitudes are $EF = 12.2\,\text{cm}$ and $AB = CD = 4\,\text{cm}$, and in Figure 4, the amplitudes are $KL = 10.88\,\text{cm}$ and $GH = IJ = 3\,\text{cm}$; referring to the dimension and calculating the areas of the polygons $AFBDEC$ and $GLHJKI$, we notice that the $\text{area}(AFBDEC) > \text{area}(GLHJKI)$; thus, there exists a significant difference between the attractors at the orders $\alpha = 0.9$ and $\alpha = 0.95$. The method adopted in this section proves the influence of the order of the Caputo derivative. To see more the impact of the order of the Caputo derivative, we consider fractional chaotic equation (7) with incommensurate order:

$$\begin{aligned} x' &= ax + y + yz, \\ y' &= -xz + yz, \\ D_c^{\alpha} z &= -bz - cxy. \end{aligned} \tag{31}$$

System (31) is obtained when $\kappa = 1$ and $\beta = 1$ in equation (7). We have the phase portraits in following Figure 5.

The Caputo derivative's impact can be observed by comparing the phase portrait in the commensurate scenario and the phase portrait in the incommensurate scenario, which have different geometries. To detect equation (7) chaotic behavior with the orders $\alpha = 0.9$ and $\alpha = 0.95$, we calculate the Lyapunov exponents. The Lyapunov exponents will permit us, in general, to recognize chaotic behaviors. The Jacobian matrix of fractional differential equation (7) with the same order is given by the following matrix, which is a fundamental tool for finding the Lyapunov exponents:

$$J = \begin{pmatrix} a & 1+z & y \\ -z & z & -x+y \\ -cy & -cx & -b \end{pmatrix}. \tag{32}$$

The Lyapunov exponents in the context of fractional calculus in the chaotic system using Matlab code are proposed in Danca's work. Following the same proposed algorithm, the Lyapunov exponents for fractional-order equation (7) with commensurate order when $\alpha = 0.95$ are given as follows:

$$\begin{aligned} \text{LYE}_1 &= 0.3449, \\ \text{LYE}_3 &= 0, \\ \text{LYE}_3 &= -2.5326. \end{aligned} \tag{33}$$

And, its associated Kaplan–Yorke dimension is given as follows:

$$\dim(\text{LYE}) = 2 + \frac{\text{LYE}_1 + \text{LYE}_2}{\left|\text{LYE}_3\right|} = 2.1362. \tag{34}$$

Following the previous results, we can give the nature of the behaviors. First of all, the fractional system is dissipative because the sum of all Lyapunov exponents gives a negative number. The second property is to detect the chaotic behavior of our presented equation (7) with the same order. We can see with equation (33), we have one positive Lyapunov exponent corresponding to the chaotic behavior of equation (7). We repeat the same analysis with the order $\alpha = 0.9$; the Lyapunov exponents are represented as the following form:

$$\begin{aligned} \text{LYE}_1 &= 0.3775, \\ \text{LYE}_2 &= 0, \\ \text{LYE}_3 &= -3.0042. \end{aligned} \tag{35}$$

And, its associated Kaplan–Yorke dimension is given as follows:

$$\dim(\text{LYE}) = 2 + \frac{\text{LYE}_1 + \text{LYE}_2}{\left|\text{LYE}_3\right|} = 2.1257. \tag{36}$$

The system is dissipative as well because the addition of all Lyapunov exponents is negative. For the nature of the behaviors, we analyze equation (35); we have the same conclusion as in the previous case, equation (7) has chaotic behavior with the order $\alpha = 0.9$. It is caused by the existence of one positive Lyapunov exponent. This section's main conclusion is when the fractional derivative orders vary in the interval $[0.9, 1)$, fractional equation (7) with the same order has chaotic behavior. To confirm this assumption, we calculate in following Table 1 the Lyapunov exponents versus the fractional-order derivative's variation into $[0.9, 1)$.

Checking the results on Table 1, we conclude that fractional-order equation (7) is dissipative at all orders in the interval $[0.9, 1)$. It is because, at all orders, the addition of the Lyapunov exponents is negative. We observe one positive Lyapunov exponent at all orders α, which means the fractional-order system's solutions have chaotic behavior.

6. Stability of the Equilibrium Points in Fractional Context Calculus

In this part, we discuss the fractional-order system's stability by using the Matignon criterion. It is a famous criterion used in fractional calculus. Stability analysis is one of the fundamental points in the chaotic and hyperchaotic system. In general, all equilibrium points when the system is chaotic fail to be stable. In this section, we consider equation (7) with

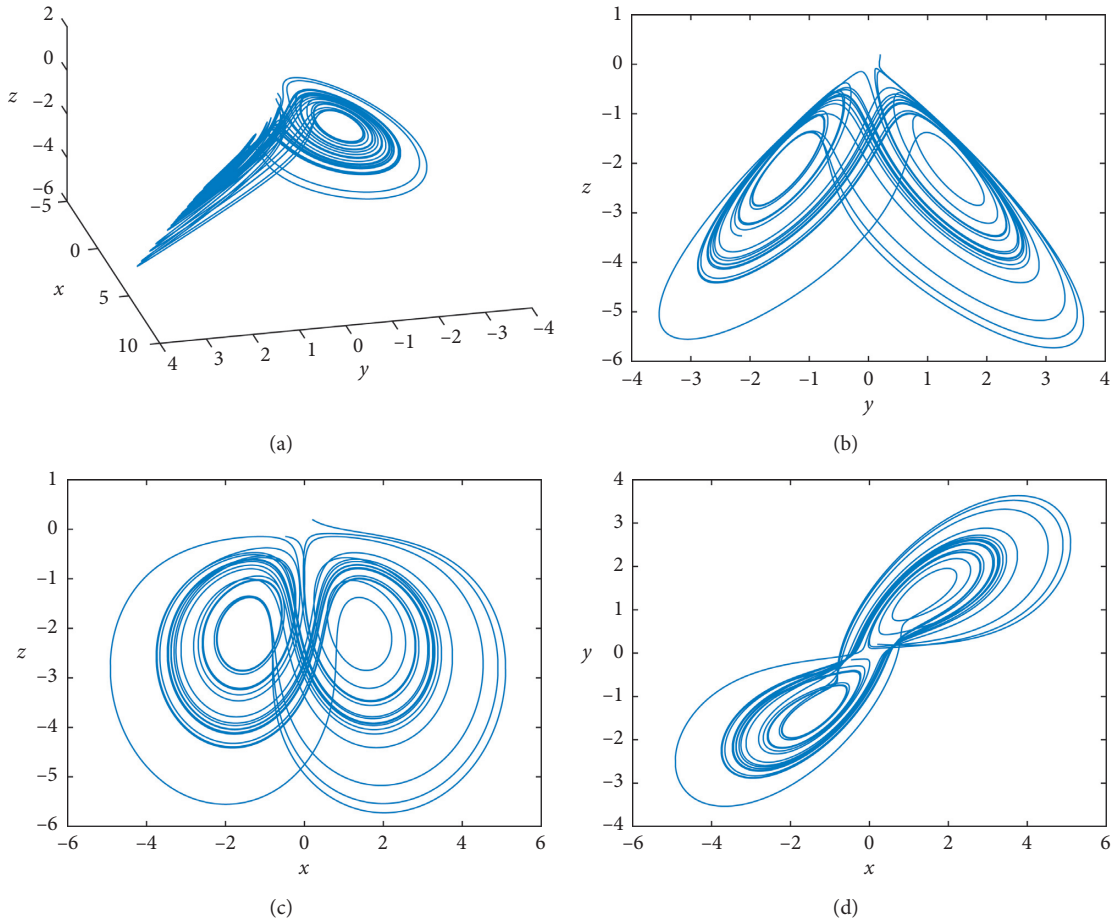

Figure 1: Phase portraits with the order $\alpha = 0.95$.

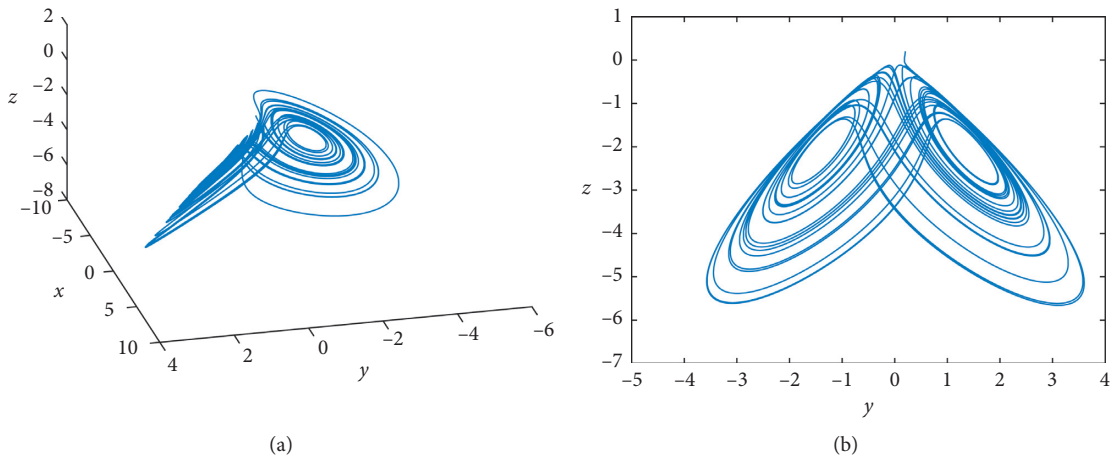

Figure 2: Continued.

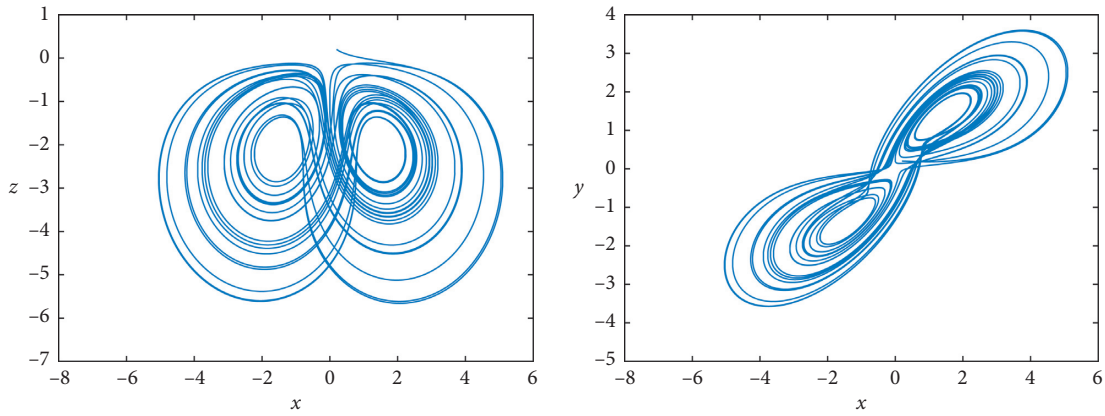

Figure 2: Phase portraits with the order $\alpha = 0.9$.

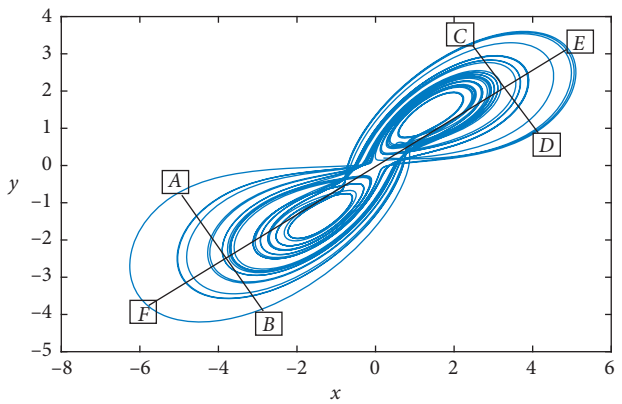

Figure 3: Phase spaces with polygon with the order $\alpha = 0.9$.

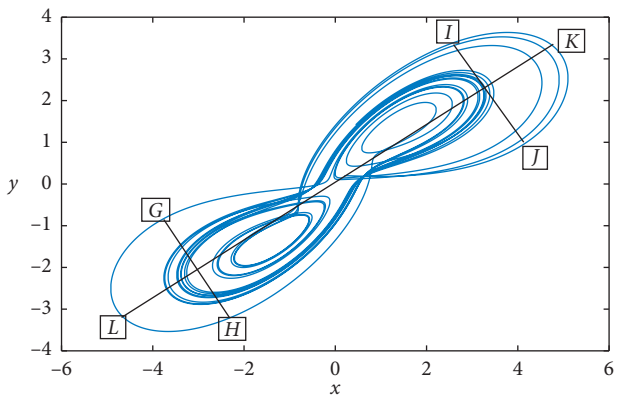

Figure 4: Phase spaces with polygon with the order $\alpha = 0.95$.

commensurate order. It is also interesting to focus on the stability of its equilibrium points. The Jacobian matrix given in the previous section will be used again. We have the matrix described by the following expression:

$$J = \begin{pmatrix} a & 1+z & y \\ -z & z & -x+y \\ -cy & -cx & -1 \end{pmatrix}. \tag{37}$$

The following points are the real equilibrium points when you exclude the complex eigenvalues:

$$\begin{aligned} P_1 &= (0, 0, 0), \\ P_2 &= (-1.41, -1.41, -2), \\ P_3 &= (1.41, 1.41, -2). \end{aligned} \tag{38}$$

The principle of the method consists of evaluating the Jacobian matrix at all points previously mentioned. For the first point P_1, the Jacobian matrix is as follows:

$$J(P_1) = \begin{pmatrix} 1 & 1 & 0 \\ 0 & 0 & 0 \\ 0 & 0 & -1 \end{pmatrix}. \tag{39}$$

The previous matrix has eigenvalues as the following numbers $\lambda_1 = 1$, $\lambda_2 = 0$, and $\lambda_3 = -1$. We notice that the third eigenvalue satisfies $|\arg(\lambda_3)| = \pi > (\alpha\pi/2)$. The first eigenvalue obeys that $|\arg(\lambda_1)| \approx 0 < (\alpha\pi/2)$ for all α. Thus, the equilibrium point is not stable for all orders α of the Caputo derivative.

The matrix in equation (37) at the point P_2 is described as the following form:

$$J(P_2) = \begin{pmatrix} 1 & -1 & -1.41 \\ 2 & -2 & 0 \\ 1.41 & 1.41 & -1 \end{pmatrix}. \tag{40}$$

The previous matrix has eigenvalues as the following numbers $\lambda_1 = 0.1230 + 1.8776i$, $\lambda_2 = 0.1230 - 1.8776i$, and $\lambda_3 = -2.246$. We remark that the third eigenvalue satisfies $|\arg(\lambda_3)| = \pi > (\alpha\pi/2)$. The first eigenvalue obeys to

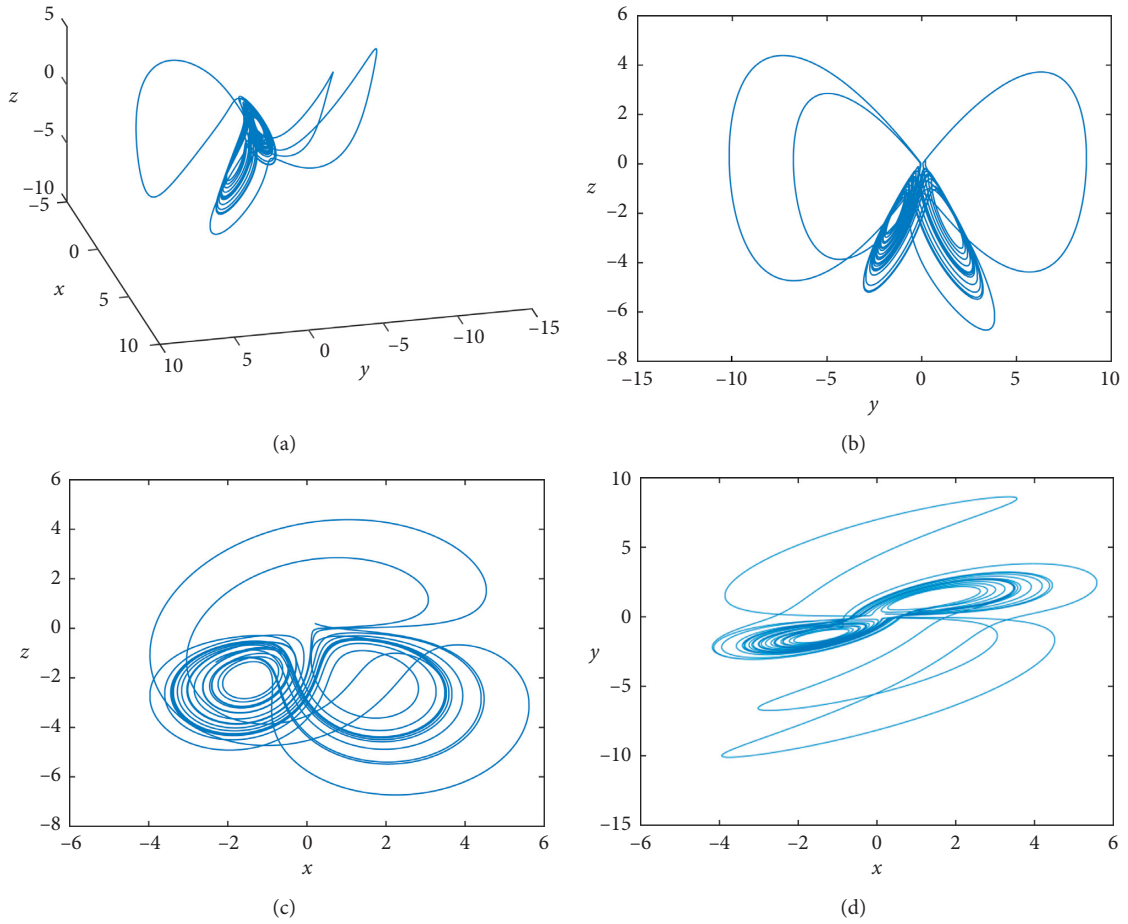

Figure 5: Phase portraits with the order $\alpha = 0.9$ in equations (32)–(34).

Table 1: Lyapunov exponents.

α	LE_1	LE_2	LE_3
0.90	0.3775	0	−3.0042
0.91	0.3581	0	−2.7858
0.92	0.3083	0	−2.8379
0.93	0.2701	0	−2.7337
0.94	0.2979	0	−2.5546
0.95	0.3449	0	−2.5326
0.96	0.2177	0	−2.3049
0.97	0.2107	0	−2.1671
0.98	0.2171	0	−2.0931
0.99	0.2402	0	−2.0701
0.9950	0.2215	0	−1.9927

$|\arg(\lambda_1)| \approx (43\pi/90) > (\alpha\pi/2)$ for all $\alpha < 0.9$ and the last eigenvalue $|\arg(\lambda_2)| \approx (43\pi/90) > (\alpha\pi/2)$ for all α. Thus, the equilibrium point is not stable when α exceeds 0.9.

The Jacobian at the point P_3 is described by

$$J(P_2) = \begin{pmatrix} 1 & -1 & 1.41 \\ 2 & -2 & 0 \\ -1.41 & -1.41 & -1 \end{pmatrix}. \quad (41)$$

The previous matrix has eigenvalues as the following numbers $\lambda_1 = 0.1230 + 1.8776i$, $\lambda_2 = 0.1230 - 1.8776i$, and $\lambda_3 = -2.246$. We have that the third eigenvalue satisfies $|\arg(\lambda_3)| = \pi > (\alpha\pi/2)$. The first eigenvalue obeys that $|\arg(\lambda_1)| \approx (43\pi/90) > (\alpha\pi/2)$ for all $\alpha < 0.9$ and the last $|\arg(\lambda_2)| \approx (43\pi/90) > (\alpha\pi/2)$ for all α. Then, the equilibrium point is not stable when α exceeds 0.9.

7. Bifurcation Diagrams and Lyapunov Exponents

This section analyzes the impact caused by the variation of the parameters a and c on chaotic behavior. Small variations are applied to a and c, and we depict the responses via the bifurcation diagrams plus phase portraits. In this section, for more clarity in the curve, we consider the step-size $h = 0.005$. All findings are obtained with equation (7) in commensurate order.

We begin our analysis with the variation of the parameter a in the interval $(0, 5)$. We fix $b = 1$ and $c = 1$. In Figure 6, we represent the bifurcation diagram versus the parameter a.

We notice that when the parameter a varies in the region $[0.6, 5)$, fractional system (5)–(8) has chaotic behavior. Note that the variation of the parameter a into

$(0, 0.5)$ generates the solutions' convergence to a stable equilibrium point. For an illustration of the chaotic behavior, we represent the phase portraits of our system at $a = 1.5$ and fixing $b = 1$ and $c = 1$ at the order $\alpha = 0.95$, see Figure 7.

We confirm the chaotic behavior with the existence of one positive and large Lyapunov exponent:

$$\begin{aligned} \mathrm{LYE}_1 &= 0.1918, \\ \mathrm{LYE}_2 &= 0, \\ \mathrm{LYE}_3 &= -2.4806. \end{aligned} \tag{42}$$

And, its associated Kaplan–Yorke dimension is given as follows:

$$\dim(\mathrm{LYE}) = 2 + \frac{\mathrm{LYE}_1 + \mathrm{LYE}_2}{\left|\mathrm{LYE}_3\right|} = 2.0773. \tag{43}$$

To validate the convergence of the solutions to a stable equilibrium point, we study the local stability of the nontrivial equilibrium point of equation (7) with commensurate order considering $a = 0.4$. The equilibrium points of equation (7) with commensurate order with $a = 0.4$ are given by $O(0, 0, 0)$, $A(-1.18, -1.18, -1.4)$, and $B(1.18, 1.18, -1.4)$. The Jacobian matrix at the point $O(0, 0, 0)$ gives

$$J(O) = \begin{pmatrix} 0.4 & 1 & 0 \\ 0 & 0 & 0 \\ 0 & 0 & -1 \end{pmatrix}. \tag{44}$$

The eigenvalues of the previous matrix are given by $\lambda_1 = 0.4$, $\lambda_2 = 0$, and $\lambda_3 = -1$. We can remark that the first eigenvalue does not obey to Matignon criterion; thus, the point $O(0, 0, 0)$ is not local stable. Thus, the convergence of the solutions of equation (7) is not at the point $O(0, 0, 0)$. We now try to a point $A(-1.18, -1.18, -1.4)$; thus, the Jacobian matrix is given by

$$J(A) = \begin{pmatrix} 0.4 & -0.4 & -1.18 \\ 1.4 & -1.4 & 0 \\ 1.18 & 1.18 & -1 \end{pmatrix}. \tag{45}$$

We obtain as eigenvalues the following values $\lambda_1 = -0.0763 + 1.4507i$, $\lambda_2 = -0.0763 - 1.4507i$, and $\lambda_3 = -1.8474$. We can observe that all eigenvalues have negative real parts. Thus, the Matignon criterion is satisfied by all eigenvalues. Thus, the point $A(-1.18, -1.18, -1.4)$ is a stable equilibrium point. We finish with the point $B(1.18, 1.18, -1.4)$. The Jacobian matrix at the point B is described as the following form:

$$J(C) = \begin{pmatrix} 0.4 & -0.4 & 1.18 \\ 1.4 & -1.4 & 0 \\ -1.18 & -1.18 & -1 \end{pmatrix}. \tag{46}$$

The eigenvalues of the previous Jacobian matrix at this point are given by $\lambda_1 = -0.0763 + 1.4507i$, $\lambda_2 = -0.0763 - 1.4507i$, and $\lambda_3 = -1.8474$. We can observe that all eigenvalues have negative real parts; thus, the Matignon criterion is automatically satisfied. Thus, the point C coincides with the stable equilibrium point. Referring to the phase portraits, the trajectories converge to the point B when $a = 0.4$.

We finish this section by the bifurcation diagram generated by the variation of the parameter $c \in (0, 25)$, and we illustrate the impact of the parameter c on the phase portraits, see Figure 8, taken at $a = 1$ and $c = 4$.

The bifurcation diagram shown in Figure 9 indicates that , in our considered interval $(0, 25)$, the system has continuously chaotic behavior. Let us $c = 4$; the chaotic behavior at this point is confirmed by the existence of one positive Lyapunov exponent; we have the following calculations:

$$\begin{aligned} \mathrm{LYE}_1 &= 0.2485, \\ \mathrm{LYE}_2 &= 0, \\ \mathrm{LYE}_3 &= -2.4311. \end{aligned} \tag{47}$$

And, its associated Kaplan–Yorke dimension is given as follows:

$$\dim(\mathrm{LYE}) = 2 + \frac{\mathrm{LYE}_1 + \mathrm{LYE}_2}{\left|\mathrm{LYE}_3\right|} = 2.1022. \tag{48}$$

For more confirmation of the chaotic region, we depict our fractional system's phase portraits at $a = 1$ and $c = 0.5$, see Figure 10.

8. Electrical Circuit Schematic of the Fractional System

In this section, we give the circuit representation associated to chaotic system (7) with incommensurate order. For more details in the context of the fractional chaotic circuit, we consider equation (7) with $\kappa = \beta = 1$ written using electronic tools:

$$x' = \frac{1}{R_1 C_1} x + \frac{1}{R_2 C_1} y + \frac{1}{R_3 C_1} yz, \tag{49}$$

$$y' = -\frac{1}{R_4 C_1} xz + \frac{1}{R_5 C_2} yz, \tag{50}$$

$$D_c^{\alpha} z = -\frac{1}{R_6 C_3} z - \frac{1}{R_7 C_3} xy, \tag{51}$$

where C_i for $i = 1, \ldots, n$ denotes the value of the capacitors and R_i represents the resistance value. To connect the results in this paper with the experimental results, we draw the circuit schematic and generate the phase portraits using oscilloscopes. We first use our numerical scheme in the previous sections to draw the phase portraits. We consider the order of the Caputo derivative as $\alpha = 0.95$. The portraits of model (49)–(51) are represented in following Figure 11.

For the circuit schematic, the values of the capacitors are given by $C_1 = C_2 = C_3 = 1$ nF, and the values of the resistors are given $R_1 = 250\,\mathrm{k}\Omega$, $R_2 = 250\,\mathrm{k}\Omega$, $R_3 = 6.25\,\mathrm{k}\Omega$, $R_4 = 6.25\,\mathrm{k}\Omega$, $R_5 = 6.25\,\mathrm{k}\Omega$, $R_6 = 250\,\mathrm{k}\Omega$, and $R_7 = 6.25\,\mathrm{k}\Omega$.

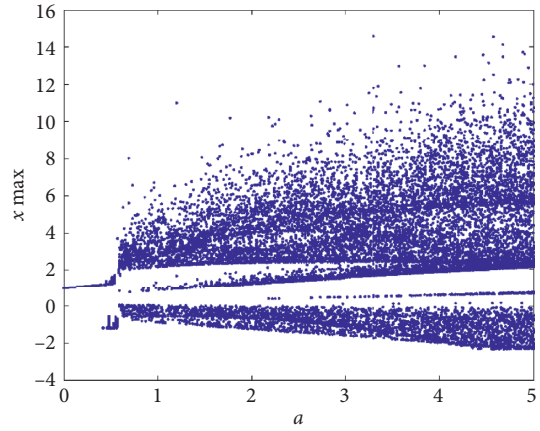

Figure 6: Bifurcation diagram versus the parameter a at order $\alpha = 0.95$.

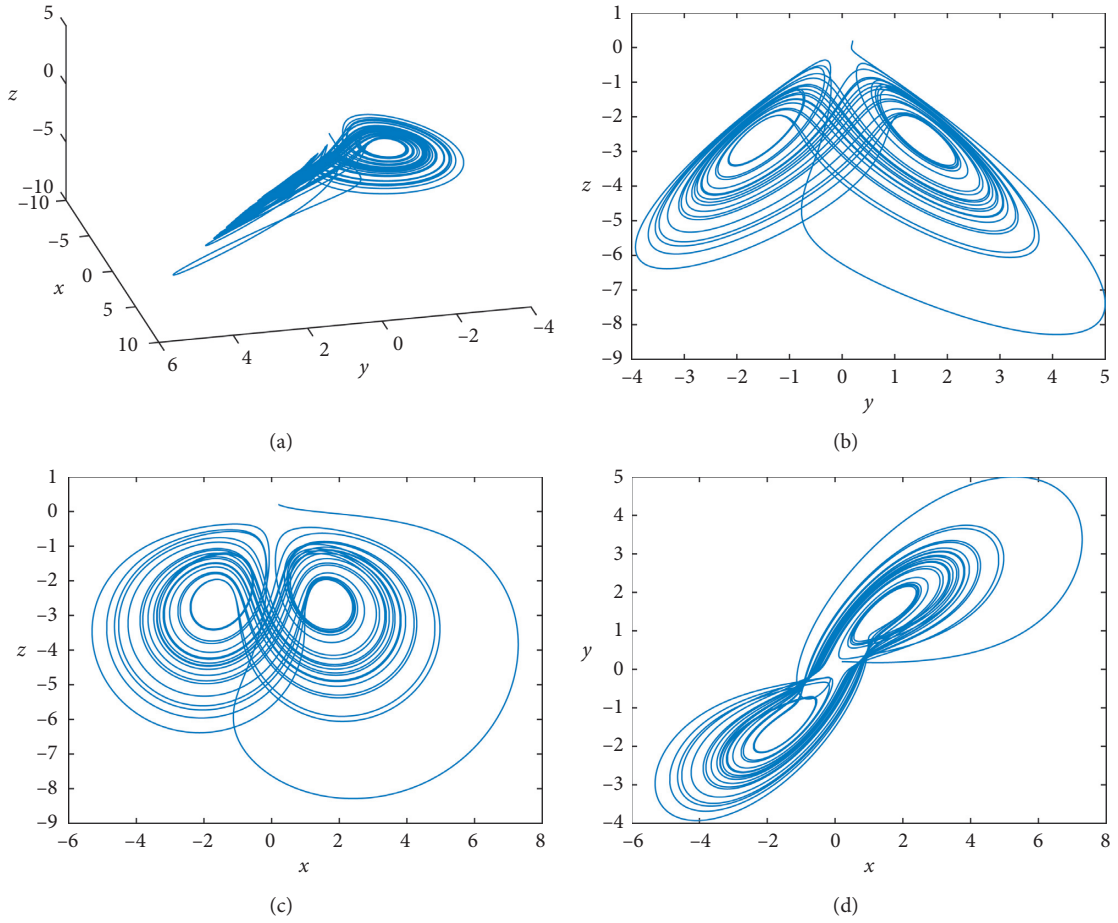

Figure 7: Phase portraits with the order $\alpha = 0.95$ and $a = 1.5$.

We need to utilize the fractional integrators associated with the order $\alpha = 0.95$ [25]; we have the following formula:

$$\frac{1}{s^{0.95}} \approx \frac{1.2862s^2 + 18.6004s + 2.0833}{s^3 + 18.4738s^2 + 2.6547s + 0.003}. \quad (52)$$

In equation (52), the third-order approximation is used, but more suitable approximations can also be used. This section's objective is the circuit schematic to validate our theoretical results; therefore, third- or fourth-order approximations can be used for illustration. The method of

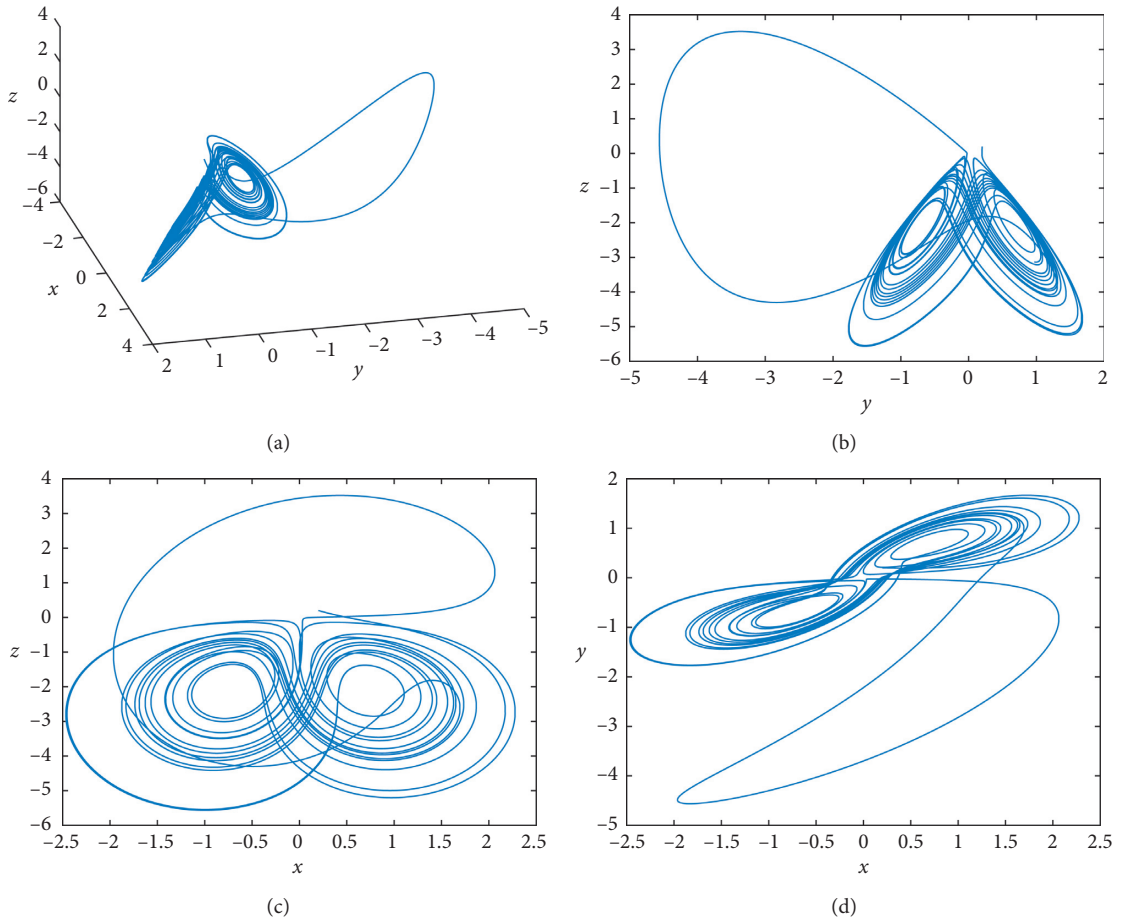

Figure 8: Phase portraits with the order $\alpha = 0.95$.

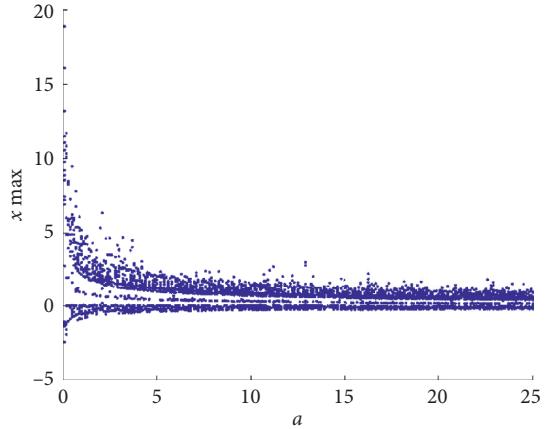

Figure 9: Bifurcation diagram versus the parameter c at order $\kappa = 0.95$.

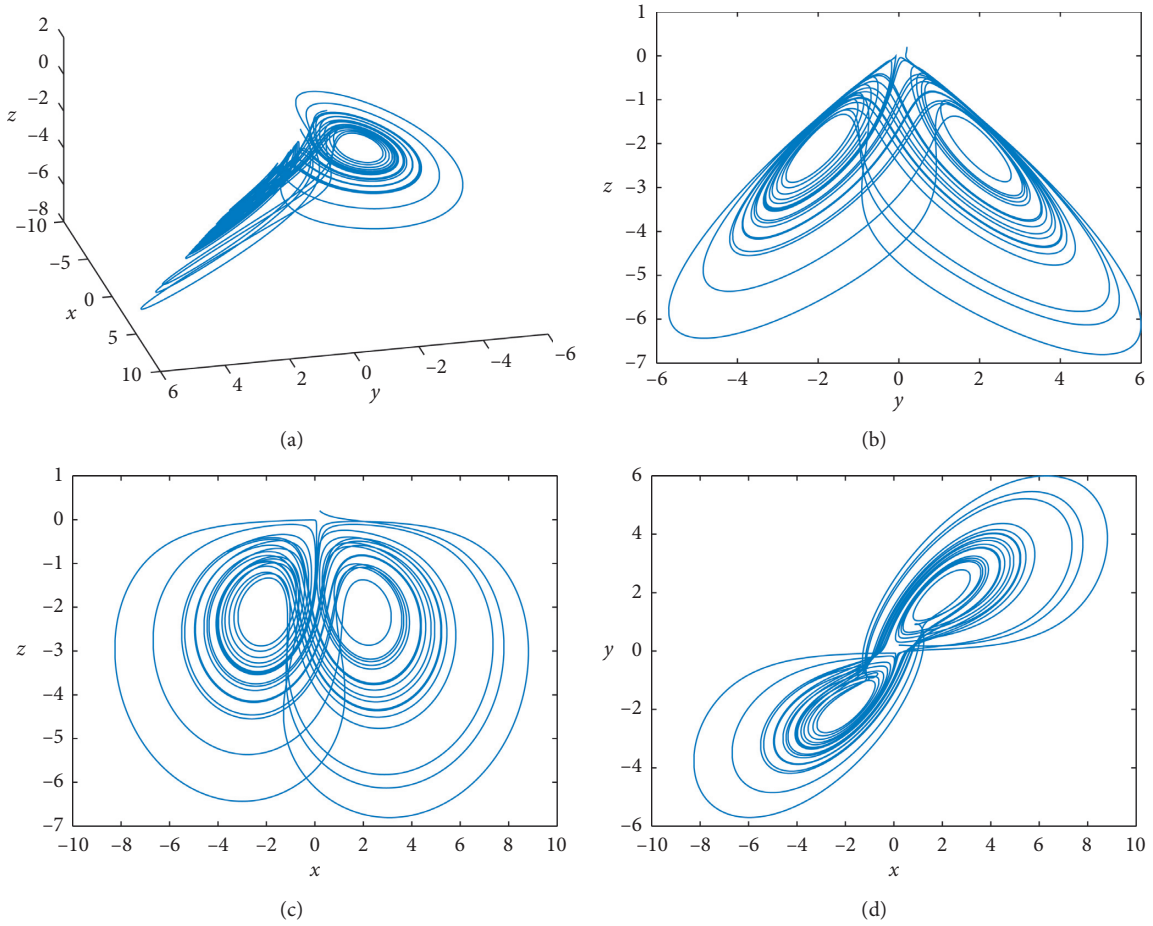

Figure 10: Phase portraits with the order $\alpha = 0.95$.

approximation in equation (52) is not unique. There also exists the 4^{th}-order approximation, which can generate a satisfactory magnitude and phase response over a considerable frequency band [26]. For more related works addressing the approximation of the fractional-order capacitor via fourth-order continued fraction expansion, see Mishra et al.'s investigation [26]. Utilizing the transfer function, the above function can be written as the following formula:

$$T(s) = \frac{(1/C_3)}{s + (1/R_9C_3)} + \frac{(1/C_4)}{s + (1/R_{10}C_4)} + \frac{(1/C_5)}{s + (1/R_{15}C_5)}. \tag{53}$$

Identifying two above equations (45) and (46), we have the following values for the resistors and the capacitors for the fractional integrator, $C_3 = 1.27\,\text{nF}$, $C_4 = 4.7\,\text{nF}$, $C_5 = 3.63\,\text{nF}$, $R_9 = 700\,\text{M}\Omega$, $R_{10} = 1.5\,\text{M}\Omega$, and $R_{15} = 15\,\text{k}\Omega$. The circuit schematic is done with the aids of 14 resistors, five capacitors, four multipliers for the 4 nonlinear functions, and others, see Figure 12.

The results corresponding to the simulation of the electronic circuit in the Multisim platform are shown in following Figures 13–15.

We can observe that the results with Matlab after simulating the numerical scheme in Figure 11 and the findings corresponding to the simulation of the electronic circuit in the Multisim platform shown in Figures 13–15 are in good agreement. This section connects the theoretical results with experimental results.

Before closing this section, we will implement the integer version of model equations (49)–(51). Therefore, the order α should be $\alpha = 1$. For the confirmation of our results obtained after the simulation of the electronic circuit in the Multisim platform, we first simulate the following differential equations:

$$x' = ax + y + yz, \tag{54}$$

$$y' = -xz + yz, \tag{55}$$

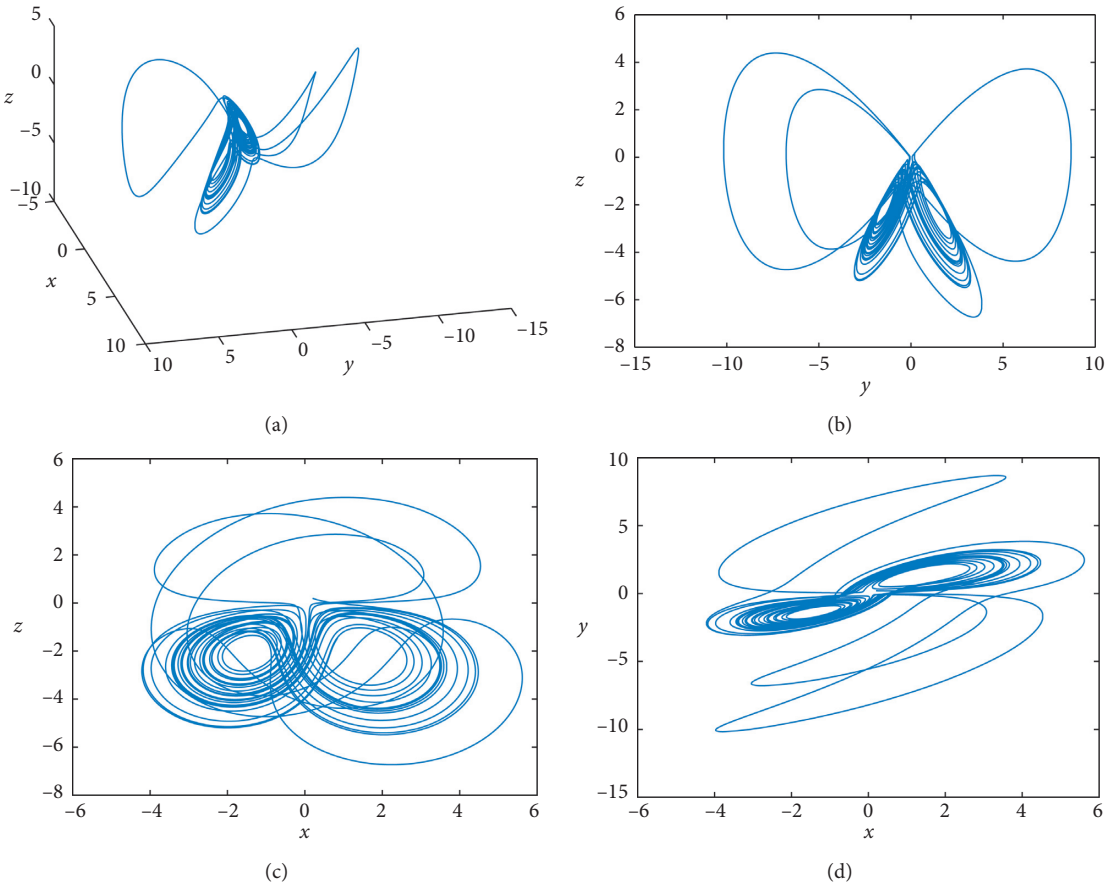

Figure 11: Phase portraits with incommensurate fractional system (42)–(44).

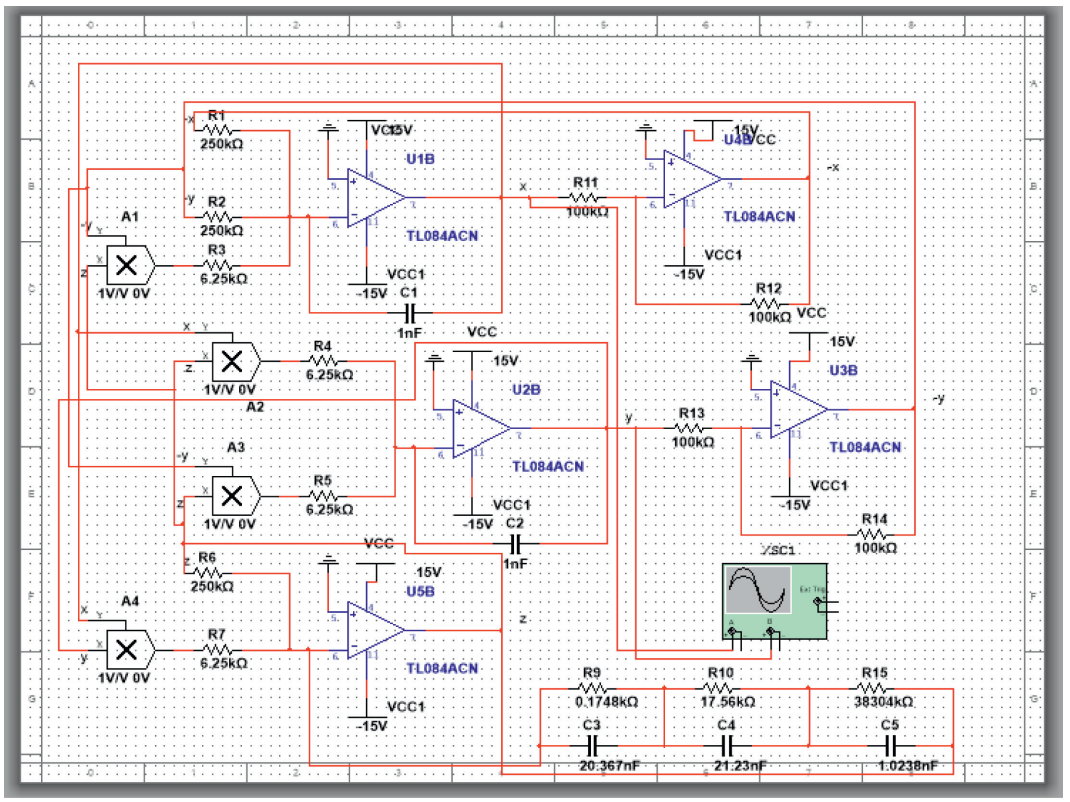

Figure 12: Circuit schematic for fractional-order system (42)–(44).

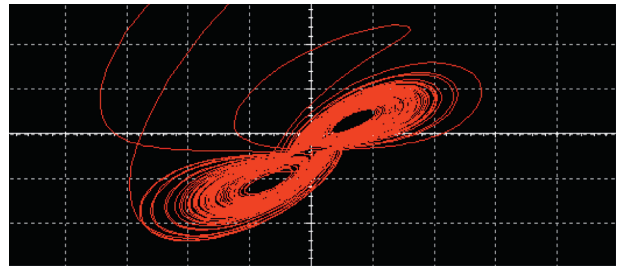

Figure 13: (x, y) space portrait of the Multisim simulation of equations (49)–(51).

$$z' = -z - cxy. \tag{56}$$

Under the initial conditions given by system (9) and with $a = 1$ and $c = 1$, the phase portraits are represented in following Figure 16.

For simulation of system (54)–(56), we rewrite equations (54)–(56) by using resistors and capacitors; we have the following representation:

$$x' = \frac{1}{R_1C_1}x + \frac{1}{R_2C_1}y + \frac{1}{R_3C_1}yz, \tag{57}$$

$$y' = -\frac{1}{R_4C_1}xz + \frac{1}{R_5C_2}yz, \tag{58}$$

$$z' = -\frac{1}{R_6C_3}z - \frac{1}{R_7C_3}xy, \tag{59}$$

where the values of capacitors are given $C_1 = C_2 = C_3 = 1\,\text{nF}$ and resistors are given by $R_1 = 250\,\text{k}\Omega$, $R_2 = 250\,\text{k}\Omega$, $R_3 = 6.25\,\text{k}\Omega$, $R_4 = 6.25\,\text{k}\Omega$, $R_5 = 6.25\,\text{k}\Omega$, $R_6 = 250\,\text{k}\Omega$, and $R_7 = 6.25\,\text{k}\Omega$. The schematic of the above system is represented in following Figure 17.

The phase portraits obtained after the simulation of the circuit in Figure 17 are in following Figures 18–20.

We can observe that the theoretical results 16 and the experimental results 18, 19, and 20 are in good agreement.

9. Sensitivity to Initial Conditions

In this section, we study the sensitivity of our model when the initial conditions change permanently. By the definition of chaos, the chaotic systems are very sensitive to the starting conditions. In this section, we try to measure the impact of the initial conditions via the bifurcation diagrams. For the rest of the paper, we consider equation (7) with commensurate order $\alpha = 0.95$. The comparisons are made with the conditions given by

$$\begin{aligned} x(0) &= x_0 = 0.2, \\ y(0) &= y_0 = 0.2, \\ z(0) &= z_0 = 0.2. \end{aligned} \tag{60}$$

We first consider the variation of the parameter a, and we influence the last initial condition z_0. The bifurcation map21 associated with the initial conditions $(0.2, 0.2, 0.2)$ (blue) and $(0.2, 0.2, 0.5)$ (red) versus the variation of the parameter a is given in following Figure 21.

The present bifurcation diagram, see Figure 21, informs us that the chaotic regions do not change significantly when the parameter a varies. Note that, for the initial condition $(0.2, 0.2, 0.2)$, the chaotic region is $(0.6, 5)$, and for the initial condition $(0.2, 0.2, 0.5)$, the chaotic region is $(0.7, 5)$. The initial conditions' impact can be observed at the beginning of the bifurcation diagram, in the interval $(0, 1)$, where system (7) trajectories converge to a stable equilibrium point. We notice that, with the first initial condition $(0.2, 0.2, 0.2)$, the system enters first in the chaotic region. The small perturbation on the starting condition can generate changes but not significantly when the parameter varies. To see the initial condition's influence according to the variation of a, we illustrate by representing the phase portraits at $a = 0.6$ and $a = 0.7$. When $a = 0.6$, we can observe that, in Figure 22, the phase space in (x, y) plane (blue) corresponding to $(0.2, 0.2, 0.2)$ is chaotic, contrary to the phase space22 in plane (x, y) (red) corresponding to $(0.2, 0.2, 0.5)$, where clearly the solutions of the system converge to an stable equilibrium point. Let us now $a = 0.7$; in Figure 22, the phase space in the plane (x, y) (blue) corresponding to the condition $(0.2, 0.2, 0.2)$ is chaotic, and the phase space22 in the plane (x, y) (red) corresponding to $(0.2, 0.2, 0.5)$ is also chaotic.

In the second, we suppose $y_0 = 0.5$, $x_0 = 0.2$, and $z_0 = 0.2$ are fixed. The variation of the parameter a is also considered in the bifurcation diagram. The sensitivity to the starting condition can also be observed in the bifurcation diagram. The bifurcation diagram, see Figure 23, associated with the conditions $(0.2, 0.2, 0.2)$ (blue) and $(0.2, 0.2, 0.5)$ (red) versus the variation of the parameter a is given in following Figure 23.

The bifurcation diagram, see Figure 23, informs us the chaotic regions $(0.6, 5)$ for the starting condition of equation (7) are given by $(0.2, 0.2, 0.2)$ and $(0.7, 5)$ for the new condition $(0.2, 0.5, 0.2)$. The influence of the initial conditions can be noticed in the interval $(0.6, 0.7)$, after this region equation (7) has strange attractors with the conditions $(0.2, 0.2, 0.2)$ and $(0.2, 0.5, 0.2)$. For illustration, see Figure 24, we consider $a = 0.65$, and we represent the phase space in the plane (x, z) for more clarity.

We finish this section with the perturbation of the first initial condition. The bifurcation diagram, see Figure 25,

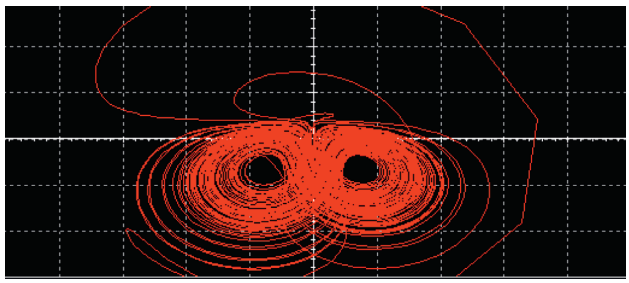

Figure 14: (x, z) space portrait of the Multisim simulation of equations (49)–(51).

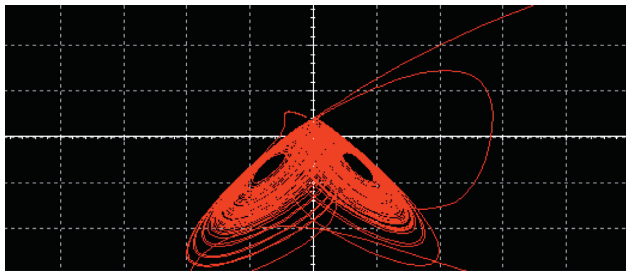

Figure 15: (y, z) space portrait of the Multisim simulation of equations (49)–(51).

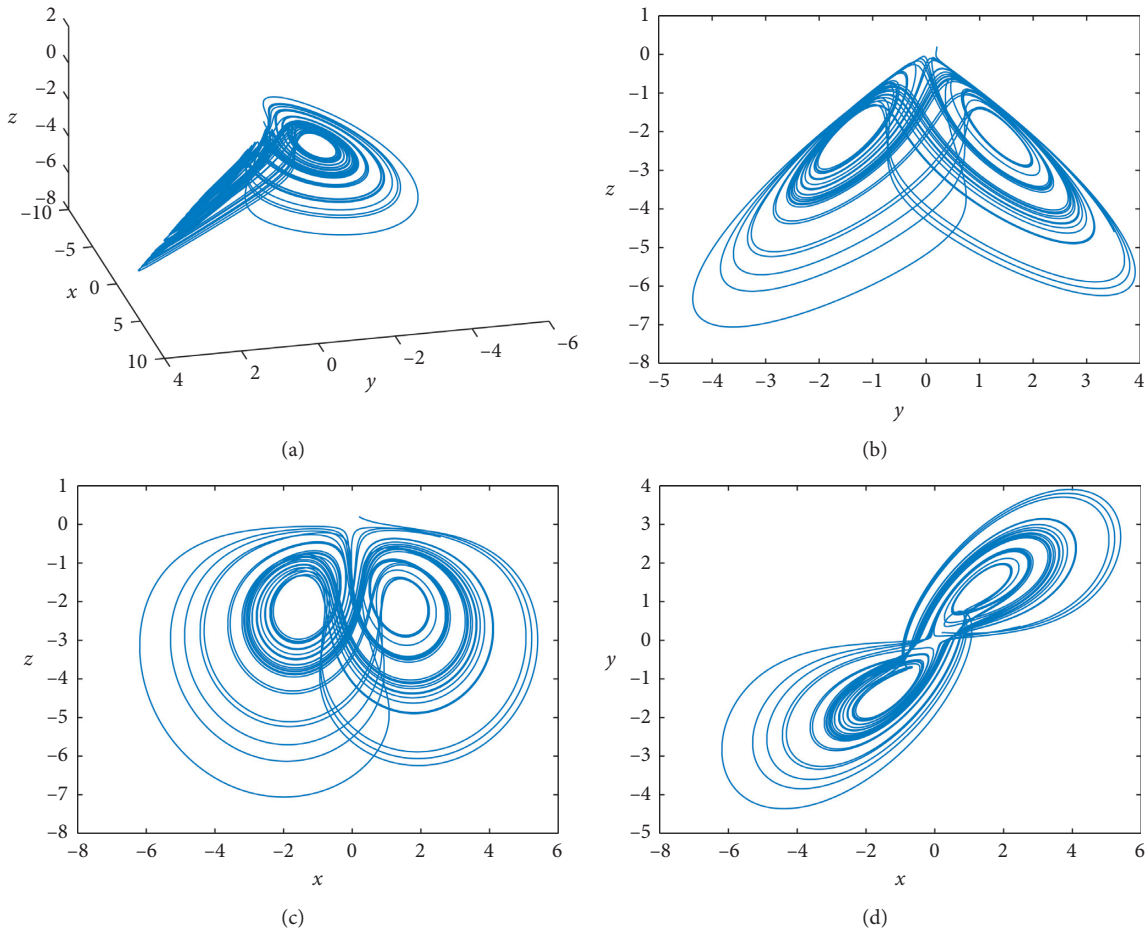

Figure 16: Phase portraits with system (54)–(56).

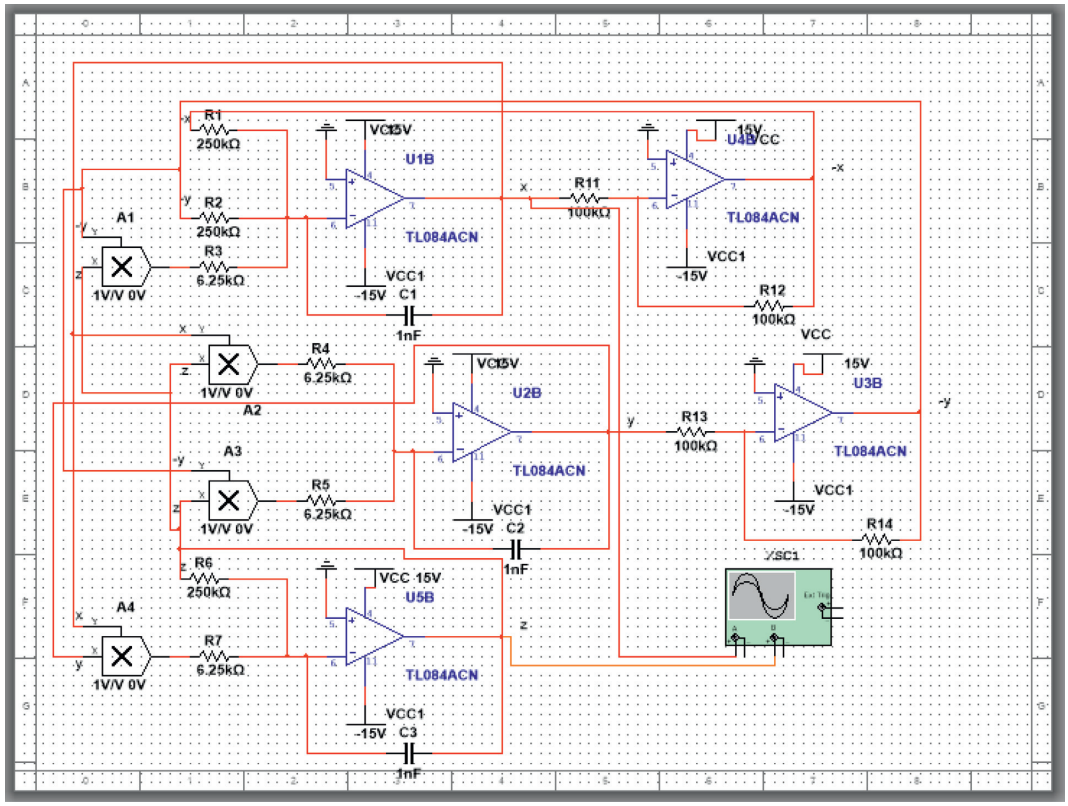

Figure 17: Circuit schematic for system (57)–(59).

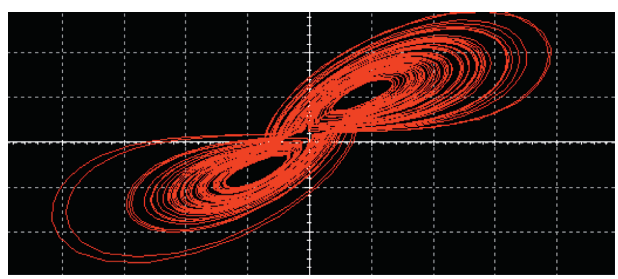

Figure 18: (x, y) space portrait of the Multisim simulation of equations (54)–(56).

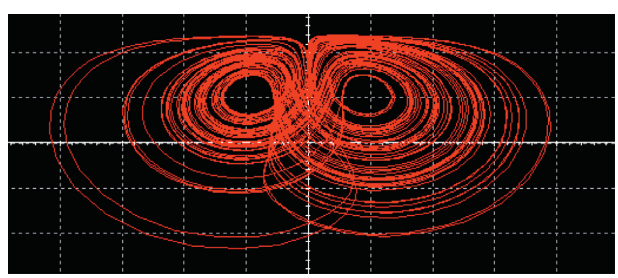

Figure 19: (x, z) space portrait of the Multisim simulation of equations (54)–(56).

associated to the initial conditions $(0.2, 0.2, 0.2)$ (blue) and $(0.5, 0.2, 0.2)$ (red) versus the variation of the parameter a is given in the following figure.

The bifurcation diagram presented in Figure 25 can be interpreted as with the condition $(0.2, 0.2, 0.2)$, the chaotic region does not change, and with $(0.5, 0.2, 0.2)$, the new chaotic region is also the interval $(0.7, 5)$. In bifurcation diagrams, see Figures 21, 23, and 25, the general observation is that the chaotic regions do not significantly change when the parameter a varies. We also observe that the chaotic

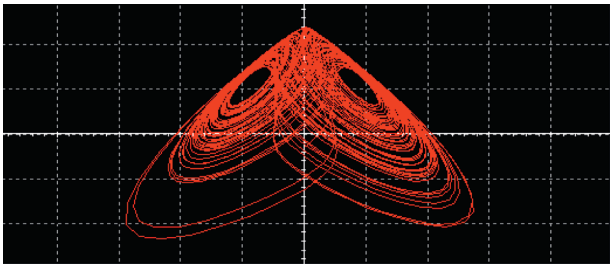

Figure 20: (y, z) space portrait of the Multisim simulation of equations (54)–(56).

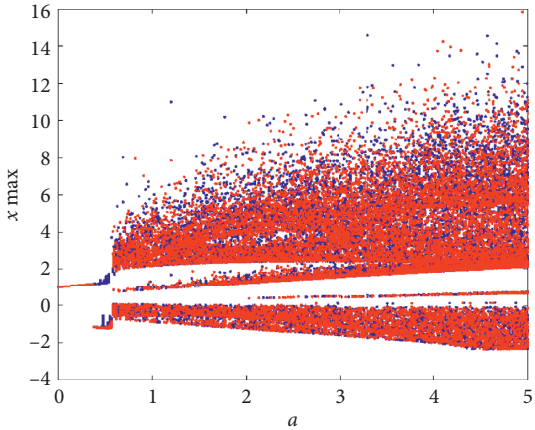

Figure 21: Bifurcation diagram versus the parameter a at $(0.2, 0.2, 0.2)$ and $(0.2, 0.2, 0.5)$.

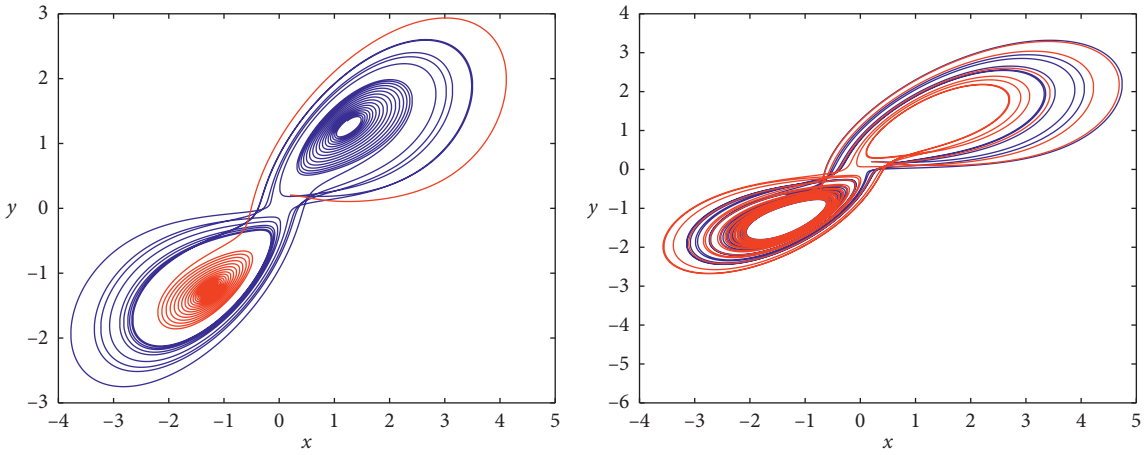

Figure 22: (a) Portrait at $a = 0.6$ in the plane (x, y). (b) Portrait at $a = 0.6$ in the plane (x, y).

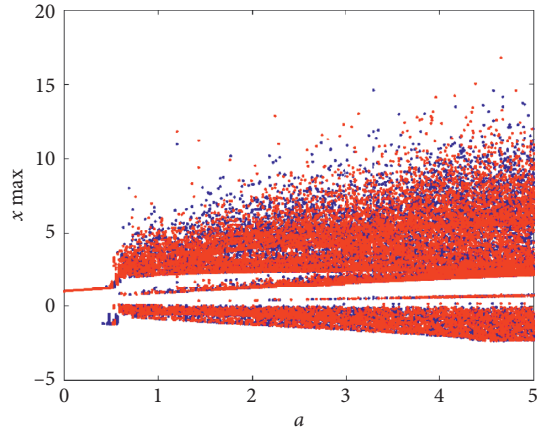

Figure 23: Bifurcation diagram versus the parameter a at $(0.2, 0.2, 0.2)$ and $(0.2, 0.5, 0.2)$.

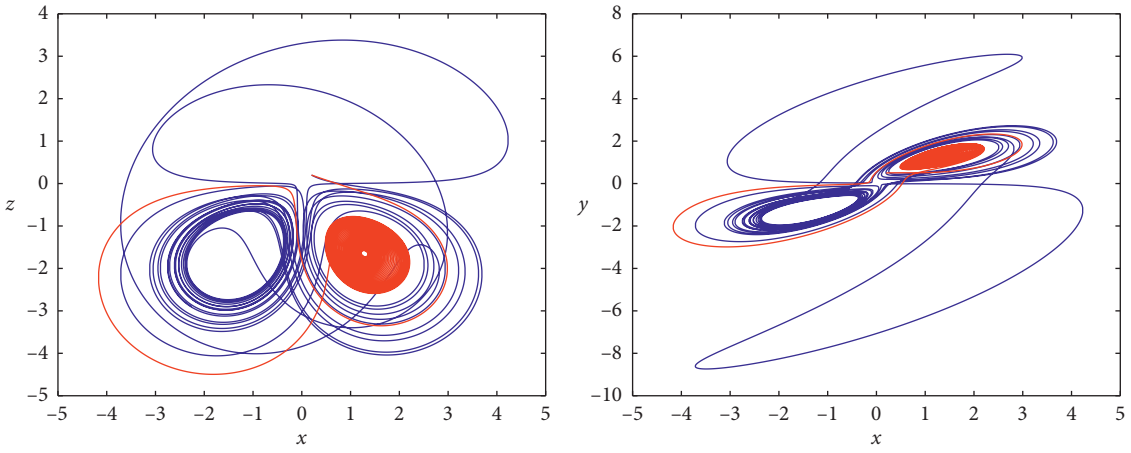

Figure 24: (a) Portrait at $a = 0.65$ in the plane (x, z). (b) Portrait at $a = 0.65$ in the plane (x, y).

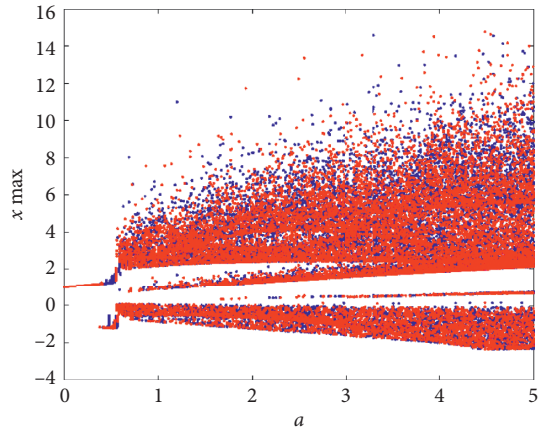

Figure 25: Bifurcation diagram versus the parameter a at $(0.2, 0.2, 0.2)$ and $(0.5, 0.2, 0.2)$.

region $(0.7, 5)$ is conserved for all new conditions $(0.2, 0.2, 0.5)$, $(0.2, 0.5, 0.2)$, and $(0.5, 0.2, 0.2)$. Thus, the small variation in the starting conditions does not affect the chaotic region of our present model.

10. Conclusion

In this paper, we have proposed a new system of differential equations that exhibit chaotic behavior and then studied with the Caputo fractional derivative. We have discussed the nature of the chaos for different orders of the fractional derivative using Lyapunov exponents. It is noticed that the fractional-order system considered in this paper has chaotic behavior when the order of the fractional derivative is into $(0.9, 1)$. The small variation of the model's parameters has been studied using bifurcation diagrams, which play an essential role in the chaos characterization. We also find that the initial condition's choice is crucial because our fractional-order system is very sensitive to the initial conditions. The investigations related to the Lyapunov exponents in the context of the fractional derivative are an open problem. The incommensurate fractional-order chaotic system can be investigated for future work. For example, how the phase portraits can be obtained in the context of incommensurate order. How can the Lyapunov exponents be calculated for a fractional-order chaotic system with incommensurate order? What about the variations of the parameters? What will be the impact of the different fractional-order derivatives?

Data Availability

No data were used to support this study.

Conflicts of Interest

The author declares that there are no conflicts of interest.

References

[1] M. Diouf and N. Sene, "Analysis of the financial chaotic model with the fractional derivative operator," *Complexity*, vol. 2020, Article ID 9845031, 14 pages, 2020.

[2] L. F. Ávalos-Ruiz, C. J. Zúñiga-Aguilar, J. F. Gómez-Aguilar, R. F. Escobar-Jiménez, and H. M. Romero-Ugalde, "FPGA implementation and control of chaotic systems involving the variable-order fractional operator with Mittag-Leffler law," *Chaos, Solitons & Fractals*, vol. 115, pp. 177–189, 2018.

[3] A. Akgul, "Chaotic oscillator based on fractional order memcapacitor," *Journal of Circuits, Systems and Computers*, vol. 28, no. 14, Article ID 1950239, 2019.

[4] Z. Wei, I. Moroz, J. C. Sprott, A. Akgul, and W. Zhang, "Hidden hyperchaos and electronic circuit application in a 5D self-exciting homopolar disc dynamo," *Chaos*, vol. 27, p. 033101, Article ID 033101, 2017.

[5] M.-F. Danca, "Lyapunov exponents of a discontinuous 4D hyperchaotic system of integer or fractional order," *Entropy*, vol. 20, no. 5, p. 337, 2018.

[6] F. Mansal and N. Sene, "Analysis of fractional fishery model with reserve area in the context of time-fractional order derivative," *Chaos, Solitons & Fractals*, vol. 140, Article ID 110200, 2020.

[7] N. Sene, B. Sène, S. N. Ndiaye, and A. Traoré, "Novel approaches for getting the solution of the fractional black-scholes equation described by Mittag-Leffler fractional derivative," *Discrete Dynamics in Nature and Society*, vol. 2020, Article ID 8047347, 11 pages, 2020.

[8] M. Yavuz and N. Sene, "Stability analysis and numerical computation of the fractional predator-prey model with the harvesting rate," *Fractal and Fractional*, vol. 4, no. 3, p. 35, 2020.

[9] S. K. Mishra, M. Gupta, and D. K. Upadhyay, "Fractional derivative of logarithmic function and its applications as multipurpose ASP circuit," *Analog Integrated Circuits and Signal Processing*, vol. 100, no. 2, pp. 377–387, 2019.

[10] S. K. Mishra, M. Gupta, and D. K. Upadhyay, "Design and implementation of DDCC-based fractional-order oscillator," *International Journal of Electronics*, vol. 106, no. 4, pp. 581–598, 2019.

[11] J. Munoz-Pacheco, E. Zambrano-Serrano, C. Volos, S. Jafari, J. Kengne, and K. Rajagopal, "A new fractional-order chaotic system with different families of hidden and self-excited attractors," *Entropy*, vol. 20, no. 8, p. 564, 2018.

[12] K. Rajagopal, L. Guessas, A. Karthikeyan, A. Srinivasan, and G. Adam, "Fractional order memristor no equilibrium chaotic system with its adaptive sliding mode synchronization and genetically optimized fractional order PID synchronization," *Complexity*, vol. 2017, Article ID 189261, , 2017.

[13] J. Gómez-Aguilar, D. Baleanu, and F. Tchier, "Chaotic attractors with fractional conformable derivatives in the Liouville-Caputo sense and its dynamical behaviors," *Entropy*, vol. 20, no. 5, p. 384, 2018.

[14] J. F. Gómez-Aguilar, K. Ali Abro, O. Kolebaje, and A. Yildirim, "Chaos in a calcium oscillation model via Atangana-Baleanu operator with strong memory," *The European Physical Journal Plus*, vol. 134, no. 4, p. 140, 2019.

[15] A. Atangana and J. F. Gomez-Aguilar, "Hyperchaotic behaviour obtained via a nonlocal operator with exponential decay and Mittag-Leffler laws," *Chaos, Solitons and Fractals*, vol. 102, pp. 285–294, 2017.

[16] C. Li, I. Pehlivan, J. Sprott, and A. Akgul, "A novel four-wing strange attractor born in bistability," *IEICE Electronics Express*, vol. 12, no. 4, pp. 1–12, 2015.

[17] K. Rajagopal, A. Durdu, S. Jafari, Y. Uyaroglu, A. Karthikeyan, and A. Akgul, "Multiscroll chaotic system with sigmoid nonlinearity and its fractional order form with synchronization application," *International Journal of Non-Linear Mechanics*, vol. 116, pp. 262–272, 2019.

[18] A. Akgul, C. Arslan, and B. Aricioglu, "Design of an interface for random number generators based on integer and fractional order chaotic systems," *Chaos Theory and Applications*, vol. 1, no. 1, pp. 1–18, 2019.

[19] A. Akgul, C. Li, and I. Pehlivan, "Amplitude control analysis of a four-wing chaotic attractor, its electronic circuit designs and microcontroller-based random number generator," *Journal of Circuits, Systems, and Computers*, vol. 26, no. 12, Article ID 1750190, 2017.

[20] A. A. Kilbas, H. M. Srivastava, and J. J. Trujillo, *Theory and Applications of Fractional Differential Equations*, North-Holland Mathematics Studies, Elsevier, Amsterdam, The Netherlands, 2006.

[21] I. Podlubny, *Fractional Differential Equations, Mathematics in Science and Engineering*, Academic Press, New York, NY, USA, 1999.

[22] J. Fahd, T. Abdeljawad, and D. Baleanu, "On the generalized fractional derivatives and their Caputo modification," *Journal*

of Nonlinear Sciences and Applications, vol. 10, pp. 2607–2619, 2017.

[23] R. Garrappa, "Numerical solution of fractional differential equations: a survey and a software tutorial," *Mathematics*, vol. 6, no. 2, p. 16, 2018.

[24] J. L. Echenausía-Monroy, H. E. Gilardi-Velázquez, R. Jaimes-Reátegui, V. Aboites, and G. Huerta-Cuellar, "A physical interpretation of fractional-order-derivatives in a jerk system: electronic approach," *Communications in Nonlinear Science and Numerical Simulation*, vol. 90, Article ID 105413, 2020.

[25] M. Borah, P. Roy, and B. K. Roy, "Synchronisation control of a novel fractional-order chaotic system with hidden attractor," in *Proceedings of the 2016 IEEE Students 'Technology Symposium'*, Kharagpur, India, September 2016.

[26] S. K. Mishra, D. K. Upadhyay, and M. Gupta, "An approach to improve the performance of fractional-order sinusoidal oscillators," *Chaos, Solitons & Fractals*, vol. 116, pp. 126–135, 2018.

Hindawi
Complexity
Volume 2021, Article ID 6653106, 10 pages
https://doi.org/10.1155/2021/6653106

Research Article

A Countable System of Fractional Inclusions with Periodic, Almost, and Antiperiodic Boundary Conditions

Ahmed Salem [1] **and Aeshah Al-Dosari** [1,2]

[1]*Department of Mathematics, Faculty of Science, King Abdulaziz University, P.O. Box 80203, Jeddah 21589, Saudi Arabia*
[2]*Prince Sattam University, Al-Kharj 16278, Saudi Arabia*

Correspondence should be addressed to Ahmed Salem; ahmedsalem74@hotmail.com

Received 22 March 2021; Accepted 28 May 2021; Published 14 June 2021

Academic Editor: Cristiana J. Silva

This article is dedicated to the existence results of solutions for boundary value problems of inclusion type. We suggest the infinite countable system to fractional differential inclusions written by ${}_{\mathrm{ABC}}D^{\alpha}[\nu_i(t)] \in \mathcal{Y}_i(t, \{\nu_i(t)\}_{i=1}^{\infty})$. The mappings $\mathcal{Y}_i(t, \{\nu_i(t)\}_{i=1}^{\infty})$ are proposed to be Lipschitz multivalued mappings. The results are explored according to boundary condition $\sigma\nu_i(0) = \gamma\nu_i(\rho), \quad \sigma, c \in \mathbb{R}$. This type of condition is the generalization of periodic, almost, and antiperiodic types.

1. Introduction

Consider the following infinite system:

$$ {}_{\mathrm{ABC}}D^{\alpha}[\nu_i(t)] \in \mathcal{Y}_i\left(t, \{\nu_j(t)\}_{j=1}^{\infty}\right), \quad i \in \mathbb{N}, t \in [0, \rho], \tag{1}$$

$$\sigma\nu_i(0) = \gamma\nu_i(\rho), \quad \sigma, \gamma \in \mathbb{R}, \tag{2}$$

where ${}_{\mathrm{ABC}}D^{\alpha}$ denotes the Atangana–Baleanu fractional derivative in the Caputo sense of order $\alpha \in (0, 1]$ and $\{\mathrm{y}_i\}_{i\in\mathbb{N}}$ is an infinite countable family of Lipschitz continuous multivalued mappings. This means there is an infinite countable sequence of continuous real-valued functions $\{\nu_i(t)\}_{i\in\mathbb{N}}$ satisfying problems (1) and (2). In this case, we can define the function $V(t)$: $[0, \rho] \longrightarrow \mathbb{R}^{\mathbb{N}}$ by $V(t) = (\nu_i(t))_{i\in\mathbb{N}}$. This function denotes the sequence of solutions for the given system.

In the field of infinite systems, the research to fractional differential problems started via ordinary derivatives (see [1–4] and the mentioned references therein). Then, many scholars were attracted to develop these problems into the ones associated with fractional derivatives. For instance, see the required results in [5–8] and references cited therein. The importance of the infinite system was arising naturally in the description of physical problems such as stochastic (stochastic metapopulation) models [9, 10], models descried by the Becker–Döring cluster [11, 12], and optimal pursuit equations [13] and the control problems for the models descried by parabolic and hyperbolic equations [14].

The concept of fractional derivative arose before 300 years when L'Hospital asked in 1695 which is addressed in Leibnitz notation for the nth derivative "What would happen if the order $n = 1/2$?". So, the idea of fractional derivative started by operators with power kernel (Riemman and Caputo derivatives). It has been industrialized due to complexities associated with the heterogeneous phenomenon. The fractional differential operators are capable of capturing the behavior of multifaceted media as they have diffusion processes. In this field, many researchers have paid attention in several ways to develop these derivatives. For instance, they found the ways for the development to new ones without the problem of nonsingularity (Caputo–Fabrizio with the exponential kernel) and then without nonlocality (Atangana–Baleanu with the Mittag–Leffler kernel). Mittag–Leffler kernel in the AB derivative helps to understand the beginning and the end of a considered phenomenon which is due to the memory effect of the Mittag–Leffler function. Additionally, in some works, it was proved that the AB derivative can generate chaotic behaviors in some linear and nonlinear systems for certain values taken

by the derivative order. In other situations, some researchers have shown that the fractional derivatives lost some of the basic properties that usual derivatives have such as the product rule and the chain rule. For the sake of solving this problem, they investigated the conformable fractional derivative. This derivative is important to develop the Lie symmetry analysis for differential equations involving different fractional derivatives such as the Caputo–Fabrizio derivative and Atangana–Baleanu derivative. In fact, the development of fractional calculus theory matches with the development of analytical and numerical methods for solving fractional differential equations and systems. For showing this importance, we refer to see [15–18] and the references therein.

In [19], we studied how to generate the differential equations and inclusions by one form (we call them as equi-inclusion problems). Then, we studied the solvability of this form. Next, in [20], we generated the fractional differential equation at resonance on the half line into the inclusion one and explored the existence results of positive solutions for this problem. After research and reading about the infinite system topic, we find that all proven treatises are linked only to single-valued operators. So, what we refer here is to survey the infinite fractional differential system proposed with multivalued mappings. This means we hatch a generalization of previous literature studies in the infinite system field. This draws a way to new and important extents for the infinite system theory of nonlinear analysis. Furthermore, it would be useful to express some descriptions of complicated physical phenomena. We have a strong anticipation that the partial differential inclusion which leads to the infinite system of fractional differential inclusions would be very influential to make a fundamental shift in the theory of complicated neural sets, huge and stochastic branching processes, and the theory of dissociation of polymers. Also, by the inclusion system with ${}_{\mathrm{ABC}}D^{\alpha}$, we think that modeling and computations will be performed to explore deep and manifold aspects of mixed convective flow of nanofluids and random flow processes of so many fluids.

Our work is concerned with the existence of anti-periodic, periodic, and almost periodic solutions for problem (1) in the Banach space $\ell_p(\mathbb{R}^{\mathbb{N}})$, $1 < p < \infty$. Theorems used here give us sufficient conditions for the existence of common solutions to the infinite family of quasi-nonexpansive multivalued operators in the uniformly convex real Banach space. The results are affected by hemicompactness, compactness, contraction properties, and the one-step iterative scheme.

It is worth remarkable to mention that the field of studying the existence and uniqueness of solutions to fractional differential equations has drawn attention of many contributors [21–28].

2. Preliminaries

We present this section with some needed definitions, facts, lemmas, theorems, and auxiliary results used to start the main theorems.

2.1. Real Sequence Banach Space. Define the space $\mathbb{V}$ to be the real sequence Banach space $\ell_p(\mathbb{R}^{\mathbb{N}})$, $1 < p < \infty$, endowed with the norm

$$\|V\|_{\ell_p} = \left(\sum_{i=1}^{\infty} |\nu_i|^p\right)^{(1/p)}, \quad V = (\nu_i)_{i\in\mathbb{N}}. \tag{3}$$

Then, from [29–31], we have the following facts.

Definition 1. (uniformly convex space). A normed space $\mathbb{V}$ is called a uniformly convex space if for any $\varepsilon \in (0, 2]$, there exists $\delta = \delta(\varepsilon) > 0$ such that if $\nu_1, \nu_2 \in \mathbb{V}$ with $\|\nu_1\| = \|\nu_2\| = 1$ and $\|\nu_2 - \nu_1\| \geq \varepsilon$, then $\|(1/2)(\nu_1 + \nu_2)\| \leq 1 - \delta$.

Lemma 1. *The space ℓ_p is uniformly convex for all $1 \leq p < \infty$.*

Theorem 1. *Adopt $1 \leq p, q < \infty$ such that $(1/p) + (1/q) = 1$. Then, the inequalities thereafter hold:*

(i) Holder inequality: let $\eta \in \ell_p$ and $\eta\prime \in \ell_q$. Then, $\eta\eta\prime \in \ell_1$ and

$$\|\eta\eta\prime\|_{\ell_1} \leq \|\eta\|_{\ell_p}\|\eta\prime\|_{\ell_q}. \tag{4}$$

(ii) Minkowski inequality: let $\eta, \eta\prime \in \ell_p$. Then, $\eta + \eta\prime \in \ell_p$ and

$$\|\eta + \eta\prime\|_{\ell_p} \leq \|\eta\|_{\ell_p} + \|\eta\prime\|_{\ell_p}. \tag{5}$$

(iii) Imbedding theorem: let Ω have a finite positive measure and $1 \leq q \leq p \leq \infty$. Then, $\ell_q(\Omega) \subseteq \ell_p(\Omega)$ and

$$\|\eta\|_{\ell_p} \leq \|\eta\|_{\ell_q}. \tag{6}$$

Theorem 2. *(compactness in ℓ_p). Let E be a Banach space and $K \subset \ell_p(E)$. Then, K is compact in $\ell_p(E)$ if and only if*

(i) K is closed and bounded

(ii) $(\sum_{r=n}^{\infty} |\nu_r|^p)^{(1/p)} \longrightarrow 0$ as $n \longrightarrow \infty$

(iii) If $D_r\colon \ell_p(E) \longrightarrow E$ defined for all $(\nu_r) \in \ell_p(E)$ by $D_r[(\nu_r)_{r\geq 1}] = \nu_r$, then $D_r(K)$ is compact for all $r \geq 1$

Corollary 1. *The subsets*

$$K_x = \left\{(\nu_r)_{r\geq 1} \in \ell_p \middle| |\nu_r| \leq |x_r|, |x_r| \longrightarrow 0 \quad \text{as } r \longrightarrow 0, 1 \leq p \leq \infty\right\} \tag{7}$$

are compact subsets of ℓ_p spaces.

2.2. Basics in Multivalued Maps. The concept of multi-operators is related to the multivalued maps. So, it is required to show some facts about them and their properties. These facts are confirmed in [32–37].

Let $(E, \|.\|)$ and $(H, \|.\|)$ be two Banach spaces. A multivalued map A: $E \longrightarrow P_{cl}(E)$ is seen as convex (closed) if for every $e \in E$, then $A(e)$ is convex (closed) and selected to be completely continuous if $A(B)$ is relatively compact for every $B \in P_b(E)$.

The map A is said to be upper semicontinuous if for each closed subset $W \subset E$, $A^{-1}(W)$ is a closed subset of E. This means the set $\{e \in E: A(e) \subseteq O\}$ is open for all open sets $O \subset E$. It is lower semicontinuous if for each open subset $Z \subset E$, $A^{-1}(Z)$ is an open subset of E. In other words, A seems to be lower semicontinuous as long as the set $\{e \in E: A(e) \cap O \neq \varnothing\}$ is open for all open sets $O \subset E$.

A map A: $[0, \varepsilon] \longrightarrow P_{cl}(E)$ is presented to be measurable multivalued if for every $e \in E$, the function $\tau \longrightarrow d(e, A(\tau)) = \inf\{d(e, a): a \in A(\tau)\}$ is $\mathscr{L}$–measurable function.

Given $C, B \in P_{cl}(E)$; then,

$$\begin{aligned} h(C, B) &= H_d(C, B) = d_H(C, B) \\ &= \max\{\sup_{c \in C} d(c, B), \sup_{b \in B} d(C, b)\} \end{aligned} \tag{8}$$

absorbs the Pompeiu–Hausdorff distance of C, B.

If we adopt A as a completely continuous function with nonempty compact values, then it is upper semicontinuous if and only if its graph is closed (i.e., if $v_n \longrightarrow v_*$ and $y_n \longrightarrow y_*$, then $y_n \in A(v_n)$ implies to $y_* \in A(v_*)$).

Definition 2. A multivalued map A: $[a, b] \times \mathbb{R} \longrightarrow P(\mathbb{R})$ is known as Caratheodory if

(1) $\forall r_n \in \mathbb{R}, n \in \mathbb{N}, \quad \tau \longrightarrow A(\tau, \{r_n\})$ is measurable

(2) For a.e. $\tau \in [a, b]$, $(\{r_n\}) \longrightarrow A(\tau, \{r_n\})$ is upper semicontinuous

In addition to assumptions (1) and (2), the map A is L^1-Caratheodory if for each $k > 0$, $\exists\, \phi_k \in L^1[a, b]$ satisfying $\sup_{\tau \geq 0} |\phi_k(\tau)| < +\infty$ and $\phi_k > 0$ and nondecreasing map Ł for which

$$\begin{aligned} \left\|A(\tau, \{r_n\})\right\| &= \sup\{|a|: a(\tau) \in A(\tau, \{r_n\})\} \\ &\leq \phi_k(\tau) Ł(\|\mathrm{r}\|), \ \mathrm{r} = (\mathrm{r_n}), \end{aligned} \tag{9}$$

for all $\|r\| < k$, $n \in \mathbb{N}$, $\tau \in [a, b]$.

Definition 3 (nonexpansive and quasi-nonexpansive multimapping). Let K be a subset of a metric space E and T: $K \longrightarrow P_{cl,b}(K)$ be a multivalued map with $\mathrm{Fix}(T) = \{v \in K | Tv = v\}$ (the set of all fixed points of T in K). Then, we have the following:

(i) T is called a nonexpansive mapping if it is contraction according to the metric. This means that, for all $v_1, v_2 \in K$, we have

$$H_d(Tv_2, Tv_1) \leq \left\|v_2 - v_1\right\|_E. \tag{10}$$

(ii) T is said to be quasi-nonexpansive if $\mathrm{Fix}(T) \neq \varnothing$ and for all $w \in \mathrm{Fix}(T)$ and all $v \in K$, we have

$$H_d(Tv, Tw) \leq \|v - w\|_E. \tag{11}$$

(iii) $\mathrm{Fix}(T)$ is a closed subset if K is closed and convex of E.

Definition 4 (hemicompactness). Let K, E, and T be defined as in Definition 3. Then, T is called hemicompact if

(i) For any sequence $(v_r)_{r \in \mathbb{N}} \in K$ such that $d(v_r, Tv_r) \longrightarrow 0$ as $r \longrightarrow 0$, there is a subsequence (v_r^s) of (v_r) with $v_r^s \longrightarrow w \in K$

(ii) T is compact

Theorem 3 (nonempty infinite intersection). *For any space W, the following statements are equivalent:*

(i) W is compact.

(ii) Every decreasing sequence $\{W_n | n \in \mathbb{N}\}$ of nonempty closed subsets of W has a nonempty intersection

$$\left((\mathrm{i.e})\, W_{n+1} \subseteq W_n, \quad \forall n \in \mathbb{N} \Rightarrow \bigcap_{n \geq 1} W_n \neq \varnothing\right). \tag{12}$$

(iii) Every collection $\{W_n | n \in \mathbb{N}\}$ of nonempty closed subsets of W satisfying the finite intersection property has a nonempty intersection

$$\left((\mathrm{i.e}) \bigcap_{s=1}^{m} W_{n_s} \neq \varnothing \Rightarrow \bigcap_{n \geq 1} W_n \neq \varnothing\right). \tag{13}$$

2.3. Fractional Calculus. In this part, we give definitions related to the used derivative, its history, the corresponding integral, and some properties [38–40].

Definition 5 (Riemann–Liouville integral). For the order $\zeta > 0$, the Riemann–Liouville fractional integral of a function $h(\tau)$: $[0, \infty) \longrightarrow \mathbb{R}$ is defined by

$$I^{\zeta} h(\tau) = \frac{1}{\Gamma(\varsigma)} \int_0^{\tau} (\tau - \varsigma)^{\zeta - 1} h(\varsigma) \mathrm{d}\varsigma \tag{14}$$

since the R.H.S is pointwise defined on $(0, \infty)$.

Definition 6 (Caputo–Fabrizio derivative). CF derivative for the order $\alpha \in [0, 1]$ and $\eta(\varsigma) \in H^1(a, b)$ is given by

$${}^{\mathrm{CF}}D^{\alpha} \eta(\varsigma) = \frac{(2 - \alpha) M(\alpha)}{2(1 - \alpha)} \int_a^{\varsigma} e^{-(\alpha(\varsigma - s)/1 - \alpha)} \eta\prime(s) \mathrm{d}s, \tag{15}$$

where $M(\alpha)$ is a normalization function such that $M(0) = M(1) = 1$.

Definition 7 (Mittag–Leffler function). The general form of Mittag–Leffler function E_{α} of order α is written by

$$E_{\alpha}(v) = \sum_{r=0}^{\infty} \frac{v^r}{\Gamma(\alpha r + 1)}. \tag{16}$$

The main derivative used in the present paper is the Atangana–Baleanu fractional derivative in the Caputo sense. It is proposed by interchanging the kernel $\exp(-(\alpha(\varsigma-s)/1-\alpha))$ in the Caputo–Fabrizio derivative by the equivalent form via the Mittag–Leffler formula that is $\sum_{r=0}^{\infty}((-a(t-s))^r/r!)$, $a=(\alpha/1-\alpha)$. After that, replace $r!$ by $\Gamma(\alpha r+1)$ and $(-a(t-s))^r$ by $(-a(t-s))^{\alpha r}$. So, in the space

$$H^1(\Omega)=\left\{\eta(\varsigma)|\eta(\varsigma),\ D^{\rho}\eta(\varsigma)\in L^2(\Omega),\quad \forall\rho\le 1\right\},\tag{17}$$

we have the following definitions.

Definition 8 (Atangana–Baleanu fractional derivative in the Caputo sense). ABC derivative for the order $\alpha\in[0,1]$ and $\nu(\varsigma)\in H^1(a,b)$ is given by

$${}_{\mathrm{ABC}}D^{\alpha}\nu(\varsigma)=\frac{M(\alpha)}{(1-\alpha)}\int_a^{\varsigma}E_{\alpha}\left[-\frac{\alpha(\varsigma-s)^{\alpha}}{1-\alpha}\right]\nu\prime(s)\mathrm{d}s.\tag{18}$$

This derivative is related to the fading memory concept and frequently used to discuss and analyze the real-world phenomena such as fluid and nanofluid models (see [41–43] and references therein). Depending on the constant $M(\alpha)$, the corresponding integral is given by the following definition.

Definition 9 (Atangana–Baleanu fractional integral). AB integral of the order $\alpha\in[0,1]$ and $\nu(\varsigma)\in H^1(a,b)$ is given by

$${}_{\mathrm{AB}}I^{\alpha}\nu(t)=\frac{1-\alpha}{M(\alpha)}\nu(t)+\frac{\alpha}{M(\alpha)}{}_{R}I_a^{\alpha}\nu(t),\tag{19}$$

where ${}_{R}I^{\alpha}$ is the Riemann–Liouville integral of order α.

Lemma 2. *For $\alpha\in(0,1)$, $t\in(a,b)$, and $\nu(t)\in AC^1[a,b]$, the following statements hold:*

a1: AB integral together with the ABC derivative satisfies the Newton–Leibniz formula

$${}_{\mathrm{AB}}I_{a^+}^{\alpha}\left[{}_{\mathrm{ABC}}D_{a^+}^{\alpha}\nu\right](t)=\nu(t)-\nu(a).\tag{20}$$

a2: they also satisfy the property

$${}_{\mathrm{ABC}}D_{0^+}^{\alpha}\left[{}_{\mathrm{AB}}I_{0^+}^{\alpha}\nu\right](t)=\nu(t)-\nu(o)E_{\alpha}\left(\frac{-\alpha t^{\alpha}}{1-\alpha}\right).\tag{21}$$

a3: AB integral is a commutative operator such that, for any two orders $\alpha,\beta\in(0,1)$, we have

$$\begin{aligned}{}_{\mathrm{AB}}I_{a^+}^{\alpha}\left[{}_{\mathrm{AB}}I_{a^+}^{\beta}\nu\right](t)&=\left[\frac{1-\alpha}{M(\alpha)}+\frac{\alpha}{M(\alpha)}{}_{\mathrm{R}}I_a^{\alpha}\right]\left[\frac{1-\beta}{M(\beta)}+\frac{\beta}{M(\beta)}{}_{\mathrm{R}}I_a^{\beta}\right]\\ \nu(t)&=\left[\frac{1-\beta}{M(\beta)}+\frac{\beta}{M(\beta)}{}_{\mathrm{R}}I_a^{\beta}\right]\left[\frac{1-\alpha}{M(\alpha)}+\frac{\alpha}{M(\alpha)}{}_{\mathrm{R}}I_a^{\alpha}\right]\\ \nu(t)&={}_{\mathrm{AB}}I_{a^+}^{\beta}\left[{}_{\mathrm{AB}}I_{a^+}^{\alpha}\nu\right](t).\end{aligned}\tag{22}$$

Lemma 3 (antiperiodic solution). *The unique solution of the problem*

$${}_{\mathrm{ABC}}D^{\alpha}[\nu(t)]=\varepsilon(t),\quad t\in[0,\rho],\tag{23}$$

$$\sigma\nu(0)=\gamma\nu(\rho),\sigma,\quad \gamma\in\mathbb{R},\ \text{with}\ \sigma\neq\gamma,\ \alpha\in[0,1],\tag{24}$$

is given by

$$\begin{aligned}\nu(t)=&\frac{1-\alpha}{M(\alpha)}\varepsilon(t)+\frac{\alpha}{M(\alpha)\Gamma(\alpha)}\int_0^t(t-s)^{\alpha-1}\varepsilon(s)\mathrm{d}s\\&+\frac{\gamma}{\sigma-\gamma}\left[\frac{1-\alpha}{M(\alpha)}\left(\varepsilon(\rho)-\frac{\sigma}{\gamma}\varepsilon(0)\right)\right.\\&\left.+\frac{\alpha}{M(\alpha)\Gamma(\alpha)}\int_0^{\rho}(\rho-s)^{\alpha-1}\varepsilon(s)\mathrm{d}s\right].\end{aligned}\tag{25}$$

Proof. By applying ${}_{\mathrm{AB}}I^{\alpha}$ to both sides of (23), we get

$$\nu(t)={}_{\mathrm{AB}}I^{\alpha}(\varepsilon)(t)+c,\tag{26}$$

which implies

$$\begin{aligned}\nu(0)&=\frac{1-\alpha}{M(\alpha)}\varepsilon(0)+c,\\ \nu(\rho)&={}_{\mathrm{AB}}I^{\alpha}(\varepsilon)(\rho)+c.\end{aligned}\tag{27}$$

Now, applying (24), we find that

$$\begin{aligned}c=&\frac{\gamma}{\sigma-\gamma}\left[\frac{1-\alpha}{M(\alpha)}\left(\varepsilon(\rho)-\frac{\sigma}{\gamma}\varepsilon(0)\right)\right.\\&\left.+\frac{\alpha}{M(\alpha)\Gamma(\alpha)}\int_0^{\rho}(\rho-s)^{\alpha-1}\varepsilon(s)\mathrm{d}s\right].\end{aligned}\tag{28}$$

□

Lemma 4 (periodic/almost periodic solution). *The unique solution of the problem*

$$\begin{aligned}{}_{\mathrm{ABC}}D^{\alpha}[\nu(t)]&=\varepsilon(t),\quad t\in[0,\rho],\\ \nu(0)&\cong\nu(\rho),\quad \alpha\in[0,1],\end{aligned}\tag{29}$$

is given by

$$\nu(t)={}_{\mathrm{AB}}I^{\alpha}(\varepsilon)(t)+c\quad\text{whenever}\tag{30}$$

$$\varepsilon(0)\cong\varepsilon(\rho),\tag{31}$$

$$\int_0^{\rho}\frac{(\rho-s)^{\alpha-1}}{\Gamma(\alpha)}\varepsilon(s)\mathrm{d}s\cong 0,\tag{32}$$

and then $c\cong-(1-\alpha/M(\alpha))\varepsilon(0)\cong-(1-\alpha/M(\alpha))\varepsilon(\rho)$.

Proof. Similar to the proof of Lemma 3, we have

$$\nu(t)={}_{\mathrm{AB}}I^{\alpha}(\varepsilon)(t)+c.\tag{33}$$

The almost periodic/periodic condition leads to

$$(1-\alpha)(\varepsilon(\rho)-\varepsilon(0))+\frac{\alpha}{\Gamma(\alpha)}\int_0^{\rho}(\rho-s)^{\alpha-1}\varepsilon(s)\mathrm{d}s\cong 0. \quad (34)$$

Under this equation, we have three cases:

p1: if $\alpha=0$, then $\varepsilon(\rho)\cong\varepsilon(0)$ must hold

p2: when $\alpha\in(0,1)$, both $\varepsilon(\rho)\cong\varepsilon(0)$ and $\int_0^{\rho}((\rho-s)^{\alpha-1}/\Gamma(\alpha))\varepsilon(s)\mathrm{d}s\cong 0$ must hold

p3: in case $\alpha=1$, we get $\int_0^{\rho}\varepsilon(s)\mathrm{d}s\cong 0$

So, we can say, in general, that there is an almost periodic/periodic solution if both (31) and (32) hold for every $\alpha\in[0,1]$. Now, substituting (31) and (32) to the value of $c=c(\sigma)$ in Lemma 3 with $\sigma\longrightarrow\gamma$ and using the continuity condition, we get $\lim_{\sigma\longrightarrow\gamma}c=-((1-\alpha/M(\alpha)))\varepsilon(0)=c|_{\sigma=\gamma}$. Hence, the periodic/almost periodic solution is given by

$$\begin{aligned}\nu(t)&={}_{\mathrm{AB}}I^{\alpha}(\varepsilon)(t)-\left(\frac{1-\alpha}{M(\alpha)}\right)\varepsilon(0)\\&=\frac{1-\alpha}{M(\alpha)}[\varepsilon(t)-\varepsilon(0)]+\frac{\alpha}{M(\alpha)\Gamma(\alpha)}\int_0^{t}(t-s)^{\alpha-1}\varepsilon(s)\mathrm{d}s.\end{aligned} \quad (35)$$

It is clear to see that $\nu(0)\cong 0\cong\nu(\rho)$ which completes the proof. □

2.4. Fixed-Point Theorems. This section is surveyed by some fixed-point theorems investigated in the uniformly convex real Banach space [44, 45].

Theorem 4. *Let $\mathbb{V}$ be a uniformly convex real Banach space and K be a closed, bounded, convex subset of $\mathbb{V}$. Let $T\colon K\longrightarrow P_{cp}(K)$ be nonexpansive multivalued mappings. Then, T has a fixed point $x\in K$ with $x\in Tx$.*

The next theorem is formulated for the infinite countable family of multioperators under the vision of the one-step iterative scheme defined as follows.

Let K be a closed, bounded, convex subset of a uniformly convex real Banach space $\mathbb{V}$. Let $\{T_i\colon K\longrightarrow P_b(K)\}$ be an infinite countable family of quasi-nonexpansive multivalued mappings with $\cap_{i=1}^{\infty}Fix(T_i)\neq\varnothing$ and $p\in\cap_{i=1}^{\infty}Fix(T_i)$. Then, for all $n\in\mathbb{N}$, the sequence $\{V_n\}$ is defined by

$$V_1\in K,\quad V_{n+1}=\sigma_{n,0}V_n+\sum_{r=1}^{n}\sigma_{n,r}V_{n,r}, \quad (36)$$

$$V_{n,r}\in T_rV_n,\ \text{such that}\ \|p-V_{n,r}\|=d(p,T_rV_n), \quad (37)$$

$$\{\sigma_{n,r}\}\subset[0,1),\ \text{with}\ \sum_{r=0}^{n}\sigma_{n,r}=1,\quad r\in\mathbb{N}. \quad (38)$$

Theorem 5. *Let K be a closed, bounded, convex subset of a uniformly convex real Banach space $\mathbb{V}$. Let $\{T_i\colon K\longrightarrow P_b(K)\}$ be a sequence of quasi-nonexpansive and continuous multivalued mappings with $\cap_{i=1}^{\infty}Fix(T_i)\neq\varnothing$ and $p\in\cap_{i=1}^{\infty}Fix(T_i)$. Let $\{V_i\}$ be a sequence defined by (36) with the condition that $\lim_{n\longrightarrow\infty}\sigma_{n,r}$ and $\lim_{n\longrightarrow\infty}\sigma_{n,n}$ exist and lie in $[0,1)$ for all $r\in\{0\}\cup\mathbb{N}$. Assume that one of $\{T_i\}$ is hemicompact. Then, the sequence $\{V_i\}$ converges strongly.*

3. Inferred Results

3.1. Auxiliary Results. Let $V(t)\colon C[0,\rho]\longrightarrow\mathbb{R}^{\mathbb{N}}$ be defined by $V(t)=(\nu_i(t))_{i\in\mathbb{N}}$. Then, for every multivalued mapping $\mathcal{Y}_i$, we have $\mathcal{Y}_i(t,\nu_1(t),\ldots,\nu_i(t),\ldots)=\mathcal{Y}_i(t,V(t))$. Define the set-valued maps $S_{\mathcal{Y}_i,V}$ such as

$$S_{\mathcal{Y}_i,V}=\{\varepsilon_i(t)|\,\varepsilon_i(t)\in\mathcal{Y}_i(t,V(t))\cap L^1(J,\mathbb{R})\},\quad J=[0,\rho]. \quad (39)$$

For the antiperiodic solutions, we define the multioperators $\{\Upsilon_i\colon\ell_p\longrightarrow\mathbb{R}\}$ for all $i\in\mathbb{N}$ as follows:

$$(\Upsilon_iV)(t)=\{\Psi_{\mathcal{Y}_i}(t)|\Psi_{\mathcal{Y}_i}(t)=\Delta(\varepsilon_i)(t),\quad \varepsilon_i(t))\in\overline{S_{\mathcal{Y}_i,V}}\}, \quad (40)$$

where

$$\begin{aligned}\Delta(\varepsilon_i)(t)&=\frac{1-\alpha}{M(\alpha)}\varepsilon_i(t)+\frac{\alpha}{M(\alpha)\Gamma(\alpha)}\int_0^{t}(t-s)^{\alpha-1}\varepsilon_i(s)\mathrm{d}s\\&\quad+\frac{\gamma}{\sigma-\gamma}\left[\frac{1-\alpha}{M(\alpha)}\left(\varepsilon_i(\rho)-\frac{\sigma}{\gamma}\varepsilon_i(0)\right)\right.\\&\quad\left.+\frac{\alpha}{M(\alpha)\Gamma(\alpha)}\int_0^{\rho}(\rho-s)^{\alpha-1}\varepsilon_i(s)\mathrm{d}s\right].\end{aligned} \quad (41)$$

For the almost periodic/periodic solutions, the multioperators $\{\Pi_i\colon\ell_p\longrightarrow\mathbb{R}\}$ for all $i\in\mathbb{N}$ are defined by

$$(\Pi_iV)(t)=\{\Theta_{\mathcal{Y}_i}(t)|\,\Theta_{\mathcal{Y}_i}(t)=\underline{\Delta}(\varepsilon_i)(t),\ \varepsilon_i(t)\in\overline{S_{\mathcal{Y}_i,V}}\}, \quad (42)$$

where

$$\begin{aligned}\underline{\Delta}(\varepsilon_i)(t)&=\frac{1-\alpha}{M(\alpha)}[\varepsilon_i(t)-\varepsilon_i(0)]\\&\quad+\frac{\alpha}{M(\alpha)\Gamma(\alpha)}\int_0^{t}(t-s)^{\alpha-1}\varepsilon_i(s)\mathrm{d}s.\end{aligned} \quad (43)$$

Consider that the following conditions hold:

(H_1) $(\mathcal{Y}_i)$ is a sequence of L^1–Caratheodory multivalued mappings that are

$$\mathcal{Y}_i\colon J\times\mathbb{V}\longrightarrow P_{cp}(\mathbb{R}), \quad (44)$$

with

(1) The maps $t\longrightarrow\mathcal{Y}_i(t,V(t))$ are measurable for all $V\in\mathbb{V}$.
(2) The maps $V\longrightarrow\mathcal{Y}_i(t,V(t))$ are measurable for all $t\in J$.
(3) For all $i\in\mathbb{N}$, there exist $\psi_i\in C[J,\mathbb{R}_+]$ such that

(H_2) y_i are Lipschitz mappings with constants $L_i\in\mathbb{R}_+$, respectively. This means

$$H_d\left(\mathscr{Y}_i(t,V_1(t)),\ \mathscr{Y}_i(t,V_2(t))\right) \le L_i\left\|V_1 - V_2\right\|, \quad \forall i \in \mathbb{N}. \tag{46}$$

$(\mathscr{H}_3)$ $\sum_{i\ge 1} L_i < \infty$ and $Z = \Xi \sum_{i=1}^{\infty} L_i < 1$ whenever

$$\Xi = 2\left(\frac{1-\alpha}{M(\alpha)}\right) + \left(1 + \left|\frac{\gamma}{\sigma-\gamma}\right|\right)\frac{\rho^{\alpha}}{M(\alpha)\Gamma(\alpha)}. \tag{47}$$

$(\mathscr{H}_4)$ $(|\nu_i|/\Xi\psi_i^*|\nu_i|) > 1$, $\psi_i^* = \sup_{t\in J}|\psi_i(t)|$.

Then, we have the following propositions.

Proposition 1. *The set-valued maps $\Upsilon_i(V)$ are bounded and contraction for all $i \in \mathbb{N}$.*

Proof. In view of $(\mathscr{H}_1)$ and $(\mathscr{H}_4)$, we have

$$\begin{aligned}\left|\Upsilon_i(V)\right| &\le \left[\frac{1-\alpha}{M(\alpha)} + \frac{t^{\alpha}}{M(\alpha)\Gamma(\alpha)} + \left|\frac{\gamma}{\sigma-\gamma}\right|\left(\left|1-\frac{\sigma}{\gamma}\right|\left(\frac{1-\alpha}{M(\alpha)}\right)\right.\right.\\ &\quad \left.\left. + \frac{\rho^{\alpha}}{M(\alpha)\Gamma(\alpha)}\right)\right]\left|\mathscr{Y}_i(t,V(t))\right|\\ &\le \Xi\psi_i^*\left|\nu_i\right| \le \left|\nu_i\right|.\end{aligned} \tag{48}$$

Thus, we prove the boundedness.

To prove the contraction condition for all $i \in \mathbb{N}$, consider that $\Psi^1_{\mathscr{Y}_i}(t) \in \Upsilon_i(V_2)$. This implies the existence of some $\varepsilon_i^1(t) \in \overline{S_{\mathscr{Y}_i,V_2}}$ subject to

$$\Psi^1_{\mathscr{Y}_i}(t) = \Delta\left(\varepsilon_i^1(t)\right), \tag{49}$$

where Δ is defined by (41). By using $(\mathscr{H}_2)$, we can define the sets

$$\overline{\Upsilon}_i(t) = \left\{\varepsilon \in \mathbb{R} \mid \left|\varepsilon_i^1(t) - \varepsilon(t)\right| \le L_i\left\|V_1 - V_2\right\|_{\ell_p}\right\}. \tag{50}$$

According to Theorem III.41 in [46], $(\mathscr{H}_1)$, and the measurability of the functions $\varepsilon_i^1(t)$ and $W(t) = L_i\|V_1 - V_2\|_{\ell_p}$, the sets $\overline{\Upsilon}_i(t)$ are also measurable for all $i \in \mathbb{N}$. Therefore, the maps $t \longrightarrow \overline{\Upsilon}_i(t) \cap \mathscr{Y}_i(t,V(t))$ are measurable with nonempty closed values. Hence, the measurability of $\Upsilon_i(t)$ and Proposition 2.1.43 in [47] drive to the existence of some $\varepsilon_i^2 \in \overline{S_{\mathscr{Y}_i,V_1}}$ for which

$$\left|\varepsilon_i^1(t) - \varepsilon_i^2(t)\right| \le L_i\left\|V_1 - V_2\right\|_{\ell_p}, \quad i \in \mathbb{N}. \tag{51}$$

Define $\Psi^2_{\mathscr{Y}_i}$ by

$$\Psi^2_{\mathscr{Y}_i}(t) = \Delta\left(\varepsilon_i^2(t)\right), \tag{52}$$

which leads to

$$\begin{aligned}\left|\Psi^1_{\mathscr{Y}_i}(t) - \Psi^2_{\mathscr{Y}_i}(t)\right| &= \left|\Delta\left(\varepsilon_i^1\right)(t) - \Delta\left(\varepsilon_i^2\right)(t)\right|\\ &\le \Xi L_i\left\|V_1 - V_2\right\|_{\ell_p}, \quad i \in \mathbb{N},\end{aligned} \tag{53}$$

where $\Xi L_i < 1$ by $(\mathscr{H}_3)$. Using the Akin relation obtained by interchanging the rules of V_1 and V_2, we conclude that, for all $i \in \mathbb{N}$, the operators Υ_i are contraction. □

Proposition 2. *For all $n \in \mathbb{N}$, define the operators T_n: $K_x \to P(K_x)$,*

$$\begin{aligned}T_n(V) &= \left(\nu_1, \ldots, \nu_{n-1}, \nu_n, \Upsilon_{n+1}(V), \ldots\right)\\ &= \left(\begin{Bmatrix}\nu_i, & i \le n\\ \Upsilon_i(V), & i > n\end{Bmatrix}\right),\end{aligned} \tag{54}$$

where K_x is created as the one in Corollary 1. The following statements are all satisfied:

(i) $T_n(V) \in P_b(K_x)$ for all $n \in \mathbb{N}$

(ii) T_n are contraction with constants $Z = \Xi\sum_{i=1}^{\infty} L_i$ for all $n \in \mathbb{N}$ if and only if there exist some $\Psi_{\mathscr{Y}_i}(t) \in \Upsilon_i(V)$ such that $\nu_i = \Psi_{\mathscr{Y}_i}(t)$

(iii) $\{T_n\}_{n\in\mathbb{N}}$ is a decreasing nested sequence which means $T_{n+1} \subseteq T_n$ for all $n \in \mathbb{N}$

Proof

(i) Using Proposition 1 and the definition of K_x, we get, for all $i \in \mathbb{N}$, that $|\Upsilon_i(V)| \le |\nu_i| \le |x_i|$. This implies $(\Upsilon_i(V))_{i\ge 1} \in K_x$. Consequently, $T_1(V) \in P_b(K_x)$, and thus, all $T_n(V) \in P_b(K_x)$ for all $i \in \mathbb{N}$.

(ii) Define the metric map G_d as

$$G_d\left(T_n(V_1), T_n(V_2)\right) = \sum_{i=1}^{\infty} H_d\left(\Upsilon_i(V_1), \Upsilon_i(V_2)\right). \tag{55}$$

Consider that there exist some $\Psi_{\mathscr{Y}_i}(t) \in \Upsilon_i(V)$ such that $\nu_i = \Psi_{\mathscr{Y}_i}(t), i = 1, \ldots, n$. Using the contraction result in Proposition 1, we find

$$\begin{aligned}G_d\left(T_n(V_1), T_n(V_2)\right) &\le \left[\Xi\sum_{i=1}^{\infty} L_i\right]\left\|V_1 - V_2\right\|_{\ell_p}\\ &= Z\left\|V_1 - V_2\right\|_{\ell_p}.\end{aligned} \tag{56}$$

Applying $(\mathscr{H}_3)$, we get the result of the contraction condition for T_n for all $n \in \mathbb{N}$.

Now, consider that, for all $n \in \mathbb{N}$, T_n are contraction and $\nu_i \notin \Upsilon_i(V)$. Define the metric

$$\begin{aligned}\overline{G}_d\left(T_n(V_1), T_n(V_2)\right) &= \sum_{r=1}^{n}\left|\nu_1^r - \nu_2^r\right|\\ &\quad + \sum_{r=n+1}^{\infty} H_d\left(\Upsilon_r(V_1), \Upsilon_r(V_2)\right).\end{aligned} \tag{57}$$

Then,

$$\begin{aligned}&\overline{G}_d\left(T_n(V_1), T_n(V_2)\right)\\&\le n\left\|V_1 - V_2\right\|_{\ell_p} + \left[\Xi \sum_{r=n+1}^{\infty} L_i\right]\left\|V_1 - V_2\right\|_{\ell_p}\\&= (n+Z)\left\|V_1 - V_2\right\|_{\ell_p},\end{aligned} \tag{58}$$

where $(n+Z) > 1$. This contradicts with the assumption that T_n are contraction operators. Hence, we get $\nu_i \in \Upsilon_i(V)$.

(iii) By (ii), we have for all $n \in \mathbb{N}$ that

$$\begin{aligned}T_n(V) &= \begin{pmatrix} \{ & \begin{matrix} \nu_i & i \le n \\ \Upsilon_i(V) & i > n \end{matrix} \end{pmatrix}\\&= \begin{pmatrix} \{ & \begin{matrix} \Psi_{\mathscr{Y}_i}(t) & i \le n \\ \Upsilon_i(V) & i > n \end{matrix} \end{pmatrix} \supseteq \begin{pmatrix} \{ & \begin{matrix} \Psi_{\mathscr{Y}_i}(t) & i \le n+1 \\ \Upsilon_i(V) & i > n+1 \end{matrix} \end{pmatrix}\\&= \begin{pmatrix} \{ & \begin{matrix} \nu_i & i \le n+1 \\ \Upsilon_i(V) & i > n+1 \end{matrix} \end{pmatrix} = T_{n+1}(V).\end{aligned} \tag{59}$$

□

Proposition 3. *For all $n \in \mathbb{N}$, define T_n such as in Proposition 2. Then,*

a1: for all $n \in \mathbb{N}, T_n$ are quasi-nonexpansive mappings

a2: for all $n \in \mathbb{N}, Fix(T_n)$ are closed subsets of K_x

a3: for all $n \in \mathbb{N}, T_n$ are all hemicompact mappings

a4: $\cap_{i=1}^{\infty} Fix(T_n) \neq \varnothing$

Proof

a1: following the theorem saying that the continuous image of the compact set is compact itself with applying Proposition 2 (I, II) implies $T_n(K_x) \subset P_{cp}(K_x)$. By Theorem 6 and Definition 3, we get $\mathrm{Fix}(T_n) \neq \varnothing$ for all $n \in \mathbb{N}$. Thus, T_n are all quasi-nonexpansive operators.

a2: from (a1) and since K_x is a closed and convex subset of Banach space, we see that $\mathrm{Fix}(T_n)$ are closed subsets of K_x according to Definition 3.

a3: due to Definition 4 and the proof of (a1), T_n are hemicompact for all $n \in \mathbb{N}$.

a4: let $p \in \mathrm{Fix}(T_{n+1})$; then, $p \in T_{n+1}(p) \subseteq T_n(p)$. Hence, $p \in T_n(p)$ which follows $\mathrm{Fix}(T_{n+1}) \subseteq \mathrm{Fix}(T_n)$. Using Theorem 3, we get $\cap_{i=1}^{\infty} \mathrm{Fix}(T_n) \neq \varnothing$. □

3.2. Main Results

Theorem 6. *Consider that $\mathscr{Y}_i: J \times \mathbb{V} \longrightarrow P_{cp}(\mathbb{R})$ satisfy $(\mathscr{H}_1)$, $(\mathscr{H}_2)$, $(\mathscr{H}_3)$, and $(\mathscr{H}_4)$. Assume that, for all $n \in \mathbb{N}$, T_n are defined by (40), (41), and (54). Also, let*

$$\Xi = 2\left(\frac{1-\alpha}{M(\alpha)}\right) + \left(1 + \left|\frac{\gamma}{\sigma - \gamma}\right|\right)\frac{\rho^{\alpha}}{M(\alpha)\Gamma(\alpha)}. \tag{60}$$

Then, infinite systems (1) and (2) are able to have a common antiperiodic solution if and only if there exist some $\Psi_{\mathscr{Y}_i}(t) \in \Upsilon_i(V)$ such that $\nu_i = \Psi_{\mathscr{Y}_i}(t)$.

Proof. Define the sequence $\{V_n\}_{n \ge 1}$ by (36)–(38). Under the vision of Theorem 5, Propositions 1–3 explain the existence of the common solution to infinite systems (1) and (2). □

Theorem 7. *Consider that $\mathscr{Y}_i: J \times \mathbb{V} \longrightarrow P_{cp}(\mathbb{R})$ satisfy $(\mathscr{H}_1)$, $(\mathscr{H}_2)$, and $(\mathscr{H}_4)$. Assume that, for all $n \in \mathbb{N}$, $\overline{T}_n$ are defined by the same way as (54) with respect to (42) and (43). Moreover, let*

$$\overline{\Xi} = 2\left(\frac{1-\alpha}{M(\alpha)}\right) + \frac{\rho^{\alpha}}{M(\alpha)\Gamma(\alpha)} \tag{61}$$

and

$(\mathscr{H}_5)$ $\sum_{i \ge 1} L_i < \infty$ and $\overline{Z} = \overline{\Xi} \sum_{i=1}^{\infty} L_i < 1$.

Then, infinite systems (1) and (2) are able to have at least a common periodic solution if and only if there exist some $\Theta_{\mathscr{Y}_i}(t) \in \Pi_i(V)$ such that $\nu_i = \Theta_{\mathscr{Y}_i}(t)$.

Proof. Similar to the proof of Theorem 6 but with respect to $\overline{\Xi}$. □

Corollary 2. *Infinite systems (1) and (2) are able to have one or more common almost periodic solutions.*

4. Examples

Example 1. Consider the problem

$${}_{\mathrm{ABC}}D^{(2/3)}[\nu_n] \in \left[\frac{1}{2^{nr}}\left(\frac{\nu_n}{1 + \sum_{s=1}^{r}|\nu_s|}\right)\right]_{r=1}^{n}, \tag{62}$$

$$3V(0) = V(\rho). \tag{63}$$

Then, we have $\mathscr{Y}_n(t, V(t)) = [(1/2^{nr})\ (\nu_n/1 + \sum_{s=1}^{r}|\nu_s|)]_{r=1}^{n}$ and

$$\left|\mathscr{Y}_n\right| \le \frac{1}{2^n}|\nu_n|. \tag{64}$$

If we take $\psi_n(t) = (1/2^n) = \psi_n^*$, we find that $(\mathscr{H}_1)$ holds. Furthermore, we have

$$\begin{aligned}&H_d\left(\mathscr{Y}_n(t, V_1(t)), \mathscr{Y}_n(t, V_2(t))\right) \le \frac{1}{2^n}\left|\nu_1^n - \nu_2^n\right|\\&= \frac{1}{2^n}\left(\left|\nu_1^n - \nu_2^n\right|^p\right)^{(1/p)} \le \frac{1}{2^n}\left\|V_1 - V_2\right\|_{\ell_p},\end{aligned} \tag{65}$$

which explains that $(\mathscr{H}_2)$ holds with $L_n = (1/2^n)$. It is known that $\sum_{n=1}^{\infty} L_n = \sum_{n=1}^{\infty}(1/2^n) = 1 < \infty$. In this case, we need to make sure that $\Xi < 1$ for the sake of obtaining $(\mathscr{H}_3)$. First, by using the rules

$$M(\alpha) = \frac{2}{2-\alpha},$$
$$\Gamma(\alpha)\Gamma(1-\alpha) = \frac{\pi}{\sin\ \alpha\pi}, \tag{66}$$

we find that

$$M\left(\frac{2}{3}\right) = \frac{3}{2},$$
$$\Gamma\left(\frac{1}{3}\right) \approx 2.6789385347077476337,$$
$$\frac{1}{M(2/3)\Gamma(2/3)} \approx 0.0086,$$
$$\left(1 + \left|\frac{\gamma}{\sigma-\gamma}\right|\right)\frac{\rho^{\alpha}}{M(\alpha)\Gamma(\alpha)} \approx 0.0129\rho^{(2/3)},$$
$$2\left(\frac{1-\alpha}{M(\alpha)}\right) = \frac{4}{9}. \tag{67}$$

Taking $\rho^{(2/3)} \leq (2/9(0.0129))$ implies that $\rho \in (0, 10.5881117)$. Therefore, $\Xi \leq (8/9) < 1$ which means that $(\mathscr{H}_3)$ holds. Finally, since $\psi_n^*\Xi \leq (8/9(2^n)) < 1$, $n \geq 1$, $(\mathscr{H}_4)$ holds. Applying Theorem 6, there exists at least one solution of antiperiodic type for problems (62) and (63).

Example 2. Assume the following problem:

$${}_{\mathrm{ABC}}D^1[\nu_n] \in \left[\frac{1}{(2+r)^n}\left(\frac{\sin\ \nu_n}{1+\sum_{s=1}^{r}|\nu_s|}\right)\right]_{r=1}^{n}, \tag{68}$$

$$V(0) = V(\rho). \tag{69}$$

In this problem, we have $\alpha = M(\alpha) = 1$,

$$\mathscr{Y}_n(t, V(t)) = \left[\frac{1}{(2+r)^n}\left(\frac{\sin\ \nu_n}{1+\sum_{s=1}^{r}|\nu_s|}\right)\right]_{r=1}^{n},$$
$$|\mathscr{Y}_n| \leq \frac{1}{3^n}|\nu_n|. \tag{70}$$

It follows that $\psi_n(t) = (1/3^n) = \psi_n^*$, and thus, $(\mathscr{H}_1)$ holds. It is clear to see that $(\mathscr{H}_2)$ holds if we take $L_n = (1/3^n)$ and then $\sum_{n=1}^{\infty} L_n = (1/2) < 1$. Since $\alpha = 1$, $\overline{\Xi} = \rho$, and $\overline{Z} = (\rho/2)$ tends to take $\rho \in (0, 2)$ in order to obtain $(\mathscr{H}_5)$. Finally, we have $(1/\Xi\psi_n^*) = (3^n/\rho) > (3/2) > 1$ which drives to $(\mathscr{H}_6)$. According to Theorem 7, problems (42), (43), (54), (62), (63), (68), and (69) have at least one periodic solution.

Remark 1. If we take problems (42), (43), (54), (62), (63), (68), and (69) with the condition $V(0) \approx V(\rho)$, then by the same results in Example 2, we get the existence result of the almost periodic solution.

5. Conclusion

By this work, we connected between three sides of generalization: first, using the generalization of fractional differential operators with the Mittag–Leffler kernel; second, generating the infinite countable system of equations by multivalued mappings; third, using the general form of periodic, almost periodic, and antiperiodic boundary conditions. We explain how to obtain the exact solutions in the three cases according to the boundary conditions. Consequently, we show the sufficient conditions for the existence results to different solutions and give some related examples to the main theorems. These results have strong impacts to give an even better description of the dynamics of real-world problems (in particular, the dynamics complex systems). These results also have practical extensions to understand the complex phenomena related to multifaceted media, chaotic behaviors, fluctuations, nanofluids, and heterogeneous phenomenon. Next time, we will work to study the generalization of the conjugate value problem with one of the most important derivatives.

Data Availability

The data used to support the findings of this study are included within the article, and other data used can be obtained from the corresponding author upon request.

Conflicts of Interest

The authors declare that they have no conflicts of interest.

Authors' Contributions

Both authors contributed equally to this work and read and approved the final manuscript.

Acknowledgments

This work was supported by the Deanship of Scientific Research (DSR), King Abdulaziz University, Jeddah (Grant no. D-146-130-1439). The authors, therefore, gratefully acknowledge the DSR for the technical and financial support.

References

[1] J. Banas and M. Lecko, "Solvability of infinite systems of differential equations in Banach sequence spaces," *Journal of Computational and Applied Mathematics*, vol. 137, pp. 363–375, 2001.

[2] M. Mursaleen and S. A. Mohiuddine, "Applications of measures of noncompactness to the infinite system of differential equations in ℓ_p spaces," *Nonlinear Analysis: Theory, Methods & Applications*, vol. 75, no. 4, pp. 2111–2115, 2012.

[3] M. Mursaleen, "Application of measure of noncompactness to infinite systems of differential equations," *Canadian Mathematical Bulletin*, vol. 56, no. 2, pp. 388–394, 2013.

[4] S. A. Mohiuddine, H. M. Srivastava, and A. Alotaibi, "Application of measures of noncompactness to the infinite

system of second-order differential equations in ℓ_p spaces," *Advances in Difference Equations*, vol. 2016, pp. 1–13, 2016.
[5] M. Mursaleen, B. Bilalov, and S. Rizvi, "Applications of measures of noncompactness to infinite system of fractional differential equations," *Filomat*, vol. 31, no. 11, pp. 3421–3432, 2017.
[6] F. Wang and Y. Cui, "Positive solutions for an infinite system of fractional order boundary value problems," *Advances in Difference Equations*, vol. 169, 2019.
[7] F. Wang, Y. Cui, and H. Zhou, "Solvability for an infinite system of fractional order boundary value problems," *Annals of Functional Analysis*, vol. 10, no. 3, pp. 395–411, 2019.
[8] A. Seemab and M. U. Rehman, "Existence of solution of an infinite system of generalized fractional differential equations by darbo's fixed point theorem," *Journal of Computational and Applied Mathematics*, vol. 364, Article ID 112355, 2020.
[9] F. Arrigoni, "Deterministic approximation of a stochastic metapopulation model," *Advances in Applied Probability*, vol. 35, no. 3, pp. 691–720, 2003.
[10] A. D. Barbour and A. Pugliese, "Asymptotic behavior of a metapopulation model, Advances," *Annals of Applied. Probablity*, vol. 15, no. 2, pp. 1306–1338, 2005.
[11] J. M. Ball, J. Carr, and O. Penrose, "The becker-döring cluster equations: basic properties and asymptotic behaviour of solutions," *Communications in Mathematical Physics*, vol. 104, no. 4, pp. 657–692, 1986.
[12] J. Carr and R. M. Dunwell, "Asymptotic behaviour of solutions to the becker-döring equations," *Proceedings of the Edinburgh Mathematical Society*, vol. 42, no. 2, pp. 415–424, 1999.
[13] G. I. Ibragimov, "The optimal pursuit problem reduced to an infinite system of differential equations," *Journal of Applied Mathematics and Mechanics*, vol. 77, no. 5, pp. 470–476, 2013.
[14] K. Deimling, *Nonlinear Functional Analysis*, Springer, Berlin, Germany, 1985.
[15] A. Salem, H. M. Alshehri, and L. Almaghamsi, "Measure of noncompactness for an infinite system of fractional langevin equation in a sequence space," *Advances in Difference Equations*, vol. 2021, p. 132, 2021.
[16] A. Salem and N. Mshary, "On the existence and uniqueness of solution to fractional-order langevin equation," *Advances in Mathematical Physics*, vol. 2020, Article ID 8890575, 11 pages, 2020.
[17] A. Salem and B. Alghamdi, "Multi-strip and multi-point boundary conditions for fractional langevin equation," *Fractal and Fractional*, vol. 4, no. 2, 18 pages, 2020.
[18] A. Salem and M. Alnegga, "Measure of noncompactness for hybrid langevin fractional differential equations," *Axioms*, vol. 9, no. 2, p. 59, 2020.
[19] A. Salem and A. Al-dosari, "Existence results of solution for fractional sturm-liouville inclusion involving composition with multi-maps," *Journal of Taibah University for Science*, vol. 14, no. 1, pp. 721–733, 2020.
[20] A. Salem, F. Alzahrani, and A. Al-dosari, "Attainabillity to solve fractional differential inclusion on the half line at resonance," *Complexity*, vol. 2020, Article ID 9609108, 13 pages, 2020.
[21] H. Baghani and J. J. Nieto, "on fractional langevin equation involving two fractional orders in different intervals," *Nonlinear Analysis: Modelling and Control*, vol. 24, pp. 884–897, 2019.
[22] R. P. Agarwal, A. Alsaedi, N. Alghamdi, S. K. Ntouyas, and B. Ahmad, "Existence results for multi-term fractional differential equations with nonlocal multi-point and multi-strip boundary conditions," *Advances in Difference Equations.*vol. 342, 2018.
[23] A. Salem, "Existence results of solutions for anti-periodic fractional langevin equation," *Journal of Applied Analysis & Computation*, vol. 10, no. 6, pp. 2557–2574, 2020.
[24] A. Salem, F. Alzahrani, and M. Alnegga, "Coupled system of non-linear fractional langevin equations with multi-point and nonlocal integral boundary conditions," *Mathematical. Problem in Engineering*, vol. 2020, Article ID 7345658, 15 pages, 2020.
[25] A. Salem, F. Alzahrani, and B. Alghamdi, "Langevin equation involving two fractional orders with three-point boundary conditions," *Differential and Integral Equations*, vol. 33, pp. 163–180, 2020.
[26] A. Salem and M. Alnegga, "Fractional langevin equations with multi-point and non-local integral boundary conditions," *Cogent Mathematics & Statistics*, vol. 7, no. 1, 2020.
[27] A. Salem, F. Alzahrani, and L. Almghamsi, "Fractional langevin equations with nonlocal integral boundary conditions," *Mathematics*, vol. 7, no. 5, pp. 1–10, 2019.
[28] A. Salem and B. Alghamdi, "Multi-point and anti-periodic conditions for generalized langevin equation with two fractional orders," *Fractal and Fractional*, vol. 3, no. 4, pp. 1–14, 2019.
[29] R. Bhatia, *Notes in Functional Analysis*, Hindustan Books Agency, New Delhi, India, 2009.
[30] I. E. Leonard, "Banach sequence spaces," *Journal of Mathematical Analysis and Applications*, vol. 54, no. 1, pp. 245–265, 1976.
[31] C. Chidume, *Geometric Properties of Banach Spaces and Nonlinear Lterations*, Springer-Verlag, Berlin, Germany, 1965.
[32] V. Georgi and Smirnov, *Introduction To The Theory Of Differential Equations*, p. 41, American Mathematical Society, Rhode Island, USA, 2002.
[33] J. P. Aubin and A. Cellina, *Differential InclusionSet-Valued Maps and Viability Theory*, Spring-Verlag, Berlin, Germany, 1984.
[34] J. P. Aubin and H. Frankowska, *Set-Valued Analysis,*Birkhauser, Bosten, MA, USA, 1990.
[35] K. Deimling, *Multi-Valued Differential Equations*, Walter De Gruyter, Berlin, Germany, 2011.
[36] C. Shiaw, K. K. Tan, and C. S. Wong, "Quasi-nonexpansive multi-valued maps and selections," *Fundamental Mathematica*, vol. 87, pp. 109–119, 1975.
[37] P. E. Howard, "Definitions of compact," *Journal of Symbolic Logic*, vol. 55, no. 2, pp. 645–655, 1990.
[38] A. Atangana and D. Baleanu, "New fractional derivatives with nonlocal and non-singular kernel: theory and application to heat transfer model," *Thermal Science*, vol. 20, no. 2, pp. 763–769, 2016.
[39] M. Al-Refai, "Fractional differential equations involving caputo fractional derivative with mittag-leffler non-singular kernel: comparison principles and applications," *Electronic Journal of Differential Equations*, vol. 2018, no. 36, 2017.
[40] D. Baleanu and A. Fernandez, "On some new properties of fractional derivatives with mittag-leffler kernel," *Communications in Nonlinear Science and Numerical Simulation*, vol. 59, pp. 444–462, 2018.
[41] D. G. Prakasha, P. Veeresha, and J. Singh, "Fractional approach for equation descriping the water transport in unsaturated porous media with mittag-leffler kernel," *Frontiers in Physics*, vol. 7, no. 193, 2019.

[42] J. Hristov, *On the Atangana-Baleanu Drivative and its Relation to Fading Memory Concept: The Diffusion Equation Formulation*, pp. 175–193, Springer Nature, Cham, Switzerland, 2019.

[43] F. Ali, S. Murtaza, N. A. Sheikh, and K. S. Nisar, "Atangana-baleanu fractional model for the flow of jeffrey nanofluid with diffusion thermo effects: applications in engine oil," *Advances in Difference Equations*, vol. 2019, 2019.

[44] T. C. Lim, "A fixed point theorem for multi-valued non-expansive mappings in uniformaly convex banch space," *Bullten of the American Mathematical Society*, vol. 80, no. 6, pp. 1123–1126, 1974.

[45] A. Bunyawat and S. Suantai, "Common fixed points of a countable family of multivalued quasi-nonexpansive mappings in uniformly convex banach spaces," *International Journal of Computer Mathematics*, vol. 89, no. 16, pp. 2274–2279, 2012.

[46] C. Castaing and M. Valadier, *Convex Analysis and Measurable Multifunctions*, Springer, New York, NY, USA, 2006.

[47] S. Hu and N. S. Papageorgiou, *Handbook of Multivalued Analysis*, Kluwer Dordrecht, Dordrecht, The Netherlands, 1997.

Hindawi
Complexity
Volume 2021, Article ID 9927607, 10 pages
https://doi.org/10.1155/2021/9927607

Research Article

Predicting Tipping Points in Chaotic Maps with Period-Doubling Bifurcations

Changzhi Li,[1] Dhanagopal Ramachandran,[2] Karthikeyan Rajagopal,[3] Sajad Jafari,[4,5,6] and Yongjian Liu[1]

[1]*Guangxi Colleges and Universities Key Laboratory of Complex System Optimization and Big Data Processing, Yulin Normal University, Yulin 537000, China*
[2]*Center for System Design, Chennai Institute of Technology, Chennai, India*
[3]*Center for Nonlinear Systems, Chennai Institute of Technology, Chennai, India*
[4]*Center for Computational Biology, Chennai Institute of Technology, Chennai, India*
[5]*Biomedical Engineering Department, Amirkabir University of Technology, Tehran 15875-4413, Iran*
[6]*Health Technology Research Institute, Amirkabir University of Technology, Hafez Ave, No. 350, Valiasr Square, Tehran 159163-4311, Iran*

Correspondence should be addressed to Karthikeyan Rajagopal; rkarthiekeyan@gmail.com

Received 18 March 2021; Accepted 24 May 2021; Published 4 June 2021

Academic Editor: Guillermo Huerta Cuellar

In this paper, bifurcation points of two chaotic maps are studied: symmetric sine map and Gaussian map. Investigating the properties of these maps shows that they have a variety of dynamical solutions by changing the bifurcation parameter. Sine map has symmetry with respect to the origin, which causes multistability in its dynamics. The systems' bifurcation diagrams show various dynamics and bifurcation points. Predicting bifurcation points of dynamical systems is vital. Any bifurcation can cause a huge wanted/unwanted change in the states of a system. Thus, their predictions are essential in order to be prepared for the changes. Here, the systems' bifurcations are studied using three indicators of critical slowing down: modified autocorrelation method, modified variance method, and Lyapunov exponent. The results present the efficiency of these indicators in predicting bifurcation points.

1. Introduction

Chaotic dynamics is interesting in the field of nonlinear systems. Real systems can present chaotic oscillations [1]. Phenomenological behaviors of chaotic systems are interesting [2]. Two types of systems can show chaos: continuous systems (flows) and discrete systems (maps) [3–5]. Chaos is still a challenge, and there are many unknown mysteries about it in both continuous and discrete chaotic systems [6–8]. Studying various dynamics of discrete and continuous systems has been a hot topic [9–11]. Hyperchaotic dynamics of coupled systems was discussed in [12]. A chaotic system with symmetry was investigated in [13]. A piecewise linear system was studied in [14, 15]. Discrete systems can show many exciting dynamics, while most dynamics can be investigated using an in-depth study of their structures [16]. The reliability of the dynamics of discrete systems is highly dependent on simulation time [17]. The finite precision of computers has a significant effect on the simulation of chaotic dynamics [18]. Critical points of the bifurcation diagram in a chaotic map were investigated in [19]. Chaotic maps have some engineering applications, such as random number generators [20, 21]. In [22], the Henon map was investigated using fuzzy logic. Fractional order of the generalized Henon map was discussed in [23]. Various dynamics of the Bogdanov map were investigated in [24]. Multistability is an interesting behavior of dynamical systems [15, 25, 26]. Multistability is a condition in which the system's attractor is dependent on the initial values [27]. Various types of multistability can be discussed, such as extreme multistability [28]. Multistability of a 1D chaotic map has been studied in [29]. Secure communication and

image encryption are some of the applications of chaotic dynamics [30, 31]. Image encryption based on the Bogdanov map is very applicable [32, 33]. Control is an important challenge in the study of chaotic dynamics [34–36].

Dynamical properties of systems can be investigated using bifurcation diagrams. In a bifurcation diagram, various dynamics of the system can be seen as well as its bifurcation points [37–39]. Nonlinear dynamical tools are very useful [40, 41]. Hidden and nonstandard bifurcations of a system were studied in [42]. The study of bifurcations of a nonautonomous memristive FitzHugh–Nagumo circuit has been done in [43]. In [44], bifurcations of memristor synapse-based Morris–Lecar were discussed. Recently, the study of bifurcation points and their predictions is interesting [45, 46]. Before the occurrence of bifurcation points, slowing down is seen in the system dynamics [47]. This slowness is useful in the indication of bifurcation points [48, 49]. Prediction of bifurcation points is vital since some bifurcations may cause an undesired new behavior. Prediction of bifurcation points of biological systems has been studied in [50]. For example, the application of slowing down of blood pressure in predicting ischemic stroke was discussed in [51]. The ability of older adults to recover was investigated as a key for antiaging issue [52]. The advantage of predicting bifurcation points using indicators is to predict approaching the bifurcation points before their occurrence. Many studies try to indicate bifurcation points [53, 54]. Prediction of noise-induced critical transitions was studied in [55]. The most exciting predictors of bifurcation points are autocorrelation at lag-1 and variance [47]. In [56], some issues in those indicators in predicting bifurcation points during a period-doubling route to chaos were studied. So, a new version of the well-known indicators was proposed to solve those issues [56]. In [57, 58], the Lyapunov exponent was studied as an indicator of bifurcation points. However, some points in the calculation of Lyapunov exponents should be considered [59].

Here, we study various dynamics of two chaotic maps. These maps show different bifurcations. The cobweb plot is used to study the dynamics of the chaotic map in which the transition of the time series is also shown in the map plot [60]. Then, using critical slowing down indicators, various tipping points of the systems are investigated.

2. The Chaotic Maps

Two chaotic maps are studied in this paper. The first one is a one-dimensional chaotic map, which is called the sine map, as shown in the following equation:

$$x_{k+1} = B \sin(\pi x_k). \tag{1}$$

To study various behavior of the system by varying initial values, cobweb diagrams of the sine map in parameter $B = 0.6$ and various initial conditions are shown in Figure 1. Here, in the cobweb plots, the map is shown in red color, the identity line is shown in cyan color, and the transition of time series is shown in black color. Figure 1 shows that the system has three equilibrium points in this parameter since its map has three intersections with the identity line where $x_{k+1} = x_k$. The origin is unstable because the slope of the map is larger than one, and the other ones are stable because the amplitude of slope is smaller than one. So, the system is multistable in this parameter, and initial conditions are crucial in the system's final state. The figure shows that different initial conditions result in various equilibrium points.

To briefly explain the dynamic of System (1), its bifurcation is presented in Figure 2. The diagram depicts that the system has various dynamics, and the amplitude of attractors is expanded by increasing the bifurcation parameter. The bifurcation diagram shows that the map has various dynamics from equilibrium points to chaotic attractors. In bifurcation parameters $0 < B < 0.318$, the system shows one fixed point at zero. Figure 3(a) shows the cobweb plot with $B = 0.2$ and initial condition $x_0 = 0.2$. By increasing parameter B, two equilibrium points are created, and the origin becomes unstable (Figure 3(b) with $B = 0.5$ and $x_0 = 0.2$). So, the two equilibrium points are coexisting. After that, an increase in parameter B causes a period-doubling route to chaos. The cobweb plot of the chaotic dynamics with $B = 1$ and $x_0 = 0.2$ is shown in Figure 3(c). So, in this interval of parameter B, the system has two stabilities, which can vary from an equilibrium point to chaos by changing the bifurcation parameter. By increasing parameter B, a crisis happens, and the chaotic attractor is expanded. Figure 3(d) shows that the attractor can move from the positive part of the sine function to the negative one and vice versa ($B = 1.001$ and $x_0 = 0.2$). After that, in $B = 1.466$, a period-two dynamic is generated, followed by the period-doubling route to chaos. Figure 3(e) shows the cobweb plot of the system in $B = 1.5$ and $x_0 = 0.2$ in which the system has a periodic dynamic. In larger parameters such as $B = 2.5$ (Figure 3(f)), an exciting dynamic appears in which increasing parameter B causes another peak of the sine function touches the identity line. It can create four new equilibrium points. Two equilibrium points are stable, and another two equilibrium points are unstable. Then, the same route to chaos happens by increasing parameter B, and the bifurcations repetitively happen, which are just different in the amplitude of the dynamics.

The sine function is symmetric concerning the origin. This property causes two different symmetric stabilities shown in the bifurcation diagram with two positive and negative initial conditions. Figure 4 shows the bifurcation diagram of System (1) with $x_0 = 0.5$ for the black diagram and $x_0 = -0.5$ for the red diagram. The system has two stable equilibria in $B \in [0.317, 0.719]$, and each of them continues with a period-doubling route to chaos. Also, in each of the periodic windows, the multistability of the system can be seen.

The second studied system is the Gaussian map. This map is formulated as follows:

$$x_{k+1} = e^{-ax_k^2} + B, \tag{2}$$

where parameter $a = 6.2$ is fixed and parameter B is the bifurcation parameter. Figure 5 shows bifurcation diagram

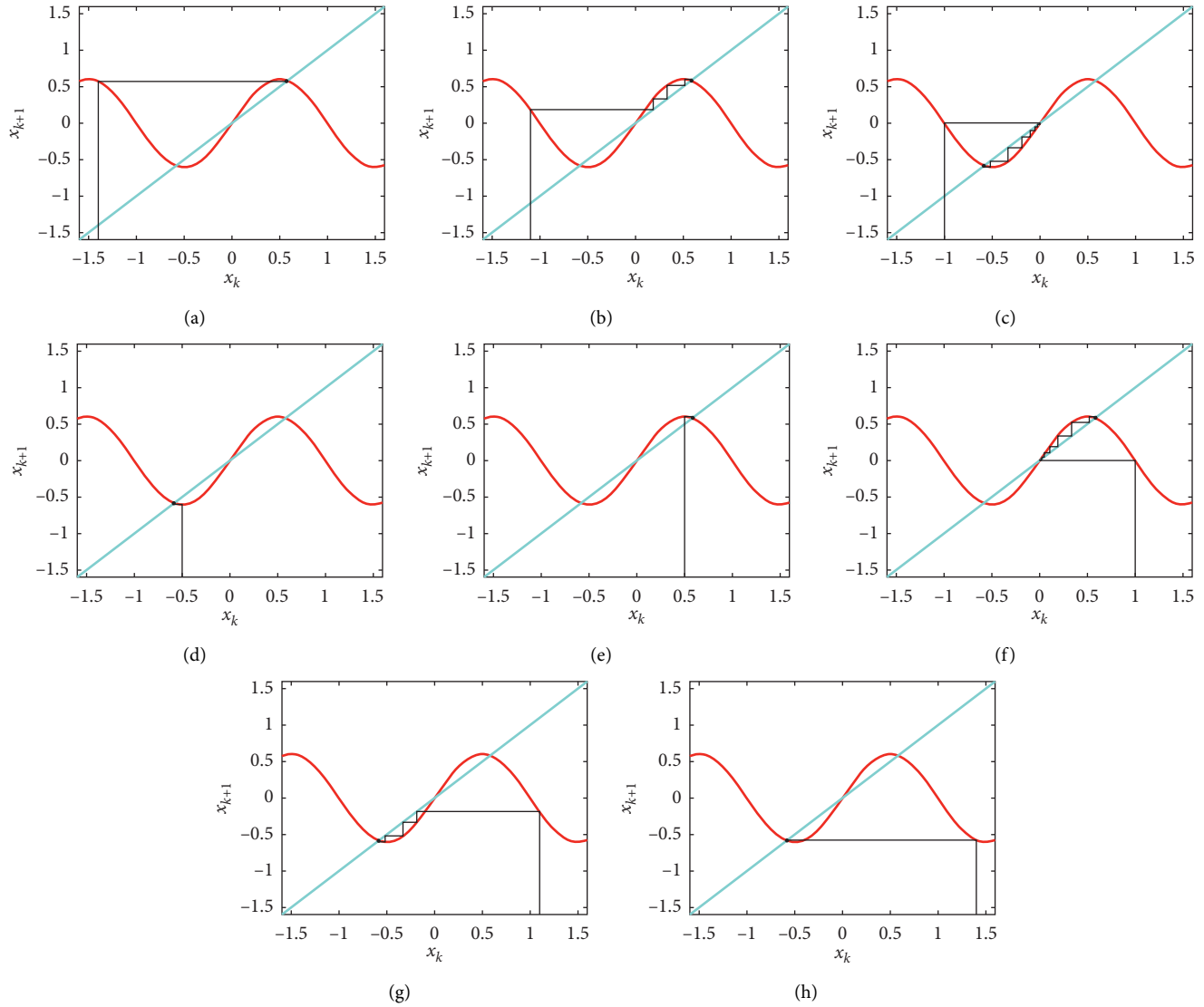

Figure 1: Cobweb diagram of System (1) in parameter $B = 0.6$ and initial condition (a) $x_0 = -1.4$; (b) $x_0 = -1.1$; (c) $x_0 = -1$; (d) $x_0 = -0.5$; (e) $x_0 = 0.5$; (f) $x_0 = 1$; (g) $x_0 = 1.1$; (h) $x_0 = 1.4$; this shows that the system has two stable equilibria in this value of parameter.

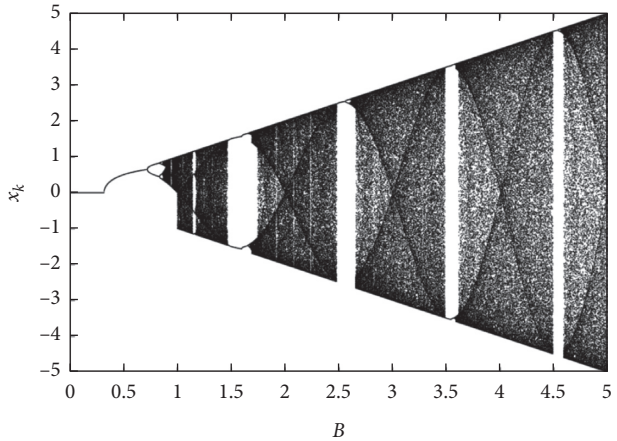

Figure 2: Bifurcation diagram by varying parameter B and constant initial condition $x_0 = 0.5$. The symmetric sine map has a period-doubling route to chaos and with periodic windows observed within.

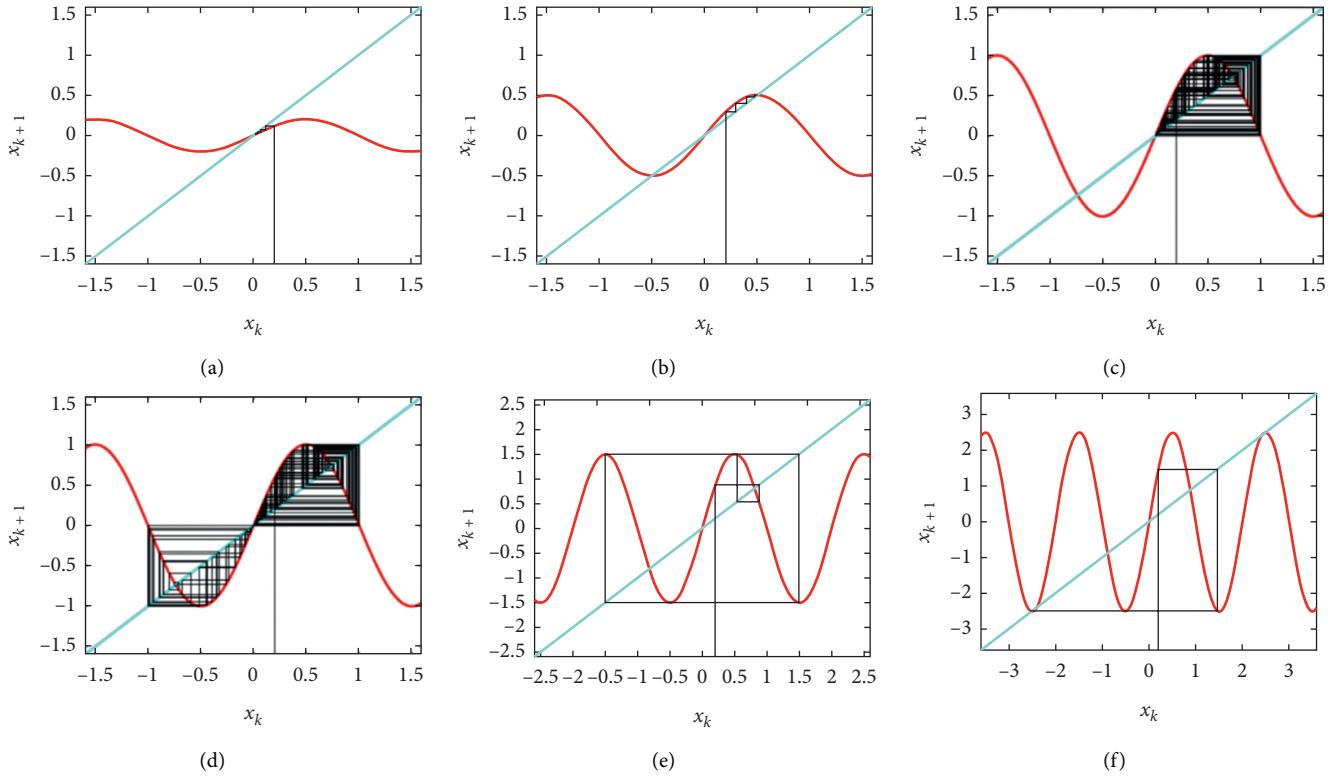

Figure 3: Cobweb diagram of System (1) in initial condition $x_0 = 0.2$ and parameter (a) $B = 0.2$; (b) $B = 0.5$; (c) $B = 1$; (d) $B = 1.001$; (e) $B = 1.5$; (f) $B = 2.5$; by increasing parameter B, the sine map changes from equilibrium points to chaos, and then increasing the parameter causes some periodic dynamics in periodic windows.

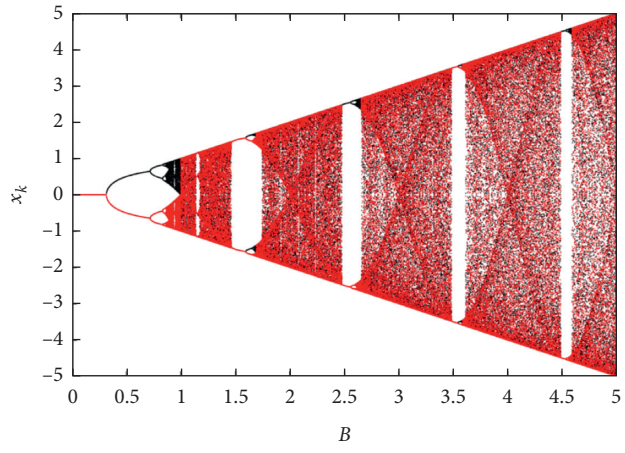

Figure 4: Bifurcation diagram by changing parameter B; the black diagram is plotted with $x_0 = 0.5$, and the red diagram is plotted with $x_0 = -0.5$; the sine map has two stabilities in some intervals of parameter B, while in some other intervals, the two stabilities merge to one attractor.

of this map by changing parameter B. It can be seen that the system shows a period-doubling route to chaos and its inverse route by increasing B.

3. Critical Slowing Down Indicators of the Chaotic Maps

Here, the bifurcations of the symmetric sine map are studied. The studies of the previous section show that the system has various dynamics and many bifurcation points. Critical slowing down is observed before the tipping points. The slowness can be characterized using the critical slowing down predictors [47]. One of the useful slowing down indicators is autocorrelation at lag-1. Before the tipping points, the system became slower, so the similarity of consecutive states increases. Another well-known indicator is variance, which increases before the bifurcation points. However, a previous study has shown that these indicators can only

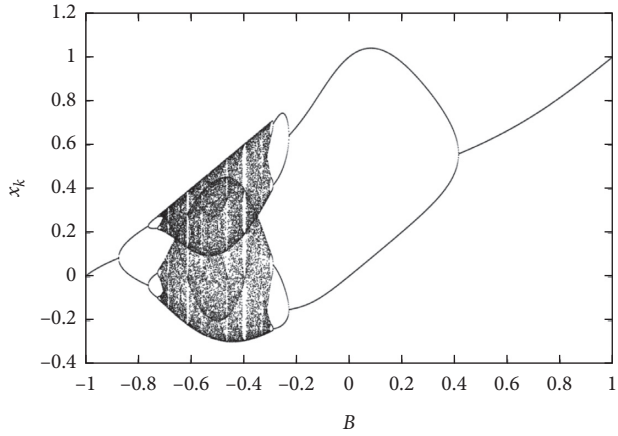

FIGURE 5: Bifurcation diagram of the Gaussian map by varying parameter B and constant initial condition $x_0 = 0$. The system shows various dynamics in its period-doubling route.

predict tipping points of type "period-one" [56]. In that work, to modify the previous indicators, the previous indicators such as autocorrelation and variance were applied to subvectors obtained from each cycle of the m-cycle attractor where m is the period of the signal [56].

The modified autocorrelation (AC) method is applied to the dynamics of the map for varying parameter B. Figure 6 shows the bifurcation diagram of the sine map in the interval $B \in [0, 5]$ in black and the absolute of the modified autocorrelation indicator in blue. The results depict that the predictor indicates various bifurcation points in the route of period-doubling to chaos. Many bifurcations can be seen in this interval. For example, in $B = 1.596$, a pitchfork bifurcation happens, which is predicted by increasing AC's value. Also, bifurcation points of the period-doubling route to chaos in the periodic window intervals such as $B \in [2.48, 2.68]$ were appropriately predicted. To have a closer look at the performance of this predictor, Figure 7(a) presents the bifurcation diagram and its correspondence modified autocorrelation in interval $B \in [0, 1.2]$. By approaching the tipping point, the absolute of modified autocorrelation approaches its maximum value (one). Then, by going far away from the bifurcation point, its value decreases to zero. Figure 7(b) shows the estimated period of the system using the algorithm proposed in [56].

The modified variance method is applied to the dynamics of System (1) (Figure 8). In Figure 8(a), the bifurcation diagram is shown in black color, and the scaled version of the logarithm of the modified variance (×0.1) is shown in blue color by changing $B \in [0, 5]$. To have a closer view, these diagrams are shown in $B \in [0, 1.2]$, in Figure 8(b). The figure shows that the modified variance increases by approaching the bifurcation point and decreases by going far away from it.

Another indicator of bifurcation points is the Lyapunov exponent [57, 58]. Lyapunov exponent goes to zero by approaching the bifurcation points. It has an exact value in various bifurcation points. Figure 9 presents the bifurcation diagram in black and Lyapunov exponent in blue color.

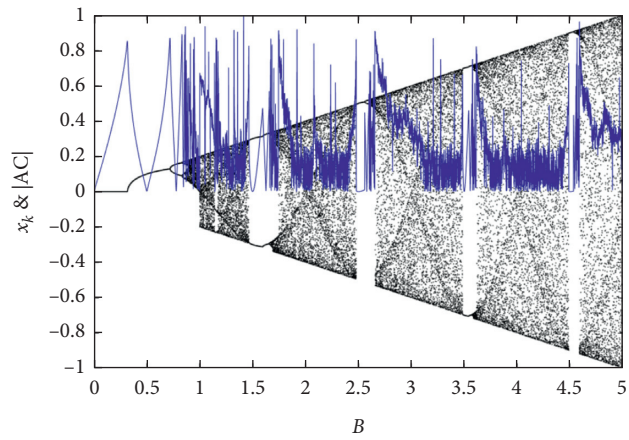

FIGURE 6: The scaled bifurcation diagram of the sine map (×0.2) for changing $B \in [0, 5]$ and initial condition $x_0 = 0.5$ in black and the absolute value of modified autocorrelation in blue color; this presents that $|AC|$ can predict various bifurcations by approaching to the value 1.

Figure 9(a) shows the diagrams in $B \in [0, 5]$ and Figure 9(b) shows in $B \in [0, 1.2]$. The results depict that the Lyapunov exponent can predict various tipping points of the sine map.

The second studied system is the Gaussian map. It was shown that the system has various dynamics and bifurcation points. To predict the bifurcations, AC, variance, and Lyapunov exponent are used. Figure 10 shows that the absolute value of AC predicts various bifurcation points. For instance, the system has a bifurcation point in $B = -0.88$ from period-1 to period-2 dynamics. The absolute value of AC increases until its value becomes one in the bifurcation point. The same trends can be seen in other bifurcation points.

Figure 11 shows the modified variance, which is calculated from the states of the Gaussian map by changing parameter B. The figure shows that the variance increases before bifurcation points, but it does not reach a constant value in various bifurcation points. So, increasing variance alarms the approaching bifurcation points.

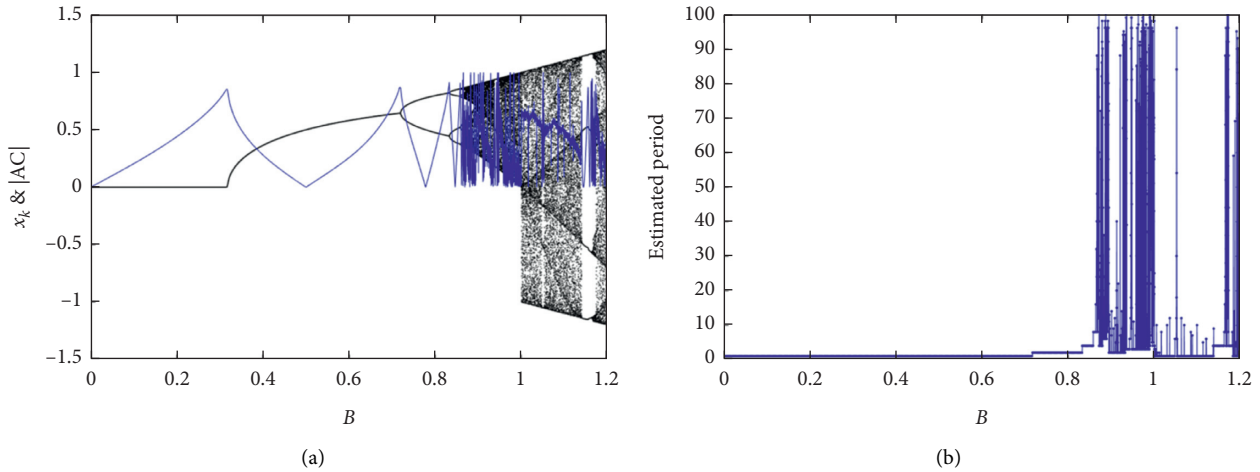

FIGURE 7: (a) The bifurcation diagram of the sine map by changing $B \in [0, 1.2]$ and initial condition $x_0 = 0.5$ in black and the absolute value of modified autocorrelation in blue color; (b) the estimated period of the sine map in $B \in [0, 1.2]$. The zoomed view shows better the ability of $|AC|$ to predict various bifurcations.

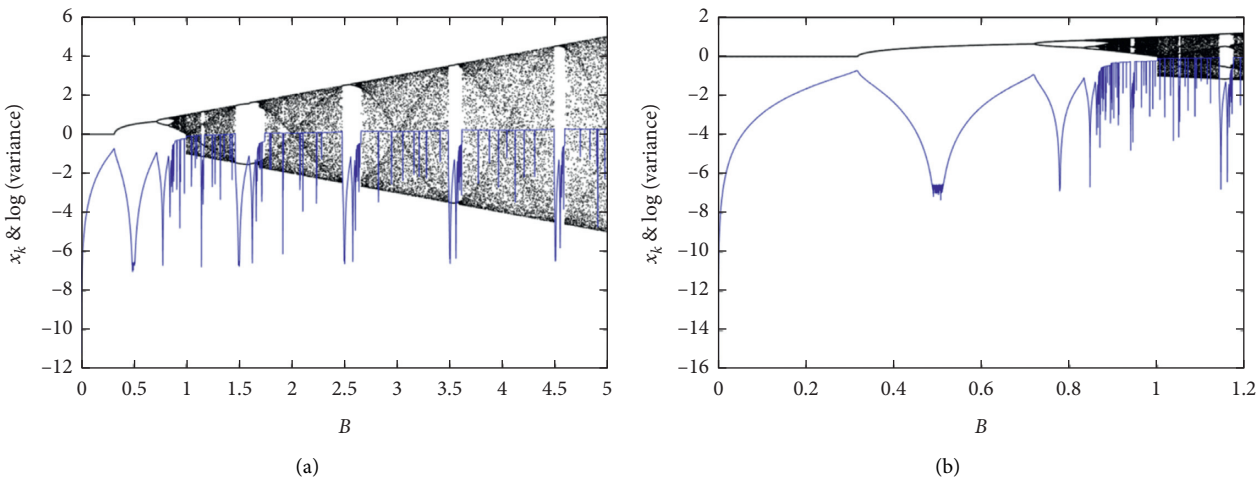

FIGURE 8: Bifurcation diagram in black color and the scaled version of the logarithm of the modified variance (×0.1) in blue color (a) by changing $B \in [0, 5]$; (b) by changing $B \in [0, 1.2]$; the results show that the variance method increases by approaching bifurcations which alarms that a tipping point is getting close.

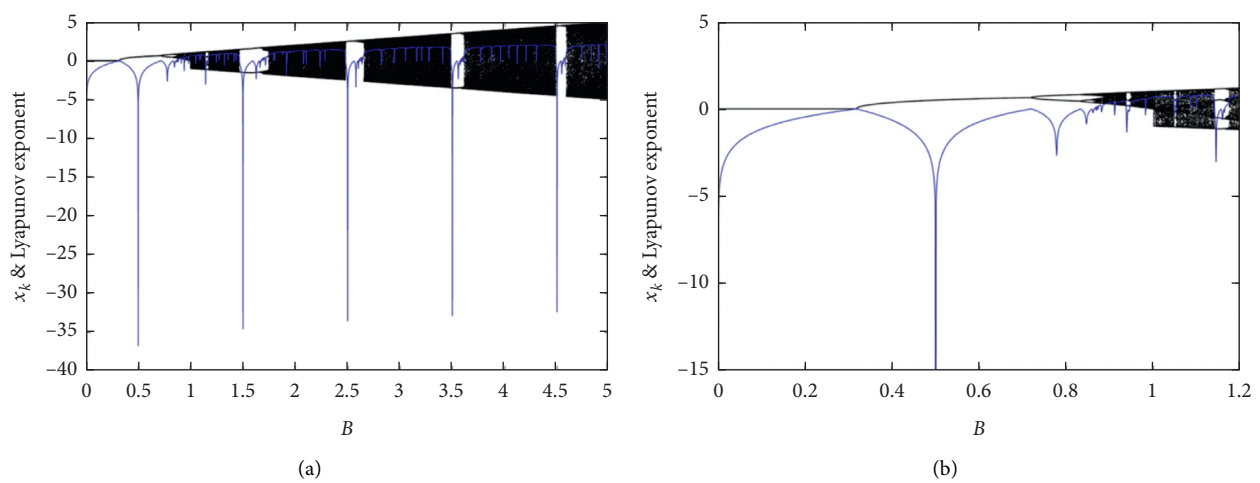

FIGURE 9: Bifurcation diagram in black and Lyapunov exponent in blue color by changing (a) $B \in [0, 5]$; (b) $B \in [0, 1.2]$; Lyapunov exponent approaches to zero by approaching bifurcation points, which can help their predictions.

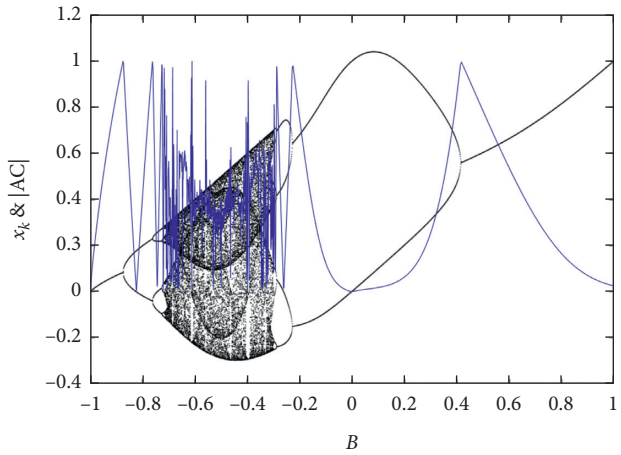

FIGURE 10: The bifurcation diagram of the Gaussian map with respect to changing $B \in [-1, 1]$ and initial condition $x_0 = 0$ in black and the absolute value of modified autocorrelation in blue color; this presents that $|AC|$ can predict various bifurcations by approaching the value 1.

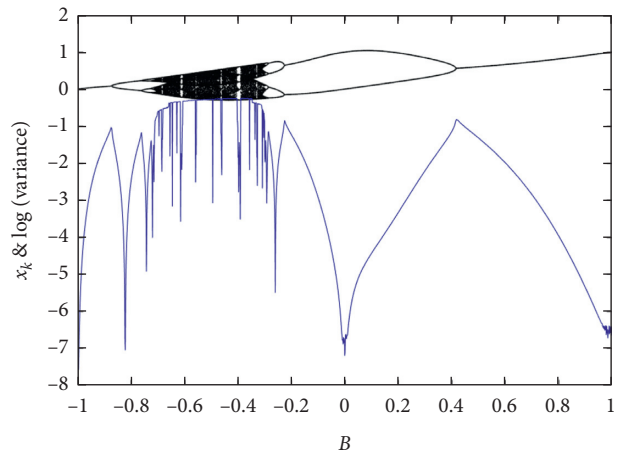

FIGURE 11: Bifurcation diagram in black color and the scaled version of the logarithm of the modified variance (×0.1) in blue color by changing $B \in [-1, 1]$; the results show that the variance method increases by approaching bifurcations, which alarms that tipping points are getting close.

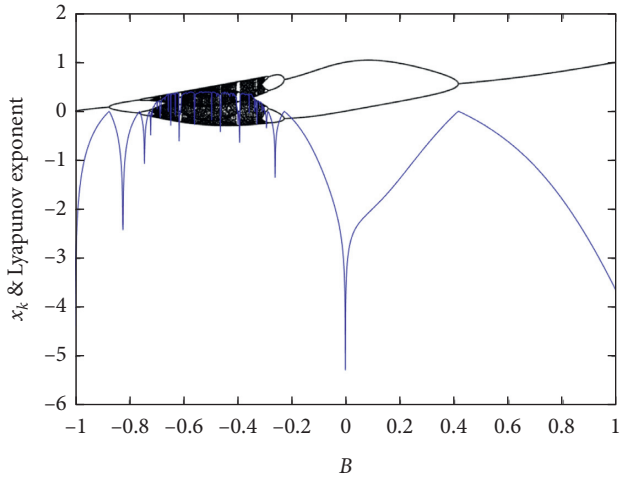

FIGURE 12: Bifurcation diagram in black and Lyapunov exponent in blue color by changing $B \in [-1, 1]$; Lyapunov exponent approaches zero by approaching bifurcation points, which can help their predictions.

Another studied indicator of the paper is the Lyapunov exponent. The results of the Lyapunov exponent are shown in Figure 12. Lyapunov exponent alarms approaching the bifurcation points by approaching zero. So, approaching zero shows that a bifurcation point is very close, while going away from it shows that the system is getting far from bifurcation points.

4. Discussion and Conclusion

This paper aimed to predict bifurcation points of chaotic maps. Two systems were studied: sine map and Gaussian map. Various dynamics of the sine map were studied, and its bifurcations were investigated. The results presented the multistability of the system because of its symmetric map. The system's critical slowing down was indicated using the modified autocorrelation method, modified variance method, and Lyapunov exponent. These studies showed that the bifurcation points of the sine map could be predicted using the indicators. The other studied system was the Gaussian map. The system shows various dynamics in a period-doubling route to chaos. Bifurcation points of the system were predicted using modified autocorrelation, modified variance, and Lyapunov exponent. Some indicators, such as autocorrelation and Lyapunov exponent, have an exact value in the bifurcation points. So, approaching the exact values indicates approaching the bifurcations. However, the variance method does not have an exact value in the bifurcation points. In the variance method, increasing the variance shows approaching the bifurcation points; however, we cannot precisely determine when it happens. The chaotic attractors are very complex dynamics. In chaotic domain, we cannot determine the transient time and slowness of dynamics. So, we cannot trust the indicators in the chaotic dynamics.

This study shows that some indications can alarm approaching the various bifurcation points. Those indicators had various natures. For example, autocorrelation calculates the short-term memory of the time series. Variance is based on the variations which increase by approaching the bifurcation points. The third method was the Lyapunov exponent, which shows the speed of the system approaching its final dynamic. The results, tested on two discrete systems, showed that these indicators had a proper trend when approaching bifurcation points that alarms their occurrences. In the future works, prediction of bifurcation points of systems with other types of bifurcations than period-doubling route to chaos can be investigated. As a suggestion for future works, some can consider the application of deep learning and reinforcement learning in the prediction of tipping points.

Data Availability

All the numerical simulation parameters are mentioned in the respective text part, and there are no additional data requirements for the simulation results.

Conflicts of Interest

The authors declare that they have no conflicts of interest to report regarding the present study.

Acknowledgments

This work was supported by the High Level Innovation Team Program from Guangxi Higher Education Institutions of China (Document No. [2018] 35). This work was funded by the Center for Computational Biology, Chennai Institute of Technology, India (funding no. CIT/CCB/2021/RD/007).

References

[1] G. Huerta-Cuellar, E. Jiménez-López, E. Campos-Cantón, and A. N. Pisarchik, "An approach to generate deterministic Brownian motion," *Communications in Nonlinear Science and Numerical Simulation*, vol. 19, no. 8, pp. 2740–2746, 2014.

[2] A. N. Pisarchik, R. Jaimes-Reátegui, R. Sevilla-Escoboza, G. Huerta-Cuellar, and M. Taki, "Rogue waves in a multistable system," *Physical Review Letters*, vol. 107, no. 27, p. 274101, 2011.

[3] E. Mliki, N. Hasanzadeh, F. Nazarimehr, A. Akgul, O. Boubaker, and S. Jafari, "Some new chaotic maps with application in stochastic," in *Recent Advances in Chaotic Systems and Synchronization*, pp. 165–185, Elsevier, Amsterdam, Netherlands, 2019.

[4] R. Lozi and A. N. Pchelintsev, "A new reliable numerical method for computing chaotic solutions of dynamical systems: the Chen attractor case," *International Journal of Bifurcation and Chaos*, vol. 25, no. 13, p. 1550187, 2015.

[5] N. Wang, G. Zhang, and H. Bao, "A simple autonomous chaotic circuit with dead-zone nonlinearity," *IEEE Transactions on Circuits and Systems II: Express Briefs*, vol. 67, no. 12, pp. 3502–3506, 2020.

[6] F. Nazarimehr, S. Jafari, G. Chen et al., "A tribute to J. C. Sprott," *International Journal of Bifurcation and Chaos*, vol. 27, no. 14, p. 1750221, 2017.

[7] J. L. Echenausía-Monroy and G. Huerta-Cuéllar, "A novel approach to generate attractors with a high number of scrolls," *Nonlinear Analysis: Hybrid Systems*, vol. 35, p. 100822, 2020.

[8] N. Wang, G. Zhang, N. V. Kuznetsov, and H. Bao, "Hidden attractors and multistability in a modified Chua's circuit," *Communications in Nonlinear Science and Numerical Simulation*, vol. 92, p. 105494, 2021.

[9] R. Lozi, V. A. Pogonin, and A. N. Pchelintsev, "A new accurate numerical method of approximation of chaotic solutions of dynamical model equations with quadratic nonlinearities," *Chaos, Solitons & Fractals*, vol. 91, pp. 108–114, 2016.

[10] J. Echenausía-Monroy, J. H. García-López, R. Jaimes-Reátegui, and G. Huerta-Cuellar, "Evidence of multistability in a multiscroll generator system," *Advances on Nonlinear Dynamics of Electronic Systems*, vol. 17, 2019.

[11] G. D. Leutcho, J. Kengne, L. Kamdjeu Kengne, A. Akgul, V.-T. Pham, and S. Jafari, "A novel chaotic hyperjerk circuit with bubbles of bifurcation: mixed-mode bursting oscillations, multistability, and circuit realization," *Physica Scripta*, vol. 95, no. 7, Article ID 075216, 2020.

[12] R. J. Escalante-González and E. Campos, "Hyperchaotic attractors through coupling of systems without equilibria,"

The European Physical Journal Special Topics, vol. 229, no. 6-7, pp. 1309–1318, 2020.

[13] G. D. Leutcho and J. Kengne, "A unique chaotic snap system with a smoothly adjustable symmetry and nonlinearity: chaos, offset-boosting, antimonotonicity, and coexisting multiple attractors," *Chaos, Solitons & Fractals*, vol. 113, pp. 275–293, 2018.

[14] E. Campos, "Derivation of a continuous time dynamic planar system with two unstable foci from a three-dimensional chaotic piecewise linear system," *Chaos: An Interdisciplinary Journal of Nonlinear Science*, vol. 30, no. 5, Article ID 053114, 2020.

[15] R. Escalante-González and E. Campos, "Multistable systems with hidden and self-excited scroll attractors generated via piecewise linear systems," *Complexity*, vol. 2020, 2020.

[16] F. Nazarimehr, S. Jafari, S. M. R. H. Golpayegani, and L. H. Kauffman, "Investigation of bifurcations in the process equation," *International Journal of Bifurcation and Chaos*, vol. 27, no. 13, p. 1750201, 2017.

[17] E. G. Nepomuceno, S. A. M. Martins, B. C. Silva, G. F. V. Amaral, and M. Perc, "Detecting unreliable computer simulations of recursive functions with interval extensions," *Applied Mathematics and Computation*, vol. 329, pp. 408–419, 2018.

[18] T. E. Nazaré, E. G. Nepomuceno, S. A. M. Martins, and D. N. Butusov, "A note on the reproducibility of chaos simulation," *Entropy*, vol. 22, no. 9, p. 953, 2020.

[19] M. Romera, G. Pastor, M.-F. Danca et al., "Bifurcation diagram of a map with multiple critical points," *International Journal of Bifurcation and Chaos*, vol. 28, no. 5, p. 1850065, 2018.

[20] A. Beirami, H. Nejati, and W. H. Ali, "Zigzag map: a variability-aware discrete-time chaotic-map truly random number generator," *Electronics Letters*, vol. 48, no. 24, pp. 1537-1538, 2012.

[21] F. J. Farsana and K. Gopakumar, "A novel approach for speech encryption: zaslavsky map as pseudo random number generator," *Procedia Computer Science*, vol. 93, pp. 816–823, 2016.

[22] D. Cafagna and G. Grassi, "Decomposition method for studying smooth Chua's equation with application to hyperchaotic multiscroll attractors," *International Journal of Bifurcation and Chaos*, vol. 17, no. 1, pp. 209–226, 2007.

[23] L. Jouini, A. Ouannas, A.-A. Khennaoui, X. Wang, G. Grassi, and V.-T. Pham, "The fractional form of a new three-dimensional generalized Hénon map," *Advances in Difference Equations*, vol. 2019, p. 122, 2019.

[24] D. K. Arrowsmith, J. H. E. Cartwright, A. N. Lansbury, and C. M. Place, "The Bogdanov map: bifurcations, mode locking, and chaos in a dissipative system," *International Journal of Bifurcation and Chaos*, vol. 3, no. 4, pp. 803–842, 1993.

[25] H. E. Gilardi-Velázquez, L. J. Ontañón-García, D. G. Hurtado-Rodriguez, and E. Campos-Cantón, "Multistability in piecewise linear systems versus eigenspectra variation and round function," *International Journal of Bifurcation and Chaos*, vol. 27, no. 9, p. 1730031, 2017.

[26] J. L. Echenausía-Monroy, G. Huerta-Cuellar, R. Jaimes-Reátegui et al., "Multistability emergence through fractional-order-derivatives in a PWL multi-scroll system," *Electronics*, vol. 9, no. 6, p. 880, 2020.

[27] A. Anzo-Hernández, H. E. Gilardi-Velázquez, and E. Campos-Cantón, "On multistability behavior of unstable dissipative systems," *Chaos: An Interdisciplinary Journal of Nonlinear Science*, vol. 28, no. 3, Article ID 033613, 2018.

[28] C. R. Hens, R. Banerjee, U. Feudel, and S. K. Dana, "How to obtain extreme multistability in coupled dynamical systems," *Physical Review. E, Statistical, Nonlinear, and Soft Matter Physics*, vol. 85, Article ID 035202, 2012.

[29] E. J. Staunton and P. T. Piiroinen, "Noise and multistability in the square root map," *Physica D: Nonlinear Phenomena*, vol. 380-381, pp. 31–44, 2018.

[30] A. Pisarchik, R. Jaimes-Reátegui, C. Rodríguez-Flores, J. García-López, G. Huerta-Cuellar, and F. Martín-Pasquín, "Secure chaotic communication based on extreme multistability," *Journal of the Franklin Institute*, vol. 358, no. 4, pp. 2561–2575, 2021.

[31] B. Cassal-Quiroga and E. Campos-Cantón, "Generation of dynamical S-boxes for block ciphers via extended logistic map," *Mathematical Problems in Engineering*, vol. 2020, 2020.

[32] S. V. Janardhanan and P. Sanjeeva, "Bogdanov map-based permuted double image encryption," *Anais da Academia Brasileira de Ciencias*, vol. 92, p. e20181207, 2020.

[33] R. N. R. Parida, S. Singh, and C. Pradhan, "Analysis of color image encryption using multidimensional Bogdanov map," in *Histopathological Image Analysis in Medical Decision Making*, pp. 202–225, IGI Global, Hershey, PA, USA, 2019.

[34] J. L. Echenausía-Monroy, J. H. García-López, R. Jaimes-Reátegui, and G. Huerta-Cuéllar, "Parametric control for multiscroll generation: electronic implementation and equilibrium analysis," *Nonlinear Analysis: Hybrid Systems*, vol. 38, p. 100929, 2020.

[35] J. L. Echenausía-Monroy, J. H. García-López, R. Jaimes-Reátegui, and G. Huerta-Cuellar, "Electronic implementation dataset to monoparametric control the number of scrolls generated," *Data in Brief*, vol. 31, p. 105992, 2020.

[36] N. Wang, G. Zhang, and H. Li, "Parametric control for multi-scroll attractor generation via nested sine-PWL function," *IEEE Transactions on Circuits and Systems II: Express Briefs*, vol. 68, 2020.

[37] R. C. Hilborn, *Chaos and Nonlinear Dynamics: An Introduction for Scientists and Engineers*, Oxford University Press, Oxford, UK, 2000.

[38] H. Bao, Z. Hua, N. Wang, L. Zhu, M. Chen, and B. Bao, "Initials-boosted coexisting chaos in a 2-D sine map and its hardware implementation," *IEEE Transactions on Industrial Informatics*, vol. 17, no. 2, pp. 1132–1140, Feb 2021.

[39] Z. Wei, B. Zhu, J. Yang, M. Perc, and M. Slavinec, "Bifurcation analysis of two disc dynamos with viscous friction and multiple time delays," *Applied Mathematics and Computation*, vol. 347, pp. 265–281, 2019.

[40] S. M. Shekatkar, Y. Kotriwar, K. P. Harikrishnan, and G. Ambika, "Detecting abnormality in heart dynamics from multifractal analysis of ECG signals," *Scientific Reports*, vol. 7, pp. 15127–15211, 2017.

[41] M.-F. Danca and G. Chen, "Bifurcation and chaos in a complex model of dissipative medium," *International Journal of Bifurcation and Chaos*, vol. 14, no. 10, pp. 3409–3447, 2004.

[42] G. Pastor, M. Romera, M.-F. Danca et al., "Hidden and nonstandard bifurcation diagram of an alternate quadratic system," *International Journal of Bifurcation and Chaos*, vol. 26, no. 2, p. 1650036, 2016.

[43] M. Chen, J. Qi, H. Wu, Q. Xu, and B. Bao, "Bifurcation analyses and hardware experiments for bursting dynamics in non-autonomous memristive FitzHugh-Nagumo circuit," *Science China Technological Sciences*, vol. 63, pp. 1–10, 2020.

[44] H. Bao, D. Zhu, W. Liu, Q. Xu, M. Chen, and B. Bao, "Memristor synapse-based morris-lecar model: bifurcation analyses and FPGA-based validations for periodic and chaotic

bursting/spiking firings," *International Journal of Bifurcation and Chaos*, vol. 30, no. 3, p. 2050045, 2020.

[45] F. Nazarimehr, S. M. R. Hashemi Golpayegani, and B. Hatef, "Does the onset of epileptic seizure start from a bifurcation point?" *The European Physical Journal Special Topics*, vol. 227, no. 7–9, pp. 697–705, 2018.

[46] M. Scheffer, J. Bascompte, W. A. Brock et al., "Early-warning signals for critical transitions," *Nature*, vol. 461, no. 7260, pp. 53–59, 2009.

[47] M. Scheffer, S. R. Carpenter, T. M. Lenton et al., "Anticipating critical transitions," *Science*, vol. 338, no. 6105, pp. 344–348, 2012.

[48] I. A. Van De Leemput, M. Wichers, A. O. J. Cramer et al., "Critical slowing down as early warning for the onset and termination of depression," *Proceedings of the National Academy of Sciences*, vol. 111, no. 1, pp. 87–92, 2014.

[49] S. V. George, S. Kachhara, R. Misra, and G. Ambika, "Early warning signals indicate a critical transition in Betelgeuse," *Astronomy & Astrophysics*, vol. 640, p. L21, 2020.

[50] M. Scheffer, J. E. Bolhuis, D. Borsboom et al., "Quantifying resilience of humans and other animals," *Proceedings of the National Academy of Sciences*, vol. 115, no. 47, pp. 11883–11890, 2018.

[51] V.-V. Le, T. Mitiku, G. Sungar, J. Myers, and V. Froelicher, "The blood pressure response to dynamic exercise testing: a systematic review," *Progress in Cardiovascular Diseases*, vol. 51, no. 2, pp. 135–160, 2008.

[52] S. Ukraintseva, K. Arbeev, M. Duan et al., "Decline in biological resilience as key manifestation of aging: potential mechanisms and role in health and longevity," *Mechanisms of Ageing and Development*, vol. 194, p. 111418, 2021.

[53] V. Dakos, S. R. Carpenter, W. A. Brock et al., "Methods for detecting early warnings of critical transitions in time series illustrated using simulated ecological data," *PLoS One*, vol. 7, no. 7, Article ID e41010, 2012.

[54] P. M. Müller, J. Heitzig, J. Kurths, K. Lüdge, and M. Wiedermann, "Anticipation-induced social tipping--can the environment be stabilised by social dynamics?," 2020, https://arxiv.org/abs/2012.01977.

[55] J. Ma, Y. Xu, Y. Li, R. Tian, S. Ma, and J. Kurths, "Quantifying the parameter dependent basin of the unsafe regime of asymmetric Lévy-noise-induced critical transitions," *Applied Mathematics and Mechanics*, vol. 42, no. 1, pp. 65–84, 2021.

[56] F. Nazarimehr, S. Jafari, S. M. R. Hashemi Golpayegani, M. Perc, and J. C. Sprott, "Predicting tipping points of dynamical systems during a period-doubling route to chaos," *Chaos: An Interdisciplinary Journal of Nonlinear Science*, vol. 28, no. 7, Article ID 073102, 2018.

[57] F. Nazarimehr, S. Jafari, S. M. R. Hashemi Golpayegani, and J. C. Sprott, "Can Lyapunov exponent predict critical transitions in biological systems?" *Nonlinear Dynamics*, vol. 88, no. 2, pp. 1493–1500, 2017.

[58] F. Nazarimehr, A. Ghaffari, S. Jafari, and S. M. R. H. Golpayegani, "Sparse recovery and dictionary learning to identify the nonlinear dynamical systems: one step toward finding bifurcation points in real systems," *International Journal of Bifurcation and Chaos*, vol. 29, no. 3, p. 1950030, 2019.

[59] M. L. C. Peixoto, E. G. Nepomuceno, S. A. M. Martins, and M. J. Lacerda, "Computation of the largest positive Lyapunov exponent using rounding mode and recursive least square algorithm," *Chaos, Solitons & Fractals*, vol. 112, pp. 36–43, 2018.

[60] R. Stoop and W.-H. Steeb, *Berechenbares Chaos in Dynamischen Systemen*, Springer-Verlag, Berlin, Germany, 2006.

Hindawi
Complexity
Volume 2021, Article ID 5578339, 9 pages
https://doi.org/10.1155/2021/5578339

Research Article

Basin of Attraction Analysis of New Memristor-Based Fractional-Order Chaotic System

Long Ding,[1] Li Cui ,[1] Fei Yu ,[2] and Jie Jin[1]

[1]*Hunan University of Science and Technology, Xiangtan, Hunan 411201, China*
[2]*School of Computer and Communication Engineering, Changsha University of Science and Technology, Changsha 410114, China*

Correspondence should be addressed to Li Cui; 348640501@qq.com

Received 7 February 2021; Revised 27 March 2021; Accepted 7 April 2021; Published 14 April 2021

Academic Editor: Guillermo Huerta Cuellar

Memristor is the fourth basic electronic element discovered in addition to resistor, capacitor, and inductor. It is a nonlinear gadget with memory features which can be used for realizing chaotic, memory, neural network, and other similar circuits and systems. In this paper, a novel memristor-based fractional-order chaotic system is presented, and this chaotic system is taken as an example to analyze its dynamic characteristics. First, we used Adomian algorithm to solve the proposed fractional-order chaotic system and yield a chaotic phase diagram. Then, we examined the Lyapunov exponent spectrum, bifurcation, SE complexity, and basin of attraction of this system. We used the resulting Lyapunov exponent to describe the state of the basin of attraction of this fractional-order chaotic system. As the local minimum point of Lyapunov exponential function is the stable point in phase space, when this stable point in phase space comes into the lowest region of the basin of attraction, the solution of the chaotic system is yielded. In the analysis, we yielded the solution of the system equation with the same method used to solve the local minimum of Lyapunov exponential function. Our system analysis also revealed the multistability of this system.

1. Introduction

Recently, chaotic systems have attracted wide attention from researchers due to their own particularities and their vast application potential in the memristor [1–4], random number generator [5, 6], secure communication [7–9], image encryption [10–14], and artificial neural network [15–20]. How to increase the complexity of a chaotic system and generate complex chaotic attractors to make it hard to encipher information in encryption system applications has become a field of interest for researchers both in and outside China. In 1971, Professor Shaotang Cai published the "Memristor-The Missing Circuit Element" [21]. After theoretic derivation of the relationships between the four basic electrical physical quantities—voltage, current, charge, and magnetic flux—Cai assumed that there exists a fourth basic circuit element: the memristor. Over the most recent decade, the use of memristors in designing chaotic circuits, such as pure memristor networks and complex circuits containing one or more memristors, has been extensively studied [22–24]. Results show that memristor-based chaotic circuits provide a greater variety of dynamic behaviors. As memristors are nanoelements which are not commercialized yet, in the current studies related to conventional memristor-based chaotic circuits, researchers tend to use existing simulation analog elements to realize a memristor analog circuit and then use it to investigate the dynamic properties of the designed system. For this reason, selecting a memristor model and designing a memristor analog circuit constitutes an important part of fundamental research.

At present, the generation and application of multistability and extreme multistability has become a very hot topic for chaotic circuit systems [25–29]. Compared with other chaotic systems, combining memristors with chaotic systems can generate chaotic attractors possessing complicated dynamic properties. Yet the multistability of a chaotic system is dependent on the initial state of the system.

In fact, a multistable dynamic system usually has a very complicated basin of attraction structure that can be defined by a fractal boundary. From a mathematical point of view, a

basin of attraction indicates that there is a chaotic attractor on the smooth hypercurve observed in a dynamic system showing invariables and a subspace with positive finite time fluctuation in addition to the invariable subspace in asymptotic termination state. Although the chaotic attractor is laterally stable, the insertion of an unstable periodic orbit in the chaotic attractor constitutes the source of losing this lateral stability. Whether the chaotic attractor will lose lateral stability is determined by how the orbit becomes unstable. Dynamically, beyond invariable manifolds, there can appear different bifurcations and different forms of basin of attraction. If there are sieve basins in a multistable chaotic system, their final state will be totally unpredictable. This is similar to a random process, for which only the probability of the final state of the system can be determined.

The purpose of this research is to take the analysis on the proposed chaotic system as an example to exhibit the nonlinear dynamical behavior of a memristor-based fractional-order chaotic system and to provide a new theoretical basis for the study of nonlinear systems. In the study, we used Adomian algorithm to solve the proposed fractional-order chaotic system and yield the chaotic phase diagram, and the bifurcation, Lyapunov exponent, and SE complexity of the chaotic system. Here, we specifically present a new analytical method of using Lyapunov exponent to describe the state of the basin of attraction of a chaotic system, from which we yielded the solution, basin of attraction region, transitional region, and divergence trajectory of the system. Our system analysis also revealed the multistability of the system.

2. New memristor-Based Fractional-Order Chaotic System

We propose a new memristor-based fractional-order chaotic system which is expressed by

$$\begin{cases} \dfrac{dx^q}{d^q t} = A(y - x), \\ \dfrac{dy^q}{d^q t} = Bx - xz - xW(w), \\ \dfrac{dz^q}{d^q t} = x^2 - Cz, \\ \dfrac{dw^q}{d^q t} = x. \end{cases} \tag{1}$$

The function of memristor [30] is

$$W(w) = 0.1w^2 + 0.6. \tag{2}$$

When $A = 5$, $B = 20$, $C = 4$, $q = 0.98$ $(0 < q < 1)$, and the initial value is (0.1, 0.1, 0.1, 0.1), Adomian decomposition algorithm is used to solve system (1) and yield the corresponding system phase diagram, as shown in Figure 1. When $q = 0.9$, the phase diagram of system (1) is as shown in Figure 2. Here, we are going to analyze the proposed fractional-order chaotic attractor subsystems for orders 0.98 and 0.9. Figure 2 is more complex than Figure 1.

2.1. Equilibrium Point and Lyapunov Exponent Analysis. The equilibrium points of system (1) can be obtained by solving the following equation:

$$\begin{cases} 0 = A(y - x), \\ 0 = Bx - xz - xW(w), \\ 0 = x^2 - Cz, \\ 0 = x. \end{cases} \tag{3}$$

Through equation (3), we get the equilibrium point for system (1) as (0, 0, 0, 0). When $q = 0.98$, the Lyapunov exponents of system (1) are LE1 = 0.7505, LE2 = −0.0297, LE3 = −0.2298, and LE4 = −9.8612, suggesting that system (1) is a chaotic system. The Lyapunov exponent of the system (1) is calculated and the corresponding index map is obtained based on predictor-corrector (PECE) method of Adams–Bashforth–Moulton type and Wolf's method. The Lyapunov exponents are shown in Figure 3.

2.2. Bifurcation and Lyapunov Exponent Spectrum Analysis. Assume that the fractional-order parameters are $q = 0.98$, $B = 20$, and $C = 4$; the control parameter A of system (1) is increased from 1 to 6; the initial value of system (1) is (0.1, 0.1, 0.1, 0.1); the step size of A is 0.01. The bifurcation diagram of the fractional-order system is as shown in Figure 4(a). We can see that when the fractional-order system is in order 0.98, system (1) is in the chaotic state. When parameters $q = 0.9$, $B = 20$, and $C = 4$ and again when control parameter A is increased from 1 to 6, the fractional-order system will come into the chaotic state through period doubling bifurcation. The bifurcation diagram is as shown in Figure 5(a) when the fractional-order parameters are $q = 0.98$, $A = 5$, and $C = 4$, the control parameter B of system (1) is increased from 10 to 22, the initial value of system (1) is (0.1, 0.1, 0.1, 0.1), and the step size of B is 0.01. The bifurcation diagram of the fractional-order system is as shown in Figure 6(a). We can see that when the fractional-order system is in order 0.98, system (1) will come into chaotic state through bifurcation. When parameters $q = 0.9$, $A = 5$, and $C = 4$ and again when control parameter B is increased from 10 to 22, the fractional-order system has hidden bifurcation. The bifurcation diagram is as shown in Figure 7(a). At the same time, the Lyapunov exponent of system (1) is calculated and the corresponding index map is obtained based on the predictor-corrector (PECE) method of Adams–Bashforth–Moulton type and Wolf's method. The Lyapunov exponents are as shown in Figures 4(b), 5(b), 6(b), and 7(b). The Lyapunov spectrum provides the parameter range when system (1) is in chaos, and these ranges are consistent with bifurcation analysis results.

2.3. SE Complexity Analysis. The complexity analysis of systems covers a range of fields. Researchers into these fields have reported different understandings about the complexity of the systems. So far, no consensus has been reached over the definition of complexity. The complexity of a

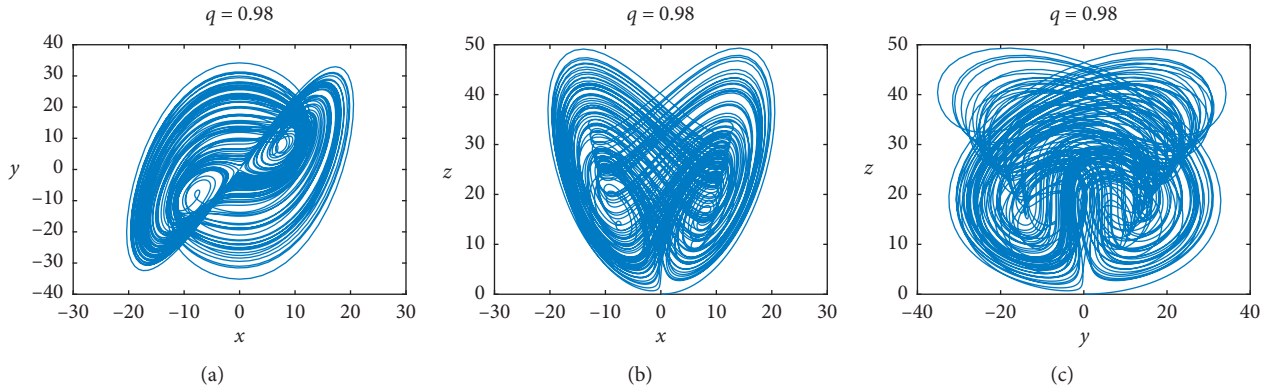

Figure 1: The chaotic attractor of system (1) with $q = 0.98$. (a) x-y plane, (b) x-z plane, and (c) y-z plane.

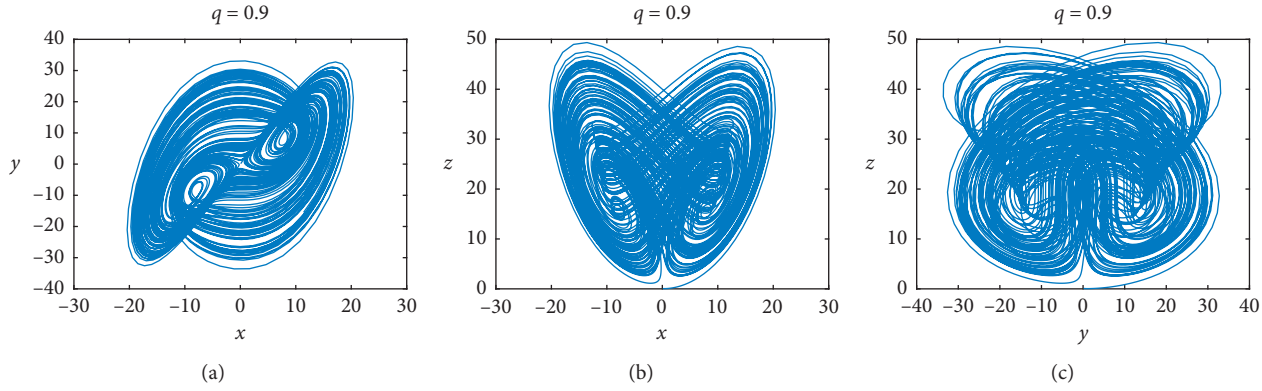

Figure 2: The chaotic attractor of system (1) with $q = 0.9$. (a) x-y plane, (b) x-z plane, and (c) y-z plane.

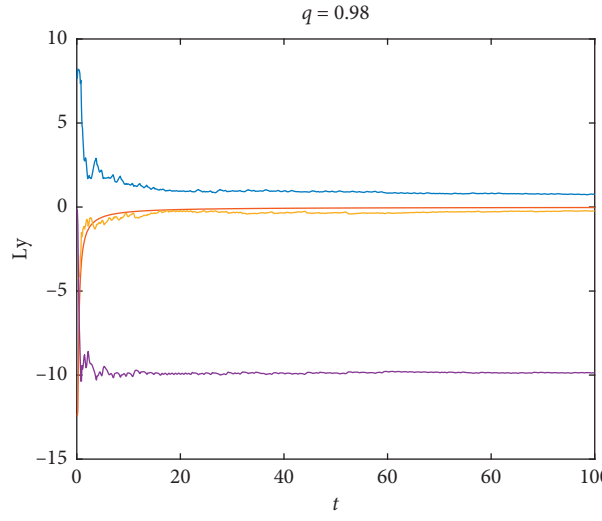

Figure 3: The Lyapunov exponents of system (1) with $q = 0.98$.

chaotic system is the random nature of the chaotic sequence. The higher the complexity of a chaotic system is, the closer the sequence is to a random one and, accordingly, the higher the security of the corresponding system becomes. The complexity of a chaotic system is essentially the complexity of chaotic dynamics. So far, many complexity algorithms have been used to measure the complexity of a system, such as multiscale entropy [31], Shannon entropy [32], fuzzy

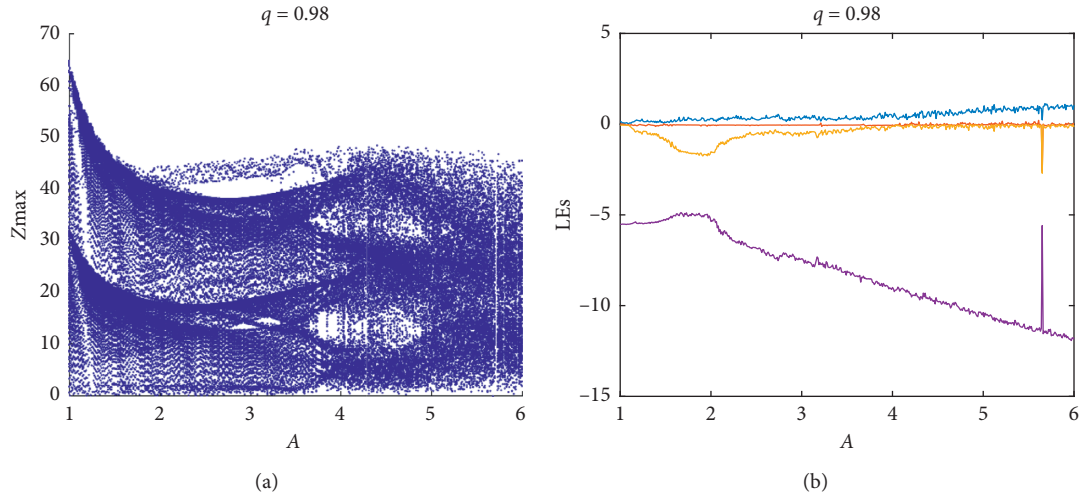

Figure 4: (a) Bifurcation diagram of parameter A of system (1) with $q = 0.98$; (b) Lyapunov exponent spectrum of parameter A of system (1) with $q = 0.98$.

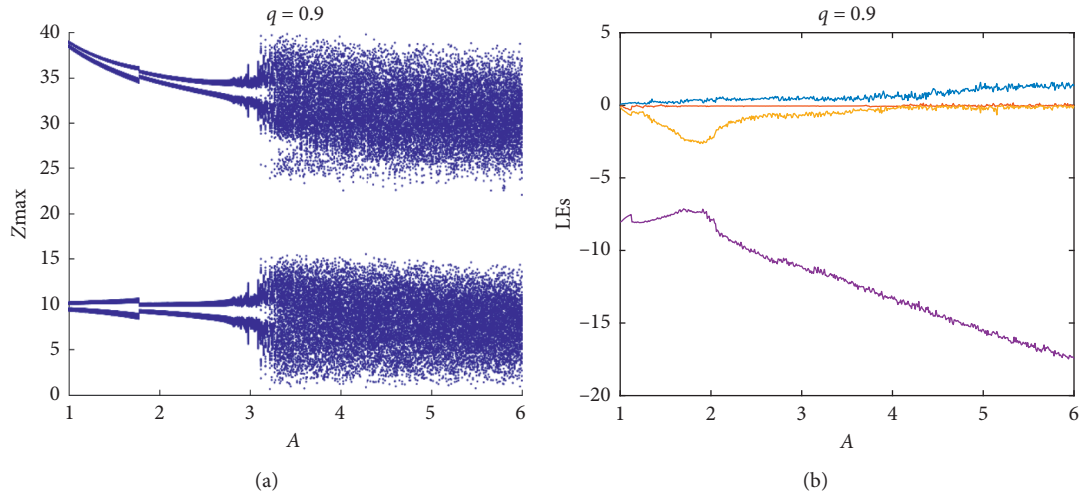

Figure 5: (a) Bifurcation diagram of parameter A of system (1) with $q = 0.9$; (b) Lyapunov exponent spectrum of parameter A of system (1) with $q = 0.9$.

entropy [33], and spectral entropy (SE) [34]. Compared with other algorithms, SE is more popular for having fewer parameters and higher accuracy. For this reason, we used SE to measure the complexity of our new chaotic system. Furthermore, chaotic mapping-based SE can provide better basis for choosing the right parameters in real applications. Figure 8 shows the SE complexity analysis related to parameter A and order q. From this diagram, we can see that the lower the order is, the darker the color is and, accordingly, the greater the complexity of the system becomes. This well agrees with the reality that the lower the order of a fractional-order chaotic system, the greater the complexity of the chaos. Within the corresponding parameters, if this system is used in a chaotic secure communication system, the confidentiality of the communication system will be improved.

2.4. Basin of Attraction Analysis. Regarding fractional-order chaotic systems, we have published two articles on basin of attraction analysis [35, 36]. In the present study, we further analyzed the characteristics of a basin of attraction and again analyzed the stability of the system by considering Lyapunov exponential function. When the system operates in the initial state, it will move towards the direction in which Lyapunov exponential function decreases until reaching its local minima. The local minima point of Lyapunov exponential function means the stable point in phase space, where each attractor will surround a substantial basin of attraction. In that sense, these points are also called attractors. These basins of attraction represent a stable chaotic state. When the stable point comes into the lowest region of the basin of attraction, the solution of the chaotic system can be yielded. The size of a basin of attraction, as indicated by the radius of attraction, can be defined

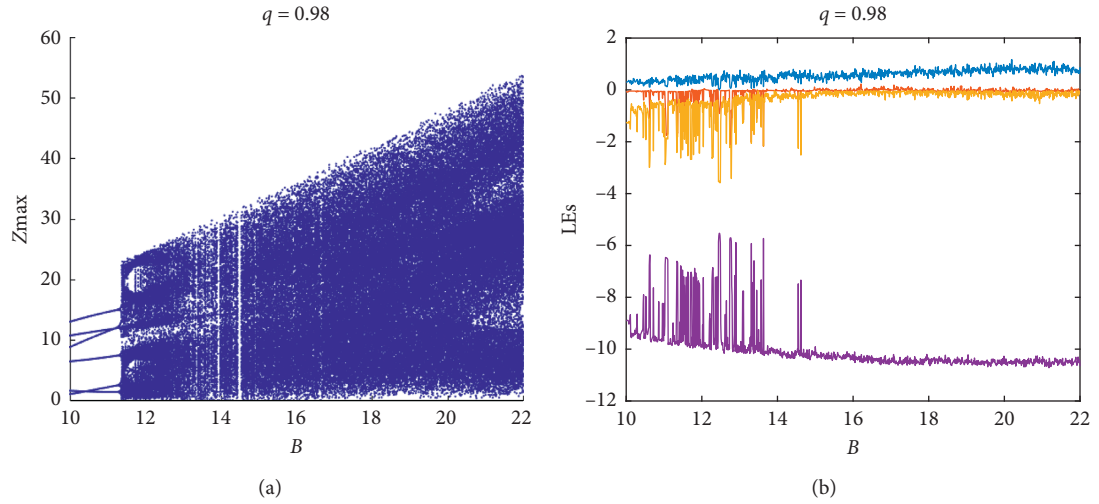

Figure 6: (a) Bifurcation diagram of parameter B of system (1) with $q = 0.98$; (b) Lyapunov exponent spectrum of parameter B of system (1) with $q = 0.98$.

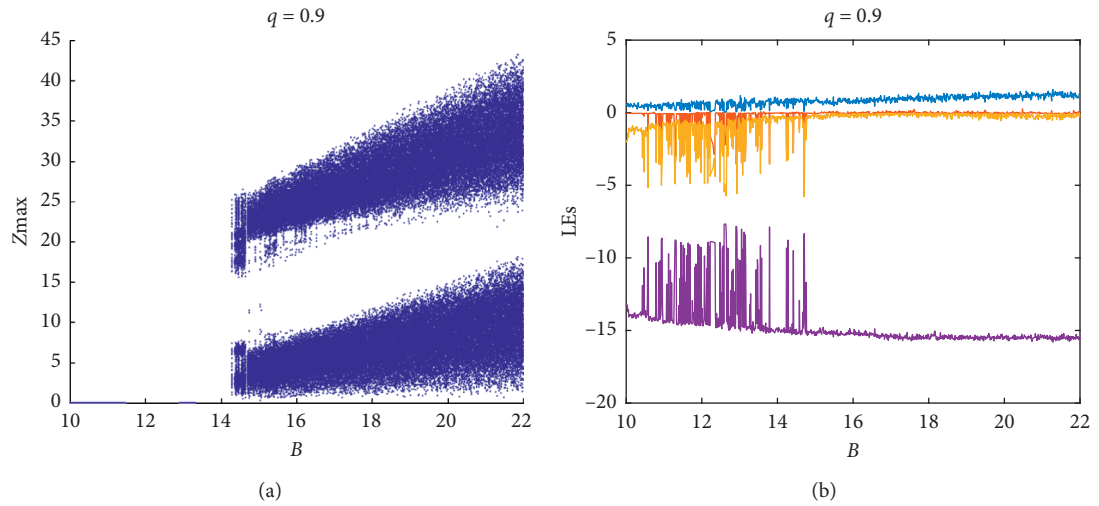

Figure 7: (a) Bifurcation diagram of parameter B of system (1) with $q = 0.9$; (b) Lyapunov exponent spectrum of parameter B of system (1) with $q = 0.9$.

as the maximum distance between all states contained in a basin of attraction or the maximum distance of the state that can be attracted by the attractor. In a dynamic system with more than one attractor, the corresponding basin may have a fractal boundary or even more complicated structure. Hence, in system (1), the representative coexistent attractors will have such a complicated basin boundary structure. The orange region is the basin of attraction for attractors at infinity which shows the coexistence of multiple attractors. In the yellow region, there is a line composed of a number of green points which fall in the center of the yellow region. They are the local minima points of Lyapunov exponential function, which indicate the stable points in phase space. They are also the solutions of a chaotic system, as well as the symmetry points of the basin of attraction. The blue region is the transitional region. From the basin of attraction diagrams for different orders, the basin of attraction section is a series of symmetric graphs which are unevenly distributed but have a self-similar appearance. From Figures 9–11 , we can see that system (1) has quite a few coexistent attractors. The basin of attraction is described by the Lyapunov exponent, so in the matlab program, we found the local minimum of the Lyapunov exponent. The green line was actually discrete points, but the figure was shrunk, making them look like a line. In the global basin of attraction figure, it can be found that the steady-state regions represented by yellow are spaced apart. So, they are multistable. Under different orders, the basin of attraction of system (1) shows different states, especially its area in the yellow region. How to use the radius of attraction to derive the size of a basin of attraction is a future field of concern. Now, that we have derived the position of the central point of the basin of attraction, the next step will be to obtain the size of the basin of attraction. Panorama of the base of attraction of system (1) with $q = 0.9$, as shown in Figure 12.

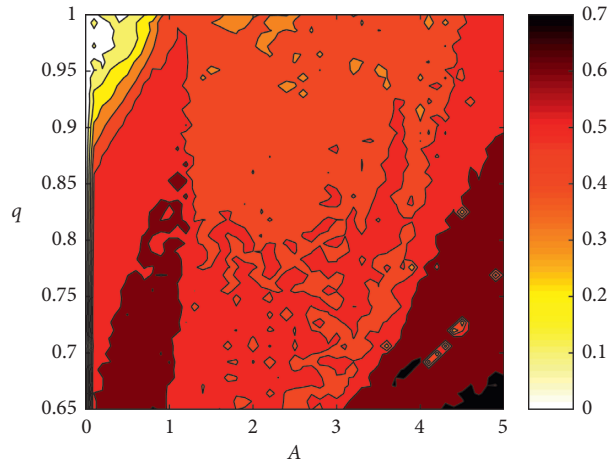

Figure 8: Chaos diagrams of fractional-order chaotic system (1): q-A plane.

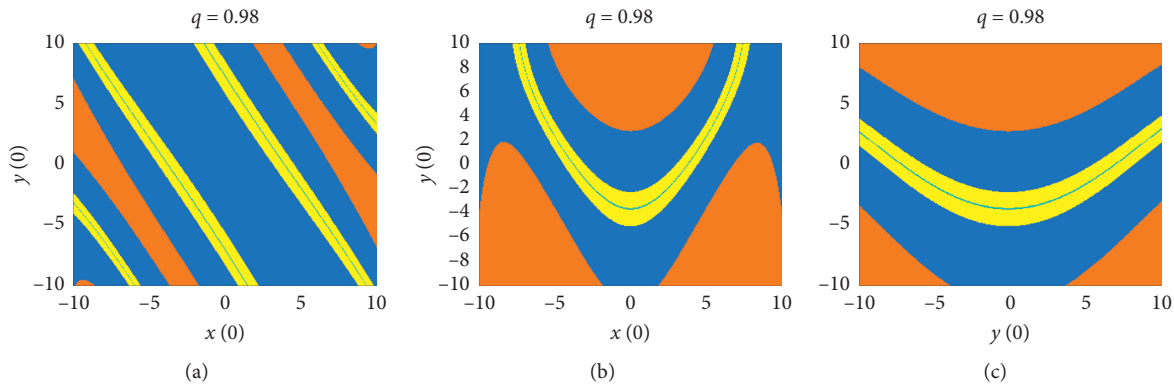

Figure 9: The basin of attraction of system (1) with $q = 0.98$: (a) $x(0)$–$y(0)$ plane, (b) $x(0)$–$z(0)$ plane, and (c) y (0)–$z(0)$ plane.

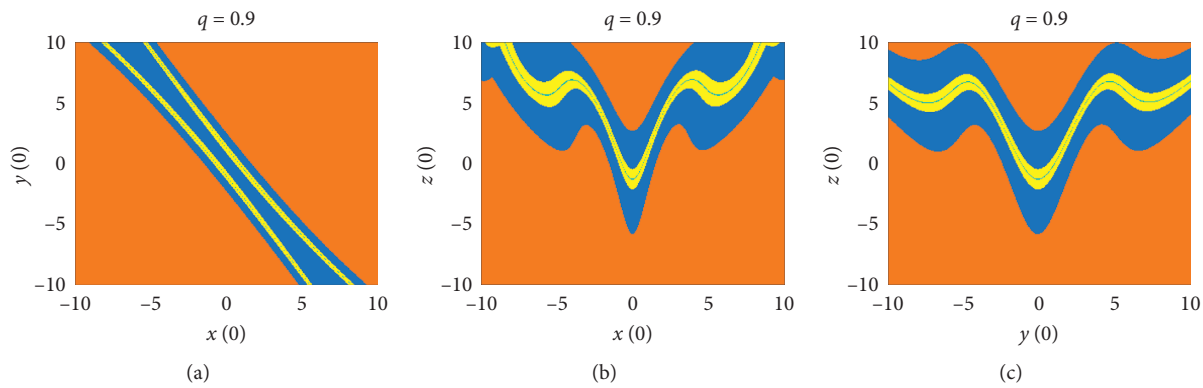

Figure 10: The basin of attraction of system (1) with $q = 0.9$: (a) $x(0)$–$y(0)$ plane, (b) $x(0)$-$z(0)$ plane, and (c) $y(0)$–$z(0)$ plane.

2.5. FPGA Implementation. The hardware experiment of system (1) with $q = 0.98$ is conducted by the method of fixed-point number, based on FPGA technology. We use Xilinx Zynq-7000 series XC7Z020 FPGA chip and AN9767 dual-port parallel 14 bit digital to analog conversion module with the maximum conversion rate of 125 MHz and adopt Vivado17.4 and the System Generator to realize the joint debugging of matlab: FPGA. Besides, we use oscilloscope to visualize the analog output. After the analysis, synthesis and compilation of Vivado. To further confirm that the chaotic system (1) is correct, after confirming that the timing simulation results are correct, generate the bit file by Vivado and download the generated bit file to the FPGA development board, convert the output of FPGA into the analog signal using AN9767 digital analog converter, and then connect AN9767 digital analog converter to the oscilloscope to observe the phase diagram of system (1) attractor. The phase diagrams displayed by the oscilloscope are, respectively, shown in Figure 13.

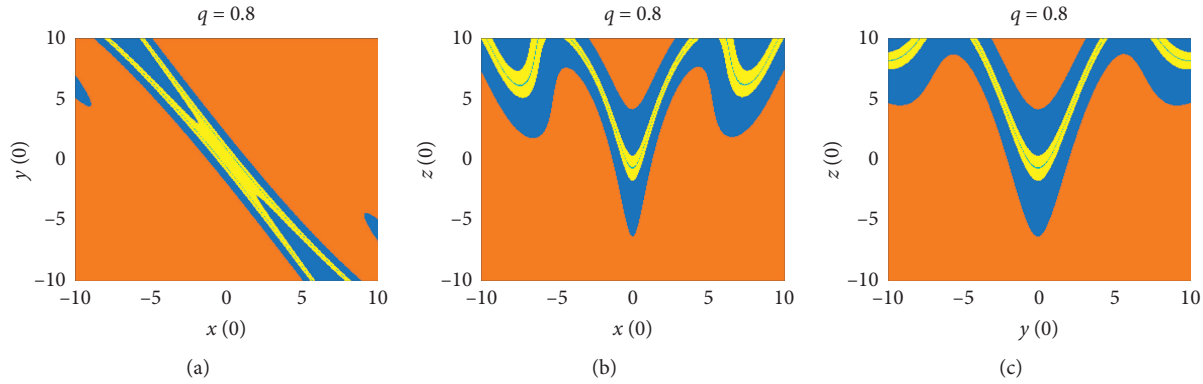

FIGURE 11: The basin of attraction of system (1) with $q = 0.8$: (a) $x(0)$–$y(0)$ plane, (b) $x(0)$–$z(0)$ plane, and (c) $y(0)$–$z(0)$ plane.

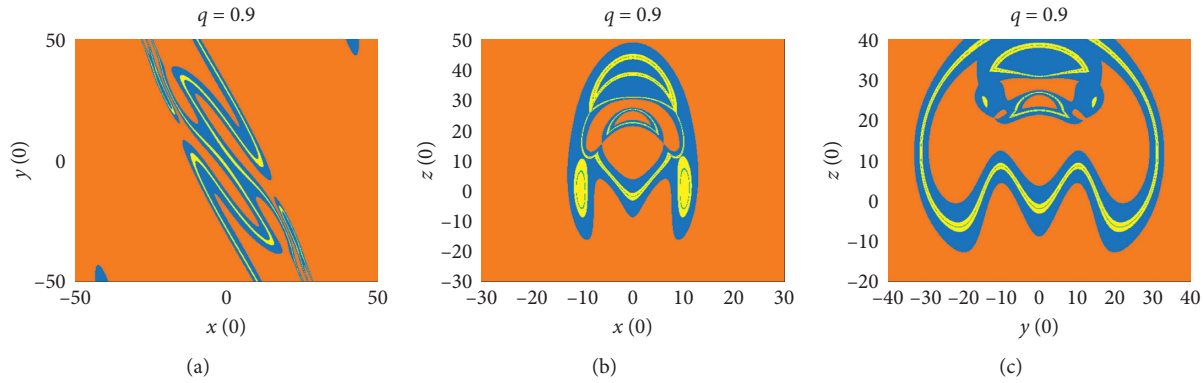

FIGURE 12: Panorama of the basin of attraction of system (1) with $q = 0.9$: (a) $x(0)$–$y(0)$ plane, (b) $x(0)$–$z(0)$ plane, and (c) $y(0)$–$z(0)$ plane.

FIGURE 13: The chaotic attractor of system (1) with $q = 0.98$. (a) x-y plane, (b) x-z plane, and (c) y-z plane.

3. Conclusions

Through the example of the memristor-based fractional-order chaotic system, this paper proposes a method to analyze the domain of attraction of the chaotic system via Lyapunov exponents. This method is used to depict the states when the orbit of the Lyapunov exponents takes different initial values, then obtain the center point of the attraction domain, and analyze the various states of the chaotic system as described under the domain of attraction at different orders. At the same time, the chaotic phase portraits are achieved by the solution of the proposed fractional-order chaotic system based on Adomian algorithm, and the dynamic analysis of the chaotic system is studied, such as

Lyaponov exponential spectrum, bifurcation, and SE complexity. Furthermore, this paper forecasts the future research directions and application areas of the domain of attraction.

Data Availability

The data used to support the findings of this study are included within the article.

Conflicts of Interest

The authors declare that they have no conflicts of interest.

Acknowledgments

This work was supported by the National Natural Science Foundation of China under Grant 61504013, Natural Science Foundation of Hunan Province under Grants 2019JJ50648 and 2020JJ4315, and Research Foundation of Education Bureau of Hunan Province.

References

[1] Z. Wen, Z. Li, and X. Li, "Transient MMOs in memristive chaotic system via tiny perturbation," *Electronics Letters*, vol. 56, no. 2, pp. 78–80, 2020.

[2] C. Wang, H. Xia, and L. Zhou, "A memristive hyperchaotic multiscroll jerk system with controllable scroll numbers," *International Journal of Bifurcation and Chaos*, vol. 27, no. 6, Article ID 1750091, 2017.

[3] S. Zhong, "Heterogeneous memristive models design and its application in information security," *Computers, Materials & Continua*, vol. 60, no. 2, pp. 465–479, 2019.

[4] M. Zhu, C. Wang, Q. Deng et al., "Locally active memristor with three coexisting pinched hysteresis loops and its emulator circuit," *International Journal of Bifurcation and Chaos*, vol. 30, no. 13, Article ID 2050184, 2020.

[5] X. Chen, S. Qian, F. Yu et al., "Pseudorandom number generator based on three kinds of four-wing memristive hyperchaotic system and its application in image encryption," *Complexity*, vol. 2020, Article ID 8274685, 17 pages, 2020.

[6] F. Yu, S. Qian, X. Chen et al., "Chaos-based engineering applications with a 6D memristive multistable hyperchaotic system and a 2D SF-SIMM hyperchaotic map," *Complexity*, vol. 2021, Article ID 6683284, 21 pages, 2021.

[7] F. Yu, S. Qian, X. Chen et al., "A new 4D four-wing memristive hyperchaotic system: dynamical analysis, electronic circuit design, shape synchronization and secure communication," *International Journal of Bifurcation and Chaos*, vol. 30, no. 10, Article ID 2050147, 2020.

[8] Y. Li, Z. Li, M. Ma, and M. Wang, "Generation of grid multi-wing chaotic attractors and its application in video secure communication system," *Multimedia Tools and Applications*, vol. 79, no. 39-40, pp. 29161–29177, 2020.

[9] F. Yu, Z. Zhang, L. Liu et al., "Secure communication scheme based on a new 5D multistable four-wing memristive hyperchaotic system with disturbance inputs," *Complexity*, vol. 2020, Article ID 5859273, 2020.

[10] B. Lu, F. Liu, X. Ge, and Z. Li, "Cryptanalysis and improvement of a chaotic map-control-based and the plain image-related cryptosystem," *Computers, Materials & Continua*, vol. 61, no. 2, pp. 687–699, 2019.

[11] H. Lin, C. Wang, F. Yu et al., "An extremely simple multi-wing chaotic system: dynamics analysis, encryption application and hardware implementation," *IEEE Transactions on Industrial Electronics*, vol. 1, 2021.

[12] J. Zeng and C. H. Wang, "A novel hyper-chaotic image encryption system based on particle swarm optimization algorithm and cellular automata," *Security and Communication Networks*, vol. 2021, Article ID 6675565, 10 pages, 2021.

[13] J. Liu, J. Li, J. Cheng et al., "A novel robust watermarking algorithm for encrypted medical image based on dtcwt-dct and chaotic map," *Computers, Materials & Continua*, vol. 61, no. 2, pp. 889–910, 2019.

[14] J. Deng, M. Zhou, C. Wang, S. Wang, and C. Xu, "Image segmentation encryption algorithm with chaotic sequence generation participated by cipher and multi-feedback loops," *Multimedia Tools and Applications*, vol. 18, 2021.

[15] W. Yao, C. Wang, Y. Sun et al., "Exponential multistability of memristive Cohen-Grossberg neural networks with stochastic parameter perturbations," *Applied Mathematics and Computation*, vol. 386, Article ID 125483, 2020.

[16] H. Lin, C. Wang, Y. Sun, and W. Yao, "Firing multistability in a locally active memristive neuron model," *Nonlinear Dynamics*, vol. 100, no. 4, pp. 3667–3683, 2020.

[17] T. Chen, L. Wang, and S. Duan, "Implementation of circuit for reconfigurable memristive chaotic neural network and its application in associative memory," *Neurocomputing*, vol. 380, pp. 36–42, 2020.

[18] H. Lin, C. Wang, W. Yao et al., "Chaotic dynamics in a neural network with different types of external stimuli," *Communications in Nonlinear Science and Numerical Simulation*, vol. 90, Article ID 105390, 2020.

[19] C. Ma, J. Mou, F. Yang et al., "A fractional-order hopfield neural network chaotic system and its circuit realization," *The European Physical Journal Plus*, vol. 135, no. 1, Article ID 100, 2020.

[20] H. Lin, C. Wang, Q. Hong, and Y. Sun, "A multi-stable memristor and its application in a neural network," *IEEE Transactions on Circuits and Systems II: Express Briefs*, vol. 67, no. 12, pp. 3472–3476, 2020.

[21] L. Chua, "Memristor-The missing circuit element," *IEEE Transactions on Circuit Theory*, vol. 18, no. 5, pp. 507–519, 1971.

[22] J. Sun, J. Han, P. Liu et al., "Memristor-based neural network circuit of pavlov associative memory with dual mode switching," *AEU-international Journal of Electronics and Communications*, vol. 129, Article ID 153552, 2021.

[23] Q. Lai, Z. Wan, P. D. K. Kuate et al., "Coexisting attractors, circuit implementation and synchronization control of a new chaotic system evolved from the simplest memristor chaotic circuit," *Communications in Nonlinear Science and Numerical Simulation*, vol. 89, Article ID 105341, 2020.

[24] Y. Peng, K. Sun, and S. He, "A discrete memristor model and its application in Hénon map," *Chaos, Solitons and Fractals*, vol. 137, Article ID 109873, 2020.

[25] C. Li, G. Chen, J. Kurths, T. Lei, and Z. Liu, "Dynamic transport: from bifurcation to multistability," *Communications in Nonlinear Science and Numerical Simulation*, vol. 95, Article ID 105600, 2021.

[26] Y. Shen and S. Zhu, "Multistability of delayed neural networks with monotonically nondecreasing linear activation function," *Neurocomputing*, vol. 423, pp. 89–97, 2021.

[27] Y. Zhang, Z. Liu, H. Wu, S. Chen, and B. Bao, "Two-memristor-based chaotic system and its extreme multistability

reconstitution via dimensionality reduction analysis," *Chaos, Solitons & Fractals*, vol. 127, pp. 354–363, 2019.

[28] A. Bayani, K. Rajagopal, A. J. M. Khalaf, S. Jafari, G. D. Leutcho, and J. Kengne, "Dynamical analysis of a new multistable chaotic system with hidden attractor: anti-monotonicity, coexisting multiple attractors, and offset boosting," *Physics Letters A*, vol. 383, no. 13, pp. 1450–1456, 2019.

[29] F. Yu, L. Liu, H. Shen et al., "Multistability analysis, coexisting multiple attractors and FPGA implementation of Yu-Wang four-wing chaotic system," *Mathematical Problems in Engineering*, vol. 2020, Article ID 7530976, 2020.

[30] L. Qiu, W. Chen, F. Wang, and J. Lin, "A non-local structural derivative model for memristor," *Chaos, Solitons & Fractals*, vol. 126, pp. 169–177, 2019.

[31] A. S. Minhas, P. K. Kankar, N. Kumar, and S. Singh, "Bearing fault detection and recognition methodology based on weighted multiscale entropy approach," *Mechanical Systems and Signal Processing*, vol. 147, Article ID 107073, 2021.

[32] P. M. Cincotta, C. M. Giordano, R. A. Silva, and C. Beaugé, "The Shannon entropy: an efficient indicator of dynamical stability," *Physica D*, vol. 417, Article ID 132816, 2021.

[33] Z. Yuan, H. Chen, T. Li et al., "Fuzzy information entropy-based adaptive approach for hybrid feature outlier detection," *Fuzzy Sets and Systems*, vol. 54, 2020.

[34] P.-Y. Xiong, H. Jahanshahi, R. Alcaraz et al., "Spectral entropy analysis and synchronization of a multi-stable fractional-order chaotic system using a novel neural network-based chattering-free sliding mode technique," *Chaos, Solitons and Fractals*, vol. 144, Article ID 110576, 2021.

[35] L. Cui, M. Lu, Q. Ou et al., "Analysis and circuit implementation of fractional order multi-wing hidden attractors," *Chaos, Solitons and Fractals*, vol. 138, Article ID 109894, 2020.

[36] L. Cui, W.-H. Luo, and Q. Ou, "Analysis and implementation of new fractional-order multi-scroll hidden attractors," *Chinese Physics B*, vol. 30, no. 2, Article ID 020501, 2021.